WBS: 1.2.21.2.2
QA: N/A

Civilian Radioactive Waste Management System
Management & Operating Contractor

Yucca Mountain Site Description

TDR-CRW-GS-000001 REV 01 ICN 01

September 2000

Prepared for:

U.S. Department of Energy
Yucca Mountain Site Characterization Office
P.O. Box 30307
North Las Vegas, Nevada 89036-0307

Prepared by:

TRW Environmental Safety Systems Inc.
1180 Town Center Drive
Las Vegas, Nevada 89144

Under Contract Number
DE-AC08-91RW00134

WBS: 1.2.21.2.2.
QA: N/A

Civilian Radioactive Waste Management System
Management & Operating Contractor

Yucca Mountain Site Description

TDR-CRW-GS-000001 REV 01 ICN 01

September 2000

Prepared for:

U.S. Department of Energy
Yucca Mountain Site Characterization Office
P.O. Box 30307
North Las Vegas, Nevada 89036-0307

Prepared by:

TRW Environmental Safety Systems Inc.
1180 Town Center Drive
Las Vegas, Nevada 89144

Under Contract Number
DE-AC08-91RW00134

VOLUME 1

DISCLAIMER

This report was prepared as an account of work sponsored by an agency of the United States Government. Neither the United States Government nor any agency thereof, nor any of their employees, nor any of their contractors, subcontractors or their employees, makes any warranty, express or implied, or assumes any legal liability or responsibility for the accuracy, completeness, or any third party's use or the results of such use of any information, apparatus, product, or process disclosed, or represents that its use would not infringe privately owned rights. Reference herein to any specific commercial product, process, or service by trade name, trademark, manufacturer, or otherwise, does not necessarily constitute or imply its endorsement, recommendation, or favoring by the United States Government or any agency thereof or its contractors or subcontractors. The views and opinions of authors expressed herein do not necessarily state or reflect those of the United States Government or any agency thereof.

Civilian Radioactive Waste Management System
Management & Operating Contractor

Yucca Mountain Site Description

TDR-CRW-GS-000001 REV 01 ICN 01

September 2000

Prepared by:

R.C. Quittmeyer
Lead Author

9/20/2000
Date

Checked by:

D. Mohr
Product Checking Group Lead Checker

9/20/00
Date

Approved by:

A. Simmons
Site Integration Department Manager

9/20/00
Date

CHANGE HISTORY

Revision Number	Interim Change No.	Effective Date	Description of Change
0	0	September 1998	Initial Issue (under Document Identifier B00000000-01717-5700-00019)
1	0	July 14, 2000	Revision to reorganize the presentation of material, update sections with new information, and meet requirements of new procedures. Reorganization included: • Added an Introduction • Split the section on Hydrologic System into sections on Surface Water Hydrology, Unsaturated Zone Hydrology, and Saturated Zone Hydrology • Split the section on Geochemistry into sections on Geochemical Framework and Factors Affecting Radionuclide Transport • Created a separate section on Tectonic Hazards • Added a section on Natural Analogs. The document was updated to include information available through the end of fiscal year 1999. In some areas, it was possible to include more recent results.
1	1	September 20, 2000	Document changed to address acceptance conditions identified in accordance with AP-7.5Q (Submittal, Review, and Acceptance of Deliverables). In addition, changes were also made to correct minor errors and for editorial purposes. Change bars in the margin mark text and tables that have been changed, with the following exceptions: in Sections 8, 9, and others where PTn was designated as "Paintbrush Tuff nonwelded unit", this has been changed to "Paintbrush nonwelded unit";

CHANGE HISTORY (Continued)

Revision Number	Interim Change No.	Effective Date	Description of Change
1	1	September 20, 2000	in addition, the term C-Holes Complex was standardized in those sections. Table 6.3-1 was deleted, and the following table renumbered. Figures 11.2-3 to 11.2-5 were deleted, and the following four figures were renumbered. Changes were also made to the following figures: 1.1-1, 2.2-1, 4.2-18, 4.3-10, 4.3-12, 4.5-30, 4.5-31, 4.8-5, 4.8-6, 4.8-13, 4.8-26 to 4.8-29, 4.8-50 to 4.8-52, 4.8-57, 4.9-4, 5.2-9, 5.2-10, 5.2-12, 5.2-14, 5.2-15, 5.3-32, 5.3-34 to 5.3-36, 6.4-12, 8.1-4, 8.2-1, 8.2-7, 8.2-12, 8.2-24, 8.2-25, 8.2-27 to 8.2-41, 8.3-4, 8.3-14, 8.5-11, 8.5-13, 9.2-1, 9.3-2, 9.3-30, 11.4-1, 11.4-2, 12.2-2, 12.3-6, 12.3-12, 12.3-31 to 12.3-48, 12.3-57, 13.3-1, 13.4-6, 13.4-7, 13.4-24, and 13.4-27

EXECUTIVE SUMMARY

The *Yucca Mountain Site Description* summarizes in a single, integrated document the current state of knowledge and understanding of the natural system at Yucca Mountain. It describes the geology, geochemistry, climatology, and hydrology of the site. In addition, it discusses factors affecting radionuclide transport, the effect of thermal loading on the natural system, tectonic hazards, and how natural analogs provide increased confidence in the understanding of natural processes operating at the site. The document also describes the geography and demography of the site, and nearby facilities that might be a factor in safety analyses.

The *Yucca Mountain Site Description* is broad in nature. It summarizes investigations carried out as part of the Yucca Mountain Site Characterization Project since 1988, but also includes work done at the site in earlier years, as well as studies performed by others. It includes both results generated in accordance with the Yucca Mountain Site Characterization Project quality assurance program and those that were not. Preparation of the document itself was not a quality affecting activity. It should not be used as a source of qualified information. Rather, the sources cited in the document and the Technical Data Management System should be consulted for information on the quality status of results presented here.

Yucca Mountain is located in Nye County in southern Nevada. The site lies in the north-central part of the Basin and Range physiographic province, within the northernmost subprovince commonly referred to as the Great Basin. The basin and range physiography reflects the extensional tectonic regime that has affected the region during the middle and late Cenozoic Era. Yucca Mountain was initially selected for characterization, in part, because of its thick unsaturated zone, its arid to semiarid climate, and the existence of a rock type that would support excavation of stable openings. Congressional action directed that Yucca Mountain be the only site characterized to evaluate its suitability for development of a geologic repository for high-level radioactive waste and spent nuclear fuel.

Geologic Setting–Yucca Mountain is composed largely of volcanic rocks that resulted from eruptions within the southern Nevada volcanic field between about 14 and 11 million years ago. The rocks are primarily pyroclastic flows and tephra fallout deposits. One of these flow deposits, the Topopah Spring Tuff, forms the horizon being considered for waste emplacement. The Tiva Canyon Tuff lies above the Topopah Spring Tuff and the Calico Hills Formation lies below it. Studies have identified the properties and characteristics of these formations as they relate to the movement of water through the rocks and the ability of the rocks to slow the transport of radionuclides. Colluvium and alluvium overlie the volcanic rocks on hillslopes and in lower lying areas. Carbonate rocks of Paleozoic age underlie the volcanic rocks at Yucca Mountain. These rocks are important in understanding the flow of water beneath the water table.

On a broad scale, the volcanic rocks can be grouped into welded and nonwelded units with differing hydrogeologic and thermal/mechanical properties. Lithophysae, cavities formed by vapor concentration as the deposits cool, characterize some portions of the welded units and can affect rock properties. Glassy (vitric) zones also are characteristic of the volcanic rocks in some horizons. The matrix mineralogy of the tuffs at Yucca Mountain consists primarily of silica polymorph minerals (cristobalite, tridymite, and quartz) and potassium feldspar. Zeolite

minerals are abundant in the Calico Hills Formation. Fracture-filling minerals consist predominantly of silica polymorphs, calcite, clays, zeolites, iron oxides, and manganese oxides.

Geologic mapping indicates a number of faults intersect the rocks forming Yucca Mountain and its vicinity. These faults can be classified as those that divide the rocks into major blocks (block-bounding faults), those that reflect deformation within blocks (intrablock faults), and those that transfer motion from one block-bounding fault to another (relay faults). Detailed studies of a number of faults provide information on their activity, if any, during the Quaternary Period. Studies of Quaternary fault activity form part of the basis for analyzing seismic hazard at Yucca Mountain.

Fractures in the rock at Yucca Mountain have been studied in natural exposures, cleared "pavements," boreholes, and underground excavations. Fractures are generally of three types: early cooling joints, later tectonic joints, and joints caused by erosional unloading. Fracture intensity and connectivity influence groundwater flow within the volcanic rocks. Values for fracture intensity and connectivity are greatest in the densely welded tuffs, least in the nonwelded units, and intermediate in lithophysal zones.

Climatology–Climate in the vicinity of Yucca Mountain affects the amount of water that can infiltrate into the mountain and the level of the water table. Studies providing evidence of past climates in the Yucca Mountain vicinity indicate climates wetter than today dominated over the past several hundred thousand years. Interglacial climates, such as the present climate, persisted only about 20 percent of the time. During much of the next 10,000 years, it is expected that the climate at Yucca Mountain will be wetter and cooler than it is today.

Surface Water Hydrology and Erosion–Studies of surface water hydrology support evaluations of infiltration and flooding. Surface waters related to the Death Valley regional groundwater flow system are limited to infrequent ephemeral streamflows following heavy rains and to isolated local areas of ponding and perennial flow fed by groundwater discharge. Most of the infrequent streamflow is returned to the atmosphere as evapotranspiration.

Long-term erosion rates at Yucca Mountain are low. Erosion on modern hillslopes occurs during infrequent, intense, short duration summer thunderstorms. Aggradation occurs in washes and on the upper alluvial fans. Landscape response under wetter conditions caused an increase of vegetation on hillslopes and greater resistance to removal of sediment. Washes, deprived of sediment supply and subject to increased streamflow, incised their valley sediment and entrenched their channels across alluvial fans. During colder intermediate climates, frost wedging of bedrock blocks occurred on hillslopes and hillslope creep resulted in the erosion of bedrock material.

Unsaturated Zone Hydrology–The Yucca Mountain site occupies an intermediate position between areas of recharge and discharge of the regional groundwater flow system. The aridity and small average rate of recharge produce a correspondingly small groundwater flux, which is readily transmitted through the extensively fractured rocks that compose most of the region. As a result of these conditions, the water table commonly is deep beneath the land surface, particularly beneath prominent ridges such as Yucca Mountain. The combination of aridity,

large topographic relief, and transmissive rocks results in a thick unsaturated zone, which is a principal hydrologic attribute of the site.

Studies of unsaturated zone hydrology address net infiltration, percolation, fracture-matrix interaction, accumulation of perched water, lateral flow, and deep percolation to the water table. These processes determine the amount of water that may seep into repository drifts, possibly come in contact with waste packages, and eventually reach the water table.

Data and interpretations from field studies at Yucca Mountain, combined with insights about hydrologic processes documented in the scientific literature, have led to a detailed understanding of the physical processes and properties that control net infiltration. These processes include precipitation, surface runoff and run-on, infiltration, evapotranspiration, and the redistribution of moisture in the shallow subsurface. Simulation results for a mean modern climate scenario indicated that average annual precipitation for the potential repository area is 196.9 mm/yr. and average net infiltration is 4.7 mm/yr. For mean monsoon and mean glacial-transition climate scenarios, the average net infiltration is 12.5 mm/yr. and 19.8 mm/yr., respectively.

Knowledge of the properties of hydrogeologic units in the unsaturated zone is needed to understand and model the hydrologic processes taking place. Properties were measured by two distinctly different methods: matrix-properties analysis of rock cores and field-scale air-injection testing. In general, porosity is related primarily to the depositional features and amount of welding of a rock, with the lowest porosities occurring in the most densely welded rocks and the highest porosities occurring in the nonwelded and bedded rocks. Mineral alteration also has a significant influence on the hydrologic properties. The six principal hydrogeologic units defined in the unsaturated zone at the site are unconsolidated alluvium, Tiva Canyon welded (TCw), Paintbrush nonwelded (PTn), Topopah Spring welded (TSw), Calico Hills nonwelded (CHn), and Crater Flat undifferentiated (CFu).

Perched water has been identified below the potential repository horizon. Accumulation of perched water seems to be caused by either the basal vitrophyre of the Topopah Spring Tuff or the vitric-zeolitic boundary in the Calico Hills Formation acting in concert with a lateral structural barrier.

Geochemical and isotopic data for waters from the unsaturated zone are consistent with a flow model in which all unsaturated zone waters, including perched waters, originate at the surface of the mountain. Although flow paths appear to be predominantly vertical, there is evidence that suggests lateral flow in some units. Isotopic data provide evidence of water that has flowed rapidly to at least the depth of the Exploratory Studies Facility (ESF). This water presumably flowed along pathways that included fractures and faults. Stable isotope values suggest pore water in the TSw probably has a post-glacial origin and is on the order of 2,000 to 10,000 years old.

Deposits of calcite and opal in fractures and cavities mark pathways of past percolation of water through the unsaturated zone. Morphologic relations, as well as chemical and isotopic compositions of these secondary minerals, provide an interpretable geochemical record of paleohydrologic conditions within Yucca Mountain. The preferred localization of secondary minerals demonstrates precipitation under water-unsaturated conditions. Results of dating of the

minerals indicate that the undersaturated conditions, at least at the level of the ESF, have persisted for several million years. There is no indication in the subsurface that deposition rates of calcite and opal varied greatly during the last million years, even though wetter and cooler climates resulted in greater recharge. These observations suggest that percolation and mineral deposition through most of the Topopah Spring Tuff may have been buffered from variations in effective moisture, except in the zones of highest flux associated with throughgoing structures.

Movement of water through the unsaturated zone is a key issue in evaluating the performance of a potential repository at Yucca Mountain. Percolation flux has been estimated using a number of different approaches. These approaches include heat-flow deficit, chloride mass-balance, hydraulic-conductivity/potential gradient, calculations based on the mass of secondary minerals in ESF fractures, estimates based on volumes and residence times of perched water, and direct estimation by multiplying the effective hydraulic conductivity of the rock at a given depth by the hydraulic gradient. These approaches yield percolation flux values in the range of near zero to about 25 mm/yr.

Investigations carried out in the ESF address subsurface hydrologic conditions. Single-hole and cross-hole air-injection tests were used to measure the permeability of the Ghost Dance fault zone. Results indicate the fault zone has permeability values about 3 to 10 times those observed in the footwall and hanging wall. Studies were also carried out to evaluate the potential for water to seep into drifts. Although there is significant uncertainty in the seepage-percentage predictions, there seems to be a low seepage probability for percolation fluxes less than 100 mm/yr.

The conceptual model of fluid flow in the unsaturated zone at Yucca Mountain consists of several important flow processes and issues. Infiltration is spatially and temporally variable because of the nature of the storm events that supply precipitation and variation in soil cover and topography. As a result of the relatively high density of interconnected fractures and low matrix permeabilities in the TCw, infiltration pulses move rapidly through the fracture system with little attenuation relative to travel times in the matrix. Because of relatively high matrix permeability and porosity and low fracture densities of the PTn, predominantly fracture flow in the TCw becomes dominantly matrix flow in the PTn. Lateral flow of liquid water seems to be insignificant within the PTn unit. Unsaturated flow of liquid water in the TSw is primarily through the fractures.

The occurrence of perched water near the TSw-CHn contact indicates that the TSw basal vitrophyre and the CHn serve as barriers to vertical flow and cause lateral flow. Below the potential repository, both the CHn and CFu units have vitric and zeolitic components that differ by the degree of hydrothermal alteration. Because the zeolitic rocks of the CHn and the CFu have low matrix permeability and some fracture permeability, a relatively small amount of water may flow through the zeolitic units. However, modeling indicates that most of the water that percolates to the zeolitic horizon is diverted laterally in the perched-water bodies and then vertically down faults. Conversely, but similar to the PTn unit, the vitric rocks of the CHn and the CFu have relatively high matrix porosity and permeability and, therefore, mostly porous-medium flow predominates in these rocks. Fracture flow is believed to be limited in these units. Fracture-matrix interaction is likely limited within the welded units in the unsaturated zone, as

evidenced by perched water derived mainly from fracture flow and by bomb-pulse chlorine-36 at the repository level in the ESF.

The conceptual model of radionuclide transport in the unsaturated zone encompasses all aspects of the conceptual model for flow. In addition, the conceptual model of radionuclide transport takes into account physical and chemical processes unique to transport. These processes include advection, matrix diffusion, fracture and matrix sorption, colloid-facilitated transport, radioactive decay, and dispersion.

Flow and transport within the unsaturated zone is modeled by a fully coupled, three-dimensional model that incorporates much of the known geologic, hydrologic, chemical, and thermal complexity of Yucca Mountain. The model was used to generate flow fields for spatially varying lower-bound, mean, and upper-bound net infiltration for the current climate, a postulated future monsoon climate, and a postulated future glacial-transition climate. Two perched-water models were investigated: a flow-through model and a bypass model.

The simulation results indicate that fracture flow is dominant both at the potential repository horizon and at the water table. At the repository horizon, fracture flow is more than 80 percent of the total percolation flux. Fracture flow at the water table ranges from 70 to 90 percent of the total flow. The model also simulated geochemical characteristics and calcite deposition to provide constraints on net infiltration and percolation flux. Simulations of flow fields depict the distribution of percolation flux at the potential repository horizon and at the water table.

Groundwater travel and tracer-transport times for both conservative and reactive constituents were estimated using the model flow fields. The simulations yielded a wide range of groundwater travel or tracer-transport times for different infiltration rates, tracers, and perched-water conceptual models. Groundwater travel or tracer transport times are inversely proportional to average net infiltration rate over the model domain. As average net infiltration increases from 5 to 35 mm/yr., average groundwater travel times for the 50 percent breakthrough decrease by a factor of 100 to 1,000.

Two models were developed that provide quantitative descriptions of potential water seepage into drifts of a potential repository at Yucca Mountain: the seepage model for performance assessment and the disturbed drift seepage submodel. Model results indicate that seepage percentage decreases with increasing van Genuchten $1/\alpha$, or fracture continuum permeability. For percolation fluxes ranging from about 5 to 15 mm/yr., seepage percentage ranged from near zero to about 70 percent. Simulation results indicated that drift degradation had little effect on seepage for the degradation conditions simulated.

Simulations of transport of radioactive solutes and colloids from the repository horizon to the water table were performed to support model development and performance assessment studies of a potential repository. The results of the simulations were used to evaluate the transport of radioactive solutes and colloids, and to determine the processes, mechanisms, and geologic features that have a significant effect on transport. The contributions of decay products of radioactive decay to transport were evaluated from the bottom of the potential repository to the water table. The effects of the various conceptual models of perched water on transport also were evaluated.

Three-dimensional simulations were run for lower-bound, mean, and upper-bound infiltration cases and incorporated three climate scenarios. The release rate of radionuclides at the potential repository was considered constant over time. Simulation results show the normalized release rate at the water table for technetium-99 has a very strong dependence on the infiltration regime. As the infiltration rate increases from low to mean present-day level, the arrival of the 10-percent relative concentration decreases from about 10,000 years to about 300 years. The sorption of neptunium-237 retards its transport through the unsaturated zone system as compared to technetium-99 and is sufficient to increase the time to reach the water table by a factor of about 40. The relative concentration of plutonium-239 never reaches 10 percent at the water table even after 1 million years of continuous release because of the strong sorption of plutonium-239. However, the decay products of plutonium-239, such as uranium-235, reach the water table much more quickly. Also, simulation results reveal that radionuclide transport from the repository to the water table is affected significantly by the faults, especially at the early times. Simulation results for three-dimensional transport of plutonium colloids show a high sensitivity to the declogging parameter.

Saturated Zone Hydrology–The saturated zone underlying Yucca Mountain and the surrounding region represents an additional component of the path along which radionuclides could be transported from the potential repository at Yucca Mountain. The Alkali Flat-Furnace Creek groundwater basin underlies the potential repository, and is a part of central Death Valley subregion of the Death Valley regional groundwater flow system. Potentiometric data from widely spaced boreholes indicate that groundwater probably flows southward from upland recharge areas in the volcanic terrain of Pahute and Rainier mesas, beneath Timber Mountain, and southward toward the Yucca Mountain area. The groundwater flows through aquifers of the Tertiary Age volcanic and volcaniclastic sequence beneath Crater Flat, Yucca Mountain, and Jackass Flats, eventually ascending into the valley-fill sedimentary deposits of the Amargosa Desert. A regional carbonate aquifer underlies the Tertiary volcanic rocks in the Yucca Mountain vicinity. Comparison of major-ion and isotopic content data from waters of the lower carbonate aquifer with those from the volcanic units implies that there has been little mixing of water from the lower carbonate aquifer with that of the overlying Tertiary volcanic aquifers beneath Yucca Mountain. Flow paths inferred based on chemical and isotopic data are in general agreement with those based on potentiometric gradients.

A model of the regional flow system is used to provide boundary conditions for a local (site-scale) flow system model. The regional model incorporates data on hydraulic heads and spring flows, hydraulic conductivities, estimated water budgets, and faults. For the regional flow model, simulated values of hydraulic head are in relatively good agreement with observed values. Evidence of some apparent model error exists based on apparent larger values of residuals for certain spring flows; however, the apparent differences between simulated and observed spring flows could be attributable in part to uncertainties or errors in some spring flow estimates.

A site-scale saturated zone flow and transport model was developed to simulate flow and transport processes at the local (site) scale. The model reasonably simulates observed water levels and hydraulic gradients, particularly in the area along the inferred flow path from beneath the potential repository. There is also good agreement between simulated and estimated specific

discharge, and flow paths simulated by the site-scale flow model generally agree with flow paths interpreted from hydrochemical data.

In the immediate vicinity of Yucca Mountain, hydrogeologic data indicate that groundwater flows towards the potential repository area from the north and from the west, and away from the potential repository initially in a southeastern direction toward Fortymile Wash and Jackass Flats, then south-southwestward toward the Amargosa Desert. Beneath the crest of Yucca Mountain, flow is entirely in the lower volcanic aquifers and deeper units. However, at Fortymile Wash, the upper volcanic aquifer dips beneath the water table and dominates the flow system. Limited data on the vertical hydraulic gradient indicates that an upward gradient exists between the carbonate aquifer and the volcanic aquifers at a location southeast of the potential repository, and could extend to the area underlying the potential repository as well.

Several lines of evidence have been examined to determine the stability over time of the elevation of the groundwater table in the vicinity of Yucca Mountain. Studies were made of natural existing spring features and paleodischarge sites, packrat midden sites, groundwater samples, and mineralogical and isotopic indicators. Results of these studies indicate that, during the past two pluvial periods, if water table gradients were similar to modern-day gradients, as is suggested by alternate-climate modeling simulations, the groundwater table could have been situated a maximum of about 115 to 120 m higher than the current water table level beneath Yucca Mountain.

Radionuclide Transport–A number of factors affect the transport of radionuclides within the unsaturated and saturated zones. These factors include radionuclide solubility and speciation, sorption, the effects of organics on sorption, matrix diffusion, and the effects of colloids. Radionuclides of concern for Yucca Mountain are neptunium, plutonium, americium, technetium, iodine, and uranium. Sorption coefficients for radionuclides of interest were obtained using water and rock samples from the site. Sorption coefficients were obtained in batch experiments performed at several pH levels to evaluate the impact of pH variations on the sorption coefficient. The potential effects of organics on actinide sorption were evaluated in batch experiments with model organic compounds in water and rock samples from the site. Models were developed to explain the sorption coefficient data and to allow prediction of coefficient values under anticipated conditions. Adsorption of radionuclides by alluvium has also been studied. Dynamic transport studies include crushed-tuff column experiments under flowing conditions, solid rock column experiments, and currently experiments with alluvium. In addition, the transport of radionuclides through fractures was examined to assess the retardation that can be provided by radionuclide diffusion into the matrix and sorption onto the minerals coating Yucca Mountain fractures. Colloid-facilitated transport of radionuclides has been studied in the laboratory using waters collected from Yucca Mountain or synthesized to reflect Yucca Mountain waters and colloidal materials either collected from the field or synthesized in the laboratory.

In addition to laboratory studies of factors affecting radionuclide transport, field studies have also been carried out. A transport test at Busted Butte was designed to validate and improve the site-scale model of flow and transport in the unsaturated zone. A mixture of conservative tracers, a reactive tracer, and fluorescent polystyrene microspheres was injected into the test block of rock and used to track flow, reactive transport, and colloid migration, respectively. To

test conceptual saturated zone transport models, two major cross-hole, forced-gradient tracer tests at the C-holes complex were carried out. Observed responses of nonsorbing tracers were consistent with matrix diffusion behavior. This result supports the use of a dual-porosity conceptual model to describe radionuclide transport through the saturated, fractured volcanic rocks near Yucca Mountain. Results also suggest that the use of laboratory-derived radionuclide sorption parameters in field-scale transport predictions is defensible.

Thermal Loading Effects–If a geologic repository is constructed at Yucca Mountain, the emplaced radioactive wastes will emit a significant amount of heat from the radioactive decay. This heat will influence hydrologic, mechanical, and chemical conditions in both the near field (drift scale) and far field (mountain scale). Consequently, there are several sets of coupled processes that must be taken into account to determine the overall performance of the repository in the unsaturated zone. These coupled processes include thermohydrologic, thermomechanical, and thermochemical processes, and combinations of these three. Both laboratory and field studies (Large Block Test, Single Heater Test, Drift Scale Test) were carried out to address these issues. Thermohydrologic behavior of a potential repository was examined for conditions that included boiling in the host rock, coalescence of boiling zones around individual drifts, heterogeneity of heating along drifts, use of backfill, and use of a drip shield.

Drift-scale models of the near-field environment of a potential repository were developed to evaluate the potential effects of coupled thermohydrologic-chemical processes on unsaturated zone flow and transport. These models include the Drift Scale Test thermohydrologic-chemical model and the thermohydrologic-chemical seepage model. The Drift Scale Test thermohydrologic-chemical model was used to predict thermohydrologic-chemical processes prior to and during the Drift Scale Test in the ESF. Results of the Drift Scale Test thermohydrologic-chemical model indicate that the strong thermal load applied to the system results in changes in temperature, liquid saturation, and gas-phase compositions, which, in turn, cause changes in the chemistry of the system.

The thermohydrologic-chemical seepage model provides an analysis of the effects of thermohydrologic-chemical processes in the near-field host rock surrounding the potential emplacement drifts on the seepage water chemistry and gas-phase composition. The thermohydrologic-chemical analysis included complete investigation of pertinent mineral-water processes in the host rock and their effect on the near-field environment. The model was used to evaluate the effects of mineral dissolution and precipitation; the effects of CO_2 exsolution and transport in the region surrounding the drift; the potential for forming calcite, silica, or other mineral assemblage precipitation caps; and the resulting changes to porosity, permeability, and seepage. Four infiltration cases were simulated; in each case, infiltration was increased with time to account for changes in climate.

Thermal-mechanical-hydrological investigations included study of thermomechanical effects on fracture flow; mechanical loading of waste packages through creep, block failures, or seismic loading; and thermal-mechanical effects on hydrology. Thermal effects on the geochemical system can affect the distribution of minerals and the geochemistry of fluids in the repository vicinity. Studies examined mineral dissolution and precipitation, mineral stability, the evolution of in-drift water chemistry, and fluid-rock interactions.

Tectonic Hazards–Volcanic and seismic activity pose tectonic hazards that might affect a repository at Yucca Mountain. These hazards have been analyzed probabilistically and are taken into account in preclosure design (seismic) and postclosure performance assessment (volcanic and seismic). Studies of the igneous features in the vicinity of Yucca Mountain supported the volcanic hazard analysis. Results of the analysis indicate that the mean annual frequency of intersection of the repository footprint by an igneous dike is 1.6×10^{-8}. The mean annual frequency of an eruptive vent forming through the emplacement block is 7.7×10^{-9}. Studies have also documented the likely characteristics of any future volcanic eruption that might disrupt a repository at Yucca Mountain.

Studies to evaluate seismic hazards at Yucca Mountain focused on characterizing the contemporary seismic environment, the history of faults active during the Quaternary Period, and the attenuation of ground motion from local and regional earthquakes. Both ground motion and fault displacement hazards were examined. For horizontal acceleration with an annual frequency of exceedance of 10^{-4}, spectral acceleration ranges from 0.168 g at 0.3 Hz to 1.160 g at 10 Hz to 0.534 g at peak ground acceleration. These values were determined for a defined reference rock condition. An analysis to incorporate the local site response must be carried out to obtain final seismic design inputs. For an annual frequency of exceedance of 10^{-5}, fault displacement hazard is insignificant, except on major block-bounding faults.

Natural Analogs–Observation of natural or anthropogenic (human-induced) analogs can help to determine whether the results of repository models are consistent with the behavior of real systems. Analogs are especially useful for investigating processes that occur over large distances and long time frames, and they can be used to evaluate the reliability and uncertainties associated with modeling. Analogs investigated were relevant to specific components of the engineered and natural barrier systems at Yucca Mountain. Anthropogenic sites, such as contaminant plumes at the Idaho National Engineering and Environmental Laboratory and at Hanford, Washington, have provided an opportunity to test numerical and conceptual models similar to those used to model unsaturated zone and saturated zone transport at Yucca Mountain.

The Nopal I uranium deposit at the Peña Blanca site in Mexico provides an analog in unsaturated, fractured, rhyolitic tuff. The uranium-series disequilibrium data indicate stability for uranium-235, uranium-238, protactinium, and thorium in fracture-filling materials over time scales of about 100,000 years. Furthermore, the sequence of uranium alteration paragenesis at Nopal I is a very good analog to alteration of uranium oxide spent nuclear fuel. At Nopal I, Palmottu, and Poços de Caldas, uranium has been transported small distances, essentially completely along fractures, and is sorbed onto iron-oxides and calcites. Matrix diffusion is an important transport mechanism at Cigar Lake and Oklo. Colloid filtration is an important process in the saturated zone at Cigar Lake, Koongarra, and Poços de Caldas.

INTENTIONALLY LEFT BLANK

CONTENTS

CONTENTS (Continued)

Page

CONTENTS (Continued)

CONTENTS (Continued)

Page

CONTENTS (Continued)

Page

CONTENTS (Continued)

Page

CONTENTS (Continued)

Page

CONTENTS (Continued)

CONTENTS (Continued)

Page

CONTENTS (Continued)

Page

CONTENTS (Continued)

Page

Page

Page

CONTENTS (Continued)

Page

CONTENTS (Continued)

CONTENTS (Continued)

Page

CONTENTS (Continued)

Page

CONTENTS (Continued)

Page

CONTENTS (Continued)

Page

CONTENTS (Continued)

Page

Page

CONTENTS (Continued)

Page

CONTENTS (Continued)

Page

CONTENTS (Continued)

Page

CONTENTS (Continued)

Page

CONTENTS (Continued)

Page

CONTENTS (Continued)

Page

CONTENTS (Continued)

Page

CONTENTS (Continued)

INTENTIONALLY LEFT BLANK

FIGURES

FIGURES (Continued)

Page

FIGURES (Continued)

Page

FIGURES (Continued)

Page

FIGURES (Continued)

Page

FIGURES (Continued)

FIGURES (Continued)

Page

FIGURES (Continued)

Page

FIGURES (Continued)

Page

FIGURES (Continued)

Page

FIGURES (Continued)

Page

FIGURES (Continued)

Page

FIGURES (Continued)

FIGURES (Continued)

Page

FIGURES (Continued)

Page

FIGURES (Continued)

Page

FIGURES (Continued)

Page

FIGURES (Continued)

Page

FIGURES (Continued)

Page

FIGURES (Continued)

Page

FIGURES (Continued)

Page

FIGURES (Continued)

FIGURES (Continued)

Page

FIGURES (Continued)

Page

FIGURES (Continued)

FIGURES (Continued)

Page

FIGURES (Continued)

Page

FIGURES (Continued)

FIGURES (Continued)

Page

FIGURES (Continued)

Page

FIGURES (Continued)

Page

FIGURES (Continued)

Page

FIGURES (Continued)

Page

FIGURES (Continued)

Page

FIGURES (Continued)

Page

FIGURES (Continued)

Page

FIGURES (Continued)

Page

FIGURES (Continued)

Page

FIGURES (Continued)

Page

FIGURES (Continued)

Page

FIGURES (Continued)

Page

FIGURES (Continued)

Page

TABLES

TABLES (Continued)

Page

TABLES (Continued)

Page

TABLES (Continued)

TABLES (Continued)

Page

TABLES (Continued)

TABLES (Continued)

Page

TABLES (Continued)

TABLES (Continued)

TABLES (Continued)

TABLES (Continued)

TABLES (Continued)

TABLES (Continued)

TABLES (Continued)

TABLES (Continued)

TABLES (Continued)

ACRONYMS AND ABBREVIATIONS

BLM	U.S. Bureau of Land Management
CFu	Crater Flat undifferentiated
CHn	Calico Hills nonwelded
CNWRA	Center for Nuclear Waste Regulatory Analyses
CRWMS	Civilian Radioactive Waste Management System
DOE	U.S. Department of Energy
DOPA	dihydroxyphenylalanine
DTN	data tracking number
ESF	Exploratory Studies Facility
GFM	geologic framework model
ISM	integrated site model
LA	License Application
M&O	Management and Operating Contractor
MM	mineralogic model
NAFA	Nordic aquatic fulvic acid
NRC	U.S. Nuclear Regulatory Commission
OIS	oxygen isotope stage
PSHA	probabilistic seismic hazard analysis
PTn	Paintbrush nonwelded
PVHA	probabilistic volcanic hazard analysis
Q	rock mass quality
RMR	rock mass rating
RPM	rock properties model
RQD	rock quality designation
TCw	Tiva Canyon welded
TSPA	total system performance assessment
TSw	Topopah Spring welded
USGS	U.S. Geological Survey
VA	Viability Assessment
YMP	Yucca Mountain Site Characterization Project

SYMBOLS

Ag	silver
Al	aluminum
Am	americium
Ar	argon
B	boron
Ba	barium
Bi	bismuth
Br	bromine
C	carbon
Ca	calcium
Ce	cerium

SYMBOLS (Continued)

Cl	chlorine
Cm	curium
Cr	chromium
Cs	cesium
Cu	copper
Eu	europium
F	fluorine
Fe	iron
H	hydrogen
He	helium
Hg	mercury
I	iodine
K	potassium
Kr	krypton
La	lanthanum
Li	lithium
Mg	magnesium
Mn	manganese
N	nitrogen
Na	sodium
Nb	niobium
Nd	neodymium
Ni	nickel
Np	neptunium
O	oxygen
Pa	protactinium
Pb	lead
Po	polonium
Pt	platinum
Pu	plutonium
Ra	radium
Rb	rubidium
Rn	radon
Sb	antimony
Sc	scandium
Se	selenium
Si	silicon
Sm	samarium
Sr	strontium
Tc	technetium
Te	tellurium
Th	thorium
Ti	titanium
U	uranium
Xe	xenon

SYMBOLS (Continued)

Y	yttrium
Zr	zirconium

INTENTIONALLY LEFT BLANK

1. INTRODUCTION

Since 1983, under the Nuclear Waste Policy Act of 1982, the U.S. Department of Energy has been investigating a site at Yucca Mountain in Nevada (Figure 1.1-1) to determine whether it is suitable for development as the nation's first repository for permanent geologic disposal of high-level radioactive waste and spent nuclear fuel. The *Yucca Mountain Site Description* presents the current understanding of the features, events, and processes composing the natural system at and near the site. Characterization of the natural system is necessary to assess the ability of the potential geologic repository to perform adequately. The natural system is the framework within which engineered components of a potential repository must be designed. The Yucca Mountain Project must demonstrate with reasonable assurance that the combined natural and engineered systems will provide for maintenance of public health and safety for 10,000 yr.

The Yucca Mountain site is located in Nye County in southern Nevada, approximately 160 km (100 mi.) northwest of Las Vegas. It is situated in the southern part of the Great Basin, the northernmost subprovince of the Basin and Range physiographic province. The mountain is an irregularly shaped volcanic upland (Figure 1.1-2) that reaches an elevation ranging from 1,500 to 1,930 m (4,920 to 6,330 ft) at the crest and has about 650 m (2,130 ft) of relief. It is bounded to the west by Crater Flat, to the east by Midway Valley and Jackass Flats, to the south by the Amargosa Valley, and to the north by Timber Mountain.

Characteristics of Yucca Mountain that led to its consideration as the site for a geologic repository include its arid to semiarid climate and the relatively great depth to the water table. For waste emplaced in the unsaturated zone, these attributes would help to limit the amount of water available to contact waste packages. This would contribute to a long lifetime for the waste packages with slow degradation of the waste form within the packages. For any radionuclides that escape the waste packages, the natural system will reduce their concentration during transport away from the potential repository, thereby limiting possible exposure to the public.

Adequate knowledge of the natural system is essential to making an informed decision about the suitability of a potential repository at Yucca Mountain for the nation's high-level radioactive waste and spent nuclear fuel. An understanding of the natural system at Yucca Mountain supports the case that the DOE is preparing regarding the long-term safety of a geologic repository at the site. The plan to complete that case is the potential repository safety strategy (CRWMS M&O 1999a, p. v) which identifies seven factors related to the safety case:

1. Limited seepage of water into the emplacement drifts
2. Performance of the drip shield
3. Performance of the waste package
4. Solubility limits of dissolved radionuclides in Yucca Mountain water
5. Retardation of radionuclide migration in the unsaturated zone
6. Retardation of radionuclide migration in the saturated zone
7. Dilution of radionuclide concentrations during migration.

The safety case will also address those features, events, and processes that might disrupt the potential repository, such as igneous events and seismic fault displacement. In addition, the

safety case will include insights from natural analogs (other sites having radionuclide features and history that have a bearing on the long-term performance of the Yucca Mountain site).

Investigations of the natural system at Yucca Mountain address these factors and potential disruptive features, events, and processes to provide an important part of the technical basis for demonstrating the long-term safety of a potential geologic repository at the site. They also provide information needed to substantiate safety during the operational period for a repository before it is permanently closed. Thus, the information on the natural system presented here supports the development of a safety case for a potential geologic repository at Yucca Mountain.

1.1 OBJECTIVE AND SCOPE

The objective and scope of this document are described in a development plan (CRWMS M&O 1999b). The primary objective is to summarize, in a single integrated document, the knowledge and understanding of the natural system affecting Yucca Mountain. In addition, this report summarizes the geographic setting and demography of the site vicinity and information on its nearby industrial, transportation, and military facilities. This document also summarizes information on how heat generated by emplaced waste would affect the ambient natural system, and presents natural analogs that may provide insights into the behavior of the potential geologic repository at the site. This information forms part of the technical basis for preparing the Site Recommendation and, if the site is found suitable, a License Application to the U.S. Nuclear Regulatory Commission. It also can be used to address the U.S. Nuclear Regulatory Commission's Key Technical Issues (Sagar 1997) related to the natural system during the pre-licensing period.

The scope of the *Yucca Mountain Site Description* consists of summarizing existing information to describe the natural system at Yucca Mountain and addressing related issues. It is based largely on reports that document activities of the Yucca Mountain Site Characterization Project (YMP). It also incorporates relevant information from reports prepared by investigators working outside of the YMP. This information includes consideration of interpretations and hypotheses that differ from those developed by YMP investigators.

During site characterization, numerous reports have been prepared to document investigations and their results. Recently, a series of Analysis and Modeling Reports and Process Model Reports have been developed to describe aspects of the natural and engineered systems and how they will be treated in assessments of total system performance. Process Model Reports related to the natural system include those addressing an integrated site model, unsaturated zone flow and transport, saturated zone flow and transport, the near-field environment, disruptive events, and the biosphere. The *Yucca Mountain Site Description* draws upon these documents, as well as the earlier reports, in summarizing the current state of knowledge and understanding.

Technical areas covered by the *Yucca Mountain Site Description* are:

- Geographic setting and demography (Section 2)
- Nearby industrial, transportation, and military facilities (Section 3)
- Geologic framework (Section 4)
- Geochemical framework (Section 5)

- Climatology and meteorology (Section 6)
- Surface water hydrology (Section 7)
- Unsaturated zone hydrology (Section 8)
- Saturated zone hydrology (Section 9)
- Factors affecting radionuclide transport (Section 10)
- Integrated natural system response to thermal loading (Section 11)
- Tectonic hazards (Section 12)
- Natural analogs (Section 13).

The description of the Yucca Mountain site and surrounding region contained in this document represents the knowledge at a particular point in time. Results described are generally those available at the end of September 1999, although some results from later analyses are also included. Investigations and analyses are ongoing in some technical areas, including unsaturated and saturated zone hydrology, climate, seismic inputs for design analyses, and natural analogs.

INTENTIONALLY LEFT BLANK

1.2 QUALITY ASSURANCE

In accordance with QAP-2-0, *Conduct of Activities*, the activity of preparing the *Yucca Mountain Site Description* was evaluated and was determined to be not quality affecting (Wemheuer 1999, p. 1). This report is not intended as a source of information that is relied upon to address safety or waste isolation issues. Information for those purposes should be obtained from source documents cited here. This revision of the *Yucca Mountain Site Description* was prepared in accordance with AP-3.11Q, *Technical Reports*.

To determine the quality status of any data discussed in this report, the Technical Data Management System of the Yucca Mountain Site Characterization Project should be consulted. Because quality status changes through data verification and qualification efforts, only the Technical Data Management System provides the status at any given point in time. For this reason, quality status of data is not documented in the *Yucca Mountain Site Description.* Similarly, the quality status of any software mentioned in this report should be obtained from the Baseline of Qualified Software.

References cited in this report are documented in the Document Input Reference System database. This database consolidates information on how references are used in each section of the document. It provides a description of the inputs and documents which page, section, figure, or table from a particular reference is being cited. It thus summarizes the information given through short citations in the text and the reference lists for each section. Because the *Yucca Mountain Site Description* is not quality affecting, the quality status of the inputs is not tracked.

INTENTIONALLY LEFT BLANK

1.3 YUCCA MOUNTAIN SITE CHARACTERIZATION PROJECT BACKGROUND

The Nuclear Waste Policy Act of 1982, which established the high-level radioactive waste disposal program for the United States, requires in Section 113 that a general plan be prepared for characterizing a candidate repository site. In 1988, the U.S. Department of Energy produced the Yucca Mountain site characterization plan (DOE 1988) called for in the Act. This plan described a comprehensive program to provide the information and data needed to evaluate the suitability of the Yucca Mountain site against criteria in U.S. Department of Energy siting guidelines and to satisfy U.S. Nuclear Regulatory Commission requirements for licensing. Implementation of this plan was intended to provide the information needed to design a repository that would work in harmony with the natural system and to evaluate the expected performance of the repository and site as a total system.

Site characterization also provides information required to analyze the suitability of the Yucca Mountain site relative to suitability criteria identified in proposed 10 CFR 963 (64 FR 67054). The preclosure analysis will consider a preliminary description of site characteristics (proposed 10 CFR 963.13(b)(1) [64 FR 67054]) and potential hazards (proposed 10 CFR 963.13(b)(4) [64 FR 67054]). The postclosure analysis will be based on the postclosure suitability criteria that reflect processes and models important to total system performance of the potential geologic repository (proposed 10 CFR 963.17 [64 FR 67054]). Site characterization results support description of:

- The geologic, hydrologic, geophysical, and geochemical properties of the site (proposed 10 CFR 963.1(a)(1) [64 FR 67054]) that are needed to analyze postclosure suitability
- Unsaturated zone flow characteristics including parameters such as climate, infiltration, unsaturated zone flux, and seepage (proposed 10 CFR 963.17(a)(2) [64 FR 67054])
- Near field environment characteristics including thermal hydrology and the near field geochemical environment (proposed 10 CFR 963.17(a)(3) [64 FR 67054])
- Unsaturated zone transport, thermal hydrology, saturated zone transport, and dilution (proposed 10 CFR 963.17(a)(7)-(8) [64 FR 67054]).

Finally, site characterization results support analysis of disruptive event criteria, which include volcanism and seismic events (proposed 10 CFR 963.17(b)(1)-(2) [64 FR 67054]).

Requirements to characterize the Yucca Mountain site are also included in proposed 10 CFR 63 (10 CFR 63.15(b) [64 FR 8640]). Regulatory requirements recognize that an understanding of the geology of the site is a key component in determining the ability of the site to house a potential geologic repository that will maintain the health and safety of the public. Geologic features, events, and processes of the site must be described in a Safety Analysis Report to the extent that the information is relevant and material to safety or performance of a geologic repository (proposed 10 CFR 63.21(c)(1) [64 FR 8640]). Information to be described includes:

- The geology, geomechanical properties, hydrology, and geochemistry of the site (proposed 10 CFR 63.21(c)(1)(ii) [64 FR 8640])

- The surface-water hydrology climatology, and meteorology of the site (proposed 10 CFR 63.21(c)(1)(iii) [64 FR 8640])
- The geologic media in which a repository would be constructed (proposed 63.21(c)(3) [64 FR 8640])
- The response of the geomechanical, hydrogeologic, and geochemical systems to anticipated thermal loading (proposed 10 CFR 63.21(c)(6) [64 FR 8640]).

Documentation of the results of site characterization activities also support the requirements of proposed 10 CFR 63.21(c)(5) and (9) (64 FR 8640) to characterize features, events, and processes that will significantly affect compliance with performance criteria and explain measures used to support models used in performance assessment.

For an integrated safety analysis of the potential geologic repository operations area, site characterization results support compliance with specifications to identify and analyze naturally occurring hazards (proposed 10 CFR 63.112(b) [64 FR 8640]). Site characteristics information also contributes to providing a technical basis for including or excluding specific hazards from the safety analysis (proposed 10 CFR 63.112(d) [64 FR 8640]). For performance assessment, site characterization results support requirements to include data related to the geology, hydrology, and geochemistry of the site, account for uncertainties and variabilities, consider alternative conceptual models and provide a technical basis for including or excluding specific features, events, and processes (proposed 10 CFR 63.114(a)-(e) [64 FR 8640]). Finally, the results also aid in demonstrating that multiple barriers, including natural barriers, are incorporated into the design of a potential repository (proposed 10 CFR 63.113(a) [64 FR 8640]).

The site characterization project, as it has evolved since 1988, has included surface-based testing and investigations, underground testing as required by U.S. Nuclear Regulatory Commission regulations, and laboratory studies and modeling activities for the evaluation of potential repository performance. Surface-based studies have included the following:

- Mapping geologic structures, including rock units, faults, fractures, and volcanic features
- Drilling boreholes into the mountain to identify the geologic units present at depth, measuring the depth of the water table and properties of the hydrologic system, observing the rate at which water moves from the surface into the rock below, and determining air and water movement properties above the water table
- Using gravitational, magnetic, electrical, and seismic methods to infer the distribution and properties of geologic units and structures at depth
- Monitoring earthquake activity
- Heating a large block of rock to observe the subsequent effects of heat on its hydrologic and chemical properties.

Boreholes provide a key source of information for characterizing the Yucca Mountain site. In addition to providing data on the stratigraphy and structure of the site, they also provide access for in situ testing and samples for laboratory testing. Boreholes have been drilled for many different purposes at Yucca Mountain (Figure 1.3-1). The convention for naming boreholes provides information on their location and purpose (see Dyer 1992).

The single largest effort of the Yucca Mountain site characterization project was constructing the Exploratory Studies Facility to gain access to the subsurface for exploration and testing at the depth of the potential repository. Work began on construction of this facility in late 1992 and excavation with a tunnel-boring machine began in September 1994. The 7.9-km (4.9-mi.) long underground tunnel (Figure 1.3-2) that constitutes the main part of the Exploratory Studies Facility was completed in April 1997. A cross drift to enhance the characterization of the potential repository block was completed in September 1998. Investigative work in the Exploratory Studies Facility focuses primarily on thermal and hydrologic testing and confirmation of the rock properties. Testing has included:

- Geologic mapping of underground openings
- Investigations of rock geotechnical properties
- Characterization of hydrologic properties of the Ghost Dance fault zone
- Air-injection and liquid-release tests to characterize fracture flow and seepage
- Single heater and drift-scale thermal tests to investigate the behavior of the natural system under thermal loads.

Laboratory testing has augmented the surface and underground tests carried out at the Yucca Mountain site. Laboratory studies allow properties and processes to be investigated under controlled conditions. Laboratory tests include those to determine mechanical, chemical, and hydrologic properties of rock samples in support of repository design and development of process models. Tests also quantify properties of radionuclides that affect their transport if released from a potential repository. Additional laboratory tests include those to examine the chemical properties of ambient water samples and the effects of heat on behavior and chemical properties of water in the host rock.

The results of these site characterization investigations, as summarized in this report, are the primary basis for the U.S. Department of Energy's description of the Yucca Mountain site. These results are supplemented by relevant information from other studies that have been carried out, including some which document alternative interpretations. Together, they document the current understanding of the natural system at Yucca Mountain.

INTENTIONALLY LEFT BLANK

1.4 REPORT ORGANIZATION

The *Yucca Mountain Site Description* is organized into 13 sections addressing 12 different technical areas. Following this introduction (Section 1), the geographic setting and demography of the site area are summarized (Section 2). Next, industrial, transportation, and military facilities are discussed as they relate to preclosure safety analyses (Section 3). Then, the geologic (Section 4) and geochemical (Section 5) frameworks of the site are presented. Following these sections, the essential role of water is addressed from its start as precipitation through its movement in the saturated zone. First to be discussed are the climatology and meteorology of the site (Section 6). Then, the surface water hydrology of the site is presented (Section 7). Descriptions of the characteristics and processes in the unsaturated zone (Section 8) and the saturated zone (Section 9) follow. The description of the site then turns to factors that affect radionuclide transport (Section 10). The effects on the ambient natural system from the thermal load generated by waste emplacement are addressed next (Section 11). Tectonic hazards are then described (Section 12) to address the likelihood that volcanic or seismic events will disrupt the potential repository at Yucca Mountain. Finally, analogs to processes that may operate at the potential Yucca Mountain repository are discussed (Section 13). These natural analogs can provide additional confidence that models used to describe the site are reasonable.

Units for values provided in this document are generally given in the system of units (metric or English) in which they were originally reported in source documents. Conversion to units of the alternative measurement system is indicated in parentheses to aid readers who are not familiar with one or the other system. For some values, for which there is no standard alternative unit, no conversion is given.

INTENTIONALLY LEFT BLANK

1.5 REFERENCES

1.5.1 Documents Cited

CRWMS M&O 1999a. *Repository Safety Strategy, Revision 3: Plan to Prepare the Postclosure Safety Strategy Case to Support Yucca Mountain Site Recommendation and Licensing Considerations.* TDR-WIS-RL-000001 REV 00. Las Vegas, Nevada: CRWMS M&O. ACC: MOL.19991129.0447.

CRWMS M&O 1999b. *Yucca Mountain Site Description, Rev. 01.* Development Plan TDP-CRW-GS-000005. Las Vegas, Nevada: CRWMS M&O. ACC: MOL.19991012.0150.

DOE (U.S. Department of Energy) 1988. *Site Characterization Plan Yucca Mountain Site, Nevada Research and Development Area, Nevada.* DOE/RW-0199. Nine volumes. Washington, D.C.: U.S. Department of Energy, Office of Civilian Radioactive Waste Management. ACC: HQO.19881201.0002.

Dyer, J.R. 1992. "Borehole Designations Used for Existing Boreholes." Letter from J.R. Dyer (DOE/YMSCO) to W.L. Clarke (LLNL), L.R. Hayes (USGS), J.A. Canepa (LANL), T.E. Blejwas (SNL), M.D. Voegele (SAIC), R.F. Pritchett (REECo), R.L. Bullock (RSN), and L.D. Foust (M&O, TRW), May 8, 1992. ACC: NNA.19920522.0070.

Sagar, B., ed. 1997. *NRC High-Level Radioactive Waste Program Annual Progress Report: Fiscal Year 1996.* NUREG/CR-6513, No. 1. Washington, D.C.: U.S. Nuclear Regulatory Commission. ACC: MOL.19970715.0066.

Wemheuer, R.F. 1999. "First Issue of FY00 NEPO QAP-2-0 Activity Evaluations." Interoffice correspondence from R.F. Wemheuer (CRWMS M&O) to R.A. Morgan, October 1, 1999, LV.NEPO.RTPS.TAG.10/99-155, with enclosures. ACC: MOL.19991028.0162.

1.5.2 Codes, Standards, Regulations, and Procedures

64 FR 8640. Disposal of High-Level Radioactive Wastes in a Proposed Geologic Repository at Yucca Mountain, Nevada. Proposed rule 10 CFR 63. Readily available.

64 FR 67054. 10 CFR Parts 960 and 963. Office of Civilian Radioactive Waste Management; General Guidelines for the Recommendation of Sites for Nuclear Waste Repositories; Yucca Mountain Site Suitability Guidelines. Readily available.

AP-3.11Q, Rev. 0, ICN 1. *Technical Reports.* Washington, D.C.: U.S. Department of Energy, Office of Civilian Radioactive Waste Management. ACC: MOL.19991130.0149.

Nuclear Waste Policy Act of 1982. 42 U.S.C. 10101 et seq. Readily available.

QAP-2-0, Rev. 5. *Conduct of Activities.* Las Vegas, Nevada: CRWMS M&O. ACC: MOL.19980826.0209.

1.5.3 Source Data, Listed by Data Tracking Number

MO0004YMP00017.000. Exploratory Studies Facility and Cross Drift. Submittal date: 05/18/2000.

MO0004YMP00031.000. Major Geographic Features in the Vicinity of Yucca Mountain. Submittal date: 04/22/2000.

MO0004YMP98102.004. Boreholes Drilled to Characterize the Yucca Mountain Vicinity. Submittal date: 04/22/2000.

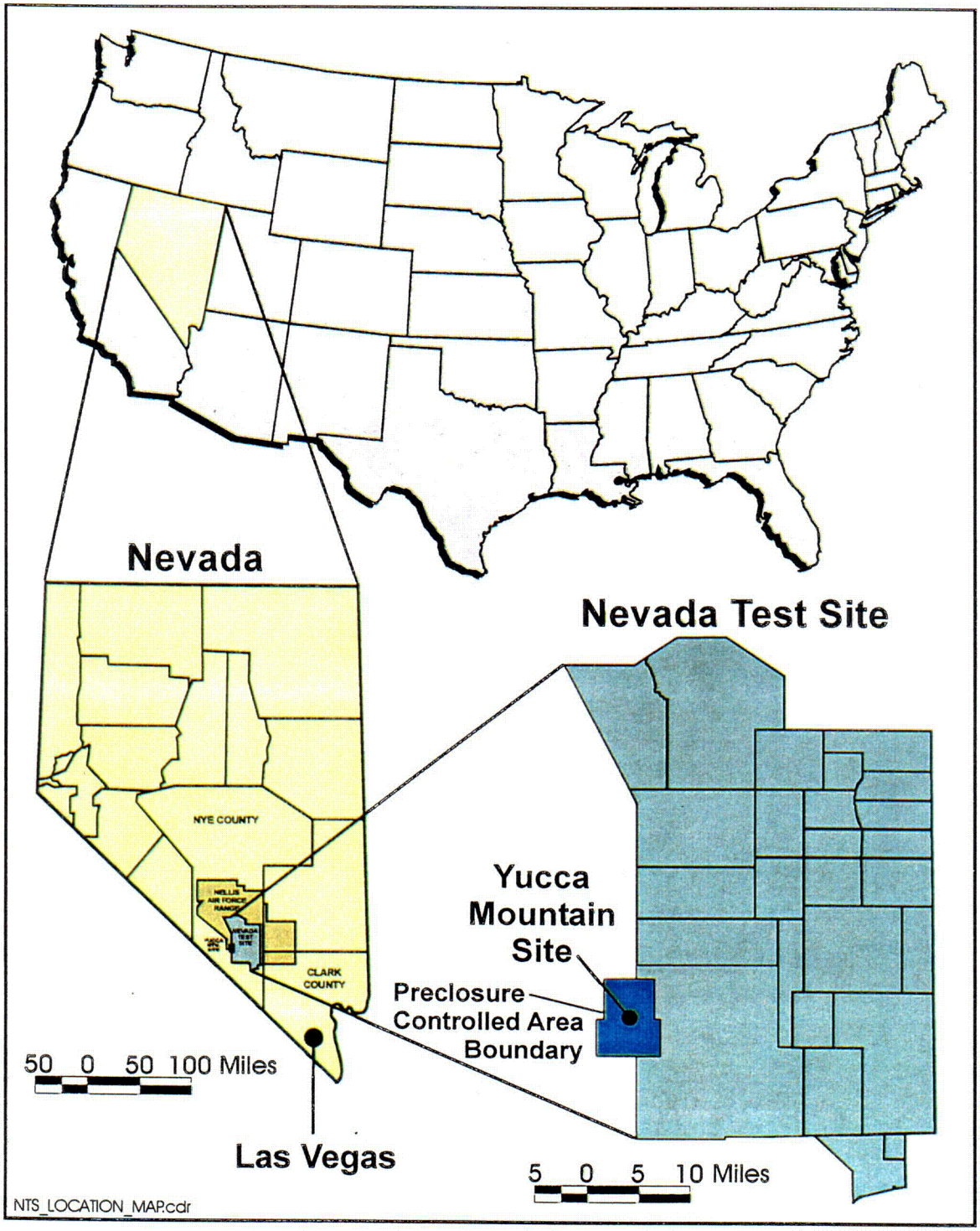

Figure 1.1-1. Location of Yucca Mountain, Nevada

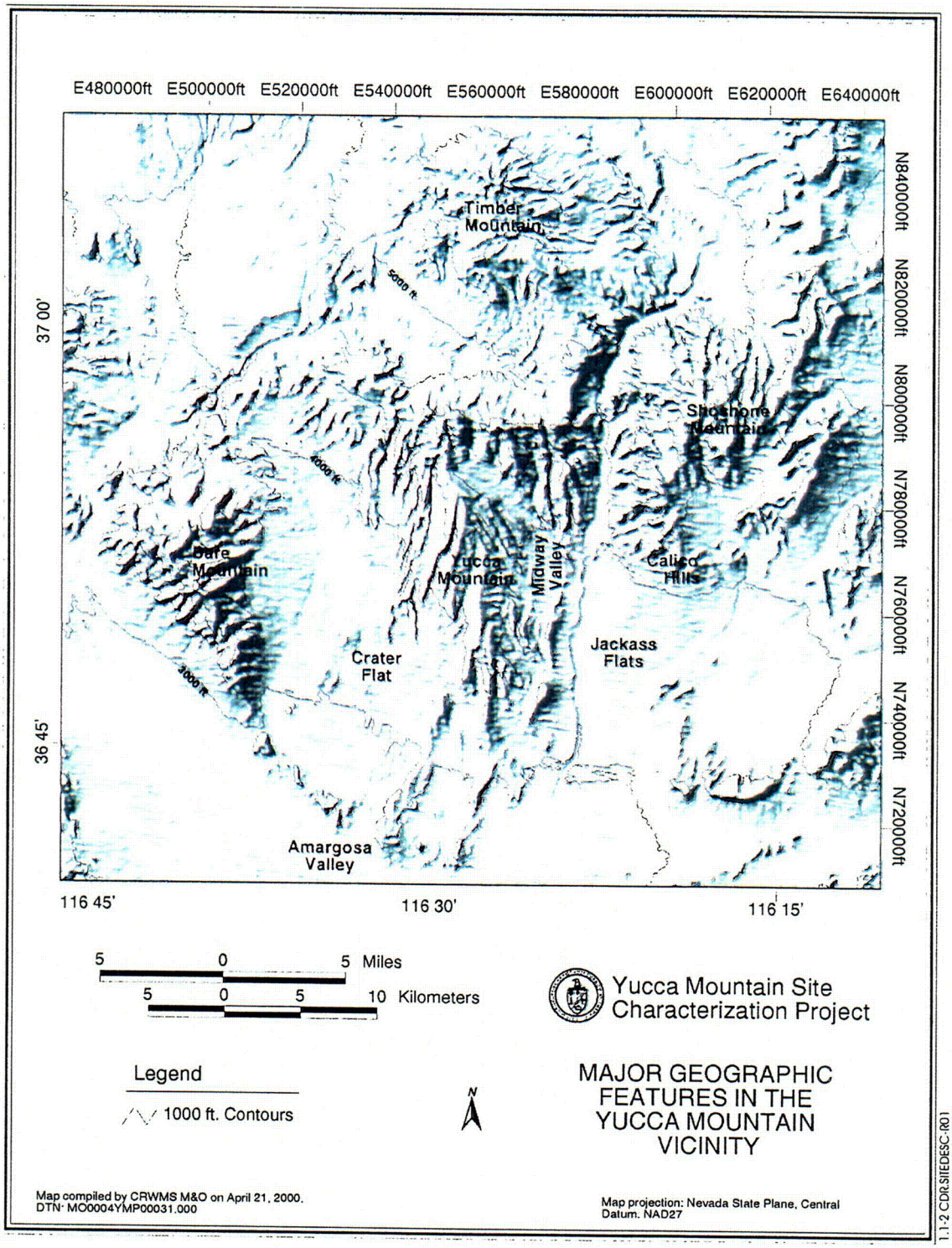

Figure 1.1-2. Major Geographic Features in the Yucca Mountain Vicinity

C02

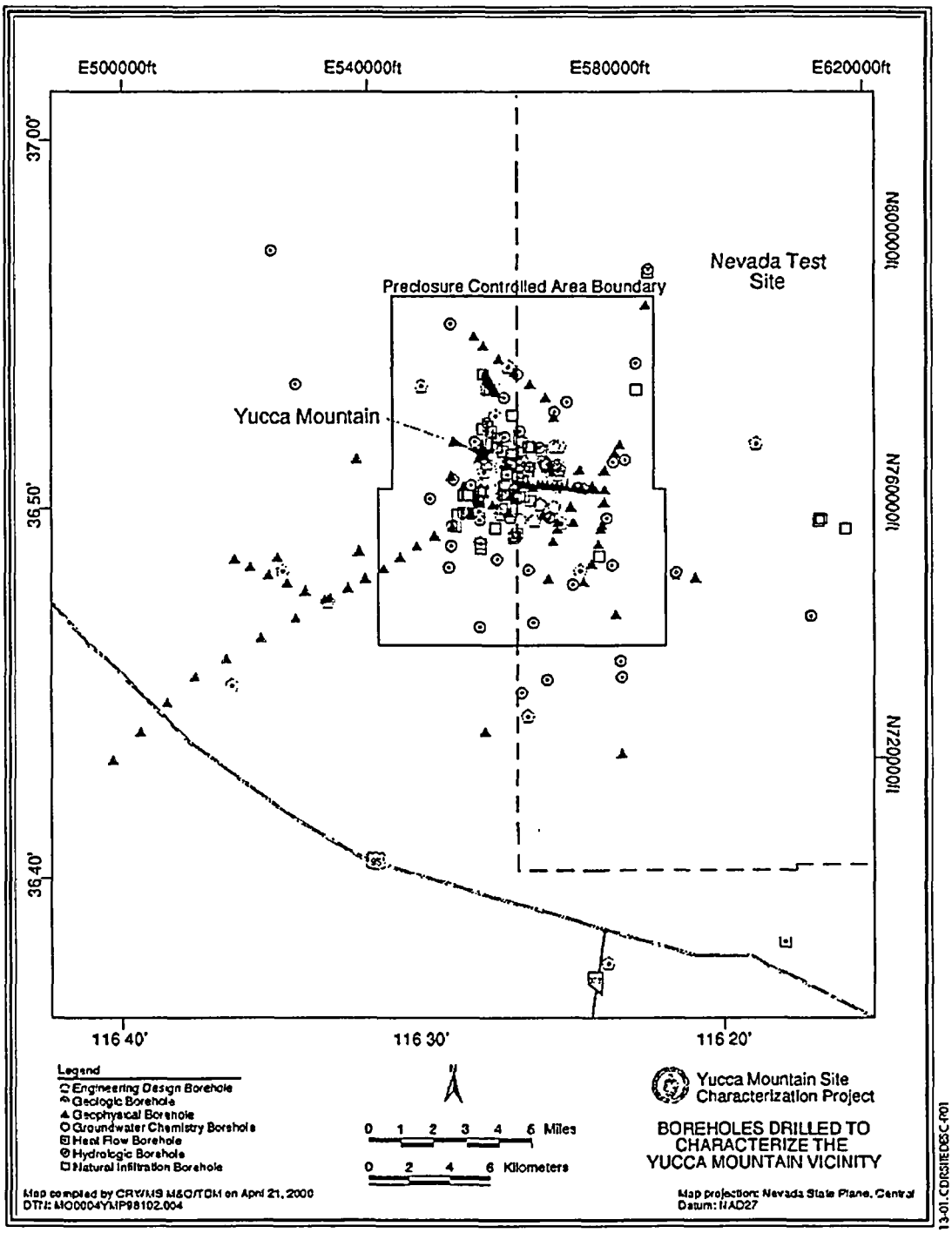

Figure 1.3-1. Boreholes Drilled To Characterize the Yucca Mountain Vicinity

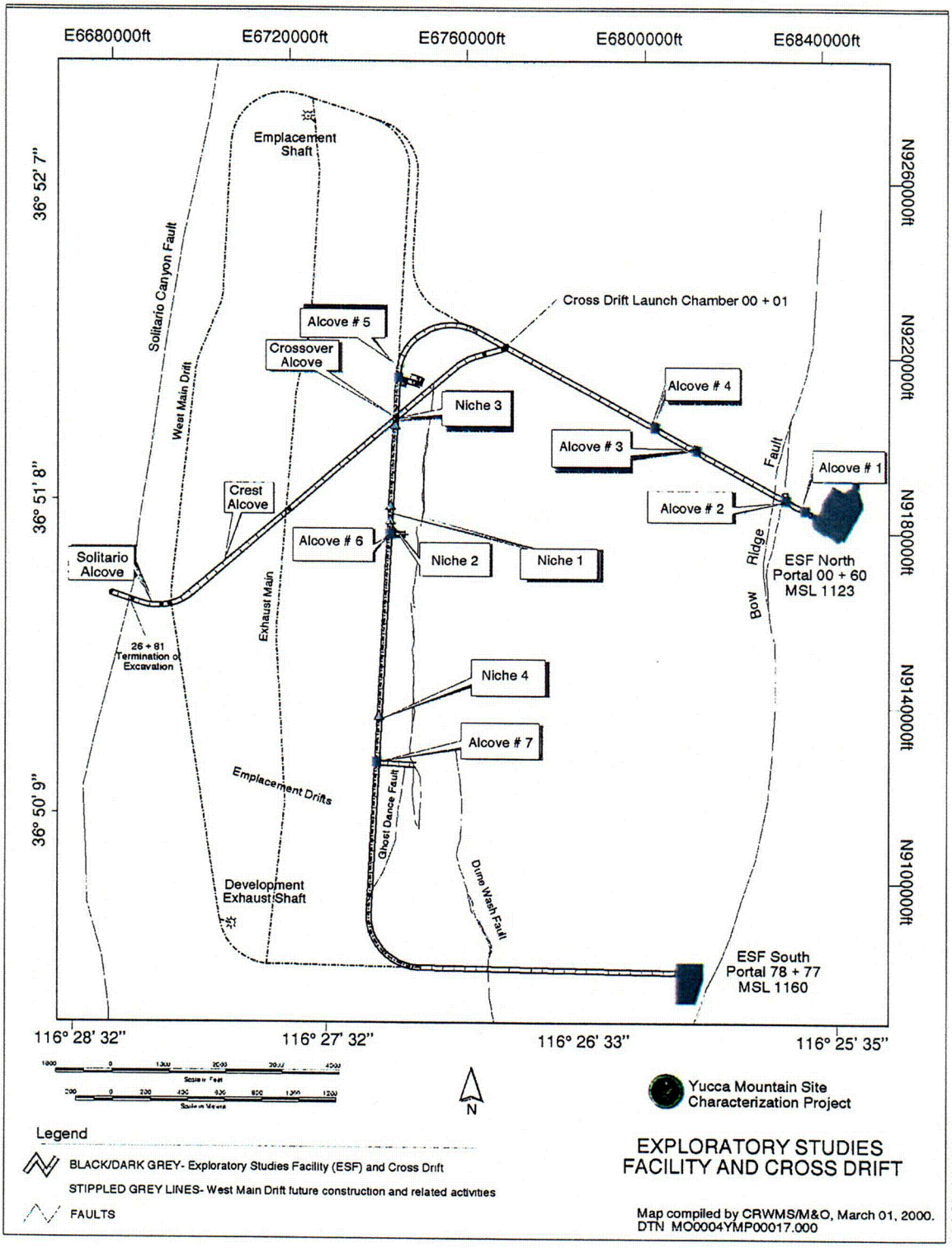

Figure 1.3-2. Exploratory Studies Facility and Cross Drift

2. GEOGRAPHIC SETTING AND DEMOGRAPHY

2.1 INTRODUCTION

This section presents an overview of the general geography and demography of the region encompassing the potential repository at the Yucca Mountain site. Section 2.1 identifies the sources of data. Section 2.2 includes a summary description of the general physiography and topography of the region (discussed in greater detail elsewhere in this document) and a more detailed description of the Yucca Mountain site, facilities, and boundaries. Section 2.3 identifies the three-county area that will receive most of the socioeconomic impacts of the potential repository; discusses the population distribution and density; and provides a brief socioeconomic overview of the region, focusing on the population within 84 km (52 mi.) of the potential repository.

The regional geographic setting, including climatic, seismic, and hydrologic information, is summarized from information discussed elsewhere in this document. Appropriate references are made to sections where citations for the data can be found. Existing and future Yucca Mountain facilities are summarized from Yucca Mountain Site Characterization Project engineering files reports. Demographic data are derived from external sources, such as the U.S. Bureau of the Census and the Nevada State Demographer's Office. Population distribution data in the vicinity of the potential Yucca Mountain repository have been developed within the Yucca Mountain Site Characterization Project using a combination of data acquired from utilities and as a result of a data-gathering activity (CRWMS M&O 1998).

INTENTIONALLY LEFT BLANK

2.2 SITE GEOGRAPHY

The Yucca Mountain site is located in Nye County in southern Nevada, approximately 160 km (100 mi.) northwest of Las Vegas (see Figures 2.2-1 and 2.2-2), on land controlled by three federal agencies: the U.S. Air Force (Nellis Air Force Range), the U.S. Department of Energy (DOE) Nevada Test Site, and the U.S. Bureau of Land Management (BLM) (see Figure 2.2-3).

The Yucca Mountain site and surrounding areas are in the southern Great Basin, the northernmost subprovince of the Basin and Range physiographic province (Figure 2.2-4). The topography of the Yucca Mountain site and surrounding region is typical of the Great Basin and the larger Basin and Range Province, which are "generally characterized by more or less regularly spaced, generally north-south trending mountain ranges and intervening alluvial basins that were formed by faulting" (DOE 1996, p. 4-74). The Yucca Mountain tectonic setting is discussed in greater detail in Section 4.3.

Elevation changes and variations in topographic relief are considerable within the area of the Yucca Mountain site. On the Nevada Test Site, elevation varies "from less than 1,000 m (3,280 ft) above sea level in Frenchman Flat and Jackass Flats to about 2,340 m (7,675 ft) on Rainier Mesa, and about 2,200 m (7,216 ft) on Pahute Mesa" (DOE 1996, p. 4-74). Within 50 mi. (80 km) south of the Yucca Mountain site, Death Valley, California, presents the lowest point in the Western Hemisphere—86 m (282 ft) below sea level at Badwater (National Park Service 1998).

Yucca Mountain is an irregularly shaped volcanic upland that reaches an elevation ranging from about 1,500 to 1,930 m (4,900 to 6,330 ft) at the crest and has about 650 m (2,100 ft) of relief. The Yucca Mountain climate is arid, and the mountain receives less than 25 cm (10 in.) of rain per year (DOE 1988a, p. A-2). Section 6.2 presents the climatic conditions in the Yucca Mountain region.

There are no perennial streams in the general vicinity of the Yucca Mountain site. As discussed in Section 7, the streams are ephemeral, fed by runoff from snowmelt and from precipitation during storms that are most common in winter. Storms also occur occasionally in spring and fall, and localized thunderstorms occur infrequently during the summer (DOE 1996, p. 4-107). Surface water runoff in the Yucca Mountain area is through Fortymile Canyon and south through Fortymile Wash. Jackass Flats, east of the Yucca Mountain site and one of the three primary valleys on the Nevada Test Site, is topographically open with drainage via the Fortymile Wash. The Fortymile drainage, in turn, intersects the Amargosa River in the Amargosa Desert about 32 km (20 mi.) southwest of the Nevada Test Site. The Amargosa River enters Death Valley at its southern end, turns to the northwest, and terminates near the center of the valley. The Great Basin subprovince is an internally draining basin (i.e., precipitation that falls over the basin has no outlet to the Pacific Ocean) (DOE 1996, p. 4-107). Figure 7.1-1 shows the surface water features of the Yucca Mountain region.

The Yucca Mountain site is in proximity to a number of natural hazards, including faults, seismic activity, and past volcanic activity, as well as man-made hazards, including weapons testing. Faults have been identified, and there has been historical seismic activity in the southern Great Basin. Section 12.3 describes the seismicity around Yucca Mountain. The southern Great Basin

has experienced volcanic activity as recently as Pleistocene time; this activity and its proximity to the Yucca Mountain site are described in Section 12.2. More than 900 nuclear tests were conducted at the Nevada Test Site, and the site is currently used to test conventional weapons and to conduct toxic waste disposal and scientific experiments. Section 3 provides additional discussion of the Nevada Test Site and other activities in the vicinity of the potential repository. Castor et al. (1999, pp. 21 to 29) researched historical mining activities near Yucca Mountain, and found evidence of prospecting activities, but confirmed that there has been no mining within 10 km of the potential repository subsurface area. A discussion of potential natural resources at the Yucca Mountain site can be found in Section 4.9.

DOE (revised) Interim Guidance, Section 121(a) (Dyer 1999, enclosure, p. 20), states that "the geologic repository operations area and the postclosure controlled area shall be located in and on lands that are either acquired lands under the jurisdiction and control of the DOE, or lands permanently withdrawn and reserved for its use." The geographic boundaries of the potential repository and the postclosure controlled area have been identified.

The Yucca Mountain Site Characterization Project (YMP) will ultimately identify an area surrounding the geologic repository operations area as the preclosure controlled area to meet the following guidelines for protection against radiation exposures and releases of radioactive material as stated in DOE Interim Guidance, Section 111(a) (Dyer 1999, enclosure, pp. 16 to 17):

> (1) The geologic repository operations area shall meet the requirements of 10 CFR Part 20.
>
> (2) During normal operations, and for Category 1 design basis events, the annual dose to any real member of the public, located beyond the boundary of the preclosure controlled area shall not exceed a [total effective dose equivalent] TEDE of 0.25 mSv (25 mrem).

DOE Interim Guidance, Section 111(b)(2) (Dyer 1999, enclosure, p. 17), also states:

> The geologic repository operations area shall be designed so that taking into consideration Category 2 design basis events and until permanent closure has been completed, no individual located on, or beyond any point on the boundary of the preclosure controlled area, will receive the more limiting of a [total effective dose equivalent] TEDE of 0.05 Sv (5 rem), or the sum of the deep dose equivalent and the committed dose equivalent to any individual organ or tissue (other than the lens of the eye) of 0.5 Sv (50 rem). The lens dose equivalent shall not exceed 0.15 Sv (15 rem), and the shallow dose equivalent to skin shall not exceed 0.5 Sv (50 rem).

A temporary preclosure controlled area has been identified. Its boundary was determined as follows. A 5 km circle was drawn around each of the four repository openings from which a repository gaseous release could occur: the North and South Portals and the north and south ventilation shafts. The resultant cloverleaf was roughly squared off to provide an area that is approximately rectangular, measuring 14 km (9 mi.) by 17 km (11 mi.), surrounding the

repository block. This temporarily identified area is shown on Figure 2.2-5 and subsequent figures in this report as the "preclosure controlled area."

Although the boundary of this preclosure controlled area is not yet final, it provides a basis in this section for discussing infrastructure and activities that are inside or outside the preclosure controlled area. As site characterization activities are completed, the YMP will identify the boundaries for the areas described below according to the License Application regulatory requirements (Section 13.1). The establishment of these regulatory-required boundaries, which will replace the designated areas discussed below, will be coordinated with identification and analysis of design basis events. The following definitions are from DOE's revised Interim Guidance (Dyer 1999, enclosure, pp. 2 to 3).

> *Underground facility* means the underground structure, backfill materials, if any, and openings that penetrate the underground structure (e.g., ramps, shafts, and boreholes, including their seals).
>
> *Geologic repository operations area* means a high-level radioactive waste facility that is part of a geologic repository, including both surface and subsurface areas, where waste handling activities are conducted.
>
> *Preclosure controlled area* means that surface area surrounding the geologic repository operations area for which the licensee exercises authority over its use, in accordance with the provisions of this part, until permanent closure has been completed. The preclosure controlled area may be traversed by a highway, railroad, or waterway, so long as appropriate and effective arrangements are made to control traffic and to protect public health and safety.
>
> *Postclosure controlled area* means a surface location, to be marked by suitable monuments, and the underlying subsurface, which area has been committed to use as a geologic repository and from which incompatible activities would be restricted following permanent closure.
>
> *Restricted area* means an area, access to which is controlled by the licensee for the purpose of protecting individuals against undue risks from exposure to radiation and radioactive materials. Restricted area does not include areas used as residential quarters, but separate rooms in a residential building may be set aside as a restricted area.
>
> *Site* means the location of the preclosure controlled area, or of the postclosure controlled area, or both.
>
> *Unrestricted area* means an area, access to which is neither limited nor controlled by the licensee.

In addition, in accordance with DOE Interim Guidance, Section 121(b) (Dyer 1999, enclosure, p. 20), "Additional Controls," the DOE will need to establish appropriate

> jurisdiction and control over surface and subsurface estates necessary to prevent adverse human actions that could significantly reduce the geologic repository's ability to achieve isolation. The rights of the DOE may take the form of appropriate possessory interests, servitudes, or withdrawals from location or patent under the general mining laws.

The DOE plan for establishing jurisdiction and control focuses on land withdrawal. The land potentially to be withdrawn and for which it is necessary to establish additional controls (postclosure controlled area) is identified in *Environmental Baseline File for Land Use* (CRWMS M&O 1999a, pp. 3 to 5). Ultimately, the area will be identified in Chapter 13 of the License Application. This potential land withdrawal area to establish additional controls would extend approximately 3 km (2 mi.) east and west of the preclosure controlled area and approximately 11 km (7 mi.) to the south. The potential land withdrawal area and the preclosure controlled area are shown on Figure 2.2-6.

Public access to the Yucca Mountain site and the Nevada Test Site is restricted, and guard stations are located at all entrances to and throughout the Nevada Test Site. Because the Yucca Mountain site is partially on BLM land (Figure 2.2-3), access to the southwestern portions of the controlled area is currently possible by crossing public lands. Prior to construction of the potential repository, appropriate withdrawal actions will be completed. These withdrawals will place the entire preclosure controlled area of the potential repository under DOE control. Access to the Yucca Mountain site is through the Nevada Test Site, which is accessed through four main, paved points. Other existing, unpaved roads can provide entrance or exit routes in case of emergency. The primary entrance to the Nevada Test Site is through Gate 100 on the Mercury Highway, which originates at U.S. Highway 95, 105 km (65 mi.) northwest of Las Vegas. A second entrance, a turnoff from U.S. Highway 95 to Jackass Flats Road, is 8 km (5 mi.) west of Mercury. This entrance is presently barricaded. A third entrance off U.S. Highway 95 is through Gate 510 at Lathrop Wells Road, approximately 32 km (20 mi.) west of Mercury. These three entrances are shown on Figure 2.2-7. A fourth entrance to the Nevada Test Site is via State Road 375 through Guard Station 700 in the northeast corner of the Nevada Test Site (DOE 1996, pp. 4-39, 4-40). Because this entrance is seldom used and because of its distance from the Yucca Mountain site (approximately 50 km [31 mi.]), it is not shown on any figure in this section. Transportation to the Yucca Mountain site through the Nevada Test Site is primarily by Lathrop Wells Road, Jackass Flats Road, Cane Springs Road, and H-Road, further augmented by a network of graded gravel roads and jeep trails (DOE 1996, p. 4-39).

The site can also be accessed by air at the Desert Rock Airport (Figure 2.2-7), located 5 km (3 mi.) southwest of Mercury. The airport is unmanned but operational; its use is controlled by the DOE. The airport has a paved runway 2 km (6,560 ft) long and 30 m (100 ft) wide. No services are available at the airport; however, existing features include an administration/control building, a fireman-standby trailer, an aircraft unloading pad, aircraft parking tie-down spurs, two lighted windsocks, and radio-activated runway lights (DOE 1996, p. 4-50).

Outside the preclosure controlled area, no facilities are operated by the YMP, although some buildings in the Area 25 Central Support Facility are occupied by YMP organizations. The Area 25 Central Support Facility and other nearby Nevada Test Site facilities outside the preclosure controlled area are shown on Figure 2.2-7, and the map coordinates for each are given in Table 2.2-1. These nearby facilities are operated by Nevada Test Site organizations and include, in addition to the Area 25 Central Support Facility:

- Test Cell C
- Engine maintenance and disassembly (EMAD) building
- Reactor maintenance and disassembly (RMAD) building
- Engine Test Stand 1 (ETS-1)
- Bare Reactor Experiment Nevada (BREN) Tower
- Treatability test facility
- Gates 100 and 510
- Control Point 300 (CP 300)
- Canyon Substation (Mercury)
- Desert Rock Airport.

In addition, there is a short railroad, known as the Jackass Wells Railroad, that was used to connect and move heavy materials between the former Nuclear Rocket Development Station facilities (DOE 1996, p. 4-49). Test Cell C, Engine Maintenance and Disassembly Building, Reactor Maintenance and Disassembly Building, and Engine Test Stand 1 are shown on Figure 2.2-7. This railroad was abandoned in place (DOE 1996, p. 4-49). In 1997, Sandia National Laboratories began a series of rocket launches from Wahmonie in Area 26 (Rogers 1997). Land uses of the Nevada Test Site and identification of areas by number are given in the Nevada Test Site environmental impact statement (DOE 1996, p. 3-6, Figure 3-1).

There are several existing and proposed "key facilities" integral to the activities of the Yucca Mountain site. Current surface facilities are those disturbed areas and structures used for exploratory studies activities. Proposed future surface facilities are those areas and structures that would be used for accepting and handling high-level radioactive waste at the site. Additional potential repository surface facilities and infrastructure outside the preclosure controlled area are to be determined.

The existing surface infrastructure used by the YMP inside the preclosure controlled area includes the North and South Portal pads, Sub-docks 1 and 2, Muck Storage Area, Borrow Pit, Booster Station, Topsoil Storage and Extension Areas, Rock Storage Area, Concrete Batch Plant, and Water Storage Tank (Figure 2.2-8). The map coordinates and size for each facility are shown in Table 2.2-2. In addition, there is a temporary trailer on the South Portal Pad and a small number of temporary trailers, a change house, and a switchgear building on the North Portal Pad. Because the trailers are temporary, and the change house and switchgear buildings are subject to major modification or removal if the potential repository becomes operational, they are not characterized here (CRWMS M&O 1999b, p. 29).

In addition to existing facilities, potential repository surface facilities and infrastructure will be located within the preclosure controlled area. At the North Portal operations area, these facilities will be in the radiologically controlled area, the balance of plant area, or the site services area.

The North Portal operations area is shown on Figure 2.2-9. Other facilities that support the subsurface development of the potential repository will be located at the South Portal development operations area, the emplacement shaft surface operations area, and the development shaft surface operations area. These four areas, plus the underground facility and muck storage, constitute the geologic repository operations area (CRWMS M&O 1999b, p. 29). The size and map coordinates for the North and South Portal facilities are shown in Table 2.2-2. The emplacement shaft surface operations area and the development shaft surface operations area are located on the mountain above the repository block. They are located at the north and south ventilation shafts, respectively, shown on Figure 2.2-5. Each will be a fenced area. The emplacement shaft surface operations area will occupy an area approximately 80 by 140 m (11,200 m^2) and the development shaft operations area will occupy an area approximately 80 by 160 m (12,800 m^2) (CRWMS M&O 1999c, p. 4-9).

Facilities in the North Portal radiologically controlled area include (CRWMS M&O 1999b, Table 4-2):

- Airlock building
- Waste handling building
- Waste treatment building
- Carrier preparation building
- Transporter maintenance building
- Carrier washdown buildings
- Switchgear building with transformer
- Change house.

Should a railspur to the repository be built, rail lines and train parking will also be built (CRWMS M&O 1999b, p. 29).

The balance of plant facilities in the North Portal operations area will include (CRWMS M&O 1999b, Table 4-2):

- Administration building
- Medical center
- Fire station
- Central warehouse
- Central shops
- Motor pool and facility service station
- Mockup building
- Utility building
- Three security stations.

The site services facilities at the North Portal operations area will include the visitor center and cooling tower. This area also includes general parking lots, but they are not shown in Figure 2.2-9 (CRWMS M&O 1999b, Table 4-2).

The facilities at the South Portal development operations area include (CRWMS M&O 1999c, pp. 4-3 to 4-7):

- Covered laydown and storage area (warehouse)
- Locomotive and railcar repair shop (including battery charger station)
- Transformer yard
- Air compressor building
- Change house (for development crews)
- Portal site offices
- Surface space: optional tuff crushing and screening plant
- Aggregate storage (area) with optional feed conveyor
- Concrete car cleanout shed
- Concrete batch plant
- Water storage tanks
- Discharge water evaporation pond
- Dispatcher house
- Two security stations (only one is shown on Figure 2.2-10)
- Diesel fuel storage tank with sump
- Truck unloading area
- Surface rail parking area for locomotives, personnel, and materials railcars.

These and other South Portal facilities are shown on Figure 2.2-10. It should be noted that the names of the facilities on the figure do not exactly match the facility names listed above.

Part of the preclosure controlled area includes a 4,255.5-acre (17.2 km^2) withdrawal area (CRWMS M&O 1999a, p. 2; 55 FR 39152) from the Mining and Mineral Leasing Laws (43 CFR 3800), precluding the staking of mining claims over the repository block. This withdrawal area is shown on Figure 2.2-11. Prior to this withdrawal, there were 10 lode mining claims in this mining and leasing laws withdrawal area that were quit-claimed after negotiations with the DOE (Castor et al. 1999, p. 29). There are currently no private land or mining claims in the preclosure controlled area (CRWMS M&O 1999a, pp. 1 to 3).

The land area that would potentially be withdrawn to provide additional controls is located on BLM land south of the preclosure controlled area, west of the Nevada Test Site, and just north of U.S. Route 95. There were 35 unpatented mining claims in this area as of May 7, 1997 (the latest update of the BLM mining claims database). These are broken down as 11 lode claims and 24 placer claims (CRWMS M&O 1999a, p. 5). Since 1991, when the government instituted an annual fee requirement for claims, the number of claims has been dropping rapidly, leaving only claims by serious miners. As the status of unpatented mining claims tends to change rapidly, it is too early to develop a strategy for dealing with claimants. However, it is reasonable to assume that any mining claims can be obtained through compensation or otherwise dealt with prior to repository closure (CRWMS M&O 1999a, p. 5). Also in this area just north of U.S. Route 95, there is a small cinder cone pit (Figure 2.2-11) being mined for raw materials for concrete blocks. This location is well outside the areas required for preclosure control, and it is possible that by the time of repository closure, approximately 100 yr. in the future, that the resource might be consumed or supplanted by new technology. It is reasonable to assume that the property can be purchased prior to closure (CRWMS M&O 1999a, p. 5). In addition, the far southwest corner

of the potential withdrawal area contains a proposed sand-and-gravel-pit development (CRWMS M&O 1999a, p. 7) and a utility corridor in the southern portion of the potential withdrawal area (DOE 1999, p. 3-9).

Additional discussion of facilities that could affect daily operations and performance of the potential repository, or that could pose health or safety or radiological health and safety hazards, is provided in Section 3.2.

2.3 SITE DEMOGRAPHY

The demographic study area surrounding the Yucca Mountain site includes five counties, four in Nevada and Inyo County in California, within 84 km of the potential repository. The primary focus is on the three southern Nevada counties of Clark, Lincoln, and Nye (Figure 2.2-2), which cover approximately 95,000 km^2 (37,000 $mi.^2$) and have an estimated population of 1,289,120 persons (Nevada State Demographer 1999a). Tables 2.3-1 and 2.3-2 present current population and areal data for Clark, Lincoln, and Nye counties. Table 2.3-3 presents population projections from the Nevada State Demographer's Office for the three counties. These projections are based upon existing growth patterns on expected scenarios related to employment growth and migration patterns. Population data are for 1998, unless otherwise noted. Additional discussions on area population can be found in the *Final Environmental Impact Statement for the Nevada Test Site and Off-Site Locations in the State of Nevada* (DOE 1996, Section 4.1.3) and the *Renewal of the Nellis Air Force Range Land Withdrawal: Legislative Environmental Impact Statement* (USAF 1999, Section 3.13.5). Discussion related to the demographics of the critical group (Dyer 1999, pp. 19 to 20) can be found in the *Biosphere Process Model Report* (CRWMS M&O 2000, Section 3.1.2).

Population and related economic activity in southern Nevada are concentrated in Clark County in the incorporated cities and in the unincorporated areas of the Las Vegas Valley. The incorporated cities include Boulder City, Henderson, Las Vegas, Mesquite, and North Las Vegas, which contain 734,070 of Clark County's 1,255,200 persons (Nevada State Demographer 1999b). Most of the remainder of the Clark County population resides in the unincorporated areas near Las Vegas, including east Las Vegas (U.S. Census Bureau 1993), Paradise, Spring Valley, and Sunrise Manor (Nevada State Demographer 1999c), which together total approximately 430,000 persons.

Lincoln County has a total population of only 4,190 persons, 3,130 (75 percent) of whom live in the incorporated town of Caliente or the unincorporated towns of Alamo, Panaca, and Pioche (Nevada State Demographer 1999a, 1999b, 1999c). The overall population density of Lincoln County is only 0.15 persons/km^2.

Nye County, where the Yucca Mountain site is located, has 29,730 persons, 0.63 person/km^2. Of this population, 27,550 persons (93 percent) live in the incorporated city of Gabbs and the unincorporated towns of Amargosa, Beatty, Manhattan, Pahrump, Round Mountain, and Tonopah. The largest population concentration is in Pahrump, with 20,080 persons, approximately 68 percent of the total county population (Nevada State Demographer 1999a, 1999b, 1999c).

Esmeralda County has a 1998 population of 1,420 (Nevada State Demographer 1999a). However, only a very small portion of the county is within the potential repository's radiological monitoring grid (Figure 2.3-1), discussed below. Population estimates by the YMP determined that this small area of Esmeralda County does not contain any residents (CRWMS M&O 1998, Table 3-3). Esmeralda County will not be further discussed.

Inyo County, California, is at its closest 36 km from the potential repository. However, the area of Inyo County within the potential repository's radiological monitoring grid (Figure 2.3-1) is

almost entirely within Death Valley National Park. Population and employment within the national park are primarily related to park activities (CRWMS M&O 1998, p. 2-5). There is no evidence that residents of Inyo County have ever been employed by the YMP (DOE 1999, p. 3-22). Population estimates in Inyo County within the potential repository's radiological monitoring grid are shown in Tables 2.3-4 and 2.3-5.

Of greater importance to the Yucca Mountain site than the population concentrations in the Las Vegas Valley is the population in the vicinity of the potential repository. Accordingly, an area of population analysis centered on the site (Easting 570433.6, Northing 765621.5, State Plane Feet, Nevada Central; Easting 551178.3, Northing 4078341.4, Universal Transverse Mercator Grid Zone 11; Longitude 116°25'33.33"E and Latitude 36°51'11.61"N [data tracking number: MO0003YMP99045.001]) has been established consistent with U.S. Nuclear Regulatory Commission regulatory guides (Regulatory Guide 1.70, Section 2.1; Regulatory Guide 1.109, Appendix D, Section 2.b), and is shown on Figure 2.3-1. The area designated the radiological monitoring grid is 84 km (52 mi.) in radius. The center has a radius of approximately 4 km (2.5 mi.). Each succeeding concentric circle has a radius 8 km (5 mi.) greater than the previous circle. As shown in Figure 2.2-2, much of the grid is located in the southernmost portion of Nye County, with smaller outer portions of the grid in the Nevada counties of Clark, Lincoln, and Esmeralda and in Inyo County in California.

Population data within the radiological monitoring grid were obtained from electrical utility data (to identify the number of households), field surveys (to supplement and verify the numbers and locations of housing units within the monitoring area), and limited interviews with residents (to identify the numbers of persons in households). The methodology is discussed in *Yucca Mountain Site Characterization Project: Summary of Socioeconomic Data Analyses Conducted in Support of the Radiological Monitoring Program, April 1997 to April 1998* (CRWMS M&O 1998, Section 2).

There are no permanent residents within 20 km (12.5 mi.) of the center of the radiological monitoring grid and only one incorporated city in Nye County, Gabbs, which is not within the grid. There are four Census Designated Places within the Radiological Monitoring Grid: Amargosa Valley, Beatty, and Pahrump in Nye County, and Indian Springs in Clark County. The closest permanent population concentration to the Yucca Mountain site is in the Amargosa Valley, a primarily agricultural-based community on the south edge of the Nevada Test Site (CRWMS M&O 1998, pp. 3-12 to 3-15). The population densities in the Amargosa Valley are 3.17 persons/km^2 or less in the inhabited grid cells (Table 2.3-5). Several grid cells have no population. Similarly, in the Beatty area, population densities in the most populated grid cells are approximately 7 and 11 persons/km^2. Populations by grid cell are provided in Table 2.3-4. Population densities for grid cells with population are provided in Table 2.3-5.

Portions of Pahrump are within the radiological monitoring grid, or 50 km (31 mi.) from the potential repository. Pahrump had a 1998 population of approximately 20,000 (Nevada State Demographer 1999c), although Nye County estimates the 1999 population at 26,231 (Williams 1999, Table 1). It is the only town within the 84-km radiological monitoring grid to have a population greater than 2,500. Rapid growth in Pahrump has been the result of increased immigration of retirees and increases in population of persons who live in Pahrump and commute to Las Vegas for employment (DOE 1996, p. 4-60).

Within the 84-km grid, population concentrations are primarily a result of agricultural, mining, tourism, and service activities (DOE 1996, pp. 4-58 to 4-61). Agricultural development is concentrated in the Amargosa Valley and Pahrump. Mining operations, tourism, general services, and employment on the Nevada Test Site and the Nellis Air Force Range help support these two towns and other unincorporated population census places located within the radiological monitoring grid, including Mercury, Beatty, Johnnie, Furnace Creek Ranch, and Death Valley Junction. Current distributions of the large percentage of federally owned land in the three counties and Nevada are shown in Table 2.3-6.

Current land use patterns and economic drivers will drive future population changes within the 84-km area. Little of the area surrounding Yucca Mountain is privately owned, and there is very little built-up or urban land (CRWMS M&O 1999a, Figure 3). Close to the Yucca Mountain site, it is likely that a large percentage of the land will remain federally owned and controlled. In addition, the Nevada Test Site is withdrawn from public use and reserved to the jurisdiction of the DOE (DOE 1996, p. 4-5). Considering the substantial disturbance of the environment on the Nevada Test Site, it is unlikely that it will be available for unrestricted public use or habitation in the near future. Consequently, it is assumed that there will be a lack of economic impetus and resulting infrastructure on the limited private land near the site sufficient to support large populations.

Within the 84-km grid, only Pahrump is expected to become a population center exceeding 25,000 persons within the foreseeable future. Table 2.3-7 shows the population in Nye County and Pahrump for 1980, 1990, and 1998. From 1990 to 1998, Pahrump grew by more than 12,600, while the rest of the county population declined by approximately 700. Clearly, Pahrump is the population center of the county, and future growth in Nye County (Table 2.3-3) is expected to be concentrated in Pahrump.

The factors that contributed to the rapid growth in Pahrump are not present in other areas of Nye County closer to the potential repository. Beatty has been, and continues to be, dependent upon the mining industry. This has placed it in a boom and bust situation for a number of years. With the closing of the Bullfrog Mine, and the subsequent loss of 320 jobs between 1996 and 2000 (Cauliflower 1998), it is expected that Beatty's population will decrease over the next several years.

The Amargosa Valley, to the south of the potential repository, has an agricultural-based economy. Infrastructure is not currently extensive, and there are no current economic drivers that would lend expectations of rapid population growth. While much of Pahrump's growth was fueled by Pahrump's proximity to the job market in Las Vegas and by a spillover of the rapid growth in Las Vegas, Amargosa Valley is probably too far removed (approximately 90 to 95 mi.) to serve as a bedroom community for Las Vegas.

The location formerly known as Lathrop Wells, at the intersection of U.S. Highway 95 and Nevada Highway 373, is at the northern end of the Amargosa Valley. It is more than 20 km (12 mi.) south of the potential repository. Population in this grid cell is currently less than 20 persons (Table 2.3-5). A limiting factor on growth is depth to groundwater. The greater the depth, the greater the cost to drill and operate wells. At the eastern area of the Amargosa Valley near Ash Meadows, and southward near Death Valley Junction, the depth to groundwater is less

than 6 m (20 ft). The depth to water increases (as does the cost to obtain water) north and west from those points to more than 90 m (300 ft) near the intersection of U.S. Route 95 and Nevada Route 373 (Kilroy 1991, Figure 4). North of U.S. Route 95, depth to groundwater continues to increase to approximately 750 m (2,460 ft) at Yucca Mountain. Depth to groundwater in the vicinity of Yucca Mountain ranges from 200 to 700 m (650 to 2,300 ft) (Luckey et al. 1996, Table 6). Depth to water is discussed in Section 9.2.4. The increased depth to groundwater in the areas north of Lathrop Wells would be a deterrent for settlement of new populations. Based on precedent, lack of existing infrastructure, cost of obtaining water, and current land ownership, it is unlikely that there would be any population locating closer to the mountain than that presently at Lathrop Wells.

Some recent events could potentially lead to some level of development in this area. One is the proposed Nevada Science and Technology Center in northern Amargosa Valley, on U.S. Route 95 just west of Nevada Highway 373. The center would include a $40 million science museum and a business park (Tetreault 1999). In addition, the Nevada Test Site Development Corporation has initiated planning for the Desert Rock Sky Park to be located at the DOE-controlled Desert Rock Airport near Mercury (NTS Development Corporation 1998). At this time, these projects are too early in the planning process to determine potential impacts on local development and population. It is noted, however, that these projects likely fall within the envelope of potential employment increases analyzed in the Nevada Test Site environmental impact statement (DOE 1996, Section 5.3.1.3). This document assumed a possible large growth in employment at the Nevada Test Site of more than 4,500 jobs above 1994 levels by the year 2005. The expanded workforce was based on the possibility that several national DOE projects, then under consideration, could be located or transferred to the Nevada Test Site. The DOE concluded there would be no significant socioeconomic impacts in Nye County from increased employment (61 FR 65551). However, since that time, DOE decisions have located many of these programs at other DOE facilities, and Nevada Test Site employment has fallen by approximately 1,200 jobs between 1995 and 1999 (data tracking number MO0003SPAEMP50.001).

2.4 REFERENCES

2.4.1 Documents Cited

Castor, S.B.; Garside, L.J.; Tingley, J.V.; LaPointe, D.D.; Desilets, M.O.; Hsu, L.C.; Goldstrand, P.M.; Lugaski, T.P.; and Ross, H.P. 1999. *Assessment of Metallic and Mined Energy Resources in the Yucca Mountain Conceptual Controlled Area, Nye County, Nevada.* Open-File Report 99-13. Reno, Nevada: Nevada Bureau of Mines and Geology. TIC: 245099.

Cauliflower, T. 1998. Repository EIS Contact Report: Employment Information for the Bullfrog Mine. Telephone conversation from T. Cauliflower (CRWMS M&O) to A. Meyers (Barrick Gold Corporation), March 20, 1998. ACC: MOL.19990429.0213.

Clark County Natural Resource Team 1997. "Existing Conditions." Chapter 1 of Clark County Federal Lands Element - Adopted: July 1, 1997. [Las Vegas, Nevada: Clark County Department of Comprehensive Planning]. Accessed May 16, 2000. TIC: 247894. http://www.co.clark.nv.us/COMPPLAN/Nrteam/Fedlands/fedland_exist_text.htm

CRWMS M&O 1998. *Yucca Mountain Site Characterization Project: Summary of Socioeconomic Data Analyses Conducted in Support of the Radiological Monitoring Program, April 1997 to April 1998.* Las Vegas, Nevada: CRWMS M&O. ACC: MOL.19980803.0064.

CRWMS M&O 1999a. *Environmental Baseline File for Land Use.* B00000000-01717-5705-00115 REV 00. Las Vegas, Nevada: CRWMS M&O. ACC: MOL.19990302.0178.

CRWMS M&O 1999b. *Repository Surface Design Engineering Files Report.* BCB000000-01717-5705-00009 REV 03. Las Vegas, Nevada: CRWMS M&O. ACC: MOL.19990615.0238.

CRWMS M&O 1999c. *Engineering File - Subsurface Repository.* BCA000000-01717-5705-00005 REV 02 DCN 01. Las Vegas, Nevada: CRWMS M&O. ACC: MOL.19990621.0157; MOL.19990615.0230.

CRWMS M&O 2000. *Biosphere Process Model Report.* TDR-MGR-MD-000002 REV 00. Las Vegas, Nevada: CRWMS M&O. ACC: MOL.20000323.0634.

DOE (U.S. Department of Energy) 1988a. *Site Characterization Plan, Yucca Mountain Site, Nevada Research and Development Area, Nevada.* DOE/RW-0199. Volume I, Part A. Washington, D.C.: U.S. Department of Energy, Office of Civilian Radioactive Waste Management. ACC: HQO.19881201.0002.

DOE (U.S. Department of Energy) 1988b. *Section 175 Report: Secretary of Energy's Report to the Congress Pursuant to Section 175 of the Nuclear Waste Policy Act, As Amended.* DOE/RW-0205. Washington, D.C.: U.S. Department of Energy, Office of Civilian Radioactive Waste Management. ACC: HQZ.19890203.0079.

DOE (U.S. Department of Energy) 1996. *Final Environmental Impact Statement for the Nevada Test Site and Off-Site Locations in the State of Nevada.* DOE/EIS 0243. Volume 1. Las Vegas, Nevada: U.S. Department of Energy, Nevada Operations Office. TIC: 226875.

DOE (U.S. Department of Energy) 1999. *Yucca Mountain Site Characterization Project Socioeconomic Monitoring Program Quarterly Employment Data Report, April 1999 through June 1999.* North Las Vegas, Nevada: U.S. Department of Energy, Office of Civilian Radioactive Waste Management. ACC: MOL.19991104.0397.

Dyer, J.R. 1999. "Revised Interim Guidance Pending Issuance of New U.S. Nuclear Regulatory Commission (NRC) Regulations (Revision 01, July 22, 1999), for Yucca Mountain, Nevada." Letter from J.R. Dyer (DOE/YMSCO) to D.R. Wilkins (CRWMS M&O), September 3, 1999, OL&RC:SB-1714, with enclosure, "Interim Guidance Pending Issuance of New NRC Regulations for Yucca Mountain (Revision 01)." ACC: MOL.19990910.0079.

Kilroy, K.C. 1991. *Ground-Water Conditions in Amargosa Desert, Nevada-California, 1952-87.* Water-Resources Investigations Report 89-4101. Carson City, Nevada: U.S. Geological Survey. TIC: 209975.

Luckey, R.R.; Tucci, P.; Faunt, C.C.; Ervin, E.M.; Steinkampf, W.C.; D'Agnese, F.A.; and Patterson, G.L. 1996. *Status of Understanding of the Saturated-Zone Ground-Water Flow System at Yucca Mountain, Nevada, as of 1995.* Water-Resources Investigations Report 96-4077. Denver, Colorado: U.S. Geological Survey. ACC: MOL.19970513.0209.

National Park Service 1998. *Death Valley National Park.* Washington, D.C.: National Park Service. TIC: 239799.

Nevada Department of Administration 2000a. "Federal Land by County, Excluding Departments of Defense Energy, Fiscal Year 1995." Land, Water, and Wildlife. Nevada Statistical Abstract. Carson City, Nevada: Nevada Department of Administration. Accessed May 22, 2000. TIC: 248068. http://www.state.nv.us./budget/saland99.htm

Nevada Department of Administration 2000b. "Federally Administrated Land in Nevada." Land, Water, and Wildlife. Nevada Statistical Abstract. [Carson City, Nevada]: Nevada Department of Administration. Accessed May 22, 2000. TIC: 248069. http://www.state.nv.us./budget/saland99.htm

Nevada State Demographer 1999a. "Nevada Population Estimates by County 1990 through 1998." Reno, Nevada: Nevada Department of Taxation. Accessed 6/14/99. TIC: 245306. http://www.state.nv.us/budget/sapop.html

Nevada State Demographer 1999b. "Population of Nevada's Incorporated Cities 1995-1998." Reno, Nevada: Nevada State Demographer. Accessed 6/11/99. TIC: 245305. http://www.state.nv.us/budget/sapop.html

Nevada State Demographer 1999c. "Population of Nevada's Unincorporated Towns--Historical Governor's Certified Series." Reno, Nevada: Nevada State Demographer. Accessed 6/11/99. TIC: 245304. http://www.scs.unr.edu/demographer

Nevada State Demographer 1999d. "Nevada Population Estimates (1997-98) and Forecasts (1999-2018) by County." Reno, Nevada: Nevada State Demographer. Accessed 6/11/99. TIC: 245303. http://www.state.nv.us/budget/sapop.html

NTS Development Corporation 1998. "Desert Rock Sky Park Master Plan: Executive Summary." Las Vegas, Nevada: NTS Development Corporation. Accessed 08/30/99. TIC: 245360. http://www.ntsdev.com/drmp/desertRock.htm

Pahrump Valley Times 2000. *Report Takes Guesswork out of Nye Land Ownership.* March 31, 2000. Page B11. Pahrump, Nevada: Pahrump Valley Times. TIC: 247895.

Rogers, K. 1997. "Fire in the Sky." Las Vegas, Nevada: Las Vegas Review Journal. Accessed June 11, 1999. TIC: 241104. http://www.lvrj.com/lvrj home/1997/apr-14-mon-1997/news/5165508.html

Tetreault, S. 1999. "Space Station Museum Proposed Near Test Site." Las Vegas, Nevada: Las Vegas Review Journal. Accessed 8/30/99. TIC: 245310. http://www.lvrj.com/cgi-bin/printable.cgi?/lvrj_home/1999/Jul-15-Thu-1999/news/11562813.html

U.S. Census Bureau 1993. "1990 Census of Population and Housing, Population and Housing Unit Counts, Nevada." *Table 9. Population and Housing Units, 1970 to 1990; Area Measurements and Density: 1990.* 1990 CHP-2-30. Washington, D.C.: U.S. Census Bureau. TIC: 245637.

U.S. Census Bureau 1996. *Land Area, Population and Density for States and Counties: 1990.* Summary Tape File 1C. Washington, D.C.: U.S. Census Bureau. TIC: 237861.

USAF (U.S. Air Force) 1999. *Renewal of the Nellis Air Force Range Land Withdrawal: Legislative Environmental Impact Statement.* Washington, D.C.: U.S. Department of the Air Force. TIC: 243264.

Williams, J.M. 1999. "Supporting Data, Tables, and Sources for Population Estimates Through the First Quarter, 1999, Nye County, Nevada; Task 2900." Memorandum from J.M. Williams (Planning Information Corporation) to L. Bradshaw (Nye County Nuclear Waste Repository Program), May 14, 1999, with enclosure. TIC: 247259.

2.4.2 Codes, Standards, Regulations, and Procedures

10 CFR 20. Energy: Standards for Protection Against Radiation. Readily available.

43 CFR 3800. Public Lands: Interior: Mining Claims Under the General Mining Laws. Readily available.

55 FR 39152. 43 CFR Public Land Order 6802. Withdrawal of Public Land to Maintain the Physical Integrity of the Subsurface Environment, Yucca Mountain Project, Nevada. Readily available.

61 FR 65551. Record of Decision: Environmental Impact Statement for the Nevada Test Site and Off-Site Locations in the State of Nevada. Readily available.

Regulatory Guide 1.70, Rev. 3. 1978. *Standard Format and Content of Safety Analysis Reports for Nuclear Power Plants LWR Edition.* Washington, D.C.: U.S. Nuclear Regulatory Commission. Readily available.

Regulatory Guide 1.109, Rev. 1. 1977. *Calculation of Annual Doses to Man from Routine Releases of Reactor Effluents for the Purpose of Evaluating Compliance with 10 CFR Part 50, Appendix I.* Washington, D.C.: U.S. Nuclear Regulatory Commission. Readily available.

2.4.3 Source Data, Listed by Data Tracking Number

MO0001GSC00040.000. Department of Energy Nevada Test Site Road and Facilities Map. Submittal date: 01/26/2000.

MO0001YMP97344.003. Boundaries and Larger Sub-Provinces of the Basin and Range Physiographic Province. Submittal date: 01/14/2000.

MO0001YMP97346.004. Land Use in the Vicinity of Yucca Mountain. Submittal date: 01/14/2000.

MO0002YMP99041.002. Existing and Proposed Infrastructure Yucca Mountain, Nevada. Submittal date: 03/14/2000.

MO0003SPAEMP50.001. Nevada Test Site Employment Data (Averages) by Standard Industrial Code (SIC): August 1995 - January 2000. Submittal date: 03/29/2000.

MO0003YMP97317.005. Nearby Active Mines and Minerals and Leasing Act Withdrawal Area. Submittal date: 03/17/2000.

MO0003YMP97345.004. Yucca Mountain Site in Proximity to Southern Nevada Counties and Adjacent California Counties. Submittal date: 03/17/2000.

MO0003YMP99040.003. Potential Withdrawal Area. Submittal date: 03/17/2000.

MO0003YMP99042.001. Nevada Test Site (NTS) Infrastructure Near to the Preclosure Controlled Area. Submittal date: 03/17/2000.

MO0003YMP99045.001. Areas Monitored for Socioeconomic Analysis Within the 84 Kilometer Radiological Monitoring Grid. Submittal date: 03/17/2000.

MO0006YMP99039.002. Preclosure Controlled Area. Submittal date: 06/07/2000.

MO0008YMP97343.006. Location of the Nevada Test Site and Yucca Mountain Site, Nevada, USA (United States of America). Submittal date: 08/29/2000.

MO9904COV8016A.000. Coverage: Nport Pots. Submittal date: 04/14/1999.

MO9904COV8016B.000. Coverage: Sport Pots. Submittal date: 04/14/1999.

MO9904COV97380.000. Coverage: ESFAREA97S. Submittal date: 04/15/1999.

MO9905NTSTRFAC.000. Nevada Test Site (NTS) Transmission Facilities. Submittal date: 05/26/1999.

INTENTIONALLY LEFT BLANK

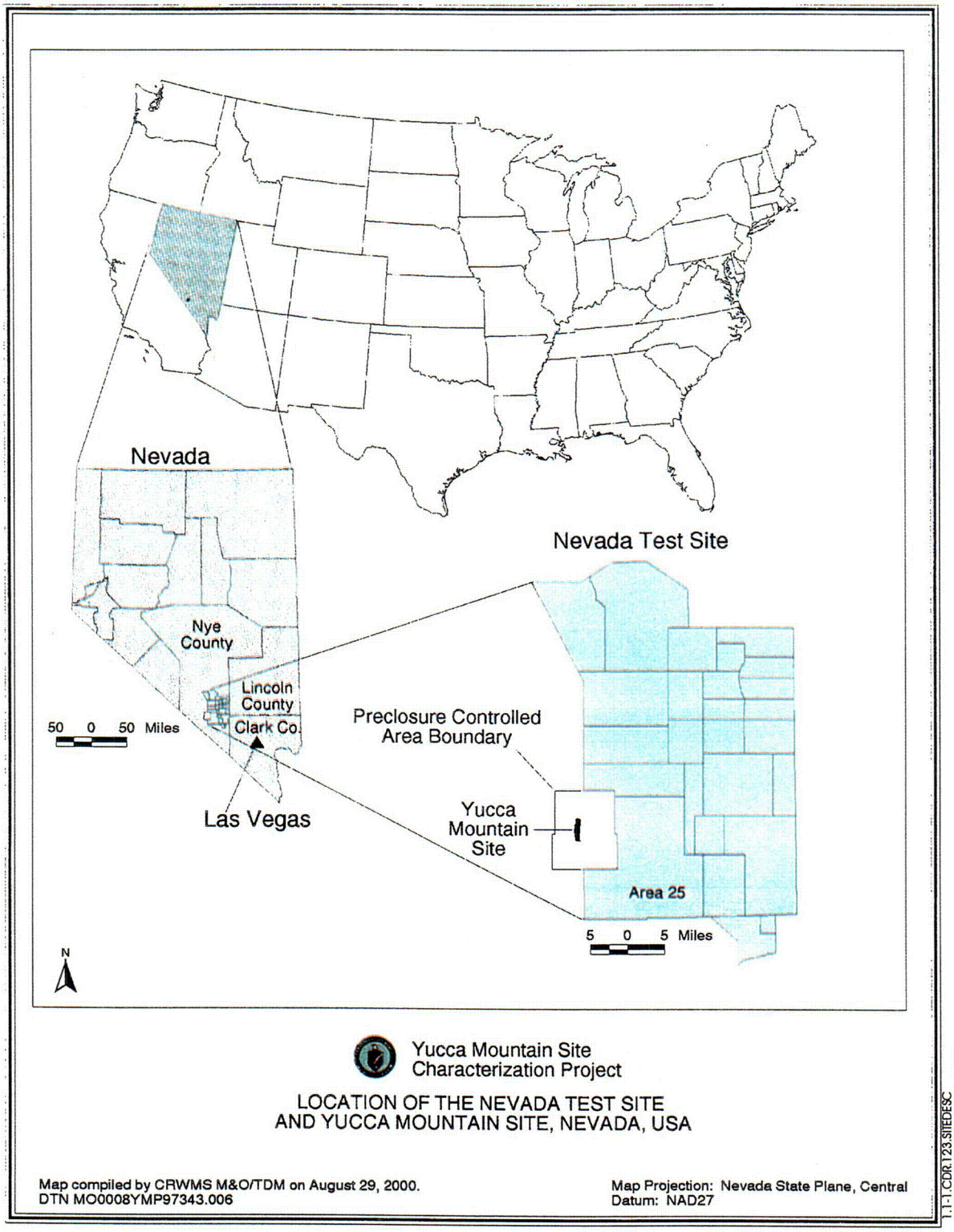

Figure 2.2-1. Location of the Nevada Test Site and Yucca Mountain Site, Nevada, USA

C04

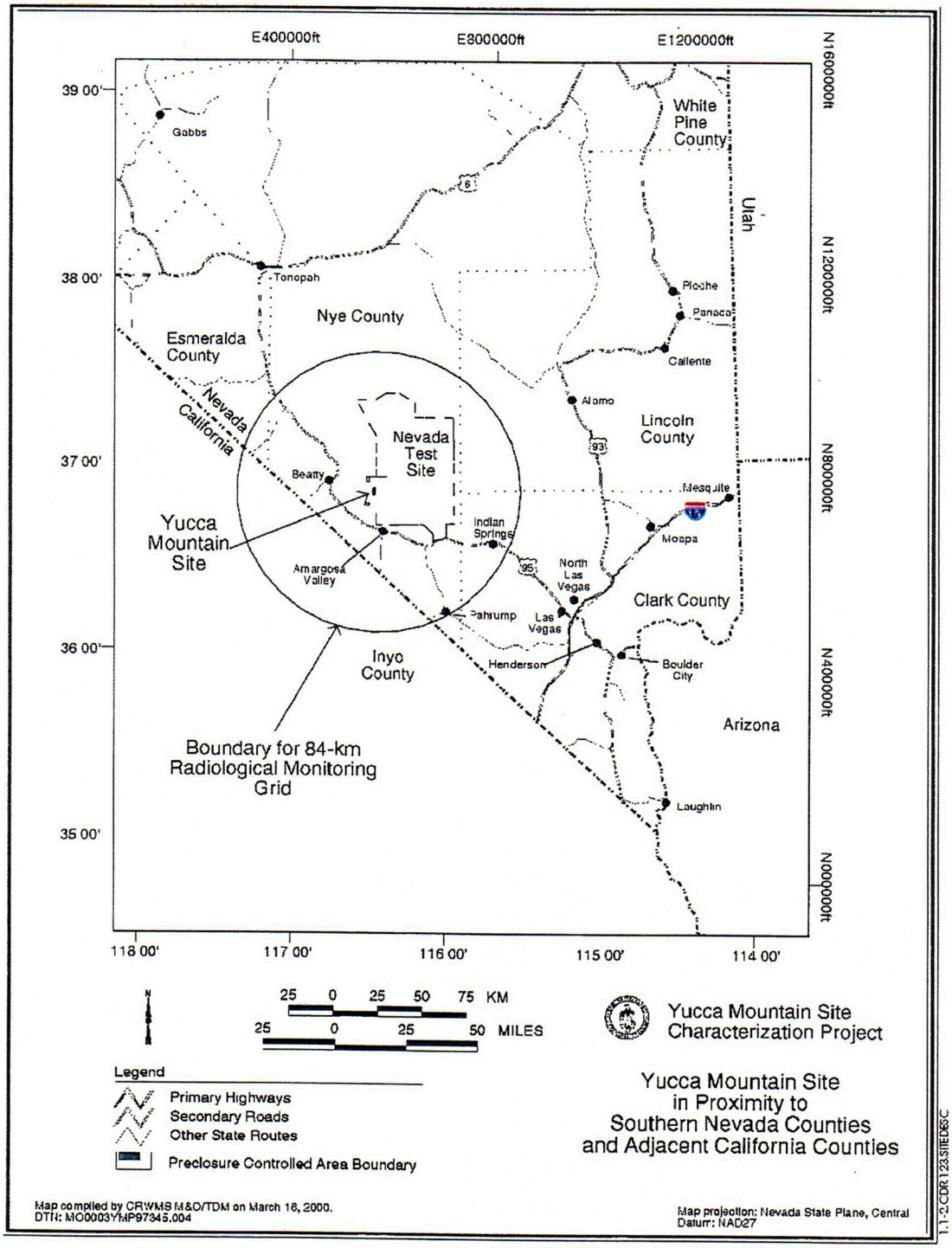

Figure 2.2-2. Yucca Mountain Site in Proximity to Southern Nevada Counties and Adjacent California Counties

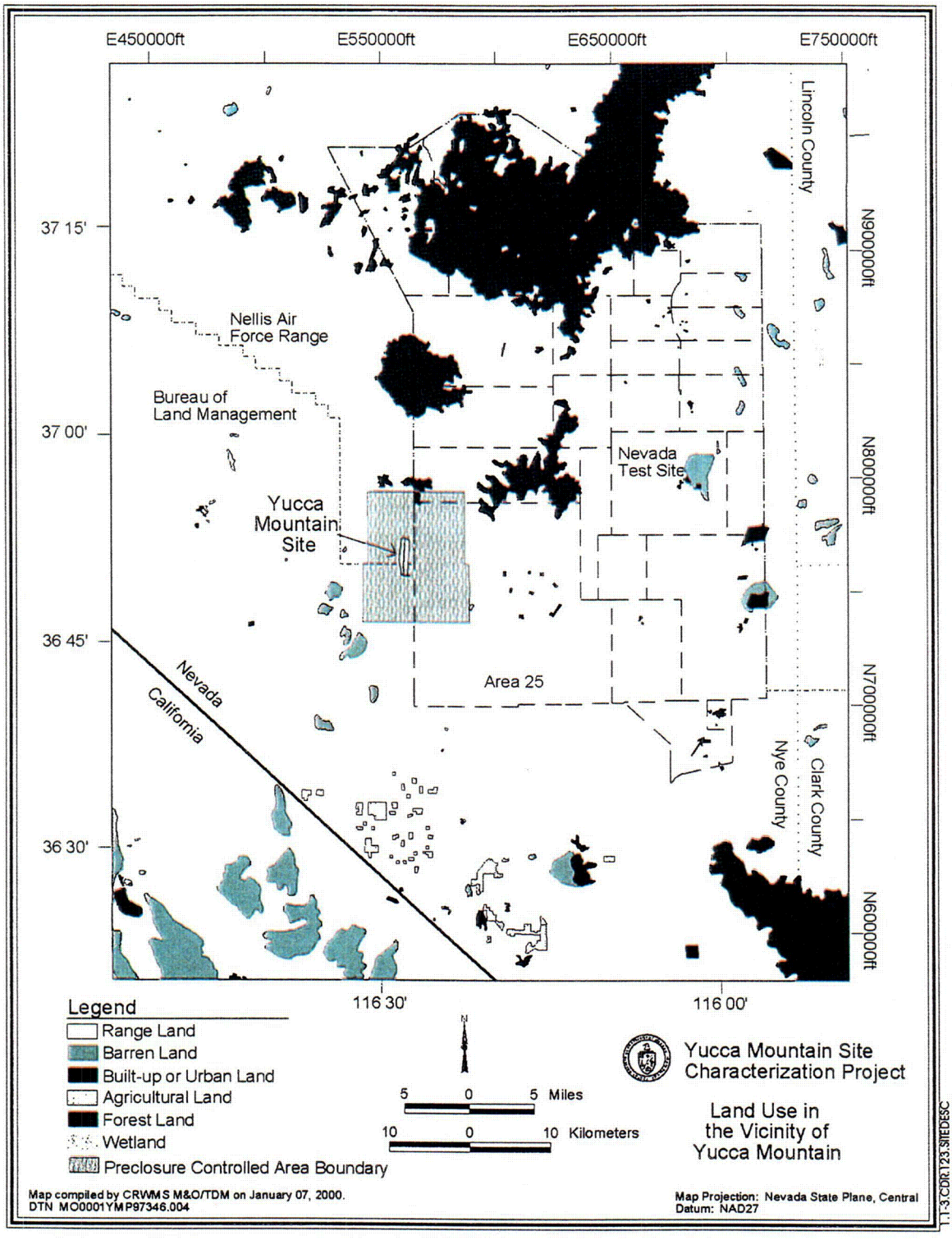

Figure 2.2-3. Land Use in the Vicinity of Yucca Mountain

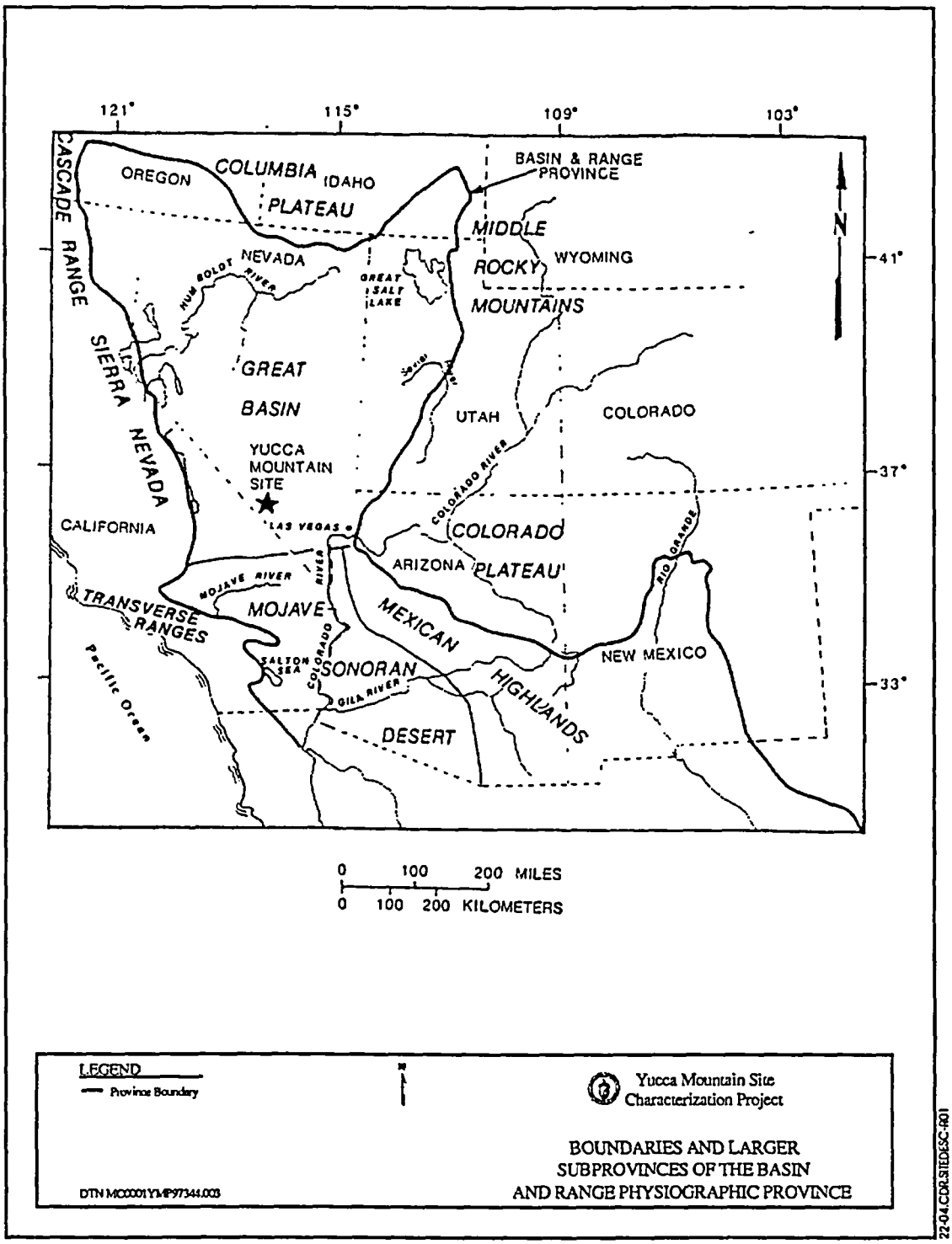

Figure 2.2-4. Boundaries and Larger Subprovinces of the Basin and Range Physiographic Province

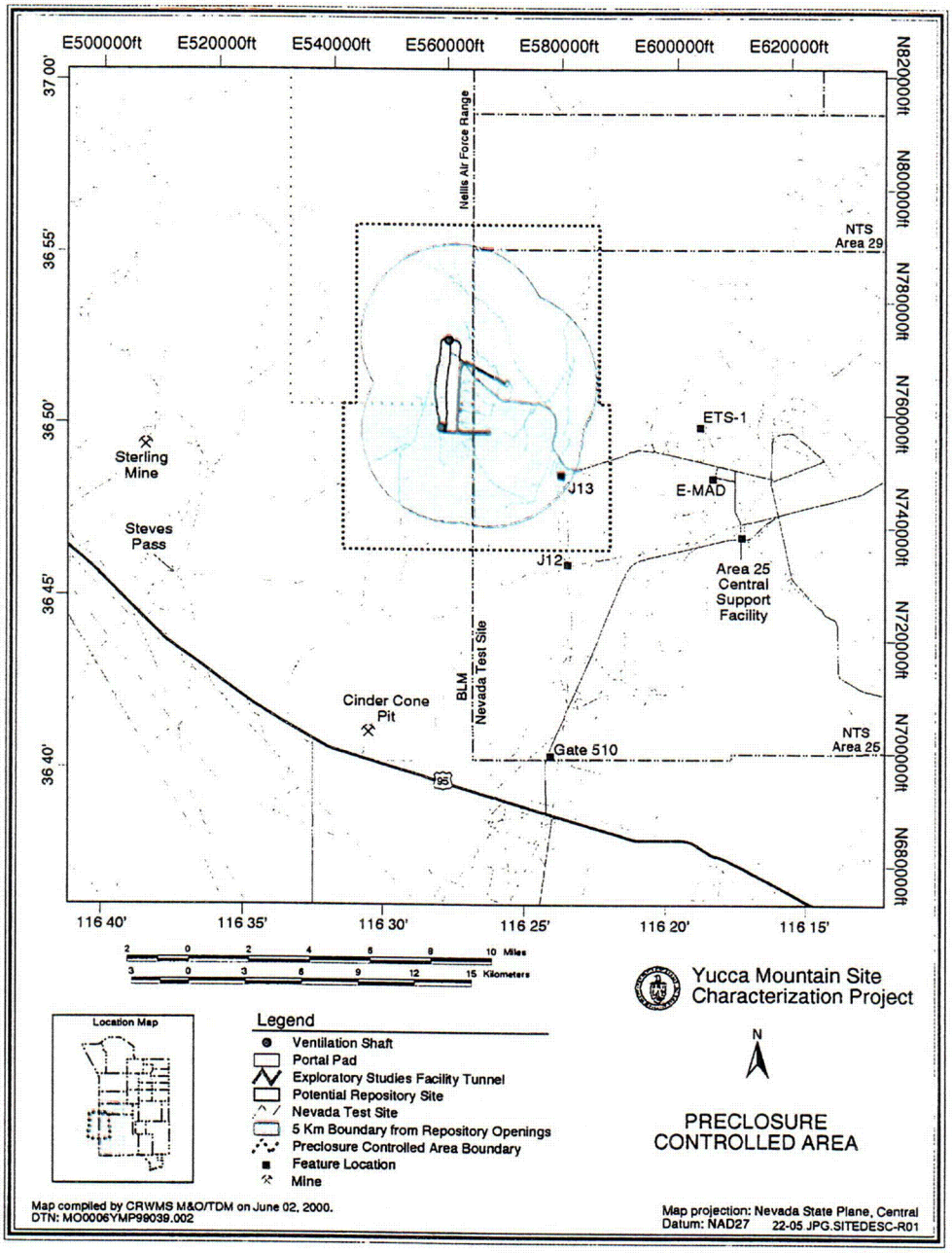

Figure 2.2-5. Preclosure Controlled Area

C07

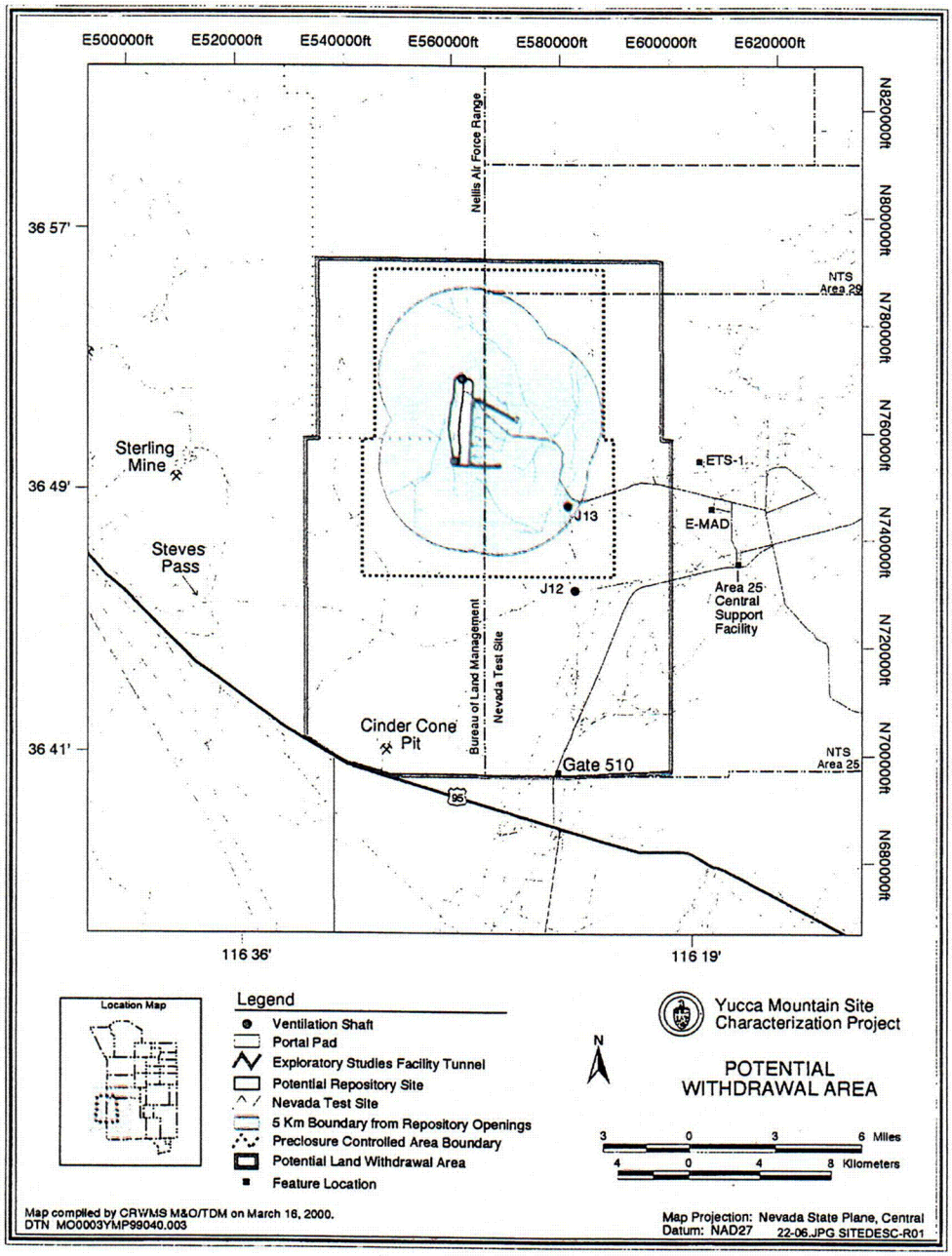

Figure 2.2-6. Potential Withdrawal Area

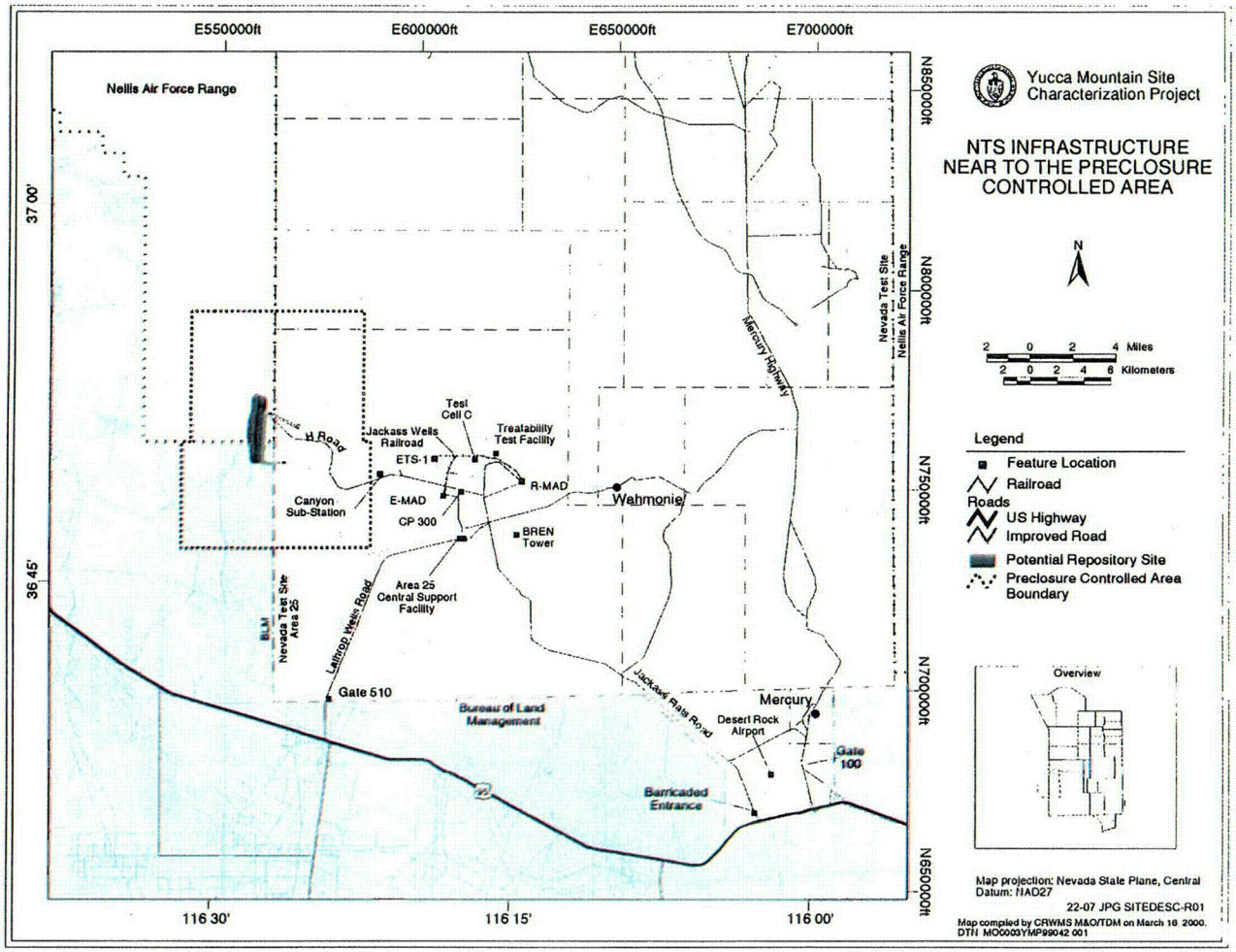

Figure 2.2-7. Nevada Test Site Infrastructure near to the Preclosure Controlled Area

C09

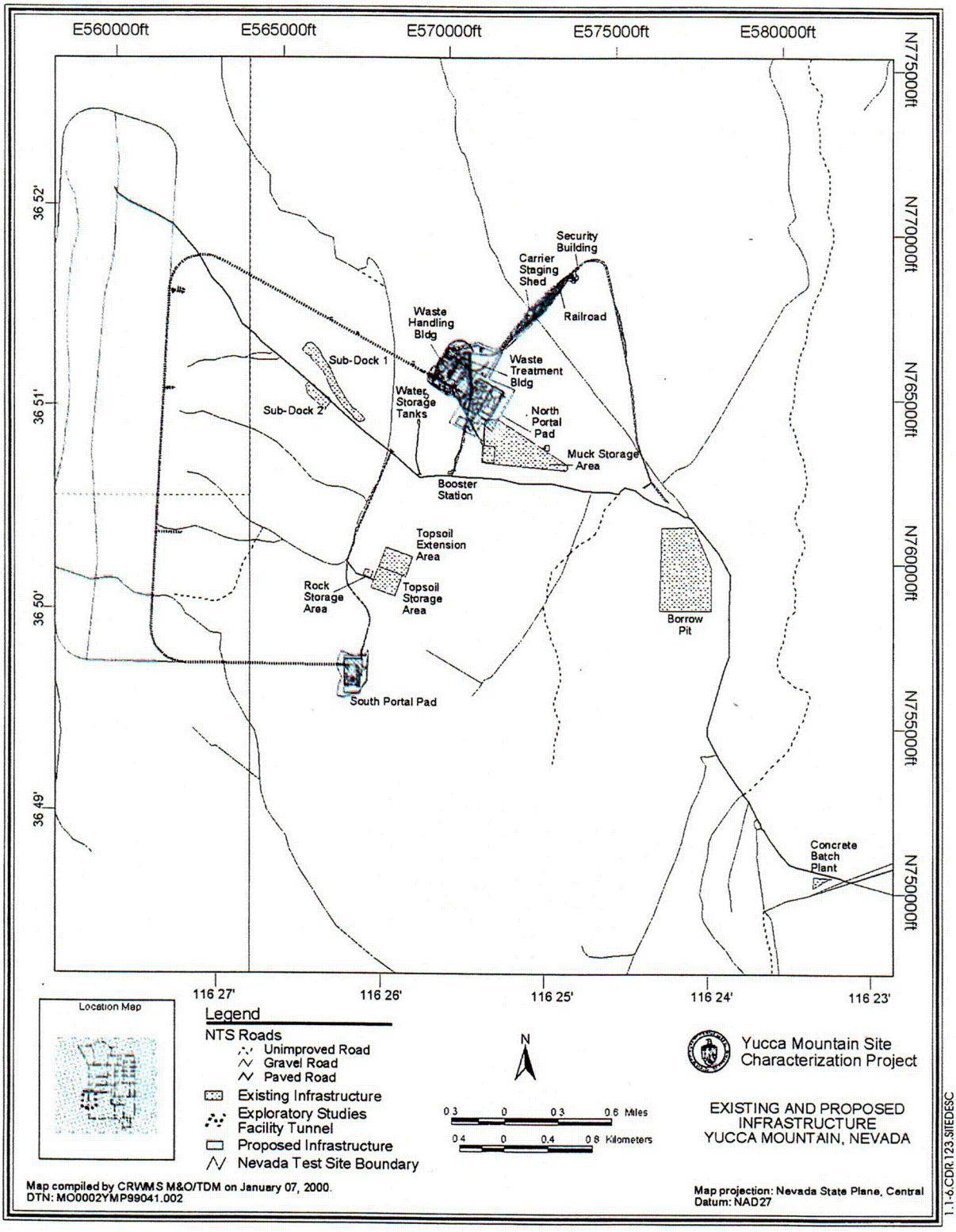

Figure 2.2-8. Existing and Proposed Infrastructure at Yucca Mountain, Nevada

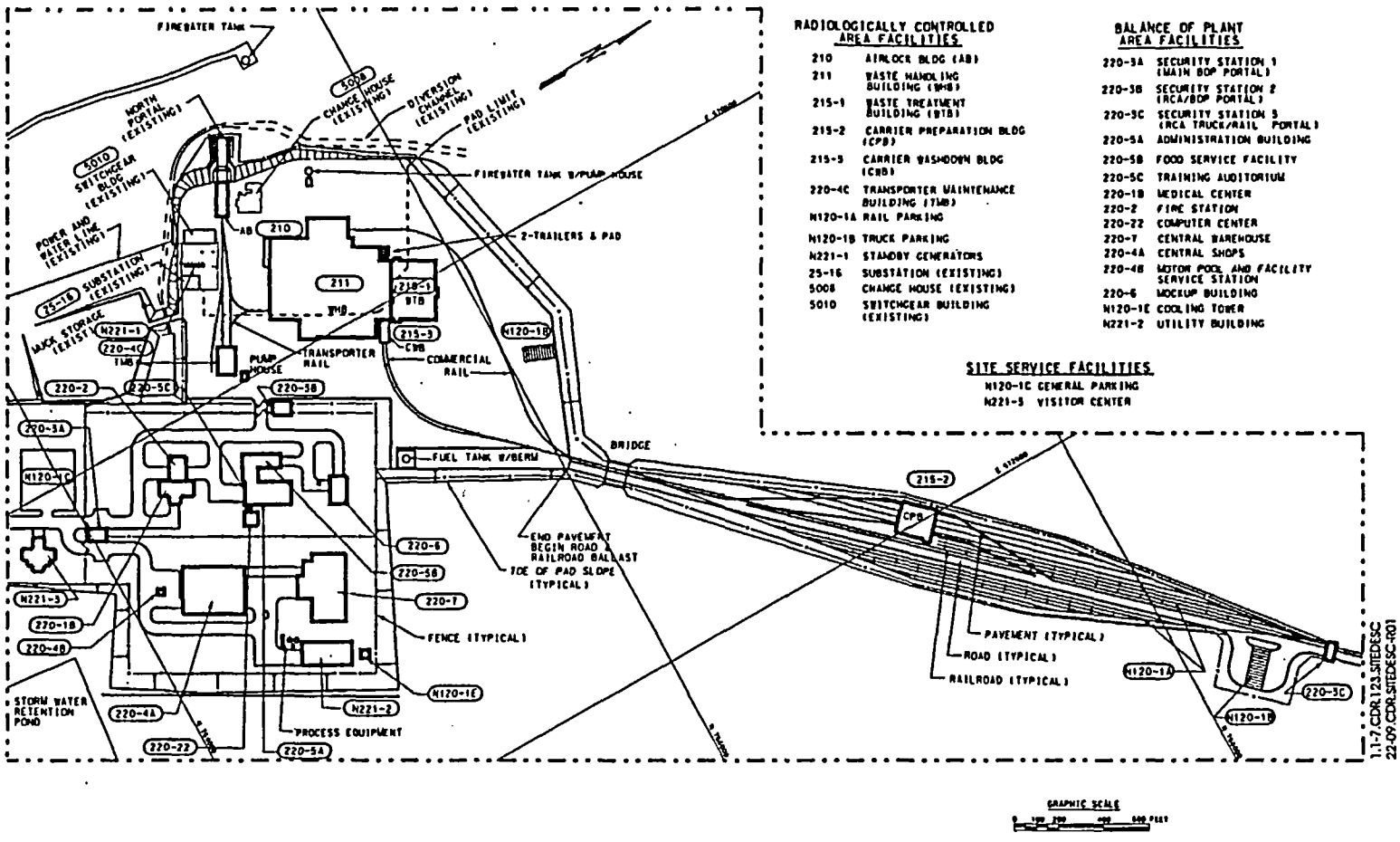

Source: CRWMS M&O (1999b, Attachment IV, Figure 4)

NOTE: This figure will be updated as the configuration of the surface facilities evolves.

Figure 2.2-9. North Portal Operations Area

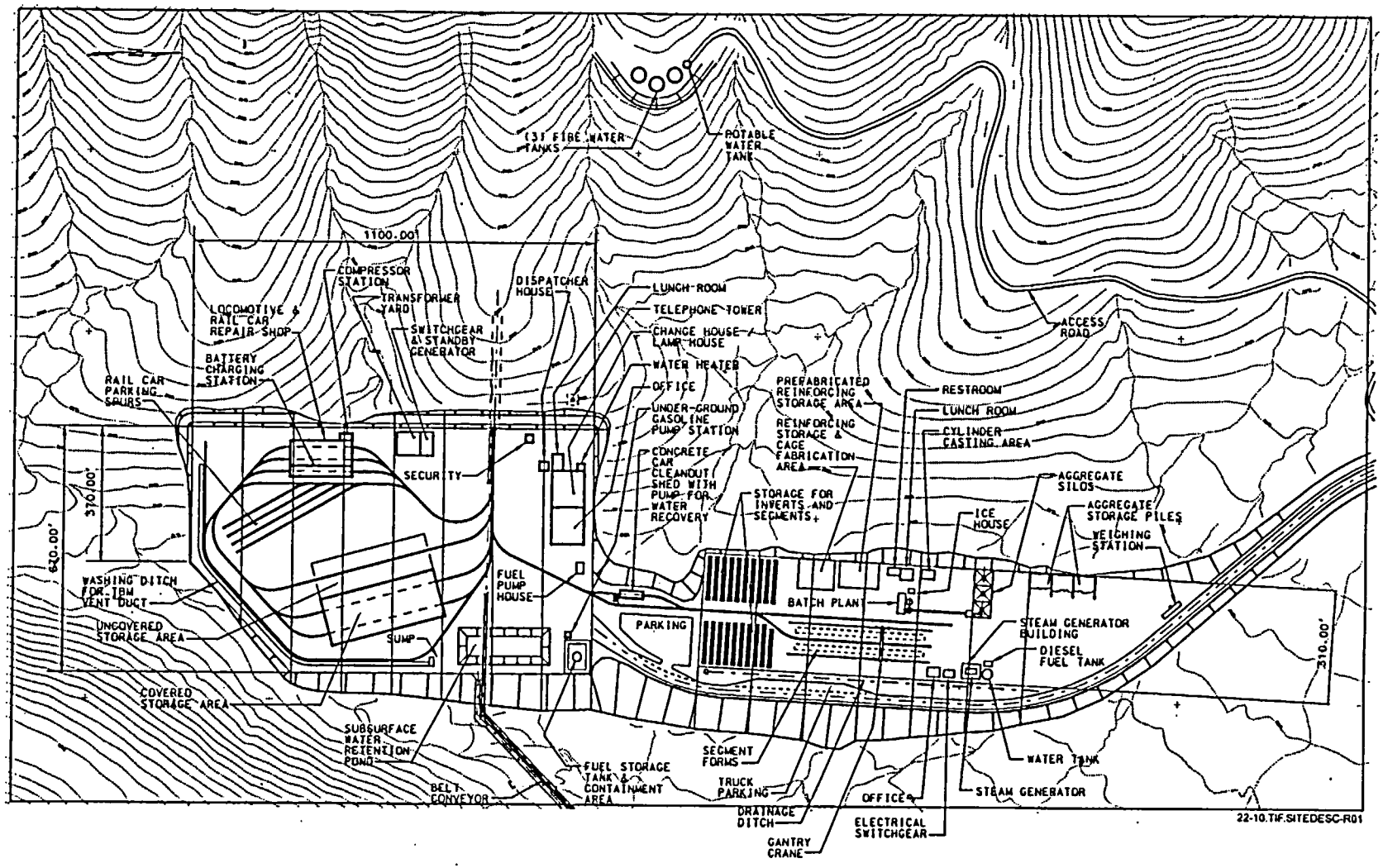

Source: CRWMS M&O (1999c, Figure 4.3.2.1-1)

NOTE: Illegibility of topographic contour values does not affect the technical content and purpose of this figure.

Figure 2.2-10. South Portal Development Operations Area

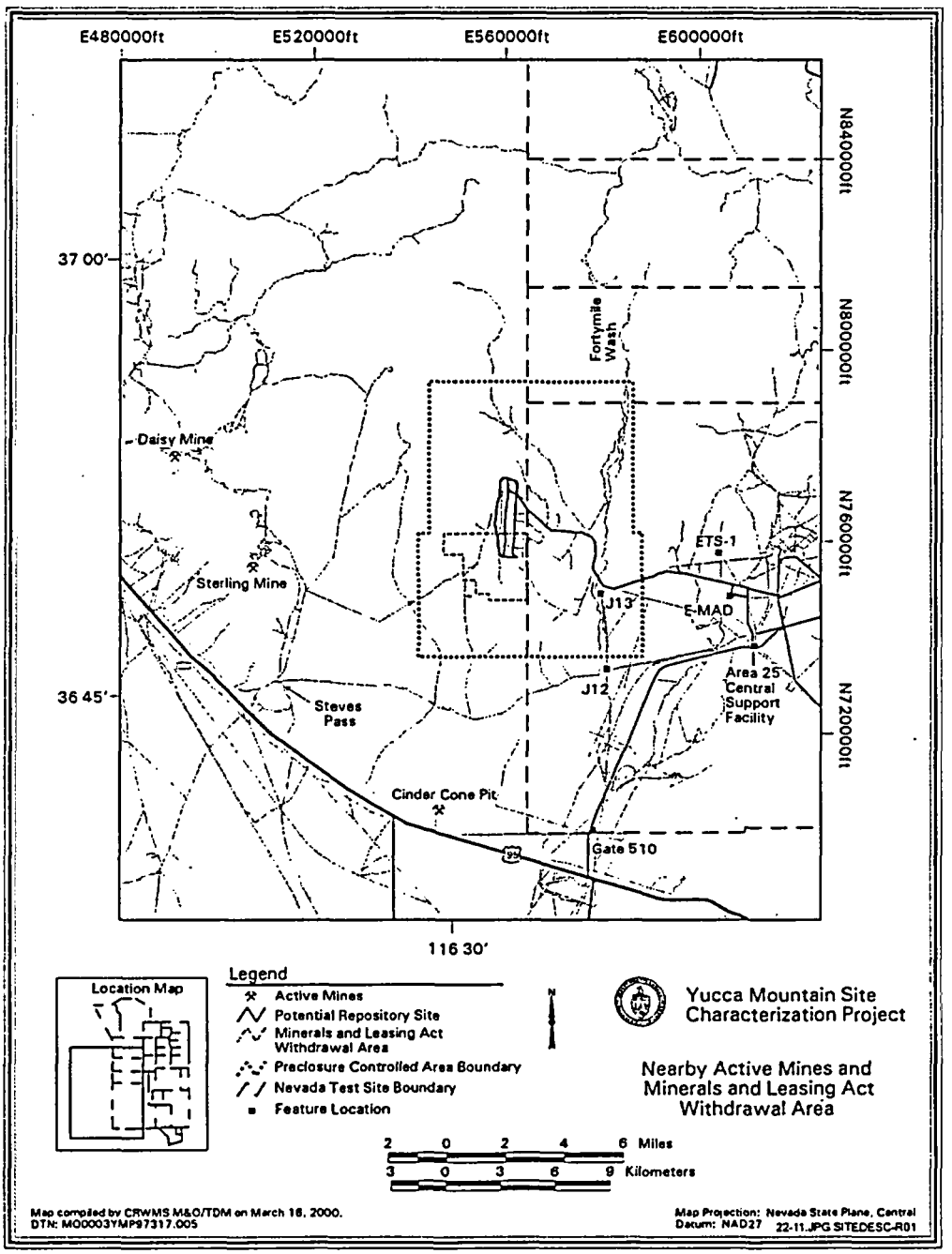

Figure 2.2-11. Nearby Active Mines and Minerals and Leasing Act Withdrawal Area

INTENTIONALLY LEFT BLANK

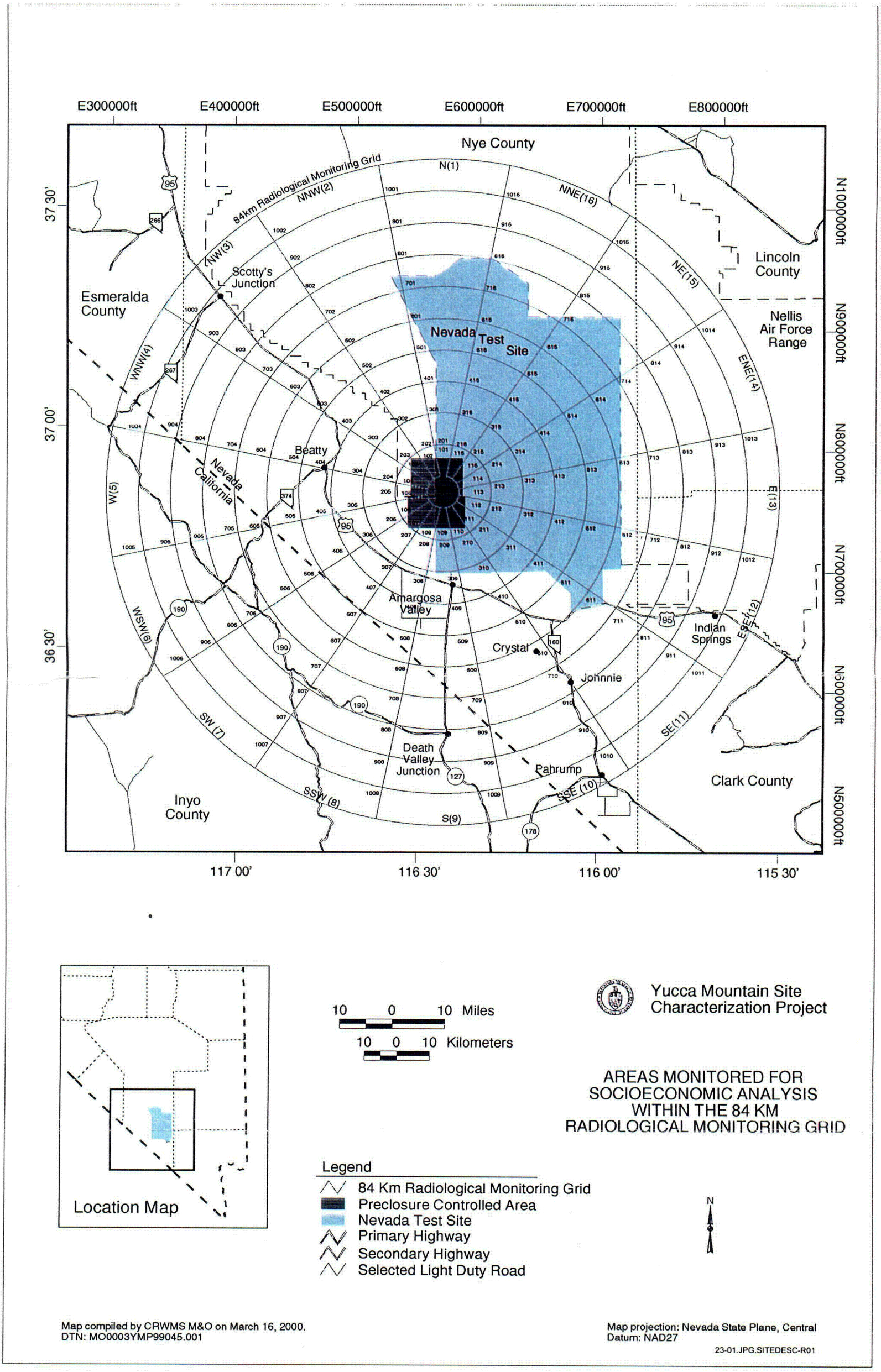

Figure 2.3-1. Areas Monitored for Socioeconomic Analysis within the 84 Kilometer Radiological Monitoring Grid

INTENTIONALLY LEFT BLANK

Table 2.2-1. Location of Facilities and Infrastructure near the Preclosure Controlled Area

Area	Facility Name	Geographic (Degree-Minute-Second)		State Plane Coordinates (feet)	
		Longitude	Latitude	Easting	Northing
Administrative Areas	Preclosure Controlled Area	TBD	TBD	TBD	TBD
	Postclosure Controlled Area	TBD	TBD	TBD	TBD
	Restricted Area	TBD	TBD	TBD	TBD
Existing Surface Facilities (Outside Preclosure Controlled Area)	Canyon Sub-Station	-116 20 33	36 49 26	594845	755047
	Test Cell 'C'	-116 16 43	36 49 49	613578	757423
	Area 25 Central Support Facility	-116 17 15	36 46 43	611074	738555
	Engine Maintenance and Disassembly Building (EMAD)	-116 18 6	36 48 29	606852	749242
	Reactor Maintenance and Disassembly Building (RMAD)	-116 14 24	36 49 12	624884	753714
	Engine Test Stand 1 (ETS-1)	-116 18 36	36 49 48	604383	757271
	Desert Rock Airport	-116 01 52	36 37 13	686477	681353
	CP-300	-116 17 21	36 48 32	610480	749636
	Mercury	-116 0 3	36 39 38	695240	696086
	Gate 100	-116 0 14	36 37 32	694418	683359
	Gate 510	-116 24 14	36 40 15	577037	699240
	Treatability Test Facility	-116 17 24	36 46 41	610309	738384
	BREN Tower	-116 14 47	36 46 33	623085	737628
	Wahmonie (Sandia National Laboratories Launch Site)	-116 09 33	36 48 42	648560	750797

DTNs: M09905NTSTRFAC.000; MO0001GSC00040.000

NOTES: TBD = to be determined
Coordinates are for geographic center of facility.

Table 2.2-2. Location and Characteristics of Facilities and Infrastructure in the Preclosure Controlled Area

Area	Facility Name	Geographic (Degree-Minute-Second)		State Plane Coordinates (feet)	
		Longitude	Latitude	Easting	Northing
Existing Surface Facilities (Inside Preclosure Controlled Area)	Booster Station	-116 25 34	36 50 40	570405	762411
	Borrow Pit	-116 24 09	36 50 11	577273	759489
	Concrete Batch Plant	-116 23 20	36 48 38	581254	738659
	Muck Storage Area (North Portal)	-116 25 12	36 50 48	572160	763235
	North Portal Pad	-116 25 36	36 51 09	570169	765355
	Rock Storage Area	-116 26 03	36 50 10	567963	759384
	South Portal Pad	-116 26 10	36 49 41	567440	756415
	Sub-Dock 1	-116 26 17	36 51 07	566883	765170
	Sub-Dock 2	-116 26 22	36 51 03	566442	764692
	Topsoil Storage Area	-116 25 58	36 50 08	568434	759142
	Topsoil Extension Area	-116 25 53	36 50 14	568784	759752
	Water Storage Tank	-116 25 45	36 50 55	569485	763937
Potential Repository Surface Facilities (Inside Preclosure Controlled Area)	**North Portal Operations Area: Radiologically Controlled Area Facilities**				
	Airlock Building	-116 25 48	36 51 00	571554	765282
	Waste Handling Building	-116 25 31	36 51 17	570599	766151
	Waste Treatment Building	-116 25 29	36 51 20	570796	766436
	Carrier Preparation Building	-116 25 04	36 51 34	572794	767932
	Transporter Maintenance Building	-116 25 30	36 51 04	570693	764887
	Carrier Washdown Buildings	-116 25 28	36 51 11	570898	765582
	Switchgear Building with Transformer	-116 25 37	36 51 06	570142	765057
	Change House (North Portal)	-116 25 37	36 51 15	570116	766002
Potential Repository Surface Facilities (Inside Preclosure Controlled Area)	**North Portal Operations Area: Balance of Plant Areas**				
	Security Station 1 (Main BOP Portal)	-116 25 26	36 51 06	571071	765040
	Security Station 2 (RCA/BOP Portal)	TBD	TBD	TBD	TBD
	Security Station 3 (RCA truck/rail Portal)	-116 24 47	36 51 41	570902	768608
	Administration Building	-116 24 49	36 51 44	574061	768952
	Medical Center	-116 25 25	36 51 00	571127	764397
	Fire Station	-116 25 26	36 51 00	571039	764446
	Central Warehouse	-116 25 17	36 51 04	571756	764815
	Central Shops	-116 25 20	36 50 59	571501	764317
	Motor Pool and Facility Service Station	-116 25 20	36 51 00	571502	764507
	Mockup Building	-116 25 21	36 51 06	571412	765062
	Utility Building	TBD	TBD	TBD	TBD

Table 2.2-2. Location and Characteristics of Facilities and Infrastructure in the Preclosure Controlled Area (Continued)

Area	Facility Name	Geographic (Degree-Minute-Second)		State Plane Coordinates (feet)	
		Longitude	Latitude	Easting	Northing
	North Portal Operations Area: Site Services Areas				
Potential Repository Surface Facilities (Inside Preclosure Controlled Area)	General Parking (multiple locations)	TBD	TBD	TBD	TBD
	Cooling Tower	-116 25 14	36 51 03	572024	764732
	Visitor Center	-116 25 26	36 50 53	571030	763754
	South Portal Development Operations Area				
	Covered Laydown and Storage Area (warehouse)	-116 26 08	36 49 38	567669	756136
	Locomotive and Railcar Repair Shop	-116 26 09	36 49 38	567518	756185
	Transformer Yard	TBD	TBD	TBD	TBD
	Air Compressor Building	-116 26 10	36 49 39	567469	756258
	Change House	-116 26 12	36 49 37	567327	756015
	Portal Site Offices	-116 26 12	36 49 38	567325	756166
	Optional Tuff Crushing and Screening Plant	TBD	TBD	TBD	TBD
	Aggregate Storage Area	TBD	TBD	TBD	TBD
	Concrete Car Cleanout Shed	-116 26 07	36 49 40	567713	756372
	Concrete Batch Plant	-116 26 07	36 49 40	567752	756313
	Water Storage Tanks	TBD	TBD	TBD	TBD
	Discharge Water Evaporation Pond	TBD	TBD	TBD	TBD
	Dispatcher House	TBD	TBD	TBD	TBD
	Diesel Fuel Storage Tank with Sump	TBD	TBD	TBD	TBD
	Truck Unloading Area	TBD	TBD	TBD	TBD
	Surface Rail Parking Area	TBD	TBD	TBD	TBD
	Security Station - Main Gate	TBD	TBD	TBD	TBD
	Security Station - South Portal Entrance	-116 26 24	36 49 48	566337	757154

DTNs: MO9904COV97380.000; MO9904COV8016A.000; MO9904COV8016B.000

Sources: CRWMS M&O (1999b, 1999c); Figure 2.2-8

NOTES: TBD = to be determined; NA = not available

Coordinates, areas, and perimeters for existing surface facilities (inside preclosure controlled area) are calculated by Geographic Information System algorithm. Area and perimeter for potential repository surface facilities (inside preclosure controlled area) are from CRWMS M&O (1999b, Table 4-2).

INTENTIONALLY LEFT BLANK

Table 2.3-1. 1998 Population of Incorporated and Unincorporated Cities and Towns in Clark, Lincoln, and Nye Counties

Place Name	Population
Clark County	1,255,200
Incorporated	
Boulder City	14,730
Henderson	159,380
Las Vegas	441,230
Mesquite	12,070
North Las Vegas	106,660
Unincorporated	
Bunkersville	850
East Las Vegas (1990)	11,087[a]
Enterprise	13,210
Glendale	80
Indian Springs	3,110
Laughlin	7,790
Moapa	590
Moapa Valley	5,370
Mt. Charleston	970
Paradise	164,170
Searchlight	740
Spring Valley	107,100
Sunrise Valley	147,680
Whitney	13,420
Winchester	30,280

Place Name	Population
Lincoln County	4,190
Incorporated	
Caliente	1,150
Unincorporated	
Alamo	480
Panaca	580
Pioche	920
Nye County	29,730
Incorporated	
Gabbs	390
Unincorporated	
Amargosa Valley	1,100
Beatty	1,600
Manhattan	140
Pahrump	20,080
Round Mountain	960
Tonopah	3,280

Sources: Nevada State Demographer (1999a, 1999b, 1999c)

NOTE: [a]U.S. Census Bureau (1993)

Table 2.3-2. Population Density of Clark, Lincoln, and Nye Counties

County	1998 Population	Area (km^2)	Persons (km^2)
Clark	1,255,200	20,488	61.27
Lincoln	4,190	27,543	0.15
Nye	29,730	47,001	0.63

Sources: Nevada State Demographer (1999a); U.S. Census Bureau (1996)

NOTE: Multiply square kilometers by 0.3861 to obtain square miles.

Table 2.3-3. Population Projections for Clark, Lincoln, and Nye Counties

County	2002	2007	2012	2017
Clark	1,529,680	1,843,920	2,166,830	2,552,270
Lincoln	4,490	4,360	4,460	4,560
Nye	39,880	48,820	56,820	64,290

Source: Nevada State Demographer (1999d)

Table 2.3-4. Estimated Population by Grid Cell within 84 Kilometers (52 Miles) of the Yucca Mountain Site, First Quarter 1998

Direction	Population by Distance (km)										
	4	12	20	28	36	44	52	60	68	76	84
S (09)	0	0	0	16	230	398	108	0	10	0	0
SSW (08)	0	0	0	0	298	38	0	0	7	0	0
SW (07)	0	0	0	0	0	0	0	804	0	0	0
WSW (06)	0	0	0	0	0	0	0	0	0	87	0
W (05)	0	0	0	0	735	17	0	0	0	0	0
WNW (04)	0	0	0	0	1,121	0	0	0	0	0	20
NW (03)	0	0	0	0	28	2	0	0	0	33	0
NNW (02)	0	0	0	0	0	0	0	0	0	0	0
N (01)	0	0	0	0	0	0	0	0	0	0	0
NNE (16)	0	0	0	0	0	0	0	0	0	0	0
NE (15)	0	0	0	0	0	0	0	0	0	0	0
ENE (14)	0	0	0	0	0	0	0	0	0	0	0
E (13)	0	0	0	0	0	0	0	0	0	0	0
ESE (12)	0	0	0	0	0	0	0	0	0	1,389	0
SE (11)	0	0	0	0	0	3	0	13	0	0	206
SSE (10)	0	0	0	0	0	23	137	11	17	4,529	9,631
Ring No.	0	1	2	3	4	5	6	7	8	9	10
Total per Ring	0	0	0	16	2,412	481	245	828	34	6,038	9,857
Grand Total 84-km Grid											19,911

Sources: CRWMS M&O (1998, p. 3-7)

NOTES: Grid cells are numbered by distance (kilometer) and direction from the center of the radiological monitoring grid. Each concentric ring around the center of the grid is consecutively numbered from 1 to 10. Each sector is numbered from 1 to 16 in a counterclockwise manner with north being 01 and north northwest being 02. For example, the grid cell that is the third ring (20 to 28 km from center) and due south of the repository would be grid cell 309 and would have a population of 16. These grid cell numbers are shown on Figure 2.3-1 and used in Table 2.3-5.

Table 2.3-5. Estimates of Resident Population and Population Density within the Radiological Monitoring Grid by Area and Grid Cell, First Quarter 1998

	Population	Area (km^2)	Population Density (persons/km^2)
Nye County, Nevada			
Amargosa Valley area			
Grid Cell 309 (Lathrop Wells)	16	75.40	0.21
Grid Cell 408 (Farming Triangle)	298	100.53	2.96
Grid Cell 409 (Farming Triangle)	230	100.53	2.29
Grid Cell 508 (Farming Triangle)	38	125.66	0.30
Grid Cell 509 (Farming Triangle)	398	125.66	3.17
Grid Cell 510 (Crystal Heights)	23	125.66	0.18
Grid Cell 511 (Specter Range)	3	125.66	0.02
Grid Cell 609 (Stateline)	108	150.80	0.72
Grid Cell 610 (Crystal)	137	150.80	0.91
Grid Cell 710 (Ash Meadows)	11	175.93	0.06
Amargosa Valley subtotal within the 84-km grid	1,262	NA	NA
Beatty area			
Grid Cell 403 (Oasis Valley)	28	100.53	0.28
Grid Cell 404 (Beatty)	1,121	100.53	11.15
Grid Cell 405 (Beatty)	735	100.53	7.31
Grid Cell 503 (Oasis Valley)	2	125.66	0.02
Grid Cell 505 (Rhyolite)	17	125.66	0.14
Grid Cell 903 (Scotty's Junction)	33	226.19	0.15
Beatty subtotal within the 84-km grid	1,936	NA	NA
Pahrump area			
Grid Cell 710 (Johnnie)	13	175.93	0.07
Grid Cell 810 (Pahrump)	17	201.06	0.08
Grid Cell 910 (Pahrump)	4,529	226.19	20.02
Grid Cell 1010 (Pahrump and Stewart Valley)[a]	9,631	251.33	38.32
Pahrump subtotal within the 84-km grid	14,190	NA	NA
Mercury	0	—	0
Clark County, Nevada			
Indian Springs area			
Grid Cell 912 (Indian Springs and Cactus Springs)	1,389	226.19	6.14
Grid Cell 1011 (Cold Creek and Willow Creek)	206	251.33	0.82
Indian Springs subtotal within the 84-km grid	1,595	NA	NA
Esmeralda County, Nevada	0	—	0
Lincoln County, Nevada	0	—	0
Inyo County, California			
Death Valley area			
Grid Cell 707 (Furnace Creek)	804	175.93	4.57
Grid Cell 808 (Ryan)	7	201.06	0.03
Grid Cell 809 (Death Valley Junction)[a]	10	201.06	0.05
Grid Cell 906 (Stovepipe Wells)	87	226.19	0.38
Grid Cell 1004 (Scotty's Castle)	20	251.33	0.08
Death Valley subtotal within the 84-km grid[a]	928	NA	NA
Grand Total in the 84-km Grid	**19,911**	**4,021.24**	**4.95**

Source: CRWMS M&O (1998, p. 3-7)

NOTES: [a] Grid cell 809 (Death Valley Junction) is not in Death Valley National Park. Stewart Valley population of 17 in California is included in Grid Cell 1010 in Pahrump.

NA = not applicable

Multiply square kilometers by 0.3861 to obtain square miles.

Table 2.3-6. Estimates of Federally Owned Land in Nevada by Entitlement Acreage and County, Fiscal Year 1995 (in Acres)

County	Bureau of Land Management	U.S. Forest Service	National Park Service	Fish and Wildlife Service[g,h]	U.S. Air Force[i,j]	Department of Energy	Other Federal Holdings	Total Federal Land Holdings	Total County Land Area	Federal Land (%)
Clark[a]	2,900,000	252,000	587,000	820,000	13,500	0	50,700	4,623,200	5,120,000	90.30
Nye[b]	6,548,338	1,966,671	107,648	24,724	1,946,504	765,795	0	11,359,680	11,619,200	97.77
Lincoln[c,d,e]	5,633,723	30,672	0	761,490	242,329	46,713	671	6,715,598	6,816,000	98.53
Nevada[f,k]	47,969,220	5,805,129	l	2,218,411	2,903,606	797,842	1,030,194	60,724,402	70,745,700	85.83

Source: [a]Clark County Natural Resource Team (1997)
[b]Pahrump Valley Times (2000, p. B11)
[c]USAF (1999, pp. ES-7, 3.10-5, 3.10-9)
[d]DOE (1996, p. 4-5)
[e]Nevada Department of Administration (2000a)
[f] Nevada Department of Administration (2000b)

NOTE: [g]Clark County contains 327,000 acres of land co-managed with U.S. Air Force (Co-location of Desert National Wildlife Range and Nellis Air Force Range).
[h]Lincoln County contains 499,000 acres of land co-managed with U.S. Air Force (Co-location of Desert National Wildlife Range and Nellis Air Force Range).
[i] U.S. Air Force totals do not include acres co-managed with U.S. Fish and Wildlife Service (Co-location of Desert National Wildlife Range and Nellis Air Force Range).
[j] U.S. Air Force land is Nellis Air Force Range in Nye and Lincoln; Nellis Air Force Base in Clark County.
[k]Data compiled at different times (1987 and 1995) and using different methods. Totals may not agree.
[l] The total is contained in "Other Federal Holdings."
Multiply acres by 0.004047 to obtain square kilometers.

Table 2.3-7. Population and Growth in Nye County and Pahrump

Location	Population				
	1980[a]	1990[b]	Growth: 1980-1990	1998[c]	Growth: 1990-1998
Nye County	9,048	17,781	8,733	29,730	11,949
Pahrump	3,311	7,425	4,114	20,080	12,655

Sources: [a] DOE (1988b, p. 15)
[b] U.S. Census Bureau (1993)
[c] Nevada State Demographer (1999a, 1999b)

INTENTIONALLY LEFT BLANK

3. NEARBY INDUSTRIAL, TRANSPORTATION, AND MILITARY FACILITIES

3.1 INTRODUCTION

This section identifies potential events associated with present and projected industrial, transportation, and military facilities and operations that occur in the vicinity of the Yucca Mountain site. These events need to be evaluated for their potential effect on daily operations and performance of the potential repository, or for their use in identifying design basis events to establish design parameters. Industrial operations include commercial operations, such as agriculture.

The U.S. Nuclear Regulatory Commission (NRC) has proposed a rule (proposed 10 CFR 63 [64 FR 8640]) to govern the licensing of the U.S. Department of Energy to receive and possess source, special nuclear, and byproduct material at a geologic repository operated in accordance with the Nuclear Waste Policy Act of 1982, as amended. The U.S. Department of Energy has issued Interim Guidance (Dyer 1999) to be used within the Yucca Mountain Site Characterization Project for planning for the Site Recommendation and draft License Application until the NRC issues its final regulations. The License Application developed in accordance with this Interim Guidance will include a Safety Analysis Report that describes and assesses features of the Yucca Mountain site that might affect the operations, design, and performance of the potential repository.

At this time, existing regulatory guidance does not define a distance from the potential repository within which all facilities and operations must be identified and analyzed for potential impact on the potential repository. Therefore, this document uses as guidance NRC requirements established for nuclear power plants, specifically NUREG 0800 (NRC 1981, Sections 2.2.1 and 2.2.2) and Regulatory Guide 1.70 (Section 2.2), which direct the identification of all facilities and activities within 8 km (5 mi.) of a power plant. Both documents also direct that facilities and activities at greater distances should be analyzed if they have the potential for affecting safety-related features.

The term "plant" is interpreted for this section to represent the existing surface facilities at the Yucca Mountain site and repository-related surface facilities (see Section 2.2) that will be active if the potential repository at Yucca Mountain is authorized for waste reception. The area within an 8-km (5-mi.) radius of the potential repository includes parts of the Nellis Air Force Range, Area 25 of the Nevada Test Site, and public lands managed by the U.S. Bureau of Land Management (Figures 3.1-1 and 3.1-2). The 8-km (5-mi.) area discussed in this section is shown on Figures 3.1-1 and 3.1-2 and is centered at the Waste Handling Building, which will be located on the North Portal Pad of the Exploratory Studies Facility.

Facilities and activities near the potential repository were screened for their potential impact on the potential repository (CRWMS M&O 2000, p. 57). Further analyses of potential impacts on the repository from nearby facilities and activities are discussed in *Industrial/Military Activity-Initiated Accident Screening Analysis* (CRWMS M&O 1999a, pp. 23, 31 to 32) and *MGR Aircraft Crash Frequency Analysis* (CRWMS M&O 1999b).

Information for this section came from both external and internal (Yucca Mountain Site Characterization Project-specific) documents. Primary external sources include the *Final Environmental Impact Statement for the Nevada Test Site and Off-Site Locations in the State of Nevada* (DOE 1996) and the *Draft Environmental Impact Statement for a Geologic Repository for the Disposal of Spent Nuclear Fuel and High-Level Radioactive Waste at Yucca Mountain, Nye County, Nevada* (DOE 1999). Additional information came from the U.S. Department of Commerce (DOC 1998) and U.S. Department of Defense flight charts (DOD 1997) used in the development of Figure 3.1-1 and the *Renewal of the Nellis Air Force Range Land Withdrawal: Legislative Environmental Impact Statement* (USAF 1999).

3.2 NEARBY FACILITIES AND ACTIVITIES WITHIN EIGHT KILOMETERS (FIVE MILES) OF THE POTENTIAL REPOSITORY

Within 8 km (5 mi.) of the potential repository are lands controlled by the U.S. Air Force, the U.S. Department of Energy (DOE), and the U.S. Bureau of Land Management. Airspace in this area is controlled by the U.S. Air Force and the DOE. This section discusses facilities and activities outside the Yucca Mountain site but within the 8-km radius identified in Section 3.1.

Airspace–The area within 8 km (5 mi.) of the potential repository is located beneath or adjacent to restricted airspace areas, control over which has been delegated to the U.S. Air Force and the DOE by the Federal Aviation Administration (USAF 1999, p. 3.1-3). This restricted airspace was established because of the classified or hazardous nature of the activities conducted within these airspaces or in the areas beneath these airspaces (USAF 1999, Section 3.1, Introduction, p. 2). Restricted area R-4807 extends north of the potential repository site over Nellis Air Force Range withdrawn lands and overlies ground support facilities for military air-to-ground weapons training, including convoys, simulated airfields, and electronic combat threat emitters. Electronic Combat (EC) South (Figure 3.1-1) is the closest subrange of R-4807 to the potential repository. Electronic Combat South is primarily used as an entry/exit corridor for the R-4807 subranges and contains manned electronic threat emitters (USAF 1999, pp. 3.1-3 to 3.1-4). No live ordnance is used in this area (USAF 1994, pp. 15, 17).

The potential repository underlies the western portion of R-4808 (R-4808W), a DOE-restricted area associated with Nevada Test Site activities (Figure 3.1-1). By agreement with the DOE, military aircraft may use flight routes within R-4808 for entering and exiting R-4807 (USAF 1999, p. 3.1-4). Nellis aircraft using R-4808 to enter and exit the Nellis Air Force Range are randomly dispersed. There are currently no set entry and exit routes. Ongoing discussions between the DOE Nevada Operations Office and Nellis Air Force Base will result in a memorandum of understanding regarding use of R-4808 for entering and exiting the Nellis Air Force Range complex.

Numerous military training routes that traverse the state are used by U.S. Air Force and Navy aircraft for low-level, high-speed flight training (DOE 1996, pp. 4-25 to 4-30). One of these routes, VR-222, lies south and west of the potential repository and outside the Nellis Air Force Range (Figure 3.1-1). *MGR Aircraft Crash Frequency Analysis* (CRWMS M&O 1999b) examines the frequencies of aircraft crashes on radioactive material control facilities at the potential repository. The analysis concluded that "the aircraft crash external event at a potential repository at Yucca Mountain is not considered a credible event" (CRWMS M&O 1999b, p. 28). See CRWMS M&O (1999b) for details on this analysis.

Nevada Test Site Area 25–Area 25, the largest area on the Nevada Test Site, occupies 223 $mi.^2$ (DOE 1996, p. 4-16) and is divided into four land use zones (Figure 3.1-2): the Yucca Mountain Site Characterization Zone; the Research, Test, and Experiment Zone; the Reserved Zone; and the Solar Enterprise Zone. The Solar Enterprise Zone is reserved for use by the Nevada Test Site for construction and operation of a solar power generation facility (DOE 1996, p. 3.1-1; 61 FR 65551, p. 65561). The Yucca Mountain Site Characterization Zone is reserved for use by the DOE for Yucca Mountain site characterization activities. The Research, Test, and Experiment Zone is used by the U.S. Army Ballistic Research Laboratory for depleted uranium

testing and other activities. Reserved Zones at the Nevada Test Site are used to provide area and facilities that allow flexible support for diverse short-term testing and experimentation. The Reserved Zone in Area 25 is used for military land navigation and training exercises (DOE 1996, pp. 4-16 to 4-17). The 8-km (5-mi.) area around the Yucca Mountain site includes a portion of the Area 25 Reserved Zone, but not the Research, Test, and Experiment Zone or the Solar Enterprise Zone. However, there are no facilities associated with the Reserved Zone within the 8-km (5-mi.) area (Figure 3.1-2). Other Area 25 facilities and activities more than 8 km (5 mi.) from the potential repository are discussed in Section 3.3.

U.S. Bureau of Land Management Land–There are no known formal industrial or commercial land uses or infrastructure on U.S. Bureau of Land Management land (exclusive of dirt roads) within 8 km (5 mi.) of the potential repository.

3.3 FACILITIES AND ACTIVITIES MORE THAN EIGHT KILOMETERS (FIVE MILES) FROM THE POTENTIAL REPOSITORY

Outside of the 8-km (5-mi.) radius from the potential repository, there are military, transportation, and industrial or commercial facilities and activities on the Nellis Air Force Range, the Nevada Test Site, and U.S. Bureau of Land Management land that could affect daily operations and performance or be used as design basis events for the potential repository.

Nellis Air Force Range–The Nellis Air Force Range "north range" extends north of Electronic Combat (EC) South (Figure 3.1-1) and is used extensively for weapons training and testing. Large amounts of live and inert ordnance are used on the northern portions of this range that are approved for ordnance use. There are substantial numbers of aircraft flights within the north range, where training missions, exercises, and weapons testing take place daily. Although Yucca Mountain is not directly beneath any military routes (DOC 1998) or in close proximity to live ordnance use on the Nellis Air Force Range (USAF 1999, pp. 3.1-3 to 3.1-4), the high density of flights in the Nellis Air Force Range and the possibility of an aircraft accident could pose a threat to daily operations and performance of the potential repository. Such accidents could be considered design basis events. Safety analyses considering Nellis Air Force Range aircraft activities on the Nevada Test Site relative to the potential repository are discussed in *Industrial/Military Activity-Initiated Accident Screening Analysis* (CRWMS M&O 1999a) and *MGR Aircraft Crash Frequency Analysis* (CRWMS M&O 1999b). The latter analysis concluded that the frequency of an aircraft crash into the potential repository is less than 1×10^{-6} per year and is not considered a credible event (CRWMS M&O 1999b, pp. 27 to 28).

Nevada Test Site (Area 25)–As discussed in Section 3.2, Area 25 is divided into four land use zones: the Yucca Mountain Site Characterization Zone; the Reserved Zone; the Research, Test, and Experiment Zone; and the Solar Enterprise Zone (Figure 3.1-2). Research sites within the Area 25 Reserved Zone include the Treatability Test Facility and the Bare Reactor Experiment Nevada (BREN) Tower. The Treatability Test Facility was established for bench-scale testing of physical processes for separating plutonium and uranium from contaminated soils. The 465-m-high BREN Tower has been used by a number of organizations to conduct sonic boom research, meteorological studies, and free-fall/gravity drop tests. The Solar Enterprise Zone is designated for the development of a solar energy power-generation facility and associated light industrial equipment and commercial manufacturing capability. In the 1980s, Area 25 was used for MX missile siting studies and canister ejection certification tests (DOE 1996, pp. 4-16 to 4-17). For point of reference, Figure 3.1-2 also shows facilities discussed in Section 2.2 and shown in Figure 2.2-7.

Nevada Test Site (Other Than Area 25)–The Nevada Test Site was the primary location of U.S. continental nuclear weapons testing from 1945 to 1992; during that period, more than 900 aboveground and below ground nuclear weapons tests were performed. Underground nuclear tests ceased in 1992 due to a testing moratorium; however, the U.S. Department of Energy (DOE) is still directed by the Executive Office to maintain a state of preparedness to test nuclear weapons in the future. Potential areas for future tests include Pahute Mesa and Yucca Flat (DOE 1996, pp. 2-4, 3-2), both of which lie within approximately 60 km of the potential repository (Figure 3.1-2). Nuclear weapons tests may affect seismicity in the region, as discussed in Section 12.3. Also, administrative policies enforced during such weapons tests

could affect the daily operations of the potential repository. In addition to maintaining preparedness for possible nuclear weapons testing, Nevada Test Site operations include destroying damaged nuclear weapons and conducting dynamic experiments under the Stockpile Stewardship Program, including impact, passive, and chemical tests (DOE 1996, p. 3-2). No activities under the Stockpile Stewardship Program, including potential resumption of underground tests, are anticipated to have adverse impacts on facilities and operations of the potential repository (CRWMS M&O 1999a, pp. 17 to 18). Another activity includes rocket launches by Sandia National Laboratories from Wahmonie in Area 26 to the Tonopah Test Range, approximately 113 km (70 mi.) to the northwest (Rogers 1997). Although these activities take place outside of the 8-km area (5-mi.) boundary, they could pose a health or safety hazard and affect daily operations or performance of the potential repository. Other activities at the Nevada Test Site, such as low-level radioactive waste disposal, waste management operations, non-proliferation experiments, and conventional weapons demilitarization activities, are discussed in *Industrial/Military Activity-Initiated Accident Screening Analysis* (CRWMS M&O 1999a, pp. 17 to 23). None of these activities is expected to have adverse impacts on the potential repository. Other current and potential uses of the Nevada Test Site are identified in the Nevada Test Site environmental impact statement (DOE 1996).

A part of the Nevada Test Site is under development for private use. In 1997, a 10-yr. use permit was signed by Nevada Test Site Development Corporation and the DOE, enabling Kistler Aerospace Corporation to begin development of launch operations for a fully reusable orbital launch vehicle (Edwards 1997). In October 1998, a final agreement to operate from Area 18 was signed. Kistler Aerospace was expected to begin construction in Area 18 of the Nevada Test Site (Figure 3.1-2) in the 1999 to 2000 time frame (although construction was not started in 1999), followed by commencement of operations (LVRJ 1998). Kistler Aerospace activities are considered here because launch and reentry activities could potentially pose a health or safety hazard to the potential repository and could be considered a design basis event if Kistler operations continue past 2010.

As the License Application Safety Analysis Report is developed, other new nearby facilities and activities that may pose special public health and safety hazards, or radiological health and safety hazards, to the development, operation, or closure of the potential repository may be identified. For example, it is noted that the DOE Nevada Operations Office is actively seeking diversification of activities at the Nevada Test Site and is promoting development of new operations and missions, including the Kistler Aerospace activities and designation by the National Aeronautics and Space Administration as a launch site for a new generation of unmanned launch vehicles, the VentureStar. Other potential Nevada Test Site activities that could impinge on the remoteness of the potential repository include the development of new transportation corridors or the promotion of mineral resource exploration and development in Area 25. It is important that should such Nevada Test Site activities be initiated, additional safety analyses will need to address such issues.

Other Areas–This document also considers commercial, industrial, and transportation operations more than 8 km (5 mi.) from the Yucca Mountain site that could pose a health or safety hazard or that could affect daily operations at the potential repository. Five such operations have been identified on land outside the Nevada Test Site and Nellis Air Force Range. The first is the Razorback Grazing Allotment (issued by the U.S. Bureau of Land Management),

which borders the southwestern corner of the Nellis Air Force Range and is located just outside the 8 km (5 mi.) area around the potential repository (Figure 3.1-2). Activities associated with grazing are not listed on the hazards list and do not appear to pose a threat to preclosure activities at the potential repository (CRWMS M&O 2000, p. 57).

The second activity is mining near Beatty and associated water usage from volcanic boreholes. Currently, borehole VH-2 is the only known volcanic borehole in the area that provides water for mining activities. Active mines, including the Daisy and the Sterling gold mines, the cinder cone pit, and volcanic boreholes near Yucca Mountain, are shown on Figure 3.1-2. The area also contains numerous other boreholes that have been drilled as part of the site characterization activities. These are not discussed in this section, but their locations are shown in the site atlas (DOE 1997). These mining activities do not present a threat to the potential repository-related activities at Yucca Mountain (CRWMS M&O 1999a, p. 23).

The third activity involves the operations of two gas and oil exploratory wells located approximately 26 km (16 mi.) south of the potential repository's surface facilities. These wells (Felderhoff-Federal No. 23 and Felderhoff-Federal No. 5-1) are south of U.S. Route 95 (and are not shown on Figure 3.1-2) and are sufficiently distant from the site to have no adverse impacts on the repository in the event of an accident (CRWMS M&O 1999a, p. 23).

The fourth activity is aircraft operations within commercial flight paths (Figure 3.1-1) south of the Nevada Test Site and the Yucca Mountain site. The centerlines of Federal Airway V 105, for air traffic below 18,000 ft mean sea level, and overlying Jet Route J-92, for air traffic above 18,000 ft mean sea level (USAF 1999, pp. 3.1-10 to 3.1-12), are approximately 25 km (15 mi.) southwest of the potential repository site. These routes travel from southeast to northwest and are primarily used by commercial air traffic between Reno and Las Vegas and other airports in the southwestern and northwestern United States. U.S. Highway 95 (Figure 3.1-1) is occasionally used as a visual reference by general aviation aircraft flying under visual flight rules through this area. The few aircraft flying under these conditions through this area are limited by Federal Aviation Regulations to altitudes below 18,000 ft mean sea level (DOC 1998). These flight activities do not present a threat to the potential repository-related activities at Yucca Mountain (CRWMS M&O 1999b, pp. 11 to 13).

Another commercial operation in this vicinity is the low-level nuclear waste site (U.S. Ecology) approximately 26 km (16 mi.) west of the surface facilities for the potential repository. There are no activities at this facility which would impact repository activities (CRWMS M&O 1999a, p. 23).

There are no other known commercial or industrial operations greater than 8 km (5 mi.) from Yucca Mountain that could pose a health or safety hazard to the potential repository (CRWMS M&O 1999a, pp. 23, 32).

INTENTIONALLY LEFT BLANK

3.4 NEARBY TRANSPORTATION ROUTES

Transportation routes of potential concern to health, safety, and normal operations at the potential repository are (1) railroads or heavy-haul truck routes that may be built or upgraded to transport high-level radioactive waste to the potential repository and (2) commercial and military flight zones and highways in the vicinity of the Yucca Mountain site. There are no streams or rivers in the Yucca Mountain region capable of supporting commercial water-based transportation.

Railroads and Heavy-Haul Truck Routes–If the potential repository is built and operated, high-level radioactive waste may be transported to Nevada by rail. When the high-level radioactive waste reaches Nevada, it may be transported from the national rail lines to the potential repository by either rail or heavy-haul trucks. There are currently no rail lines to the potential repository at Yucca Mountain; if the rail alternative is selected, a line will have to be constructed. If the heavy-haul alternative is selected, either heavy-haul routes will have to be constructed or existing routes upgraded. There are currently five potential heavy-haul truck routes and five potential rail corridors in Nevada being considered for transportation of high-level radioactive waste to Yucca Mountain. These potential routes have been planned with consideration of necessary rights-of-way, land withdrawals, use restrictions, and land use conflicts. The planning methodology is described in the *Nevada Potential Repository Preliminary Transportation Strategy Study 2* (CRWMS M&O 1996, Volume I, Executive Summary). The potential routes are described and analyzed in *Draft Environmental Impact Statement for a Geologic Repository for the Disposal of Spent Nuclear Fuel and High-Level Radioactive Waste at Yucca Mountain, Nye County, Nevada* (DOE 1999, Volume I, Section 6.3). Only a small portion of each route is close enough to the potential repository to potentially affect daily operations or performance. Scenarios for onsite high-level radioactive waste transportation hazards are being evaluated.

Flight Corridors and Highways–Military and commercial air transportation corridors and activities are described in Sections 3.2 and 3.3. Aside from commercial air corridors, U.S. Highway 95 is the primary transportation route near the Yucca Mountain site. U.S. Highway 95 lies in a northwest/southeast orientation and passes approximately 21 km (13 mi.) to the southwest of the surface facilities at the potential repository (CRWMS M&O 1999a, p. 31). Using methods similar to those described in U.S. Nuclear Regulatory Commission Regulatory Guide 1.91, *Evaluations of Explosions Postulated to Occur on Transportation Routes Near Nuclear Power Plants,* an evaluation was made of potential impacts due to explosion or fire associated with highway transportation accidents. No adverse effects on surface facilities at the potential repository were identified in the evaluation (CRWMS M&O 1999a, p. 32). However, U.S. Highway 95 is the primary land-based route to the potential repository and is heavily relied upon for the transportation of workers and materials to the Nevada Test Site and the Yucca Mountain site. A traffic event on U.S. Highway 95, particularly between Las Vegas and the entrances to the Nevada Test Site (Figure 2.2-7), could disrupt the delivery of high-level radioactive waste, materials, and employees to the potential repository and, hence, affect daily operations or performance, although such an event would likely be of short duration.

INTENTIONALLY LEFT BLANK

3.5 REFERENCES

3.5.1 Documents Cited

CRWMS M&O 1996. *Nevada Potential Repository Preliminary Transportation Strategy Study 2.* B00000000-01717-4600-00050 REV 01. Two volumes. Las Vegas, Nevada: CRWMS M&O. ACC: MOL.19960724.0199; MOL.19960724.0200.

CRWMS M&O 1999a. *Industrial/Military Activity-Initiated Accident Screening Analysis.* ANL-WHS-SE-000004 REV 00. Las Vegas, Nevada: CRWMS M&O. ACC: MOL.20000307.0381.

CRWMS M&O 1999b. *MGR Aircraft Crash Frequency Analysis.* ANL-WHS-SE-000001 REV 00. Las Vegas, Nevada: CRWMS M&O. ACC: MOL.19981221.0203.

CRWMS M&O 2000. *MGR External Events Hazards Analysis.* ANL-MGR-SE-000004 REV 00. Las Vegas, Nevada: CRWMS M&O. ACC: MOL.20000310.0069.

DOC (U.S. Department of Commerce) 1998. *IFR Enroute Low Altitude - U.S.* Chart L-5. 18 June 1998 to 13 August 1998. Washington, D.C.: U.S. Department of Commerce. TIC: 240419.

DOD (U.S. Department of Defense) 1997. *Area Planning Military Training Routes, North and South America.* Flight Information Publication AP/1B. St. Louis, Missouri: National Imagery and Mapping Agency. TIC: 239798.

DOE (U.S. Department of Energy) 1996. *Final Environmental Impact Statement for the Nevada Test Site and Off-Site Locations in the State of Nevada.* DOE/EIS 0243. Volume 1. Las Vegas, Nevada: U.S. Department of Energy, Nevada Operations Office. TIC: 226875.

DOE (U.S. Department of Energy) 1997. *Yucca Mountain Site Characterization Project Site Atlas 1997.* Washington, D.C.: U.S. Department of Energy. TIC: 236826.

DOE (U.S. Department of Energy) 1999. *Draft Environmental Impact Statement for a Geologic Repository for the Disposal of Spent Nuclear Fuel and High-Level Radioactive Waste at Yucca Mountain, Nye County, Nevada.* DOE/EIS-0250D. Summary, Volumes I and II. Washington, D.C.: U.S. Department of Energy, Office of Civilian Radioactive Waste Management. ACC: MOL.19990816.0240.

Dyer, J.R. 1999. "Revised Interim Guidance Pending Issuance of New U.S. Nuclear Regulatory Commission (NRC) Regulations (Revision 01, July 22, 1999), for Yucca Mountain, Nevada." Letter from J.R. Dyer (DOE/YMSCO) to D.R. Wilkins (CRWMS M&O), September 3, 1999, OL&RC:SB-1714, with enclosure, "Interim Guidance Pending Issuance of New NRC Regulations for Yucca Mountain (Revision 01)." ACC: MOL.19990910.0079.

Edwards, J.G. 1997. "Kistler Closer to Liftoff." Las Vegas, Nevada: Las Vegas Review Journal. Accessed September 7, 1999. TIC: 245334. http://www.lvrj.com/plweb-cgi/fastweb?ge...er%26closer%26to%26liftoff%29%3AHEADLINE

LVRJ (Las Vegas Review Journal) 1998. "In Brief: Kistler, NTS Sign Test Site Agreement." Las Vegas, Nevada: Las Vegas Review Journal. Accessed September, 7, 1999. TIC: 245333. http://www.lvrj.com/plweb-cgi/fastweb?ge...er%26closer%26to%26liftoff%29%3AHEADLINE

NRC (U.S. Nuclear Regulatory Commission) 1981. "Identification of Potential Hazards in Site Vicinity." Chapter 2, Section 2.2.1 - 2.2.2 of *Standard Review Plan for the Review of Safety Analysis Reports for Nuclear Power Plants.* LWR Edition. NUREG 0800, Rev. 2. Washington, D.C.: U.S. Nuclear Regulatory Commission. TIC: 239428.

Rogers, K. 1997. "Fire in the Sky." Las Vegas, Nevada: Las Vegas Review Journal. Accessed June 11, 1999. TIC: 241104. http://www.lvrj.com/lvrj home/1997/apr-14-mon-1997/news/5165508.html

USAF (U.S. Air Force) 1994. *Air Force Instruction 13-212.* AFI 13-212. Washington, D.C.: U.S. Department of the Air Force. TIC: 236940.

USAF (U.S. Air Force) 1999. *Renewal of the Nellis Air Force Range Land Withdrawal: Legislative Environmental Impact Statement.* Washington, D.C.: U.S. Department of the Air Force. TIC: 243264.

3.5.2 Codes, Standards, Regulations, and Procedures

61 FR 65551. Record of Decision: Environmental Impact Statement for the Nevada Test Site and Off-Site Locations in the State of Nevada. Readily available.

64 FR 8640. Disposal of High-Level Radioactive Wastes in a Proposed Geologic Repository at Yucca Mountain, Nevada. Proposed rule 10 CFR 63. Readily available.

Nuclear Waste Policy Act of 1982. 42 U.S.C. 10101 et seq. Readily available.

Regulatory Guide 1.70, Rev. 3. 1978. *Standard Format and Content of Safety Analysis Reports for Nuclear Power Plants LWR Edition.* Washington, D.C.: U.S. Nuclear Regulatory Commission. Readily available.

Regulatory Guide 1.91, Rev. 1. 1978. *Evaluations of Explosions Postulated to Occur on Transportation Routes Near Nuclear Power Plants.* Washington, D.C.: U.S. Nuclear Regulatory Commission. Readily available.

3.5.3 Source Data, Listed by Data Tracking Number

MO0003YMP99043.001. Industrial, Commercial and Military Facilities/Activities in Proximity to Yucca Mountain. Submittal date: 03/17/2000.

MO0003YMP99044.001. Transportation Facilities/Activities in Proximity to Yucca Mountain. Submittal date: 03/17/2000.

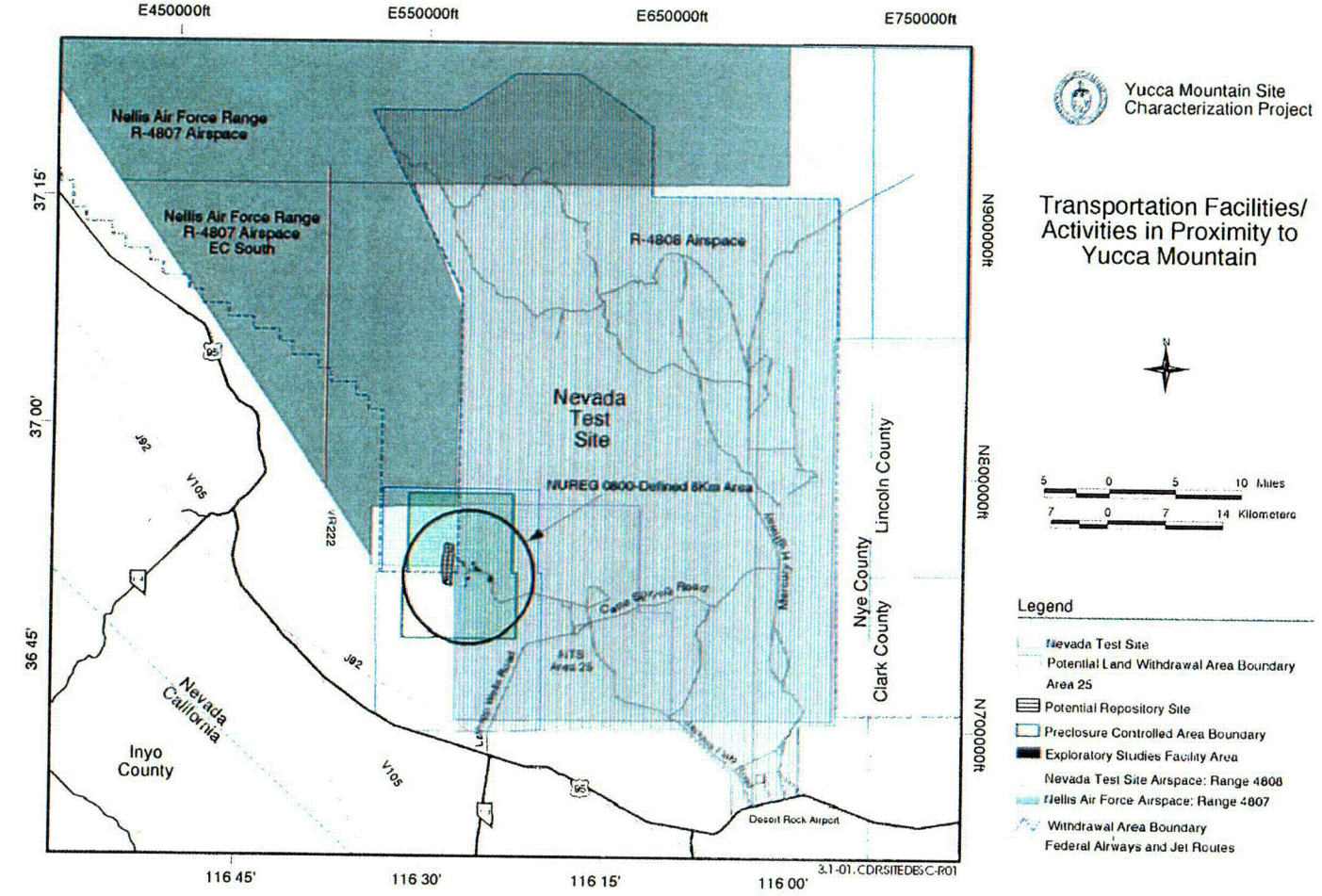

Map compiled by CRWMS M&O/TDM on March 16, 2000.
DTN MO0003YMP99044.001

Map projection: Nevada State Plane, Central
Datum: NAD27

Figure 3.1-1. Transportation Facilities/Activities in Proximity to Yucca Mountain

C12

INTENTIONALLY LEFT BLANK

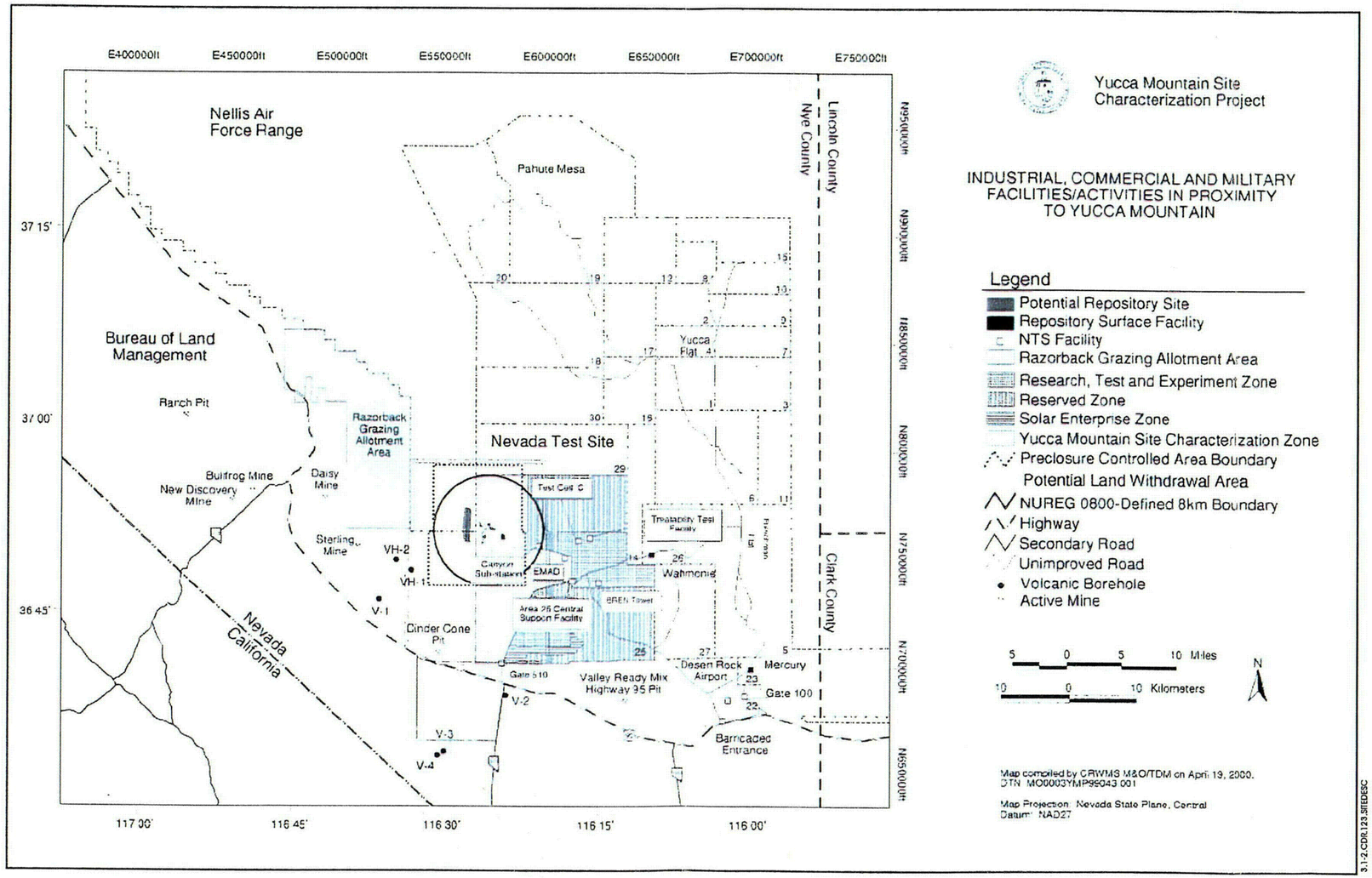

Figure 3.1-2. Industrial, Commercial, and Military Facilities/Activities in Proximity to Yucca Mountain

INTENTIONALLY LEFT BLANK

4. GEOLOGIC FRAMEWORK

4.1 INTRODUCTION

The geology of Yucca Mountain and the surrounding region provides a framework for understanding the natural system at the site. This understanding forms part of the technical basis for the contribution of the natural system to the potential repository's safety. The geology of the site controls in part the manner in which water moves through and away from the mountain. It also dictates the ability of the site to provide an adequately sized rock body with appropriate characteristics for construction of a radioactive waste repository. Understanding of the geologic framework for Yucca Mountain has, therefore, been a key goal of site characterization activities.

4.1.1 Regulatory Framework

In addition to the general requirements of proposed 10 CFR 63 (64 FR 8640) to describe the site with appropriate attention to the features, events, and processes that might affect design or performance assessment (Section 1), additional U.S. Nuclear Regulatory Commission (NRC) documents are relevant to some of the work presented in this section. The NRC has identified "Repository Design and Thermal-Mechanical Effects" as a key technical issue (NRC 1999a). The discussion of site geotechnical properties in Section 4.7, including rock thermal properties, contributes to addressing this technical issue. The NRC has also identified "Structural Deformation and Seismicity" as a key technical issue (NRC 1999b). Two subissues associated with this key technical issue are "Fracturing and Structural Framework of the Geologic Setting" and "Tectonic Framework of the Geologic Setting." Information presented in Sections 4.2,4.3, and 4.6 contribute to addressing these subissues. Information on regional tectonic models also contributes to addressing the NRC's key technical issue "Igneous Activity" (Reamer 1999). In addition, the understanding of the geologic system at Yucca Mountain also supports resolution of the key technical issues of "Radionuclide Transport" and "Total System Performance Assessment and Integration" (NRC 1999c, 2000). Potential relevance of other selected standards and NRC documents is evaluated in CRWMS M&O (1999b).

4.1.2 Key Observations

Assessments of the geologic framework for Yucca Mountain have resulted in the following key observations:

- Stable underground openings can be excavated at Yucca Mountain and rocks forming the potential repository horizon have sufficient lateral extent to support repository development.
- Tectonic models proposed for the Yucca Mountain vicinity include a caldera model for Crater Flat, extensional and detachment style fault models, rift/graben models, and lateral shear pull-apart basin models. All these models were considered in analyzing volcanic and seismic hazards.
- Neogene volcanic rocks dominate the exposed stratigraphic sequence at Yucca Mountain. These rocks consist mostly of pyroclastic-flow and fallout tephra deposits

with minor lava flows and reworked materials that were erupted from the southwestern Nevada volcanic field during the period 15.2 to 11.4 Ma.

- Most lithostratigraphic units are laterally extensive within the site area and typically have a stratiform geometric shape.

- The hierarchy of structures that affect the Miocene Paintbrush Group at Yucca Mountain comprises north-striking block-bounding faults spaced 1 to 4 km (0.6 to 2.5 mi.) apart, commonly with hundreds of meters (about a thousand feet) of normal-sense Tertiary displacement; northwest-striking relay faults that transfer displacement between block-bounding faults; smaller intrablock faults, commonly with 1 to 20 m (3 to 66 ft) of displacement; and a network of joints and tectonic fractures that, where best developed, divides the rock mass at the cubic-meter scale.

- The relatively simple nature of Tertiary extensional deformation in the central and northern parts of Yucca Mountain (1- to 4-km-wide [0.6- to 2.5-mi.-wide] fault-bounded panels with stratigraphic units dipping to the east) give way to more complex deformational patterns with greater interaction between individual block-bounding faults that characterize the more highly extended terrain of southern Yucca Mountain and the area directly north of Yucca Mountain.

- The most important controls on fracture attributes are primary, lithologic controls. The degree of welding, lithophysae development, vapor-phase alteration, and pumice content are all primary controls that affect fracture spacing, type, number of sets, continuity of individual fractures, and (probably) connectivity of the entire network. Structural controls on fracture distribution, such as proximity to faults, are secondary to primary lithologic controls.

- Site characterization data are integrated into a three-dimensional model of the distribution of stratigraphic units, rock properties, and mineral composition at Yucca Mountain, which provides a framework for modeling natural processes at the site.

- The Yucca Mountain site contains no identified metallic mineral or uranium resources; has no unique or economically exploitable deposits of industrial minerals; has low potential for energy resources, including oil and gas, and has very low potential for coal, tar sands, or oil shale; and has no economically viable geothermal resources.

4.1.3 Organization

The following sections describe the geologic framework of Yucca Mountain. Section 4.2 provides the regional geologic setting. Section 4.3 describes the tectonic models that have been proposed for the site vicinity. Section 4.4 discusses surficial geology and Quaternary stratigraphy. Sections 4.5 and 4.6 present the site stratigraphy and site structural geology, respectively. Section 4.7 summarizes geoengineering properties of the site and Section 4.8 discusses the integrated model of geology, rock properties, and mineral distribution for the site area. Section 4.9 assesses the potential for natural resources at Yucca Mountain. Finally, Section 4.10 summarizes the findings concerning the geologic framework.

4.2 REGIONAL GEOLOGIC SETTING

The regional geologic setting for Yucca Mountain consists of those tectonic, stratigraphic, and structural elements that contribute to the makeup and evolution of the site. The setting provides a context for understanding the processes currently acting at Yucca Mountain and for evaluation of its geology. Conclusions regarding the site geology need to be consistent with the regional framework. The regional geologic setting thus constrains the descriptive and process models that will be used to assess the ability of the natural system to play a role in the satisfactory performance of the site.

The information presented in this regional geologic setting is more general than the information focusing on the Yucca Mountain site provided in subsequent sections. Regional information is drawn mainly from existing geologic literature; that is, papers and reports were not prepared specifically for the Yucca Mountain Site Characterization Project (YMP). Therefore, the data they contain were not collected and their analyses were not carried out under the YMP quality assurance program. The papers and reports did, however, undergo peer review for publication. Differences in interpretation among scientists are to be expected and are reflected in this discussion of regional geology. These differences are especially apparent in some of the maps in this section, since a geologic map is both a summary of field observations and an interpretation of those observations.

Maps that summarize the surface distribution of rocks of different age groups are compiled from a number of sources. The maps that depict locations of thrust faults, folds, detachment faults, and shear zones are also drawn from existing publications to show specific features discussed in the text. The maps therefore differ in details, depending on the investigation and the subject emphasized.

The main value of a review of regional studies is to provide a context within which structural interpretations and tectonic models of the Yucca Mountain site can be judged or validated on the basis of investigations beyond the immediate area of Yucca Mountain.

4.2.1 Tectonic Setting

Tectonic setting refers to the geological architecture or structural configuration of the different rock masses in the area. The overall tectonic setting, the Great Basin, generally consists of fault-bounded basins and mountain ranges (including Yucca Mountain) greatly complicated by volcanic activity that has occurred within the past 15 m.y. Typically, faults in this setting are normal or strike-slip faults that reflect the extensional deformation caused by plate tectonic interactions at the western margin of the North American continent during the middle and late Cenozoic Era (e.g., Bohannon and Parsons 1995). The Great Basin is segmented into tectonic domains, structurally bounded blocks of the Earth's crust characterized by deformations that distinguish them from adjacent domains. Tectonic domains exist at different scales; this section addresses domains at a regional scale. Three regional tectonic domains characterize Yucca Mountain and its surrounding environs: the Walker Lane domain, which includes the site; the Basin and Range domain, to the northeast; and the Inyo-Mono domain, to the southwest (Figure 4.2-1).

4.2.1.1 Walker Lane Domain

Yucca Mountain lies within the Walker Lane domain, an approximately 100-km-wide (60-mi.-wide) structural belt along the western side of the Basin and Range domain (Figure 4.2-1). The domain, also referred to as the Walker Lane belt (Stewart 1988) or simply the Walker Lane, extends northwestward from the vicinity of Las Vegas, subparallel to the Nevada-California border, into northern California. The domain is characterized as an assemblage of crustal blocks separated by discontinuous northwest-striking right-lateral faults and northeast-striking left-lateral faults (Stewart 1988, p. 686; Carr, W.J. 1990, p. 284). Because of its structural heterogeneity, the Walker Lane is recognized as a tectonic terrane distinct from the Basin and Range only at a regional scale. The local northwest-striking faults give the domain its overall structural grain and deformation style, and they obscure basin and range structure to varying degrees (Section 4.2.1.2). While there is no definitive eastern structural boundary to the Walker Lane as a whole, the Las Vegas Valley shear zone (Figure 4.2-1) can be interpreted as an eastern bounding structure for the domain's southern segment.

The Walker Lane domain is subdivided into sections, each of which is characterized by a distinct structural pattern (Stewart 1988, p. 686). With respect to the tectonic setting of Yucca Mountain, only three of these sections are of concern: the Goldfield section, which contains the Yucca Mountain site and is characterized by irregular (in places arcuate) ranges, lack of major northwest-striking strike-slip faults, and a scarcity of major "basin-range" faults (Stewart 1988, p. 694); the Spotted Range-Mine Mountain section, which abuts the Goldfield section to the south and is dominated by northeast-striking left-lateral faults; and the Spring Mountains section, which is dominated by Paleozoic and Precambrian rocks that largely preserve pre-Basin and Range structural patterns (Figure 4.2-1).

4.2.1.2 Basin and Range Domain

The Basin and Range domain (Figure 4.2-1) is also a physiographic province, the physiography being virtually a direct expression of the bedrock structure (Stewart 1980, p. 110). Structurally, the province is characterized by generally north-south aligned ranges separated by basins with thick alluvium deposits derived from the adjacent ranges (Figure 4.2-2). The ranges are separated in the north-south direction by distances of roughly 25 to 30 km (16 to 19 mi.), but many ranges arc toward each other and merge along the strike. The general small-scale spatial pattern was aptly likened by G.K. Gilbert (1875) to an "army of caterpillars marching north out of Mexico." This pattern is the result of generally east-west directed extension that began in Tertiary time and continues at present (e.g., Stewart 1980, p. 105f; Hamilton and Myers 1966, p. 527). Rocks of every age, from Precambrian to Pleistocene, are deformed by this extension; deformation is typically expressed as complex normal faulting that has facilitated the rotation of blocks to various dips around nearly horizontal axes. Thus, each range is fundamentally an assemblage of tilted fault blocks and is bounded by a major range-front fault. Seismic reflection profiles show that this style of deformation extends beneath the intervening basins, where it is buried by alluvium (Catchings 1992).

4.2.1.3 Inyo-Mono Domain

The Inyo-Mono domain includes all of the extended terrane west of the Furnace Creek-Death Valley fault zone, east of the Sierra Nevada front, and north of the Garlock fault (Figures 4.2-1 and 4.2-2). Its northern end is defined by the termination of the Fish Lake Valley fault and a major right step in the population of active northwest-striking faults along a "northeast-striking structural zone" (Carr, W.J. 1984, p. 30, Figure 3). However, on the basis of gross structure and landform pattern, the domain could be projected northward to the northern terminus of the White Mountains (Stewart 1988, p. 693) (Figure 4.2-2). It includes modern basins and ranges with great structural and topographic relief, including Death Valley Basin and the Panamint Range. Because of its ongoing tectonic activity and exposure of originally deep-seated crustal rocks, the Inyo-Mono domain is an important part of the regional geologic setting of Yucca Mountain; it contains some of the more tectonically active structures in the Yucca Mountain region.

The Inyo-Mono domain was identified by W.J. Carr (1984, pp. 9, 26) as a subsection of the southwestern Great Basin, distinct from the Walker Lane domain. W.J. Carr (1984, p. 26) emphasized the pronounced northwest structural and physiographic trends, particularly the "long, linear valleys of north-northwest trend that are outlined by pronounced, throughgoing structures with abundant evidence of Holocene and local historic faulting." He contrasted this tectonic pattern with the "display of adjacent transform-like offsets or large-scale oroflexing common to many elements of the Walker Lane belt" (Carr, W.J. 1984, p. 26). Stewart (1988, p. 692), citing W.J. Carr (1984), also recognized the distinct tectonic character of the Inyo-Mono domain, but he included it as a section of the Walker Lane domain because of the major north-northwest striking right-lateral faults.

Extension in the Inyo-Mono domain is dominated by dextral strike-slip and oblique transtension resulting in elevated crustal blocks and intervening deep, high-relief basins (Blakely et al. 1999, p. 5). Structural relief is very high, in part because detachment faulting has unroofed some of the ranges, including the Funeral Range and the Black Mountains. Distinctive as this domain is, it may be partly represented within the Walker Lane domain by less developed features, including Amargosa Valley and Sarcobatus Flat, and perhaps even the Amargosa Desert rift zone of L.A. Wright (1989, p. 2). Further discussion with implications for Yucca Mountain is appropriate under evaluation of tectonic models (Section 4.3).

4.2.2 Regional Stratigraphy and Lithology

The stratigraphy and lithology of the regional geologic setting are relevant to the assessment of Yucca Mountain because these geological elements provide much of the history of deposition and deformation that has affected the site. They also constitute the framework for understanding other aspects of the Yucca Mountain site, including its structural geology and tectonics, geoengineering properties, mineral resource potential, hydrology, and geochemistry. Regional stratigraphy is not relevant to the tectonic domains described in the previous section because deposition and metamorphism reflect a series of evolving geologic environments that preceded formation of the domains and that no longer exist in the Great Basin. The following sections describe rock stratigraphic units at a regional scale. Section 4.5.4 contains detailed descriptions of stratigraphic units occurring in the immediate vicinity of Yucca Mountain.

Stratigraphic units are grouped below from oldest to youngest. The units are defined in terms of group and formation names, but are described as lithosomes. Thus, bodies of rock are characterized in terms of gross lithology, thickness, and mineralogy, as well as lateral variations in these parameters, all of which reflect their genesis and depositional environments. Features associated with the history and distribution of these layered rocks are also discussed, including the character of regional unconformities, intrusive rocks, and alteration phenomena. Outcrop locations are generalized in terms of geographic area or physiographic features, such as named ranges; the referenced studies provide detailed locations. Stratigraphic units are summarized in Tables 4.2-1 (Precambrian and Paleozoic), 4.2-2 (Permian and Mesozoic), and 4.2-3 (Tertiary and Quaternary).

4.2.2.1 Pre-Cenozoic Rocks

Pre-Cenozoic rocks in the Yucca Mountain region comprise chiefly upper Precambrian (Proterozoic) through Paleozoic marine strata. Mesozoic rocks are of minor significance to Yucca Mountain, as they are preserved in the western part of the Inyo-Mono domain (chiefly marine strata) and near the southern part of the Walker Lane domain (chiefly continental strata). Small Mesozoic igneous intrusions are found near Yucca Mountain. The Precambrian section is dominated by siliciclastic strata; the Paleozoic section is dominated by limestones and dolomites. These rocks have undergone successive generations of faulting, fracturing, and broad to local folding about both vertical and subhorizontal axes (Table 4.2-1). In the area of the southwestern Nevada volcanic field and within the Goldfield section of the Walker Lane, the pre-Cenozoic rocks are not well exposed; hence, their pre-middle Miocene structural configuration is uncertain near Yucca Mountain. The pre-Cenozoic rocks are important, however, because they include the main regional aquifers and aquitards.

4.2.2.1.1 Precambrian Rocks

Precambrian rocks comprise two major assemblages: an older, metamorphosed basement assemblage (no basal contact is exposed), and a younger, metasedimentary assemblage, the uppermost unit of which is partly Cambrian. The older assemblage consists chiefly of quartzofeldspathic gneisses and quartz-feldspar-mica schists of metasedimentary or metaigneous origin. The gneisses and schists are typically intruded by migmatitic veins or larger, deformed bodies of granite or pegmatite.

Rocks of this assemblage crop out in Monarch Canyon in the Funeral Mountains (Wright, L.A. and Troxel 1993), at a railroad cut through the Bullfrog Hills (Maldonado 1990; Hoisch et al. 1997, p. 2823f), and in the Trappman Hills (Ekren, Anderson et al. 1971, p. 6) north of Yucca Mountain in the Goldfield section of the Walker Lane (Figure 4.2-3; except for Trappman Hills). East of Yucca Mountain, except in eastern Clark County, the metamorphic basement is not exposed in the Basin and Range domain (Stewart 1980, p. 9, Figure 6).

The older metamorphic rocks are well exposed in the Panamint Range (Figure 4.2-3), where they are mapped as the "World Beater Complex" (Lanphere et al. 1964), and have been radiometrically dated by U-Pb zircon methods at about 1,800 Ma (Lanphere et al. 1964, p. 269). The World Beater Complex is unconformably overlain by rocks of the Pahrump Group (Wright, L.A., Troxel et al. 1981, p. 4), which includes three formations: the basal Crystal

Spring Formation, the Beck Spring Dolomite, and the overlying Kingston Peak Formation (Stewart 1970, p. 14). In some places (e.g., the southern Death Valley region), however, Pahrump Group rocks are missing and the World Beater Complex is overlain directly by the Noonday Dolomite (Table 4.2-1). Originally sandstones, siltstones, dolomite, and conglomerate, the strata of the Pahrump Group are locally metamorphosed to facies ranging from greenschist to amphibolite similar to that of the high-grade rocks of the underlying World Beater Complex. High-grade to medium-grade metamorphism characterizes the Pahrump Group in the central Panamint Range and the northern Funeral Mountains (Labotka 1980, p. 688; Troxel 1988, p. 48), where the Pahrump Group is most widely exposed.

The age of the Pahrump Group is not well determined. The Crystal Spring Formation contains diabase sills radiometrically dated using the U-Pb method on baddeleyite at about 1,080 Ma (Heaman and Grotzinger 1992, p. 639). The Kingston Peak Formation consists partly of conglomerates that are inferred to be of glacial origin (tillites) and, therefore, have been assigned an age of about 700 Ma on the basis of regional correlation (Miller, J. 1985, p. 1539).

The Pahrump Group is overlain at an erosional unconformity by Upper Proterozoic units—the Noonday Dolomite and the Johnnie Formation—which, in turn, are capped by the Stirling Quartzite and the Wood Canyon Formation. The Wood Canyon Formation, a siltstone or locally calcareous silty sandstone, spans the Proterozoic-Cambrian boundary. The Upper Proterozoic formations are widely exposed in the Panamint Range of the Inyo-Mono domain (Labotka, Warasila et al. 1985, p. 10,359); in the Spring Mountains section of the Walker Lane; in the Funeral Mountains; and at Bare Mountain, the Striped Hills, and the Specter Range (Figure 4.2-3; exposures in the Striped Hills and the Specter Range are too small to show at the scale of the figure). The Stirling Quartzite and the Wood Canyon Formation are exposed locally east and north of Yucca Mountain (Ekren, Anderson et al. 1971, pp. 7, 9). The metamorphic facies of the Upper Proterozoic strata is lower greenschist over wide areas of exposure, but in some places, notably the northwestern corner of Bare Mountain, the section as high as the Wood Canyon Formation reaches garnet-amphibolite facies of metamorphism.

Regionally, the Upper Proterozoic units thicken and become increasingly calcareous from southeast to northwest (Stewart 1970, p. 7; Diehl, P. 1976, p. 58). They form the basal units of a miogeoclinal section and represent a marine depositional environment characterized by passive margin conditions and simple lithologies, chiefly siliciclastic rocks that grade upward into Paleozoic carbonate rocks. The cumulative thickness of the exposed Precambrian section in the Yucca Mountain region ranges from 100 m (328 ft) to more than 6 km (3.7 mi.) and forms a sedimentary wedge that thickens to the northwest (Stewart 1970, p. 7). The Proterozoic rocks, with their weakly to strongly metamorphosed fabrics, form a regional aquitard or barrier to groundwater flow (Winograd and Thordarson 1975, p. C39).

4.2.2.1.2 Paleozoic Rocks

Paleozoic rocks in the Yucca Mountain region comprise three lithosomes: a lower, Cambrian through Devonian, dominantly carbonate lithosome; a middle, Mississippian, fine-grained siliciclastic lithosome; and an upper, Pennsylvanian to Mid-Permian, carbonate lithosome. The lower carbonate lithosome represents deposition in a deep to shallow marine passive continental margin (outer shelf to upper rise) setting (e.g., see Poole, Stewart et al. 1992, p. 46). By Late

Devonian time these conditions were interrupted by the Antler Orogeny, the main result of which in the Yucca Mountain region was an influx of clay, silt, and sand into the depositional record (Trexler, J.H. et al. 1996, p. 1739). A carbonate platform (continental shelf) depositional environment was reestablished in Pennsylvanian time across much of the region, except in the Inyo-Mono domain, where a deeper trough or slope environment was formed (Stewart 1980, p. 46; Dunne 1986, p. 5).

The lower part of the lower carbonate lithosome is represented by a shallow water, mixed clastic to carbonate succession represented by the upper two-thirds of the Wood Canyon Formation, the Zabriskie Quartzite, and the Carrara Formation (Table 4.2-1). This succession is overlain by a thick interval of monotonous, dark-gray Cambro-Ordovician limestone, dolomite, and minor shale: the Bonanza King and Nopah formations and the Pogonip Group (Goodwin Limestone, Ninemile Formation, and Antelope Valley Formation). The Cambro-Ordovician carbonates are well exposed in the central part of Bare Mountain, and in the Specter Range to the southeast (Figure 4.2-4). A portion of the sequence was penetrated in the Felderhoff Federal No. 25-1 well that was drilled in the eastern Amargosa Basin (Grow et al. 1994, p. 1300; Carr, W.J., Grow et al. 1995). The Bonanza King Formation is widely exposed in the CP Hills and in the Halfpint Range (Figure 4.2-4); about 1,400 m (4,593 ft) of section is present in the Halfpint Range (Barnes, Christiansen et al. 1962, p. D29). The Upper Cambrian Nopah Formation is similarly widespread, extending at least from the Halfpint Range southwest to the Nopah Range (Figure 4.2-4) as a variegated dolomite with subordinate silty-shaley and cherty intervals.

Although the Cambrian carbonates are strong and resistant to erosion, in many places they are characterized by stratally confined brecciation. At least two generations of breccia are present, the oldest of which may be of primary origin (submarine debris flows). One or more post-consolidation breccias, most likely of tectonic origin, are associated with interclastic voids in many parts of the calcareous section. This condition has enhanced cavernous dissolution, favoring the flow of groundwater. This feature, as well as the regional extent and uniformity, provides the conditions that make the lower carbonate lithosome a regional aquifer (the lower carbonate aquifer of Winograd and Thordarson [1975, p. C14]).

The character of the Cambro-Ordovician carbonate section described above differs markedly from that of the Upper Ordovician Eureka Quartzite. The upper part of the Eureka Quartzite is typically a dense, white, sucrose quartzite that forms a unit as much as 150 m (492 ft) thick that is closely fractured. These characteristics promote the use of the Eureka Quartzite as a decorative building aggregate; they also enhance its properties as a fracture-flow aquifer. In many places, the Eureka Quartzite is stained red by hematite deposited in fractures by groundwater. It is widely distributed and is lithologically persistent (Ekren, Anderson et al. 1971, p. 18). The Eureka Quartzite is succeeded by the shallow water Ely Springs Dolomite, which marks a recurrence of the carbonate depositional regime. Ordovician strata grade up through the Ely Springs Formation, interrupted by minor erosional gaps, into dolomites that form the Siluro-Devonian section (Stewart 1980, pp. 25, 28).

The Silurian system is thin and areally restricted relative to the rest of the Paleozoic section in southern Nevada (Stewart 1980, p. 28); it is generally about 600 m (1,968 ft) thick in the Yucca Mountain region (Stewart 1980, p. 28). The Silurian section in much of eastern Nevada consists of the Middle to Upper Silurian Laketown Dolomite, a gray, thin-to-thick, bedded to massive

dolomite, presumably of shallow water origin (Stewart 1980, p. 29, Figure 18). It is exposed in the Pintwater Desert, Pahranagat, and Pahroc ranges. To the west, this facies grades into a thin- to slabby-bedded to laminated, very dark gray to black limestone that is locally sandy, cherty, or carbonaceous, and presumably of outer shelf origin (Stewart 1980, p. 29). The two Silurian carbonate facies are recognized at Bare Mountain (Figure 4.2-5), where the lower (deeper water), thin-bedded facies is assigned to the Roberts Mountains Formation and the upper, massive (shallow water) dolomitic facies is assigned to the Lone Mountain Dolomite (Cornwall and Kleinhampl 1961; Monsen et al. 1992). The Roberts Mountains Formation appears to be regionally unconformable on the Ordovician Ely Springs Dolomite. It ranges in age from late Early Silurian to probably latest Silurian and is about 200 m (656 ft) thick (Monsen et al. 1992). The gradationally overlying Lone Mountain Dolomite is about 490 m (1,608 ft) thick; it is assigned a Silurian to perhaps Early Devonian age on the basis of lithology and stratigraphic position above the Roberts Mountains Formation (Cornwall and Kleinhampl 1961; Monsen et al. 1992).

In the Yucca Mountain area, the Roberts Mountains Formation crops out only in northern Bare Mountain (Sawyer, Wahl et al. 1995, p. 30). The Roberts Mountains Formation and the Lone Mountain Dolomite are the only Paleozoic units penetrated by a borehole at Yucca Mountain (Carr, M.D. et al. 1986, p. 1). Below 1,244 m (4,081 ft), well UE-25p#1 (see Carr, M.D. et al. 1986, Plate 1) penetrated about 563 m (1,847 ft) of dolomite equivalent to the Roberts Mountains Formation and Lone Mountain Dolomite exposed in Chuckawalla Canyon on the east flank of Bare Mountain (Carr, M.D. et al. 1986, pp. 18 to 19). At Chuckawalla Canyon, the Roberts Mountains Formation crops out as a dark gray to black, finely crystalline, cherty dolomite; the overlying Lone Mountain Dolomite is a light gray, fine- to medium-grained, crystalline dolomite. To the east, in the Spotted Range and Ranger Mountains, correlative Silurian strata are exposed in the lower part of the dolomite of the Spotted Range (Figure 4.2-5) (Poole et al. 1965; Ekren, Anderson et al. 1971, p. 19), but only the Lone Mountain Dolomite is lithologically similar to the chronostratigraphically correlative (Lower to Upper Silurian, chiefly Wenlockian) dolomite of the Spotted Range.

West of Bare Mountain, the Silurian section is included in the lower part of the Hidden Valley Dolomite, a unit equivalent to the Laketown Dolomite. The Hidden Valley Dolomite ranges in thickness from about 350 m (1,148 ft) in the Inyo Mountains to about 415 m (1,362 ft) in the Death Valley area (Corbett, K. et al. 1988, p. 271), and between 90 and 400 m (295 and 1,312 ft) in the Nopah Range and the Montgomery Mountains (Burchfiel, Hamill et al. 1983, p. 1364).

Devonian rocks in the Yucca Mountain region consist of a succession of limestone and dolomite that typically includes intervals of thick-bedded, gray, crystalline dolomite; fossiliferous, thin- or slabby-bedded or cherty limestone; and silty-sandy or quartzitic beds. The lithologic and stratigraphic variability, the fossil assemblage, and the presence of numerous erosional breaks indicate deposition in shallow (shelf to upper slope) water, dominated at times by reef bank environments. Devonian strata tend to be siltier upsection and toward the northwest, a lithostratigraphic distinction that becomes more pronounced in the overlying Mississippian section (Stevens, C.H. et al. 1991, p. 884). Johnson, J.G. et al. (1988) provided discussions of facies and depositional environments of Devonian rocks in the western United States, including lithofacies maps that show the complexity of regional stratigraphic relations across the Yucca Mountain region.

In the older literature, the Devonian section in the vicinity of Yucca Mountain is grouped into three main units: the informal "Dolomite of the Spotted Range" (the upper part of which is Lower Devonian) (Ekren, Anderson et al. 1971, p. 19), the Nevada Formation (Lower and Middle Devonian) (Merriam 1940, pp. 9, 14; Ekren, Anderson et al. 1971, p. 20; Barnes, Ekren et al. 1982), and the Devils Gate Limestone (Middle to Upper Devonian) (Merriam 1940, pp. 9, 16). This tripartite designation is widely applied in southern Nevada, but the stratigraphic nomenclature for Devonian units east of Yucca Mountain now more commonly adheres to unit designations defined by Nolan (1935): the Lower Devonian is represented by the upper part of the Sevy Dolomite; the Middle and Upper Devonian are represented by the Simonson Dolomite and by the Guilmette Formation (Johnson, J.G. et al. 1988, p. 169) (Table 4.2-1). Upper Devonian strata are also included in the lowermost part of the Eleana Formation, a unit defined at the Nevada Test Site (Poole, Houser et al. 1961, p. D-110) (Table 4.2-1).

The Devonian section is thick and extensive across southern Nevada. Perhaps the thickest (1,844 m [6,505 ft]) and most complete Devonian section in the Yucca Mountain region is located in the Pahranagat Range (Tschanz and Pampeyan 1970, p. 32). In the Nevada Test Site area, the Devonian section is estimated to have a total thickness of about 1,000 m (3,280 ft) (Robinson, G.D. 1985, p. 6). The Sevy Dolomite or its correlative strata (Nolan 1935) extends over an area of about 260,000 km^2 (100,600 $mi.^2$) (Osmond 1957, p. 1869; Johnson, J.G. et al. 1988, p. 166), from western Utah to Eureka, Nevada, and south to the Inyo Range in California, as a homogeneous, microcrystalline, generally unfossiliferous, well-bedded, gray dolomite capped in many places by a quartz sandstone (Tschanz and Pampeyan 1970, pp. 32 to 33). At the Nevada Test Site, the Sevy Dolomite is about 265 m (870 ft) thick (Tschanz and Pampeyan 1970, p. 33). The Simonson Dolomite is nearly as widespread, but is lithologically more variable and is fossiliferous. The Nevada Test Site probably has at least 240 m (787 ft) of Simonson Dolomite (in the southwest corner of Lincoln County) (Tschanz and Pampeyan 1970, p. 35; Poole, Houser et al. 1961, p. D-110). The Guilmette Formation is conspicuous for its massive reef breccia limestone facies and presence of sandy to silty limestones. About 470 m (1,542 ft) of Guilmette Formation (i.e., Devils Gate Limestone and Narrow Canyon Limestone) are present at the Nevada Test Site (Johnson, M.S. and Hibbard 1957, pp. 355 to 356, Plate 33).

The Simonson Dolomite and Guilmette Formation crop out at the southeastern corner of Shoshone Mountain, at Mine Mountain, and at the southernmost end of the Belted Range around the northern margin of Yucca Flat (Figure 4.2-5). These units are also well exposed at the southern end of the Spotted Range in and around Mercury Ridge and in the southern part of the Ranger Mountains (Figure 4.2-5). The Sevy and Simonson dolomites and the Guilmette Formation are widely exposed south of the Specter Range thrust, and rocks of equivalent age and lithology crop out in the Calico Hills and form the westernmost outliers of the Striped Hills (Figure 4.2-5).

At Bare Mountain, the Devonian section (Figure 4.2-5) is represented by evenly-bedded dolomite and less abundant limestone and sandstone, designated the Fluorspar Canyon Formation (Cornwall and Kleinhampl 1961), a unit equivalent to the Nevada Formation (Table 4.2-1) and about 250 m (820 ft) thick. However, thrust faulting has juxtaposed two different facies here; accordingly, Monsen et al. (1992) subdivided the Fluorspar Canyon Formation, retaining that name for well-bedded strata in the upper thrust plate and designating more clastic, locally coralline strata below the thrust as "rocks of Tarantula Canyon." Both the

Fluorspar Canyon Formation of Monsen et al. (1992) and the rocks of Tarantula Canyon are conformable with the underlying Silurian Lone Mountain Dolomite (equivalent to the lower part of the Sevy Dolomite), which is present on both sides of the thrust fault. However, the rocks of Tarantula Canyon are overlain by a silty-shaley unit designated the Eleana Formation by Monsen et al. (1992) and the Meiklejohn Formation by Cornwall and Kleinhampl (1961). Monsen et al. (1992) interpreted a conformable contact at Tarantula Canyon and inferred that the lower part of the Eleana here may be Devonian, whereas Cornwall and Kleinhampl (1961) interpreted the contact as a thrust and thereby designated the entire Meiklejohn Formation (i.e., Eleana Formation) as a displaced Mississippian section.

Farther west, Devonian rocks are exposed in the Nopah and Montgomery Mountains (Nevada Formation unconformable on Silurian strata in the Nopah Range) (Burchfiel, Hamill et al. 1983, p. 1359; Hazzard 1937, pp. 280, 327) (Figure 4.2-5). In the Nopah Range, the Middle Devonian unit, about 270 m (886 ft) thick, was formerly known as the Sultan Dolomite (Hazzard 1937, p. 276). In the southern Funeral Mountains and the Cottonwood Mountains of California, the Devonian section comprises the Lost Burro Formation, a carbonate unit about 750 m (2,460 ft) thick, and the top of the Hidden Valley Dolomite equivalent to the Sevy Dolomite (McAllister 1974, pp. 3, 6, 13, Plate 2) (Figure 4.2-5). The Lost Burro Formation is a pale gray, crystalline dolomite, locally cherty, with minor quartzite layers. It is equivalent to the Guilmette Formation and the Simonson Dolomite (Tschanz and Pampeyan 1970, pp. 35, 40). Middle Devonian strata in the Nopah Range are about 270 m (886 ft) thick (Sultan Dolomite) (Hazzard 1937, p. 276). Devonian strata become increasingly argillaceous to the west (indicating a deep depositional trough), and pinch out in the Inyo Mountains (Snow 1992, p. 97). The Hidden Valley Dolomite thins to the south and pinches out in the middle of the Panamint Range, the Nopah Range, and the Spring Mountains (Snow 1992, p. 96) (Figure 4.2-5), whereas Upper Devonian dolomite (the Lost Burro Formation) extends across a Middle Devonian unconformity on into Nevada.

Mississippian strata in the Yucca Mountain region are represented by sharply contrasting but locally intertonguing lithologies: a shale-siltstone section that thickens to more than 3,000 m (9,842 ft) toward its westward source (Stewart 1980, p. 41), and a comparatively thinner and more uniform carbonate section that extends southeastward from the vicinity of Mercury and the Spotted Range, where it is about 300 m (984 ft) thick (Barnes, Ekren et al. 1982). Stevens et al. (1996, p. 11) recognized three general but contrasting lithofacies belts of Mississippian age based on regional studies in southern Nevada and east-central California:

- A southeastern, predominantly limestone belt representing an extensive carbonate platform (Monte Cristo Group, Narrow Canyon Formation, Indian Springs Formation)
- A central, mixed limestone and siliciclastic belt representing slope and base-of-slope environments (Mercury Limestone, Tin Mountain Limestone, Perdido Group, Chainman Shale)
- A northwestern, dominantly siliciclastic belt deposited primarily in a base-of-slope and basinal environment (Eleana Formation, Rest Spring Shale).

Barnes, Ekren et al. (1982) mapped three Mississippian carbonate units at the Nevada Test Site: the Narrow Canyon Limestone (transitional with the underlying Devonian Devils Gate Limestone, or Guilmette Formation), the Mercury Limestone, and the informal limestone of Timpi Canyon (Table 4.2-1). Farther east, these Mississippian units are represented by the Rogers Spring and the Monte Cristo Limestones (Table 4.2-1). The Monte Cristo is now elevated to group status, with the inclusion of an uppermost unit correlative with Mississippian clastic rocks of the Spotted Range (Sawyer, D.A., Wahl et al. 1995, p. 29). Along the west side of Yucca Flat (Figure 4.2-6), the Mississippian section is mostly the shaley, western facies, represented by the Eleana Formation (Table 4.2-1). The Eleana Formation is well exposed in its type locality, the Eleana Range (Figure 4.2-6), where it is more than 2,300 m (7,546 ft) thick (Poole, Houser et al. 1961, p. D-104; Cole, Wahl et al. 1989, Figure 3, pp. 436 to 437) and consists of thin-bedded turbidites, laminated siltstones, and chert and/or quartz clast conglomerates that bottom as massive channel fills (Cole, Trexler et al. 1994, p. 69). The upper part of the Eleana Formation is chiefly calcareous turbidites, which is represented farther east and south by the Chainman Shale (Table 4.2-1), a monotonous siltstone or mudstone several hundred meters thick, interbedded with sparse quartz sandstone. The Chainman Shale crops out in the CP Hills and the core of the Calico Hills (Maldonado et al. 1979, p. 1; Cole, Trexler et al. 1994, pp. 68, 71; Sawyer, D.A., Wahl et al. 1995, p. 29) (exposures too small to display in Figure 4.2-6). Correlative strata crop out in the northeastern corner of Bare Mountain (Cornwall and Kleinhampl 1961; Monsen et al. 1992).

About 770 m (2,526 ft) of Chainman Shale were penetrated by borehole UE-25 a-3 in the Calico Hills. The hole bottomed in Silurian or Devonian dolomite (Maldonado et al. 1979, p. 1). The borehole revealed low-grade thermal metamorphism of the shale, which provides one possible explanation for a magnetic anomaly that encompasses the Calico Hills (Majer et al. 1996, Plate 2). Alternatively, the anomaly could be explained by a depositionally thick section of Miocene tuff above the Paleozoic contact.

A section of Upper Devonian to Lower Mississippian strata above the Guilmette Formation at Shoshone Mountain (Figure 4.2-5) may be a transitional facies between the Eleana turbidite facies to the northwest and the carbonate-platform facies of the Spotted Range to the southeast. The lowest Mississippian strata consist of pale-green siltstone and shale, platy limestone, and black chert lenses, all of which may correlate with thin, Lower Mississippian limestone beds in the Spotted Range (Barnes, Ekren et al. 1982). The highest preserved intervals of the green quartz siltstone and calcareous shale at Shoshone Mountain probably correlate with the Chainman Shale (Cole, Trexler et al. 1994, p. 71). Mississippian rocks in the Funeral Mountains (exposures too small to show at the scale of Figure 4.2-6) are assigned to the Tin Mountain Limestone and the Perdido Formation (Monte Cristo Formation in the Nopah Range) (Table 4.2-1).

Rocks of Pennsylvanian to Permian age in the Yucca Mountain region are represented by the Tippipah Limestone (Table 4.2-1), a thick- to thin-bedded, gray limestone, but locally silty and cherty (Frizzell and Shulters 1990). The Tippipah is exposed only at the east side of the Nevada Test Site, at the southern end of the Eleana Range (Syncline Ridge), and at the southern end of the CP Hills (Figure 4.2-6), where it is disconformable with the Chainman Shale (Cole, Trexler et al. 1994, p. 75). The disconformity represents an erosional hiatus of as much as 10 m.y., which was followed by essentially synchronous regional carbonate shelf deposition (Cole,

Trexler et al. 1994, p. 75). The Pennsylvanian section is about 1,000 m (3,280 ft) thick at the Nevada Test Site (Frizzell and Shulters 1990), and about as thick in the Spring Mountains (Figure 4.2-6), where it is designated the Bird Spring Formation (Table 4.2-1) (Longwell and Dunbar 1936, p. 1203; Longwell et al. 1965, p. 30; Rich 1961, p. 1160). With the exception of much of the Lower Pennsylvanian at the Nevada Test Site (Cole, Trexler et al. 1994, p. 75), the section represents nearly continuous deposition during Pennsylvanian time and into Lower Wolfcampian time (Tschanz and Pampeyan 1970, pp. 55 to 56). Pennsylvanian strata have not been found at Bare Mountain, but the Bird Spring Formation is exposed farther south in the Nopah Range (Figure 4.2-6) (Burchfiel, Hamill et al. 1983, Figure 2, p. 1359; Hazzard 1937, p. 337).

The Death Valley region approximates the location of a carboniferous facies transition from a carbonate-quartzite lithology (shallow water platform environment) to the southeast to a siltstone-shale lithology (deep water environment) to the northwest (Snow 1992, p. 100; Stevens 1986, pp. 20, 23). The transition is marked by occurrence of the Upper Mississippian Rest Spring Shale (Table 4.2-1) in the Darwin Plateau area (Stone, Dunne et al. 1989; Snow 1992, p. 97). The Rest Spring Shale is a variegated, generally black shale and siltstone with minor sandstone, equivalent to the Chainman Shale (Stevens et al. 1996, p. J5). In the Cottonwood Mountains, the Pennsylvanian carbonate platform environment changes to a clastic rise section across a span of about 35 km (22 mi.) (Snow 1992, p. 100). The stable carbonate platform began to collapse in mid-Wolfcampian time, as indicated by a stratigraphic interval more than 50 m (164 ft) thick consisting of turbidites, debrites, and argillaceous limestones (Snow 1992, p. 100).

The Paleozoic section of the Inyo Mountains is only 2,760 m (9,055 ft) thick. It generally documents increasing water depth from Ordovician to Late Mississippian time (Stevens 1986, p. 24). Thereafter, the depositional environment is very complex, reflecting tectonic activity farther west. In the Darwin Plateau area, deep water environments in Late Pennsylvanian through Early Permian time are represented by massive, micritic limestone and turbidites; rapid shallowing occurred in Middle to Late Permian time (Corbett et al. 1988, p. 271), ultimately resulting in at least local subaerial exposure and deposition of coarse, terrigenous clastic rocks presently exposed in the Inyo Mountains (Dunne 1986, p. 5; Snow 1992, p. 101). A nearly unbroken Paleozoic section from Cambrian to Middle Pennsylvanian is exposed in and south of the Nopah Range (Figures 4.2-4, 4.2-5, and 4.2-6), totaling more than 7,500 m (24,600 ft) thickness (Burchfiel, Hamill et al. 1983, p. 1359). The only major unconformity in the section is at the base of the Devonian Nevada Formation, on the Silurian Hidden Valley Dolomite and the Ordovician Ely Springs Dolomite (Burchfiel, Hamill et al. 1983, p. 1359). The total thickness of the pre-Tertiary section at the Nevada Test Site is estimated at about 11,500 m (37,730 ft) (Frizzell and Shulters 1990).

4.2.2.1.3 Mesozoic Rocks

Stratified Mesozoic rocks have not been found within a 100-km (62-mi.) radius of Yucca Mountain; their closest occurrence is at the periphery of this area, south and east of Charleston Peak, in the Spring Mountains (Figure 4.2-7). There, at the latitude of Las Vegas, a thick, well-exposed section of Mesozoic rock forms Wilson Cliffs (Longwell et al. 1965, Plate 1) (Figure 4.2-7). Although Mesozoic strata are not a factor in the hydrologic or tectonic

phenomena relevant to Yucca Mountain, a discussion is included here as an integral part of the geologic history of the Yucca Mountain region.

Carbonate deposition in the Yucca Mountain region continued into Late Permian time, but gradual uplift, accompanied by erosion, resulted in the development of a Paleozoic-Mesozoic unconformity. Deeper stratigraphic levels were exposed toward the west, whereas deposition of younger strata encroached from the east, progressively covering much of the eroded carbonate rock. Consequently, in the western Spring Mountains, Lower Triassic strata unconformably overlie Middle to Lower Permian levels of the Bird Spring Formation, whereas in the southeastern Spring Mountains, the Permian section is more nearly complete, containing Permian red beds and the Toroweap and Kaibab Formations. As the erosional hiatus across the unconformity diminishes toward the east, the younger Paleozoic strata below the unconformity reflect shallower, near-shore depositional environments, as do the Lower Triassic beds that lie above the unconformity. Farther east, in the Colorado Plateau, a virtually complete Permian through Triassic section is present.

Lower Triassic strata are assigned to the Moenkopi Formation (Stewart 1980, p. 60) (Table 4.2-2). This unit includes interbedded silty limestone, reddish-brown siltstone to fine-grained sandstone, gypsum and local limestone pebble conglomerates, and facies that indicate a shoaling, marine to alluvial near-shore environment of deposition. Upper Triassic strata comprise the Chinle Formation and its basal member, the Shinarump Conglomerate (Table 4.2-2). The Shinarump consists of widespread chert-pebble conglomerate in sandstone matrix; the Chinle is chiefly weakly consolidated red shale, claystone, siltstone, and fine sandstone. Unconformably above the Chinle are Lower Jurassic red beds equivalent to the Moenave and Kayenta formations of the Colorado Plateau (Stewart 1980, p. 60). Conformably above these beds lies the Lower Jurassic Aztec Sandstone (Stewart 1980, p. 67), the youngest Mesozoic deposit in the region (Table 4.2-2). The Aztec consists of conspicuously cross-bedded, pink to red, fine- to medium-grained quartzose sandstone, as much as 750 m (2,460 ft) thick in the Wilson Cliffs (Figure 4.2-7). The top of the Aztec Sandstone is either eroded away or sliced off by an overthrust Paleozoic section (Longwell et al. 1965, Plate 1).

The Mesozoic section in the Spring Mountains (Figure 4.2-7) indicates that regional uplift continued and expanded eastward in Middle to Late Triassic time, exposing strata of the Moenkopi Formation to slight erosion and, during a later phase of uplift, exposing the Chinle Formation to erosion (Marzolf 1990, p. 495). By Early Jurassic time, the region evolved from an alluvial plain to a desert, and dune sands of the Aztec Sandstone were laid down (Marzolf 1990, Figure 13).

In California, Mesozoic strata are present in a band that stretches along the Inyo Mountains and the Darwin Plateau, then into the Argus Range (Figure 4.2-7) (Stone and Stevens 1986, p. 45). The section includes two Triassic lithosomes: a lower, marine to near-shore alluvial lithosome consisting of about 800 to 900 m (2,625 to 2,953 ft) of Lower to perhaps Middle Triassic micritic limestone and mudstone (Dunne 1986, pp. 6 to 7; Stone and Stevens 1986, p. 45), and an Upper Triassic (and perhaps even younger) continental volcanic and volcaniclastic lithosome as much as 150 m (492 ft) thick (Dunne 1986, p. 7). Here, as in Nevada, the change in environment of deposition, from marine to continental, reflects regional uplift associated with tectonism. The Upper Triassic lithosome in California comprises an eastward prograding assemblage of fan

deposits that were derived from the evolving Sierra Nevada plutonic-volcanic terrane to the west, now represented by the exposed Sierra Nevada batholith (Dunne 1986, p. 6; Dunne et al. 1978, p. 195). Most California Triassic sediments are metamorphosed as a result of igneous intrusion and concomitant crustal thickening (Dunne 1986, p. 8). Igneous intrusion in this region occurred from about 186 to 147 Ma (Chen and Moore 1982, p. 4774; Dunne et al. 1978, p. 196), and metamorphism from 80 to 70 Ma (Labotka, Warasila et al. 1985, pp. 10, 359).

Mesozoic rocks younger than Early Jurassic in the Yucca Mountain setting are intrusive, consisting of widely scattered granitic stocks and mafic dikes. Granitic stocks near Yucca Mountain (Figure 4.2-7) include the Climax and Gold Meadow stocks (101 Ma and 93.6 Ma, respectively) (Naeser and Maldonado 1981, pp. 45 to 46) and a buried intrusive body near Yucca Flat (102 Ma) (Cole, Harris et al. 1993), as well as numerous lamprophyre dikes (about 101 Ma) (Cole, Trexler et al. 1994, p. 69). In California, a widely distributed population of mafic dikes that are aligned about N25°W (the Independence dike swarm) (Chen and Moore 1979, Figure 1) is Late Jurassic (about 148 Ma) (Chen and Moore 1979, p. 129). The dikes represent an early phase of regional extension that is oriented N65°W (Chen and Moore 1979, p. 133). The intrusion of granitic stocks represents a period of crustal thickening and heating that culminated probably in Late Jurassic to Early Cretaceous time. Metamorphism of the Proterozoic rocks in the Funeral Mountains has been attributed to intrusive activity in Mesozoic time. Many intrusive rocks are exposed at structural levels that indicate removal by erosion of several kilometers of rock since the time of intrusion and crystallization.

4.2.2.2 Cenozoic Rocks

Cenozoic rocks of the Yucca Mountain geologic setting fall into three general groups: pre-Middle Miocene sedimentary (including volcaniclastic) rocks that predate creation of the southwestern Nevada volcanic field; the Middle to Late Miocene volcanic suite that constitutes the southwestern Nevada volcanic field; and the Plio-Pleistocene basalts and basin sediments. These lithostratigraphic groups are not well defined in terms of system boundaries (e.g., Tertiary or Quaternary), so systemic distinctions will not be emphasized in the following sections.

At Yucca Mountain and in the surrounding area, Cenozoic rocks overlie complexly deformed Paleozoic and Precambrian rocks along a profound erosional unconformity. The distribution, geometry, and attitudes of these older rocks, and the extent to which these factors influenced the distribution and structure of the Cenozoic units, is indeterminable, given the present paucity of subsurface data. The age of the regional unconformity is also unknown, but erosional down-cutting, possibly associated with extension, most likely was under way in Late Cretaceous (post-Santonian) time, as the various Cretaceous stocks and dikes are all post-kinematic or indicate the influence of an extensional stress field during emplacement. The age of the basal Cenozoic deposits is unknown; the oldest such deposits within a 100-km (62-mi.) radius of Yucca Mountain are at least late Oligocene, but such deposits may include older basal colluvium or lag conglomerates.

The erosional surface shows evidence of considerable weathering, suggestive of a warm, bi-seasonal savannah environment. The carbonates show a characteristic red (terra rosa) clay-rich weathering rind, local solution weathering, and rounded hill forms having relief of perhaps 100 m (328 ft) or less. Late Cretaceous to Eocene climatic conditions were most likely

conducive to such weathering. Cavernous weathering is only sparsely or weakly developed in the Paleozoic carbonates (Winograd and Thordarson 1975, p. C16), and the character of the early Tertiary surface is in marked contrast to the sharply etched, high-relief surface formed in post-Miocene time. Also, much of the relief expressed in the exposed Paleozoic rocks owes its origin to late Miocene extensional faulting. High structural relief is locally associated with the pre-late Oligocene surface, but it is ordinarily affected by weathering. The relative contributions of erosion/weathering and tectonic displacement to the formation of paleo-relief are presently undetermined.

4.2.2.2.1 Tertiary Rocks

Pre-middle Miocene sedimentary rocks are widely distributed in Nevada (Stewart 1980, p. 87). The distribution and heterogeneous continental character of the Tertiary deposits implies that they were laid down in restricted basins that may have been precursors to the present basins (cf. Stewart 1980, p. 92). The deposits in the Yucca Mountain area typically comprise a basal conglomerate, lacustrine limestone, and tuffs. The conglomerate is composed of locally derived clasts (Precambrian or Paleozoic provenance), commonly of cobble to boulder size, and is typically poorly sorted and set in an oxidized matrix. Its textural characteristics range from those associated with colluvial deposits to those associated with fanglomerates and stream channel gravels. The conglomerate typically intertongues with and is overlain by a characteristically pinkish-cream to buff or tan crystalline or clayey-silty lacustrine limestone. In outcrop, the limestone commonly shows soft-sediment deformation features, local slump folding, and algal mat structures. Upsection, the limestone is interbedded with and ultimately overlain by tuffaceous sandstone and distal air-fall tuffs of uncertain provenance.

Strata of this age and lithologic assemblage are found in and near Rock Valley, east of Yucca Mountain (Figure 4.2-8). These strata are informally designated as the "rocks of Winapi Wash" (Table 4.2-3). Strata of similar age and lithology are exposed to the east in the Pahranagat area; the coeval section includes up to 330 m (1,083 ft) of strata called the Hells Bells Canyon Formation (Dolgoff 1963, p. 878f). The thickest sections of this type and age (1,500 to 1,800 m [4,921 to 5,906 ft]) are present in the Spotted and Pintwater ranges (Tschanz and Pampeyan 1970, p. 67). To the west, along the east side of the Funeral and Grapevine Mountains and in small patches at the northeast corner of Bare Mountain, a section as much as 900 m (2,953 ft) thick forms the Titus Canyon Formation (Stock, C. and Bode 1935; Cornwall and Kleinhampl 1964, p. J7). Tuffs in the Titus Canyon Formation give radiometric ages ($^{40}Ar/^{39}Ar$) as old as 34 to 30 Ma (Saylor and Hodges 1994, p. 88). Tertiary sediment older than Miocene is very sparse west of the Funeral Mountains (Dunne 1986, p. 16), but thick lower Tertiary conglomerates are reported in the Cottonwood Mountains (Snow and White 1990, p. 416f).

Basin deposits of similar lithologies are found in the ranges east of Yucca Mountain (Guth et al. 1988, p. 241; Tschanz and Pampeyan 1970, p. 67), but ages have not been adequately determined to clearly discriminate the Oligocene Winapi Wash succession from a lithologically similar section that belongs to the Miocene Horse Spring Formation. The lacustrine limestone deposits generally are not more than 30 m (98 ft) thick in any locality near Yucca Mountain (Tschanz and Pampeyan 1970, p. 68).

The presence of air-fall tuffs high in the Oligocene section heralds a period of catastrophic explosive volcanism that began in Oligocene time and culminated 15 to 7.5 Ma with the creation of the southwestern Nevada volcanic field (Stewart et al. 1977, p. 67; Carr, W.J. et al. 1986, p. 3; Sawyer et al. 1994, p. 1304) (Figure 4.2-9) (see also Section 12.2). The earliest of these great eruptions is represented by the Monotony Tuff, a unit dated 27.3 Ma and exposed mainly north of Yucca Mountain in the Belted Range and the Rhyolite Hills (Sawyer, D.A., Wahl et al. 1995, p. 28) (Figure 4.2-10). The Monotony Tuff has a maximum exposed thickness of about 700 m (2,297 ft); it originated from a caldera located in the area of the present Pancake Range and northern Reveille Range (Ekren, Anderson et al. 1971, p. 25; Sawyer, D.A., Wahl et al. 1995, p. 28). (The Pancake Range is north of the Reveille Range.) The sequence of upper Oligocene through middle Miocene tuffs and associated sediments forms an important part of the Tertiary section in the setting north and east of Yucca Mountain; Ekren, Anderson et al. (1971, p. 24) cite more than 6,000 m (20,685 ft) of such strata ranging in age from 27 to 7 Ma.

Deposition of the tuffs and establishment of the great caldera complexes interrupted and locally obliterated the established Tertiary depositional regime in the Yucca Mountain geologic setting. This regime continued elsewhere, however, with modifications imposed by tectonism, until nearly the end of the Miocene, when fundamental changes in climate and regionally active extensional faulting put an end to it throughout the southern Great Basin.

In the vicinity of Yucca Mountain, in Rock Valley, the Oligocene rocks of Winapi Wash are succeeded by a complex assemblage of bouldery and poorly sorted stream gravel, volcanic arkose, shale and siltstone, freshwater limestone and marl, and a variety of tuffs. This assemblage is informally designated "rocks of Pavits Spring" (Hinrichs 1968) (Table 4.2-3). The fluvial-lacustrine environment inherited from the Oligocene persisted in Rock Valley until the Ammonia Tanks Tuff was deposited at 11.4 Ma. Gravel (unit Tsd) (Carr, M.D. et al. 1986, Figure 12, pp. 28, 30) possibly correlative with the rocks of Pavits Spring was penetrated by well UE-25 p#1 at Yucca Mountain, near the Paleozoic unconformity (Figure 4.5-3). Lacustrine sediments similar to those of the rocks of Pavits Spring crop out at the northeast corner of Bare Mountain. Here also are exposed the "rocks of Joshua Hollow," an assemblage of gravel, siltstone, shale, and crystal tuff of inferred middle to early Miocene age (Monsen et al. 1992). These strata are in fault contact with Paleozoic rocks of Bare Mountain; they are lithologically equivalent to the rocks of Pavits Spring. Sediment equivalent to the rocks of Pavits Spring is also exposed at the southern end of Bare Mountain (unit TsT) (Frizzell and Shulters 1990).

Along the eastern flank of the Funeral Mountains, in the Bat Mountain area, Cenozoic strata include a basal conglomeratic unit overlain by interlayered limestone, siltsone and sandstone, and tuff that provided a K/Ar age of 25 Ma (Cemen and Wright 1990, p. 308). The upper Oligocene strata are succeeded by sandstones, limestone, and conglomerate that range upsection to the middle Miocene Bat Mountain Formation (Cemen and Wright 1990, p. 308) (Figure 4.2-8; Table 4.2-3). The Bat Mountain Formation consists largely of alluvial fan and basin strata similar to the rocks of Pavits Spring. A similar succession crops out in the Mount Helen area (Sawyer, D.A., Wahl et al. 1995, p. 20) and in the Weepah Hills and Silver Peak Range in the northwest corner of the Yucca Mountain region. The section in the Silver Peak Range that is comparable to the Miocene rocks of Pavits Spring is called the Esmeralda Formation (Turner 1900, p. 168) (Table 4.2-3). The formation is unconformable on an upper Oligocene or lower Miocene tuff and ranges in age from about 16 Ma to about 6 Ma (Stewart 1980, p. 89; Stewart

and Diamond 1990, p. 462). The total Tertiary thickness here may be as great as 5,400 m (17,716 ft) (Stewart and Diamond 1990, p. 452).

The conditions under which the rocks of Winapi Wash were deposited apparently persisted in the area east of Las Vegas well into Miocene time, as indicated by the Horse Spring Formation. Lithologic similarities between the rocks of Winapi Wash and the Bitter Ridge Member of the Horse Spring Formation led Hinrichs (1968) to correlate the former unit in Rock Valley with the much younger Horse Spring Formation near Las Vegas. The Horse Spring Formation ranges in age from 20 to 12 Ma (Bohannon 1984, p. 12). Cemen and Wright (1990, p. 308) remark on the lithologic similarity of the Oligocene strata (25 Ma) at Bat Mountain with the type Horse Spring Formation. Apart from their geographic isolation, these Oligocene through Miocene units could be considered different parts (older and younger) of a single lithosome.

The explosive volcanism that led up to and culminated in the formation of the southwestern Nevada volcanic field is the most significant depositional event of the Cenozoic era with respect to Yucca Mountain. It resulted in the formation of at least six major calderas between about 15 and 7.5 Ma (Sawyer, D.A., Fleck et al. 1994, p. 1304), created Yucca Mountain, and brought to a close the regional deposition that spans domains of the Yucca Mountain geologic setting. The record of regional tuff deposition begins within the rocks of Pavits Spring. Tuff deposition is also documented in the eastern part of the Nevada Test Site, where Redrock Valley Tuff (15.3 Ma) (Sawyer, D.A., Wahl et al. 1995, p. 26) and the tuff of Yucca Flat (15 Ma) (Sawyer, D.A., Wahl et al. 1995, p. 26) are significant components. The succession of tuff and lava units that form Yucca Mountain are listed in Table 4.2-3 and described in detail in Section 4.5. Several units that are widely distributed in the southwestern Nevada volcanic field include the Crater Flat Group (about 13.25 Ma), the Calico Hills Formation (12.9 Ma), the Paintbrush Group (12.8 to 12.7 Ma), and the Timber Mountain Group (11.6 to 11.4 Ma) (Sawyer, D.A., Fleck et al. 1994, p. 1305). The lowest of the tuffs that form the foundation of Yucca Mountain is the Lithic Ridge Tuff (14 Ma) (Sawyer, D.A., Fleck et al. 1994, p. 1305). Although pre-Lithic Ridge tuffs are found in the rocks of Pavits Springs and beneath Yucca Mountain, little is known about their extent, age, and stratigraphic relationships. In fact, caldera sources for all but the Tiva Canyon Tuff and the Timber Mountain Group tuffs are uncertain (Sawyer, D.A., Fleck et al. 1994, p. 1304).

Lipman et al. (1966, p. F1) first noted that the Topopah Spring Tuff and the Tiva Canyon Tuff of the Paintbrush Group might represent eruptions from a zoned magma chamber. They attributed the zoning to fractional crystallization such that the upper portion of the chamber had evolved to a rhyolitic composition that was the first magma erupted and thus formed the base of each ash-flow sheet. Eruption from successively deeper portions of the magma chamber produced less siliceous ejecta with a higher proportion of crystals (which had settled into a deeper part of the magma chamber) such that the upper levels of the ash-flow sheets are crystal-rich quartz latites. Noble, D.C. and Hedge (1969, p. C137) noted that Sr was more radiogenic in the first (older) erupted parts of the ash flows and concluded that the upper part of the magma chamber had assimilated crustal rocks. Working in a similar volcanic sequence, Stuckless and O'Neil (1973, p. 1995) used Sr and O isotopes and bulk rock chemistry to show that fractional crystallization and wall-rock assimilation occurred simultaneously such that early-formed crystals were less radiogenic than their enclosing matrix. They proposed that the ash-flow complexes were generated by partial melting in the lower crust, but Nd isotope studies of several ash-flow

complexes, including those of the Timber Mountain area, suggest a large component of mantle-derived basalt (Perry, DePaolo et al. 1993, p. 879).

In another interpretation, Broxton, Warren et al. (1989, p. 5984) proposed that small volume eruptions at the caldera complex occurred in a series of cycles from individual shallow magma reservoirs. Broxton, Warren et al. (1989, p. 5983) infer that the differentiation/emplacement process was repeated for each major eruption sequence, or group. Peak volcanism in the southwestern Nevada volcanic field occurred during eruption of the Paintbrush and Timber Mountain groups when more than 4,500 km^3 (1,078 $mi.^3$) of magma were erupted in two episodes separated by a span of about 1.1 m.y. (Table 4.2-3) (Sawyer, D.A., Fleck et al. 1994, p. 1311).

The Wahmonie Formation (Poole, Elston et al. 1965) forms a sequence of andesite and dacite lava flows erupted from a source north of Skull Mountain and south of Shoshone Mountain. The Wahmonie Formation forms a distinctive marker between the Crater Flat Group tuffs and the Calico Hills Formation east of Yucca Mountain (Figure 4.2-11). Rocks of the Wahmonie Formation are characteristically dark, Fe-rich, massive or thick-bedded lava flows, autoclastic breccias, and agglomerates. The lower part of the Wahmonie Formation includes interbedded volcaniclastic sediments—debris flows, lahars, and mudslides—that indicate initial deposition in a relatively high-relief setting. The basal volcanic and volcaniclastic interval was formerly called the Salyer Formation (Poole, Elston et al. 1965; Frizzell and Shulters 1990), but is now reduced to member status (Sawyer, D.A., Wahl et al. 1995, p. 19).

The Calico Hills Formation is named for exposures in the northwest part of the Calico Hills (Sawyer, D.A., Fleck et al. 1994, p. 1307). It consists of rhyolite lavas, bedded and locally zeolitized tuffs, and nonwelded ash-flow tuffs. In the Yucca Mountain area, it is 50 to 300 m (164 to 984 ft) thick (Sawyer, D.A., Wahl et al. 1995, p. 18; Sawyer, D.A., Fleck et al. 1994, p. 1307). In earlier maps and reports, the unit is referred to informally by various designations, such as Rhyolite of Calico Hills (Lipman and McKay 1965), tuffs and lavas of Calico Hills (Carr, W.J. et al. 1986, p. 4, Figure 2), or rhyolite lavas and tuffaceous beds of Calico Hills (Frizzell and Shulters 1990).

The largest and most important contribution to the volume of Yucca Mountain is the Paintbrush Group (Table 4.2-3). It consists of a succession of well-stratified rhyolites and quartz latites totaling about 610 m (2,000 ft) thick at Yucca Mountain. The group includes four members, from the bottom up, the Topopah Spring Tuff (12.8 Ma), the Pah Canyon Tuff, the Yucca Mountain Tuff, and the Tiva Canyon Tuff (12.7 Ma). The Topopah Spring Tuff directly overlies tuff of the Calico Hills Formation at Yucca Mountain (Sawyer, D.A., Fleck et al. 1994, p. 1308). The Topopah Spring Tuff is subdivided into eleven members (Day et al. 1998b) based on crystallinity, degree of welding, and development of lithophysae. The Topopah Spring Tuff is the host rock for the potential radioactive waste repository; the unit is discussed and described in appropriate detail in Section 4.5.4.5.

The Paintbrush Group was faulted and eroded following deposition of the 12.7-Ma Tiva Canyon Tuff, thus forming an unconformable contact with the overlying Timber Mountain Group (Fridrich 1999, p. 184). Although the Timber Mountain Group forms a major eruptive volume of siliceous rhyolites and quartz latites, it is sparsely present at Yucca Mountain (chiefly at Plug

Hill and Rainier Ridge [Day et al. 1998b]). In general, distribution of the two major units of the Timber Mountain Group, the Rainier Mesa Tuff and the Ammonia Tanks Tuff, is extensive within the western half of Crater Flat Basin and at the western end of the south-bounding cuesta. Outcrop thickness as great as 240 m (787 ft) is recorded (Fridrich 1999, p. 187). The unit is described in detail in Section 4.5.4.7.

Other eruptive sequences and calderas associated with the southwestern Nevada volcanic field include the Ammonia Tanks Tuff (11.45 Ma), the Black Mountain caldera (9.4 Ma), and the Stonewall Mountain volcanic center (7.5 Ma) (Figure 4.2-11) (Sawyer, D.A., Fleck et al. 1994, pp. 1305 to 1306). The various tuffs and lavas erupted in the post-11-Ma period form important volumes of rock in the Pahute Mesa-Sarcobatus Flat-Bullfrog Hills area northwest of Yucca Mountain. They are not, however, directly relevant to the history or makeup of Yucca Mountain. The youngest tuff at Yucca Mountain is the Rainier Mesa Tuff of the Timber Mountain Group.

Physical properties of the tuff and lava units of the southwestern Nevada volcanic field contrast greatly across formational contacts, but tend to be uniform laterally over wide areas. This characteristic results from:

- The conditions of deposition—large batches of homogenized material laid down quickly over large areas
- Differences in initial composition of each eruptive batch
- Post-depositional processes of welding, vapor phase crystallization, autolytic and pneumatolytic alteration, and gas dispersion.

As a result, some of the tuff units are physically similar to ceramics or glass, whereas others are loose and porous, or vesicular and closely fractured or chemically altered. Understanding the spatial variation of these properties contributes to modeling the behavior of a potential repository under thermal loading and to modeling of hydrologic processes. More detailed information on these rocks is found in Sections 4.5, 4.7, 4.8, and 12.2.

Miocene rocks west and south of Yucca Mountain, in the Inyo-Mono domain, that are chiefly of igneous origin are younger than about 16 m.y. These include the central Death Valley volcanic field (Wright, L.A., Troxel et al. 1981, p. 7) and an irregular belt of volcanic rocks that extends from the Owlshead Mountains and southern Panamint Range eastward toward the Kingston Range, the Greenwater Range, the Black Mountains, and the Furnace Creek basin (Figure 4.2-9). Tuffs of the Artists Drive Formation date from about 14 to 6 Ma (Wright, L.A., Thompson et al. 1991). Above this lie the Furnace Creek and Funeral formations, with a combined total thickness of about 3,600 m (11,811 ft) of pyroclastic sediments, basalt flows, intertonguing conglomerates, sandstones, and mudstones. Basalts near the base of the Funeral Formation are dated at about 4 Ma (McAllister 1973). Wright, L.A., Thompson et al. (1991) note that this rock assemblage is most likely the direct result of Neogene local basin subsidence and extension.

The central Death Valley volcanic field is underlain by the Willow Springs Pluton, a diorite dated between 11.6 and 10 Ma, exposed along the west side of the Black Mountains (Figure 4.2-9) (Asmerom et al. 1990, pp. 224 to 225). The diorite is intruded by small granite bodies. Basalt extrusion in the Resting Springs Range of about the same age (11.7 m.y.) was

followed by extensive silicic to mafic volcanism during the 10.5- to 5-Ma period. Volcanism culminated in the 8.5- to 6.5-Ma period with eruption of the Shoshone volcanic suite, chiefly dacites and rhyodacite tuffs (with associated sediments) exposed in the eastern Black Mountains and southern part of the Greenwater Range (Figure 4.2-9). Silicic volcanism ceased in this area about 5 to 6 Ma with deposition of rhyolites of the Greenwater volcanic suite (Noble, L.F. 1941, p. 956; Drewes 1963, p. 42). Thereafter, diminishing basaltic volcanism continued into Late Pleistocene time, as in the Goldfield section of the Walker Lane domain to the east.

The advent of basaltic volcanism at about 11 Ma signaled the end of crustal magmatism in the construction of Yucca Mountain. It indicates generation of small, discrete batches of basaltic magma at upper mantle depths (60 km [37 mi.]) capable of making their way quickly to the surface in Crater Flat basin (Crowe, Perry et al. 1995, pp. 5-16 to 5-17). The history, evolution, and character of Plio-Pleistocene basaltic volcanism proximal to Yucca Mountain (within 25 km [15 mi.] of the potential repository) is treated by Crowe, Perry et al. (1995) and by Vaniman et al. (1982).

The oldest basalts in Crater Flat are dated at about 11.3 Ma, indicating that episodes of basaltic volcanism began very shortly after eruption of the Ammonia Tanks Tuff (11.45 Ma). However, no further basaltic volcanism occurred in Crater Flat until 3.7 Ma, when a group of five northwest-aligned scoria cones and lava flows were emplaced in southeastern Crater Flat (Figure 4.2-12). This latter episode represents the largest volume basaltic emplacement in Crater Flat. The complex formed largely from Hawaiian-type fissure eruptions and aa flows. Lava-filled fissures and feeder dikes are oriented north-south. The deposit was subsequently cut by faulting that produced dip-slip offsets of more than 1 m (3 ft), west side down (Crowe, Perry et al. 1995, pp. 2-19 to 2-20).

4.2.2.2.2 Quaternary Rocks and Sediments

Quaternary deposits consist of alluvial sediments and infrequently erupted basalts. The basaltic eruptions represent a continuation of the activity during the Late Tertiary. Following the episode at 3.7 Ma, a subsequent basaltic eruption episode occurred between 1.7 and 0.7 Ma. It consists of four cinder cones (Little Cones, Red Cone, Black Cone, and Makani Cone) aligned north-northeast along the axis of Crater Flat (Figure 4.2-12). Most of the volume from this episode is associated with Red and Black cones. The area of this episode spatially overlaps the area of the earliest eruption (11.3 Ma).

The most recent episode of basaltic volcanism created the Lathrop Wells Cone (Figure 4.2-12). The Lathrop Wells Cone complex comprises fissure eruptions, spatter and scoria cones, and aa flows. Satellite spatter cones at the east base of the main cone have a northwest alignment. The Lathrop Wells Cone complex is probably about 80 ka (Heizler et al. 1999, pp. 767 to 768). The complex emplacement history of this volcanic center is discussed by Crowe, Perry et al. (1995), by Heizler et al. (1999), and in Section 12.2.2.4.

Other basaltic groups in the Yucca Mountain vicinity include the 380-ka Sleeping Butte centers, located 45 km (30 mi.) northwest of Yucca Mountain, and the Amargosa Valley basalt, located about 3 km (1.8 mi.) south of Amargosa Valley crossroads (Crowe, Perry et al. 1995, p. 2-19). The basalt is buried, but was sampled by drilling; basalt samples gave $^{40}Ar/^{39}Ar$ isochron ages of

3.8 and 4.4 m.y. (Crowe, Perry et al. 1995, p. 2-19). The eruptive history of Quaternary basaltic volcanism in the Yucca Mountain region is discussed in more detail in Section 12.2.2.4.

Apart from sporadic and volumetrically minor basaltic volcanism, Quaternary deposition in the Yucca Mountain geologic setting is chiefly restricted to alluvial basin deposition. In many basins, alluvial deposition is a continuation of sediment infilling that was well under way in late Miocene time. For example, in Mid Valley (Figure 4.2-13), a continuous alluvial section 300 to 400 m (984 to 1,312 ft) thick includes a several-meter-thick (10-ft-thick) interval of 7.5-Ma ash-fall Spearhead Tuff (McArthur and Burkhard 1986, pp. 26 to 27, 41). The tuff, penetrated by two boreholes, is overlain by about 360 m (1,181 ft) of fine to coarse sand and sandy gravel derived from the basin flanks.

Closed basins in the area received alluvial sediment hundreds of meters (about 1,000 ft) thick throughout the Plio-Pleistocene, in response to continuing faulting, subsidence, and range flank erosion. Frenchman Flat and Yucca Flat basin, Mid Valley, Crater Flat basin, and especially the basins of the Inyo-Mono terrane (Figure 4.2-13) contain sediment that includes coarse alluvial clastic facies (e.g., debris flow deposits, colluvium, fan sheet gravel) and lakebed-playa deposits (e.g., siliceous clays, marls, evaporites). In some basins, such as Crater Flat basin, aggradation has reached levels sufficient to have formed spillways, so that alluvial deposition is graded to an adjacent valley (here Amargosa Valley) (Figure 4.2-13) or basin.

Within the Yucca Mountain region, broad valley or trough-like areas of subsidence are linked by graded fan assemblages and washes to form two separate drainage systems: the Las Vegas Valley watershed and the Amargosa Valley watershed (Figure 4.2-13). Colluvium and scree commonly litter the range flanks. This sediment typically is brought to the basins as debris flows or mud flows during the infrequent torrential rains that are characteristic of the present interpluvial climate.

An overall regional tilt to the south, established during the past 8 m.y. (Carr, W.J. 1984, p. 82), seems to have driven regional drainage southward, resulting in a general ponding at the southern ends of major basins and the development of spillways. Drainage through Amargosa Valley, for example, was ponded at a former Tecopa Lake, which was receiving sediment in late Pliocene to early Pleistocene time. The lake was breached and the Tecopa Lake beds are being incised as drainage flows through the Sperry Hills, then west into Death Valley (Figure 4.2-13).

Although present deposition and erosion generally occur at very low rates and sporadically because of the arid climate, the middle to late Pleistocene depositional record (locally dated by distal ash layers like the 760-ka Bishop Ash) indicates a highly variable and localized succession of sedimentary deposits, perhaps analogous to the middle Miocene rocks of Pavits Spring, but without the tuffaceous volcanic component. Sediment input is dominated by highly local sources that control the lithologies of the coarse clastic components; lake or pond deposits are virtually the only datable records because they contain fine sediment and rare but radiometrically datable volcanic ash beds. In some places, large accumulations of eolian silts and sands are banked up against range flanks or as dune accumulations, notably Big Dune, south of Bare Mountain (Figure 4.2-13). Further details on Pleistocene stratigraphy and depositional and erosional processes can be found in Section 4.4.3.3.

4.2.3 Regional Structure and Tectonic Deformation

The geologic setting of Yucca Mountain is characterized structurally by two distinctly different tectonic deformation styles: an earlier compressional "mountain building" style of regional folding and overthrusting, and a later extensional "basin forming" style of regional normal and strike-slip faulting. The following sections discuss the structures resulting from these two styles of deformation.

4.2.3.1 Compressional Tectonics of the Yucca Mountain Region

The compressional style records orogenic events that occurred primarily during Paleozoic deposition, followed by a peak event that occurred in the Mesozoic and terminated marine deposition. Compressional deformation of Precambrian age is also recorded in Proterozoic and older rocks, but no orogenic pattern has been determined from the sparsely exposed rocks.

The earliest mountain building event that affected Paleozoic rocks in the Yucca Mountain geologic setting is the Antler Orogeny (Stewart 1980, p. 36, Figure 22). Antler orogenic deformation is expressed chiefly by the Roberts Mountains overthrust belt, which is located well north of Yucca Mountain (Figure 4.2-14). The thrusting created a mountain range and a marine foredeep basin along its eastern margin into which the coarse sediment that eroded from the thrust belt was deposited. An alternative interpretation (Ketner 1998), characterizes the Antler Orogeny as involving primarily vertical tectonics, without a strong compressional component.

The coarse, clastic sediment derived from the Antler highlands beginning in Middle Devonian time and continuing into the Mississippian period constitutes the Eleana Formation, exposed at the Nevada Test Site (Trexler, J.H. et al. 1996, p. 1740). Farther east, a correlative section of shale (Chainman Shale) was deposited in an environment that has aspects of an inner shelf as well as a subsiding basin (Trexler, J.H. et al. 1996, p. 1750); east of that was a carbonate platform environment uninfluenced by the Antler Orogeny (Figure 4.2-14). Similar depositional effects of the Antler Orogeny are found in the Inyo-Mono domain, where the Upper Mississippian Rest Spring Shale and the shaley lower part of the Lower Mississippian Tin Mountain Limestone represent erosion of the Antler highlands (Dunne 1986, p. 5) and, therefore, are part of the Eleana-Chainman lithosome.

The Antler Orogeny is significant in the Yucca Mountain region for two reasons:

- The fine-grained, terrigenous lithology of the Eleana (and especially the Chainman Shale) lithosome forms a major Paleozoic aquitard north and east of Yucca Mountain, as well as a potential source rock for hydrocarbons.
- The subsequent juxtaposition of three distinct but coeval facies (i.e., Antler-derived clastic debris, black Chainman Shale, and Mississippian and older carbonates) aids in recognizing the structural configurations that formed during the subsequent Sevier-Cordilleran Orogeny.

Mountain building in the near vicinity of Yucca Mountain began with eastward-encroaching uplift in latest Permian to Triassic time and culminated during the Mesozoic with the Sevier Orogeny (Stewart 1980, p. 77; Fleck 1970a; Armstrong 1968, p. 429f). The Sevier Orogeny

resulted in a broadly north- to northeast-trending fold-thrust system (Figure 4.2-15). The thrust sheets are typically complicated by overturned or dismembered folds and local reverse or overthrust faults. The major thrusts are continuous along strike for distances of more than 100 km (62 mi.) and exhibit stratigraphic juxtapositions that indicate translations of tens of kilometers. Nevertheless, the history of thrust faulting in the Yucca Mountain region, and the identity of each fault from place to place, is uncertain because of erosion, subsequent extension, and burial beneath Tertiary and Quaternary rocks and surficial deposits over wide areas. Therefore, only a general treatment, with an emphasis on geometric relations relevant to issues concerning Yucca Mountain, is presented below.

Two major thrusts are recognized in the vicinity of Yucca Mountain: the Belted Range thrust (Caskey and Schweickert 1992, p. 1318; Cole and Cashman 1999, p. 8) and the CP thrust (Caskey and Schweickert 1992, p. 1316; Barnes and Poole 1968, p. 233; Carr, W.J. 1984, p. 52). The Belted Range thrust (Figure 4.2-15) is the structurally lower and older thrust. It is represented in outcrop at Bare Mountain (there referred to as the Meiklejohn Peak thrust), perhaps in the core of the Calico Hills (see discussion of Calico Hills below), and by exposures at the southern end of the Belted Range west of Yucca Flat (Figure 4.2-15) (Caskey and Schweickert 1992, pp. 1318, 1321; Cole and Cashman 1999, p. 7). Displacement across the Belted Range thrust is estimated from at least 7 km (4.3 mi.) (Cole and Cashman 1999, p. 8) to more than 25 km (15.5 mi.) (Caskey and Schweickert 1992, p. 1320). Below the Belted Range thrust, a stack of imbricate slices or "plates" place Middle Devonian strata and the Eleana Formation over the Chainman Shale along a subhorizontal thrust exposed in the Eleana Range (Trexler, J.H. et al. 1996, p. 1756). Thrusts that form the base of this duplex zone cut upsection into Mississippian strata, then form a décollement within the weak Chainman Shale (Trexler, J.H. et al. 1996, p. 1757). The duplex stack extends about 7 km (4.3 mi.) outboard (east) of the main Belted Range thrust; it includes structures at Calico Hills (Calico Hills plate), Mine Mountain (Mine Mountain plate), the Eleana Range (Castle plate, Dolomite Hill plate, and Grouse Canyon plate), and Quartzite Ridge at the northern border of the Nevada Test Site (Figure 4.2-15) (Trexler, J.H. et al. 1996, p. 1739; Cole and Cashman 1999, pp. 10, 11). A component of the duplex stack in this northern area was identified as the Tippipah thrust by Robinson (1985, p. 7). Westward projection of the Belted Range thrust implies that the magnetic gradient present beneath the volcanic deposits at the northern end of Yucca Mountain represents the duplex stack thrust southward against the Silurian rocks penetrated by well UE-25 p#1 (Carr, M.D. et al. 1986, p. 16).

The CP thrust is a west-vergent back-thrust that lies to the east of, and is structurally above and younger than, the Belted Range thrust (Figures 4.2-15 and 4.2-16) (Caskey and Schweickert 1992, p. 1326). It generally emplaces Precambrian through Cambro-Ordovician strata over Mississippian and Pennsylvanian strata. The CP thrust is a large, complex structure that extends for more than 180 km (112 mi.) on strike and has about 8.5 km (5.3 mi.) of stratigraphic throw (Caskey and Schweickert 1992, pp. 1318, 1327). Rocks of the upper plate are imbricately faulted, highly folded, and locally overturned to the west. Large-scale, west-vergent, nearly recumbent folds occur in both the lower and upper plates of the CP thrust (Caskey and Schweickert 1992, p. 1316). The CP thrust was originally defined from a small patch of outcrop in the CP Hills, which form the west flank of Yucca Flat (Figure 4.2-15) (Barnes and Poole 1968, p. 233). Early work at the Nevada Test Site assigned all thrust structures in the area to the CP thrust (Barnes and Poole 1968, p. 233; Carr, W.J. 1984, p. 52),

but Caskey and Schweickert (1992, p. 1314) distinguished the CP thrust from the Belted Range thrust on the basis of lower plate folds that indicate westward thrusting of the CP thrust in opposition to eastward thrusting of the Belted Range thrust.

The complex structural relations between the Belted Range and CP thrust systems are reflected in the conflicting interpretations in geologic reports. Exposures north and west of the CP Hills have been variously interpreted. East-vergent thrusting at Mine Mountain is cited by Burchfiel, Pelton et al. (1970, p. 213) and Ekren, Anderson et al. (1971, p. 69) and assigned to the CP thrust; Barnes and Poole (1968, p. 238) and Caskey and Schweickert (1992, p. 1318) recognized west-vergent thrusting at Mine Mountain and linked the Mine Mountain and CP thrusts. W.J. Carr (1984, p. 52) and G.D. Robinson (1985, p. 16) tentatively proposed that the older over younger block assemblage at Mine Mountain could be a dismembered gravity slide. This was substantially documented by Cole, Wahl et al. (1989, p. 444). Cole, Wahl et al. (1989) considered that the structure at Mine Mountain, the CP Hills, and the Calico Hills could best be interpreted as low-angle gravity sliding of middle Miocene age; only the faults at Bare Mountain could be considered indisputable thrusts. More recently, structure at Mine Mountain is interpreted to be a complex overprinting of west-vergent thrusting of the CP thrust over the lower plate of the older east-vergent Belted Range thrust, as well as later extensional faulting (Cole and Cashman 1999, p. 16).

Caskey and Schweickert (1992, p. 1324) carried the CP thrust west through the Calico Hills and correlated it to the Panama thrust at the southern end of Bare Mountain (Figure 4.2-15). This interpretation suggests that the CP thrust extends through the Paleozoic substrate beneath Yucca Mountain, possibly placing Silurian rocks above buried Eleana Formation rocks or forming a north-vergent thrust south of and subparallel to the inferred Belted Range thrust duplex mentioned above. In other words, beneath Yucca Mountain there may exist two opposing thrusts, one correlating with the Meiklejohn Peak thrust and the other with the Panama thrust at Bare Mountain.

The structure exposed in the core of the Calico Hills could be assigned to gravity sliding or to the Belted Range thrust (Trexler, J.H. et al. 1996, p. 1756; Cole and Cashman 1999, p. 18), the CP thrust (Caskey and Schweickert 1992, p. 1324), or both (Cole and Cashman 1999, p. 25). Uncertainty exists because of the difficulty in recognizing indisputable thrust-related deformation that expresses vergence, and because either thrust system could reasonably be projected through the Calico Hills. Simonds and Scott (1996, p. 34) could not resolve the uncertainty, but tentatively advocated a thrust structure rather than a gravity slide structure.

Apart from the Calico Hills exposure, the east- and west-vergent thrust systems are separated by a span of rock that probably was never overthrust. Conodont alteration indices data indicate that the Chainman Shale at Syncline Ridge, located between the thrust systems (Figure 4.2-15), was never tectonically buried, hence neither thrust ever extended much beyond its present position (Trexler, J.H. et al. 1996, p. 1757). Conodont alteration indices from the Silurian rocks penetrated by well UE-25 p#1 at Yucca Mountain indicate the rocks reached maximum temperatures of 140° to 180°C. M.D. Carr et al. (1986, p. 49) concluded that these temperatures could have been achieved by normal burial depths for Silurian rocks in the Great Basin. This observation supports an interpretation that the Silurian rocks in UE-25 p#1 were not overthrust. The gap between the thrust fronts probably extends to Bare Mountain, where the Meiklejohn

Peak thrust (Belted Range thrust system) and the Panama thrust (CP thrust system) are presently separated by about 6.5 km (4 mi.). Small klippen of the Panama thrust near the center of the mountain (Monsen et al. 1992) indicate the gap, if it existed, was originally smaller, or perhaps the Panama thrust originally overrode the Meiklejohn Peak thrust (Cole and Cashman 1999, p. 27).

Farther east, the Spotted Range thrust, named for its exposure in the Spotted Range (Figure 4.2-15) (Barnes, Ekren et al. 1982), placed Middle Cambrian strata over Upper Devonian and Mississippian strata, with more than 25 km (15.5 mi.) of offset (Caskey and Schweickert 1992, pp. 1318, 1320; Tschanz and Pampeyan 1970, p. 108). Lower plate strata have tight to isoclinal folds overturned to the southeast. Accordingly, the Spotted Range thrust cannot be correlated with the CP thrust (as proposed by Barnes and Poole 1968, p. 235). Caskey and Schweickert (1992, p. 1320) observed that the lower plate of the Spotted Range thrust is structurally equivalent to the upper plate of the west-vergent CP thrust (Figure 4.2-16). Therefore, the Spotted Range thrust is an eroded, eastern outlier (klippe) of the Belted Range thrust.

The Spotted Range thrust has been extended westward by correlation with the Specter Range thrust (Wernicke, Snow et al. 1988, p. 257). The Specter Range thrust is exposed for a strike distance of about 4 km (2.5 mi.) in the Specter Range (Sargent and Stewart 1971), where it is expressed as a N60°E, N50° to 60° fault that places the Cambrian Bonanza King Formation over Lower and Middle Ordovician strata (Sargent and Stewart 1971; Burchfiel 1965, p. 179), a stratigraphic displacement of more than 1,700 m (5,577 ft) (Burchfiel 1965, p. 179). The correlation with the Spotted Range thrust was argued by Snow (1992, p. 96) on the basis of structural position, stratigraphic throw, association with a footwall syncline, and distance from other distinctive structures. However, Cole and Cashman (1999, p. 30) pointed out that the Specter Range thrust and the Spotted Range thrust represent different stratigraphic levels (cf. Burchfiel 1965, p. 185; Caskey and Schweickert 1992, p. 1326), and that stratigraphic displacement decreases to the east such that the Specter Range thrust dies out beneath Mercury Valley. Burchfiel (1965, p. 186, Plate 3) inferred that the Specter Range thrust continues east and south of Mercury Valley as a strike-slip fault, the northern end of the Las Vegas Valley shear zone (discussed below).

The Gass Peak thrust is a large, east-vergent thrust that places upper Precambrian and Cambrian rock over highly folded and locally overturned Pennsylvanian and Permian carbonate strata (Figure 4.2-17) (Longwell et al. 1965, p. 76; Guth 1981, p. 767) for at least 140 km (87 mi.) along the east side of the northern part of the Sheep Range and through the Las Vegas Range (Longwell et al. 1965, p. 75). It is traceable southward into the Spring Mountains (as the Wheeler Pass thrust) because of its consistent structural level (Figure 4.2-17) (Guth 1990, p. 240). Net horizontal displacement could exceed 30 km (19 mi.) (Guth 1981, p. 764). Because no major thrusts occur between the Gass Peak thrust and klippen of the Spotted Range thrust, the lower plate of the Spotted Range thrust is also equivalent to the upper plate of the Gass Peak thrust (Figure 4.2-16) (Caskey and Schweickert 1992, p. 1322). Therefore, the Gass Peak thrust and the CP thrust define the eastern and western structural boundaries of the same allochthon.

Late Paleozoic and Mesozoic thrust systems in the Inyo-Mono domain are more extensive and complex than any exposed east of the Funeral Mountains, but their structural relations are more

clearly defined. The most extensive thrust system, the Last Chance thrust system (Figure 4.2-17), includes (from oldest to youngest) the Last Chance, the Talc City, the Race Track, the Marble Canyon, and the Lemoigne thrusts (Dunne 1986, p. 9). The system comprises imbricate, northeast-trending, generally east-vergent thrusts having at least 7 to 35 km (4.3 to 22 mi.) of displacement in aggregate. The thrusts place rocks as old as Precambrian on rocks as young as Permian. Deformation typically involves locally recumbent and isoclinal folds in the overridden plates, but most folds are upright and open. The system was probably most extensively active from middle Triassic to early Jurassic time (Dunne 1986, p. 11), but thrusting could have begun as early as Permian time (Snow 1992, p. 102). The Last Chance thrust system predates the 167- to 185-Ma Hunter Mountain batholith (Dunne et al. 1978, p. 197). It may predate intrusion of the pre-late Triassic White Top stock in the Cottonwood Mountains (Snow 1992, p. 91; Caskey and Schweickert 1992, p. 1327). The Last Chance thrust system essentially comprises the Death Valley thrust belt (Snow 1992, p. 81).

Numerous attempts have been made to correlate thrusts of the Death Valley thrust belt across the Furnace Creek-Death Valley fault into the Walker Lane and the Nevada Test Site area. Caskey and Schweickert (1992, p. 1326) argued that only three thrust plates exist at the Nevada Test Site, not five as in the Death Valley thrust belt (Snow 1992, p. 81; Wernicke, Snow et al. 1993, p. 453):

- Strata above the Belted Range thrust
- Strata below the Belted Range thrust and the CP thrust
- Strata above the CP thrust and the Gass Peak thrust.

Accordingly, Caskey and Schweickert (1992, p. 1325) tentatively correlate only two thrusts, the Belted Range thrust with the Last Chance thrust. Caskey and Schweickert (1992, p. 1317, Figure 3) and Snow (1992, p. 94) continue the Belted Range thrust west, connect it with the Grapevine thrust, and thereby correlate it with the Last Chance thrust system (Figure 4.2-17). Snow (1992, p. 97) correlates the Meiklejohn Peak duplex zone (Calico Hills plate of Trexler, J.H. et al. [1996, p. 1739]) with the Racetrack duplex zone beneath the Last Chance thrust. Snow (1992, p. 84, Table 1) also correlated the White Top thrust (or backfold) with the Panama thrust-CP thrust (Figure 4.2-17), but this correlation is disputed by Cole and Cashman (1999, p. 33). The Marble Canyon thrust is correlated with the Specter Range thrust via the Scwaub Peak thrust in the Funeral Mountains (Wernicke, Snow et al. 1988, p. 257; Snow 1992, pp. 94, 96; Cole and Cashman 1999, p. 33).

Attempts to trace thrusts across the Spring Mountains section of the Walker Lane domain into the Inyo-Mono domain are hampered because of dextral offset along the Stewart Valley fault and as much as 3.5 km (2.2 mi.) of normal offset along the Grapevine fault (Figure 4.2-17) (Burchfiel, Hamill et al. 1983, p. 1371). The structurally lowest thrust in the Spring Mountains section, and in the entire Yucca Mountain geologic setting, is the Birdspring thrust, which places the Bonanza King Formation on the Lower Jurassic Aztec Sandstone; however, at its northern end, the thrust loses throw and merely duplicates Permian red beds (Burchfiel and Davis 1988, p. 89). The Birdspring thrust is the base of a duplex sheet of imbricate faults and folds, all cut out by the overlying Keystone thrust (Figure 4.2-17), which puts Bonanza King over younger Cambrian and overturned Triassic strata.

In tracing thrusts west out of the Spring Mountains and into the Montgomery Mountains, Burchfiel, Hamill et al. (1983, p. 1375) tentatively concluded that the Wheeler Pass thrust is correlative with the Chicago Pass and Shaw Pass thrusts in the northern part of the Nopah Range (Figure 4.2-17). The Chicago Pass thrust and the closely related Shaw thrust have a net stratigraphic throw of about 5 km (3 mi.) to the south. The thrust overrides a footwall syncline that infolds lowest Devonian to highest Carboniferous strata with a 300-m (984-ft) wavelength (Burchfiel, Hamill et al. 1983, pp. 1367, 1369). The Montgomery thrust places Stirling Quartzite over Ordovician rocks and Devonian Devils Gate Limestone in a tight overturned syncline having a wavelength of about 1 km (0.6 mi.) across a dip of about 30° to the northwest (Burchfiel, Hamill et al. 1983, pp. 1366 to 1367). Wernicke, Axen et al. (1988, p. 1743), Wernicke, Snow et al. (1988, p. 257), and Snow (1992, p. 82) correlated thrusts as far west as the Panamint Range or the Slate Range in eastern California with the Wheeler Pass-Gass Peak thrust system.

At present, the only aspects of the Mesozoic Orogeny that are well known in the Yucca Mountain geologic setting are the geometry and the stratigraphic relations among the various thrust sheets. Questions regarding where the faults are rooted, how they climb sections, and to what levels of the crust thrusting is involved remain unresolved.

Many thrust systems in the Yucca Mountain region are associated with regional folds. One example of a large fold is the Panamint-Greenwater anticlinorium (Wright, L.A., Troxel et al. 1981, p. 10), described by Dunne (1986, p. 15) as a "northwest-pointing tongue of Precambrian rock exposed in the Panamint, Black, and Greenwater Ranges." The fold is bounded by west-dipping strata of the East Sierra thrust system in the Argus Range, and by east-dipping strata in the Resting Spring and Nopah ranges (Figure 4.2-15). Structural relief is probably about 7 km (4.3 mi.). The fold may be a large ramp anticline resulting from the generally eastward movement of a thrust stack of Proterozoic crystalline basement up and over a west-facing ramp (Dunne 1986, p. 15). Robinson (1985, p. 5) inferred that the major structure encompassing Yucca Mountain is a synclinorial basin spanning the area between Bare Mountain and the Halfpint Range, a distance of more than 80 km (50 mi.) (Figure 4.2-18). In his interpretation, the basin is asymmetric, having steep to overturned limbs on the Bare Mountain side and along Rock Valley. The basin is bounded to the south by the Rock Valley fault zone and to the northeast by a "major northeast-trending thrust system," the Tippipah thrust zone (Robinson 1985, p. 5) (the Belted Range thrust of Caskey and Schweickert [1992] and Trexler, J.H. et al. [1996]). The principal deformation within the basin consists of broad, concentric folds 8 to 24 km (5 to 15 mi.) apart that trend about N30°E and plunge northward (Figure 4.2-19). Robinson (1985, pp. 5, 19) based his interpretations of fold structure on exposed dips, data from well UE-25 p#1, and aeromagnetic data. As a corollary to this tectonic interpretation, Robinson (1985, p. 16) inferred that the Mine Mountain and CP thrusts are minor structures; he suggested they were local slides that occurred in response to regional folding. Whether Robinson's (1985) assessment of fold geometry, and the relative magnitudes of folding and thrusting, is correct, there is little doubt that large-amplitude, regional folds have accompanied thrust faulting in the region.

East of Yucca Mountain, the Gass Peak thrust plate is folded into large, north-trending open folds (Guth 1990, p. 238) and, more broadly, arched to form the Pintwater anticline (Longwell 1945, p. 111f) and the Spotted Range syncline (Barnes, Ekren et al. 1982), a regional

fold pair traceable for about 100 km (62 mi.) and having a combined width that spans four mountain ranges (i.e., the Sheep, Desert, Pintwater, and Spotted ranges) (Figure 4.2-15). Structural relief is probably as great as 7 km (4.3 mi.) (Caskey and Schweickert 1992, p. 1322). The west limb of the Pintwater anticline probably controls the ramp-like Pintwater thrust (Longwell et al. 1965, p. 72), a steeply west-dipping thrust fault that extends about 25 km (16 mi.) along the west side of the Pintwater Range (Figure 4.2-15) and has about 1 km (0.6 mi.) of stratigraphic separation (Guth 1990, p. 241).

Burchfiel, Hamill et al. (1983, pp. 1366, 1375) argued that a large, recumbent east-trending anticline-syncline pair in the northwestern Spring Mountains (Montgomery thrust) correlates with the east-trending Pintwater anticline at the southern end of the Spotted Range. The Pintwater anticline and the Spotted Range syncline represent a broad regional fold pair having a pre-extensional structural relief of as much as 7 km (4.3 mi.) (Caskey and Schweickert 1992, p. 1322). The Montgomery thrust is inferred to pass through the northwestern part of the Spring Mountains, degenerating into a fold pair ultimately correlating with the Pintwater Range anticline (Figure 4.2-15).

It is unclear when overthrusting and regional folding generally ceased in the Yucca Mountain region. The presence of undeformed Late Cretaceous intrusives indicates that deformation did not continue through Cretaceous time. The Belted Range thrust, as correlative to the Last Chance thrust, probably originated prior to latest Middle Triassic and ceased activity by about 93 Ma, the age of the Climax stock (Naeser and Maldonado 1981, p. 46), a granodiorite intruded in complexly folded Ordovician strata north of Yucca Flat (Houser and Poole 1960). The age of the CP and the Gass Peak thrusts, which cut the Belted Range thrust (Figure 4.2-16), would be younger. The Keystone thrust was probably moving by Early Jurassic time (Burchfiel, Fleck et al. 1974, p. 1021). By late Jurassic time, deformation was well under way in the Great Basin (Armstrong 1968, p. 449). Thus, the Sevier Orogeny (Armstrong 1968, p. 451; Fleck 1970a, p. 1718) was a short-lived compressional event in the Yucca Mountain region. Compressional tectonism in the Inyo-Mono terrane appears to have ceased completely in Paleogene time (Dunne 1986, p. 16).

4.2.3.2 Extensional Tectonics of the Yucca Mountain Region

Extension in the Yucca Mountain region was active by late Oligocene time (Axen et al. 1993, p. 64; Sawyer, D.A., Fleck et al. 1994, p. 1314; Hardyman and Oldow 1991, p. 285; Ekren and Byers 1984, p. 214; Dilles et al. 1993, p. 425) and probably earlier (Eaton 1982, p. 412; Hodges and Walker 1992, p. 563; Axen et al. 1993, p. 64; Applegate et al. 1992, p. 519; Smith, D.L. 1991, p. 189). This early phase of extension, sometimes referred to as "pre-basin and range faulting" (Zoback et al. 1981, p. 420), continued into middle Miocene time. It is thought to have evolved by gravitational collapse of thrust-thickened crust following diminution of subduction-generated compression from the west (Stewart 1978, p. 25; Wernicke, Christiansen et al. 1987, p. 203; Cole et al. 1993; Hodges and Walker 1992, pp. 566 to 567; Scholz et al. 1971, p. 2987). The result was a thinner, closely faulted crust and lithosphere heated and elevated by upper mantle convection (Stewart 1978, p. 26; Hamilton, W.B. 1989, p. 770; Eaton 1982, pp. 411, 422; Scholz et al. 1971, p. 2981, Figure 3). Extension during this early phase is thought to have migrated from east-northeast to west-southwest and to have been unaffected by oblique shear (Seedorff 1991, Figures 5 to 8). Although this phase of regional

extension progressed under the influence of a generally uniform west- to southwest-directed least principal stress (Zoback et al. 1981, p. 204), northwest-directed oblique shear did influence the course of extension toward the west side of the widening province at an early date (Stewart 1992, pp. 7; 9). By early Miocene time (and likely by Middle-Late Oligocene), the characteristic features of the Walker Lane had been established, namely discontinuous north-northwest striking dextral faults and east-northeast striking sinistral faults (Ekren and Byers 1984, p. 203; Hardyman and Oldow 1991, p. 289; Stewart 1988, p. 686). Deep-seated detachment may also have been a significant mechanism of Paleogene extension in this region. Geobarometry and fission-track age dates indicate that subhorizontal mylonites, presumably indicative of predetachment shear (Hamilton 1987, pp. 157, 165; Hamilton, W.B. 1988, p. 80), were generated at depths of at least 15 km (9.3 mi.) beneath the Funeral-Bare Mountains area during this phase of deformation (Hoisch and Simpson 1993, pp. 6823 to 6824; Hoisch et al. 1997, p. 2830).

The main extensional features within the tectonic setting of Yucca Mountain were established by about 15 Ma, namely a basin and range structural pattern defined chiefly by north-south oriented basins or troughs and fault zones associated with the Walker Lane, including the Rock Valley fault zone.

The Late Oligocene interval was punctuated by deposition of ash-fall tuffs from eruptions east and north of Yucca Mountain (Axen et al. 1993, p. 62). The advent of siliceous volcanism marks an important tectonic development in the early phase of extension: it signals a culmination of regional crustal heating, the so-called "ignimbrite flare-up," during which large volumes of siliceous magma were emplaced in the middle to upper crust (Seedorff 1991, p. 133).

Like the progress of early extension, magmatism proceeded from north to south through the Great Basin; in the south it seems to have generally lagged behind the extension. Thus, the southwestern Nevada volcanic field may have been generated in an area of crust weakened by deep extensional basins and therefore conducive to volcanic venting (Axen et al. 1993, pp. 68, 73); but an alternative interpretation by Sawyer, D.A., Fleck et al. (1994, pp. 1314, 1316) proposes that the Oasis Valley-Timber Mountain caldera complex formed in an area of minor crustal extension and that significant extension proximal to Yucca Mountain occurred after formation of the caldera complex. A basin analysis by Blakely et al. (1999) indicates that the southwestern Nevada volcanic field (including Yucca Mountain) formed within an assemblage of deep extensional basins, which suggests that the present basin configuration was well established prior to the formation of Yucca Mountain. A clastic sedimentary deposit, the rocks of Pavits Spring (Hinrichs 1968), and the comparable Esmeralda Formation (Stewart and Diamond 1990), also imply that deepening and integration of basins in the Yucca Mountain region occurred prior to formation of the southwestern Nevada volcanic field.

The rocks of Pavits Spring record basin integration and increased structural and topographic relief by way of thick, torrential stream boulder gravels and volcanic arkoses. Increasingly proximal volcanic activity is indicated by increasing contributions of tuffs upsection, including, ultimately, the major components of the southwestern Nevada volcanic field, beginning around 14 Ma with units of the Crater Flat Group.

The course and extent of basin evolution in the Yucca Mountain area are only generally perceived, but it seems clear that considerable extension and basin deepening preceded the volcanic activity that created Yucca Mountain.

The culminating tectonic event in the geologic evolution of the region and, coincidentally, the initiating event for the structural formation of Yucca Mountain was the creation of the southwestern Nevada volcanic field. This field was produced by a succession of at least five voluminous and numerous smaller eruptions that occurred over 7.5 m.y., from about 15 to 7.5 Ma. The greatest of these eruptions created the volcanic pile (the Paintbrush and Timber Mountain groups) of which Yucca Mountain is a part. Post-eruptive deflation likely created at least some of the present structural framework of Yucca Mountain, assuming that some post-Paintbrush Group subsidence of Crater Flat basin can be attributed to withdrawal of the underlying magma chamber (cf. Carr, W.J. 1990, p. 300). Local domainal extension, involving some strike-slip displacements, clockwise rotation of crustal blocks, basin subsidence, and range uplift, continued in the Walker Lane during the phase of siliceous volcanism (Sawyer, D.A., Fleck et al. 1994, p. 1314). Yucca Mountain was affected by this activity in the 12.7- to 9-Ma interval, as evidenced by continued subsidence and extension across the Crater Flat basin and the collapse of the Jackass Flats area and of volcanic terrane farther east.

The advent of basaltic volcanism at about 11 Ma signals the end of crustal level magmatism in the vicinity of Yucca Mountain. It indicates generation of small, discrete batches of basaltic magma at upper-mantle depths (45 to 60 km [28 to 37 mi.]) capable of making their way quickly to the surface (Crowe, Perry et al. 1995, pp. 4-1, 5-6).

From about 11 to 7 Ma, the style of tectonic deformation in the Yucca Mountain region became more clearly one of narrow basin subsidence, possibly accompanied by adjacent range uplift. Analysis of faults near Yucca Flat and in the Basin and Range province to the east indicate that the present stress regime originated around 9 Ma; before then, the least compressive stress was oriented in a more westerly or southwesterly direction (Zoback et al. 1981, p. 212; Minor 1995, p. 10,524). Minor (1995, p. 10,525) concluded that the stress field in the Yucca Mountain region rotated clockwise as much as 65° in the 11- to 8.5-Ma interval. The clockwise stress rotation is recognized elsewhere in the region (Carr, W.J. 1984, p. 84; Zoback et al. 1981, pp. 207, 209; Michel-Noël et al. 1990, pp. 155, 169), but estimates of its timing vary (Wernicke, Axen et al. 1988, p. 1756). Hardyman and Oldow (1991, p. 295) envision a clockwise stress rotation of as much as 90° in the northern Walker Lane that began in the late Oligocene and attained its present state in the late Miocene. This style of tectonism continues at present, focused most conspicuously at Frenchman Flat and Yucca Flat east of Yucca Mountain and in Death Valley to the west. Some basins are quiescent or have not been active since the middle Pleistocene, including Mid Valley, Jackass Flats, and Amargosa Valley. Nevertheless, historic seismicity and occasional large earthquakes accompanied by subsidence, such as the Cedar Mountain-Fairview Peak-Dixie Valley earthquakes, indicate that basin subsidence is sporadic. Presently, strike-slip faulting is active in Rock Valley (Coe, Yount et al. 1996, p. 4.13-6f) and in the Inyo-Mono terrane to the west.

4.2.3.2.1 Contemporary Deformation

Large earthquakes on range-front faults during the past 100 years indicate that Basin and Range extension is still under way. Epicenter distribution patterns and geodetic strain data indicate that strain presently is concentrated primarily north of Yucca Mountain, in a zone along latitude 37°N (the intermountain seismic belt), in the eastern California shear zone, and in the central Nevada seismic zone (Figure 4.2-1) (Bennett et al. 1999, p. 373, Figure 1). High geodetic extension rates characterize these active areas (Bennett et al. 1998, p. 566; Savage et al. 1995, pp. 20, 266). Dixon et al. (1995, p. 762) note that northwest motion of the Sierra Nevada block is accomplished by a combination of east-west extension on north-striking normal faults, and by dextral motion on northwest-striking strike-slip faults of the Walker Lane and eastern California shear zone (Figure 4.2-1). Geologic evidence suggests that the eastern California shear zone has been a zone of high strain since late Miocene time (10 to 6 Ma) (Dixon et al. 1995, p. 760). Dixon et al. (1995, p. 761) report 8.8 mm/yr. (0.35 in./yr.) at N9°± 5° W. The integrated strain rate across the eastern California shear zone is 12.1 ± 1.2 mm/yr. (0.48 ± 0.05 in./yr.) at N38° ± 5°W (Dixon et al. 1995, p. 767).

The kinematic boundary condition for Basin and Range deformation (the relative motions of the Pacific and North American plates) has been nearly constant for at least the past 3.4 m.y. (Harbert and Cox 1989, p. 3061), which is within the time span for activity of the Inyo-Mono domain (Hodges et al. 1989, p. 462). During this time, tectonic activity has gradually shifted westward, from the Death Valley-Furnace Creek fault to the Owens Valley fault (Dixon et al. 1995, p. 765). Dixon et al. (1995, p. 765) suggest that the Walker Lane accommodates significant dextral shear. The central Nevada seismic zone trends obliquely across the older Walker Lane (Savage et al. 1995, pp. 20, 267). Therefore, it would seem that the westward migration of tectonism in the Inyo-Mono domain and the historical surface-rupturing earthquake activity along the central Nevada seismic zone represent a concentration of crustal strain of regional extent and significant longevity. This strain zone appears to be shifting westward and perhaps northward (Dixon et al. 1995, p. 769), away from any involvement with Yucca Mountain.

The driving mechanism for ongoing extension may be a mantle plume associated with generation of the Yellowstone hot spot (Saltus and Thompson 1995, p. 1235) or assimilation of previously subducted oceanic lithosphere (Severinghaus and Atwater 1990, p. 17; Bohannon and Parsons 1995, p. 957). A mantle plume may also be holding the Great Basin at relatively high elevations north of 37°N (Parsons et al. 1994, p. 85, Figure 1). However, arguments have been presented against the hot spot/mantle plume interpretation (Hamilton, W.B. 1989, p. 758).

The extensional tectonic evolution of the Yucca Mountain region produced significant structures that bear on interpretations of the history of deformation and on the development of tectonic models that include Yucca Mountain. The following sections identify and discuss these regional structures: the Funeral Mountains detachment; the Bullfrog Hills detachment; the Las Vegas Valley shear zone; the Death Valley-Furnace Creek-Fish Lake Valley fault; and northeast-trending strike-slip fault zones located east of Yucca Mountain.

4.2.3.2.2 Funeral Mountains Detachment

A major detachment fault has denuded the core of the Funeral Mountains, revealing the broad, smooth lower plate surface. It seems clear that the lower plate (i.e., the subjacent crust) rose up during or shortly following detachment to give the range its present crest and perhaps much of its overall relief (hence the expression "turtleback" [Wright, L.A., Otton et al. 1974, p. 53]). Uplift occurred late during the phase of regional Miocene extension. Fission track dates of apatite, sphene, and zircon from the lower plate rock indicate that cooling through the temperature interval 285° to 120° (equivalent to about 10- to 5-km [6.2- to 3.1-mi.] burial depth) took place between 10 and 9 Ma (Holm and Dokka 1991, p. 1777), with surface exposure having occurred sometime after 6 Ma (Hoisch and Simpson 1993, p. 6822).

The elongate domiform or arch-like Funeral Mountains detachment and its lower plate of highly metamorphosed Upper Proterozoic rocks plunge gently northwestward beneath the almost unmetamorphosed upper plate of Upper Proterozoic to Miocene rocks of the Grapevine Mountains, which in most of the range dip gently. Restoration of southern Grapevine rocks atop those of Funeral Mountain indicates the former to have been transported about 30 km (19 mi.) west-northwestward along the detachment surface (Hamilton, W.B. 1988, p. 61). The Boundary Canyon fault, or perhaps more correctly the scarp face of the upper plate, more or less rims the Funeral Mountains and is most accessible at Boundary Canyon (Figure 4.2-19), for which it is named.

Rocks comprising the upper plate of the Funeral Mountains detachment are well exposed along the eastern flank of the Funeral Mountains in the vicinity of the Bird Track Hills (Figure 4.2-19). The lower part of this rock sequence consists of the chlorite-grade Stirling Quartzite and the Wood Canyon Formation, which are complexly and irregularly faulted. This Precambrian section is overlain unconformably by the Titus Canyon Formation and tilted panels of the Paintbrush Group Tuff.

The contact between the upper plate and the lower plate along the east side of the Funeral Mountains shows evidence of pronounced shearing, but the amount of slip is unknown. The Titus Canyon Formation and a thick lower Miocene lava flow and associated tuff are much faulted, but can be seen on both remote sensor imagery and mapping to be generally continuous along the Grapevine Mountains for at least 22 km (14 mi.), thus precluding major deformation before eruption of the middle Miocene ash flows. Most of the Cenozoic extension postdates 9 Ma, but may predate 7.5 Ma. This accords with the late Miocene cooling ages, determined by fission-track studies by Hoisch and Simpson (1993, p. 6805) and Holm and Dokka (1991, p. 1775) that record the tectonic denudation of the northwest end of the lower plate of the Funeral Mountains. Tectonic denudation of these midcrustal rocks and the rotation and detachment faulting of the Miocene supracrustal rocks were thus of about the same age and must have been linked kinematically.

4.2.3.2.3 Bullfrog Hills Detachment

The Bullfrog Hills are an assemblage of highly disrupted and structurally discordant, variably tilted blocks of tuff of the southwestern Nevada volcanic field that are spread out into Amargosa Valley from a source located between the northern flank of Bare Mountain and the western side

of Oasis Valley. The assemblage is separated from Bare Mountain by the shallow, north-dipping, generally east-striking Fluorspar Canyon fault. This fault represents the near-headwall of the detachment, as well as the accommodation plane for westward translation. The headwall (or breakaway) fault of the Bullfrog Hills is exposed along a north-trending line that defines at least 1 km (0.6 mi.) of stratigraphic offset that occurred between 12.7 and 11.6 Ma (Fridrich 1998, p. 36, 1999, p. 184, Figure 6). This line or zone connects with the Fluorspar Canyon fault. The more evident high-angle faults that segment the Bullfrog Hills farther west terminate against the trace of the low-angle Fluorspar Canyon fault (Figure 4.2-20). After 12.7 Ma, the breakaway zone occupied at least three successively more westward positions (Fridrich 1998, p. 17, 1999, p. 189).

Extension of the Bullfrog Hills began with northwest-side down faulting during the 11.6- to 12.7-Ma interval (Hoisch et al. 1997, p. 2818). The faulting produced translation and tilting that ranges from 45° at the head to at least 70° in the hills just east of Beatty (Figure 4.2-20) (Fridrich 1998, p. 15, 1999, p. 184). The translated and rotated blocks are separated by small wedge-shaped troughs filled with rockslide breccia and coarse alluvium (Fridrich 1998, p. 15, 1999, p. 186). This entire assemblage was then largely blanketed by the Timber Mountain Group tuff and rhyolite of Fleur-de-lis Ranch, which was subsequently faulted; Ammonia Tanks Tuff is tilted 20° to 55° eastward. A cap of 10.7-Ma basalt is also faulted, but is much less tilted (Hoisch et al. 1997, p. 2818). Severe brecciation and sliding occurred in the 11.4-Ma rhyolite and sediments in the northern Bullfrog Hills (Minor and Fleck 1994, p. 75). The faulting appears to have become inactive and the Bullfrog Hills stabilized between about 9.8 Ma (Weiss et al. 1991a, p. A246) and 6.3 Ma (Weiss et al. 1988, p. A399), following the opening of the western Amargosa Valley and Sarcobatus Flats basins (Figure 4.2-20) after 10 Ma (Weiss, Noble, Worthington et al. 1993; Hoisch et al. 1997, p. 2819).

West of Beatty, the Bullfrog Hills rest on pre-Tertiary rocks along the subhorizontal Bullfrog fault, which apparently is a distal extension of the Fluorspar Canyon fault. The Bullfrog fault separates Precambrian schist containing veins of foliated granite from overlying tilted blocks of Miocene tuff. Heating of the Precambrian section during the Miocene was apparently strong enough to reset the radiometric systems so that the rocks now yield Miocene ages (McKee 1983, p. 17). In places, a selvage of highly fragmented Paleozoic section lies above the Bullfrog fault and below the Miocene tuffs (Hamilton 1988, p. 57). This geometry prompted Maldonado and Hausback (1990) to infer two stacked detachment faults west of Beatty. The lower one, the Bullfrog fault, is clearly the more consequential fault, being an inferred link between the Boundary Canyon fault of the Funeral Mountains detachment and the Fluorspar Canyon fault (Figure 4.2-19) (Hoisch et al. 1997, p. 2816). If this inferred fault continuity is correct, there are significant implications for the history of Bare Mountain.

A detachment at Bare Mountain is indicated by the Gold Ace fault (Fridrich 1999, p. 180), a north-striking, east-dipping fault that separates high-grade metamorphic rocks to the west (lower plate) from low-grade to nonmetamorphosed rocks to the east (upper plate). The Gold Ace fault projects to intersect the Fluorspar Canyon fault at a high angle (Fridrich 1999, p. 180, Figure 5). Near the northern limit of outcrop, the Gold Ace fault intersects a west-striking fault (Monsen et al. 1992) that also juxtaposes high- and medium-grade metamorphic rocks, the Conejo Canyon fault (Fridrich 1999, p. 180). Hoisch et al. (1997, p. 2819) and Hoisch (1995, p. 19) inferred that the Conejo Canyon fault is actually a west-striking segment of the Gold Ace fault, and that this

combined fault merges with the Fluorspar Canyon fault (Hoisch 1995, Figure 2.2, pp. 19, 44). Because the Gold Ace fault separates rocks of contrasting metamorphic grade, as does the Boundary Canyon fault of the Funeral Mountains, Hoisch (1995, p. 44) inferred that the Boundary Canyon fault is also a continuation of the Fluorspar Canyon fault. On this basis, Hoisch (1995, pp. 17, 44) concluded that the Boundary Canyon fault extends into Bare Mountain via the Bullfrog-Fluorspar Canyon faults, which thereby define a single regional detachment.

Hoisch (1995, p. 44) inferred that the present east dip of the north-trending grade discordance fault may be explained by horizontal axis rotation from an initial northwest dip, or (less likely) the north-trending, east-dipping grade discordance fault may be a remnant of a system of large mullions within a regional Funeral Mountains-Bullfrog Hills-Bare Mountain detachment. The mullion interpretation requires that Bare Mountain be rotated 30° counterclockwise to bring a mullion structure into proper northwest alignment with the Bullfrog detachment. Furthermore, the alignment would be enhanced by locating Bare Mountain 5 to 10 km (3.1 to 6.2 mi.) to the west or southwest in late Miocene time while maintaining the basement exposures in the southern Bullfrog Hills at their present locations. Hoisch (1995, p. 42) further speculated that translation and rotation were integral components of crustal extension in this region, perhaps leading to opening of the Amargosa Desert basin as well. Notions of wholesale block rotation and translation to accommodate structural alignments and juxtapositions in this region are also argued by Snow and Prave (1994, p. 720); their arguments hinge on pre-Tertiary features and regional strike-slip fault mechanisms. However, work by Stamatakos et al. (1998, p. 1544) demonstrates insignificant, if any, Tertiary vertical axis rotation of Bare Mountain. These mechanisms are discussed in the evaluation of tectonic models (Section 4.3).

Mechanisms of extension west of Bare Mountain require far-traveled translation via detachment, as well as significant uplift (on the order of several kilometers). W.B. Hamilton (1988, p. 80) reconciled these mechanisms by inferring that regional detachment began as deep-seated normal faulting. The Gold Ace fault was initially a normal fault that dipped steeply west-northwestward, reaching rocks that were then about 15 km (9.3 mi.) deep (they had been about 25 km (15.5 mi.) deep in Cretaceous time) in the vicinity of the eastern Bullfrog Hills. The present length of the fault along the lower plate as defined is no more than 22 km (13.7 mi.), so in order to descend 15 km (9.3 mi.) and cut the presently exposed metamorphic rocks, its initial dip would have to have been no gentler than 45°. This dip also accounts for the depth of formation of the garnet-staurolite rocks of northwesternmost Bare Mountain. W.B. Hamilton (1988, p. 55) inferred that the initial fault gave way at about the 15-km (9.3-mi.) level to ductile flattening, which presumably accords with the detachment geometry and metamorphic petrology of the present Funeral Mountains.

As slip proceeded on the initially steep fault, the footwall rose and flattened, stranding the thin northeast Bare Mountain upper plate on the rising lower plate as a hinge migrated westward in the lower plate (Hamilton, W.B. 1988, pp. 50, 81; Hoisch et al. 1997, p. 2830). Faulting started before 12.7 Ma, and by 8 Ma was inactivated as far west as the northwest Bare Mountain. At about 10 Ma, the active fault dipped steeply beneath the Bullfrog Hills region, where mid-crust rocks that were subhorizontal when faulting began were rising into the footwall of the active fault (Hoisch et al. 1997, p. 2829). The shallow hinge of flattening and the deep hinge of pickup of mid-crustal rocks both migrated westward for another 2 m.y. or so, progressively stranding backtilted panels of Miocene rocks and bringing deep rocks to or near the surface. The tectonic

lenses and breccias of Paleozoic rocks, now present between lower-plate metamorphic rocks and the panels of Miocene supracrustal rocks of the Bullfrog Hills, were scraped from the hanging wall of a retreating Grapevine megablock (Hamilton 1988, pp. 55; 61). Klippen of these lenses also lie on topographic crests on the metamorphic rocks south of Fluorspar Canyon. When the system was inactivated at 7 or 8 Ma, the final master fault dipped steeply beneath the Grapevine Mountains, which before 12 Ma lay close to the unmetamorphosed Paleozoic strata of Bare Mountain. The trace of the steep, active fault in these terms migrated about 35 km (22 mi.) in 4 or 5 m.y. at a rate of about 7 to 9 mm/yr. (0.3 to 0.4 in./yr.). Hoisch et al. (1997, p. 2830) calculate a rate of 12 mm/yr. (0.6 in./yr.) that operated until about 10.3 Ma.

4.2.3.2.4 The Las Vegas Valley Shear Zone

The Las Vegas Valley shear zone (Figure 4.2-1) represents the eastern boundary of the Walker Lane south of Rock Valley (Stewart 1988, pp. 688, 695). The Las Vegas Valley shear zone is important to the Yucca Mountain geologic setting because it forms a major domain boundary (Figure 4.2-1) and plays a role in some tectonic models applicable to Yucca Mountain. However, nothing precise is known about the Las Vegas Valley shear zone because it is buried by Pleistocene alluvium, exhibits little or no seismic activity, and cannot be well characterized using available geophysical data. The shear zone is generally thought to be a right-lateral strike-slip fault, chiefly on the evidence of displaced traces of Mesozoic thrust faults on either side (Longwell 1974, p. 985; Stewart 1988, p. 695) and the clockwise curvature of the major ranges on the east side. The generally accepted displacement of more than 40 km (25 mi.) along the central part of the shear zone (Burchfiel 1965, p. 185) is thought to have occurred between 15 and 10 Ma (Bohannon 1984, p. 59; Hudson, M.R. et al. 1994, p. 273).

The northern reach of the Las Vegas Valley shear zone is subject to widely disparate interpretations (Hinrichs 1968; Fox and Carr 1989, p. 42; Caskey and Schweickert 1992, p. 1325, Figure 3; Burchfiel 1965, p. 186). Burchfiel (1965, p. 186) considered the northwestern projection of the zone to continue into the Specter Range thrust, as shown on Figure 4.2-21. Burchfiel's interpretation requires an episode of substantial south-southeast-directed compression in early Tertiary times to effect 6,000 ft (1,830 m) or more of stratigraphic offset along the 50° to 60° northwest-dipping Specter Range thrust, as well as approximately 35 km (22 mi.) of right-lateral offset along the Las Vegas Valley shear zone as projected into Mercury Valley.

The Las Vegas Valley shear zone also has been interpreted as an accommodation zone (Guth 1981, p. 769; Carr, W.J. 1984, p. 13; Hamilton, W.B. 1988, p. 79) or a "transfer fault" (Duebendorfer and Black 1992, p. 1109) that marks the lateral margin of a large tract of detachment faults thought to include the Spotted Range and ranges farther southeast (Guth 1981, p. 770). This interpretation avoids structural problems at the northern end of the shear zone by inferring that lateral displacement decreases to zero somewhere northwest of Indian Springs, a consequence of extension in this region (Guth 1981, p. 769). The accommodation model of Duebendorfer and Black (1992) requires 10 to 20 km (6 to 12 mi.) of slip to be absorbed by oroclinal bending in the Specter Range, but evidence for such compression during the 14- to 13-Ma interval has not been recognized in or near Rock Valley. Therefore, arcing the Las Vegas Valley shear zone to the west through Mercury Valley into alignment with the left-lateral Rock Valley fault zone is not a viable tectonic interpretation. However, independent calculation by

Caskey and Schweickert (1992, p. 1328) implies that the amounts of extension between correlative structures found both north and south of the shear zone are not significantly different, which diminishes the importance of an accommodation or transfer mechanism.

The Las Vegas Valley shear zone is thus plausibly related to one of two opposed tectonic mechanisms: (1) lateral accommodation that attends detachment faulting, or (2) north-south oriented lateral compression that has resulted in oroclinal bending and some right-lateral slip. The issue of oroclinal bending is of considerable tectonic interest because it implies a mechanism of lateral compression (or "constriction") (Wernicke, Axen et al. 1988, p. 1754) in a tectonic regime thought to be dominated by or exclusively in extension.

As much as 55 km (34 mi.) of late to middle Miocene north-south crustal shortening is estimated in the northern Black Mountains along the Lake Mead fault zone (Anderson, R.E., Barnhard et al. 1994, p. 1381), which is compatible with both right-lateral slip and domain-boundary compression along the Las Vegas Valley shear zone (Anderson, R.E., Barnhard et al. 1994, p. 1403). Paleomagnetic studies indicate that the vertical-axis, clockwise bending in ranges along the north side of the Las Vegas Valley shear zone is not a consequence of simple fault drag (Sonder et al. 1994, p. 786), but represents a broad zone of combined crushing and local rotation of blocks on the order of a few kilometers laterally (Nelson, M.R. and Jones 1987, p. 13; Sonder et al. 1994, p. 782).

The sedimentological character of Tertiary strata and structural features near the southern end of the Spotted Range suggest that the apparent range-scale drag folding (oroflexing) associated with the Las Vegas Valley shear zone was formed in pre-late Oligocene time (Cole and Cashman 1999, p. 35). Right-lateral transpression seems to have culminated in a Late Miocene event that involved crushing and bending of extended terrane north and east of the shear zone. Extension in the Sheep and Desert ranges evidently continued late, during deposition of strata tentatively correlated with the Miocene Horse Spring Formation (Guth 1981, pp. 766 to 767). In that case, right-lateral transpression that possibly had begun as early as 29 Ma must have peaked prior to about 14 to 13 Ma (Hudson, M.R. et al. 1994, p. 258).

4.2.3.2.5 Death Valley-Furnace Creek-Fish Lake Valley Fault

The combined Death Valley-Furnace Creek-Fish Lake Valley fault system forms the only major, throughgoing fault system in the Yucca Mountain region (Figure 4.2-22). The fault system is significant because it is a major domain boundary that separates a region of high strain rate and seismic activity (the Inyo-Mono domain) from one of relatively low strain rate and highly diverse structure and seismic activity (the Walker Lane). The fault system varies in structural style along strike, and links with associated lateral structures are uncertain. Therefore, its role in local fault development is open to speculation. It may represent the eastern border of a series of transtensional pull-aparts (Burchfiel and Stewart 1966, p. 439; Blakely et al. 1999, p. 13), or it may represent range front faults linked by strike-slip segments that are evolving into an increasingly coherent structure propagated northward along a strike distance of about 350 km (220 mi.).

The southern part of the fault system, the Death Valley fault segment, is primarily an oblique right-lateral range-front fault. It follows the salients and reentrants of the Black Mountains front,

varying in strike from north-south to N40°W. For the most part, the Death Valley fault dips moderately to steeply west, but toward its southern end, dips range from 35° to 65° east or northeast (Piety 1996, pp. 141, 318). Fault length is uncertain because of disagreement on definition of its poorly exposed end points. A minimum length of 51 km for the Death Valley fault is based on nearly continuously exposed west-facing scarps (Piety 1996, p. 142); a minimum length for the Furnace Creek fault is 105 km (65 mi.) (Piety 1996, p. 190); and a minimum length for the Fish Lake Valley fault is 80 km (50 mi.) (Piety 1996, p. 181).

The total offset of the Death Valley fault is unknown, but the dip-slip component, estimated from bedrock relief, is about 4,570 m (15,000 ft) (Wills 1989, p. 197). Hooke (1972, p. 2091) estimated a Holocene (about 10 to 11 ka) dip-slip displacement of about 63 m, based on elevation differences of coeval lakeshore features on the east and west sides of Death Valley. Fleck (1970b, p. 2811) considered that most of the vertical displacement on the Death Valley fault is ancient, probably having its inception before deposition of the Furnace Creek Formation (about 6 Ma). Estimates of total lateral offset toward the southern end of the fault range from 1.7 to 50 km (1 to 31 mi.), depending on the age of offset rock units (Piety 1996, p. 319). Estimates of late Tertiary and Quaternary offset range from 35 km (22 mi.) (Butler et al. 1988, p. 406) to about 20 km (12.4 mi.) (Brady 1986, p. 2). Estimates of Pleistocene offset toward the southern end of the fault range from about 15 to 200 m (50 to 656 ft), with estimates of 1.2 to 3 m (4 to 10 ft) per event based on displaced drainage (Piety 1996, pp. 321 to 322). Toward the southern end of the Black Mountains, the Death Valley fault has mostly strike-slip displacement (Piety 1996, p. 319). Holocene activity along the Death Valley fault is expressed by a 10.5-m (34-ft) scarp in an alluvial fan near Mormon Point; the average per event displacement is estimated to be about 2.5 m (8 ft) (Klinger and Piety 1996, p. 56).

The Furnace Creek fault is chiefly a right lateral strike-slip fault that extends through alluvial fans along the central part of Death Valley. The continuous fault trace is well expressed in most remote sensor images, probably because of the well-developed Pleistocene to Holocene scarp that ranges in cumulative relief from 0.3 to 23 m (1 to 75 ft) (Piety 1996, p. 190). Estimates of total lateral offset, based on displaced Precambrian units, are uncertain: they range from 128 km (80 mi.) to less than 8 km (5 mi.) (Wright, L.A. and Troxel 1967, p. 937; Piety 1996, p. 190). Piety (1996, p. 191) reports estimates of Pleistocene lateral offset of 21 m (69 ft) and 46 m (151 ft) and of single-event Holocene offsets of 1.5 to 2.7 m (5 to 9 ft) or less. Klinger and Piety (1996, p. 56) report an average lateral displacement per Holocene event of 4.5 m (15 ft).

A link between the Death Valley fault and the Furnace Creek fault is not well established. The main trace of the Furnace Creek fault may veer southeastward along the southern end of the Funeral Mountains and into the Amargosa trough, and even link up with structures along the east side of Amargosa Valley (Wright, L.A. and Troxel 1967, p. 947, Figure 2). The Death Valley fault may intersect or merge with the Furnace Creek fault across the alluvial-filled valley between the Funeral and Black mountains, a 19-km-long (12-mi.-long) gap termed the "transition zone" by Klinger and Piety (1996, pp. 9, 44). The structural nature of the inferred linkage is unclear, except that here fault traces and fold forms are relatively short, trend in various directions, and form a relatively wide zone (Klinger and Piety 1996, p. 44).

Toward its northern end, between the Grapevine Mountains (Figure 4.2-22) and the Last Chance Range to the north, the Furnace Creek fault is distributed into a number of fault planes forming a

zone that extends into Fish Lake Valley. The Fish Lake Valley fault is thought to have propagated northward from the Furnace Creek fault sometime between 12 and 4 Ma (Reheis 1993, p. 376). The fault dies out in a series of folds near the northern end of Fish Lake Valley (Stewart 1967, pp. 133 to 139). The northernmost 80 km (50 mi.) or more of this zone of strike-slip and primarily dip-slip range front faults is called the Fish Lake Valley fault. Estimates of maximum lateral displacement range from 25 km (15.5 mi.) (Piety 1996, p. 182) to 50 km (31 mi.) (McKee 1968, p. 512). Estimates of maximum vertical displacement range up to 750 m (2,461 ft) (Reheis and McKee 1991, p. 40). The upper Pleistocene dip-slip component on this fault is as great as 64 m (210 ft) (Brogan et al. 1991, p. 1), and a Pleistocene lateral displacement as great as 122 m (400 ft) is recorded (Sawyer, T.L. 1991, p. 126). Pleistocene activity along the fault has been high; vertical displacement of as much as 540 m (1,772 ft) may have accrued within the past 740 ka (Reheis and McKee 1991, p. 38). However, modeling by Dixon et al. (1995, p. 765), based on space geodesy, implies that activity along the Death Valley-Furnace Creek-Fish Lake Valley fault system has slowed during the past few million years as slip is increasingly taken up to the west, mainly along the Owens Valley fault zone. This transference of right-lateral slip activity to the west is reflected by the historical seismicity along the eastern California shear zone (Figure 4.2-1) (Dixon et al. 1995, p. 765) and its convergence northward with the Fish Lake Valley fault.

4.2.3.2.6 Northeast-Trending Strike-Slip Fault Zones and the Spotted Range-Mine Mountain Structural Zone

The Spotted Range-Mine Mountain structural zone (Figure 4.2-1) (Carr, W.J. 1984, p. 30; Stewart 1988, p. 694, referred to as "section") is distinguished by prominent east-northeast trending, left-lateral, strike-slip faults and fault zones: the Rock Valley fault zone, the Mine Mountain fault, the Wahmonie fault zone, and the Cane Spring fault (Figure 4.2-23). The structural zone forms a discrete section of the Walker Lane domain (Stewart 1988, pp. 694 to 695); it does not have a counterpart in the adjacent Basin and Range or Inyo-Mono domains.

The largest and most tectonically significant structural component of the Spotted Range-Mine Mountain structural zone is the Rock Valley fault zone (Coe, Yount et al. 1996), an unusually well-exposed domain section boundary against the Spring Mountains section of the Walker Lane (Figures 4.2-1 and 4.2-23) (Stewart 1988, p. 695). It is presently seismogenic and comprises a seismic source exceeded in size only by the Furnace Creek fault, which occurs at a greater distance from Yucca Mountain.

The Rock Valley fault zone coincides with a band of broad aeromagnetic lows bounded by a parallel gradient (-300 to -400 nT) (Glen and Ponce 1991) along the south side of Little Skull Mountain and extending eastward to Frenchman Flat, a distance of about 40 km (25 mi.). The geophysical data and local stratigraphy and structure indicate that the fault zone is part of a complex structural trough about 5 km (3 mi.) wide. Three major fault sets comprise the Rock Valley fault zone:

- Continuous, dominantly strike-slip faults that strike N65° to 80°E for distances of 15 km (9 mi.) or more
- Shorter normal, strike-slip, and/or reverse bridging faults that strike N25° to 50°E

- Minor normal and strike-slip faults that strike N10° to 15°W.

The zone is further complicated by N25°E-striking faults that project into Rock Valley from the north. These faults might be related tectonically (but not specifically) to the Cane Spring fault and to the Wahmonie fault zone, which strikes through the gap between Skull and Little Skull mountains (Figure 4.2-23).

A seismic reflection profile (Majer et al. 1996, p. 23) was shot across the Rock Valley fault zone about midway along its length. The southern end of the profile (Figure 4.2-24) is located north of a complex bounding fault or within a zone of complex fault-controlled structure that defines the southern margin of Rock Valley and the inferred structural trough, the footwall of which is indicated by Paleozoic outcrop south of the profile's end of line. One of three major Rock Valley fault strands, fault RV3, appears to be the southernmost plane of a zone of faulting perhaps 100 m (328 ft) wide. Disruption in interval A and a general down-to-the-north flexure of Tertiary strata mark the location of the zone in the profile (Figure 4.2-24). Inferred offset of the Paleozoic contact is about 400 ft (122 m) down to the north. This is possibly the major structural expression of the southern fault strand of the Rock Valley fault zone. Another mapped southern fault strand, RV4, is not expressed at all in the seismic profile. This is also the case for the mapped medial strand (RV1). The vertical offset component for these two strands is probably less than acoustic resolution.

The biggest structural break on the profile is at the step fault, located 300 m (984 ft) north from RV1 (Figure 4.2-24). The step fault perhaps bridges the northern and medial strands of the Rock Valley fault zone. The seismic profile shows that this deep fault forms the southern side of a depression about 1,640 ft (500 m) wide and 650 ft (198 m) deep filled with Pleistocene sediment. The Paleozoic contact is downdropped by about 600 ft (183 m) along the step fault.

The north side of the trough may mark the location of the northern fault strand (down to the south). However, there is no trace of a throughgoing fault at the surface or in the uppermost few hundred feet of the seismic profile. The trace of the northern fault strand is not expressed in the mapped geology or in aerial photographs within 2 to 3.5 km (1.2 to 22 mi.) to either side of the seismic profile. In other words, the profile crosses a 5.5-km (3.4-mi.) gap in the surface trace of the northern fault strand. The profile indicates a down-to-the-south fault at about CDP Station 320 that is buried by about 400 ft (122 m) of Pleistocene alluvium, and/or Wahmonie dacite (Twt).

Offsets along the fault planes are rarely demonstrable because cross-cutting features are uncommon. Estimates of total lateral offset of no more than 1.5 to 4 km (0.9 to 2.5 mi.) are based on regional considerations (Barnes, Ekren et al. 1982) and geophysical data (Kane and Bracken 1983, p. 9). A few observed lateral offsets are in the range of 30 to 40 m (98 to 131 ft). However, they appear to be pre-Pleistocene, and a more precise age constraint is unlikely to become available. These large displacements may actually be the cumulative results of several series of smaller events that were spaced closely enough in time to have prevented erosional discrimination of smaller component slips.

Historically, earthquakes have been frequent toward the west end of Rock Valley, in the vicinity of Little Skull Mountain, the Striped Hills, and the Specter Range. Data summarized by Rogers,

A.M., Harmsen et al. (1981, pp. 9, 15, 1987, p. 37) indicate that the earthquakes were mostly small magnitude events (M 4.0) that occurred from near surface to about 10 km (6.2 mi.) depth on north- to northeast-striking faults that had left-lateral strike-slip and oblique slip mechanisms (Rogers, A.M., Harmsen et al. 1987, p. 31). Most of the strike-slip mechanisms occurred in the 4- 9-km (2.5- to 5.6-mi.) depth range. Fault-plane solutions for these pre-1993 earthquakes are in accord with the sense of slip of the mapped faults, but no individual seismogenic faults have been identified (Rogers, A.M., Harmsen et al. 1987, p. 37).

The Cane Spring fault is expressed as a conspicuous rectilinear fault-line scarp lineament (Reheis and Noller 1991, Plate 3) that strikes N54°E along the north flank of Mount Salyer (Figure 4.2-23). The Cane Spring fault itself is mapped for a total length of about 8 km (5 mi.). The fault evidently controls the location of Cane Spring, a large perched spring that gives the fault its name. Mapping by Ekren and Sargent (1965) provides little support for a southwest fault projection into Rock Valley, since faults mapped across the eastern flank of Skull Mountain are curvilinear normal faults of varied and minor displacement. These appear to be local faults unrelated to any inferred throughgoing strike-slip zone; in any event, they are old bedrock faults having no morphological expression.

Outcrops show the Cane Spring fault to be a subvertical shear zone about 1.5 m (5 ft) wide. The fault plane controls a discontinuous scarp that locally attains a relief as great as 3 m (10 ft) across the beds of a few downslope gullies that cross the lineament west of Cane Spring. Local kinematic features imply left-lateral offset, but gross lithologic contacts indicate a dominantly normal, north-side-down movement. Poole, Elston et al. (1965) inferred three generations of alternating dip slip ("yo-yo tectonics") in addition to strike slip, but the basis for this inference is unclear. The contrast in landforms across the fault is pronounced, suggesting that the bulk of the offset has been dip-slip. The southeast side of the fault (upthrown block) shows numerous lineaments diverging south from the fault trace at angles of 30° to 45°. These probably represent splay faults or fractures indicative of the sinistral mechanism. Total offset along the Cane Spring fault remains unknown. No indications of late Pleistocene activity were observed; aerial photos show that the oldest and deepest stream courses on this slope cross the fault and are not offset by it. The most recent activity may have been 100 ka or older.

The Mine Mountain fault (Orkild 1968) extends along the south flank of Mine Mountain as two N35°E-striking subparallel faults that are separated by as much as 200 m (656 ft). The faults interconnect and splay and apparently entrain slices tens of meters across. At Mine Mountain, the Tiva Canyon Tuff is offset for a distance of 1.2 km (0.7 mi.) in a left-lateral sense across the fault zone. No exposures of the fault have been found, so the attitude of the fault plane(s) is unknown. Orkild (1968) interpreted the faults as oblique left-lateral, down to the south. The offset Tertiary units dip about 30°W, so given a steeply south-dipping fault (85° or more), purely normal displacement of about 500 to 600 m (1,640 to 1,970 ft) could produce the apparent left-lateral offset shown on the geologic map (Orkild 1968). Considering slip relations on other faults in the region, an oblique slip seems most likely.

As no detailed Quaternary mapping has been done in the Mine Mountain quadrangle, the relation of faulting to Quaternary stratigraphy is unknown. The surficial Skull Mountain quadrangle map to the south (Swadley and Huckins 1990) indicates that the fans overlying the projected Mine Mountain fault zone are constructed of late to middle Pleistocene alluvium (Q2b and Q2c)

(Swadley and Huckins 1990). Reconnaissance along and across the southern alluvial flank of Shoshone Mountain, and examination of aerial photos of this area, revealed evidence of complex faulting, but no evidence of late Quaternary displacements or any scarps in alluvium, or any transcurrent fault trace in alluvium that extends southwest of Mine Mountain. Weakly etched, short lineaments are found where the bedrock pediment is thinly covered; these features probably represent erosion focused by shattered bedrock. No throughgoing fault plane was found among the variously tilted and sheared pediment blocks, but a strong northeast-oriented, shear-controlled fabric is evident in numerous bedrock exposures within fan gullies. The breccia is typically sliced by irregular, subplanar fractures having no slip indicators that strike N20° to 45°E, 85°S to 90°.

The total late Tertiary normal displacement along the Shoshone Mountain range front is difficult to judge because faulting is distributed across a zone more than 1 km (0.6 mi.) wide and because the volcanic units were deposited on a surface of high relief (as much as 100 m [328 ft]) eroded in faulted Paleozoic blocks and in the overlying Wahmonie Formation. Where evident, the style of displacement is one of obverse dip away from the slope rather than toward it, in the sense of a rotated slump block. This style, along with the sinistral shear component, suggests that Shoshone Mountain pulled away obliquely west-southwest from a subsiding basin and that faulting was preceded by formation of a down-to-basin monocline.

No lineaments or other expressions of Quaternary faulting have been recognized to define a projection of the Mine Mountain fault in the fan deposits graded to Yucca Valley to the east. A smooth 32-mGal gravity gradient that defines the structural west flank of Yucca Valley (Healey et al. 1987) suggests that the fault does not project into Yucca Valley. To the southwest, the situation is more problematic.

The northern strand of the Mine Mountain fault zone was projected by Orkild (1968) southwest across Mid Valley along the southeast flank of Shoshone Mountain, where it is depicted as a down-to-the-south range front fault. Seismic profiles illustrated and interpreted by McArthur and Burkhard (1986, pp. 61, 63, 67, 69) cross the projection of the Mine Mountain fault zone in Mid Valley. The profiles indicate disruption of reflections along the projection of the fault zone, but the nature of deformation is ambiguous. Simple large-scale block tilting is not in evidence. The garbled reflections suggest distributed shear rather than a few individual fault planes. Because reflections cannot be traced north across the inferred fault plane profiles, lateral offset rather than normal displacement is indicated.

Maldonado (1985) retained Orkild's range front fault projection, but also projected the more southerly of the two Mine Mountain fault strands southwest across Mid Valley and out across Jackass Flats to a point due west of Little Skull Mountain (Figure 4.2-23). A range front fault certainly exists where Orkild has mapped it, but YMP field work did not reveal any evidence for the left-lateral fault trace projection of Maldonado (1985). Nevertheless, there is good evidence for strike-slip faulting in bedrock exposures along the base of Shoshone Mountain and in a low bluff of Paintbrush Tuff (evidently an outlier of the Little Skull Mountain block) located just west of the Field Operations Center.

The 1:100,000 Bouguer gravity map of the Nevada Test Site (Healey et al. 1987) provides little indication of a significant crustal fault along the inferred projection of the Mine Mountain fault

zone in northern Jackass Flats. Here, the fault projection passes across an area in Jackass Flats of virtually no gradients or conspicuous anomalies. In Mid Valley, the projection passes along the northwest flank of a large minimum that represents the main depression of Mid Valley, and the fault could thus be considered a bounding structure to the depression (Figure 4.2-23).

The 1:100,000 aeromagnetic map of the Beatty quadrangle (Glen and Ponce 1991) shows strongly aligned gradients and separation of distinct anomaly patterns along the projection of the Mine Mountain fault zone into Jackass Flats. The aeromagnetic gradients indicate that the fault zone projection is about 800 m (2,625 ft) wide along Shoshone Mountain, and that it widens to about 1.5 km (0.9 mi.) as it crosses Jackass Flats south of Calico Hills. This zone of aligned steep gradients and linear and positive anomalies extends into a crudely annular anomaly pattern of short, steep highs rimmed with negative anomalies, about 8 km (5 mi.) in diameter, centered west of the Field Operations Center.

The westward extent and the possible interaction of the convergent, westward extensions of the Rock Valley fault zone and the Mine Mountain fault are unknown. W.J. Carr (1984, p. 16) projected the Spotted Range-Mine Mountain structural zone of the Walker Lane belt, which is characterized by northeast-striking left-lateral faults, west into California to the Furnace Creek fault zone (Figure 4.2-25). However, no faults resembling the Rock Valley fault zone are known to transect the Funeral Mountains. The Rock Valley fault zone probably extends no farther west than a line drawn from the west side of Little Skull Mountain south to the west end of the Skeleton Hills (Figure 4.2-23). Laterally sheared Paleozoic rocks and local Miocene volcanic rocks exposed along this line imply the existence of a N5°- to 15°E-striking fault or shear zone. A fault along this trend is also indicated by gravity and aeromagnetic anomaly gradients, a hydraulic barrier (Winograd and Thordarson 1975, p. C75), and seismic reflection data (Brocher, Carr et al. 1993, p. 35), as well as sparse west-facing scarps in alluvial fans.

Attempts to find a segment of the Rock Valley fault zone west of the line described above (the gravity fault) have been unsuccessful. Lineaments in the Amargosa Valley, however, suggest that a segment of the Rock Valley fault zone exists beneath the Amargosa Valley. On the other hand, the main strands of the Rock Valley fault zone veer to the south into the Specter Range east of the Striped Hills (Figure 4.2-23). Thus, it is still unclear whether the zone extends all the way to the western end of Rock Valley, let alone into Amargosa Valley.

INTENTIONALLY LEFT BLANK

4.3 REGIONAL TECTONIC MODELS

A regional tectonic model represents the structure of a portion of the Earth's crust and illustrates how the structural assemblage has evolved through time. A tectonic model integrates three basic components: geometry and spatial relations among structures; mechanisms by which structures interact and respond to regional stress; and the succession, duration, and evolution of deformation events. Tectonic models for Yucca Mountain and its vicinity attempt to explain current geologic structure and geophysical data in light of regional tectonic processes by integrating discrete data sets such as the histories of volcanism, deposition, and fault movement. The observations are integrated into a plausible structural evolution of the site and surrounding area, compatible with existing data and earth physics, which is the tectonic model.

4.3.1 Conceptual Tectonic Models: Elements and Constraints

4.3.1.1 Model Elements

Tectonic models can be expressed in various ways (e.g., physical, mathematical). This section presents conceptual models, illustrated by maps and cross sections. The elements of a tectonic model for Yucca Mountain include:

- **Physical Extent**–The space to which the model applies
- **System Geometry**–The shape, orientation, and distribution of tectonic features (e.g., fault and block geometry, volcanic vent distribution)
- **Boundary Conditions**–External forces and processes at the model boundary, and bounding fault character and activity
- **Driving Forces**–Active processes (e.g., stresses, strain rates) that may produce the observed features
- **System Response/Dynamics**–Consequences of the driving forces and boundary conditions acting on the system geometry within the model's physical domain (e.g., fault activity, including rates, interactions, rupture patterns, distribution of seismic potential; type and rates of volcanism; effects on groundwater flow and water table elevation; extension rate and distribution of effects).

As discussed in more detail in Section 4.3.4, most tectonic models published for Yucca Mountain do not include all these elements.

4.3.1.2 Model Constraints

Tectonic models are constrained by data at both regional and local scales. In this section, regional constraints are briefly presented. In the next section, local constraints are described in more detail.

Any tectonic model for Yucca Mountain must be compatible with the plate tectonic setting of the western United States. Yucca Mountain is located in the Basin and Range province, a region

characterized by high heat flow, thin crust, bimodal basalt-rhyolite volcanism, high topography, block and detachment faulting, and west-northwest oriented crustal extension (e.g., Thompson, Catchings et al. 1989, p. 178; Zoback and Zoback 1989, p. 530). Tectonic deformation within the Basin and Range province results from the interplay of boundary forces and internal buoyancy forces. The boundary forces are related to the interaction of the Pacific plate with the North American plate; internal buoyancy forces are due to local density contrasts and the high topographic elevation of the province (e.g., Thatcher, Foulger et al. 1999, p. 1714; Flesch, Holt et al. 2000, p. 834).

Geodetic and satellite global positioning system (GPS) data indicate that the Pacific plate is moving northwest at 46 to 48 mm/yr. (1.81 to 1.88 in./yr.) relative to the North American plate interior (Bennett, Davis, and Wernicke 1999, p. 371). Of this movement, the San Andreas fault system accounts for approximately 35 mm/yr. (1.37 in./yr.); the remaining 13 mm/yr. (0.51 in./yr.) is distributed through the Inyo/Mono domain and the Walker Lane, which includes Yucca Mountain (Bennett, Davis, and Wernicke 1999, p. 371; Thatcher, Foulger et al. 1999, p. 1716). East of the Walker Lane and Central Nevada Seismic Belt, tectonic strain comprises about 3 mm/yr. (0.12 in./yr.) of east-west oriented extension (Thatcher, Foulger et al. 1999, p. 1716; Flesch, Holt et al. 2000, pp. 834, 835). A viable tectonic model of Yucca Mountain must accommodate the driving forces of right lateral shear and buoyancy-driven crustal extension.

On a less broad, but still regional scale, Yucca Mountain is located in the Goldfield section of the Walker Lane domain (Section 4.2.1.1). The Goldfield section is characterized by irregular (in places arcuate) mountain ranges, a lack of major northwest-striking strike-slip faults, and a scarcity of major basin-and-range normal faults (Stewart 1988, p. 694). The Goldfield section also contains the southwestern Nevada volcanic field.

At a local level, Yucca Mountain is located in the Crater Flat domain (Fridrich 1999, p. 170). The following Section 4.3.2 describes key tectonic elements and deformational constraints of this domain, with an emphasis on their relevance to evaluating Yucca Mountain tectonic models.

4.3.2 The Crater Flat Domain – Tectonic Constraints for Yucca Mountain

The Crater Flat domain (Fridrich 1999, p. 170) (Figure 4.3-1)is characterized by a distinct system geometry consisting of closely spaced, west-dipping normal faults that are best exposed across Yucca Mountain. The faults are described in detail in Section 4.6. The normal fault system extends westward into Crater Flat where it is mostly buried by alluvium, though it is partly exposed at Crater Flat's northern and southern edges. East of Yucca Mountain, the west-dipping normal fault system may extend under the alluvium of Jackass Flats.

The western boundary of the Crater Flat domain is marked by the east-dipping Bare Mountain range-front fault (Figure 4.3-1). No well-defined structure marks the Crater Flat domain eastern boundary, but it is clear that the domain boundary lies west of the Striped Hills and the western flank of Little Skull Mountain (Figure 4.3-1), features that exhibit structures not found at Yucca Mountain. The buried, west-dipping Gravity fault (Figure 4.3-1) (Winograd and Thordarson 1975, p. C75) could represent the eastern domain boundary, but no distinct bounding structure is expressed at the northern end of Jackass Flats or along the southern or western flank

of the Calico Hills (Simonds and Scott 1996, p. 37, Figure 9). Despite a pronounced geomorphic expression, the channel of Fortymile Wash (Figure 4.3-1) does not appear to follow a significant structural break (Day et al. 1998b, p. 15; Brocher et al. 1998, p. 965, Figure 6), and therefore is not the eastern boundary.

The northern boundary of the Crater Flat domain is marked by a transition from systematic down-to-the-west normal faults to the short, numerous, radial faults associated with the southern margin of the Timber Mountain/Claim Canyon caldera (Minor et al. 1997, p. 8) (Figure 4.3-1). The northern boundary is projected east-southeast along Yucca Wash. The pronounced linear trend of Yucca Wash (Figure 4.3-1) suggests fault or fracture control, but no fault offset has been observed along or across the wash (Day et al. 1998b, p. 11). The southern end of the Crater Flat domain is marked by a low, north-dipping ridge that dips into Crater Flat. The low ridge extends west from the southern end of Yucca Mountain to nearly the southern end of Bare Mountain at Steve's Pass (Figure 4.3-1). The west-dipping normal fault system found at Yucca Mountain and in Crater Flat extends into the ridge (Simonds et al. 1995).

The structural definition of the Crater Flat domain is supported by geophysical data. Isostatic gravity maps and profiles (McCafferty and Grauch 1997; Healey et al. 1987; Snyder and Carr 1982, Plate 1) show that the Crater Flat domain is underlain by a structural basin about 4 km (2.5 mi.) deep (Blakely et al. 1999, p. 12). It is defined on its west side by a steep, approximately 30 mGal gradient (Snyder and Carr 1982, p. 20) that represents the Bare Mountain fault (Figure 4.3-2). The basin narrows and becomes shallow to the south, its margin essentially coincident with the north-dipping low ridge described above. Aeromagnetic maps show that the fault pattern expressed at Yucca Mountain continues to the west into Crater Flat, and that it also extends eastward into Jackass Flats (McCafferty and Grauch 1997). A deep seismic reflection profile (Crater Flat seismic profile track, Figure 4.3-1) shows that the Crater Flat structural basin is asymmetric, deepening westward toward the Bare Mountain fault (Brocher et al. 1998, p. 960). Although normal faults within the upper 1 km (0.6 mi.) of crust are not clearly depicted in the seismic reflection profile, the geophysical and geological data jointly support the interpretation of Crater Flat basin as a structural trough having the style of a half graben (Brocher et al. 1998, p. 947; Fridrich et al. 1999, p. 198), with the Yucca Mountain fault system antithetic to a master Bare Mountain fault.

Geophysical data indicate a number of relationships that are not explained by geological mapping. Gravity data show that Yucca Mountain lies along the west flank of a basement high that defines the eastern margin of the Crater Flat structural basin that separates Crater Flat and Yucca Mountain from Jackass Flats (Snyder and Carr 1982, p. 25) (Figure 4.3-2). Although the east flank of Yucca Mountain rests partly on this basement high, the highest elevations of Yucca Mountain lie a few kilometers (a mile or so) to the west, within the structural basin itself (Snyder and Carr 1982, p. 18). The elevation of Yucca Mountain relative to the basin rim is anomalous; the only structure at Yucca Mountain that conforms to the trend of the basement high is the combined Paintbrush Canyon and Stagecoach Road faults.

None of the Yucca Mountain and Crater Flat faults are exposed south of the north-dipping ridge that marks the southern end of the Crater Flat domain. Apparently they terminate at the margin of the gravity-defined basin. This interpretation is supported by aeromagnetic data (McCafferty

and Grauch 1997). However, the nature of the structural terminations or transitions in this area is unclear.

The Crater Flat structural basin widens and deepens northward toward the Timber Mountain/Claim Canyon caldera complex (Blakely et al. 1999, p. 11). The caldera complex appears to be a large intrusive/extrusive igneous plug emplaced within a basement trough several kilometers deep (a mile or two). North of the caldera complex, the pattern and style of normal faults expressed in Pahute Mesa are aligned with the fault pattern of the Crater Flat domain, suggesting a link between the two areas (Figure 4.3-3) (Carr, W.J. 1990, pp. 291, 293).

In the following sections, geologic features of the Crater Flat domain are discussed in some detail to help constrain, and distinguish among, tectonic models for the Yucca Mountain area.

4.3.2.1 Yucca Mountain Fault System

To establish a basis for tectonic models, faults at Yucca Mountain are discussed in this section to provide the overall geometry, timing, and relationships between fault sets. More detail on Yucca Mountain faulting is provided in Section 4.6. In general, the faults comprise two major populations: a fundamental block-bounding set of west-dipping normal faults propagated up from the pre-Tertiary basement that floors the Crater Flat structural basin, and a secondary set that includes northwest-striking and intrablock faults that are not directly related to the block-bounding faults (Day et al. 1996, p. 2-2). A third population comprises fractures and small faults resulting from cooling and alteration.

The exposed rocks of Yucca Mountain were extended west-northwestward, by as much as 40 percent during middle and late Miocene time (Fridrich et al. 1999, p. 197). Since that time there has been little further extension (Fridrich et al. 1999, p. 208). Most faulting and tilting occurred between the eruptions of the Tiva Canyon Tuff (12.7 Ma) and the Rainier Mesa Tuff (11.6 Ma) (Day et al. 1998b, pp. 17 to 18). Extension apparently began prior to deposition of the Tiva Canyon Tuff (Fridrich 1999, p. 189; Scott, R.B. 1990, p. 268), and probably peaked during or shortly after its deposition. Paleomagnetic directions indicate that tilting (due to faulting) of some blocks occurred before magnetic remanence was locked in (Rosenbaum et al. 1991, p. 1972). Stratigraphic relationships at Yucca Mountain indicate that dip-slip offset on the west-dipping normal faults generally increases toward the south (Day et al. 1998b). Strikes of faults at the northern end of Yucca Mountain are generally north-south (approximately 000° to 010°), while strikes at the southern end are generally north-northeast (approximately 020° to 035°). In addition, fault dips decrease toward the south. These changes in strike, dip, and displacement indicate increasing relative local crustal extension toward the south (Fridrich et al. 1999, p. 208).

The relationship of Yucca Mountain faults to faults in the Paleozoic/Precambrian basement is uncertain. Block-bounding faults such as the Solitario Canyon and Paintbrush Canyon faults (Figure 4.3-1) penetrate deeply into the basin. Evidence for deep penetration includes relatively high groundwater temperatures measured in wells close to these faults, suggesting upward leakage of warm groundwater from the deep carbonate aquifer (Sass et al. 1995, p. 165). Another indication of deep penetration of the Solitario Canyon fault is the presence of a basalt dike approximately 10 Ma (Carr, W.J. and Parrish 1985, p. 30) located along part of the fault plane exposed in trench 10 (Figure 4.4-3), where it is offset by the fault. However, almost

nothing is known about faulting in the pre-Tertiary section. Nearby exposures of Paleozoic/Precambrian rocks at Bare Mountain, the Specter Range, and the core of the Calico Hills indicate that faulting is very complex. A similar complexity is assumed to occur in the pre-Tertiary section under the Crater Flat structural basin.

4.3.2.2 Vertical Axis Rotation

Rotation of fault-bounded blocks provides another constraint on tectonic models for Yucca Mountain. Paleomagnetic data (Rosenbaum et al. 1991, p. 1964; Hudson, M.R., Sawyer et al. 1994, p. 270) show that toward the south, Yucca Mountain has been progressively rotated clockwise 25° to 30° following deposition of the Tiva Canyon Tuff (12.7 Ma). Apparently most of the rotation occurred prior to deposition of the overlying Timber Mountain Group; rotation of the Ammonia Tanks Tuff (11.45 Ma) amounts to only 6° ± 13° (Hudson, M.R., Sawyer et al. 1994, p. 270). Vertical axis rotation appears to have begun approximately 11.6 Ma (Minor et al. 1997, p. 20). Virtually no rotation has occurred at the north end of Yucca Mountain. Paleomagnetic declinations change gradually toward the south (Rosenbaum et al. 1991, p. 1974). The southward increase in paleomagnetic pole rotations (and, therefore, block rotation) coincides with a decrease in topographic elevation, a change in strike of block-bounding faults from northerly to northeasterly, a decrease in fault dips, an increase in stratal dips, and an increase in total extension from 10 to 20 percent (Fridrich 1999, p. 206). The axis along which these changes occur can be extended northwestward across Crater Flat, where paleomagnetic data from 23 sites in western and northern Crater Flat also indicate 10° to 20° of clockwise rotation (Minor et al. 1997, p. 15). The sinistral (left-lateral) component of slip on most block-bounding faults at Yucca Mountain also appears to increase to the south, which is compatible with clockwise block rotation.

The cause of late Miocene vertical axis rotation is uncertain. It has been ascribed to dextral shear at or near the south end of Yucca Mountain (Sonder et al. 1994, p. 769; Burchfiel 1965, p. 186) or the influence of a strain gradient resulting from differential extension above a detachment fault (Wernicke and Axen 1988, p. 850; Hagstrum and Gans 1989, p. 1840; Scott, R.B. 1990, pp. 275, 279). Rotation has also been attributed to extension of Crater Flat as a pull-apart basin (Fridrich 1999, p. 210), an increase in listric faulting toward the south, and development of relay ramp slices between fault segments (Stamatakos and Ferrill 1998, p. 158). A local cause is supported by poor correlation between fault strikes and paleomagnetic declinations within fault blocks, which also suggests that only a fraction of the change in fault strikes toward the south can be attributed to oroclinal bending (Stamatakos and Ferrill 1998, pp. 154, 155). Because large rotations are also recorded in northwestern Crater Flat, where total extension is small (Minor et al. 1997, pp. 2, 3), listric faulting cannot be the only cause of rotation. Whatever the cause, vertical axis rotation is a local phenomenon; wider areal paleomagnetic data do not indicate a broad distribution of clockwise rotations north of Yucca Mountain (Hudson, M.R., Sawyer et al. 1994, p. 274).

4.3.2.3 Basaltic Volcanism

The history, evolution, and character of Pliocene-Pleistocene basaltic volcanism proximal to Yucca Mountain (within 25 km [15.5 mi.] of the potential repository) are extensively described

by Crowe, Perry et al. (1995) and summarized in Section 12.2. A brief description is provided here, with an emphasis on constraints for tectonic models.

The oldest eruptive basalts in Crater Flat, dated at about 10.5 to 11.3 Ma (Fridrich 1999, p. 189) (Figures 4.2-12, 4.3-4), shortly followed eruption of the Ammonia Tanks Tuff (11.45 Ma). The next eruptions occurred about 3.7 Ma, when a group of five northwest-aligned scoria cones and lava flows were emplaced in southeastern Crater Flat from north-south oriented fissures and feeder dikes. This group represents the largest volume basaltic emplacement in Crater Flat (Figures 4.2-12, 4.3-4). Subsequently west-side-down faulting produced dip-slip offsets of more than 1 m (Crowe, Perry et al. 1995, p. 2-20).

The next younger basaltic eruption, about 1.0 Ma, consists of four cinder cones (Little Cones, Red Cone, Black Cone, and Makani Cone) aligned north-northeast along the axis of Crater Flat (Figures 4.2-12, 4.3-4). Lava of this group overlaps the eruption area of the earliest (10.5- to 11.3-Ma) episode (Figures 4.2-12, 4.3-4). The most recent episode of basaltic volcanism created the Lathrop Wells Cone (about 80 ka [Heizler et al. 1999, p. 802]), which lies south of the older eruption groups (Figures 4.2-12, 4.3-4). The Lathrop Wells Cone complex comprises fissure eruptions, spatter and scoria cones, and aa flows. Satellitic spatter cones at the east base of the main cone have a northwest alignment.

The episodic nature of basaltic eruptions (11.3 Ma, 3.7 Ma, 1.0 Ma, 80 ka), the aligned series of emplacements, the generally consistent alkalic compositions of the basalts, and the generally north-south structural alignment in Crater Flat basin indicate that emplacement depends on recurrent tectonic conditions that involve the entire thickness of the crust and part of the upper mantle beneath the basin (Crowe, Perry et al. 1995, pp. 5-1, 5-14). The small volume of basalt erupted during each episode, the short and abrupt duration of emplacement, and the evidence of high volatile content and rapid degassing (scoria, aa) indicate that the basaltic melt did not force its way though the crust by virtue of thermal energy and bulk buoyancy, but ascended as a relatively low-temperature, low-viscosity, hydrous melt having virtually no crustal residence time. A hydrous mantle source for the Crater Flat basalts is consistent with their low rubidium content, relative to other incompatible trace elements (Crowe, Perry et al. 1995, p. 4-6). The basalt dikes apparently created their own fracture pathways near the surface because the basaltic center locations are largely independent of faults that cut the surface.

The northwest alignment of the eruptive groups along with the north-northeast orientation of individual eruptive features suggests the recurrent influence of a dextral shear zone or perhaps a group of north-striking faults or fracture zones susceptible to dextral transtension along the trend of the eruptive centers. These fractures apparently dilate episodically and tap the upper mantle basaltic magma source. The occurrence of basaltic tephra in some of the fault fissure fills of Quaternary age along Yucca Mountain indicates that, in at least one episode, eruption essentially coincided with normal fault movement (Ramelli, Oswald et al. 1996, p. 4.7-49).

4.3.2.4 Structure of Crater Flat

Crater Flat is the alluvium-covered area west of Yucca Mountain within the Crater Flat structural domain (Figure 4.3-1). The structure of Crater Flat is central to several of the tectonic models

proposed for the Yucca Mountain region. Because it is covered by alluvium, the structure of Crater Flat is largely inferred from geophysical data and exposures in the surrounding hills.

The fault pattern exposed at Yucca Mountain continues west beneath the alluvium of Crater Flat. The westernmost faults observed at the surface are the Crater Flat fault (Figure 4.2-12) and an extension, the West Lava fault (Ramelli, Bell et al. 1988). The West Lava fault has a less-than-1-m (less-than-3-ft) scarp formed in alluvium with an estimated age of 17 to 30 ka (Ramelli, Bell et al. 1991, pp. I-63, I-64). Drill holes VH-1 and VH-2 (Carr, W.J. 1982, p. 12; Carr, W.J. and Parrish 1985, p. 6, Table 1) (Figure 4.3-1) indicate that the alluvium, consisting of fan debris, is at least 350 m (1,150 ft) thick. The basin also contains 2 to 4 km (1.2 to 2.5 mi.) of tuff of the southwestern Nevada volcanic field (Ackermann et al. 1988, p. 30; Brocher, Hart et al. 1996, p. 6; Majer et al. 1996, p. 49).

Crater Flat has the structure of a half-graben controlled by the Bare Mountain fault. Seismic and gravity data indicate that the Crater Flat basin is deepest on the west side (Snyder and Carr 1984, Plate 1; Majer et al. 1996, pp. 45, 46; Brocher, Hart et al. 1996, p. 31). This conclusion is supported by the general westward thickening of units exposed along the basin's southern and northern margins (Fridrich 1999, p. 177). There is some evidence of a low longitudinal arch near the basin axis , a feature interpreted as a rollover above the Bare Mountain fault (Faulds et al. 1994). A narrow zone (0.5 to 2 km [0.3 to 1.2 mi.]) along the basin's westernmost edge contains east-dipping faults (Fridrich 1999, p. 176) .

The southern end of Crater Flat is defined by the low ridge that extends between Steve's Pass and the southern terminus of Yucca Mountain. Outcrops indicate that the Miocene tuffs are faulted down against Paleozoic rock to the west, but strata along the ridge dip about 10° north. The ridge is estimated to have formed post-10 Ma, and appears to be the only major tilting that is not an expression of older extensional patterns (Fridrich 1999, p. 190).

4.3.2.5 Bare Mountain Fault

The Bare Mountain fault forms the structural and physiographic western boundary of Crater Flat and the Crater Flat structural domain. The fault extends from Steve's Pass, at the southern end of Bare Mountain, north to Tram Ridge (Figure 4.3-1), where it splays into the Tram Ridge fault and the Tate's Wash fault (Fridrich 1999, p. 174). These faults decrease in throw and become part of a population of similar faults exposed along the caldera rim that flanks the north end of Crater Flat.

Gravity data (McCafferty and Grauch 1997; Oliver and Fox 1993, pp. 1813, 1814; Ponce, Harris et al. 1988; Snyder and Carr 1982) show Crater Flat to have an asymmetric gravity field with a steep eastward gradient east of Bare Mountain and a gentle westward gradient west of Yucca Mountain. The isostatic low trends generally northward in the eastern part of the basin, where dense pre-Tertiary strata are about 3 to 4 km (1.8 to 2.5 mi.) deep (Figure 4.3-2). The steepest gradient is along the southern part of Bare Mountain, at the east base of Black Marble Hill, where the low is only about 1 km (0.6 mi.) east of the topographic mountain front. The gradient continues north, becoming gentler, though its total relief remains high, and the low is centered 2 to 3 km (1.2 to 1.9 mi.) east of the topographic mountain front along central and northern Bare Mountain.

The deep seismic reflection profile (Crater Flat seismic profile track, Figure 4.3-1) (Brocher et al. 1998, p. 956) indicates the southern end of the Bare Mountain fault dips about 65° east to a depth of about 3.5 to 6 km. The fault cannot be projected to deeper than 6 km because it is not imaged on the seismic data (Brocher et al. 1998, p. 959). The Bare Mountain fault has been interpreted as both a single, large-displacement fault and as a series of faults. Faults synthetic to Bare Mountain fault have been reported from 0.5 to 2 km (0.3 to 1.2 mi.) east of it in Crater Flat (Fridrich 1999, p. 176).

Bare Mountain underwent rapid uplift during the peak and early declining phases of Yucca Mountain deformation (Hoisch et al. 1997, p. 2819). Episodes of significant fault displacement are indicated by slide breccias located in Crater Flat that were derived from Bare Mountain prior to 11.6 Ma and after 11.4 Ma (Simonds and Fridrich 1995, p. 82). No major post-Miocene faulting has been documented along the fault. The Bare Mountain fault has been active in the Pleistocene (Anderson, L.W. and Klinger 1996, p. 4.12-67) and has shown oblique dextral displacement near the southern end of Bare Mountain where the Bare Mountain fault curves to a northwest strike (Fridrich 1999, p. 177). Recurrent late Pleistocene and Holocene faulting has been suggested (Reheis 1988, p. 110), but topographic profiles preclude large displacements during late Quaternary faulting (Klinger and Anderson 1994). Fault exposures on the low ridge at the south end of Crater Flat do not indicate Pleistocene offset, or offset that postdates the approximate 10-Ma formation of the ridge (Fridrich 1999, p. 190).

The Bare Mountain fault south of Crater Flat cannot be projected with certainty. The fault or a related structure is exposed along the east side of Black Marble Hill where early Miocene rocks (equivalent to the rocks of Pavits Spring) are in fault contact with the Rainier Mesa Tuff (11.6 Ma). Fault offset is estimated at a few hundred meters. An alignment of gravity anomalies suggests that the fault continues to the south out of Crater Flat and marks the western border of the Amargosa Valley. The Bare Mountain fault may be either a long pre-middle Miocene fault with only the Crater Flat section showing significant late Miocene offset (Carr, W.J. 1988, p. 46), or it may be a shorter middle to late Miocene fault that splays into smaller faults at the southern end of Crater Flat.

4.3.2.6 Eastern Structural Boundary of the Crater Flat Domain

As discussed in Section 4.3.2, the eastern boundary of the Crater Flat domain is not clearly defined. A feature identified by gravity surveys, and referred to as the Gravity fault (Winograd and Thordarson 1975, p. C-75) trends north beneath surficial deposits along the west side of the Striped Hills (Figure 4.3-1). This feature, which extends farther south, is inferred to be a normal fault with down-to-the-west displacements ranging from 150 to about 1,000 m (500 to several thousand ft). The footwall includes the Striped Hills and associated structures not present at Yucca Mountain; therefore, the gravity fault could be part of the eastern domain boundary. The Gravity fault cannot be traced north of Little Skull Mountain using gravity or aeromagnetic data; therefore the northeastern boundary of the Crater Flat domain is uncertain. The northeast boundary has been dealt with two ways (Figures 4.3-4A and 4.3-4B). First, arbitrary lines were drawn to connect a northern projection of the Gravity fault with a southeastern projection of an inferred strike-slip fault in Yucca Wash (Fridrich 1999, Figure 3) (Figure 4.3-4A). Second, based on seismic reflection and potential field data (Brocher et al. 1998, p. 948) an approximate boundary of diffuse west-dipping faults was projected from the Gravity fault northward along

Fortymile Wash to the Ammonia Tanks caldera (Figure 4.3-4B). The diffuse nature of the boundary is supported by geologic map data, which show the pattern of north-striking normal faults that characterizes the Yucca Mountain area merging into a pattern of radial faults north of the Calico Hills (Simonds and Scott 1996, p. 38, Figure 9).

4.3.2.7 Tectonic Implications of Eruptions in the Southwestern Nevada Volcanic Field

The temporal and spatial association between extensional tectonics and magmatic activity in the southwestern Nevada volcanic field is poorly understood. Local extension was contemporaneous with caldera activity between 13 and 11 Ma (Fridrich 1999, p. 174), however there is no clear evidence for active extension in the region during the initiation of caldera formation (Axen et al. 1993, p. 56; Sawyer, D.A., Fleck et al. 1994, p. 1314). Cumulative middle- to late-Miocene extension in the central part of the southwestern Nevada volcanic field is small relative to surrounding parts of the southern Great Basin. The surrounding areas underwent episodic nonuniform periods of extension at different times (Sawyer, D.A., Fleck et al. 1994). For example, Shoshone Mountain and Rainier Mesa provide evidence for Paintbrush Group and Timber Mountain Group deposition along the caldera complex in the absence of extension or local uplift. The eroded south flank of Shoshone Mountain shows that middle Miocene tuffs of the Paintbrush Group and younger units were deposited on a rugged terrain of eroded 13-Ma volcanics of the Wahmonie Formation, and on faulted Paleozoic carbonates. Middle Miocene tuffs filled in the eroded surface and formed a plateau that completely masked underlying relief. Although the 13-Ma Wahmonie Formation has not been extended appreciably, the Paleozoic units show evidence of considerable block rotation and extension prior to deformation of the Wahmonie Formation. Post-caldera extension (younger than the 11.45-Ma Ammonia Tanks Tuff) occurred only in restricted outlying areas (Sawyer, D.A., Fleck et al. 1994, p. 1314). Although magmatism in the southwestern Nevada volcanic field and regional extension were broadly coeval, there is no apparent genetic link, or at least no correlation in relative extent or amount of activity (Sawyer, D.A., Fleck et al. 1994. p. 1316).

The lack of correlation between extension and magmatism may be explained in two ways. First, regional basin-and-range extension may have occurred during the period of peak volcanism, but its effects may only have been imprinted in the southwestern Nevada volcanic field during or after periods of post-caldera magmatic deflation, presumably when the upper crust regained shear strength. Second, local domains may have been influenced differently by magmatic activity resulting in different styles of extension or no extension at all. Typical basin-and-range structures are not developed within 15 to 20 km (9 to 12 mi.) of the caldera complex, including most of Yucca Mountain. Beyond 15 to 20 km (9 to 12 mi.), deformation is more typical of the Basin and Range province. The superposition of caldera magmatic stresses upon the regional stress field resulted in temporary stress changes within the zone of influence surrounding the caldera complex (Minor 1995, p. 10527, Figures 4, 5, and 6).

The relatively short periods of eruption were apparently preceded by lengthy periods of buildup (Sawyer, D.A., Fleck et al. 1994, p. 1312, Figure 4), during which large amounts of heat and volatiles transferred high into the crust. Abrupt caldera collapse and strain release is the probable cause of local extension in areas adjacent to the southwestern Nevada volcanic field.

4.3.2.8 Faulting at Pahute Mesa

As discussed in Section 4.3.2, the north-trending fault system that characterizes the Crater Flat domain appears similar to the fault pattern north of the Timber Mountain caldera at Pahute Mesa (Carr, W.J. 1990, Figure 6) (Figure 4.3-3). A genetic link would imply that faulting at Pahute Mesa may provide constraints on tectonic models for the Crater Flat domain. The pre-Timber Mountain Group volcanics (12.7 Ma) are tilted northeastward 2° to 4° in the subsurface of Pahute Mesa (Warren, Byers et al. 1985, p. 6). The Rainier Mesa Tuff (11.6 Ma) is considerably thicker across down-to-the-west faults on the western side of Pahute Mesa than it is on the east side, indicating greater extension toward the west in the 12.7- to 11.6-Ma interval (Fridrich 1998, p. 15). Fault offsets in the Rainier Mesa Tuff also increase from east to west across Pahute Mesa, similar to the pattern of increase to the west seen in the Crater Flat domain (Fridrich 1998, p. 15). Fault activity at Pahute Mesa declined after the 11.6-Ma volcanic pulse, as is true in Crater Flat (Fridrich 1998, p. 16). Evidence for the decline includes minor normal faulting (offsets of approximately 80 m [262 ft] on main faults) and less than 2° tilting of the Thirsty Canyon Tuff (9.4 Ma) on Pahute Mesa (Orkild, Sargent et al. 1969).

The similarities of fault style, attitude, and timing suggest a common genetic relationship that has been attributed to extension localized within the Kawich-Greenwater rift (Carr, W.J. 1990, pp. 284, 286) (Figure 4.2-9). This spatial and temporal association implies that the rift may not only be a focus for this style of extension and for Miocene magma emplacement, it may also be a focus for whatever post-caldera extension has occurred. The moderate, north-striking, west-directed extension centered in the rift has apparently not affected adjacent terrain to the east or west.

4.3.3 Tectonic Stress and Strain in the Yucca Mountain Region

The histories of stress and strain provide critical constraints on a tectonic model. In the following sections, stress and strain are discussed in terms of both site-specific data and data from the surrounding structural domains.

4.3.3.1 Contemporary Stress and Paleo-Stress

In the Yucca Mountain area, the least principal stress vector ($\sigma 3$), which controls the extension direction, is essentially horizontal and trends N50° to 70°W (Carr, W.J. 1974, p. 1; USGS 1984, p. 4; Zoback and Zoback 1980, p. 523; Wernicke, Axen et al. 1988, p. 1752; Zoback 1989, p. 7105). Observations from boreholes at Yucca Mountain provide data on the state of stress within the upper 2,000 m (6,562 ft) of the mountain (USGS 1984, p. 21; Stock and Healy 1988, p. 87). Measured $\sigma 3$ values are low, near the margin of stability for normal faults that strike N25° to 30°E with a coefficient of static friction that is equal to or greater than 0.6 (Figure 4.3-5). If pore pressure (hydrostatic stress) were elevated to equal or exceed values of $\sigma 3$ obtained at Yucca Mountain, such faults would slip (USGS 1984, p. 59; Stock and Healy 1988, p. 92). Although local in situ stress measurements at Yucca Mountain accord well with conditions of normal faulting, local factors, such as static stresses, composition, and fabric anisotropies, influence the shallow stress field from place to place. At Rainier Mesa for example, least principal stress directions are oriented as much as 20° more northerly than $\sigma 3$ measured at Yucca Mountain (Carr, W.J. 1974, pp. 10, 11, Figure 3; Springer and Thorpe 1981,

Figures 7, 8). Near-surface stresses may not reflect conditions at seismogenic depths where strike-slip and oblique-slip focal mechanisms are common (Rogers, A.M., Harmsen et al. 1987, p. 1). Because strike-slip and dip-slip mechanisms occur throughout the uppermost 15 km (9.3 mi.) of the crust, the relative magnitudes of $\sigma 1$ and $\sigma 2$ at depth must be nearly equal, a relationship described as axially symmetric (Rogers, A.M., Harmsen et al. 1987, p. 66) (Figure 4.3-6).

Analysis of faults near Yucca Flat and in the Basin and Range to the east indicate that the present stress regime originated around 9 Ma. Prior to that time, $\sigma 3$ was oriented in a more westerly or southwesterly direction (Zoback et al. 1981, p. 189; Minor 1995, Figure 9). The stress field in the Yucca Mountain region rotated clockwise as much as 65° in the 11- to 8.5-Ma interval (Minor 1995, p. 10527). The clockwise stress rotation is recognized elsewhere in the Great Basin (Carr, W.J. 1984; Angelier et al. 1985, p. 347; Zoback et al. 1981, p. 213), but estimates of its timing vary (Wernicke, Axen et al. 1988, p. 1753). The relative magnitudes of $\sigma 1$ and $\sigma 2$ attained their present values during Plio-Pleistocene time (Bellier and Zoback 1995, p. 588).

History of the stress field is an important factor for the tectonic evolution of the Walker Lane and associated vertical axis rotation at Yucca Mountain (Section 4.3.2.2) (Minor, Hudson et al. 1997, p. 2). A characteristic tectonic feature of the Walker Lane is the complex interrelationship between strike-slip faulting and Basin-and-Range-style normal faulting. The Walker Lane can be considered in two ways. One, as a transition zone between the dominantly west-directed extension of the Basin and Range to the east and the dominantly strike-slip fault regime of California (Carr 1984, p. 9); or two, as having an independent stress history as a broad band of distributed dextral shear, superimposed on earlier extension (Wernicke, Axen et al. 1988, p. 1756; Minor, Hudson et al. 1997, p. 33). The uncertainty between these two models has a bearing on tectonic models applied to Yucca Mountain.

Based on paleo-stress studies (Scott and Hofland 1987; Throckmorton and Verbeek 1995), Yucca Mountain may lie within the eastern boundary of the Walker Lane (Figure 4.3-7) (Minor, Hudson et al. 1997, Figure 1). Yucca Flat basin (northeast of Yucca Mountain) may have opened under the influence of a regional normal-slip stress field characterized by a west-southwest $\sigma 3$ orientation. Yucca Flat basin was not affected by the clockwise stress rotation seen in the Crater Flat domain, because it is younger and outside the Walker Lane (Minor 1995, p. 10525).

Stress analyses are subject to several inherent limitations. First, field data are often ambiguous. For example, fault slip indicators in the Rock Valley fault zone could be interpreted as stress field rotations or simply as block rotations within the fault zone (Frizzell and Zoback 1987, p. 90). Second, stress measurements are point data, and often reflect local anisotropies and local variations in rock mechanical strength. Third, stress measurements at failure may not contribute to understanding changes of stress through time. In a mechanical environment of pronounced spatial heterogeneity and a wide variety of faults with differing shear strengths, the theoretical bases of stress analysis are not met. Therefore, stress data are not good predictors of future deformation.

4.3.3.2 Contemporary Strain

Analysis of strain rates and patterns provides a more direct assessment of deformation than does stress analysis. Any tectonic model for the Yucca Mountain region must account for modern strain directions and rates. Strain data are obtained from earthquake focal mechanisms, trilateration networks, very long baseline interferometry observations, and satellite geodesy.

Strain surveys show that the direction of extension in the Great Basin is toward the northwest, comparable to the direction of $\sigma 3$, the least compressive stress (Minster and Jordan 1984, p. 13; 1987, p. 4802; Gordon et al. 1993; Dixon et al. 1995; Savage, J.C. et al. 1995; Keefer et al. 1997). However, there are important spatial variations in the extensional strain rate. The northern Basin and Range appears to be moving at 4.9 ± 1.3 mm/yr. (0.19 ± 0.05 in./yr.), S82°W with respect to the continental interior (Savage, J.C. et al. 1995, p. 20267) by means of crustal extension. In contrast, the southern Basin and Range has an extension rate of 3 mm/yr. (0.12 in./yr.) or less (Sauber 1989, p. 123). The boundary between these two regions of differing extension is at about 37°N latitude (Harmsen and Rogers 1986, p. 1561; Smith, R.B. and Arabasz 1991, p. 192, Figure 7), a boundary that may represent a regional shear zone (Savage, J.C. et al. 1995, p. 20258) containing local and perhaps transient seismicity zones (Rogers, A.M., Harmsen et al. 1987, p. 77).

The relatively high strain rate of the northern Basin and Range is at least partly accommodated by the Central Nevada Seismic Zone (Figure 4.2-1). The motion of the Sierra Nevada block relative to Ely, Nevada, is 9.1 ± 1.5 mm/yr. (0.36 ± 0.06 in./yr.) at N16° ± 8°W (Savage, J.C. et al. 1995, p. 20257). Trilateration data show that at least 2.7 mm/yr. (0.11 in./yr.) of this extension is taken up by the Central Nevada Seismic Zone, a rate calculation constrained by a 40-km-wide (25-mi.) network (Savage, J.C. et al. 1995, p. 20265). The dextral slip rate along the Eastern California Shear Zone (which includes most of the Inyo-Mono domain) may be as high as 12 mm/yr. (0.47 in./yr.) (Sauber et al. 1994, p. 264), but the component of west-directed extension across the Eastern California Shear Zone, reflected by normal faulting is less than 4 mm/yr. (0.16 in./yr.) (Dixon et al. 1995, p. 767). Geologic evidence suggests that the Eastern California Shear Zone has been a zone of high strain since late Miocene time (10 to 6 Ma) (Dixon et al. 1995, p. 760).

The Crater Flat domain is located outside the zones of high strain rate defined by the Central Nevada Seismic Zone, the Eastern California Shear Zone, and the shear belt at 37°N latitude. A 50-km-aperture (31-mi.-aperture) trilateration network centered on Yucca Mountain and operated from 1983 to 1993 showed a strain accumulation of less than 2 mm/yr. (Savage, J.C. et al. 1994, p. 18106; Savage et al. 1999, p. 17627). This low rate is comparable to strain rates in the Great Basin south of 37°N. Higher strain rates have been proposed for the Yucca Mountain area (Wernicke et al. 1998), but these high rates are not supported by trilateration network data (Savage, J.C. et al. 1994, 1999).

The strain data discussed above have tectonic implications for Yucca Mountain. Contemporary strain patterns are partitioned into zones of relatively high deformation that are not clearly correlated with structurally defined tectonic domains. The high strain rate zones , such as the Central Nevada Seismic Zone, may represent concentrations of active deformation among relatively stable crust blocks (Savage, J.C. et al. 1995, p. 20265). The low strain rate

(Savage, J.C. et al. 1995, p. 20263, Figure 9) and low seismicity levels (Rogers, A.M., Harmsen et al. 1987, p. 82) (Section 12.3) in the Crater Flat domain suggest that the site area is in a tectonic domain that may be isolated from zones of high strain to the west and north.

4.3.4 Evaluation of Tectonic Models

In this section, the various tectonic models proposed for the Yucca Mountain vicinity or surrounding region are described and evaluated. These models vary considerably in detail: some were designed to explain a relatively narrow data set or hypothesis and, in some cases, boundary conditions and driving forces were not addressed. Hence, each model is discussed primarily in terms of its structural elements and the hypothesized mechanism of deformation. Each model has shortcomings, and no single model satisfies all the data.

4.3.4.1 Regulatory Background and Section Organization

The U.S. Nuclear Regulatory Commission identified five viable models (NRC 1999b, pp. C1 to C4):

- Half-Graben with Moderate Depth Detachment Model
- Half-Graben with Deep Depth Detachment Model
- Elastic-Viscous Model
- Crater Flat Pull-Apart Basin Model
- Lateral Shear Model

Each model and its variations are discussed in the following sections. In addition, the Crater Flat caldera model is described for completeness. Treatment of the models in terms of volcanic and seismic hazards assessment is presented in Sections 12.2 and 12.3, respectively.

To facilitate discussion, the models are grouped by similarities in structural elements, similar to the U.S. Nuclear Regulatory Commission groupings above. The groups are:

- Crater Flat caldera model
- Detachment fault models
- Rift/graben (elastic-viscous) models
- Lateral-shear/pull-apart basin models.

In the following sections, each model type is discussed in the same format: brief description, elements, evidence for, and evidence against.

4.3.4.2 Crater Flat Caldera Model

Crater Flat basin is a conspicuous depression within the Kawich-Greenwater rift (Figure 4.3-1), the axis of which is defined by aligned gravity anomalies that indicate basement depressions (Carr, W.J. 1990, p. 287, Figure 3). The Crater Flat caldera model was formulated (Carr, W.J. 1982, p. 9; 1984, pp. 2, 3, 70, Figure 9; 1988, p. 41, Figure 4-4) to account for: (1) the unknown source for the Crater Flat Tuff and (2) the form and structure of the Crater Flat basin. Briefly, the model postulates that Crater Flat basin reflects the structure of a subsided (now buried) caldera (the Crater Flat caldera) from which the Crater Flat Tuff was erupted.

4.3.4.2.1 Model Elements

The elements of the Crater Flat caldera model are as follows:

- **Physical Extent**–The model applies to the Crater Flat domain.
- **System Geometry**–The model implies a broad zone of arcuate faults exposed at the ground surface centered on a structural low at the location of the presumed caldera, and deep-seated faults with displacements measured in kilometers encircling the caldera proper.
- **Boundary Conditions**–At the time the presumed caldera formed it was at the southern margin of the southwestern Nevada volcanic field. Heat flow and volcanism would have been greater to the north.
- **Driving Forces**–Formation of the caldera would have been driven by volcano-tectonic processes associated with formation of the southwestern Nevada volcanic field; these are no longer active. Reactivation of favorably oriented faults would have been possible as a result of west-northwest oriented Basin and Range extension and/or right-lateral shear resulting from interaction of the North American and Pacific plates.
- **System Response/Dynamics**–Not specified. The model explains aspects of the fault pattern within the Crater Flat domain and provides a possible source for the Crater Flat Tuff, but says nothing about current volcanism and faulting.

4.3.4.2.2 Evidence for the Crater Flat Caldera Model

The caldera concept was based on the following general relationships:

- A thick sequence of welded Bullfrog Tuff was penetrated in drill hole USW-VH-1 (Figure 4.3-8), within the area of a broad positive aeromagnetic anomaly thought to indicate the presence of a thick, circular volcanic rock body representing a resurgent dome (Figure 4.3-3).
- The negative gravity anomaly of Crater Flat is indicative of an underlying graben-like structure; the basin outline appears to conform to a caldera shape.
- The location of several structural and volcanic features (including the Bare Mountain fault and some Yucca Mountain faults, and the Lathrop Wells basalt cone) could be controlled by an inferred caldera rim.

Two other buried calderas were inferred to lie farther north of the inferred Crater Flat caldera: the Tram caldera (Carr, W.J., Byers et al. 1984, p. 32), also referred to as the Prospector Pass Segment of the Crater Flat caldera, and an older-tuffs caldera beneath Yucca Mountain (Carr, W.J. 1982, p. 11) (Figure 4.3-8). The Tram caldera was inferred based on:

- Arcuate dikes in Bare Mountain that seem to correspond in age and composition to lava beneath the Tram Tuff; the lavas were thought possibly to represent early eruptions from the Tram caldera

- Thick Tram Tuff (457 m [1,499 ft]) in Beatty Wash (near the northern margin on Figure 4.3-8)

- Truncation of the Tram Tuff in northern Crater Flat by a fault that may be a caldera wall (Carr, W.J. 1982, p. 10).

Furthermore, the Tram and Lithic Ridge tuffs are underlain by and contain dacites, suggesting that dacite lavas formed an extensive pile beneath Crater Flat prior to eruption of the Crater Flat Group.

4.3.4.2.3 Evidence against the Crater Flat Caldera Model

A lack of demonstrable associations between a supposedly buried caldera and more recently acquired data negates the caldera model. For example:

- Paleomagnetic studies (Rosenbaum et al. 1991; Hudson, M.R., Sawyer et al. 1994) explain the curvature of faults at Yucca Mountain (which form part of the proposed caldera outline) as having been partly a result of vertical axis rotation that occurred about 12.7 Ma and later.

- Analysis of aeromagnetic data indicates that the prominent positive anomaly in Crater Flat originated within the Precambrian or Paleozoic section rather than from structures within the Tertiary section (Brocher, Hart et al. 1996, p. 39; Langenheim and Ponce 1995, p. 15).

- A seismic reflection profile across Crater Flat gives no evidence for deformation in Crater Flat apart from block faulting of broadly warped, essentially conformable Tertiary strata (Brocher et al. 1998, Figure 8).

The caldera model places peak tectonic activity in Crater Flat at about 14 Ma and requires that all subsequent deformation was guided by relict caldera rim structures. This hypothesis does not address the origins and mechanism of Late Neogene and Quaternary strain effects, such as distributed and recurrent faulting at Yucca Mountain; the origins and impetus for basaltic volcanism in Crater Flat; the mechanisms for vertical axis rotation at the southern half of Yucca Mountain and the strike-slip component of faulting; the post-10-Ma uplift of Bare Mountain; the evidence for Quaternary faulting at Busted Butte; and the fact that styles of faulting similar to those at Yucca Mountain in Mid Valley, Yucca Flat, and Pahute Mesa have originated independent of any relict guiding caldera structures.

4.3.4.3 Detachment Fault Models

A detachment fault is a regionally extensive normal fault with shallow dip (less than 30°). Above a detachment fault at shallow crustal levels, subparallel sets of concave-upward (listric) normal faults merge into the detachment fault and form elongate fault blocks that are all steeply tilted in the same direction. Rollover of the beds in the hanging wall is a characteristic of listric faulting and is caused by the curvature of such faults.

Low-angle normal faulting creates a succession of rotated fault blocks that rest on the low-angle fault plane atop older rocks that may not be involved in the extensional faulting—hence the name "detachment," as upper plate faulting appears detached from the lower plate. Extension is thus accomplished in the shallow crust by multiple normal faults that jointly separate and rotate upper plate blocks in a common direction. In the upper crust, this deformation mode is simple shear, in which one geometric axis of the deforming body rotates out of its original orientation.

4.3.4.3.1 Model Elements

The elements of the detachment fault model are as follows:

- **Physical Extent**–The model applies to the Crater Flat domain, the region east as far as the Sheep Range and southwest as far as Death Valley. To the north, the Timber Mountain caldera complex is not included within this model.

- **System Geometry**–The model implies a gently southwest-dipping normal fault at or below the Cenozoic-Paleozoic contact; subparallel, steeply west-dipping listric faults in the upper plate; west vergent normal faults with hanging wall rollover; horizontal extension of 100 percent or more in the upper plate; and ductile deformation of the lower plate. Other interpretations involve two or more detachments, with secondary east-vergent displacement on some.

- **Boundary Conditions**–Regional crustal extension would provide the driving force. Elevated heat flow would cause the brittle-ductile transition to rise to a relatively shallow level within the crust, reducing the thickness of the brittle crust and affecting deep fault geometries. Major extensional structures in the headwall area on the east are implied.

- **Driving Forces**–Thermal processes that may have promoted detachment faulting are no longer active in the Crater Flat domain. Reactivation of favorably oriented faults would be possible as a result of west-northwest oriented Basin and Range extension and/or right-lateral shear resulting from interaction of the North American and Pacific plates.

- **System Response/Dynamics**–Not specified. The model explains aspects of the fault pattern within the Crater Flat domain but says nothing about current volcanism and faulting.

4.3.4.3.2 Evidence for Detachment Fault Models

Detachment models have been applied largely on the strength of four major arguments to Yucca Mountain and its tectonic setting:

1. **Proximity**–Late Miocene detachment faulting occurred west of Yucca Mountain at Bare Mountain, the Bullfrog Hills, and the Funeral Mountains.

2. **Geometry**–Closely spaced west-dipping faults and hanging wall strata rotation at Yucca Mountain suggest geometries that accompany detachment faulting.

3. **Field Observation**–Detachments were reported at the Tertiary-Paleozoic contact in places east and south of Yucca Mountain.

4. **Regional Tectonic Interpretation**–A major deep detachment has been proposed to extend from near the Sheep Range, Nevada, west to Death Valley, California (Death Valley breakaway fault zone [Wernicke, Axen et al. 1988, p. 1746], Sheep Range detachment [Guth 1981, p. 763]).

Taking these four points into account, detachment faults have been proposed beneath and near Yucca Mountain (Hamilton 1988, p. 62; Scott, R.B. 1990, p. 273; Wernicke, Axen et al. 1988, p. 1746; Fox and Carr 1989, p. 37; Ferrill et al. 1996, p. 6-4; Oliver and Fox 1993, p. 1812; Ofoegbu and Ferrill 1995, p. 1-1; and McKague et al. 1996, p. 4-5). Figures 4.3-9 through 4.3-15 illustrate the various interpretations of detachment faulting applicable to the Yucca Mountain region. The original detachment fault model for Yucca Mountain included a regional "rolling hinge." Bare Mountain constituted the uplifted footwall, while the east-sloping flank of Bare Mountain was interpreted to be the exhumed detachment plane (Figure 4.3-9) (Hamilton, W.B. 1988, p. 62). The chronology of uplift at Bare Mountain implies that if a detachment exists at Yucca Mountain, it would have ceased slip at about 10 Ma (Fridrich 1999, p. 192). The resemblance of Yucca Mountain faults to tilted dominos and rollover (local increase of hanging wall dip toward the footwalls) suggest that they are listric faults (fault-plane dips that become shallower with depth) (Scott, R.B. 1990, p. 251).

An interpreted detachment fault at the Tertiary-Paleozoic contact in the Calico Hills, Rock Valley, and Point of Rocks led to the conclusion that a detachment fault forms the Tertiary-Paleozoic contact beneath Yucca Mountain at a depth of 1.5 to 2.5 km (0.9 to 1.6 mi.) (Figure 4.3-10) (Scott 1990, p. 258, Figure 4). Crater Flat has been interpreted as a pull-apart basin that controlled fault activity at Yucca Mountain (Figure 4.3-12) (Fox and Carr 1989, p. 47). A low-angle extensional fault proposed at the base of the Tertiary section was interpreted as a fragment of a subregional Miocene detachment fault that was locally reactivated during the Quaternary by sliding toward the extensional axis of Crater Flat (Fox and Carr 1989, p. 46).

The east side of the Kawich-Greenwater rift (Figures 4.2-9 and 4.3-1) that encompasses Yucca Mountain has been interpreted to be the headwall of a major detachment to the west (Carr, W.J. 1990, pp. 81 to 82). The Yucca Mountain-Crater Flat faults have been projected to depth as essentially planar with the interpretation that they need not be underlain by a regional detachment (Carr 1990, p. 300) (Figure 4.3-13). Nevertheless, these faults were considered to be largely gravitational features of a breakaway zone within the Kawich-Greenwater rift (Figures 4.2-9, 4.3-1, and 4.3-13).

Two model variants (Figure 4.3-14) were based on syntheses of previous proposals. Model A (Figure 4.3-14b) assumes that the Yucca Mountain faults developed as the headwall of the Bullfrog Hills detachment system, which was thought to accommodate as much as 275 percent extension (Ferrill et al. 1996, p. 6-4). According to this model, Yucca Mountain faults were isolated from the Bullfrog Hills system by rise of the Bare Mountain block along the Bare Mountain fault, which truncated the Yucca-Bullfrog detachment. Continued motion of the Bare Mountain fault led to formation of a deeper, east-directed detachment plane. According to this model, the older, shallower, west-directed detachment accounts for the imbricate faulting at

Yucca Mountain. The younger, deeper, east-directed detachment accounts for hanging wall collapse into rollover and formation of Crater Flat basin. Model B (Figure 4.3-14c) accounts for hanging wall rollover and imbricate faulting at Yucca Mountain directly by assuming that the Bare Mountain fault is the driving listric (detachment) fault and that Yucca Mountain faults are simply antithetic to the deep, master, east-directed Bare Mountain detachment (Ferrill et al. 1996, p. 6-4). These models may explain the westward subsidence of Crater Flat with time; they are compatible with a succession of relatively young east-dipping faults in Crater Flat (Brocher et al. 1998, Figure 18), even though the model cross-sections do not explicitly show such faults.

Detachment faulting models for Yucca Mountain have been analyzed using geophysical data and simulation. For example, a half-graben or structural trough was modeled beneath Crater Flat (Figure 4.3-2) (Snyder and Carr 1982, Figures 8 and 9). The same data were later used to create a simulated gravity profile based on juxtaposition of slices of differing density and angular relations (Oliver and Fox 1993, p. 1812). The simulated gravity profile of the second study fit the first study profile when the slices were arranged to give the Bare Mountain fault a 27° dip and the Yucca Mountain detachment a 12° dip (Figure 4.3-15) (Oliver and Fox 1993, p. 1812).

Computer simulation techniques have been used to evaluate the common detachment hanging wall deformation mechanisms (flexural slip, slip line, domino, vertical shear) (e.g., Young et al. 1993). The assumptions required to model detachment-style rollover at Yucca Mountain did not comply well with field data. Vertical shear provided the most acceptable mechanism for creating appropriate rollover. However, much of the vertical shear used to explain hanging wall rollover at Yucca Mountain (Scott 1990, pp. 259, 269) is conceptual and not based on field evidence (Figure 4.3-10).

A five-layer, linear, elastic, finite-element model was applied to the problem of detachment-related fault slip at Yucca Mountain (Figure 4.3-14b) (Ofoegbu and Ferrill 1995). In order for the model to work, it was necessary to treat each fault as a weakly cohesive or cohesionless layer at least 150-m (492-ft) thick and decoupled from confining rock. Slip was forced to occur on a selected fault by reducing its coefficient of static friction. Under reasonable confining stress, a friction angle of 0.93° is required. The model also implies that a significant proportion of fault displacement is taken up by deformation of the hanging wall and footwall. Slip rates in the detachment fault were six orders of magnitude greater than in the steep, off-branching perturbed fault. Under the model's assumptions, a detachment fault is likely to slip aseismically in response to slip events on the off-branching steep faults (Ofoegbu and Ferrill 1995, pp. 1-3, 4-6, 4-15). The model implies that detachment can only work along a weak layer that has an unusually low angle of friction or that presents significant rheological contrast with the suprajacent layer.

Detachment fault models adequately explain the distributed normal fault system at Yucca Mountain and the hanging wall rollover exhibited by each fault block. These models also adequately explain vertical axis rotation at Yucca Mountain as a consequence of differential slip rate rather than profound crustal shear mechanisms linked to deformation of the Walker Lane. Because all rotated normal faults of the upper plate are rooted in a common slip plane (the detachment), all faulting is necessarily distributed.

4.3.4.3.3 Evidence against Detachment Fault Models

Detachment fault models for the Yucca Mountain region are controversial. Most of the detachment fault models were advanced prior to geophysical data acquisition and detailed geologic mapping, which indicate that a shallow detachment at the Tertiary-Paleozoic contact (Scott 1990, p. 276, Figure 15) can be eliminated as a credible interpretation. Tertiary-Paleozoic contacts exposed east and south of Yucca Mountain are erosional contacts, not slip surfaces (Simonds and Scott 1996, p. 20), and interpretation of the deep seismic reflection profile across Yucca Mountain (Brocher et al. 1998, p. 967) shows that high-angle faults offset the Tertiary-Paleozoic contact, thus precluding a shallow detachment at the mountain.

The history of deformation in and around the Crater Flat domain constrains the timing and extent of detachment fault models. Models that incorporate the Bare Mountain fault or that involve a deformation scheme within and west of Bare Mountain (Hamilton 1988, p. 55; Scott 1990, p. 276, Figure 15; McKague et al. 1996, p. 3-11, Figure 3-6) are limited in timing and geometry. Uplift of Bare Mountain (and creation of Crater Flat basin) occurred within the 1-m.y. period from 12.7 to 11.6 Ma; by this time Bare Mountain was already an elevated range that had shed metamorphic rock debris as early as Crater Flat Group time (prior to 13 Ma) (Fridrich 1999, p. 192). The Bare Mountain fault dips steeply to a depth of about 3.5 km (2.2 mi.) and possibly as deep as 6 km (3.7 mi.) (Brocher et al. 1998, p. 966). Displacement on the Bare Mountain fault would have severed detachments at crustal depths above about 6 km (3.7 mi.) at about 12.7 Ma. Furthermore, any regional deep crustal detachment slip at or above the brittle-ductile transition was terminated by about 14 Ma, when dike intrusion and differential uplift along the Bare Mountain front isolated any deep crustal connection Bare Mountain may have had with detachment farther east. The Bullfrog Hills detachment heads along the west flank of Tram Ridge (Fridrich 1999, p. 173, Figure 3). No structural continuity between the Bullfrog Hills and the Crater Flat faults can be found that supports a model having detachment that extended through the Bullfrog Hills and Yucca Mountain (McKague et al. 1996, p. 3-4, Figure 3-2a; p. 3-11, Figure 3-b). Any shallow detachment that occurred west of the Fluorspar Canyon fault after 14 Ma was isolated from any comparable deformation in Crater Flat east of Tram Ridge (Fridrich 1999, p. 181, Figure 6). The Bullfrog Hills formed from 2 to 3 m.y. after the initial phase of Yucca Mountain faulting (Maldonado 1990, p. 1004), and the transport vector of the Bullfrog Hills projects eastward to the Rainier Mesa caldera, diverging some 20° from the orientation of the transport vector of Yucca Mountain.

Deep detachment faults (or systems) projected west of the Sheep Range by Guth (1981) and Wernicke, Axen et al. (1988, p. 1746) are incompatible with structures mapped at the Nevada Test Site because they ignore the significant strike-slip deformation of the Walker Lane. They are not comparable to structure exposed in the Funeral Mountains, the Bullfrog Hills, or Bare Mountain. In fact, chronologic and kinematic relationships among these latter structural assemblages are still unresolved. Interpretations of Miocene extensional structures east of Yucca Mountain are complicated by strike-slip faulting within the Spotted Range-Mine Mountain structural zone and by east-vergent extension east of the CP Hills. Crater Flat basin's deformation history is incompatible with detachment fault models. The Yucca Mountain faulting pattern does not reflect a systematic vergence to the west and the rate and progress of extension across Crater Flat is diachronous (Fridrich 1999, p. 193; Brocher, Hart et al. 1996, p. 955; Simonds et al. 1995). The structural style of the Crater Flat basin has progressively

changed during its tectonic evolution, and the area of active tectonism in the basin has been progressively shrinking toward the southwest corner (Fridrich 1999, p. 192). Crater Flat is young relative to Yucca Mountain, and its structural style is different from the 12.7- to 11.6-Ma style of Yucca Mountain (Fridrich 1999, p. 190). The low ridge along the southern flank of the basin formed after about 10 Ma and involves stratal tilting of as much as 10° north into the basin, a style of deformation that is not a continuation of earlier structural patterns (Fridrich 1999, p. 190).

All detachment fault models presented for Yucca Mountain have similar deficiencies: they are based on single cross-sections that do not account for the northern and southern boundaries of Crater Flat basin. Each model depends on buried (or exhumed and therefore inoperative) structures that extend beyond the Crater Flat domain's east or west structural borders and are not resolved with respect to known or postulated boundary structures. Because the hidden structures are presumed to be subhorizontal slip planes within the brittle crust, they effectively isolate lower plate deformation from structure expressed within the upper plate or at the surface, and in fact, they depend on a substantial contrast in structural style across the detachment. Consequently, these models require consideration of two superimposed seismic source zones (an upper plate and a lower plate seismic source zone), and they provide no explanation for basaltic magma passage through the lower crust. Listric fault mechanisms require a fixed (or rigid) headwall scarp that does not participate in deformation related to extension. For example, the rigid headwall does not undergo uplift in response to unloading of the footwall (or lower plate, Figure 4.3-16). Listric fault models that make the Bare Mountain fault a headwall fault do not account for the up to 5 km (3.1 mi.) of uplift of Bare Mountain since 13 Ma (Fridrich 1999, p. 182). None of the detachment fault models provide a structural solution for the Crater Flat domain eastern border, as no fixed headwall has been identified.

The model cross sections shown on Figure 4.3-14 place the headwall east of Little Skull Mountain, but this construction does not correspond to mapped structure there; incorporating Little Skull Mountain into the listric upper plate creates a tectonic problem. Because Little Skull Mountain is a north-dipping low ridge cut by down-to-the-west oblique faults, the northward tilt requires a post-9-Ma tectonic event not provided by the listric fault model, which attempts to link the post-9-Ma down-to-the-west faults at Little Skull Mountain with the pre-11.6-Ma faults at Yucca Mountain and the Bullfrog Hills.

No detachment fault models address lateral boundary conditions to extension in Crater Flat. For example, immediately north of Yucca Mountain a large volume of magma resided in the crust (Broxton, Warren et al. 1989, p. 5983) throughout the period of inferred maximum detachment activity. The effects of large volumes of molten or near-molten rock on the inferred detachment mechanism have not been addressed. The models assume that detachment occurred within brittle rock having no rheological perturbations.

Additionally, the concept of contemporary detachment faulting is complicated by a paucity of seismicity and conflicts with observations of historical earthquakes (Arabasz and Julander 1986, p. 63; Jackson, J.A. and White 1989, p. 17; Wernicke 1995). For example, the Little Skull Mountain earthquake occurred at about 11-km (6.8-mi.) depth on a N60°E-striking, 65°-to 70°-SE-dipping fault (Sheehan et al. 1994). This fault projects to the surface west of the Field Operations Center, approximately along the southwest projection of the Mine Mountain fault.

Aftershocks projected along this fault occurred at depths of less than 5 km (3.1 mi.). Aftershocks also occurred on a variety of other local faults; however none had a shallow detachment aspect. This evidence suggests that the Little Skull Mountain earthquake fault extended through any relict detachment fault and/or its headwall.

The sparse record of small (M_L equal to or less than 2.0) earthquakes at or near Yucca Mountain give focal depths as great as 9 km (5.6 mi.). Fault-plane solutions indicate oblique left-lateral normal slip on faults that dip from 55° to 88° (Harmsen and Bufe 1992, p. 33). Applying stress values for Yucca Mountain inferred by Stock et al. (1985) to the Mohr-Coulomb failure criterion, Harmsen and Bufe (1992, p. 34) calculated that applied shear stress is equal to or greater than 0.7 times the effective normal stress on the inferred fault plane of the primary solution having a 74° dip. Their calculations imply that fault slip beneath Yucca Mountain occurs on steeply dipping faults of moderate frictional strength, at depths where detachment faults are inferred to exist in some models.

Detachment faulting could have occurred during the period of peak east-west extension at Yucca Mountain as a short-lived local phase of deformation, but there is no evidence for a widely extended, long-lived system linked to tectonic activity outside the Crater Flat domain, and there is no evidence for any such activity in post-late Miocene time. Significant deficiencies of these models are that they do not accord with local structural variations and domain boundaries, and that they do not accord with the post-late Miocene history of deformation, including basaltic volcanism, recurrent fault slip, and local deformation trends within the Crater Flat domain.

Detachment fault models are deficient in accounting for the significant strike-slip faulting in the region (the Walker Lane and Rock Valley fault zone) and lack of demonstrable structural continuity between the Crater Flat domain and detachment faults to the west and southwest. The models do not explain or account for the differences between structural domains in the region or their boundaries. As all proposed detachment models are based on a single or a few cross-sections, they do not account for third-dimensional problems such as the north-dipping ridge at the south end of Crater Flat and its relationship to caldera complexes north of Yucca Mountain, which were active at the potential times of detachment faulting.

4.3.4.4 Rift-Graben (Elastic-Viscous) Models

Rift-graben models (the elastic-viscous models of NRC [1999b, pp. C-1 to C-4]) assume a mobile, viscous middle crust that is overlain by internally deformable, passive, brittle upper crust. In these models, the dominant mode of deformation approximates pure shear wherein the orientations of geometric axes of the deforming body remain unchanged during deformation. For example, a cube may become stretched or flattened, but its shape is not rotated or skewed from its original rectilinear shape. In the rift-graben models, the result is a variety of rift-like or graben-like elongate basins in the upper crust that have their long axes normal to the extension direction; fault vergence may vary across the basin. Intervening ranges may collapse or extend into adjacent basins in a manner that reflects local rock strength, stress history, or other constraints. Two general rift-graben models have been applied to the Crater Flat domain: a half-graben model and a pull-apart rift model. These models are also called planar fault models, because faults do not change dip (become listric) with depth. In the half-graben model, Crater Flat basin is the hanging wall of the Bare Mountain fault. Slip on the fault controls basin

subsidence, and the block-bounding faults of Yucca Mountain are antithetic to the Bare Mountain fault. In the pull-apart rift model, a master fault is not required; rather, behavior of internal fault sets determines the structural configuration. In addition, rift terminations may be defined by strike-slip faults (Section 4.3.4.5). In this model, Crater Flat is underlain by an axial fracture zone; widening is normal to the fracture and the basin is a lateral propagation of the deep axial fracture. Both models are driven by pure shear deformation of a ductile or viscous lower crust that controls the pattern and evolution of the upper-crustal faults.

4.3.4.4.1 Model Elements

The elements of the rift-graben (elastic-viscous) model are as follows:

- **Physical Extent**–The model applies to the Crater Flat domain and the surrounding region. Model limits are not specified, but probably include most of the Great Basin.

- **System Geometry**–The model implies subparallel rifts and half-graben with opposing vergence directions, domino-style fault blocks, planar faults with seismicity extending 10 km (6.2 mi.) or deeper, and fault-controlled linear belts of basaltic volcanism; strike-slip faults at basin terminations are permitted.

- **Boundary Conditions**–Regional-scale plastic deformation and extension of the lower crust and continental mantle would drive rift-graben formation in the upper crust. Elevated heat flow would cause the elastic-ductile transition zone to rise to a relatively shallow level within the crust.

- **Driving Forces**–Passive deformation of the elastic-brittle crust would result from plastic flow of the lower crust. The cause of lower crustal plastic deformation probably involves elevated sublithospheric heat flow and instability in the asthenosphere. The extreme thermo-tectonic processes that were responsible for the Kawich-Greenwater rift are no longer active in the Crater Flat domain. Reactivation of favorably oriented faults would occur as a result of west-northwest-oriented Basin and Range extension and/or right-lateral shear resulting from interaction of the North American and Pacific plates.

- **System Response/Dynamics**–Not fully specified. The model explains aspects of the fault pattern and basaltic volcanism within Crater Flat. Pull-apart rifting causes extension of the entire thickness of the crust, which allows ascent of low viscosity basaltic melts with short crustal residence times. The half-graben model implies that basaltic intrusion in Crater Flat could be guided by faults, but any inference that the Yucca Mountain block-bounding faults would guide intrusion toward Yucca Mountain, or that Crater Flat east-dipping faults would guide magma away from Yucca Mountain, would depend on the model variants.

4.3.4.4.2 Evidence for Rift-Graben Models

Rift-graben models are consistent with Basin and Range structure, but the substructure is not demonstrable in outcrop. Seismicity suggests that present-day extension occurs throughout most of the southern Great Basin as normal-faulting earthquakes along steeply dipping faults originating at depths approaching 19 km (11.8 mi.) (Doser and Smith 1989, p. 1385).

Deep seismic reflection profiles (Hauge et al. 1987, p. 329) and refraction profiles (Catchings and Mooney 1991, p. 6250) across central Nevada support rift-graben models. Seismic data reveal a layered crust, defined by both acoustic reflection and interval velocities, in which upper crust acoustic velocities vary by about 0.3 km/s (0.18 mi./s). Ranges cored with Mesozoic rocks have an acoustic velocity of 6.0 km/s (3.72 mi./s) and basins (or intervening ranges) underlain chiefly by Tertiary rocks have an acoustic velocity of 5.7 km/s (3.54 mi./s) (Catchings 1992, p. 1182). Upper crustal tectonic depressions filled with deposits having velocities of 5.7 km/s (3.54 mi./s) are similar to a model of Dixie Valley having highly broken rock to a depth of 20 km (12.4 mi.) (Okaya and Thompson 1985, p. 122). The seismic velocity structure implies the crust as a whole is extending laterally in boudinage fashion, compatible with a pure shear mechanism (Catchings 1992, p. 1189).

Crater Flat basin is a conspicuous depression within the Kawich-Greenwater rift (Figures 4.2-9, 4.2-11, and 4.3-1), the axis of which is defined by aligned gravity anomalies that indicate the occurrence of basement depressions (Carr, W.J. 1990, p. 287, Figure 3). The Crater Flat domain section of the volcano-tectonic rift is interpreted to have experienced several episodes of magmatic inflation, doming, and caldera and sector collapse within a steep-sided basement trough (Carr, W.J. 1990, pp. 290, 300). In this interpretation, the Yucca Mountain faults are essentially planar subsidence structures created by opening of the rift (Carr, W.J. 1990, p. 300). Figure 4.3-13 shows that opening of the rift was bidirectional, centered on an axis obscured by intrusion, with an abrupt western side (i.e., Bare Mountain fault), resulting in an asymmetric graben (Carr, W.J. 1990, p. 286). Crater Flat basin has been interpreted as a sector graben caused by evacuation of a body of magma from the base of the crust (Carr, W.J. 1990, p. 300). This interpretation accords well with the timing and magnitude of initial faulting of Yucca Mountain, as well as the basin shape and position.

A regional mechanism for Kawich-Greenwater rift genesis that would link Crater Flat basin to the entire extent of the rift presumes that the rift formed the headwall for detachments west of Crater Flat (Carr, W.J. 1990, p. 299). Two important observations relate to this model: (1) inferred detachment of the Bullfrog Hills is unrelated spatially or chronologically to faulting at Yucca Mountain, and (2) the rift mechanism provides a structural link between the fault systems in Crater Flat/Yucca Mountain and at Pahute Mesa to the north (Figure 4.3-3). This rift-like aspect of the model implies that Pleistocene extensional faulting at Yucca Mountain is not a function of antithetic slip controlled by the Bare Mountain fault, but is instead controlled by axial fractures within the deepest part of the Crater Flat basin. It implies that future tectonic activity will be concentrated toward the southern tip of the basin. The model provides a mechanism for recurrent basaltic volcanism within the rift confines and it accounts for a population of east-vergent faults beneath Crater Flat (Brocher et al. 1998, Figure 18) (Figure 4.3-17).

A rift model for Yucca Mountain, as part of the Amargosa Desert rift zone (Figure 4.3-4B), was described by Brocher et al. (1998, p. 968). Although they referred to the Amargosa Desert rift zone as an asymmetric half-graben (Brocher et al. 1998, p. 947), they presented evidence for a kind of evolved pull-apart model that depends on changing behavior of the brittle crust in response to its changing thickness through time. The rift zone was divided into two subdomains based on fault block tilt: a west-tilted Crater Flat domain and an east-tilted Yucca Mountain domain (Brocher et al. 1998, p. 950) (Figures 4.3-17, 4.3-18). The fault configuration was interpreted entirely on the basis of a seismic reflection profile and aeromagnetic anomalies that

indicate the presence of east-side-down faults in Crater Flat (Brocher et al. 1998, p. 961). However, no fault is mapped at the surface of Crater Flat west of borehole USW VH-1 (Brocher et al. 1998, p. 961), and east-facing scarps east of the borehole and along the seismic line (Faulds et al. 1994; Simonds et al. 1995) cannot confidently be traced in the seismic profile beneath the Paleozoic-Tertiary contact (event A, Brocher et al. 1998, p. 961) (Figure 4.3-17). Nevertheless, Brocher et al. (1998, pp. 956, 962) infer these faults to be present as far east as the Solitario Canyon fault on the basis of the westward tilt and apparent discontinuities of reflections (event B, Figure 4.3-17) within the Bullfrog Tuff in the upper 700 m (2297 ft) of the profile. The longitudinal extent of the east-dipping faults is unknown.

The Brocher et al. (1998, Figure 18) model geometry implies that as the brittle crust thickens and the basin widens, east-dipping faults synthetic to the Bare Mountain fault should slip, and those antithetic to the Solitario Canyon fault that are unable to slip should be cut by new west-dipping faults. This model is too specifically tied to the seismic profile to be applied to the whole Crater Flat basin. If Crater Flat basin is a pull-apart basin, it differs from those in Death Valley (Blakely et al. 1999, p. 12) or others modeled as a rhomb-shaped graben or half-graben, that are linked genetically to strike-slip faults (Sims et al. 1999, p. 549).

An elastic-viscous rift-graben mechanism explains the fundamental graben-like structure of Crater Flat basin. Because this mechanism can be tied directly to lower crustal ductile deformation, it accounts for extension throughout Quaternary time. Rift-graben models are consistent with Crater Flat domain earthquakes that exhibit steep fault planes and occur at various depths in the seismogenic brittle crust. The model is also consistent with the locations and genesis of basaltic intrusions in Crater Flat and elsewhere in the Amargosa trough. The rift-graben models account for both uplift and subsidence of block faulted crust. These models can be modified to include vertical axis rotation, which is not easily accounted for in detachment fault models. Rift-graben models imply that faulting and volcanism are coupled processes, that future volcanism will either penetrate the Bare Mountain fault or focus on deep fault intersections at the southern end of the basin, and that faulting in Crater Flat may precede and accompany volcanism.

4.3.4.4.3 Evidence against Rift-Graben Models

The half-graben model is adequate only near the central latitudinal axis of the Crater Flat domain. However, it fails to account for the decreased throw and splitting of the Bare Mountain fault in the vicinity of the caldera complex. It also does not account for the structural style at the southern end of Crater Flat. However, if dextral shear is imposed across the model (Section 4.3.4.5) some problems are resolved by treating the Timber Mountain caldera complex as a fixed plug that concentrates strain along its southern margin. The half-graben may have formed prior to the caldera complex. The model allows post-middle Miocene faulting and vertical axis rotation to be unique to the Crater Flat domain, which is isolated from deformation north of the caldera complex. The half-graben model also fails to account for a cumulative Pleistocene dip slip on the Bare Mountain fault that is less than that measured across Yucca Mountain. The half-graben model creates compression adjacent to the master fault plane (Figure 4.3-15), which gives less total extensional strain than the detachment models (Bruhn and Schultz 1996, p. 3410).

The rift-graben model does not explain the origin of the low ridge that bounds the southern rim of Crater Flat basin, which shows no evidence of axial symmetry. The model also does not account for hanging wall rollover if, as the model implies, each block-bounding fault at Yucca Mountain extends as an independent plane through the brittle crust. The model does not account for the asymmetry of Crater Flat basin, for uplift of Bare Mountain, or for vertical axis rotation in Crater Flat.

The rift model based on seismic reflection data is not a purely rift-type model, but invokes changing behavior of the brittle crust in response to changing thickness through time (Brocher et al. 1998, p. 969). The overall structure, however, is that of a rift. This model is narrowly focused on a single seismic reflection profile, and does not account for other data that would make it applicable to the entire Crater Flat domain. The seismic data are ambiguous and noisy (Brocher et al. 1998, Figures 11 through 14), so that a number of viable interpretations of faults and fault blocks could be made, including some that support detachment models, pull-apart basin models, or others. The rift interpretation does not account for apparently contradictory structures north and south of the profile, including mapped west-dipping faults in the area interpreted as an east-dipping fault domain. The model also does not explain why Crater Flat formed before Yucca Mountain (as it proposes) or why the early, east-dipping faults in Crater Flat deepened the basin while the west-dipping faults at Yucca Mountain left the mountain anomalously high. The model contradicts field evidence that subsidence and extension in the Crater Flat domain progressed toward the west, resulting in an asymmetric basin (Fridrich 1999, pp. 169 to 170).

4.3.4.5 Lateral-Shear and Pull-Apart Basin Models

Lateral-shear models apply horizontal shear stress to create translation (lateral offset) as well as tension (pull-apart basins). The result is an alignment of strike-slip fault segments that link pull-apart basins dominated by oblique faulting (Sims et al. 1999; Burchfiel and Stewart 1966; Blakely et al. 1999). In this model, Crater Flat is described as having been opened (pulled apart) between linked strike-slip and dip-slip faults. This deformation style, also termed transtension, is well documented in the Inyo-Mono domain west of the Death Valley-Furnace Creek fault. Death Valley has been modeled as a series of obliquely extending rhombochasms (Wright, L.A. and Troxel 1973) connected by northwest-striking dextral faults (Wright, L.A. 1989; Blakely et al. 1999, p. 13). Evidence of right-lateral shear is widespread in the Walker Lane, but evidence for transtensional basins linked by strike-slip faults is limited (Blakely et al. 1999, p. 13).

4.3.4.5.1 Model Elements

The elements of the lateral-shear and pull-apart basin model are as follows:

- **Physical Extent**–The model applies to the Crater Flat domain and the surrounding region, except for the Timber Mountain caldera complex to the north. Model limits are not specified, but they include the Walker Lane, Death Valley, and the Central Nevada Seismic Zone.

- **System Geometry**–The model implies the presence of northwest-striking, right-lateral strike slip faults, and conjugate northeast-striking left-lateral faults. Lateral-slip faults

may occur on a continuum between discrete, continuous faults with tens of kilometers (miles) of displacement, to diffuse, kilometers-wide (miles-wide) belts of distributed faulting that have modest displacements on individual faults. The dominant strain regime is transtensional; faults may terminate in rhombochasm or sphenochasm pull-apart basins.

- **Boundary Conditions**–Lateral-slip faulting becomes dominant to the west in the Death Valley region; it is less important to the east. Vertically, the faults penetrate the entire thickness of the elastic crust.

- **Driving Forces**–Transtensional lateral-slip faulting is due to the interplay of west-northwest oriented Basin and Range extension and right-lateral shear resulting from interaction of the North American and Pacific plates.

- **System Response/Dynamics**–Not specified. The model explains aspects of the fault pattern within the Crater Flat basin. Basaltic volcanism in the basin is the result of transtension within a zone of distributed right-lateral faulting that allows ascent of low-viscosity basaltic melts with short crustal residence times coincident with faulting episodes.

4.3.4.5.2 Evidence for Lateral-Shear and Pull-Apart Basin Models

Crater Flat was characterized as a type of half graben known as a rhombochasm (a pull-apart basin modified by distributed dextral shear) or as a sphenochasm (a pull-apart anchored at one end, so that the basin opens like a Chinese fan) (Fridrich 1999, p. 193). This model was based on surface geologic mapping and interpreted projections of surface structures to depth.

A north-northwest-striking dextral strike-slip fault at depth beneath Yucca Mountain is inferred on the basis of displacement of Bare Mountain and the Striped Hills, now separated by about 20 km (12.4 mi.) (Caskey and Schweickert 1992, p. 1324) to more than 30 km (18.6 mi.) (Schweickert and Lahren 1994, p. A-250; 1997, p. 25). The offset is based on the premise that Bare Mountain and the Striped Hills once formed a continuous Mesozoic fold structure. The inferred fault was defined as the Amargosa fault system by Schweickert and Lahren (1994, p. A-250; 1997, p. 25) (Figure 4.3-19), a system that comprises the Stewart Valley, Pahrump Valley, Stateline, and Ivanpah faults for a total length of about 250 km (155 mi.). Evidence for the fault system includes gravity, seismic, structural, stratigraphic, and paleomagnetic data; the distribution of springs and basaltic volcanic centers; and patterns of late Quaternary surface faulting (Schweickert and Lahren 1997, p. 25).

A N25°W-striking structural alignment in the Crater Flat domain is known informally as the hinge line (Fridrich 1999, p. 177) (Figure 4.3-4). The hinge line separates paleomagnetic rotations of Tiva Canyon Tuff of 10° or less to the north from rotations of 20° or more to the south (Minor et al. 1997, p. 18) (Figure 4.3-20). The boundary is more strongly indicated by the divergence of aeromagnetic gradient alignments across the mountain, and by landform terminations along the trace of the hinge line. Although the hinge line separates predominantly north-striking faults to the northeast from northeast-striking faults that have relatively larger

displacements to the southwest (Fridrich 1999, p. 177), it is the change in paleomagnetic pole azimuths that provides the hinge-like aspect of this line, not the segregation of fault attitudes.

Conceptually, the hinge line marks a strain gradient across which extension, fault displacement, and vertical axis rotation are greater south of the hinge line. Physically, the hinge line may express one of the following conditions:

- A relatively broad zone of shearing (Minor et al. 1997, p. 20)
- The marginal area of a zone in which dextral shear and extension is concentrated to the southwest (Fridrich 1999, p. 177)

The hinge line does not represent a discrete structure that forms a boundary between Yucca Mountain and Crater Flat. The hinge line could represent the distal northwestern projection of the Pahrump-Stewart Valley fault zone into Crater Flat basin, but this projection does not constitute a fault or any mappable structural feature; rather, it is a gradient across which the intensity of lateral shear varies.

The projected contours of rotation across Crater Flat imply presence of a zone of diffuse dextral shear that is aligned with and perhaps part of a larger belt of clockwise rotation and dextral shear that extends at least 60 km (37 mi.) farther to the northwest (Hudson et al. 1996, p. A-451; Minor et al. 1997, p. 20). The data imply that middle Miocene normal extension was essentially confined to the Crater Flat domain and may have been associated with caldera magmatism (Minor et al. 1997, p. 28), whereas later vertical axis rotation was imposed from outside the domain via dextral shear associated with evolution of the Walker Lane (Minor et al. 1997, p. 33).

Paleomagnetic studies (Hudson, M.R., Sawyer et al. 1994, p. 258) suggest dextral shear affected the southwestern Nevada volcanic field region in discrete zones that were discontinuous in length and diachronous in age. Nonsystematic distributions of vertical axis rotations in time and space within the southwestern Nevada volcanic field imply that individual basins responded uniquely to distributed northwest-oriented dextral shear driven by post-12.7-Ma extension south of Yucca Mountain and west of the Spring Mountains (Brocher, Carr et al. 1993, p. 45; Hudson, M.R., Sawyer et al. 1994, p. 274).

Diffuse shear limited to Crater Flat basin can explain locations of basaltic volcanism and late concentration of extension toward the southwestern corner of Crater Flat. Recognition of the hinge line in the Crater Flat domain provides a means to reconcile aspects of strike-slip faulting outside Crater Flat with diffuse dextral shear deformation within Crater Flat.

A discrete shear zone that passes through Crater Flat would account for vertical axis rotation and for the centers of Quaternary and Neogene basaltic volcanism inside and outside Crater Flat. This model implies that future volcanism in Crater Flat will be narrowly confined. The model is not only compatible with detachment faulting, it requires detachment in order to hide the transcurrent shear zone in the lower crust. The model implies that slip on the buried strike-slip fault could activate listric faulting across Yucca Mountain.

4.3.4.5.3 Evidence against Lateral-Shear and Pull-Apart Basin Models

Projection of the Pahrump-Stewart Valley shear zone into Crater Flat (Schweickert and Lahren 1994, p. A-250; 1997) is problematic. No surface expression of the proposed shear zone is evident, and no throughgoing surface displacement has been reported in the northern Amargosa basin or in the vicinity of Crater Flat. Proposed lateral displacement of the Striped Hills and Bare Mountain by 20 to 30 km (12.4 to 18.6 mi.) (Caskey and Schweickert 1992, p. 1324; Schweickert and Lahren 1994, p. A-250; 1997 p. 25) is not supported by map data (Snow 1992, p. 94; Snow and Prave 1994, p. 713). The map data include projections of the Striped Hills fold to the Winter Peak anticline and an anticlinal axis in the Funeral Mountains, and lack of offset in folds and south-vergent structures that lie along the inferred trace of the shear zone.

Stamatakos and Ferrill (1998, p. 152) report that exhumation ages, original burial depths, and structural plunges of the Striped Hills and Bare Mountain are too different for them to have been originally adjacent. At Bare Mountain, north-striking faults presumed to be right-lateral shears are actually pre-Miocene normal faults with down-to-the-southeast displacement that have been rotated out of their original attitudes (Stamatakos and Ferrill 1998, p. 152). Rotation alone could not account for the postulated 25-km (15.5-mi.) displacement (Stamatakos and Ferrill 1998, p. 154) required in the Miocene volcanic section by projection of the Pahrump-Stewart Valley shear zone (Schweickert and Lahren 1997). These observations suggest that the pull-apart basin models that involve extension of the Pahrump-Stewart Valley shear zone into Crater Flat (Caskey and Schweickert 1992; Schweickert and Lahren 1994, 1997) are not viable.

Additional observations that are inconsistent with the existence of a large throughgoing dextral fault beneath Crater Flat include the following:

- No throughgoing surface fault exists in the tuffs of the southwestern Nevada volcanic field.
- Basin analysis finds no clear expression of the Amargosa fault system north of Amargosa Valley; it shows, rather, that the Stateline fault zone may merge with the northwestern margin of the Funeral Mountains (Blakely et al. 1999, p. 10).
- The inferred movement along the fault appears to have been intermittent with long periods of inactivity. The fault system seems to have been active into Late Oligocene time, then inactive until about 12.7 Ma, when it experienced activity during volcanism. Another period of quiescence followed and activity resumed about 3.7 Ma (Schweickert and Lahren 1997).
- Observations of vertical axis rotation are not necessarily diagnostic of a discrete fault zone. For example, in the Sleeping Butte-Tolicha Peak area near Black Mountain, 13.7-Ma Grouse Canyon Tuff is rotated 10° to 30° clockwise, whereas the unconformably overlying Rainier Mesa Tuff (11.6 Ma) is unrotated. Ten kilometers (6.2 mi.) southwest, Rainier Mesa Tuff is rotated 30° clockwise, whereas Ammonia Tanks (11.45-Ma) and Thirsty Canyon (9.4-Ma) tuffs are unrotated (Hudson et al. 1996). This temporal and spatial variability is incompatible with a fixed throughgoing fault.

- Vertical axis rotation within the Crater Flat basin cannot accommodate 25 km (15.5 mi.) of dextral offset. None of the post-Miocene features between the Sleeping Butte basalts and Stewart Valley account for any significant dextral offset. A best-fit profile across the inferred shear zone in Crater Flat suggests that only 10 km (6.2 mi.) of lateral offset can be accounted for by vertical axis rotation (Stamatakos and Ferrill 1998, p. 154).

Other interpretations of Quaternary and late Tertiary strain phenomena suggest that Quaternary transcurrent features are more likely oriented oblique to the Walker Lane than along it (Carr, W.J. 1984, p. 30; Rogers, A.M., Harmsen et al. 1983, p. 4;). These observations indicate that present extensional strain leading to active faulting is currently being concentrated along the Eastern California Shear Zone and the Central Nevada Seismic Zone rather than along a 250-km-long (155-mi.) fault system within and subparallel to the Walker Lane.

Lateral shear deformation that created pull-apart basins in conjunction with right-lateral slip has operated, and continues to operate, in the Inyo-Mono domain west of the Funeral Mountains (Blakely et al. 1999), however this deformation style is not evident at Yucca Mountain. Crater Flat basin appears to have formed by orthogonal extension and lateral shear was imposed on the basin during a subsequent episode of deformation (Minor et al. 1997, p. 33). Whether the lateral shear was diffuse or more narrowly confined is uncertain.

In explaining Quaternary faulting at Yucca Mountain, the lateral-shear model implies northwest-striking Quaternary slip outside the basin, because such slip is required by the model mechanism to drive deformation at Yucca Mountain. The model does not explain structure at the caldera rim or structure along the low ridge at the southern end of the basin where evidence for the entire history of late Miocene deformation is exposed.. Furthermore, the strike-slip model is not compatible with the structural evolution of the Crater Flat domain, nor with present-day right-lateral shear in and near the Walker Lane.

Models that call on diffuse shear, requiring individual basins to deform independently at different times, are not well formulated. Lateral-shear models for Yucca Mountain are difficult to support in general because of the lack of evident shear structures required to drive local deformation. They appeal to hidden, buried, or intermittently active crustal features that require mechanisms that cannot be verified or that would be unique in the overall tectonic environment.

4.3.5 Application of Tectonic Models to Hazard Analysis

Tectonic models provide a framework in which volcanic and seismic hazards are addressed. Hazards analyses are based on the suite of tectonic models discussed above. Volcanic and seismic hazards are discussed in Sections 12.2 and 12.3.

For evaluation of volcanic hazards, an expert panel was convened (CRWMS M&O 1996h). The panel offered two conclusions concerning possible tectonic control of magma ascent: (1) location and timing of intrusion is a function of mantle petrogenesis, and (2) location and timing of intrusion is controlled by crustal tectonics. The panel concluded that magma ascent is related to extension, but tectonic models were not consistently discussed in relation to volcanism. A pull-apart basin controlled by local, deep-seated normal faults was the most commonly cited model, and strike-slip faulting related to the Walker Lane was acknowledged as a possible factor.

No panel member cited detachment faulting in relation to volcanism. The experts' use of tectonic models is summarized in Section 12.2.

For probabilistic seismic hazards analysis, an expert panel evaluated each tectonic model and assigned it a weight (Wong and Stepp 1998). The panel assigned the greatest weight to the planar fault model in combination with a component of dextral shear (a pull-apart basin model) (Table 4.3-1) (Wong and Stepp 1998, Table 4-1). According to this model, Crater Flat is a graben-like structure bounded by normal faults and modified by dextral shear (but not cut by a strike-slip fault) (Wong and Stepp 1998). The detachment model was assigned lower weight, and the lateral-shear model (strike-slip faulting extending into Crater Flat) was assigned the least weight (Table 4.3-1). The expert panel did not consider the Crater Flat caldera model viable (Wong and Stepp 1998) (Table 4.3-1). The experts' use of tectonic models is summarized in Section 12.3.

4.4 QUATERNARY STRATIGRAPHY AND SURFICIAL PROCESSES

An understanding of the Quaternary stratigraphy in the Yucca Mountain vicinity and the surficial processes that are largely responsible for its development are important for assessing a number of issues related to the design and performance of the potential repository. The Quaternary stratigraphy provides information that can be used to evaluate how recently faults have moved, determine the interval between large earthquakes on major faults, assess recent tectonic activity, determine the characteristics of recent volcanism, assess past climates, and estimate erosion rates. The landforms created by surficial processes are also a factor underlying current land use in the vicinity of Yucca Mountain, which is a consideration in developing a biosphere model for performance assessment. An understanding of surficial processes also has proved valuable in evaluating the genesis of some deposits found near the surface. The results of these studies, when integrated with other Yucca Mountain Site Characterization Project (YMP) findings, contribute to addressing some of the U.S. Nuclear Regulatory Commission (NRC) key technical issues.

4.4.1 Regional Physiographic Setting

The regional physiographic setting provides the context for understanding the local physiographic setting at Yucca Mountain. This section provides a brief description of the structural and climatological components of the regional physiographic setting.

4.4.1.1 Structural Setting

The Yucca Mountain region lies in the north-central part of the Basin and Range Physiographic Province, within the northernmost subprovince (commonly referred to as the Great Basin) that encompasses nearly all of Nevada as well as adjacent parts of Utah, Idaho, Oregon, and California. The regions surrounding Yucca Mountain can be further subdivided into several well-defined physiographic areas that reflect regional variations in their geologic characteristics (Section 4.2). These areas include (Figure 4.4-1):

- The large elongate north-northeast-trending basins and ranges of the central Great Basin
- The somewhat smaller, more arcuate, and more closely spaced basins and ranges of the southeast Great Basin
- The massive ranges and deep basins of the southwest Great Basin (Inyo-Mono subsection of W.J. Carr [1984, pp. 9, 26])
- The highly variable terrane of the Walker Lane belt, which trends northwest between the southeastern and southwestern segments of the Great Basin to the south, and between the central Great Basin and the Sierra Nevada to the north (Figure 4.4-1).

The southern margin of the Great Basin subprovince is considered to be the Garlock fault and its northeast projection. South of this feature lies the northeastern part of the Mojave Desert, characterized by relatively small, irregularly shaped basins and ranges.

The mountain ranges of the Great Basin, mostly tilted fault-bounded blocks, may extend for more than 80 km (50 mi.), are generally 8 to 24 km (5 to 15 mi.) wide, rise 300 to 1,500 m (1,000 to 5,000 ft) above the floors of the intervening basins, and occupy approximately 40 to 50 percent of the total land area. The deep structural depressions forming the basins contain sedimentary fills of late Tertiary and Quaternary ages, ranging in thickness from a few hundred meters (hundreds of feet) to more than 3 km (1.8 mi.). The floors of closed basins are nearly level to gently sloping and are commonly covered, in part, by playas. Open basins are generally moderately to deeply dissected with axial drainage ways. Within this landscape, erosion and erosional processes are concentrated in the high, steep, and relatively wet uplands, whereas deposition and depositional processes are generally concentrated in the low, relatively arid lowlands.

The Yucca Mountain area is located within the Walker Lane belt. This belt is a major structural lineament considered to be a zone of transition between the central and southeastern parts of the Great Basin (Figure 4.4-1). It is characterized by dip-slip normal faulting and typical basin-and-range topography; the southwestern Great Basin is characterized by both dip-slip and right-lateral strike-slip faulting and by irregular topography (Carr, W.J. 1984, p. 9). Yucca Mountain itself is situated on the south flank of the southwestern Nevada volcanic field. This feature consists of a series of volcanic centers from which large volumes of pyroclastic flow and fallout tephra deposits were erupted from about 14.0 to 11.4 Ma (Sawyer et al. 1994, Table 1; Byers et al. 1976, p. 5-7) (Sections 4.2 and 12.2). Accordingly, the mountain and many adjacent landforms carry the imprint of the area's extensive volcanic and deformational history. The geologic relations suggest that many (perhaps most) of these landscape features took on their basic topographic form during the period 12.7 to 11.7 Ma.

Yucca Mountain itself lies near the center of the upper Amargosa River drainage basin, which originates in the Pahute Mesa–Timber Mountain area to the north and includes the main tributary systems of Beatty and Fortymile washes (Figure 4.4-2). The basic drainage pattern of the area was established soon after the caldera collapse and resurgent dome formation that followed the Late Cenozoic eruptions in the southwestern Nevada volcanic field, and the gross pattern has changed little since then (Huber 1988, p. 1).

4.4.1.2 Climatic Setting

Climatic conditions in the Yucca Mountain region, and over Nevada and much of the southwestern United States, are described in several publications that address this general subject (e.g., Spaulding 1985; Houghton et al. 1975). In general, the climate of south-central Nevada can be characterized as arid to semiarid, with average annual precipitation ranging from 100 to 200 mm (4 to 8 in.) in most lowland areas, 200 to 400 mm (8 to 16 in.) over parts of the uplands, and more than 400 mm (16 in.) along some mountain crests. This climate exists because the Sierra Nevada Mountains (Figure 4.4-1) are a major barrier to moist air moving in from the west. Precipitation from Pacific air masses that do reach the potential repository area accounts for about 50 percent of the total amount and occurs during the months of November through April. Precipitation in the form of snow is infrequent.

Summer is generally the driest time of year; the limited summer precipitation commonly occurs as localized thunderstorms rather than from large-scale frontal activity. These storms have a

much greater flood potential than the frontal precipitation that occurs during the winter months because of their release of significant amounts of rainfall in relatively short periods of time. Thunderstorm activity produces a secondary precipitation peak during July and August.

A detailed discussion of the climate at and near Yucca Mountain can be found in Section 6.

4.4.2 Physiographic Setting of Yucca Mountain and Vicinity

This section presents the local physiographic setting of Yucca Mountain and vicinity. It describes the major landform elements and tectonic influences on the area's geomorphology.

4.4.2.1 Major Landform Elements around Yucca Mountain

The area surrounding Yucca Mountain can be subdivided into eight clearly defined physiographic elements (Figure 4.4-2) that combine to produce a variable and diverse terrane typical of the Walker Lane. These are summarized as follows:

Amargosa Desert–The Amargosa Desert occupies a broad northwest-trending basin approximately 80 km (50 mi.) long and as much as 30 km (19 mi.) wide. The basin is one of the largest in the southern Great Basin. Its floor slopes gently southeastward from elevations of about 975 m (3,200 ft) at the north end, near Beatty, to about 600 m (1,968 ft) toward the south end. The channel of the Amargosa River, into which the streams draining the Yucca Mountain area empty, extends southeastward along the basin axis, then swings west and northwest, and terminates in the internal drainage system of Death Valley.

Bare Mountain–Bare Mountain is an upfaulted block that bounds the west side of Crater Flat and consisting of complexly deformed sedimentary and metasedimentary rocks of Paleozoic and Precambrian age. The range, roughly triangular in plan view, is about 20 km (12 mi.) long and less than 2 km (1.2 mi.) to about 10 km (6.2 mi.) wide. Adjacent piedmont surfaces, sloping southwestward into the Amargosa Desert basin and eastward into Crater Flat, respectively, are generally steep and slightly to moderately dissected proximal to the range flanks, but flatten and are largely undissected toward the basin centers. The piedmont-range junction on the east side of Bare Mountain rises gradually from about 915 m (3,000 ft) at the south end to almost 1,200 m (3,937 ft) at the north end. Elevations along the range crest vary between 1,460 and 1,925 m (4,790 and 6,316 ft). The southwestern flank of the range is embayed by steep, flat-floored valleys. The eastern flank is sharply defined and only slightly embayed, being structurally controlled by the bounding high-angle, east-dipping Bare Mountain normal fault, which was active into Quaternary time.

Crater Flat–Flanked by Bare Mountain on the west and Yucca Mountain on the east, Crater Flat is a structural basin approximately 24 km (15 mi.) long and 6 to 11 km (3.7 to 6.8 mi.) wide. The basin has the overall form of a graben, its west side having been down-dropped several kilometers along the east-dipping Bare Mountain fault and its east side down-dropped a few hundred meters (several hundred feet) along a series of west-dipping normal faults next to the western slope of Yucca Mountain (Carr, W.J. 1984, pp. 64 to 70; Simonds et al. 1995; Fridrich 1998, p. 173). The axial part of the basin floor, covered by alluvial deposits that overlie a thick (as much as 3 km [1.8 mi.]) sequence of late Cenozoic volcanic rocks, rises gradually from altitudes of about 840 m (2,756 ft) at the south end to as much as 1,280 m (4,200 ft) at the

foot of Yucca Mountain to the north. Four basaltic vents and their associated lava flows form prominent cones that attain heights ranging from 27 to 140 m (88 to 460 ft) above the alluviated surface of the central basin area. These volcanic features are described in more detail in Section 12.2.

Yucca Mountain–Yucca Mountain is an irregularly shaped upland, 6 to 10 km (3.7 to 6.2 mi.) wide and about 35 km (22 mi.) long. The crest of the mountain reaches elevations of 1,500 to 1,930 m (4,921 to 6,332 ft), about 650 m (2,132 ft) higher than the floors of adjacent washes in Crater Flat and Jackass Flats. The dominantly north-trending en echelon pattern of ridges and valleys that characterizes this prominent upland is controlled by high-angle faults (Scott and Bonk 1984; Day et al. 1998a, 1998b) with displacements of several hundred meters in places. The fault blocks, composed of fine-grained volcanic rocks, are tilted eastward, so that the fault-bounded west-facing slopes are generally high, steep, and straight in contrast to the gentler and commonly deeply dissected, east-facing slopes. With the exception of the caprock-protected dip slopes that characterize some of the crest areas, the ridge crests are mostly angular and rugged. The valleys are generally narrow and V-shaped along their upper and middle reaches, but locally contain flat, alluviated floors in their lower reaches. Valley morphology ranges from shallow, straight, steeply sloping gullies and ravines to relatively deep, bifurcating, gently sloping valleys and canyons. The hillslopes between ridge crests and valley floors typically include at least three general forms: narrow upper convexities, extensive straight segments, and broad lower concavities. Drainage from the west flank of the mountain flows southward down narrow fault-controlled canyons and out into Crater Flat. Drainage from the east flank flows southeastward down Yucca, Drill Hole, and Dune washes into Fortymile Wash.

Fortymile Wash–Fortymile Wash drains an area of approximately 620 km^2 (240 $mi.^2$) east and northeast of Yucca Mountain. From its northern headwaters, it flows southward through Fortymile Canyon, a steep-sided drainage course some 300 m (984 ft) deep along the east side of Pinnacles Ridge, and continues down the south-sloping piedmont that forms the west end of Jackass Flats. Along this latter reach, the wash has cut a nearly linear trench, 150 to 600 m (492 to 1,968 ft) wide and as much as 25 m (82 ft) deep, into the Quaternary alluvial deposits of the piedmont. This entrenchment gradually decreases downslope until the wash merges with the general level of the piedmont near the northeastern margin of the Amargosa Desert basin.

Jackass Flats–Jackass Flats is an asymmetric alluviated basin, 8 to 10 km (5 to 6.2 mi.) wide and nearly 20 km (12.4 mi.) long, that lies east of Yucca Mountain and Fortymile Wash. It is formed principally by piedmonts that slope away from bounding highlands to the north, east, and south, merge in the central basin area, and descend gradually westward and southwestward toward Fortymile Wash. Toward the highlands, the piedmont areas are moderately dissected, with shallow (5- to 10-m [16 to 33 ft] deep) arroyos and rounded interfluves; elsewhere, the basin floor is largely undissected. Topopah Wash is the main axial drainage.

Pinnacles Ridge–Pinnacles Ridge is a roughly triangular upland, about 11 km (6.8 mi.) long and 6 km (3.7 mi.) wide, that is bounded by Beatty Wash on the north, Fortymile Wash on the east, and Yucca Mountain on the southwest. The ridge is contiguous with and extends southeastward from the northeastern flank of Yucca Mountain. Its south flank is structurally and lithologically similar to Yucca Mountain, and its crest is the eroded southern margin of the Timber Mountain caldera, one of the main centers of eruption in the southwestern Nevada volcanic field

(Sections 4.2, 12.2). The ridge crest rises 250 to 670 m (820 to 2,200 ft) above the prominent washes that surround it, and tributaries to these washes have cut deep, linear valleys into its flanks.

Beatty Wash–Beatty Wash, one of the larger tributaries of the upper Amargosa River, drains an irregularly shaped area of about 250 km^2 (96 $mi.^2$) north of Yucca Mountain and Pinnacles Ridge. The basin topography is generally steep and irregular, with valley depths ranging from about 200 to 790 m (656 to 2,592 ft). Total relief from the mouth of the basin to the crest of Timber Mountain to the north exceeds 1,200 m (3,937 ft).

4.4.2.2 Tectonic Influences on Geomorphology

Seismic and volcanic activity have had a strong influence on the geomorphology of the Yucca Mountain area. This section briefly describes those influences.

4.4.2.2.1 Faulting

As described above, Yucca Mountain is one of a series of en echelon fault blocks formed by a series of parallel, north-striking, primarily dip-slip faults that have sliced up a broad apron of Miocene ash-flow tuffs. The faults have been active during the Quaternary, as shown by detailed mapping (Simonds et al. 1995) and by trenching studies on each fault (Whitney and Taylor 1996, Section 4.0.2). The details of Quaternary paleoseismic behavior at Yucca Mountain are summarized in Section 12.3.

Quaternary offset along block-bounding faults has influenced depositional patterns on hillslopes and on adjacent valley or basin floors. Average offset rates from the middle Quaternary to the present range from 0.001 to 0.04 mm/yr. (0.00004 to 0.0016 in./yr.) for all faults; the average for all faults is about 0.01 mm/yr. (0.0004 in./yr.), or about 1 m (3.3 ft) of offset every 100 k.y. These are very low offset rates , and the paleoseismic studies on each fault indicate that surface-faulting earthquakes have long return times, about 5- to over 100 k.y. (Whitney and Taylor 1996). This low faulting rate has resulted in subtle landforms, and has been a contributing factor to the preservation of early and middle Pleistocene deposits on Yucca Mountain hillslopes (Whitney and Harrington 1993, pp. 1013 to 1017). A striking feature of Yucca Mountain hillslopes is the lack of well-defined, rounded alluvial fans at the base of the slopes. On the west side of Yucca Mountain, hillslopes are of nearly uniform gradients, decreasing gradually from 32° near ridge tops to about 15° near the base. This characteristic results from the homogeneous nature of the underlying volcanic tuff at the ridge crest and from the low rates of uplift, which have not caused over-steepened slopes or high relief. The lower slopes of Yucca Mountain appear more like pediments than alluvial fans. This pedimentation of lower hillslopes is evident in fault trenches (Figure 4.4-3) on the Bow Ridge fault (Trench 14D) and the main Yucca Mountain western hillslope (Trench SCF-T1). In these trenches, early and middle Pleistocene deposits are truncated and overlain by a thin veneer (less than 1 m [3.3 ft] thick) of late Pleistocene-Holocene alluvium.

Fault scarps are commonly visible along the block-bounding faults. The scarps are generally located between the bedrock footwall and colluvium on the hanging wall. The bedrock scarps appear sharp, with fault dips of 55° to 75° (Simonds et al. 1995) because the volcanic bedrock

weathers very slowly (see bedrock weathering rates below). The exposed fault scarps along the Solitario Canyon and Northern Windy Wash faults were exposure-dated by cosmogenic ^{14}C to determine whether Holocene surface ruptures may have formed the scarps (Harrington et al. 1994, p. A303). Analyses of the in situ cosmogenic radiocarbon from both scarps indicate that both scarps have been exposed for more than 20 k.y. A pattern of enhanced erosion at the base of the scarps near channels and rills indicates that the scarps have been significantly enhanced by hillslope erosion. The Stagecoach Road fault also exhibits a prominent scarp where eolian sand has washed away from a scarp formed in a well-cemented, reworked tuff. Thus, most prominent scarps at Yucca Mountain appear to be fault-line scarps, tectonic in origin but significantly enhanced by erosion.

4.4.2.2.2 Volcanology

Although Yucca Mountain is composed entirely of volcanic rocks, none of the original morphology is preserved except for the eastward dip-slope formed by tilting of the block by movement along the block-bounding faults. The volcanic morphology of the Timber Mountain caldera is fairly well preserved, such that the topographically high resurgent dome in the caldera center and the surrounding moat are readily visible in both aerial photographs and topographic maps. The morphology of younger volcanic features in the immediate vicinity of the mountain varies from poorly to extremely well preserved. Details on igneous activity in the Yucca Mountain area are found in Sections 4.2 and 12.2.

The volcanic topography associated with the 3.7-Ma basaltic centers in central Crater Flat (Figures 4.4-2, 4.2-12) has been strongly modified by erosion. The original volcanic cones are deeply eroded, exposing dikes that formed along fissures from which the lava was extruded into these centers. The limited area of flow surfaces exposed along the Windy Wash fault possesses no original topography and is everywhere formed on the nonvesicular basalts of the flow interior.

Four middle Quaternary cinder cones (about 1 Ma) are fairly well preserved. Several near-surface features, such as pressure ridges and bombs with original morphology, are preserved at these eruptive centers.

The youngest volcanic center is the Lathrop Wells crater. Cosmogenic ^{3}He and ^{36}Cl dating of the flow surfaces of the Lathrop Wells center (CRWMS M&O 1998d, p. 2-52) demonstrate there has been no apparent topographic modification (pristine flow structure is still present), although the surfaces have been exposed to the climatic conditions of the last approximately 80 k.y. The Lathrop Wells cone itself shows little sign of degradation, which initially prompted speculation that it might be as young as 10 ka (Wells et al. 1990a).

4.4.3 Surficial Geology

4.4.3.1 Surficial Geologic Mapping in the Yucca Mountain Area

Surficial mapping of Quaternary deposits in the Yucca Mountain site area has been progressively refined over the years. Table 4.4-1 compares various units designated by different studies within the region.

Early work in the Nevada Test Site region differentiated three major late Cenozoic stratigraphic units using correlation characteristics (e.g., Hoover, D.L. et al. 1981; Hoover, D.L. 1989). This original work was patterned after work done in the Vidal Junction area in the Mojave Desert (e.g., Bull 1991, pp. 102 to 103). The concept of correlation characteristics utilizes physical and morphologic characteristics of landscape elements, including landform, drainage network, soils (presence or absence of the Av horizon), topographic position, desert pavement, desert varnish, depositional environment, and lithology. According to these original studies, the oldest surficial unit, QTa, is Quaternary (early Pleistocene) or Tertiary in age or both. Units Q2 and Q1 represent middle-to-late Pleistocene and Holocene deposits, respectively. Each major geologic unit of Hoover, D.L. et al. (1981) is divided, yielding a total of 10 subunits. According to Hoover, D.L. et al. (1981, p. 8), "three additional subunits of uncertain age may belong in unit Q2" in the Nevada Test Site region. Swadley (1983), Swadley and Carr (1987), Swadley and Parrish (1988), Swadley and Hoover (1989a), Swadley and Hoover (1989b), Swadley and Huckins (1989), and Swadley and Huckins (1990) mapped the major late Cenozoic stratigraphic units on the east and west sides of Yucca Mountain. For Midway Valley, a detailed surficial geologic map subdividing these units was published by Taylor (1986, p. 5, Figure 2).

Taylor (1986, pp. 11 to 17) mapped six Tertiary to Quaternary geologic units along Yucca and Fortymile washes. Geologic units were distinguished, and pedogenic soil profiles were described from these units, to assess the influence of time and climate on soil development, and to quantify the variability in past Quaternary climates by modeling the degree of development of the calcic horizon. The ages of map units were assigned based on an inferred correlation with the stratigraphy and numerical ages of Hoover, D.L. et al. (1981, Figure 2, p. 26), Szabo et al. (1981, Tables 1, 3), and Swadley and Hoover (1989a, 1989b). Taylor (1986, p. 192, Appendix G) demonstrated that age correlates with soil morphology and the progressive accumulation of secondary carbonate, clay, and silica. Calcium carbonate, calcium-magnesium carbonate, and other carbonate species in soils were not distinguished; the term carbonate was used to refer to all pedogenic carbonate species. The term silica was used to refer to pedogenic silica species, which was shown to be predominantly opal-CT (short-range cristobalite [C] and tridymite [T] stacking within otherwise amorphous hydrous silica) (Vaniman, Chipera, and Bish 1994, pp. 8 to 11). Taylor's (1986) work clearly demonstrated the usefulness of soils for stratigraphic correlations and the estimation of surficial unit ages within the Yucca Mountain area.

Six major allostratigraphic units were mapped by F.F. Peterson (1988, Appendix B), Faulds et al. (1994), and F.F. Peterson et al. (1995, pp. 380 to 385) in the Crater Flat area, located 5 to 10 km (3.1 to 6.2 mi.) west of Midway Valley. The primary purpose of their soils-geomorphic study was to evaluate the ages and correlations of the Quaternary surficial deposits stratigraphy (QTa, Q2, and Q1) of Hoover (1989). Two allostratigraphic units were delineated within areas previously mapped as QTa, two allostratigraphic units were delineated in areas previously mapped as Q2bc (undifferentiated Q2b and Q2c), and the use (in earlier studies) of the Av horizon as a major criterion for distinguishing Pleistocene from Holocene surfaces was questioned by F.F. Peterson (1988, Appendix B). Additionally, numerical ages of allostratigraphic units are younger than numerical age estimates of surficial deposit units of earlier studies by factors of about 2 to 10. However, the numerical age estimates for both the earlier and more recent studies are uncertain because of the experimental nature of U-trend dating (Rosholt 1980; Rosholt et al. 1985) and radiocarbon dating of rock varnish, varnish cation-ratio dating, thermoluminescence dating of coarse alluvial deposits, and U-series dating of

pedogenic carbonate and silica (Harrington and Whitney 1987; Dorn 1988; Harrington et al. 1990; Szabo et al. 1981; Szabo and O'Malley 1985). Several authors have questioned the reliability of U-trend, radiocarbon dating of rock varnish, and varnish cation-ratio dating (Paces et al. 1995; Krier et al. 1990; Bierman and Gillespie 1990, 1991, 1994; Reneau and Raymond 1991; Reneau et al. 1992; Reneau 1993; Beck et al. 1998).

Wesling et al. (1992) mapped the surficial geology of Midway Valley at a scale of 1:6,000. This study delineates alluvial geomorphic surfaces, as defined by Bull and Ku (1975, Appendix 2.5G) and Bull (1991, pp. 51 to 52), that represent informal allostratigraphic units consisting of deposits separated by bounding unconformities, such as geomorphic surfaces. Eight alluvial geomorphic surfaces (Q0 through Q7) ranging in age from Plio-Pleistocene to Holocene, as well as colluvium and eolian deposits, are identified on these maps and are described in Section 4.4.3.3.

4.4.3.2 Geochronology

Quantitative dating of Quaternary units is difficult, particularly in desert areas. This difficulty arises from the paucity of chronometers well-suited to the last 1 m.y. and the lack of material that meets ideal geochronologic criteria, such as closed system behavior for isotopic systems and a short period of formation relative to the system age . Soils, for example, may form over periods of thousands of years and be only a few thousand to tens of thousands of years old. Several different methods have been used on a variety of materials in an attempt to quantify timing and rates of surficial processes in the Yucca Mountain vicinity. A compilation of age determinations for Quaternary materials in the Yucca Mountain region is given in Whitney and Taylor (1996, Table 4.1.4). Figure 4.4-3 shows the locations of fault trenches in the immediate vicinity of Yucca Mountain from which many of the samples were obtained.

Age estimates exhibit variability with respect to their inferred Quaternary stratigraphic unit. This scatter is due to several causes. Some data were collected during the early stages of the YMP when geochronologic techniques were just under development. Each technique includes explicit assumptions that may not be met by each sample. In using age estimates to support interpretations, scientific judgment is required.

The dating techniques include methods that provide:

- Estimates of ages of surfaces, which can be done using cation-ratio dating of rock varnish and in situ cosmogenic nuclide dating such as ^{10}Be, ^{36}Cl, or ^{14}C. These methods assume that the material sampled has been on the surface for the entire history of the surface, and, as such, they represent minimum ages. Uncertainties include the possibility that sampled material has a history prior to its inclusion on the surface being dated.

- Estimates of deposit ages by included material, which can be done on the basis of archaeology, ^{14}C on charcoal, or tephrochronology. These assume that the material did not have a prehistory or, in the case of charcoal, that the sample has not gained or lost C since burial.

- Soil age estimates, which can be done using thermoluminescence on the fine-grained component of soil or U-series dating on the secondary carbonate or silica. The

secondary carbonate yields a minimum age, because the soil had to exist prior to the buildup of carbonate. Thermoluminescence-based age estimates assume that samples collected below the modern surface do not contain secondary eolian additions and that the sample was not exposed to sunlight or high temperatures at some point during its history.

Each technique provides an age estimate with consequent geologic interpretations. Ideally, more than one dating technique should be used at each site to estimate the time of a tectonic event or the age of a stratigraphic unit. However, this occurs infrequently in the study area because of the lack of suitable materials.

Carbon-14 and Cation-Ratio Dating on Rock Varnish–Rock varnish dates have been determined for samples from surfaces in the Crater Flat area. These dates provide the age of surface samples and, thus, give a minimum age for the underlying deposit. The range of applicability for ^{14}C is about 500 yr. to 60 k.y. (Jackson 1997, p. 96). The cation-ratio technique is limited by regional calibration points (Section 7.4.2.2.3) to about 1.5 Ma in the Yucca Mountain area. Note that the ^{14}C method of dating rock varnish has recently been challenged (Beck et al. 1998).

In Situ Cosmogenic Nuclide Method–The in situ cosmogenic nuclide method determines a rock surface exposure history from measurements of rare nuclides produced in rocks by cosmic radiation. The method records the time a rock has been exposed on the earth's surface. The chief uncertainty associated with this method relates to temporal variation in the cosmic ray flux (Gosse et al. 1996). The main method used was the measurement of ^{10}Be.

Archaeology–One artifact has been recognized in soil about 50 cm below the surface in a trench excavated on the east side of Bare Mountain. An artifact produced during a distinct time interval by early inhabitants of the region, collected from within a deposit, can provide an estimate of the maximum age of the deposit. Although bioturbation of the soil may incorporate a younger artifact into an older deposit, no evidence for reworking was noted at the sample site.

Carbon-14 on Charcoal–Charcoal from a few sites near Beatty has been dated. Although ^{14}C is a well-accepted dating technique, its use in the Yucca Mountain region is severely limited by the paucity of datable material. If it is assumed that the datable material was deposited with the alluvium shortly after it formed, dates obtained provide a maximum age estimate for the deposit.

Tephrochronology–Ash has been collected from sand ramps, trenches, and spring deposits. The presence of an air-fall ash, which is geochemically distinct or otherwise recognizable, provides an age estimate based on a known age for the ash. Ash samples should not be reworked, because a reworked ash will record the age of the air-fall event and not the younger age of deposition. The presence of air-fall ash in a deposit provides a maximum age estimate for the deposit.

Thermoluminescence–Material collected in the Yucca Mountain area has included soil vesicular A horizons (buried and at the surface), colluvium with reworked eolian sand (sand ramps), buried alluvial fine-grained overbank deposits, eolian-rich tectonic wedges, silica-cemented Bt horizons, and fine-grained groundwater discharge deposits. Several of these applications differ significantly from materials for which the technique was developed. For

example, translocation of fine-grained material to depth within a deposit can result in ages that are too young. The thermoluminescence technique provides an age when the material dated was last exposed to sunlight and, as such, provides a minimum age for a deposit.

Uranium-Series–Uranium-series dating has been used on pedogenic calcium carbonate and silica. The early dating (pre-1993) used alpha spectrometry to measure isotopic concentrations, whereas more recent dating has utilized the more accurate mass spectrometric technique. Uranium-series dating assumes that carbonate or opal, once precipitated, is in a closed system. The technique produces a minimum age of the soil in which the dated minerals formed.

Uranium-Trend Analyses–Uranium-trend ages were based upon an assumed open system following the model proposed by Rosholt (1980). Recent work has shown that these ages are usually unreliable and that there is no way to determine which ages are in error (Paces et al. 1995).

4.4.3.3 Quaternary Stratigraphy

Quaternary stratigraphy is discussed in this section because of its strong tie to surficial geology. Site stratigraphy with an emphasis on pre-Quaternary deposits is described in Section 4.5. The regional stratigraphic framework for Yucca Mountain is presented in Section 4.2.

4.4.3.3.1 Quaternary Stratigraphy Symbols

The symbols for Quaternary and Tertiary stratigraphy used in this section are as follows. Uppercase letters Q or T indicate age of the unit as Quaternary or Tertiary, respectively, or that the unit could be either or both when both letters are used. If the uppercase letter is followed by a lowercase letter, that letter indicates the type of deposit: a = alluvium, c = colluvium, e = eolian, sd = spring deposits, and no letter = undifferentiated as to the type of deposit. Qu represents Quaternary deposits that are undifferentiated with respect to age or stratigraphic position. Numbers in the symbol indicate relative stratigraphic position, with 0 being the oldest. Letters after a number represent subdivisions of a unit. General characteristics of surfaces and soils developed on surficial deposits and geomorphic surfaces are given in Table 4.4-2.

4.4.3.3.2 Quaternary Deposits, Soils, and Geomorphic Surfaces

An alluvial geomorphic surface is the same as the top of an allostratigraphic unit. An allostratigraphic unit is defined as a mappable stratiform body that is delineated based on its bounding discontinuities (North American Commission on Stratigraphic Nomenclature 1993). Primary characteristics used to assess the relative stratigraphic ages of the map units include relative stratigraphic and geomorphic position, lithologic characteristics, degree of desert pavement development, amount and degree of desert varnish accumulation, degree of preservation of original bar-and-swale topography, and degree of soil profile development.

Surficial deposits in the Yucca Mountain area include alluvium that underlies alluvial fan and fluvial terrace surfaces and is deposited along active washes, colluvium and debris-flow deposits that occur along the base and mantle the lower parts of the hillslopes, areas of mixed bedrock and thin colluvium, and eolian deposits.

The allostratigraphic units mapped around Yucca Mountain have age-dependent surface properties that reflect interactions and feedback mechanisms among soil development, eolian deposition, clast weathering, desert varnish accumulation, biological activity, and progressive erosional instability. Young units (Qa5 to Qa7) exhibit relatively unaltered original surface characteristics, including incipient to weak soil development, no to nascent desert varnish accumulation, little to no desert pavement development, relatively unaltered bar-and-swale relief, and minimal eolian accumulations in the upper horizons of soil profiles. Older units (Qa2 to Qa4) have more strongly developed desert pavement, more continuously and darkly varnished clasts, greatly reduced bar-and-swale relief, strongly developed soils, and relatively thick accumulations of silt and fine sand in the upper parts of soil profiles. The oldest units (QT0 and Qa1) have degraded surface characteristics and soil profiles reflecting erosional modification of geomorphic surfaces.

The relative ages of the deposits, soils, and geomorphic surfaces around Yucca Mountain are well established, but there is only limited direct numerical age control. Most numerical ages are derived from colluvium in trenches dug to evaluate activity on the major faults.

Available numerical age control, relative-age data, and regional soil-stratigraphic correlations (Table 4.4-1) were used to assign ages to map units. Establishing exact numerical ages of surficial units in arid environments is difficult because of the time-transgressive nature of fluvial deposition and geomorphic surface development, the paucity of suitable materials for dating, and the imprecise nature of dating complex geomorphic and pedogenic systems using available dating methodologies (U-series dating of pedogenic carbonate and thermoluminescence dating of the silt-size fraction of eolian and fluvial sediments). The presence of the 0.76-Ma Bishop tephra and several minor late Pleistocene basaltic ashes in Quaternary sediments of the Yucca Mountain region potentially can contribute significantly to numerical dating studies (e.g., Sarna-Wojcicki et al. 1997). However, the usefulness of the basaltic ashes may be limited because of extensive reworking of the tephras at some localities, the apparent inability to differentiate geochemically among different tephras, and large age uncertainties that result from indirect dating of the tephras. Correlations to other desert soil chronosequences based on soil-stratigraphic studies is another important technique for estimating the ages of surficial units, but quantitative soil chemistry and particle-size data are unavailable to rigorously assess ages. Based on these considerations, a multiple-parameter dating approach was used to estimate the ages of surficial units. The geologic epoch for the principal alluvial units, based on age estimates from thermoluminescence dates, tephrachronology, U-series dates, and correlations of soils to other desert chronosequences, is as follows:

- Qa7–late Holocene to latest Holocene
- Qa6–middle Holocene to late Holocene
- Qa5–late Pleistocene to middle Holocene
- Qa4–late Pleistocene
- Qa3–middle to late Pleistocene
- Qa2–middle Pleistocene
- Qa1–early to middle Pleistocene
- QT0–Pliocene to early Pleistocene.

The approximate numerical ages for the above subdivisions of the Tertiary and Quaternary periods are shown in Table 4.4-3.

4.4.3.3.2.1 Alluvial Deposits and Geomorphic Surfaces

Whitney and Taylor (1996) describe the alluvial deposits and geomorphic surfaces in the Yucca Mountain area. The following summary of Quaternary stratigraphic units is taken largely from their work.

Alluvial geomorphic surfaces compose the bulk of boundaries for surficial units in the Yucca Mountain site area. Deposits associated with these surfaces include alluvium and minor eolian and debris-flow sediments. Sedimentologic properties of the various alluvial units are very similar. In general, fluvial deposits are predominantly sandy gravel with interbedded gravelly sand and sand. Fluvial facies present in these deposits include relatively coarse-grained channel bars and intervening finer-grained swales. The grain size of the bars and swales is dependent on their position within the landscape (proximal or distal fan region) and the sediment source. In the proximal alluvial fan regions, grain size is greater where larger material is available for transport and where streamflow is concentrated. In the distal reaches of the fans, sediment is finer grained, although coarser-grained facies are present locally. Gravel size ranges from pebble to boulder, and clasts generally are subangular to subrounded. In soil-pit and stream-cut exposures of Qa5, Qa6, and Qa7, the cross-sectional bar-and-swale characteristics are so well preserved that the changes in facies between the bars and swales are readily observed. The deposits associated with depositional bars include nonindurated, cobble-boulder gravel and a finer-grained sand and gravel deposit. The deposits associated with swales include a finer-grained, silt-rich, sandy gravel and gravelly sand. The boulder gravel associated with the bars typically is about 0.5 m (1.6 ft) thick. Unweathered deposits are light gray (10YR 7/2 d), poorly to moderately sorted, massive to well bedded, and clast supported to matrix supported. (Notation refers to Munsell Soil Color Chart [Munsell Color Company 1994; d = dry, m = moist].) Rodent burrows are ubiquitous on Qa5 and Qa6, most likely reflecting the ease of excavation. Qa5 and younger deposits are relatively loose and do not hold a well-formed free face when excavated. In soil pits and stream-cut exposures, buried soils are commonly observed in intervals less than 2 to 3 m (6.5 to 9.8 ft) thick. These buried soils may be older stratigraphic mapping units that have been buried, or they may represent a hiatus in the aggradational sequence of a single depositional unit. In cases where the buried soils represent a hiatus in a single depositional sequence, the surface soil characteristics reflect these variations in the amount of time they have been exposed. These variabilities are expressed in the range of soils developed on a single mapping unit.

Debris-flow deposits were observed locally in natural outcrops, soil pits, and trenches (Whitney and Taylor 1996, p. 4.1-9). These deposits are matrix supported and have pebbly to cobbly, silty, fine to medium sand texture. The gravel fraction composes approximately 15 to 30 percent of the deposit. Debris-flow deposits are nonbedded and massive and have a relatively hard consistency.

Given the similarities in sedimentologic properties of deposits among the various map units, distinctive surface properties and soil profile characteristics were the primary features used to delineate and correlate map units. These features, along with available numerical age information, serve as a basis for assigning ages to units and for correlating with sections in local

and regional soil-stratigraphic studies. The characteristics of eight identified alluvial geomorphic surfaces, their associated soil profiles, the available numerical age control, and correlations with local and regional studies are described below for each major mapped unit.

Pliocene to Early Pleistocene Alluvium (QT0)–QT0 consists of a single terrace remnant on the upthrown block of the Paintbrush Canyon fault at the north end of Alice Ridge. This unit is also found and mapped outside the Yucca Mountain area in Mercury Valley. The surface forms a pronounced topographic bench (elevation 1,168 m [3,832 ft]) that is 25 m (82 ft) higher than Qa1 and 46 m above the active channel of Yucca Wash. Deposits associated with QT0 consist of lag gravel on a bedrock surface eroded into the Tiva Canyon Tuff. Clast lithologies that include the rhyolites of Fortymile Wash are sufficiently abundant and distinct to indicate that they are exotic to Alice Ridge. Because of its limited areal extent and the extensive post-depositional erosion of the surface, no detailed soils data were collected for the QTa0 surface. One unique characteristic of the deposit is that the cemented matrix is commonly more resistant to erosion than the clasts. The thickness of the unit is unknown but is probably less than a few meters (10 ft).

The age of QT0 is probably Pliocene to early Pleistocene based on its stratigraphic position relative to Qa1, its highly dissected and eroded nature, and its rounded landform morphology. Although no soil was observed on QT0 (eroded), the partially preserved soil on Tgp has a strongly developed K horizon about twice as thick as the K horizon of the Qa1 soil. If these units are correlative, QT0 is probably Tertiary in age.

Early to Middle Pleistocene Alluvium (Qa1)–Qa1 is preserved at the surface on the Yucca Wash alluvial fan north of Sever Wash in Midway Valley; the fan surface has been dissected by younger drainages and is preserved as somewhat rounded interfluves. Qa1 also is found on the west flank of Yucca Mountain and in northeastern Crater Flat. Locally, the desert pavement associated with the Qa1 surface is very well developed, but in most areas it has been extensively degraded (Table 4.4-2). Several characteristics, including freshly exposed rock surfaces on clasts, fragments of secondary carbonate and silica platelets, and surface or near-surface calcic horizons, collectively impart a lighter tonal quality to the unit when viewed in the field or on aerial photographs. Although darkly varnished clasts are present in some areas, surface clasts typically are not darkly varnished. No original depositional bar-and-swale morphology is preserved on the surface, and larger clasts appear to be distributed randomly rather than being concentrated in areas that define depositional bars. Angular unvarnished rock fragments are common on the surface because of spallation of larger varnished clasts and exposure of fresh rock surfaces. Many clasts are fractured and strongly weathered. The total thickness of Qa1 cannot be determined from available exposures. A buried soil was observed beneath Qa1 at a depth of 2.5 m (8.2 ft) in one soil pit, but no buried soils were encountered to depths of more than 3.3 m (10.8 ft) in other soil pits on Qa1.

The strongly developed Qa1 soil is greater than 1.5 to 2.0 m (4.9 to 6.6 ft) thick and has a laminar petrocalcic horizon (Kqm) with stage IV carbonate morphology (Gile et al. 1981, Table 20) at or near the surface (Table 4.4-2). The petrocalcic horizon may be overlain by as much as 30 cm (12 in.) of eolian fine sand and silt. Soil development on the eolian deposits is characterized by brownish to reddish (10 to 7.5YR hues) Btk and Btkq horizons that have strong, medium subangular blocky structure and continuous, moderately thick clay films. The soil

developed in the overlying eolian sand and silts appears to be much younger than the underlying petrocalcic horizon formed in alluvial sediments.

Age control for Qal indicates that the unit is probably early to middle Pleistocene. Swadley et al. (1984, p. 88) designated Qal as QTa in northern Midway Valley where Qal is present, and Hoover (1989, pp. 19 to 21) notes that the best developed soils and landforms that are representative of QTa occur in northern Midway Valley. These workers assign a Pliocene to early Pleistocene age to QTa, but Hoover (1989, pp. 19 to 21) notes that the unit is probably only Pleistocene in age. In other parts of the Yucca Mountain area, deposits mapped as QTa overlie alluvial sediments of the ancestral Rock Valley Wash that contain a 2.1-Ma ash. Swadley and Hoover (1989a, 1989b) and Hoover (1989, pp. 24 to 29) note that eolian (Q2e) and alluvial (Q2c) sediments younger than QTa contain the Bishop tephra (about 760 ka) (Sarna-Wojcicki and Pringle 1992; van den Bogaard and Schirnick 1995) at several locations within the Yucca Mountain area. However, Peterson, F.F. et al. (1995) report Bishop tephra within alluvial deposits that were shown as QTa by Swadley et al. (1984, Plate 1) in northeastern Crater Flat. Peterson, F.F. et al. (1995, Figure 1) map this unit in Crater Flat as their Solitario geomorphic surface and assign a numerical age between about 430 to 760 ka based on the varnish cation-ratio ages and the reported presence of the Bishop tephra. The evaluation of stratigraphic position and geochemical identification of these tephras is in progress.

An early to middle Pleistocene age for Qal is supported by regional soil-stratigraphic correlations (Table 4.4-1). The somewhat rounded, eroded morphology of Qal surfaces and the strongly developed soil on Qal are similar to those on early to middle Pleistocene units in Nevada and California (Taylor 1986, Table 1; Wells et al. 1990a, pp. 551 to 552; Harden et al. 1991a, Table 1; 1991b, Table 1; Slate 1991, Table 3; Reheis et al. 1992, Table 1; McDonald and McFadden 1994, p. 207).

Middle Pleistocene Alluvium (Qa2)–Qa2 is recognized at the surface primarily as thin, elongated patches of alluvium in Midway Valley, where it is inset into Qal. On color aerial photographs, Qa2 surfaces have a darker, more reddish hue than the other units. This darker color and reddish hue reflect more compact and continuous desert pavement, better developed desert varnish, and the presence of reddish Bt horizons near the surface. Qa2 has a well-developed desert pavement that contains darkly varnished clasts (Table 4.4-2). Some clasts are split and fractured, and varnish has also developed on some fractured surfaces of clasts. The original bar-and-swale morphology has been reduced to the height of the larger clasts above the surface. The upper part of the unit typically has a cap of eolian silt and fine sand ranging from 30 to 50 cm (12 to 20 in.) thick. The total thickness of Qa2 varies from 2.5 (8.2 ft) to more than 3.5 m (11.5 ft) as observed in soil pits.

The moderately developed Qa2 soil has a 40-to 70-cm (15.7 to 27.5 in.) thick, reddish (7.5-5YR hues) argillic horizon (Btkq) and a zone of carbonate and silica accumulation having stage III to IV carbonate morphology (Table 4.4-2). The upper solum (Av and Btkq horizons) of the Qa2 soil is cumulate and has formed in the eolian sediments that have accumulated on the surface (Table 4.4-2). The upper part of the Btkq horizon lacks significant carbonate, but contains a silica-cemented zone that is reddish brown to yellowish red (5YR 5/4-6 d) in color and is laminar in appearance. Therefore, the morphology of the upper part of the soil is controlled by silica accumulation, whereas the morphology of the lower part of the soil is controlled by both

carbonate and silica accumulation. This gives the Qa2 soil an appearance of overall stage IV morphology.

Two factors support a middle Pleistocene age for Qa2. Stratigraphically, it lies between the early to middle Pleistocene Qa1 and the middle to late Pleistocene Qa3. The degree of soil profile development is also consistent with a middle Pleistocene age. The degree of soil profile development on the Qa2 alluvial geomorphic surface appears to be similar to that on Q2c or QTa of Taylor (1986, Table 1) and Harden et al. (1991b, Table 1). Based on correlations with local and regional soil chronosequence studies (Taylor 1986; Wells et al. 1990a; Harden et al. 1991a, Table 1; 1991b, Table 1; Slate 1991, Table 3; Reheis et al. 1992, Table 1; McDonald and McFadden 1994, p. 207), Qa2 is probably middle Pleistocene in age.

Middle to Late Pleistocene Alluvium (Qa3)–Qa3 occurs as large remnant alluvial fan surfaces and as fluvial terraces. It is one of the dominant map units in the Yucca Mountain area and underlies the main Fortymile Wash terrace. A well-developed desert pavement that contains darkly varnished clasts characterizes the Qa3 surface (Table 4.4-2). It has a dark brown or black tone on color aerial photographs. Larger clasts, some more than 30 cm (12 in.) in diameter, are distributed on the surface in diffuse, poorly defined bars. (Clast size as given in this section is maximum intermediate diameter unless otherwise stated.) The original depositional bar-and-swale morphology has been reduced to the height of individual clasts above the surface. The thickness of Qa3 averages approximately 2 to 2.5 m (6.6 to 8.2 ft) and may exceed 3.3 m (10.8 ft) locally as observed in soil pits.

The strongly developed Qa3 soil has a 20- to 75-cm-thick argillic (Bt and Btkq) horizon overlying a 100-to 130-cm- (39 to 51 in.) thick horizon of secondary carbonate and silica accumulation (Table 4.4-2). Clay films, reddening (7.5YR hue), and strong blocky structure are characteristic of the argillic horizon that also commonly has accumulations of secondary carbonate and silica. A Bkq or weakly developed Kq horizon having stage II to III carbonate morphology typically underlies the Btkq horizon.

Stratigraphic relations, numerical dating, and correlations with local and regional soil-stratigraphic studies all support the middle to late Pleistocene age for Qa3. Areas mapped as Qa3 (Wesling et al. 1992, p. 26-29, Unit 3) within Midway Valley have been mapped as Q2 by Swadley et al. (1984, Table 3) and Q2c by Taylor (1986, Table 1) and Harden et al. (1991b, Table 1), who originally considered the unit to be 270 to 440 ka on the basis of U-trend dating of deposits exposed in fault trenches (Swadley and Hoover 1989a, 1989b).

Menges et al. (1994, p. 2383; 1997, p. 22) correlate colluvial deposits in Trench 14D with Qa3 on the basis of a similar degree of soil profile development on these units. Uranium-series and thermoluminescence dating techniques were used to obtain ages for samples from these deposits (Menges et al. 1997, pp. 22 to 23). Uranium-series dating of pedogenic carbonate associated with colluvial deposits in the trench yielded an age estimate of 234 +47/-35 ka. A thermoluminescence age of 132 ± 23 ka was obtained on a mixed eolian-colluvial unit that composes the middle part of the sequence correlated with Qa3. Four U-series ages of about 100 to 145 ka also were obtained on pedogenic carbonate in the uppermost part of the Q3 sequence in Trench 14D.

Apparent similarities in soil profile development may indicate that Qa3 correlates with the early Black Cone surface in Crater Flat (Peterson et al. 1995, Tables 1, 2). However, the correlation of these units based on soil profile data is uncertain because of the extremely shallow nature of soil pits that were dug on the early Black Cone surface. The middle Pleistocene age of greater than 159 to 200 ka was assigned to the early Black Cone surface based on varnish cation-ratio dates (Peterson et al. 1995, Table 2).

The degree of soil development on Qa3 is similar to that on middle to late Pleistocene soils in other parts of the western United States (Taylor 1986, Table 1; Wells et al. 1990a; Harden et al. 1991a, 1991b, 1991c; Slate 1991; Reheis et al. 1992; McDonald and McFadden 1994). Table 4.4-1 shows the correlation of Qa3 with regional chronosequence studies that indicate stage III carbonate morphology generally occurs in middle to late Pleistocene soils.

Late Pleistocene Alluvium (Qa4)–Qa4 consists of small, inset fluvial terrace and alluvial fan remnants on the east side of Yucca Mountain and of thin alluvial deposits overlying older basin deposits in Crater Flat. The desert pavement of the Qa4 surface ranges from loosely to tightly interlocking and is noticeably less well developed than pavements formed on the older fluvial surfaces. Although desert varnish is discernible on surface clasts of the Qa4 pavement, it occurs at a much lower percentage than on surface clasts of older units (Table 4.4-2). Indistinct depositional bars are preserved as diffuse accumulations of larger clasts; bar-and-swale relief on Qa4 has been mostly reduced to clast height above the surface. The thickness of Qa4 averages about 1 m (3.3 ft) and does not exceed 2 m (6.6 ft) where observed in soil pits and trench exposures.

The well-developed Qa4 soil is characterized by a reddened (7.5YR hues) argillic horizon and accumulations of carbonate and silica (Table 4.4-2). The upper part of the soil has silica accumulation, stage II to III carbonate morphology, and a strongly developed Btkq horizon with a sandy or silty clay loam texture. Continuous, thin to moderately thick clay films coat pedologic faces of the Btkq. An Av horizon overlies the Btkq horizon.

Qa4 is estimated to be late Pleistocene in age on the basis of its stratigraphic position, thermoluminescence ages from fault trenches, and the degree of soil profile development. A thermoluminescence age of 25.7 ± 8 ka (Paces et al. 1994, p. 2397, Table 2) was obtained for an Avb horizon of Qc4 in Trench MWV-T5. The Avb represents postdepositional eolian accumulation on Qc4; therefore, the age represents a minimum estimate for the depositional age of Qc4. Eolian/colluvial sediments that have similar soil profile development as Qa4 yielded thermoluminescence ages of 38 ± 6 k.y. and 73 ± 9 k.y. in Trench MWV-T4 (Paces et al. 1995, Table 9, Figure 15). In Trench 14D, a preliminary thermoluminescence age of 48 ± 20 k.y. is reported (Paces et al. 1995, Table 14, Figure 24) for the upper part of a unit with a strongly developed Btkq horizon, which Menges et al. (1994, Table 1) correlate with Qa4. Additionally, a late Pleistocene age for Qa4 appears to be reasonable based on comparison of soil morphology data with that of regional chronosequences (Table 4.4-1).

Late Pleistocene to Middle Holocene Alluvium (Qa5)–Qa5 covers large areas of alluvial fans and occurs as inset terraces along drainages. The desert pavement is loosely packed and poorly formed, and surface clasts have minor accumulations of rock varnish (Table 4.4-2). Qa5 surfaces display well-developed bar-and-swale morphology. The amount of bar-and-swale relief

is related to landscape position and sediment sources; coarsest-grained bars lie in the proximal fan regions. Smaller, lower, partly buried bars lie on distal fans where the intervening swales are partly filled by fine-grained eolian silts and sands. Surface clasts are relatively unweathered. In soil pit and trench exposures, the average thickness of Qa5 is approximately 1 m (3.3 ft), and the maximum observed thickness is about 2.5 m (8.2 ft).

Weakly developed soils are formed on Qa5 (Table 4.4-2). Soil development is stronger in the swales where a silt-rich zone occurs in the upper 30 to 40 cm (12 to 16 in.) of the unit; soils are more weakly developed on bars. The Qa5 soil typically has a Bwk or incipient Btjk horizon with 10YR hues, weak subangular blocky structure, and colloidal stains on grains. Carbonate is disseminated in the matrix. Below about 30 cm (12 in.) depth in the Bk horizon, the bottoms of clasts have powdery coats of carbonate (stage I carbonate morphology). Where Qa5 is sufficiently thick, the carbonate content decreases below the Bk to form a transitional horizon (BC or CB) or a Ck; where Qa5 is relatively thin and underlain by a buried soil, the Bk persists to the base of the unit.

Qa5 is assigned a latest Pleistocene to early Holocene age based on numerical ages from the Yucca Mountain region and correlations to regional soil-stratigraphic studies. This age assignment is consistent with a maximum age determined for Qc5/Qa5 based on a thermoluminescence age of 25.7 ± 8 k.y. (Paces et al. 1994, p. 2399) on the Av horizon of a buried Qc4/Qa4 soil that lies directly beneath Qc5 in Trench MWV-T5. It is also consistent with a thermoluminescence age of 27 ± 5 k.y. for a Qa5 sample in soil pit MWV-P10 (Paces et al. 1995, Table 36, Figure 55). These dates suggest that the age of Qc5/Qa5 is latest Pleistocene or younger. Qa5 in soil pits MWV-P10 and MWV-P14 yielded thermoluminescence ages of 6.9 ± 1.2 k.y. and 4.0 ± 0.7 k.y., respectively (Paces et al. 1995, Table 36, Figures 55 and 56). The presence of extensive burrowing in Qa5/Qc5 and translocation of fine material by soil-forming processes may account for the somewhat younger than expected thermoluminescence ages for deposits in these soil pits. In Stagecoach Road Trench SCR-T1, sandy colluvium, capped by a weak calcic soil that exhibits similar profile development as the Qa5 soil, has yielded thermoluminescence ages of 8.9 ± 1.2 k.y. and 12 ± 6 k.y. (Menges et al. 1994, Table 4). Carbonized wood obtained from alluvial unit Q1c of Swadley et al. (1984, Table 3) near Beatty, Nevada, yielded a radiocarbon age of 8.3 ± 0.075 k.y.; reconnaissance investigation of that site during this study indicates that Q1c has a soil profile similar to that of Qa5. Based on radiocarbon dating of rock varnish in Crater Flat, minimum ages of 6 to 11 k.y. were obtained for the Little Cones unit, which has a profile similar to the Qa5 soil (Peterson et al. 1995, Tables 1, 2).

The weakly developed Qa5 soil appears to have profile characteristics similar to latest Pleistocene to Holocene units described in nearby and regional soil-stratigraphic studies (Table 4.4-1) (Taylor 1986, Table 1; Wells et al. 1984, p. 72-77; Harden et al. 1991a, 1991b; Reheis et al. 1992, Table 1). The cambic B horizon that is characteristic of most Qa5 soil profiles indicates that the unit may be as young as early to middle Holocene in age (Dohrenwend et al. 1991).

Middle to Late Holocene Alluvium (Qa6)–Qa6 occurs along the active washes as low flood plains less than 1 m above the active channels and as vegetated bars. No desert pavement has developed (Table 4.4-2), and surface clasts are unvarnished and unweathered. Relief on the Qa6

surface is primarily the result of preservation of original bar-and-swale morphology. Locally, an eolian cap as much as 5 to 10 cm (2 to 4 in.) thick may bury all but the largest surface clasts. Natural outcrops and man-made exposures indicate that the total thickness of Qa6 does not exceed 2 m (6.6 ft).

Qa6 soils lack a significant eolian cap that is common to the older surfaces (Av horizon), and soil development is limited to minimal oxidation of the deposit (Cox formation) and sparse accumulations of carbonate (Table 4.4-2). Carbonate is more concentrated toward the upper 10 cm (4 in.) of the deposit, although the matrix typically contains widely disseminated carbonate. Clasts in the upper 30 cm (12 in.) have little visible carbonate, but samples effervesce when hydrochloric acid is applied. Carbonate varies from isolated patches on the undersides of clasts to thin, relatively continuous coatings. Evidence that many clasts within the deposit have been reworked from older deposits includes randomly oriented carbonate coatings on clasts and percussion marks where the coatings are chipped from the clasts.

Qa6 is assigned a middle Holocene to historic age because of its very weak to weak soil development and its inset nature within Qa5. There is no color or structural B-horizon development and carbonate morphology varies from incipient to stage I. Historic is given as a minimum age because Qa6 receives sediments during overbank runoff events. As shown in Table 4.4-1, several middle to late Holocene alluvial units are recognized in the region.

Late to Latest Holocene Alluvium (Qa7)–Qa7 consists of the deposits along active channels and the adjacent flood plains. No desert pavement has formed on the Qa7 surface (Table 4.4-2). No desert varnish occurs on clasts, except where it is apparently inherited. Thick, dark desert varnish is present in small protected areas (small fractures and exposed voids) of some surface and subsurface clasts. However, varnish is too well developed to be actively accreting in modern channels and apparently has been reworked from older surfaces. Clasts are unweathered, and the original depositional bar-and-swale relief is unaltered. The total exposed thickness of Qa7 does not exceed 2 m (6.6 ft).

No in situ pedogenic alterations were observed for Qa7 deposits (Table 4.4-2). The overall deposit color is pale brown to brown (10YR 5-6/3 d). The deposit matrix contains reworked, disseminated carbonate. Reworking of older surficial units is indicated by numerous clasts that have thick carbonate accumulations. These clasts appear to be distributed randomly throughout Qa7. The coatings, which originally formed on the bottoms of the clasts, have no preferred orientation in the reworked deposits. Carbonate is generally not apparent on the undersides of clasts, but noticeable effervescence occurs when hydrochloric acid is applied. This unit includes modern deposition in channels (Qa7) and on hillslopes (Qc7).

4.4.3.3.2.2 Colluvial and Eolian Deposits

Colluvial deposits (Qcu) are undifferentiated because of their limited areal extent and the limited exposure of all but the youngest deposits. These deposits include colluvium, debris-flow deposits, and in situ weathered bedrock that locally mantles hillslopes. Colluvium is also intermixed or mantled with eolian deposits in some locations. Eolian deposits also occur as thin accumulations of fine sand and silt on surfaces and in soils, as well as in lenses within predominantly alluvial sequences.

Sequences of colluvial deposits are exposed in fault trenches around Yucca Mountain and in soil pits at the potential surface facilities site on the east side of Exile Hill. The colluvial stratigraphy of Midway Valley is primarily based on trench and soil-pit exposures.

Middle Pleistocene to Holocene Undifferentiated Colluvium (Qu)–This unit occurs as colluvial and debris-flow deposits and in situ weathered bedrock mantling hillslopes and, locally, includes areas mantled by eolian and reworked eolian deposits. The colluvial deposits consist of gravelly silty sands and silty fine to medium gravel with pebble to small cobble clasts. The color of the colluvial deposits is very pale brown (10YR 7/4 d) to reddish yellow (7.5YR 6/6 d) with white (10YR 8/1 d) for the older carbonate-cemented units. The colluvial deposits and debris flows are poorly sorted and nonbedded to very crudely bedded. They are predominantly matrix supported and are locally clast supported with as much as 90 percent gravel. The gravels are predominantly medium to very coarse, subangular to angular pebbles, with lesser abundances of cobbles to 20 cm (7.8 in.) in diameter and small boulders to 30 cm (12 in.) in diameter. The thickness of individual colluvial units is generally less than 2 to 3 m (6.6 to 9.8 ft) based on trench and soil-pit exposures (Whitney and Taylor 1996, p. 4.1-21).

The younger colluvial deposits, possibly equivalent to Qa5, have thin, weakly developed soils with an AB horizon over a weakly developed Bwk horizon. Colluvial deposits of probable Qa4 age display well-developed Btkq textural B horizons, 40 to 50 cm (16 to 20 in.) thick. Colluviums, possibly equivalent to Qa3 and Qa2, have multiple superimposed soils consisting of Bkq and Btjkq horizons that have stage II to III carbonate morphology. The oldest exposed colluviums have strongly developed Kqm horizons (Whitney and Harrington 1993, pp. 1011 to 1013).

At the surface, most hillslope areas mapped as undifferentiated colluvium (Qu) have surface characteristics of Qa5 and Qa6. Colluvium, having surface characteristics similar to Qa4 surfaces, commonly occurs near the toe of the hillslope. Relict Q1 to Q3 colluvial deposits are generally found elevated 1 to 2 m (3.3 to 6.6 ft) above the modern slope and coated with dark desert varnish. The oldest dated Quaternary deposit on Yucca Mountain is the colluvium on the lower western slope of Yucca Mountain. Stage IV carbonate soil on this deposit, dated by U-series, is about 1 Ma.

Eolian Deposits (Qe)–Three types of eolian deposits are observed in the Yucca Mountain area:

- Reworked eolian deposits within sand ramps surrounding Busted Butte, against the west slope of Fran Ridge, and along the flanks of the southern ridges of Yucca Mountain
- Thin accumulations of silt and fine sand in most surface soils and buried soils, and small coppice dunes on desert pavements
- Lenses of eolian sand in predominantly alluvial sequences.

Middle Pleistocene to Holocene Eolian-Colluvial Deposits (Qeu)–Sand ramps at Busted Butte and in southeastern Midway Valley are composed of a stacked sequence of eolian-colluvial units that have textures of pebbly, silty, fine to medium sand interbedded with some sandy, pebble to cobble gravel. Minor, alluvial sandy pebble gravel deposits are present locally within the sand ramp deposits. Sand ramp deposits vary from very pale brown to light gray (10YR 7/2-4 d), are

poorly to moderately sorted, and are moderately bedded to massive. This unit type is predominantly matrix supported, although the alluvial gravel and parts of some colluviums are locally clast supported. Gravel clasts are angular to subangular and commonly less than 5 cm (2 in.) in diameter, although some clasts are as large as 50 cm (20 in.) in diameter. The maximum thickness of the sand ramp deposits exceeds 15 m (50 ft). A weakly to moderately interlocking desert pavement occurs over most of the surface. Soil development in near-surface deposits consists of a well-developed reddish yellow (7.5YR 6/6 d) Btkq horizon with a sandy clay loam texture that appears to be similar to the soil formed on Qa4. Typically, one or more buried soils occur within the sand ramp deposits in Midway Valley. The buried soil observed within Trench MWV-T4 has a Kq horizon with stage IV carbonate morphology. Additionally, multiple buried soils have been observed within Busted Butte sand ramp deposits south of Midway Valley (Whitney et al. 1985, p. 750; Whitney and Muhs 1991, p. 119; Menges et al. 1994, pp. 2373 to 2390).

The presence of Bishop tephra in lower sand ramp deposits at Busted Butte (Whitney et al. 1985, p. 750; Menges et al. 1994, pp. 2373 to 2390) and at other localities near Yucca Mountain (Hoover 1989) indicates that these landforms began forming within the region sometime around 760 ka. Multiple buried soils above the Bishop tephra suggest that accumulation of the sand ramps is episodic and punctuated by surface stabilization and soil formation. At Busted Butte, some buried soils have been dated as middle to late Pleistocene using U-series disequilibrium methods (Menges et al. 1994, pp. 2373 to 2390). Thermoluminescence dates from the upper 3 m (10 ft) of sand ramp deposits in southern Midway Valley (between 38 ± 6 and 73 ± 9 ka) (Whitney and Taylor 1996, Table 4.1.4) and Busted Butte (36 ± 10 ka) indicate that the two most recent major depositional episodes on sand ramps occurred about 35 to 40 ka and about 60 to 80 ka. A thermoluminescence age of 6.2 ± 1.3 k.y. on the surface A horizon of a sand ramp in southern Midway Valley indicates that small-scale eolian additions have occurred in the Holocene.

4.4.3.3.2.3 Eolian Accumulations on Geomorphic Surfaces

A few centimeters (inches) to several tens of centimeters (a foot) of eolian silt and fine sand have accumulated on most alluvial geomorphic surfaces and have been incorporated into soil profiles formed on those surfaces. These eolian accumulations are not mapped separately, in spite of their broad areal distribution, because of their relatively thin and discontinuous nature. Models of desert pavement and soil formation recognize the importance of eolian accumulations as a source for the fine earth fraction, carbonate, and other soluble salts that occur in otherwise clean sandy gravel deposits in arid regions (McFadden 1982; Birkeland 1984, pp. 290 to 291; McFadden et al. 1987, pp. 504 to 508; McFadden and Weldon 1987, pp. 280 to 293; McDonald and McFadden 1994, pp. 205 to 213; Wells et al. 1984, pp. 69 to 87). With time, surface weathering, soil formation, and eolian additions result in incremental modifications to geomorphic surfaces. These modifications include reduction of original surface topographic relief (bar-and-swale relief), formation of Av horizons, desert pavement development, the accumulation of desert varnish on surface clasts, and weathering of surface clasts. In Midway Valley, these modifications have produced a distinctive surface morphology for a unit of a given age, and the surface morphology is used as a basis for mapping alluvial geomorphic surfaces. Relative to younger surfaces, older surfaces generally have a more subdued surface topography, stronger desert pavement development, darker and thicker desert varnish on surface clasts, and

stronger soil development. The relative thickness of eolian accumulations generally is greater on older units. Eolian additions to Qa6 and Qa7 are minimal at best, whereas eolian sediments plug the upper part of Qa5 deposits and partially fill paleo-swales to form a muted bar-and-swale topography. The surfaces of units Qa2, Qa3, and Qa4 are plugged with eolian sediments that form a continuous surface sheet and result in a nearly flat topography. The original eolian mantle on Qa1 has been stripped and replaced by a younger eolian mantle.

4.4.3.3.2.4 Spring Deposits (Late? to Middle Pleistocene)

Spring deposits are discussed in Section 9.4.2, which gives the age distribution of this type of deposit. These deposits are formed in an environment where groundwater has intersected the surface. Parts of deposits are uniformly fine-grained silt deposits, pale yellowish brown, and unconsolidated (CRWMS M&O 1996e, pp. 2-46 to 2-48). They may be massive to very poorly bedded. Locally, they are weakly cemented by calcium carbonate and weather into popcorn-shaped nodules covering the modern surface. Also locally, they contain white diatomite beds up to 75 cm (30 in.) thick. The diatomite deposit locally bears minor reworked ash and small pumice lapilli of the 760-ka Bishop Tuff.

4.4.3.4 Comparison of Regional Quaternary Stratigraphy

The Quaternary stratigraphy at Yucca Mountain is similar to that seen regionally, much of which has good age control (Table 4.4-1). The section at Silver Lake, California, provides a sequence of Quaternary stratigraphic units with ages based on radiocarbon dating of shell material and tufa from shoreline features (Reheis et al. 1989, p. 1129, Table 1; Wells et al. 1984, p. 78, Table 3). This stratigraphy includes 10 units with age control in the Holocene. The Kyle Canyon Fan in southern Nevada provides a comparable stratigraphy based on U-series age estimates on secondary carbonate rinds formed in limestone gravel. Fish Lake Valley, north of Death Valley (Slate 1991, pp. 105 to 106, Table 3; Reheis and Sawyer 1997, Table 2) and the Providence Mountains in the eastern Mojave Desert (McDonald and McFadden 1994, p. 207; Wang et al. 1996, p. 387, Table 5) also provide stratigraphies that suggest similar age ranges for timing of deposition and soil formation.

All areas, except Kyle Canyon, preserve at least three Holocene depositional units represented by the modern wash, a slightly elevated terrace in the range of 1 k.y., and the dominant late Pleistocene-early Holocene unit primarily deposited during the onset of a drier and hotter regional climate following the last major glaciation. The late Pleistocene unit in these regional studies has an estimated age range of 30 to 100 k.y. with a preferred age on the order of 50 k.y. This unit represents a major period of soil formation. The timing of deposition of this late Pleistocene unit is coincident with regional climatic records of transition from a wetter to drier climate (Winograd et al. 1992, p. 257), similar to that noted for the late Pleistocene-early Holocene (Table 4.4-1) (Section 6.3.4). A middle Pleistocene stratigraphic unit, apparently formed during another period of transitional climate, is common to the Yucca Mountain and Providence Mountain regions; however, no unit of similar age is mapped in Fish Lake Valley. Age constraints for this time period are poor in the Providence Mountains for the unit (Q3f); however, the reported preferred age of 150 k.y. falls within the middle Pleistocene Q3 unit age of the Yucca Mountain region, for which the estimated age is 100 to 250 k.y. Middle Pleistocene

deposits are preserved in all regional study areas, and the presence of buried Bishop ash at or near the base of several deposits constrains their maximum ages.

The problem with using age estimates from trenches exposed to look for tectonic offset of depositional units is that the trenches are not in locations typical of the local and regional Quaternary geology. These trenches are located at and adjacent to active mountain fronts where erosion, deposition, and eolian processes are different than on stable alluvial surfaces, which dominate the broad flat valleys. Once the ages were determined from samples collected in the fault trenches, the Quaternary mapping unit exposed in the trench was determined. Many investigators familiar with the local and regional Quaternary geology were present when these unit assignments were made. Uncertainties associated with any geologic mapping are inherent in the assignment of stratigraphic units.

4.4.3.5 Distribution of Quaternary Deposits in the Yucca Mountain Area

The Quaternary landscape in the Yucca Mountain area has been affected by physical weathering. It also reflects colluvial, eolian, and alluvial processes that have responded to varying climates and climatic changes. The topography of the mountain and adjacent basins that have been formed by extensional tectonic processes over the past 14 m.y. is an additional factor influencing landscape development at Yucca Mountain. Patterns of Quaternary deposits reflect both the tectonic environment and climatic history in the area.

One noteworthy map pattern at Yucca Mountain is the preservation of early and middle Quaternary colluvial deposits on many hillslopes (e.g., Whitney and Harrington 1993, p. 1008). Cosmogenic isotopes, volcanic ashes, cation-ratio dating, and U-series dating on colluvial soils have been used to determine the ages of these deposits. The preservation of older Quaternary deposits indicates that hillslope erosion processes have been ineffective in eroding colluvial deposits that were weathered from bedrock during the colder, pluvial climatic episodes (Whitney and Harrington 1993, p. 1014, Table 1). The slow removal of hillslope colluvium is also reflected in the lack of either large or steep alluvial fans at the base of the slopes at Yucca Mountain. The lack of fans along the base of tilted fault blocks is a strong indication of very low rates of tectonic activity. As discussed in Section 12.3, Quaternary uplift rates are generally 0.01 mm/yr. (0.0004 in./yr.) or less for the faults in the site area.

Another interpretation can be made from the preservation of older Quaternary deposits at Yucca Mountain: the amount of climatic time that erosional processes dominate the landscape is less than the time during which hillslopes are mostly stable. Recent studies by Paces, Marshall et al. (1997) on the paleodischarge deposits south of Yucca Mountain suggest that this scenario may be true. Climatic conditions appear to have been wetter and cooler than present about 80 percent of the time during the last 100 k.y. (Section 6.3.4).

As described in Section 4.4.3.3.2.2, a relatively unique deposit called a sand ramp mantles southern and eastern hillslopes around Yucca Mountain. These deposits are dominated by eolian sand that has blown against hillslopes and washed back down the slope, usually with an added component of coarse debris. The primary origin of the sand is the vast alluvial fan and terraces of Fortymile Wash and other washes that deposit fine-grained sediment in the Amargosa Valley. Sand ramps are as thick as 30 m (12 in.) around Busted Butte, along part of Fran Ridge, and on

slopes of the unnamed flanks of southern Yucca Mountain. These sandy deposits are products of a very dry and windy climate that took place during some part of the interglacial component of the climatic cycle. Up to six buried soils have been found in some sand ramps, which demonstrate the cyclic nature of dry, arid conditions at Yucca Mountain (Menges and Whitney 1996, p. 4.4-5). The presence of Bishop ash near the base of several sand ramps indicates that eolian sand deposition goes back at least 760 k.y. The preservation of essentially unconsolidated sand on Yucca Mountain hillslopes underscores again the ineffective hillslope erosional processes during the last half of the Quaternary.

The distribution of Quaternary deposits of different ages in Crater Flat appears to reflect the ongoing opening, or extension, of the basin. Deposits of Q1 to Q3 age are concentrated on the eastern side of the basin near or adjacent to Yucca Mountain. Deposits of Q5 and Q6 age are concentrated along the basin's southwestern and southern margin , the area of maximum subsidence defined on the regional seismic reflection line (Brocher et al. 1998, Figure 6) (Section 4.3). A strong contrast in runoff patterns can be seen between the east-flowing alluvial fans from Bare Mountain and the southerly slope of the drainage of central Crater Flat. This drainage contrast probably reflects the presence of a buried fault in central Crater Flat, and possibly a buried splay of the Bare Mountain fault near the base of the Bare Mountain fans. The Bare Mountain fans are not rounded in typical fan shape, but terminate against a sharp, north-trending lineament defined only by a change in drainage patterns. Fault-controlled sedimentation has occurred along the Windy Wash and Fatigue Wash faults. Uplifted early to middle Quaternary alluvium is juxtaposed with late Quaternary alluvium and colluvium.

On the east side of Yucca Mountain, sedimentation patterns do not appear to reflect active tectonism, except where colluvial wedges have deposited locally against fault scarps. The northerly trend of Fortymile Wash, which is parallel to but not coincident with the Paintbrush Canyon fault, has raised questions about whether its origin is in part tectonically influenced. Several geophysical studies, summarized in the geophysical synthesis report (Oliver et al. 1995, pp. 44, 109 to 111), suggest that a very shallow graben may exist beneath the central alluvial portion of the wash (south of the canyon); however, the regional seismic reflection line does not show any significant offset of the Tertiary-Paleozoic contact beneath the wash. No evidence of Quaternary tectonic activity has been associated with the wash. The southerly depositional pattern of the wash is controlled by the base level of the huge Amargosa Valley.

Midway Valley is underlain largely by Q1 and Q2 deposits because of a stream capture of Yucca Wash that appears to have taken place during the middle Quaternary (Taylor 1986, pp. 17 to 21). During Q1 time, Yucca Wash flowed southeastward into Fortymile Wash through the gap between Alice and Fran ridges. After Q2 time, Yucca Wash flowed eastward into Fortymile Wash north of Alice Ridge. In general, colluvial deposits that are produced during pluvial climates dominate hillslopes. The erosion and redistribution of these deposits takes place during drier climates, when hillslopes are no longer stabilized by vegetation. Hence, most of the alluvial map units in the basins and valleys, which dominate the landscape at Yucca Mountain, were deposited during interpluvial episodes. Eolian deposits record exceptionally dry and windy conditions that occurred in the climatic cycle, whereas paleodischarge deposits from springs were deposited during the wetter and cooler conditions of the pluvial part of the cycle. (Section 9.4.2 contains a complete description of paleodischarge deposits and history.) Multiple

dating and descriptions of soils, surfaces, and deposits support these deposition patterns on Yucca Mountain.

4.4.4 Paleoenvironmental History of Yucca Mountain

The eight map units identified on and around Yucca Mountain represent more than a million years of paleoenvironmental history. The landscape has experienced many cycles of Quaternary climatic change while tectonic activity has continued at a slow, almost imperceptible, rate. The surficial deposits at Yucca Mountain have left a fragmented record of climate history by recording sedimentary deposits, soils, and erosional unconformities that relate to the predominant geomorphic processes associated with past climatic episodes. The geologic record becomes more fragmented and indistinct with older map units because of poor exposure, burial by younger units, and because they generally cover greater periods of time. Nevertheless, many trends that can be interpreted in younger deposits with better age control can be assigned to older units on the basis of sedimentological characteristics and soil type.

Fortunately, a nearly continuous climatic record exists near Yucca Mountain at Devils Hole. The length and intensity of cool-wet to warm-dry climatic cycles for the southern Great Basin is well defined for about 417 k.y. (Winograd et al. 1992; Szabo et al. 1994). Long climatic records with some erosional breaks are also available from the studies of lacustrine cores from Owens Lake (Smith, G.I. et al. 1997) and especially from Death Valley (Li et al. 1996), which receives waters from the Amargosa drainage basin. (These records, as well as Amargosa paleodischarge records, packrat midden studies, and other Great Basin climatic records are discussed in detail in Section 6.3.) These more continuous climatic histories are used here to help evaluate the climatic conditions that existed at Yucca Mountain when each identified map unit was deposited, soils were formed, and erosional intervals dominated the landscape.

As discussed earlier, the Quaternary stratigraphy of Yucca Mountain is dominated by coarse colluvium and alluvium, and by eolian deposits. However, a small area of fine-grained spring discharge and marsh deposits is located at the south end of Crater Flat and at the north edge of the Amargosa Desert. Paces, Neymark, Kwak et al. (1996) have concluded that these deposits are analogous to spring discharge deposits along the Spring Mountains formed by regional groundwaters that discharged at the surface during pluvial episodes (Quade et al. 1995, Table 2). In the vicinity of Yucca Mountain, pluvial recharge may have raised the water table around 100 m (328 ft) (Quade et al. 1995, p. 228).

A summary of age ranges for Yucca Mountain stratigraphic units and interpreted erosional intervals is shown on Figure 4.4–4. Also shown are time lines and paleoclimatic records from SPECMAP (based on deep-sea cores), Devils Hole, Death Valley, and Owens Valley to compare with Yucca Mountain stratigraphy.

Given the inherent difficulty of dating coarse, arid-region deposits primarily by the time-transgressive soils that formed on them, a good to very good correlation exists between cyclic climate change and erosion and deposition at Yucca Mountain. Dated stratigraphic units at Yucca Mountain for approximately the last 150 k.y. show a strong correlation of spring deposition and stream incision during pluvial episodes (OIS-2, -4, and -6), and hillslope erosion accompanied by valley and basin alluvial deposition during interglacial climates (OIS-1, -3, -5,

and -7), and times of rapid climatic change. The correlation of Quaternary units at Yucca Mountain with units of similar age in nearby areas discussed above (Section 4.4.3.4) strengthens the interpretation that episodes of erosion and deposition have been climatically controlled. A model of landscape response to climatic change in the southern Great Basin is discussed in Section 7.4.2.1.

4.4.5 Use of Quaternary Studies to Address the Existence of a Potentially Higher Water Table at Yucca Mountain

In Sections 4.4.1 through 4.4.4, the Quaternary stratigraphy and surficial processes in the Yucca Mountain area were described at a summary level. Discussions included the types of deposits present, their age and geomorphic characteristics, and their distribution in the area. Correlations with regional Quaternary deposits were presented and a paleoenvironmental history provided that link the deposits to cyclic climate change. Some uses of the Quaternary stratigraphic record were discussed, such as estimating the timing and amount of displacement of surface rupturing earthquakes on faults in the area. In this section, another use of Quaternary studies is described to address the possible existence of a potentially higher water table at Yucca Mountain.

The occurrence of pedogenic carbonate, over both as slope-parallel deposits and as remobilized fracture fillings, has generated a controversy as to the possible existence of a adverse condition. Szymanski (1987, 1989) postulated that these deposits were formed by groundwater rising to the surface and, therefore, through the potential repository horizon. This section summarizes the work done to resolve this question and describes reasoning behind the YMP's conclusion that there are no paleogroundwater discharge deposits in the immediate vicinity of Yucca Mountain. In fact, the closest such deposit is approximately 15 km (9.3 mi.) to the southwest (Section 9.4.2).

The concerns over the carbonate deposits were raised in 1982 when the west side of Exile Hill was excavated to examine the Bow Ridge fault as part of the Quaternary faulting investigation in the vicinity of Yucca Mountain (Swadley et al. 1984, p. 34, Table 1). The 2-m-deep (6.6-ft) excavation, designated Trench 14 (Figure 4.4-3), exposed a vein-like deposit of calcium carbonate and subordinate opaline silica (Figure 4.4-5), as well as breccia deposits in the bedrock that contain drusy quartz. The trench was deepened in 1984 to 4 m (13 ft) to further elucidate the deposits' origin. Two workshops on the Trench 14 deposits were held in Las Vegas, Nevada, in early 1986. The first addressed the present state of knowledge (Voegele 1986a); the second proposed methods of investigation (Voegele 1986b). Both were open to the public and were attended by representatives of the NRC and the State of Nevada.

Following the workshops, the U.S. Department of Energy (DOE) established a five-member peer review panel to examine the issue. The review panel summarized four main categories of depositional models and suggested ways to investigate and evaluate the origin of the deposits. The depositional models proposed were:

- Pedogenic, which includes any origin involving the interaction of meteoric waters and surficial materials with subsequent deposition of calcium carbonate and silica within soil profiles and/or fractures

- Hydrothermal springs, which involves movement of hot or warm water (temperature more than 30°C [86°F]) up along faults with deposition of minerals
- Cold springs, which involves movement of regional or perched groundwater along normal hydrological gradients with deposition of minerals
- Seismic pumping, which involves the movement of hot or cold water up along faults in direct response to pressures generated by tectonism.

All but the first model imply that groundwater could have risen to the surface through the potential repository horizon, thereby creating a potentially adverse condition to waste isolation. The panel's recommendations (Hanson et al. 1987) were factored into development of the Quaternary Regional Hydrology study plan from DOE (1988, Section 8.3.1.5.2.1). The study plan was reviewed by more than 20 YMP scientists and consultants, the NRC, and the State of Nevada.

Concurrent with the YMP activities, Jerry Szymanski, a DOE physical scientist, proposed a hypothesis of catastrophic upwelling of groundwater, similar to the seismic pumping model, for the origin of the deposits. DOE requested that he draft a report to DOE management (Szymanski 1987). The YMP office performed an internal review of his report (DOE 1989, p. 1) and found it to be in need of extensive revision. Szymanski produced a revised report (Szymanski 1989). In 1990, the DOE convened a five-member review panel, external to the DOE or its YMP contractors. The panel completed its review in 1991 and, because it was unable to reach a consensus, provided its findings in two reports (Powers et al. 1991; Archambeau and Price 1991). A 17-member panel convened by the National Research Council was asked by the DOE in 1990 to "evaluate (1) if the water table had risen in the geologically recent past to the level of the proposed Mined Geologic Disposal System, and (2) if it is likely that it would happen in the manner described in the DOE staff geologist's final report within the 10,000-year period covered by the regulations" (National Research Council 1992, p. 2). The panel completed its review and provided its findings in a final report (National Research Council 1992); its findings are presented in Section 4.4.5.1.10.

The following sections present the results of work, primarily by YMP scientists, to address the possible existence of a potentially adverse condition at Yucca Mountain. Section 4.4.5.1 describes calcite deposits along faults, fractures, and at the surface. Section 4.4.5.2 provides detail on the petrology, mineralogy, and chemistry of surface deposits, and how pedogenic deposits are distinguished from spring deposits.

4.4.5.1 Calcite Deposits along Faults, Fractures, and at the Surface

A key approach to evaluating the possible past upwelling of groundwater through the potential repository area is to determine the physical and chemical attributes of the observed calcite deposits and compare them with pedogenic and spring deposits to see which they resemble. The following sections present the results of such studies. The section concludes with a summary of the National Academy of Sciences and National Research Council assessment of the issue.

4.4.5.1.1 Field Data

Comparison of the physical and chemical characteristics of the calcite-silica deposits exposed at Trench 14, with those of pedogenic and spring deposits, favors a pedogenic origin for the Trench 14 deposits (Taylor and Huckins 1986). Trench 14 exposes slope-parallel, calcium-carbonate-enriched zones (Figure 4.4-5), which are laterally extensive for thousands of square meters and follow topography (Taylor and Huckins 1995, p. 19), unlike springs, which form discrete mounds. The slope-parallel deposits are physically typical of carbonate-enriched pedogenic deposits that occur throughout the southwestern United States and other semiarid regions of the world (Bachman and Machette 1977). The carbonate-enriched horizons exposed in Trench 14 can be traced upslope and over the fault and fracture fillings. Locally, the near-vertical veins and the carbonate horizons merge. In addition, the deepened portion of Trench 14, in the area of the near-vertical veins, exposes the veins pinching out and becoming discontinuous with depth (Taylor, E.M., Coe et al. 1996, Figure 4.6.1). At depth, where the Bow Ridge fault is intersected by the Exploratory Studies Facility, deposits are restricted to the footwall of the fault. In contrast to these observations, feeders for spring mounds typically maintain subparallel walls over depths of tens to hundreds of meters (hundreds to thousands of feet).

The calcite-silica veins contain a black ash that must have washed into open fractures. It is difficult to explain the presence of the ash in an environment where water is issuing from an open fissure. Other physical features for distinguishing between pedogenic and nonpedogenic carbonate deposits are summarized by Taylor and Huckins (1995, Table 5).

4.4.5.1.2 Mineralogic and Textural Data

Earlier studies of the vein deposits in Trench 14 and similar deposits around Yucca Mountain emphasized the similarity of calcite-opal-sepiolite mineralogy to that of the widely distributed slope calcretes (Vaniman et al. 1984, p. 22; 1988, pp. 46 to 51). This similarity suggests that one depositional mechanism accounts for both slope and vein calcretes. On a centimeter scale, distinctions between slope and vein calcretes based on orientation become meaningless. Laminae within the calcretes often reveal multiple episodes of fracturing and cross-cutting deposition. These structural complications are particularly prominent in the blocky rubble near faults.

The vein material in Trench 14 is poorly indurated and fine grained. This contrasts sharply with the typical discharge feeder veins, which are well indurated and coarse grained. As described in Section 4.4.5.2.1, the centimeter-scale (half-inch) banding at Trench 14 consists of:

- Laminae with abundant root casts
- Laminae with abundant ooids and pellets
- Denser laminae that show evidence of shearing
- Thin (less than 5 mm [0.2 in.]) laminae of opal
- Rare sepiolite-rich laminae.

The ooids are generally less than 0.5 mm (0.02 in.) in diameter and have concentric coatings (mainly calcite or opal). Pellets are larger round or ellipsoidal calcite-opal bodies that generally include several detrital fragments and may include earlier formed ooids.

Because ooids and pellets contain one or more detrital fragments, laminae with an abundance of ooids and pellets contain the most detritus. The detritus consists of tuffaceous volcanic rocks and minerals from the immediate vicinity of Trench 14, plus a small amount of exotic rock fragments. The dense, sheared laminae generally contain less tuff detritus than those laminae with abundant preserved root fossils or ooids. Some of the dense laminae consist of closely intergrown calcite and opal with essentially no detritus, but to date the only pure mineral separates from the calcretes have been of opal, either from the opaline laminae or calcite from large root fossils (Vaniman, Chipera, and Bish 1995, pp. 13 to 14). Calcite crystals are small; most (more than 95 percent) are less than 5 μm, and calcite is closely intergrown with opal or, more rarely, sepiolite. All attempts to obtain pure calcite separates by crushing and density separation have failed because of intimate intergrowth with other minerals. These intimate intergrowths and the existence of ooids and pellets are atypical of any type of spring deposits (Vaniman et al. 1988, pp. 14, 45; Stuckless et al. 1992, p. 930), but are common in soils (Bachman and Machette 1977, p. 55).

The intimate intergrowth of calcite and opal in the Yucca Mountain calcretes is atypical of spring deposits. Cool and warm springs, from deep or perched sources, have higher water flow and can maintain stable pH regimes that precipitate either calcite or silica, but rarely both, in significant abundance (White et al. 1956, p. 51; Viles and Goudie 1990, p. 28). In contrast, evaporative processes within arid soils formed of siliceous detritus can cause a rise in pH from only slightly alkaline to greater than 9 (Chadwick et al. 1989; Boettinger and Southard 1990, pp. 414 to 415), passing from regimes of calcite dissolution and silica precipitation into those of calcite precipitation and silica dissolution (Watts 1980). Numerous wetting and drying cycles can thus lead to repeated pH-driven dissolution-precipitation cycles, which can account for the complex calcite and opal intergrowths seen in the Trench 14 calcretes. The closest analogous spring deposits are surface discharges that may deposit both calcite and silica, as at GMC and IMV spring localities. In these deposits, however, the opal and calcite are largely segregated or easily separable and not as intimately intergrown as the Yucca Mountain calcretes. Local spring deposits have a greater bulk density than the Yucca Mountain calcretes (Vaniman, Chipera, and Bish 1995, p. 19). This is particularly true for vein deposits at known spring localities. However, the more porous tufa mounds, as at Nevares, can develop deposits with densities low enough to approach those of the densest Yucca Mountain vein deposits. Other physical and chemical features provide more definitive distinctions between the calcite-silica deposits of spring or soil-process origins.

Many of the same authigenic minerals (calcite, opal, and sepiolite) that occur in the calcretes can also be found in known spring or seep deposits. However, there are certain key differences in the deposits that form in these two different environments. Veins of pure calcite are common at spring localities but not in calcretes. Individual calcite crystals of more than 1 cm (0.4 in.) are common in travertine veins at springs, but not in any calcretes, including vein calcretes. Where comparable fine-grained calcite does occur in travertine mounds at springs, it is still very common to obtain deposits of relatively pure calcite with characteristic bacterial clumps and ostracode fossils. Fossil casts from the stems of phreatophyte plants, connected by meniscal septae (Figure 4.4-6a), provide readily visible field evidence of spring activity. No such features are found in the Yucca Mountain calcretes.

Springs and evaporative seeps retain biogenic evidence of their past higher water content, including ostracode fossils, casts of phreatophyte plants, and algal or diatomaceous deposits of opal-A.

Pedogenic calcretes have a different set of fossils. Calcified filaments are typically pedogenic. Superficially similar calcareous filaments occur as algal products in active springs, but these delicate filaments are not preserved in accumulated inactive spring deposits, whereas bacterial shrub structures commonly are (Chafetz and Folk 1984; Viles and Goudie 1990). In contrast, the calcified filaments in the Yucca Mountain calcretes are found in the oldest as well as the youngest laminae. Moreover, algal filaments in springs are not restricted to associations with fossil roots, as are the calcified filaments of the Yucca Mountain calcretes. Needle-fiber calcites are unlikely to form and less likely to be preserved in spring discharge areas.

The delicate fossils within root casts provide two important constraints on the origins of the siliceous calcretes. First, the fragile fossil forms are preserved even within the earliest-formed calcrete laminae (Figure 4.4-7); such preservation would be unlikely if the calcretes were emplaced by successive forceful fluid injections with catastrophic brecciation. Indeed, the pervasive distribution of root fossils suggests that root penetration plays a distinctly noncatastrophic but nevertheless forceful role (Klappa 1980) in the brecciation of these calcretes. The dense, sheared laminae are pervaded by root-fossil remnants and may represent collapsed zones where coarser roots were once concentrated. Second, similar needle-fiber calcites and calcified filaments within fossil roots are characteristic of pedogenic calcretes (Klappa 1979; Phillips and Self 1987; Wright, V.P. 1986, 1989). In evaporative seeps and in calcareous tufa mounds around springs, the fossilization of vascular plants typically leaves casts of the plant form without preserving such fine features of root decay. The high water flux in seeps and springs flushes out the products of decay, leaving only the plant casts behind. Calcified filaments, needle-fiber calcites, and other delicate fungal fossils within root forms thus provide an important guide to pedogenic calcretes, particularly where they occur beneath a genetically related B-horizon. Intermittently saturated desert soils without pedogenic horizonation might retain delicate fungal fossils (Mack and James 1992), but the retention of such features is unlikely in zones of forceful spring discharge.

4.4.5.1.3 Major-Element and Trace-Element Data

Chemical composition of the overlying soil can be an important factor in evaluating calcrete origin. If the calcrete is pedogenic, the detritus incorporated into it is likely to carry with it the effects of surface exposure and soil-zone processing. Nonpedogenic calcretes may also incorporate soil detritus, but if they originate from upwelling waters, the veins should show more evidence of interaction with their wall rock than with the surface soil. This will particularly be the case for vein deposits as seen in Trench 14, where the "deep origin" hypothesis involves explosive injection and wall-rock brecciation by the vein-forming fluids (Archambeau and Price 1991, p. 4; Szymanski 1989). Chemical data for the calcretes and the overlying soils have similar lanthanide-element signatures, even where x-ray diffraction data detect no detritus. A similar effect is seen in the Fe and Sc data, where the Fe/Sc ratios of both the calcretes and the overlying soils are very similar (YMP 1993, p. 22; Vaniman et al. 1994). Examination of abundances as well as ratios indicates that many individual laminae in the calcretes have high Fe and Sc contents, even though the laminae contain no more than 25 percent detritus. The Fe and Sc enrichments result from weathering of detritus (Vaniman et al. 1994). This suggests that the detritus in the calcretes must be derived from surface soils with the same Fe/Sc ratio, but higher Fe and Sc content than the tuff. Few volcanic rocks at Yucca Mountain have sufficiently high Sc; those that do differ from the calcrete detritus by having very different La/Yb or other

chemical ratios, and by lacking key minerals, such as sphene, that characterize the detritus in the calcretes.

4.4.5.1.4 Accumulation Rates for Authigenic Calcite and Opal

Archambeau and Price (1991, p. 59) have suggested that there is too much calcite and opal in Trench 14 to be accounted for by pedogenic accumulation. This is not the case. The subsurface accumulation of calcite and opal is greatest within the fault (2.25-m-maximum-width (7.38 ft) calcrete vein near the surface and wedging down to a few centimeters (inches) wide at 4.75-m [15.58-ft] deep). Approximately 60 percent of the material in this wedge is laminated calcrete; the remainder consists of blocks of the wall-rock tuffs. Average bulk density of the calcretes is 1.6 g/cm^3 (0.058 lb./in.^{3}). The average calcite weight fraction of the calcretes is 53 percent, leading to an estimated calcite abundance of 1.2×10^6 g/m^2 (47,188 oz/yd^2) of surface overlying this wedge of vein calcrete. Estimates of eolian carbonate accumulation rates for the southwestern United States range from 0.3 to 5 g/m^2/yr. (0.0088 to 0.1474 oz/yd^2/yr.) (Machette 1985; Reheis et al. 1992). At these rates, the amount of calcite within the excavated veins at Trench 14 could accumulate over a time span between 4 m.y. and 240 k.y. This represents a maximum estimate, because the extensive area of impermeable bedrock upslope, where dust could accumulate and be washed to the fault, is not considered. Furthermore, C and O isotope data suggest that most of Trench 14 calcite was deposited during colder and wetter climates (Quade and Cerling 1990, p. 1550; Whelan and Stuckless 1990, p. 930), when carbonate accumulation rates were relatively rapid. The time spans estimated here could allow pedogenic accumulation of about 0.4 to about 7 times the amount of the Trench 14 calcite within the 1.6 m.y. of the Pleistocene. Separate studies of calcite deposits in fractures of the unsaturated zone tuffs indicate that these calcites are derived from the surface, probably as the surface calcites are dissolved and transported downward (e.g., Whelan et al. 1994; Vaniman and Chipera 1996). Based on the analysis here, it appears that with the more rapid accumulation rates, and considering only the Pleistocene accumulations, about six times the amount of Ca bound in surface calcrete may be deposited as calcite at depth. This amount does not include the earlier deposits of isotopically distinct calcite that have been reported by Paces, Marshall et al. (1997).

Because the Trench 14 calcretes are siliceous, it is possible to compare the rates of silica and calcite accumulation. Within the same calcrete wedge described above, the average opal weight fraction is 36 percent, leading to an estimated opal abundance of 0.8×10^6 g/m^2 (23,591 oz/yd^2). The solubility of SiO_2 in arid soils containing abundant siliceous glass may exceed 0.07 g/L (0.00058 lb./gal) (Chadwick et al. 1989). However, waters in local higher-elevation soils at Rainier Mesa, Nevada, have SiO_2 contents of 0.02 to 0.04 g/L (0.00017 to 0.00033 lb./gal) (Kerrisk 1987). For the SiO_2 concentration range of 0.07 to 0.02 g/L (0.00058 to 0.00017 lb/gal), 1.1 to 4.0×10^6 cm/cm^2 (433,071 to 1,574,803 in./in.^{2}) of rainwater can form enough soil water to deposit the opal within the calcrete wedge. Current rainfall at the elevation of Trench 14 is about 15 cm/yr. (6 in./yr.) (Spaulding 1983, p. 15). At this precipitation rate, sufficient rainwater could infiltrate, dissolve local silicates, and evaporate to form the opal in the vein calcrete within 70 to 270 k.y. The longer time estimate may be most appropriate, since the wetter and cooler climates that prevailed during calcrete formation (Quade and Cerling 1990, p. 1550) may have resulted in deposition from relatively silica-poor soil waters like those of Rainier Mesa. A 30- to 100-percent increase in rainfall during the Pleistocene (USGS 1984) could shorten the longer estimate to as little as 135 k.y. As with the calcite calculations, the 1.6-m.y.-duration of Pleistocene time would allow about 6 to

about 12 times the amount of opal deposited at the surface to be deposited in fractures of the unsaturated zone tuff. However, trace-element studies of calcites in the unsaturated zone suggest that glasses at depth have also been dissolved. The silica budget at depth in the unsaturated zone may therefore exceed that of calcite. This contradicts the results of Exploratory Studies Facility studies by Paces, Neymark, Marshall et al. (1996), which suggest approximately six times as much calcite as opal in unsaturated zone fracture deposits. Perhaps the most important consideration in assessing this discrepancy is the general undersaturation of Yucca Mountain waters with respect to amorphous silica (Vaniman and Chipera 1996, p. 4432). This result suggests that much of the silica dissolved from the surface will continue to travel to the water table, whereas calcite precipitation may be locally favored in the unsaturated zone.

4.4.5.1.5 Stable Isotope Data

Carbon and O isotopes in the Trench 14 vein carbonates (Whelan and Stuckless 1990, Figure 1) match those in pedogenic carbonate (Cerling et al. 1989, Table 1; Quade et al. 1989, Table 1) collected over a wide area of southern Nevada (Figure 4.4-8). In detail, the isotopic compositions suggest pedogenic deposition of the Trench 14 calcites under cooler climate conditions with a mean temperature of about 15°C (59°F) (Quade and Cerling 1990, p. 1552). Samples of soil carbonates and vein infilling from both Trench 14 and Busted Butte show that the isotopic compositions of O and C of most samples are similar for the two locations and for the two types of deposits, soils and veins (Whelan and Stuckless 1990, Figure 1). A few Busted Butte soil carbonates are slightly enriched in ^{13}C and ^{18}O (Figure 4.4-9), but the variability in the data is small enough that all soil and vein carbonate can be explained by pedogenesis.

The calculated C and O isotopic compositions of hypothetical calcites formed in equilibrium with Yucca Mountain area groundwaters are very different from those measured for the vein calcites (Figure 4.4-10). This difference shows that the veins could not have formed directly from groundwaters, like those present in the region today. Most available groundwater data are for the Cenozoic aquifer, for which the water table is at a depth of 460 to 700 m (1,509 to 2,297 ft) in the Yucca Mountain vicinity (Waddell et al. 1984, p. 1). Calculations based on lower temperatures for calcite precipitation would produce better agreement with the observed O compositions of the vein calcites, but some waters would have to be cooled to impossibly low temperatures (0°C [32°F] and lower) to precipitate calcite with the appropriate isotopic composition (Figure 4.4-10). The isotopic compositions of Trench 14 calcites could be derived through deposition from water similar to modern precipitation at reasonable temperatures (5° to 22°C [41° to 72°F]).

Carbon isotopes do not fractionate significantly between dissolved carbonate and calcite at the temperatures in question (Friedman and O'Neil 1977) . About half the groundwater samples, including the one analyzed from the Paleozoic aquifer, are either too enriched or too depleted in ^{13}C to be possible sources for the vein carbonates. Based on the similarity of C isotopic data in soils and the Trench 14 deposits, the most likely source for C in the Trench 14 calcites is pedogenic.

The preceding discussion assumes that the isotopic composition of groundwater beneath Yucca Mountain is representative of groundwater that might have formed the Trench 14 veins. However, groundwaters beneath Yucca Mountain have apparent ^{14}C ages of less than 20 ka in

the Tertiary aquifer and about 30 ka in the Paleozoic aquifer (Benson and McKinley 1985, Table 1), whereas the Trench 14 deposits are much older, with ages greater than 400 ka (Szabo and O'Malley 1985, Table 2), and as young as 92 ± 5 ka (YMP 1993, Table A-9).

The isotopic composition of ancient groundwaters in the Yucca Mountain region cannot be determined. However, the Ash Meadows flow system, which is located east of the groundwater flow system that underlies Yucca Mountain (Winograd and Thordarson 1975, p. C75, Plate 1), has left a long-term record near its discharge site. Uranium-series ages have been obtained for individual laminae within a vein of continuously deposited calcite at Devils Hole (Winograd et al. 1988, p. 1275; Ludwig et al. 1992, p. 1568). Oxygen isotope analyses of these laminae (Figure 4.4-11) show a variation that is generally less than ± 1 per mil about the present-day value during the last 560 k.y. (Winograd et al. 1988, p. 1277; Coplen et al. 1994, Figure 2). A similar variation for waters beneath Yucca Mountain would be reasonable, because the isotopic composition of both flow systems should be governed by the same climatic conditions. Even if a similar per mil increase (at currently observed temperatures) did occur for groundwater beneath Yucca Mountain, precipitated calcites would not have the isotopic compositions of those observed at Trench 14.

4.4.5.1.6 Radiogenic Tracer Isotope Data

Studies of Sr isotopes in calcite from the Yucca Mountain area support a pedogenic origin for the veins exposed in Trench 14 and argue against a groundwater origin (Marshall et al. 1990, p. 923; Marshall et al. 1991, p. 1427; Stuckless et al. 1991, p. 553). Strontium isotopes do not fractionate in nature, and the isotopic composition of Sr in calcite therefore provides a record of the isotopic composition of water from which it precipitated (Peterman and Stuckless 1993, p. 61). There is almost no overlap between the isotopic compositions of Sr for groundwater within the Tertiary aquifer near Yucca Mountain (less than 2.0) (Figure 4.4-12) the Trench 14 vein carbonates ($\delta^{87}Sr = 4.54 \pm 0.32$, N = 27) (YMP 1993, p. 56). Samples from the tertiary aquifer with the lowest values were taken in the presumed upflow direction of Trench 14 (Figure 4.4-12). For Trench 14, calcites to be derived from Tertiary aquifer water with higher isotopic compositions, such as seen south and west of Yucca Mountain (Figure 4.4-12), saturated zone flow would have to reverse direction. A bailed sample from the Paleozoic aquifer ($\delta^{87}Sr = 3.60 \pm 0.13$ for UE-25 p#1) is also significantly different from the Trench 14 veins. Thus, none of the saturated zone waters sampled to date in the Yucca Mountain area can be related genetically to the Trench 14 calcite deposits.

Data from Devils Hole can again be used to evaluate the likely compositional changes in ancient groundwater beneath Yucca Mountain. Strontium-87/strontium-86 values for water presently issuing from Devils Hole and for six samples of calcite deposits ranging in age from approximately 100 years to 600 ka (Figure 4.4-13) differ by only 0.71 per mil (Marshall et al. 1990, Figure 1). Strontium-87/strontium-86 values of water within the Cenozoic aquifer in the Yucca Mountain area probably behaved in a similar fashion, because the recharge area and host aquifer have probably not changed during the Quaternary, as suggested by the general geomorphic and tectonic stability of the landscape noted earlier in this section. Furthermore, the isotopic composition of Sr is more variable in the Paleozoic aquifer (Peterman et al. 1992, Figure 1) than in the Cenozoic aquifer (Peterman and Stuckless 1993, Figure 2) and, therefore, is potentially susceptible to larger fluctuation at its discharge region as a function of time. Thus, it

is highly unlikely that water beneath Yucca Mountain ever had high enough $^{87}Sr/^{86}Sr$ values to have been a source for the Sr in the Trench 14 deposits.

The isotopic compositions of Sr in calcite in the near-vertical vein and subhorizontal deposits at Trench 14 show a fairly close correspondence, but the vein materials, on average, have a somewhat higher value (Marshall et al. 1990, p. 922). Over a broader region around the Nevada Test Site, the correspondence between vein (0.71238 ± 0.00026, N = 39 [$\delta^{87}Sr$ = 4.48]) and pedogenic calcite (0.71233 ± 0.00028, N = 37 [$\delta^{87}Sr$ = 4.41]) is much stronger (Marshall et al. 1991, p. 1426).

The isotopic composition of the vein carbonate at Trench 14 and Busted Butte may have been influenced in part by reaction of depositing fluids with entrained solid material, and the isotopic composition may also be affected by reaction with the host wall rock (Stuckless et al. 1992, p. 933). However, most Sr in the subhorizontal deposits (and, by geochemical analogy, Ca as well) seems to come from a well-homogenized source, such as wind-blown dust. Limited data for eolian carbonate do not provide an exact match to isotopic compositions of pedogenic carbonate, which caused Marshall and Mahan (1994, p. 2685) to conclude that "an additional source or past variation of Sr composition is required to model the pedogenic carbonate system."

The remarkable homogeneity of Sr isotopic composition in pedogenic deposits over a broad geographic region argues against deposition from groundwater, because the isotopic composition of groundwater is very inhomogeneous in the vicinity of the Nevada Test Site (Peterman et al. 1992; Peterman and Stuckless 1993, Figure 2). Water emerging at the surface would impart this inhomogeneous characteristic to deposited calcite.

Lead isotopic data yield the same general conclusions as Sr (Zartman and Kwak 1993a, p. 1), although a direct comparison between the isotopic compositions of water beneath Yucca Mountain and the carbonate deposits has not been attempted because of the very low Pb concentrations of water from springs (less than 1 ppb) (Table 4.4-4) and the high probability of contamination during sampling. The contamination problems are severe, even when sampling slightly enriched (1 to 5 ppb) groundwaters (Gulson 1986), and at Yucca Mountain, water is several hundreds of meters below the surface. There is no adequate way to evaluate the potential contamination problems that may have developed from the drilling equipment and fluids or the sampling equipment. Even carefully cleaned tubing hundreds of meters long could contain more Pb than the sampled water. This may explain the anomalously large Pb concentrations found in water from two wells (Table 4.4-4).

The Pb in the calcite silica deposits has two isotopically distinguishable fractions (Zartman and Kwak 1993a, p. 1, 1993b, p. 1953). The carbonate fraction of Pb can be leached from the sample with dilute (0.8 N) acetic acid. This Pb is much more radiogenic ($^{206}Pb/^{204}Pb$ = 18.11-20.21 and $^{208}Pb/^{204}Pb$ = 38.60–39.34) than that in the wall rock ($^{206}Pb/^{204}Pb$ = 18.12-18.35 and $^{208}Pb/^{204}Pb$ = 38.74–39.20) that hosts the carbonate vein deposits (Zartman and Kwak 1993a, p. 1), and, consequently, more radiogenic than that expected for water within the Cenozoic rocks. The silicate Pb, which remains after removal of the carbonate Pb, is very similar isotopically ($^{206}Pb/^{204}Pb$ = 18.09–18.84 and $^{208}Pb/^{204}Pb$ = 38.51–39.16) to that in the Miocene volcanic rocks (Zartman and Kwak 1993a, p. 1). The carbonate Pb in pedogenic samples is also distinctly radiogenic, thereby suggesting a genetic relationships between the vein and pedogenic

carbonates. The ultimate source of this radiogenic component is not known; two samples of eolian dust lack this radiogenic component. Locally, unmetamorphosed limestones and dolomites contain radiogenic Pb (Zartman and Kwak 1993b, Table 1) as would the Precambrian crystalline rocks to the west. Thus, as with the Sr isotopic data, a change in the eolian component of the pedogenic carbonates as a function of time is required in order to match the observed data.

Groundwater in southern Nevada typically exhibits $^{234}U/^{238}U$ greater than 2.0 for samples from both the Paleozoic and the Tertiary/Quaternary aquifers (Osmond and Cowart 1982, Figure 9.12; Ludwig et al. 1993, Figure 2), but vein and soil calcites at Trench 14 and Busted Butte were largely deposited by waters with a $^{234}U/^{238}U$ less than 1.5 (Figure 4.4-14). The difference between water and initial vein compositions is even more pronounced in the vicinity of Yucca Mountain, where three samples from the Tertiary/Quaternary aquifer have values greater than 5.0, and one sample from the Paleozoic aquifer is 2.71 ± 0.09. The two analyzed vein samples have initial $^{234}U/^{238}U$ less than 1.4 (Stuckless et al. 1991, p. 553). Thus, the veins and groundwaters cannot be genetically related. In contrast, the initial $^{234}U/^{238}U$ for soils of the Yucca Mountain area is generally less than 1.40 with only one value out of 132 as high as 1.6 (Rosholt et al. 1985, Table 2). These values agree well with those observed for the Trench 14 carbonate veins, and therefore support a pedogenic origin for the fault infillings.

The record from Devils Hole can again be used to evaluate the variability of the $^{234}U/^{238}U$ during the past 300 k.y. The ratio in Devils Hole calcites has ranged from 2.65 to 2.85 (Figure 4.4-15). If a similar variability has occurred in waters beneath Yucca Mountain, the veins at Busted Butte and Trench 14 cannot have been precipitated from either of the regional aquifers.

4.4.5.1.7 Paleontological Data

Taylor and Huckins (1995, p. 18) note that the calcareous deposit at Trench 14 is devoid of fossil ostracodes or other aquatic life forms. Eight samples of soil and vein carbonate were taken from the Trench 14 area to determine if calcareous microfossils were present. No ostracodes or other aquatic animals, such as mollusks, were found. The absence of such fossils implies that the carbonate veins were not deposited in an environment that was saturated with water for periods longer than about 1 mo., which is roughly the time needed for the animals' life cycle. Ostracodes are common in oxygenated hydrologic environments of southern Nevada today, including lacustrine settings, perched springs, and discharge points for the regional aquifers, with a wide range of temperatures (Forester 1991, p. 187). Quade et al. (1995, p. 214) report abundant fossils at paleodischarge sites in the southern Great Basin.

Vaniman et al. (1994, p. 14) note that pedogenic calcretes lack aquatic fossil assemblages but typically contain delicate filaments that are not preserved in fossil spring deposits. These are remains of bacteria and fungus that are flushed out by water fluxes typical of seeps or springs, and would certainly not be preserved in the high-energy environment proposed by Szymanski (1987, 1989) for Trench 14 veins. Extremely fine, needle-fiber calcites and filaments are common at Trench 14 in oldest through youngest material, suggesting that the entire deposit is pedogenic.

Eleven soil and vein samples were collected from the Trench 14 area to look for chrysophyte cysts (the resting stage of certain forms of freshwater algae) (YMP 1993, p.34). Rare cysts were found in two vein samples. In the modern environment, cysts are far more common in places where dilute surface waters are entering the hydrologic system (recharge areas) than in places where relatively concentrated groundwater is emerging (discharge areas). In fact, modern chrysophyte cysts have been found in modern mud at the bottom of Trench 1 on the crest of Yucca Mountain. Taken together, the two types of paleontological data argue against any type of spring environment for deposition of the Trench 14 calcite and opaline silica veins; therefore, the data are consistent with a pedogenic depositional mode for the veins.

4.4.5.1.8 Possibility of Perched Water

The isotopic data are not particularly useful in evaluating a possible perched spring origin for the Trench 14 deposits, because isotopic data are not available for perched waters. However, geologic and paleontologic data suggest that a perched origin is highly unlikely. Perched water occurs above aquitards such as air-fall tuffs (Winograd and Thordarson 1975, p. C50) or nonwelded and unfractured tuffs (Waddell et al. 1984, p. 18). Such aquitards are more than 100 m (328 ft) deep in the vicinity of Exile Hill, and the veins pinch out along the fault contact with the welded tuff at Trench 14, which is highly fractured and very permeable. Perched springs today support ostracodes and other biologic forms that should leave a fossil record, and, as noted above, no such fossils have been found. These facts and the relatively small catchment area upgradient from Trench 14 argue against a perched spring origin for the Trench 14 vein deposits.

4.4.5.1.9 Data Pertaining to a Hypogene Origin

Hill et al. (1995) have recently asserted that much of the data available for the calcite/opal deposits can be explained by the upwelling of warm, CO_2-rich water along faults. Once these waters reach the surface, they are postulated to flow downhill, acquiring a pedogenic character and depositing the slope-parallel deposits. In a critique of this hypothesis, Stuckless et al. (1998, p. 70) conclude that "the paper contains several misstatements of fact, some important omissions of pertinent and readily available information, and some misleading generalizations that together bias the reader toward the erroneous conclusion that the hypogene model remains viable." There are no recent results that suggest that the fracture-filling and slope-parallel deposits are other than pedogenic in origin.

4.4.5.1.10 National Academy of Sciences and National Research Council Findings

The National Academy of Sciences and the National Research Council were requested by the DOE to evaluate whether the water table had been raised in the geologically recent past to the level of the potential repository, and whether a water table rise was likely to occur over the proposed life of the repository in the manner proposed by Szymanski (1989). A panel, established by the National Academy of Sciences and the National Research Council for this purpose, reviewed the pertinent literature and available data, consulted with scientists involved in field and laboratory studies, and spent several days in the field visiting the sites of calcite-silica deposits. The overall conclusion (National Research Council 1992, p. 3) was that none of the

evidence cited as proof of groundwater upwelling in and around Yucca Mountain could reasonably be attributed to that process. Further, the panel stated,

> The preponderance of features ascribed to ascending water clearly were related to the much older (13-10 Ma) volcanic eruptive processes that produced the rocks (ashflow tuffs) in which the features appear, contained contradictions or inconsistencies that made an upwelling groundwater origin geologically impossible or unreasonable, or were classic examples of arid soil characteristics recognized world wide. (National Research Council 1992, p. 130)

Based on physical and textural evidence from the veins in the trenches, the panel concluded that a sedimentary, low-temperature origin from descending meteoric water was supported rather than an origin involving upwelling of thermal water from deep within the crust. In addition, the panel concluded "that to date the preponderance of evidence supports the view that the calcretes and other secondary carbonates in veins of the area formed from meteoric water and surface processes" (National Research Council 1992, p. 56).

The panel added its own field observations to the database. It observed that at Busted Butte, slope-parallel deposits are thinner downslope from the vertical fracture fillings than the slope-parallel deposits above the fracture and that delicately calcified roots of plants are found wrapped around cobbles of volcanic rocks. Both observations are deemed inconsistent with formation by upwelling water. Formation of these slope-parallel deposits by upwelling water from the vertical fracture would thus require that the water flow upslope in greater quantity than downslope. Upwelling water would also be expected to flow over the land surface and form deposits at the land surface rather than specifically in the root zone. Both observations are consistent with the soil and vein carbonates forming from normal arid climate soil-forming processes.

Occurrence of mosaic breccias at Yucca Mountain and Busted Butte has been suggested as support for upwelling of pressurized groundwater. These breccias consist of angular fragments of local bedrock encased in a matrix of calcite and opaline silica. These rocks have been interpreted as forming either as a result of large and fast buildups and releases of fluid pressure or rapid downslope sliding of bedrock, with simultaneous infilling of spaces between the fragments by minerals precipitated from upwelling deep-seated fluid. Based on the field evidence, the National Academy of Sciences panel disagreed with both interpretations . Three types of breccia were noted: talus breccia, fault breccia, and small pipe-like structures with breccia cemented in them. The panel concluded that the carbonate cementing the talus breccia was deposited by evaporating rain water, progressively and simultaneously with accumulation of the talus deposit. Based on grain size, structural characteristics, and the presence of older detrital zircons, the carbonate cementing the fault breccia was concluded to be of pedogenic or surface origin,. The most likely origin of the small, irregular, breccia-filled pipes in the Topopah Spring Tuff was thought to be channeling of steam and of the volatiles degassing during the cooling of the ash-flow tuff. As a final note, the panel concluded that there was no good evidence in support of upwelling deep hot water to account for the brecciation or the silica-carbonate cementation.

The panel also evaluated the theoretical basis for the model of upwelling water. They considered the experience of historical earthquakes and the results of different types of modeling of

earthquake responses. Credible assumptions and various types of modeling indicate that the seismic pumping mechanism is inadequate to raise the water table more than tens of meters and that significant water table excursions to the design level of the potential repository are unlikely. With regard to a heat source to drive upwelling water, the panel noted that the geologic record indicates that during the lifetime of the potential repository, a low-volume basaltic intrusion is the only likely style of intrusion in the Yucca Mountain area. The panel concluded that the elastic effect of dike intrusion would result in raising the water table no more than a few tens of meters.

4.4.5.2 Petrography, Mineralogy, and Chemistry of Tertiary and Quaternary Surface Deposits

The mineralogic, petrologic, and geochemical features of Tertiary and Quaternary surface deposits are illustrated in this section by comparing B horizons and soil calcretes with spring deposits. Some relevant information on plant roots and their impact on surficial-deposit development at Yucca Mountain is included because of the important mineralogic, geochemical, and fossil aspects of plant development within Yucca Mountain soil deposits. This information also has significant bearing on the distinction between pedogenic and spring deposits.

4.4.5.2.1 Petrography of Calcretes, B Soil Horizons, Plant Roots, and Spring Deposits

Petrography of Calcretes, Soils, and Plant Roots–The petrographic data collected on calcretes from Exile Hill include thin-section and backscattered-electron-scanning-electron microscopy analysis of grain size, texture, density, and fossil structures. These data are summarized in Vaniman, Chipera, and Bish (1995). Petrographic analysis permits mapping of five general types of laminae within the siliceous calcretes. The list below is arranged in order from laminae with most detritus to laminae with essentially no detritus. The laminae can be found in both the vein-like and slope-parallel deposits, but are best developed in the veins. An example of a calcrete, vein-like deposit containing all of these lamina types is shown on Figure 4.4-7.

- **Porous and Friable Ooidal Laminae**–These laminae contain abundant ooids and pellets. Ooids consist of single detrital grains or fragments of recycled calcrete enveloped by concentric layers of calcite and opal, often with some sepiolite. (It should be noted that in these calcretes, the structure of authigenic mineral rims around ooid cores is always concentric, never radial.) Pellets are composite grains of either single or multiple detrital or calcrete fragments encased in fine-grained calcite and opal without internal structure. Pellets are generally larger than ooids (pellets; 70 μm to 1 mm (0.04 in.), average 520 ± 610 μm: ooids; 50 μm to 1 mm (0.04 in.), average 200 ± 160 μm). The abundance of inherited rock and mineral fragments in both ooids and pellets gives these laminae a large component of detritus (for typical examples, 3 to 31 percent, average 14 percent detritus).

  Within this classification is a relatively rare set of laminae in the vein calcretes that stand out in exposures because they are dark in color. These laminae are largely vertical and, although discontinuous, seldom have low-angle crosscutting orientations. The dark color of these laminae is due, in part, to their relatively abundant basaltic ash. However, the bulk of the detritus in these laminae is derived from tuffaceous rocks. Modal

analysis of one such lamina shows 48 percent tuffaceous detritus, 4 percent basaltic ash, and 48 percent authigenic calcite plus silica. This analysis is in good agreement with the results of quantitative x-ray diffraction of this lamina indicating 54 percent detritus (percent by weight). Although detritus-rich, the ooid forms in these ash-bearing laminae have thin and poorly developed rinds of authigenic minerals, indicating either young or arrested authigenic mineralization.

- **Root-Rich, Friable Laminae**–These laminae are weakly consolidated, porous, and contain abundant root fossils. The root fossils in these laminae are generally about 1 mm in diameter or less; coarser root features are not preserved. The characteristic root fossil in these laminae is an opalized root sheath, preserving the cell structure of the root wall (rhizoderm). The interior cells (the cortical parenchyma) are not fossilized, leaving a void that is typically lined by calcified filaments (hollow tubules about 5 μm in diameter and tens of μm long, made up of small, equant, subhedral to euhedral calcite crystals less than 1 μm in size). Within this lining of calcified filaments, the void left by the cortical parenchyma contains extremely delicate splays of needle-fiber calcites. Descriptive references for the terms listed above can be found in Jaillard et al. (1991) (root structure) and in Klappa (1979, p. 966), Phillips and Self (1987), Wright, V.P. (1986, 1989), and Vaniman, Chipera et al. (1994) (calcified filaments and needle-fiber calcites). Calcified filaments are common in pedogenic calcretes, where they may be formed by a number of microorganisms or by calcite precipitation around root hairs (Klappa 1979, Table 1). The small diameters and hyphae-like morphology of the calcified filaments, and the demonstration of calcite precipitation by soil fungi in culture experiments (Monger et al. 1991), support a fungal origin for these features. Needle-fiber calcite has been described from a number of pedogenic environments and attributed to calcification of fungal hyphae within decaying roots (Phillips and Self 1987; Wright, V.P. 1986, 1989). Also found within some of the root casts are extremely delicate acicular microcrystals, tapering from about 0.5 μm at their bases to narrow points (Vaniman, Chipera et al. 1994, Figure 2). This fossil form can develop within fungal hyphae and consists of either calcite or calcium-oxalate crystals (Klappa 1979, pp. 957, 960; Simkiss and Wilbur 1989). The root-rich, friable calcrete laminae have variable amounts of rock and mineral fragments, giving them a range of detrital-mineral content (detritus, 0 to 13 percent, average 5 percent).

- **Dense and Resistant Laminae**–These laminae often show evidence of shearing within the vein calcretes. They consist of densely intergrown, fine-grained (less than 5 μm) calcite plus opal; they constitute the hardest component in the calcretes, appearing dense in hand sample with vitreous luster and brown to white color. Evidence of shearing is best seen in thin section as a sigmoidal fabric within some of the dense laminae. These dense laminae also commonly contain root fossils, like the root-rich, friable laminae that are much softer (see above). However, the root fossils within the dense laminae include the delicately opalized roots described above, with calcified filaments and needle-fiber calcites in dense laminae that are unsheared, and root fossils in which the cells of the cortical parenchyma are sometimes outlined by opal (and/or sepiolite) and often filled by calcite crystals. Other root fossil forms include relicts of calcareous fossilization in which the root fossil and its surroundings have been opalized. As in the root-rich, friable laminae described above, root fossils larger than about 1 mm are not preserved.

The dense and resistant laminae generally have few detrital rock or mineral grains (detritus, 0 to 9 percent, average 2 percent).

- **Rare Sepiolite-Plus-Calcite Laminae**–Although rare, these laminae can be found, but are only well developed in the vein-like deposits. Sepiolite, a chain-structure clay mineral [$Mg_4(Si_2O_5)_3(OH)_2\ 6H_2O$], is common in all of the laminae described above but only in abundances less than about 5 percent. There are rare, discontinuous laminae with higher sepiolite concentrations and one sample block from the south wall of Trench 14 in which a late-formed lamina of intergrown calcite-plus-sepiolite drapes earlier laminae in a small-scale unconformity.

- **Laminae of Pure Opal**–Pure opaline laminae are discontinuous and thin. They occur within fractures, particularly in the vein calcretes. They provide the only authigenic minerals that can readily be separated from other authigenic minerals in the calcretes; the other common authigenic minerals (calcite and sepiolite) are too fine grained and too intimately intergrown to be separated. In all other laminae, the opal is also too intimately intergrown with fine grained calcite to be separated. In contrast, the pure opaline laminae may be a few millimeters wide and several centimeters long. Most of these laminae occur in open fractures and have a botryoidal surface morphology, indicating precipitation against one wall of the fracture and outward growth into the fracture void. Both opal-A and opal-CT can occur as pure laminae; these laminae often contain no detectable detritus.

In addition to the petrographic analysis of calcrete laminae, thin-section and/or scanning electron microscope studies were made of the overlying B-soil horizons and of plant roots from some of the species currently growing at Exile Hill (creosote bush, *Larrea divaricata*; Mormon tea or Nevada joint fur, *Ephedra nevadensis*; and desert thorn or twin fruit, *Menodora spinescens*) and some that have been inferred to have grown in the vicinity under past pluvial climates (piñon, *Pinus monophylla*; juniper, *Juniperus osteosperma*). Further discussion of these and other plants, with their relevance to the calcretes at Exile Hill, can be found in Quade and Cerling (1990, p. 1550).

In the B-horizon soils, weathered detrital grains are abundant and include both vitric and devitrified tuff fragments, as well as mineral fragments of quartz, tridymite, cristobalite, alkali feldspars, biotite, pyroxenes, amphiboles, iron-titanium-oxide minerals, sphene, and zircon. Smectite with weathered mica remnants is common; opal is seldom visible but can be seen associated with calcite in deposits that coat the undersides of pebbles. Rare occurrences of gypsum and halite are associated with decayed roots. In the lower (2Btj) horizon at Trench 14, above the calcrete, opalized root fossils occur with a form similar to those that occur in the underlying root-rich, friable laminae of the calcretes.

The petrographic observations on roots from living plants are limited; most of the plant solids are amorphous, and although whewellite ($CaC_2O_4 \bullet 2H_2O$) occurs as a mineral in all of the roots studied, it is seldom visible as discrete crystals. The sole exception is in the roots of the creosote bush, where whewellite can be seen as equant crystals (Figure 4.4-16).

Petrography of Spring Deposits–Spring deposits of the Amargosa Valley and Death Valley, as well as calcified plant material from a paleo-seep at Crater Flat, were studied for comparison with

the Exile Hill soil deposits. The vein deposits and tufa mounds associated with spring activity are laminated, but the laminae are markedly different from those observed in the calcretes. Laminated vein deposits at spring localities typically include millimeter-scale or finer bands that represent growth bands within splays of calcite crystals that radiate from the fracture walls toward the vein center (Figure 4.4-17). Alternations in texture, crystal size, and morphology typically parallel the fracture walls. Massed growths of fibrous calcites are common, although in some veins individual crystal sizes range up to 1 cm (0.4 in.) or more. The laminae in tufa mounds are developed without the fine-growth banding seen in the veins but contain, instead, a variety of fine-grained calcite textures. Most spring deposits contain fossil remnants of a wide range of organisms, ranging from bacteria and algae to encrusted remains of vascular plants (Pentecost 1992, pp. 161 to 164). Common in the surface deposits of springs in the vicinity of Yucca Mountain are bacterial clumps and ostracode shells (Figure 4.4-18). Chafetz and Folk (1984, pp. 304 to 305) identified bacterial clumps (brownish spots included within single crystals or aggregates of sparry calcite, 10 to 60 μm in diameter) as the elementary building blocks of travertines. Such features are typical of spring mounds in the vicinity of Yucca Mountain but not of the calcretes and B-horizon soils at Exile Hill.

The fossilized remains of vascular plants in spring deposits of the Yucca Mountain vicinity are particularly important, because they contrast markedly with those found in the calcretes at Exile Hill (Figure 4.4-6). Root fossils are typical of the Exile Hill calcretes, with common preservation of calcified filaments and needle-fiber calcites. In contrast, plant remains associated with spring discharge in the region are dominated by calcite casts that have formed around the stems of plants, preserving none of the cell structure and lacking the delicate filaments and needle-fibers that are characteristic of the calcretes. Indicative of standing water between and within the fossilized plant remains are meniscal septae, formed by small calcite crystals that formed by precipitation at the water-air interface. A root fossil from the paleo-seep at Site 199 has complete calcite replacement of the root form with poor preservation of cellular structure but with abundant bacterial clumps. Features like this are not found in the calcretes and B-soil horizons at Exile Hill.

4.4.5.2.2 Mineralogy of Soils, Eolian Deposits, and Relevant Playa, Seep, and Spring Deposits

Mineralogy of Calcretes, Soils, Seeps, and Springs–Calcretes at the surface of Yucca Mountain represent the most extensive near-surface authigenic mineralization. The only pure mineral separates obtained from the calcretes have been of opal, from the opaline laminae as mapped on Figure 4.4-7. Large opaline root fossils have also been collected from sand ramps east of Exile Hill (Vaniman, Bish, and Chipera 1988, Figure 22). In all other calcrete laminae, calcite and opal, or calcite and sepiolite, are closely intergrown. Calcite crystals are small; most (more than 95 percent) are less than 5 μm. Attempts to obtain pure calcite separates by crushing and density separation have failed because of intimate intergrowth with other minerals. Sepiolite is locally abundant (about 40 percent) in only a few laminae (Figure 4.4-7); the overall abundance of sepiolite and amorphous iron-, manganese-, titanium-oxides is less than 1 percent. Smectites and weathered micas are abundant in the overlying B horizons, but these phyllosilicates are of mostly eolian origin. Rare evaporite minerals (gypsum and halite) have been found in association with decayed roots in a B-soil horizon.

Calcite Compositional Ranges–Calcite is the most abundant authigenic mineral in the calcretes. Calcite contents of the calcretes, determined by quantitative x-ray diffraction, range from 26 to

70 percent for individual laminae (with the exception of ash-bearing laminae containing only 17 percent calcite and pure opaline laminae containing no calcite). Averages representing multiple laminae (bulk or channel samples) contain 47 to 59 percent calcite. There are no pure-calcite laminae and, as noted above, the fine-grain size and intimate intergrowth of calcite with other minerals made separation and concentration of calcite impractical. Contrasted with its abundance in the calcretes, calcite is only a rare constituent of the overlying B horizons. Calcite can be seen in hand sample and in thin section in Btk horizons as fine-grained coatings on the undersides of pebbles, where the calcite is commonly associated with opal.

Although chemical compositions of pure calcite in the calcretes could not be determined on mineral separates, some calcites in thin section are large enough (greater than 10 μm) to permit electron-microprobe analysis. Calcite analyses from the calcrete are listed in Table 4.4-5, along with calcite and dolomite analyses from the seep at Site 199 and calcite analyses from several springs. The seep locality in particular is exceptionally Mg rich, with an association of high-Mg calcite and dolomite. In general, spring deposits have higher-Mg calcite than the calcretes (Vaniman, Chipera, and Bish 1995, Table 4, Figure 22). Electron microprobe analyses of 20 calcrete calcites from Trench 14 indicate a lack of any calcites with MgO greater than 1 percent. This result contrasts with the calcites from seeps and springs. Although calcites from seeps and springs may have such low MgO contents, generally their MgO contents are higher (Table 4.4-5). The generally higher MgO content of most spring calcites sampled is in accord with the minor occurrence of dolomite along with calcite in several samples from Travertine Point veins and from an active spring mound at Nevares.

Calcite is the only significant reservoir for Ca and Sr in the calcretes; even though calcite could not be separated for analysis, the chemical and quantitative x-ray diffraction data for the calcretes can be used to plot Sr against either percent CaO (with 56 percent CaO representing ideal calcite) or against the x-ray-diffraction-determined percent calcite to estimate the range of Sr content in calcites of the calcretes. The calculated range of Sr content in calcrete calcite is from about 800 to 2,100 μg/g (ppm) (Vaniman, Chipera, and Bish 1995, p. 20). Comparable Sr contents are found in the Site 199 seep calcites and in the spring deposits (Table 4.4-5). The coarsest calcite observed in the calcretes, anhedral crystals of up to about 60 μm intergrown in open voids, has no detectable Sr in electron microprobe analysis (Table 4.4-5), although the calculation discussed above indicates that the more typical, fine-grained calcrete calcites should have SrO content ranging from about 0.09 to 0.25 percent. It is worth noting that the highest SrO content observed in any sample are in ostracode fossils from the spring mound at Nevares (Sample 760,t1a) (Table 4.4-5).

Opal Compositions–The Yucca Mountain calcretes are siliceous, containing variable amounts of opaline silica. The opal forms in these deposits include both opal-A (amorphous silica) and opal-CT (largely amorphous, but with both cristobalite-like and tridymite-like stacking). Opal contents of individual calcrete laminae range from 0 to 57 percent (with the exception of about 100 percent pure opaline laminae). Averages representing multiple laminae (bulk or channel samples) contain 31 to 42 percent opal. As in the calcretes, both opal-A and opal-CT are found in spring deposits. However, the opal-A that occurs in springs is generally in algal mats near active discharge zones. Small veins of opal-CT occur in older, inactive portions of some springs, sometimes as massive white nodules of vitreous luster, often several centimeters in diameter. A notable distinction from the calcrete silica deposits is the occurrence of masses or bands of authigenic quartz, which has not been found in any calcrete deposits.

Sepiolite–Sepiolite is ubiquitous in the calcretes but reaches significant abundance (up to 39 percent) only in rare laminae, where sepiolite is intergrown with calcite in pods several millimeters long. Elsewhere in the calcretes, sepiolite can occur within ooid rims, as a component of fossilized roots, as small fibrous deposits, or as clasts reworked into later-formed calcretes. The abundances of sepiolite in individual laminae containing these other occurrences do not exceed 5 percent. Sepiolite has not been found in the B-horizon soil samples. Vaniman, Chipera, and Bish (1995, pp. 21 to 23) find that there is a range of sepiolite compositions in the calcretes. The ideal sepiolite formula is $Mg_4(Si_2O_5)_3 \bullet (OH)_2 \bullet 6(H_2O)$, or $4MgO + 6SiO_2 + 7H_2O$. The data from calcretes show some substitution of Al for Si, plus substitution of Al, Fe, Ca, Na, and/or K for Mg.

Amorphous Iron-, Manganese-, Titanium-Oxides–Voids in the calcretes and B-horizon soils at Yucca Mountain may contain fillings or linings of amorphous iron-, manganese-, titanium-oxides. These deposits are a minor constituent of the vein calcretes (generally less than 1 percent), but because of their often high Fe content, they can be a significant reservoir for Fe and associated elements (especially Sc). The possibility of some crystallinity within these features cannot be ruled out, but the compositions of these metal-rich deposits are highly variable, suggesting largely amorphous composition or a fine-grained mixture of poorly crystalline phases (Vaniman, Chipera, and Bish 1995, pp. 23 to 24). Electron-microprobe data analyses suggest some intergrowth of calcite and opal with these oxide deposits, as well as intermixtures of lesser amounts of Mg and Al, particularly within the more Mn-rich deposits. In some instances, these deposits appear to fill root-fossil voids; in other instances, they line cavities or fractures of inorganic origin in the calcretes. Electron-microprobe analyses separate these opaque deposits into three types: Fe-rich deposits with minor amounts of Mg; Ti-rich deposits with minor amounts of Al; and complex Mn-rich deposits with appreciable amounts of Si, Al, and Mg. Energy-dispersive spectra of some Fe-rich amorphous deposits indicate minor amounts of sulfur, Cu, zinc, and perhaps Ni. These are many of the same elements that are highly elevated in the root-ash samples.

Smectite and Illite–Smectites vary widely in abundance (about 1 to 34 percent) in the Yucca Mountain calcretes. X-ray diffraction analyses of the separated smectites indicate poor crystallinity. What appears as a well-crystallized illitic component in the 1- to -3-μm fraction is generally much degraded in the less-than-0.35-μm fraction (Vaniman, Chipera, and Bish 1995, p. 24, Figure 20). This poorer crystallinity with finer grain size, plus the exceptionally Fe-rich composition of the finest (less-than-0.35 μm) clay fraction (more than 5 percent FeO), indicate that the illitic component is, in fact, largely due to degradation of detrital biotite (Vaniman, Chipera, and Bish 1995, p. 24). Much of the clay may be eolian. Long-range eolian transport is especially effective at size ranges of about 2 to 40 μm (Junge 1979, pp. 52 to 56).

The clay minerals in the spring deposits often include a well-crystallized illite component, unlike the B-horizon soils and calcretes at Exile Hill where the clays consist of smectite, sepiolite, and an illitic component that appears to be predominantly a degradation product of detrital biotite.

Other Minerals in Yucca Mountain Soils–The only other authigenic minerals yet found associated with B-horizon soils or calcretes at Yucca Mountain are whewellite, gypsum, and halite. Gypsum and halite are rare; they are found in trace amounts in the B-horizon soils in association with decaying roots or with deposits in open soil voids. Gypsum occurs within some voids as small, curved crystals resembling the gypsum cave flower forms found in some underground deposits. Whewellite appears to be strictly restricted to occurrences within living roots. Despite this

restriction, whewellite may be a significant contributor of Ca to the near-surface calcite deposits by virtue of many repetitions of root growth and death cycles in the upper 15 m (50 ft) of soil and rock into which roots penetrate (Vaniman and Whelan 1994).

Other Minerals in Spring Deposits–The active deposits at Grapevine Spring include surface efflorescence features that are white, fragile, and have a slightly bitter taste. X-ray diffraction analysis of this efflorescence reveals major amounts of the minerals halite, trona ($Na_3H[CO_3]_2 \bullet 2H_2O$), and thenardite ($Na_2SO_4$), with minor amounts of aphthitalite ($K_3Na\ [SO_4]_2$) and possible burkeite ($Na_6CO_3\ [SO_4]_2$). Halite, trona, and burkeite have also been reported from efflorescence deposits in Oasis Valley (Vaniman et al. 1988, p. 29). With the exception of halite, none of these minerals have yet been identified at Yucca Mountain, and, certainly, no significant deposits comparable to those at Grapevine Spring have been found.

The Paleozoic dolomite of the Roberts Mountain Formation was collected from drill core UE-25 p#1. This sample consists almost entirely of dolomite, with minor calcite and quartz. Deep carbonates with abundant dolomite could be contributors of Mg to the relatively Mg-rich carbonates found in spring deposits of the region.

4.4.5.2.3 Chemistry of Calcretes, B Soil Horizons, Plant Roots, and Spring Deposits

A detailed discussion of the chemical data for calcretes, soils, roots, spring deposits, and seeps can be found in Vaniman, Chipera, and Bish (1995, pp. 29 to 38, 41 to 47). The calcretes that form surface slopes and those within faults (vein calcretes) were analyzed. Included in that report are separate discussions of lanthanide elements, Zr, U, and Fe-Sc, Ca-Sr, and gold-arsenic systematics. In this section, focus is on specific aspects of the chemical data.

Calcium-Strontium Systematics–Strontium contents of calcites in the calcretes could not be measured directly, because pure calcite separates could not be obtained for instrumental neutron activation analysis. The Sr content of the pedogenic calcites can be estimated at about 800 to 2,100 μg/g (ppm) based on comparisons of Sr with Ca data for calcretes and use of quantitative x-ray diffraction data for calcite abundances in the calcrete samples. All other constituents within the calcretes have relatively low Ca contents, with the exception of the ashed-root samples. Strontium contents of calcretes, spring deposits, ashed plant roots, soil materials, and Roberts Mountain Formation dolomite are plotted against CaO on Figure 4.4-19. The ashed-root samples, with the exception of piñon, have a narrow range of Ca compositions. There is exceptionally high Sr in two of the common plants presently found at Exile Hill (boxthorn and creosote bush). The plants that are now absent at Exile Hill but were more common in the past cooler and wetter climates (piñon and juniper) have lower Sr contents in their root ashes and Ca-Sr ratios more similar to the calcretes. If plant life played a significant role in determining the Ca-Sr ratio of calcretes, the data are consistent with stable isotope data that suggest that most of the calcrete was deposited during cooler and wetter conditions (Quade and Cerling 1990, pp. 1550 to 1551). The Ca-Sr ratios for most soil and spring calcites are fairly similar to those for calcretes, but the concentrations of these elements are generally much greater.

Uranium–Uranium is associated with opal in the calcretes and in the B-horizon soil samples (Figure 4.4-20). A pure opal-A lamina from Trench 14 vein calcrete contains 23 μg/g (ppm) U, and a pure opal-CT lamina from the slope calcrete contains 18 μg/g (ppm) U. These contents of U in

opal compare with the lower end of the approximately 0 to 450 μg/g (ppm) range for U in opals from the unsaturated zone at Yucca Mountain (Paces, Marshall et al. 1997, Table D1). Except for the separates of pure opaline laminae, the greatest U contents in the calcretes are typically for laminae that are dense and sheared.

Gold-Arsenic Systematics–The gold and arsenic data discussed in this section were collected by instrumental neutron activation analysis. These data are summarized on Figure 4.4-21. Weiss et al. (1991b) report gold contents determined by graphite furnace-atomic absorption spectrometry and arsenic contents determined by inductively coupled plasma emission spectrometry for large (2 to 10 kg [4.4 to 22 lb.]) samples. Their detection limits for gold (0.20 ng/g [ppb]) are lower than those obtained by instrumental neutron activation analysis (generally more than 0.8 ng/g [ppb]); the detection limits for arsenic by instrumental neutron activation analysis, however, are generally comparable (approximately 0.2 μg/g [ppm]). They are capable, therefore, of reporting measurable gold contents for volcanic rocks with less than 1 ng/g gold (ppb) that are below detection limits in this data set. In this data set, only one tuff sample (an opalized sample of Tiva Canyon Tuff from Trench 14) had measurable gold (12.6 ng/g [ppb]). However, gold was measurable in most of the calcrete samples and can be compared directly with the data of Weiss et al. (1991b). They report a range of 0.5 to 7.3 ng/g (ppb) gold and 4 to 12 μg/g (ppm) arsenic from Trench 14. The arsenic and gold values for calcrete samples cover essentially the same range, although the opaline laminae contain little or no arsenic, and the gold values for most calcrete samples are somewhat higher (2 to 12 ng/g [ppb]). Two particular laminae from the vein calcretes are outliers with respect to gold content: a sepiolite-plus-calcite lamina (15 ng/g [ppb] gold) and a clay-rich, zeolite-rich lamina (29 ng/g [ppb] gold). The absence of such large gold values from the analyses by Weiss et al. (1991b) may be due to the fact that they analyzed large, bulk samples, which diluted the anomalies in small individual calcrete laminae. These relatively large gold values in calcrete laminae, however, are small compared to the contents of most of the root-ash materials, with the exception of the juniper sample and the outer part of the creosote-bush root (Figure 4.4-21). The ashed material of plants is typically enriched in gold relative to the soils in which the plant grows, with greater gold content in the ultrastructure than in the roots (Boyle 1979). In this regard, most of the plants that now exist at Trench 14, and one (piñon) that once existed there, appear to concentrate gold in their root-ash components by moderate amounts (average of approximately 8 times).

Arsenic is sometimes useful as a pathfinder element in gold exploration. Figure 4.4-21 shows considerable arsenic variation and an apparent lack of strong correlation with gold. The ashed-root materials that are strongly gold-enriched have little arsenic. Any correlation of gold with arsenic is weak in the calcretes and nonexistent in the root-ash materials.

Transition Metals and Eolian Contributions–Petrographic, chemical, and x-ray diffraction data indicate an enrichment in the Bt-soil horizons of heavy minerals, principally biotite, amphibole, oxide minerals, and some clinopyroxene (Vaniman, Chipera, and Bish 1995, p. 39). This effect is most notable in the smaller than 45 μm and clay fractions; indeed, the clays are notably Fe-rich (5 percent FeO, compared to less than 1 percent FeO in the bulk tuffs) and may be derived principally from the weathering of mafic minerals. Total concentrations of the heavy minerals are 4 to 6 percent in the smaller than 45 μm size range in B-soil horizons, but these minerals are detectable only in trace amounts in the wall-rock tuffs. Disaggregation of the wall-rock tuffs in surface weathering, with subsequent deflation or slopewash, may remove lighter minerals and leave

the heavier minerals behind. However, a contributing factor in this process may be the addition of mafic eolian minerals.

Both the Bt horizons and the calcretes contain small amounts (less than or equal to 1 percent) of amphibole fragments with characteristic pleochroism (α = light yellow-brown, β = brown, γ = green). These amphiboles occur as small grains, mostly smaller than 45 μm in diameter. The FeO contents of these small amphibole grains are mostly higher than the amphibole compositions that occur in the Tiva Canyon Tuff that is a local source of detritus (Warren, Byers, Broxton et al. 1989). Many of these amphibole fragments may be derived from distant sources and brought to Exile Hill by eolian processes.

If detrital grains, particularly those of silt to clay size, are in part brought to the site by eolian processes, then the mineralogic makeup of those sources may provide constraints on the relative proportions of local and distant contributions. Guthrie, Raymond et al. (1993, Tables 1, 2, 3, 4) have analyzed eolian dusts from four natural dust traps (under boulders, above soil horizons, or from fractures within boulders, above the soil) near Exile Hill. They used x-ray diffraction methods to determine the quantitative mineralogy of the smaller-than-425-μm fractions of these eolian samples and of several size fractions from one of them (Table 4.4-6).

In general, the mineral constituents of these eolian deposits are similar to the corresponding smaller-than-425-μm and smaller-than-45-μm fractions of the Btk-soil and 2Btj-soil horizons (Vaniman, Chipera, and Bish 1995, p. 40). Notable differences, however, are the rarity of tridymite and absence of cristobalite, higher feldspar content, and lower clay content (particularly smectite) in the eolian deposits. These differences may reflect the modifications that occur when local detritus is mixed with the eolian materials. Most important to this discussion, however, is the high content of Fe-rich heavy minerals in the eolian samples (amphibole, biotite, chlorite, and hematite total 3 to 7 percent in the smaller-than-425-μm material and 9 percent in the smaller-than-45-μm material).

Of the Fe-rich minerals common to the Bt-soil horizons and the calcretes, hematite is the most ubiquitous (Vaniman, Chipera, and Bish 1995, p. 41). Electron microprobe data for Fe-Mn and Fe-Ti contents of fine-grained (smaller than 45 μm) hematites from these three rock and soil types are summarized on Figure 4.4-22. The data available show strong similarities between hematites of the Bt-soil horizons and the calcretes but generally lower TiO_2 and higher MnO in the hematites of the local bedrock (Tiva Canyon Tuff). These differences indicate that there is a common source for hematite detritus in both the Bt-soil horizons and the calcretes. Although the data do not prove that the Bt horizon and calcrete hematites are brought in by eolian processes, the foreign compositions of amphiboles and hematites in the Bt horizons and calcretes suggest a large component of eolian input.

The most abundant detrital component of the calcretes, however, is the smaller-than-425-μm fraction that provides almost all of the detrital nuclei for the very common calcrete ooids (detrital nuclei for the ooids average 163 ± 154 μm; only 5 percent are smaller than 45 μm). For this size fraction in the B-soil horizons, Sc/FeO ratios and other chemical signatures align very well with those of the calcretes and with local tuffs (Vaniman, Chipera, and Bish 1995, pp. 32 to 35). In this size range, detritus can be moved as drifting sand but is unlikely to be carried as an aerosol suspension from distant sources (Junge 1979, pp. 52 to 56). Silt-sized and clay-sized material in the B-soil horizons, however, may be partly to largely eolian in origin.

INTENTIONALLY LEFT BLANK

4.5 SITE STRATIGRAPHY

4.5.1 Introduction

Characterizing the stratigraphy of Yucca Mountain is fundamental to site characterization and assessing the performance of the potential geologic repository at Yucca Mountain. The stratigraphy forms the framework for modeling and analyses of rock properties, mineral distributions, faulting, fracturing, hydrologic flow, radionuclide transport, performance assessment, and subsurface repository design. The purpose of this section is to summarize what is known about the stratigraphic features that are important to these models and analyses.

Mid-Tertiary volcanic rocks dominate the exposed stratigraphic sequence at Yucca Mountain. These rocks consist mostly of pyroclastic flow and fallout tephra deposits with minor lava flows and reworked materials (Figure 4.5-1). They were erupted from the southwestern Nevada volcanic field during the period 15.2 to 11.4 Ma (Sawyer, D.A., Fleck et al. 1994) (Section 4.2.3.2). Figure 4.5-2 shows both the location of Yucca Mountain with respect to the southern part of the nested caldera complex that comprises the eruptive source of this extensive volcanic field and the general distribution of the principal stratigraphic units. Regionally, the thick series of volcanic rocks (and older Tertiary rocks, where present) that form Yucca Mountain overlies Paleozoic sedimentary strata along a pronounced unconformity. The Paleozoic strata found in the region are discussed in Section 4.2.2.1.2. The volcanic rocks, in turn, are covered in many areas by a variety of late Tertiary and Quaternary surficial deposits (Section 4.4.5). Detailed descriptions of the Precambrian, Paleozoic, Mesozoic, Cenozoic, Tertiary, and Quaternary stratigraphy have been compiled into the *Yucca Mountain Project Stratigraphic Compendium* (CRWMS M&O 1996e). The compendium also includes information on each borehole in the area, regional and site geologic mapping, borehole geologic logs, available geochronology, and various figures, charts, and graphs related to the stratigraphy in the Yucca Mountain area.

Because of their importance toward understanding of geologic systems at Yucca Mountain, the volcanic rocks have been a major focus of stratigraphic studies being conducted as part of the site characterization program. Summaries of geologic studies in the Yucca Mountain area have been published periodically (e.g., Eckel 1968; USGS 1984; Carr, W.J., et al. 1986; Carr, M.D. and Yount 1988; DOE 1988; Buesch, Nelson et al. 1996), and reports describing the results of specific stratigraphic studies are numerous. In particular, data on the thickness, lateral extent, correlation, and lithologic characteristics of the rocks, in both surface and subsurface settings, were obtained during detailed studies of cores from boreholes at key localities (e.g., Spengler, Byers et al. 1981; Carr, M.D. et al. 1986; Spengler and Chornack 1984; Scott, R.B. and Castellanos 1984). Geologic mapping at a scale of 1:12,000 also provided key information (Scott, R.B. and Bonk 1984). These studies revealed the lateral continuity of the major formations along approximately west-to-east and south-to-north profiles (Figures 4.5-3 and 4.5-4).

In recent years, a large number of boreholes and cores from these boreholes were examined and analyzed, and several surface sections of the volcanic units were measured and described (Figure 4.5-5). These studies provide new lithostratigraphic data that substantially supplement and refine the stratigraphic framework that had been developed during the earlier geological

investigations (e.g., Geslin and Moyer 1995a; Geslin et al. 1995; Moyer and Geslin 1995; Moyer, Geslin, and Buesch 1995; Buesch, Spengler et al. 1996a; Rautman and Engstrom 1996a, 1996b; Buesch and Spengler 1999a, p. 17-14). Much of this work was conducted within what is referred to as the "Central Block of Yucca Mountain." This area is bounded on the west by the Solitario Canyon fault, on the east by the Bow Ridge fault, on the north by Yucca Wash, and on the south by Abandoned Wash (see Day et al. [1998a] for a detailed geologic map of the central block area).

Many investigations of the Yucca Mountain area have focused on lithostratigraphic, hydrogeologic, and thermal-mechanical properties, and each has developed a stratigraphic system (Scott, R.B. and Bonk 1984; Spengler and Fox 1989; Moyer and Geslin 1995; Moyer, Geslin, and Buesch 1995; Buesch, Spengler et al. 1996a; Day et al. 1998a, 1998b; Montazer and Wilson 1984; Flint, L.E. 1998; Ortiz et al. 1985). Tables 4.5-1 and 4.5-2 show how these different stratigraphic systems correlate to each other. Each type of investigation has obtained a wide variety of data that is unique to each discipline, but all have a common foundation in the use of rock properties, such as density and porosity. Therefore, the systems are only semi-independent, with lithostratigraphy often serving as the common framework.

Based on variations of geologic features in the rocks, formations within the Paintbrush Group have been divided into members, members into zones, zones into subzones, and subzones into intervals. Other formations have also been divided into these principal units (Buesch, Spengler et al. 1996a; Moyer and Geslin 1995; Moyer et al. 1996; Sawyer, D.A., Fleck et al. 1994). Separating the sequence into several hierarchical units and subunits has enabled other types of studies that depend upon stratigraphic data to be conducted at scales necessary to achieve their objectives. Examples of these scales include:

- Geologic mapping at relatively small scales (1:6,000 or 1:24,000; Section 4.6) in the site area or at much larger scales (1:2,400 or larger) along some fault zones, on cleared exposures for fracture studies, on walls of excavated trenches, and in the Exploratory Studies Facility (ESF)
- Defining and correlating hydrogeologic and thermal-mechanical units at borehole to mountain scales
- Three-dimensional modeling of rock properties across the site area.

Thus, the system of lithostratigraphic unit identification and nomenclature that has been developed provides a consistent stratigraphic framework that can be applied in other studies.

Six principal results culminate from these lithostratigraphic studies and provide the context for the sections that follow:

- Nineteen formations and interstratified bedded tuffs have been described in detail.
- Identification of lithostratigraphic units is based on changes in depositional features, development of welding and devitrification zones, and, in some rocks, the development of alteration, such as the formation of clay and zeolite minerals.

- The nomenclature and symbols of lithostratigraphic units consist of a systematic and hierarchical structure that enables unit identification and mapping at very detailed to generalized scales.

- The detailed lithostratigraphic system provides a framework within which the vertical and lateral continuity or variation of units can be evaluated, and although some units only occur locally, most are laterally extensive within the site area; therefore, lithostratigraphic units typically have a stratiform geometric shape.

- Rock properties, including density and porosity, are used in identification of lithostratigraphic units, and some of these properties are important in determining hydrogeologic and thermal-mechanical units.

- Lateral correlation of lithostratigraphic units that comprise the hydrogeologic and thermal-mechanical units, especially those units within the Topopah Spring Tuff that form the host rock of the potential repository (lower part of the Tptpul down to the base of the Tptpln [Tables 4.5-2 and 4.7-1]), indicates that the geometric volume and continuity of the rocks are conducive to continued evaluation for a potential repository at Yucca Mountain.

4.5.2 Data Types

A number of different types of information contribute to understanding the site stratigraphy at Yucca Mountain. These data include: stratigraphic, mineralogic, and geochemical analysis of samples from boreholes and underground excavations; geologic mapping; geophysical logs of boreholes; and measured stratigraphic sections. More specific details concerning the use of particular data sets can be found in the references cited in this section.

4.5.3 Criteria for Differentiating Volcanic Rock Units

Three principal criteria were used to differentiate the volcanic rocks at Yucca Mountain:

- Lithology and rock properties
- Mineralogy
- Geophysical log characteristics.

The principal stratigraphic subdivisions at Yucca Mountain and the criteria for differentiation are discussed in Sawyer et al. (1994) and Buesch, Spengler et al. (1996a).

Separation of formations into subunits is based on macroscopic features (degree of welding, glass or devitrified, etc.) of the rocks as they appear in core and outcrop (Buesch, Spengler et al. 1996a, p. 1). Their identification is augmented by quantitative mineralogy (Bish and Chipera 1986; Chipera, Vaniman et al. 1995), borehole geophysics (Muller and Kibler 1984; Nelson, P.H. et al. 1991; Nelson, P.H. 1996; CRWMS M&O 1997d, 1996b), and rock properties, such as density and porosity (e.g., Moyer et al. 1996, pp. 55 to 80; Flint, L.E. 1998).

The Yucca Mountain volcanic sequence is composed primarily of pyroclastic flow deposits (also referred to as ignimbrites or ash flows) with volumetrically small amounts of bedded tephra

deposits and localized lava flows and redeposited material. Most formations, which are shown on Figure 4.5-1 and identified with the three-lettered symbols, have some part that is at least partially welded, and typically some part of the section that has devitrified during cooling of the deposit. Additionally, the vitric (glassy) parts of many formations have been partly altered to clay and zeolite minerals, and all rocks have developed various amounts of fractures resulting from cooling or tectonic activity.

An understanding of the processes that formed and subsequently modified the volcanic units is critical for documenting and interpreting the lithostratigraphic sequence. Volcanic units (as observed today) are the result of primary, secondary, and tertiary processes. This tripartite division of processes represents distinctive segments of the geologic history that occur up to the time of deposition (primary), within the first ten to several hundred years after deposition (secondary), and subsequently hundreds to millions of years after deposition (tertiary). These increments of time result from general limitations deduced from stratigraphic relationships for Yucca Mountain rocks and are constrained by age determinations (Figure 4.5-1), studies of other areas, and numerical modeling of welding and cooling in pyroclastic flow deposits. This division into primary, secondary, and tertiary processes is not entirely exclusive; some processes such as faulting can occur during or shortly after deposition, or local alteration to clays and zeolites can occur during the cooling of a pyroclastic flow deposit (Levy and O'Neil 1989). Ross and Smith (1961) and R.L. Smith (1960a, 1960b) have described general features of ash-flow tuffs or pyroclastic deposits.

At Yucca Mountain, although detailed lithostratigraphic relations may exist locally, the overlap of depositional and zonal features typically results in an internal stratigraphy that is stratiform on regional and subregional scales (Moyer and Geslin 1995; Buesch, Spengler et al. 1996a; Moyer et al. 1996). Zones of welding and crystallization are variously developed in the Rainier Mesa, Tiva Canyon, Yucca Mountain, Pah Canyon, Topopah Spring, Prow Pass, Bullfrog, and Tram tuffs (Figure 4.5-1). Figure 4.5-6 conceptually illustrates how development of depositional features of a simple flow unit and the zones of welding and crystallization can result in a complex lithostratigraphic sequence. In this illustration, depositional features include changes in phenocryst content and abundance of pumice clasts. Welding zones are nonwelded and partially, moderately, and densely welded. Crystallization zones include vitric, devitrified, vapor-phase mineralization, and lithophysal zones. Although this illustration is designed to conceptually show the sequential overprinting of depositional features by welding and crystallization zones, it also represents a simplified rendition of zones in the Tiva Canyon Tuff.

Based on the vertical succession of formations and interstratified deposits, development of the zones of welding and crystallization, and subsequent alteration and fracturing, there are myriad lithostratigraphic units; however, only 23 rock types actually make up Yucca Mountain (Figure 4.5-7). Sixteen rock types are extensive and characteristic of large volumes of rock. Seven rock types are not common, but possibly have local importance to hydrogeologic or thermal-mechanical process modeling. Six rock types occur only locally and do not (at this time) appear to be volumetrically or spatially important to hydrogeologic or thermal-mechanical process modeling.

4.5.3.1 Lithologic and Rock Property Criteria

Division of formations into lithostratigraphic units and their associated symbols was initially proposed by Warren, Sawyer et al. (1989, p. 387) for rocks in the Yucca Mountain area that are a part of the southwestern Nevada volcanic field (e.g., Lipman et al. 1966). Buesch, Spengler et al. (1996a, p. 3, Table 1) extended this terminology in greater detail in the Yucca Mountain area. Several formations in the southwestern Nevada volcanic field have an upper crystal-rich (greater than 10 percent phenocrysts) member and a more voluminous, lower crystal-poor (less than 5 percent phenocrysts) member, with a relatively thin transition in phenocryst abundance between members (Lipman et al. 1966, Figures 4A, 6, 7, 10, 11, 12; Broxton, Warren et al. 1989, pp. 5968 to 5978). In the vicinity of Yucca Mountain, the Tiva Canyon and Topopah Spring tuffs of the Paintbrush Group, which are the most widespread bedrock units in the potential site area, are classic examples of this compositional zonation (Lipman et al. 1966, pp. F2 to F3). This transition in phenocryst abundance is typically 5 to 10 m thick and is included as a crystal transition zone at the base of the crystal-rich member (Buesch, Spengler et al. 1996a, p. 3).

Zones, subzones, and intervals are identified on the basis of textures, structures, and lithic fragments associated with pyroclastic flow and bedded deposits (depositional processes), zones of welding and crystallization (post-depositional processes), and geometry and surface roughness of fractures (mechanical properties of the rock) (Buesch, Spengler et al. 1996a, p. 3). Zones are defined by:

- Vitric versus devitrified pyroclasts
- Occurrence of lithophysae and related light gray rims and spots and amount of pale red-purple groundmass versus the pale brown to light gray groundmass that is typical of nonlithophysal rocks
- Planar versus irregular geometry of fractures and smooth versus rough fracture surfaces.

Subzones and intervals are defined by:

- Surface roughness
- Abundance of pumice clasts
- Amount of welding
- Type of crystallization or alteration of pumice clasts
- Interstratification of thin units with characteristics of adjacent zones or subzones.

Bedded tuff units within the Paintbrush Group (Tpbt1 to Tpbt4, Table 4.5-2) that are not identified with any established formation are arbitrarily placed with the next overlying tuff sequence (i.e., the pre-Tiva Canyon Tuff bedded tuff underlies the Tiva Canyon Tuff). This terminology is consistent with previous usage (Spengler and Rosenbaum 1980, Tables 1 to 4; Diehl, S.F. and Chornack 1990). This nomenclature has been extended to the bedded tuffs that underlie the Calico Hills Formation and Prow Pass Tuff (Moyer and Geslin 1995, Tables 3, 5). The post-Tiva Canyon Tuff bedded tuff (Tpbt5), which is an exception to this arbitrary assignment, is identified only where rocks associated with the rhyolite of Comb Peak (the youngest of the Paintbrush Group) can be identified. Many of the bedded tuffs consist of tuffaceous rocks not correlated with known eruptive units based on detailed tephrostratigraphic

studies, and they commonly are capped by paleosols that separate them from the superjacent rocks.

Individual formations in the volcanic sequence that underlies Yucca Mountain represent either volumetrically significant eruptive units or a series of products interpreted to have formed from compositionally distinct magma batches. Many of the interstratified bedded tuffs and the locally occurring lava flows are distinct from the superjacent and subjacent formations and probably represent small volume eruptions.

Distribution of physical properties, such as bulk density, porosity, and pore size, are controlled largely by variations in grain size and sorting, the abundance of volcanic glass, degree of welding, types and abundance of crystallization, amount and type of alteration to clay or zeolite, and fracture characteristics. Thickness, geometry, and internal heterogeneity of these lithologic components are influenced by the primary processes of eruption and deposition, the secondary processes of cooling and crystallization of lava flows or welding and crystallization of some pyroclastic flow deposits, and the tertiary processes of alteration of glass to clay and zeolites by reaction with aqueous solutions and fracturing or faulting from tectonism. Numerous papers describe how physical properties relate to hydrologic and hydrogeologic properties (Scott, R.B., Spengler et al. 1983, pp. 298 to 311; Montazer and Wilson 1984, Table 1; Flint, L.E. and Flint 1990; Rautman and Flint 1992; Istok et al. 1994; Moyer et al. 1996, pp. 55 to 80; Rautman et al. 1995, pp. 9 to 16; Flint, L.E., Flint, Rautman et al. 1996, p. 6-40; Flint, L.E. 1998). To varying degrees, several of these papers discussed the influence of the primary, secondary, and tertiary processes on hydrogeologic properties, although various authors do not always use this tripartite division or consistent terminology of processes. Several papers describe the relationship of physical properties, primarily porosity, to mechanical properties (Price, R.H., Martin et al. 1993; Brechtel et al. 1995); the correlation of thermal properties to porosity is addressed in CRWMS M&O (2000b) (see Section 4.8.3). Therefore, knowledge of these rock-forming processes provides important tools for estimating and predicting the lateral continuity and heterogeneity of key properties of the stratigraphic, mineralogic, hydrologic, and thermal-mechanical frameworks.

Different eruption types (effusive versus explosive) and transport and deposition mechanisms combine to produce deposits with a range of depositional features. For example, depositional features result from variations in the amounts of components (glass shards, phenocrysts, and clasts of pumice and lithic fragments), their size and shape, and the degree of sorting of grain sizes. Depositional features can change abruptly within millimeters, such as contacts between bedded tephra beds and pyroclastic flow deposits. Other contacts, such as changes in abundance of lithic or pumice clasts within a pyroclastic flow or fallout tephra deposit, can be gradational across decimeters to many meters. Some contacts (e.g., the amount of phenocrysts in the crystal-rich and crystal-poor members of the Tiva Canyon and Topopah Spring tuffs) can have transition zones that are 5 to 10 m (16 to 33 ft) thick. These contacts are identified by a threshold value, such as the decrease down-section to 5 percent (or less) phenocrysts at the top of the crystal-poor member.

Welding occurs in pyroclastic flows and bedded tephra deposits (more rarely) where glass shards and pumice clasts plastically deform as a result of combined deposit thickness (i.e., lithostatic load) and glass viscosity (a function of geochemical composition and temperature)

(Smith, R.L. 1960a, pp. 823 to 826; Smith, R.L. 1960b, p. 151; Ross and Smith 1961, pp. 24, 34). Depositional processes and the ability of interstitial gas to diffuse out of the deposit at low lithostatic pressure can enhance welding in some deposits (Buesch and Valentine 1989). Welding is the process whereby glass particles deform, porosity is reduced, and the geometry and connectivity of pore spaces are restricted. The concomitant increase in bulk rock density with increased welding results from the reduction in pore space with no change in density of the nonporous glass. Matrix density of vitric high-silica rhyolite and quartz latite (or trachyte), which are the two most common compositions in the rocks at Yucca Mountain, is typically 2.35 and 2.40 g/cm^3 (146.7 and 149.8 165 lb./ft^3), respectively. These nonporous glass densities provide a composition-based end member for evaluating the degree of welding determined from bulk rock measurements of core or from geophysical logs. Most rocks at Yucca Mountain contain some phenocrysts and lithic clasts, and most have devitrified during cooling or exhibit some alteration to clay or zeolite minerals. All of these nonglass constituents have different densities. Most of the nonglass constituents are higher in density than glass, with the exception of most clay and zeolite minerals, which have lower densities. Therefore, these constituents will influence the bulk density, porosity, and particle density that are measured or calculated from bulk rock samples.

In their classic papers on welding zones, R.L. Smith (1960b) and Ross and Smith (1961, pp. 33 to 34) divided tuffs into nonwelded, partially welded, and densely welded zones, but provided no quantified measures of the amount of welding in each zone. An attempt to quantify this tripartite division of degree of welding has been based on bulk density and porosity (Sheridan and Ragan 1977) and measurements of the aspect ratios of pumice clasts (Peterson, D.W. 1979, pp. 196 to 199). Vitric rocks have been divided into nonwelded rocks with porosity greater than 45 percent of the total volume, partially welded rocks with 45 to 10 percent porosity, and densely welded rocks with less than 10 percent porosity (Sheridan and Ragan 1977, p. 712).

At Yucca Mountain, rocks are divided into zones of nonwelded, partially welded, moderately welded, and densely welded rock based on macroscopic and microscopic textures (Spengler, Byers et al. 1981, Table 3; Maldonado and Koether 1983, pp. 56 to 83; Scott, R.B. and Castellanos 1984, pp. 94 to 121; Spengler and Chornack 1984, pp. 62 to 77; Moyer and Geslin 1995, Tables 3, 5; Buesch, Spengler et al. 1996a, pp. 9 to 10; Moyer et al. 1996, Table 3). Examples of nonwelded and densely welded zones are shown in Figure 4.5-8. Based on the comparison of macroscopic features and measured porosity in core, these welding zones have approximate ranges of 65 to 45 percent porosity for nonwelded rocks, 45 to 25 percent porosity for partially welded rocks, 25 to 10 percent porosity for moderately welded rocks, and less than 10 percent porosity for densely welded rocks. These ranges, especially the boundaries of partially to moderately welded and nonwelded to partially welded, should not be held as absolute thresholds between the zones because the values for these zone boundaries can vary from 22 to 30 percent and from 40 to 50 percent, respectively. Processes such as incipient crystallization, vapor-phase corrosion and mineralization, and alteration can result in modification of these general thresholds and ranges.

Welded zones are vertically distributed in a simple cooling unit, with nonwelded rocks at the top and bottom and increasingly welded rocks toward the center of the deposit (Smith, R.L. 1960b, pp. 153 to 157). Thick deposits can have the complete welding range, both laterally and vertically, but thin deposits can lack the more welded central parts.

Lithophysal zones occur where vapor concentrates in the densely welded part of ignimbrites to form lithophysal cavities (Ross and Smith 1961, p. 38); lithophysae can also form in lava flows. Lithophysae consist of a cavity, which is commonly coated with vapor-phase minerals on the inner wall, surrounded by a fine-grained zone, which in turn is surrounded by a thin, very fine-grained border (Figure 4.5-9). In the Tiva Canyon and Topopah Spring tuffs, lithophysae typically range in size from 1 to 50 cm (0.4 to 20 in.) in diameter. Surface exposures, borehole videos, and exposures in the ESF locally contain lithophysae with diameters as much as 1 m (3.3 ft); thus, regions of poor core recovery might indicate large lithophysae. Locally, lithophysae can be relatively uniform in size and shape but can also occur locally in a wide range of sizes and shapes within a lithophysal zone. Lithophysae can be nearly spherical, with aspect ratios (length/height) of approximately 1 to 2, or highly oblate, with aspect ratios greater than 10 or 20. Some lithophysae are extremely oblate, with cavities only 1 to 2 mm (0.04 to 0.08 in.) thick and 20 to 40 cm (7.9 to 15.7 in.) long, which results in an aspect ratio of as much as 400. These lithophysae appear to merge with larger features that have no macroscopic aperture, such as stringers and vapor-phase partings observed in the ESF. Rims of lithophysae are as much as 3 cm (1.2 in.) wide. Associated with the lithophysae are light gray to grayish-orange and pink spots 1 to 5 cm (0.4 to 2 in.) in diameter. Some spots may represent the cross sections of rims on lithophysae, whereas others have a crystal or lithic clast in the core that may have acted as a nucleation site.

Lithophysal zones in the Tiva Canyon and Topopah Spring tuffs are identified by a combined occurrence of lithophysae, spots, and fracture characteristics (Figure 4.5-9). Lithophysae shapes, spots, and rim widths can be diagnostic of specific lithophysal zones. Lithophysal zones have fewer fractures than nonlithophysal zones. The fractures are typically irregular in profile and have rough surfaces; a few fractures are high-angle, planar, and smooth. Near the contacts of lithophysal zones and subzones, localization of vapor-phase activity is indicated by an increase of veinlets and streaks in boreholes and cores. In the ESF there are larger features, such as stringers and vapor-phase partings. Within the Yucca Mountain site area, the Yucca Mountain and Pah Canyon tuffs do not contain lithophysae, but lithophysal zones are well developed in adjacent areas where these formations are thickest.

Lithophysae are found in rocks that are densely welded, and infrequently in rocks that are moderately welded, presumably where the vapor phase accumulated at superlithostatic pressure to inflate a cavity and resulting in deformation of the matrix. This deformation must have occurred early in the post-depositional history, while the matrix was still viscous glass and prior to groundmass crystallization. Some lithophysae appear to have formed in pumice clasts, and might have used the slight structural discontinuity of the pumice clast relative to the matrix as an initial point of weakness. There is no direct evidence that minerals forming rims and spots have crystallized from the vapor phase (i.e., the morphology appears completely different from the cavity and fracture coating minerals that are typically interpreted as vapor-phase precipitates). These minerals, however, appear to have crystallized in the presence of vapor that probably diffused into the matrix surrounding the lithophysal cavity or along fractures.

There are few specific matrix-property data concerning lithophysae rims or spots, but these features are very porous and have a lower density than the surrounding groundmass. Partial inclusion of these features in a core sample or as part of the borehole probably creates some of the high variability of properties measured in the lithophysal zones. During the 1980s, the

general practice was to coat the core with water to enhance contrast of features and colors during the photographic sessions. Within minutes, the rims and spots were visibly dried, probably from adsorption, whereas the adjacent groundmass remained wet much longer.

Fumarolic alteration locally produces argillic and possibly zeolitic alteration mineralization, which replaces glass or is deposited interstitially in pore space, sillar textures (nonwelded, incipiently crystallized with possible lithification by vapor-phase mineralization), and oxidation of Fe in glass to form variegated red and orange colors. The most commonly recognized and documented type of fumarolic alteration occurs at localized points or along fractures where the vapor phase is released from the top of a cooling ignimbrite (Fenner 1920, pp. 583 to 585; Smith, R.L. 1960b, p. 157; Ross and Smith 1961, pp. 30 to 31). This geometry of fumarolic alteration differs from that of the vapor-phase zones of corrosion and mineralization, or the vapor-phase zone as described by R.L. Smith (1960b, p. 155). Vapor-phase zones are much more laterally extensive and pervasive, although there can be localized variations in the amount to which this geometry is developed. There is also a difference in source of the vapor phase between the vapor-phase zones and fumaroles. In vapor-phase zones, the vapor phase is derived from the escape of gas that was interstitial to the grains of pyroclasts and lithic clasts, in addition to vapor released during crystallization of the glass. In fumaroles, the vapor phase can be released from the interior parts of the deposit, or can result from the formation of steam as meteoric water percolates downward and encounters the hot, but cooling, parts of the deposit.

Fumarolic alteration and crystallization zones are not common in most Yucca Mountain rocks. However, they occur locally in the crystal-rich, vitric, nonwelded subzone of the Topopah Spring Tuff and the pre-Pah Canyon Tuff bedded tuff (Levy, Norman et al. 1996, pp. 786, 788; Barr et al. 1996; Peterman, Spengler, Singer et al. 1996a; Buesch, Spengler et al. 1996a, p. 19; Buesch and Spengler 1999a, pp. 36, 39) (see Table 4.5-2 for rock descriptions and units). Buesch and Spengler (1999a, p. 39) proposed that during the cooling of the Topopah Spring Tuff there was diffuse, but widespread, fumarolic activity near the paleogeomorphic surface. This interpretation is based on the widespread occurrence of an argillically altered layer (labeled unit C by Moyer et al. [1996, pp. 47, 50]) within the pre-Pah Canyon Tuff bedded tuff observed in borehole cores and at exposures in Solitario Canyon, in Harper Valley in the south-central part of Yucca Mountain (Levy 1993, p. 545), and in the ESF (Barr et al. 1996; Levy, Norman et al. 1996, p. 788; Peterman, Spengler, Singer et al. 1996a). One critical aspect of this fumarolic activity is that it can be very tightly constrained based on lithostratigraphic relations whereby deposits in the uppermost part of the pre-Pah Canyon Tuff bedded tuff (unit D in Moyer et al. 1996, p. 47) and superjacent deposits of the Pah Canyon Tuff and pre-Yucca Mountain Tuff bedded tuffs are not altered.

In most of the formations, contacts between vitric and devitrified boundaries (including zones of vapor-phase corrosion and mineralization) are commonly marked by intervals of several millimeters to several meters that contain clay and/or zeolite alteration minerals. In some of the deeper formations, vitric rocks near this vitric-devitrified contact are pervasively altered to zeolite, but typically there appear to be two alteration stages. The contact between the nonlithophysal zone (Tptpln) and the vitrophyre of the vitric densely welded subzone (Tptplv) in the crystal-poor member of the Topopah Spring Tuff (Table 4.5-2) represents a relatively abrupt contact between high-temperature devitrified rock and underlying glassy rock. However, commonly there is a thin transition interval consisting of well-developed argillic or zeolitic

alteration (Levy 1984a, pp. 27 to 31; Levy 1984b; Levy and O'Neil 1989, p. 322; Chipera, Vaniman et al. 1995, p. 17; Buesch and Spengler 1999a, p. 36). Reexamination of core, cuttings, borehole video, and borehole geophysical logs shows that this alteration interval occurs in most Yucca Mountain site area boreholes, and locally is as much as several meters thick. Levy and O'Neil (1989, p. 325, Table 1) determined that the alteration to clays and zeolites near this contact occurred at a moderate temperature, approximately 40° to 100°C (104° to 212°F), and proposed that this alteration occurred during the cooling phase of the Topopah Spring Tuff. Recognizing that argillic and zeolitic alteration occurred near the crystallization front in many formations, this moderate temperature alteration might be a more common phenomenon than previously thought. The significance of this moderate temperature alteration has not been evaluated for hydrogeologic and thermal-mechanical modeling. Two possible additional locations of this type of alteration in Paintbrush Group rocks include the argillic alteration that is common near the vitric-devitrified contact in the crystal-poor Tiva Canyon Tuff, and the zeolitic alteration that occurs near the vitric-devitrified contact in the crystal-rich Topopah Spring Tuff (quantitative mineralogic data in UZ#16 from Chipera, Vaniman et al. [1995, p. 18]).

4.5.3.2 Mineralogical Criteria

Lithostratigraphic units are also identified on the basis of mineralogy, particularly crystallization and alteration. Five crystallization zones occur in ash-flow tuffs: (1) vitric, (2) high-temperature devitrification, (3) vapor-phase corrosion and crystallization, (4) lithophysal, and (5) fumarolic alteration and crystallization zones (Smith, R.L. 1960b, pp. 155 to 157). Vitric zones occur where the original glassy components remained as glass after the period of high-temperature crystallization and final cooling of the deposit had ended. The clastic texture is typically well defined, except where completely fused in some densely welded rocks. Material less than about 2 mm (0.08 in.) is referred to as matrix.

High-temperature devitrification forms rocks composed mostly of feldspar and silica minerals (quartz, cristobalite, or tridymite) with a variety of minor amounts of other minerals, which texturally form the groundmass that has crystallized within the glass particles. Grain sizes and shapes are typically small (less than 1 mm [0.04 in.]), intricately intergrown, and referred to as microgranophyric. As defined by R.L. Smith (1960b, p. 156), a granophyric zone has grain sizes that are macroscopically identifiable; however, this zone typically occurs only where deposits are very thick, such as intercaldera fill, and therefore has not been an important zone in the outflow facies that form most rocks at Yucca Mountain. Locally, groundmass minerals can have distinctive morphologic forms that are referred to as spherulitic and axiolitic.

R.L. Smith (1960b, p. 155) defined the vapor-phase zone where crystals grow in pore spaces, but detailed work at Yucca Mountain has shown that this zone can be divided into vapor-phase corrosion and vapor-phase mineralization (Buesch and Spengler 1999a, pp. 22 to 24). During initial high-temperature periods, the vapor phase is capable of corroding glass to form a secondary porosity. For example, initially solid glass shards can be corroded to form pores that mimic the shard shapes (Figure 4.5-10). Vapor-phase corrosion enhances porosity by corroding pumice, shards, and interstitial dust, and therefore changes pore-size geometry and distribution. Vapor-phase mineralization occurs as the temperature cools and precipitates minerals such as tridymite or cristobalite, sanidine, and minor amounts of other minerals (Vaniman, Bish, Broxton et al. 1984, Figure 4; Buesch, Spengler et al. 1996a, p. 12). Vapor-phase mineralization also

reduces pore-size geometry and distribution. The balance between vapor-phase corrosion and mineralization results from the vapor-phase gas activity, and locally, either process can dominate the system. Both do not always occur at the same location. The importance of the results of vapor-phase corrosion and mineralization has only recently been recognized (Buesch and Spengler 1999a, pp. 22 to 24) and are currently being documented. Thus the ability to model these processes and their distribution is still preliminary. Pore-size geometry and distribution has an important effect on hydrogeologic and thermal-mechanical properties, but at this stage of understanding the interplay of corrosion and mineralization processes and the results of these processes cannot be predicted.

Analyses of samples from the Yucca Mountain unsaturated zone indicate that smectite, clinoptilolite, and mordenite are the dominant low-temperature alteration products (Bish and Chipera 1989, pp. 12 to 13). The low-temperature alteration potential of any lithologic unit depends on rock composition, rock texture, proximity to structure, and water-rock interaction (Buesch and Spengler 1999a, p. 36). Volcanic glass that crystallized at high temperatures generally is not susceptible to alteration, except under high-temperature hydrothermal conditions. However, high porosity and permeability, whether inherited from the deposition process or induced by fracturing, typically promote alteration of glass because of the high surface area of the particles. As a result of zeolitization, glass shards can be partially or completely replaced, and porosity can be reduced by in-filling with zeolite (Figure 4.5-11). Moderately to densely welded glassy rocks, including the crystal-poor vitrophyre of the Topopah Spring Tuff or obsidian in lava flows, have relatively low porosity and permeability and do not readily alter except along fractures, as observed in some boreholes (see below).

Alteration to clays and zeolites occurs in three fundamentally different lithostratigraphic, structural, and hydrologic settings (Broxton, Bish et al. 1987): two in the unsaturated zone (faults and fractures, and perched water horizons) and one in the saturated zone. Alteration within the unsaturated zone is suspected to be associated with faults, throughgoing fracture systems, and perched water horizons or horizons of lateral flow. One example of the importance of alteration along fractures is illustrated in numerous boreholes where borehole video shows that the crystal-poor, vitric, densely welded subzone of the Topopah Spring Tuff has been significantly altered along high-angle fractures (Levy 1984b, pp. 961, 963). Other sources of clay minerals not described by Broxton, Bish et al. (1987) are several paleosols and beds of redeposited materials, where clays probably result from pedogenic processes. Rocks beneath ancient or present saturated zones can be pervasively altered (Broxton, Bish et al. 1987, p. 104). The contact between vitric to pervasively zeolitized rock in nonwelded tuffaceous rocks occurs at or within a single bed in a few boreholes, but in others the transition can be as much as 30 m (98 ft) thick; the gradational alteration depends on grain size.

4.5.3.3 Geochemical Criteria

In addition to the stratigraphic variations of rock properties discussed above, the volcanic rocks at Yucca Mountain show systematic variations in their chemical and isotopic compositions. Such variations between different ignimbrite sheets are the result of igneous differentiation and assimilation processes in the magma chamber. The differentiation leads to vertical zonations in the chamber and to inverse zonations in the ash-flow sheets as the volcanic eruption proceeds to tap increasingly deeper portions of the magma chamber (Lipman et al. 1966, pp. F2, F41).

Crystallization and vapor-phase activity during cooling may cause redistribution of some elements within individual ignimbrite sheets. Also, percolation of surface water into the rocks can deposit secondary minerals that locally modify the original igneous chemistry.

The results of comprehensive geochemical studies of the volcanic rock sequence at Yucca Mountain are presented in Section 5. Many examples, some in this section and others given in Section 4.5.4, can be cited wherein geochemical stratigraphy supports and augments the stratigraphy derived from detailed outcrop and borehole core studies.

Compositionally, the most important chemical constituents of both vitric and devitrified tuffs are SiO_2 and Al_2O_3. Figure 4.5-12 compares the abundance of these constituents in unaltered representatives of the major rock types, which include high-silica rhyolites (more than 75 percent SiO_2), low-silica rhyolites (72 to 75 percent SiO_2), and quartz-latites (less than 75 percent SiO_2). In summary, the data show that (1) the Calico Hills Formation, Yucca Mountain Tuff, and crystal-poor members of the Tiva Canyon and Topopah Spring tuffs are predominantly high-silica rhyolites; (2) the Crater Flat Group tuffs exhibit a compositional range that falls between high-silica and low-silica rhyolites; (3) the Lithic Ridge and Pah Canyon tuffs consist of low-silica rhyolites; and (4) the crystal-rich members of the Tiva Canyon and Topopah Spring tuffs are largely quartz latites (Figure 4.5-12). In unaltered rock samples, geochemical analyses provide background information that can be used to assess post-depositional alteration processes.

Analyses were also performed to determine the distribution and concentrations of rare earth and trace elements in the various lithostratigraphic units at Yucca Mountain. Variations in these elements, reflecting differences in magma sources and differentiation histories, are likewise useful for stratigraphic correlation and for the identification of altered zones. A series of diagrams (Figures 4.5-13 to 4.5-19) show chondrite-normalized lanthanide patterns for the different rock types that occur within the Crater Flat Group and younger formations. Discussions of these patterns are included in Section 4.5.4.

Often, analyses of rock samples from several different outcrop localities and boreholes in the Yucca Mountain site area show that trace element concentrations vary systematically with stratigraphic position. Based on studies of samples from borehole a#1 (borehole locations are shown on Figure 4.5-5), Peterman, Spengler, Futa et al. (1991, p. 690) determined that the crystal-rich member (Tpcr) (Table 4.5-2) is clearly distinguishable from the crystal-poor member (Tpcp) of the Tiva Canyon Tuff. Rocks in the vitric zone of the Topopah Spring Tuff (Tptpv) have been altered, and this alteration is marked by an increase in Sr concentrations with a corresponding change in Sr isotopic ratios. Spengler and Peterman (1991) discuss the trace element geochemistry of core samples from boreholes G-1 and G-3/GU-3, with emphasis on the volcanic units beneath the Topopah Spring Tuff. Detailed variations of trace elements within the crystal-rich member (Tpcr) of the Tiva Canyon Tuff provide a relatively precise indication of stratigraphic position; Singer et al. (1994) provide an example of this application of geochemical stratigraphy. Peterman and Futa (1996, pp. 6 to 18) summarize the detailed geochemical stratigraphy of the Tiva Canyon Tuff from borehole NRG#3 and compare it to three outcrop sections. Lateral variation in the Tiva Canyon Tuff is evident and a possible fault in borehole NRG#3 was identified (Peterman and Futa 1996, p. 16) based on a missing portion of the geochemical stratigraphic section. Also, geochemical stratigraphy was used to document separation on several strands of the Ghost Dance fault (Taylor, E.M., Menges et al. 1996). To

compare outcrop samples of the deeper volcanic section with the core samples, Peterman, Spengler, Singer et al. (1993, 1996b) provide geochemical and Sr isotope stratigraphy for a large suite of samples from Raven Canyon and Paintbrush Canyon (see Figures 4.5-2 and 4.6-1 for location). These analyses show that the drill core, although sampled below the water table, has geochemical characteristics comparable to the surface samples. In a study designed to evaluate the potential for a large-scale meteoric-hydrothermal system, Marshall et al. (1996) analyzed a large suite of surface samples of the Tiva Canyon Tuff. These samples were analyzed for a larger array of trace elements in order to identify anomalous metal contents and to evaluate the relative mobility of different elements during cooling of the ignimbrite sheet.

Borehole G-1 provides core samples extending from within the Topopah Spring Tuff down through the older Tertiary volcanic section to a total depth of 1,806 m (5,925 ft). As an example of the distribution of relatively immobile trace elements, Zr and Ti concentrations are shown on Figure 4.5-20. Large variations both between formations and within formations are evident; these variations are primarily due to original magmatic compositional variation. Another deep borehole, a#1, shows similar variations in these elements (Figure 4.5-21), confirming the general lateral continuity of the Tertiary volcanic rocks. In this borehole, which extends to younger rocks in the stratigraphic sequence than were penetrated in borehole G-1, the break between the crystal-poor and crystal-rich members of the Topopah Spring Tuff is easily distinguished as the point at which the Zr and Ti abundance begins to increase upsection.

Knowledge of the normal, igneous variations in the geochemistry allows identification of altered zones based on trace element abundance. Unlike Zr and Ti, post-depositional fluid movements and transport of carbonate by infiltrating water more easily mobilize Sr. Even outcrop samples are susceptible to Sr and Ca additions because of the abundant soil carbonate at Yucca Mountain. Zeolitization and clay alteration are evident in the crystal-poor, vitric, densely welded rocks of the Topopah Spring Tuff in borehole a#1. Sr concentrations increase dramatically due to addition of Sr to the rock during alteration (Figure 4.5-22). Peterman, Spengler, Futa et al. (1991, p. 692) calculate water/rock ratios of at least 100 during alteration, assuming that groundwater is the altering fluid.

In borehole NRG#3, Zr, Ba, and Ti increase upsection in the crystal-rich member of the Tiva Canyon Tuff (Figure 4.5-23), whereas Nb and Rb decrease in the same interval (Figure 4.5-24). A striking feature of most of the geochemical profiles is the constancy of concentrations within the crystal-poor members of both the Topopah Spring and Tiva Canyon tuffs. A comparison of the geochemistry of the crystal-rich member of the Tiva Canyon Tuff with that of the crystal-poor member of the Tiva Canyon Tuff in borehole NRG#3 (Figure 4.5-25) shows the general enrichment of compatible elements (Ca, Ti, Sr, Zr, Ba, La, Ce) in the crystal-rich member, consistent with igneous crystal fractionation in the source magma chamber prior to eruption.

Strontium isotopic variations have also been documented in borehole NRG#3 (Figure 4.5-26). Not only have the crystal-rich and crystal-poor members of the Tiva Canyon Tuff evolved to very different isotopic compositions over their 12.7-m.y. history, but calculated initial ratios also vary, indicating that the source magma chamber varied in isotopic composition due to crustal melting processes. These Sr isotope variations provide another stratigraphic criterion that is useful for inferring small amounts of alteration and addition of Sr from infiltrating fluids.

In summary, the geochemical stratigraphy supports and augments the stratigraphy derived from detailed petrography and field characteristics. In some cases, the geochemistry helps to refine stratigraphic picks and can be used to verify small-scale fault offsets. In unaltered samples, the geochemical analyses provide background information that can be used to assess post-depositional alteration processes.

4.5.3.4 Borehole Geophysical Log Criteria

Lithostratigraphic units can be identified based on geophysical log characteristics. Geophysical logs reflect changes in rock properties, and hence lithostratigraphic features, that range from zones 10 to 60 m (33 to 197 ft) thick and defined by relatively consistent attributes to distinctive intervals or beds less than 1 m (3.3 ft) thick. Lithophysal and nonlithophysal zones can be identified from bulk density logs and calculated porosity and water saturation values (Nelson, P.H. 1994; CRWMS M&O 1996b). Many nonlithophysal vapor-phase corroded rocks, such as those near the top and bottom of the Tiva Canyon Tuff and in the upper parts of the Topopah Spring and Prow Pass tuffs (Buesch, Spengler et al. 1996b), can also be identified in this manner.

A suite of borehole geophysical logs was collected from 57 boreholes concentrated in the Central Block of Yucca Mountain, with several located near the site area's bounding edges (Nelson, P.H. 1996, Figure 1; CRWMS M&O 1997d). In most boreholes, the suite commonly includes caliper, gamma ray, density, induction, resistivity, and neutron logs. For a few boreholes, there are magnetic, p- and s-velocity, and borehole gravimeter logs. With the aid of geophysical logs, many lithologic features can be correlated across the potential repository site (Nelson, P.H. et al. 1991; Buesch, Spengler et al. 1996b; CRWMS M&O 1996b). Welding and devitrification or alteration are important geologic controls on log response (Nelson, P.H. et al. 1991), and locally the grain size, sorting, and lithic clast content also can affect log response (Buesch, Spengler et al. 1996b). Increased welding causes matrix density to increase and porosity to decrease. Devitrification increases density, but porosity can remain unchanged, or it can increase or decrease depending on the amount of vapor-phase corrosion or mineralization. Mineral alteration (from clays and zeolites) causes a decrease in resistivity and an increase in neutron absorption, resulting in a high apparent neutron porosity. The magnetic susceptibility and remanence differs between formations, depending on the chemistry of the rock and the earth's magnetic field at the time of eruption and deposition. Additionally, volcanic glass can retain some magnetic properties, but devitrification (because it requires high temperatures and occurs shortly after deposition) forms highly magnetic minerals that typically increase the magnetic field of the rocks. Alteration typically reduces the intensity of many magnetic properties.

In addition to supporting the identification of stratigraphic contacts, borehole geophysical data, along with laboratory measurements and geologic information, also supported the development of a three-dimensional representation of rock properties at the site. This model is discussed in Section 4.8.3.

4.5.3.4.1 Correlation of Lithology and Geophysical Log Response

Boreholes G-3/GU-3 and UZ#16 were continuously cored and, therefore, provide a coherent context for correlating geophysical logs with lithostratigraphic features (Figures 4.5-27 and 4.5-28). Many boreholes, including WT-2, were drilled with techniques that produced only cuttings and no core, but the geophysical logs have signatures indicative of various lithostratigraphic features (Figure 4.5-29). Based on core measurements and a study of geophysical logs from 40 boreholes scattered across the Yucca Mountain area, P.H. Nelson et al. (1991) observed the general relationships listed below between lithologic features and gamma-ray, density, resistivity, and magnetic log responses. These relationships have been reinforced and expanded upon with the addition of calculated porosity values derived from geophysical logs (Nelson, P.H. 1994, 1996) and inclusion of observations from geophysical logs from recently drilled boreholes (Buesch, Spengler et al. 1996b; Rautman and Engstrom 1996a, pp. 33 to 41; Rautman and Engstrom 1996b, pp. 33 to 38; Engstrom and Rautman 1996; CRWMS M&O 1997d, 1996b).

The primary relationships between lithology and geophysical log response are:

- The Tiva Canyon Tuff (Tpc) exhibits relatively uniform, high-density log responses, alternating with lower and more erratic density log responses; a uniform, high-intensity gamma-ray log; high resistivity; and a low-amplitude, reverse-remnant magnetic field.

- The contacts of bedded tuffs (units Tpbt4, 3, and 2) interstratified between the Tiva Canyon (Tpc) and Topopah Spring tuffs (Tpt) (Table 4.5-2) typically show sharp, moderate to large changes in density, resistivity, neutron response, and computed porosity that mimic the bedded characteristics of these units. The pre-Pah Canyon Tuff (unit Tpbt2) characteristically has a broad, relatively smooth decrease in density and increase in resistivity and porosity that is bounded at the top and bottom by slightly more dense, lower resistivity, higher neutron, and lower porosity log responses.

- The Yucca Mountain (Tpy) and Pah Canyon tuffs (Tpp), which are interstratified with bedded tuffs Tpbt4, 3, and 2 in the central and northern parts of Yucca Mountain, are almost indistinguishable on geophysical logs from the bedded tuffs in the southern part of their extent, where they are thin, vitric, nonwelded ignimbrites (Figures 4.5-28 and 4.5-30). In the northern part of the site area, these two tuffs display characteristic welding profiles, are increasingly welded, devitrified, and vapor-phase corroded, and therefore are distinctive in relation to the bedded tuffs (Nelson, P.H. et al. 1991; Buesch, Spengler et al. 1996b).

- The Topopah Spring Tuff (Tpt) is characterized by relatively uniform, high-density log values alternating with lower, more highly variable density log values; a highly uniform, high-intensity gamma-ray log; high resistivity; and a low-amplitude, normal-remnant magnetic field.

- Tuffaceous rocks of the Calico Hills Formation produce low-amplitude gamma-ray log values, low-density and resistivity log values, and a nonperturbed magnetic field. The formation is typically altered to clays and zeolites, except where it is vitric (in the

southwestern part of the Central Block and at Busted Butte). Compared to vitric rocks, altered rocks have a slightly higher density and lower resistivity. Effective porosity is usually slightly lower.

- The upper part of the Prow Pass Tuff (Tcp) is characterized by high resistivity and enhanced gamma-ray activity; a normal-remnant magnetic field anomaly at the top serves as an excellent marker.

- The Bullfrog Tuff (Tcb) appears as a zone of high-amplitude gamma radiation and erratically higher density and resistivity, with a large-amplitude, normal-remnant magnetic field. A decrease in welding at the top and bottom of the formation helps to define it on the logs.

- Tram Tuff (Tct) has two different geophysical log signatures. The upper unit of the Tram Tuff is easily recognized by its very-high-amplitude, reverse-remnant magnetic field log and by high values of gamma radiation, density, and resistivity. The lower unit of the Tram Tuff, which is typically lithic rich, shows only low-level magnetic field perturbations and moderate values for gamma radiation, density, and resistivity.

Buesch, Spengler et al. (1996b) summarized the following correlations of lithostratigraphic features with geophysical logs. Calculated porosity and water saturation values can be used to identify, but cannot distinguish between, argillic and zeolitized rocks. This is especially evident near the devitrified-vitric boundary near the base of the Tiva Canyon Tuff (between units Tpcpln and Tpcpv2) (Table 4.5-2), near the top of the pumiceous tephra deposited on top of the Topopah Spring Tuff (unit Tpbt2), and at the devitrified-vitric tuff contact in the lower part of the Topopah Spring Tuff (unit Tptpv3a at the Tptpln-pv3 contact). In many boreholes, the bulk density and calculated porosity and water saturation values respond to depositional changes in texture and composition, including fallout tephra deposits interbedded with pyroclastic flow deposits, fine versus coarse-grained bedded tephra, and increases in the amount and size of lithic clasts. Although characteristic mineralogic variations between formations are not detected in the standard geophysical log suite, many eruptive sequences are capped by redeposited material or paleosols that commonly can be recognized on bulk density, calculated porosity and water saturation, epithermal neutron, induction, or resistivity logs.

4.5.3.4.2 Correlation of Rock Properties and Geophysical Log Response

For many lithostratigraphic features and units, there is a good correlation of borehole geophysical logs (especially density, epithermal neutron, resistivity, and calculated porosity values) with matrix properties, such as density and porosity, mineralogy, and borehole video observations. Figure 4.5-28 shows the relationships between lithostratigraphic units (Geslin et al. 1995, pp. 38 to 39), porosity calculated from borehole geophysics (CRWMS M&O 1996d), matrix porosity measured at 105°C (221°F) and relative humidity conditions (Flint, L.E. 1998, p. 17, Figure 2), quantitative mineralogy (Chipera, Vaniman et al. 1995), and the location of minor water seeps observed in borehole video. Intervals where the differential porosity (calculated by subtracting the relative humidity porosity from 105°C [221°F] porosity) is greater than 5 percent (Flint, L.E. 1998, Figures 8, 9, Table 9) are also plotted. Calculated total porosity in UE-25 UZ#16 used the calculations of P.H. Nelson (1996) and Thompson (CRWMS

M&O 1996d). Five basic relationships are depicted on Figure 4.5-28 (formations have three-letter symbols and zones or units have shortened symbols):

1. Devitrified, moderately to densely welded rocks of the Tiva Canyon (Tpc), Topopah Spring (Tpt), and Prow Pass (Tcp) tuffs have porosities less than 25 percent and differential porosities less than 5 percent. They are primarily "high-temperature" mineral assemblages with mostly quartz+feldspar and moderate amounts of cristobalite or tridymite, and have very minor amounts of "low-temperature" minerals such as clay (smectite+mica), zeolites (clinoptilolite+mordenite), and opal-CT. Lithophysal zones of the Topopah Spring Tuff and vapor-phase corroded zones of the Topopah Spring and Prow Pass tuffs have calculated porosities as much as 45 percent and matrix porosity from core measurements as much as 30 percent.

2. Vitric, nonwelded to partially welded rocks near the base of the Tiva Canyon Tuff (Tpc), nonwelded bedded tuffs (Tpbt4, 3, and 2) and Yucca Mountain Tuff (Tpy), and the nonwelded to partially welded rocks near the top of the Topopah Spring Tuff (Tpt) have porosities greater than 30 percent. Locally they have differential porosities greater than 5 percent and are mostly glass, with minor amounts of quartz+feldspar and clay.

3. Vitric, densely welded rocks of the Topopah Spring Tuff (Tpt) typically have porosities less than 10 percent, have differential porosities less than 5 percent, and are mostly glass. Rocks near the top of the crystal-poor, vitric, densely welded subzone of the Topopah Spring Tuff are pervasively altered to zeolite, form the altered interval (Tptpv3a), and have a porosity greater than 10 percent, with a differential porosity greater than 5 percent.

4. Rocks of the moderately welded to nonwelded subzones of the Topopah Spring Tuff (Tptpv2 and Tptpv1), the nonwelded pyroclastic flow deposits and bedded tuffs of the Calico Hills Formation (Tac4, 3, 2, 1, and Tacbt), and the nonwelded rocks of units 4 and 2 in the Prow Pass Tuff (Tcp4 and Tcp2) are pervasively zeolitic and have a calculated 105°C (221°F) porosity typically between 20 and 35 percent and differential porosities greater than 5 percent.

5. Two minor water seeps are associated with a 6-cm-thick bedded tuff at the base of unit c4 and at the top of the bedded tuff near the base of the Calico Hills Formation. Both seeps occur where there is a textural change in the rocks (fallout tephra deposits overlain by pyroclastic flow deposits) and an increased number of lithic clasts in the bedded tuff compared to the pyroclastic flow deposits. These textural and compositional changes are represented in the calculated porosity log and quantitative mineralogy.

In borehole WT-2 (Figure 4.5-29), similar relations occur for lithostratigraphic units, calculated total and water-filled porosity (Nelson, P.H. 1996), and quantitative mineralogy for cuttings samples (Bish and Chipera 1989, p. 49). Compared with the same lithostratigraphic units found in borehole UZ#16: (1) calculated total porosity appears slightly greater; (2) calculated water-

filled porosity has values similar to the relative humidity porosity; (3) separation in total and water-filled porosity in the lithophysal zones and vapor-phase corroded zones of the Topopah Spring Tuff (Tpt) is similar to the difference between calculated total porosity and matrix porosity; and (4) the crystal-poor, vitric, densely welded, altered interval in the Topopah Spring Tuff (Tptpv3a) can be identified on the porosity logs at a depth of approximately 1,190 ft (362.7 m).

There are two significant differences in lithostratigraphic features and geophysical logs between boreholes UE-25 UZ#16 and WT-2 (Figures 4.5-28, 4.5-29, and 4.5-31). First, the vitric-zeolitic boundary (where rocks above the boundary are mostly, if not completely, vitric and those below are pervasively altered to zeolite and indicated by the symbol CHnv-z) occurs very near the base of the vitric, densely welded subzone of the Topopah Spring Tuff (Tpt) in UZ#16. However, in WT-2 this boundary is very near the base of unit 3 in the Calico Hills Formation (Tac3) (Figures 4.5-28 and 4.5-29). P.H. Nelson (1994) describes the rationale for interpreting that the rocks have more water than can be accommodated in pores. First, some of the water is in the mineral phase (this is also referred to as structural or bound water). Second, the upper part of unit 3 in the Prow Pass Tuff (Tcp3) shows a large separation in total and water-filled porosities, which corresponds to the vapor-phase corroded part of the unit. There are almost no clays and zeolites in this part of the section; therefore, comparing this unit in these two boreholes might indicate lateral variation in the development of the secondary porosity and pore geometry.

Geophysical logs have been invaluable in correlating lithostratigraphic features and units across Yucca Mountain. The logs can be used to calculate porosity and saturation curves (Nelson, P.H. 1993, 1994, 1996; CRWMS M&O 1996d) that serve as primary input for porosity and property models (Rautman 1996; see also Section 4.8).

Regardless of the usefulness of geophysical logs, great care must be taken to properly correlate and interpret these data. An apparently spurious result from geophysical logs that occurs in several boreholes involves the localized alteration of the crystal-poor, vitric, densely welded subzone of the Topopah Spring Tuff (Tpt) (Buesch and Spengler 1998, p. 249). This pervasively altered material, referred to as the altered interval of the vitric, densely welded subzone (Unit Tptpv3a) (Table 4.5-2), is associated with the vitric zone because glass can alter to clays and zeolites, whereas minerals resulting from devitrification processes typically do not alter under most temperature and geochemical conditions at Yucca Mountain (Bish and Aronson 1993, pp. 156 to 159). Figure 4.5-32, a conceptual composite from several logs, illustrates the general relationships of devitrified, vitric, and altered rock near the contact between the lower nonlithophysal and crystal-poor vitric zones of the Topopah Spring Tuff. Lithostratigraphic relations, which have been observed in several boreholes, include vitric pumice clasts near the base of the lower nonlithophysal zone (Tptpln1), spherulites in the upper part of the vitric, densely welded subzone, and alteration along the contact and the high-angle fractures (Tptpv3a). Based on measured and calculated techniques, the typical grain density for densely welded (0 percent porosity) devitrified rock is 2.55 g/cm^3 (159.19 lb./ft^3), that for densely welded (0 percent porosity) vitric rock is 2.35 g/cm^3 (146.71 lb./ft^3), and that for alteration (clay and zeolite) minerals is 2.10 g/cm^3 (131.10 lb./ft^3). Ideally, crystal-poor, densely welded tuff with no lithic clasts that devitrified with porosity less than 10 percent will vary in bulk density from 2.24 to 2.55 g/cm^3 (139.84 to 159.19 lb./ft^3), whereas vitric rocks with porosity less than 10 percent will vary from 2.12 to 2.35 g/cm^3 (132.35 to 146.71 lb./ft^3).

Figure 4.5-32a illustrates typical variations across a nonaltered contact where vitric rocks result in a decrease in the density log. Figure 4.5-32b illustrates a pronounced decrease in the density log within a narrow width where the contact is altered and a pronounced but sustained decrease in the density log where the contact is altered (Profile A) and the borehole traverses a near-vertical fracture (Profile B). The host rock is the vitric, densely welded subzone. Thus, using geophysical logs, localized alteration of the upper contact of the crystal-poor, vitric, densely welded subzone of the Topopah Spring Tuff can often be identified.

4.5.4 Descriptions of Stratigraphic Units

Formations within the Paintbrush Group are divided into members, members into zones, zones into subzones, and subzones into intervals (Buesch, Spengler et al. 1996a). The underlying Calico Hills Formation and the Prow Pass Tuff of the Crater Flat Group are also subdivided into several lithostratigraphic units (Moyer and Geslin 1995). However, volcanic rocks older than the Prow Pass Tuff and younger than the Paintbrush Group (Timber Mountain Group), which are known primarily from core logs, borehole drill cuttings, and observations of limited outcrops, were not subjected to the same degree of separation into individual units as were the Prow Pass Tuff, the Calico Hills Formation, and formations within the Paintbrush Group. The Prow Pass, Bullfrog, and Tram tuffs are informally subdivided into units based on devitrification and degree of welding (Buesch and Spengler 1999b, pp. 62 to 64).

Lithologic descriptions are provided in two tables: Table 4.5-1, which includes generalized descriptions of the pre-Prow Pass Tuff volcanic rocks that were not subjected to a large degree of subdivision, and Table 4.5-2, which includes detailed descriptions of all the members, zones, subzones, and intervals that were defined within the Prow Pass Tuff (of the Crater Flat Group), the Calico Hills Formation, and formations of the Paintbrush Group, as well as generalized descriptions of the next overlying units of the Timber Mountain Group. Only summary discussions of the larger stratigraphic units (formations and members, or other principal subdivisions) are given below. In general, stated borehole thicknesses are apparent, depending on the borehole geometry and the dip of stratigraphic units. Locations of measured surface sections and boreholes are shown on Figure 4.5-5.

4.5.4.1 Pre-Cenozoic Rocks

Pre-Cenozoic rocks, believed to consist primarily of upper Precambrian and Paleozoic strata, underlie the Tertiary volcanic rocks at Yucca Mountain, but little detailed information is available on their thickness and overall lithology. The only direct evidence of their presence is in borehole p#1, (about 2 km [1.2 mi.] east of Yucca Mountain), which penetrated Paleozoic carbonate rocks in the depth interval 1,244 to 1,805 m (4,081 to 5,922 ft) (Figure 4.5-3). These rocks, almost entirely dolomites, have been correlated with the Lone Mountain Dolomite and Roberts Mountains Formation on the basis of exposures at Bare Mountain to the west, and on the presence of Silurian-age conodonts (Carr, M.D. et al. 1986, pp. 17 to 18). Descriptions of pre-Cenozoic rocks in the Yucca Mountain region are given in Section 4.2 and further details are compiled in the *Yucca Mountain Project Stratigraphic Compendium* (CRWMS M&O 1996e, pp. 4-1 to 4-25).

4.5.4.2 Pre-Lithic Ridge Volcanic Rocks

The oldest known volcanic rocks in the Yucca Mountain region were deposited approximately 14 Ma and underlie the Lithic Ridge Tuff (Sawyer, D.A., Fleck et al. 1994, Table 1). Because these pre-Lithic Ridge Tuff rocks are not exposed at Yucca Mountain, little is known about their extent and stratigraphic relations except locally, where they have been penetrated in boreholes. In boreholes G-1, G-2, and G-3 (Figure 4.5-4), the pre-Lithic Ridge Tuff sequence consists of bedded tuffaceous deposits, pyroclastic flow deposits, and quartz-latitic to rhyolitic lavas and flow breccia (Broxton, Byers et al. 1989, p. 7). Penetrated thicknesses vary from approximately 45 m (148 ft) in G-3 to approximately 350 m (1,148 ft) in G-2. In borehole p#1, 180 m (590 ft) of older, altered tuff occurs between the Lithic Ridge Tuff and Paleozoic strata (Muller and Kibler 1984, Table 1). Initial compositions of these older tuffs are poorly known, but the pre-Lithic Ridge rocks contain alteration products, such as clays, calcite, and chlorite (Spengler, Byers et al. 1981, pp. 18 to 25, 37 to 39; Bish and Vaniman 1985, Figure B-7). These data have been used to determine an alteration history of these older rocks (Bish and Aronson 1993, pp. 154 to 155). Details of pre-Lithic Ridge rock stratigraphy are compiled in the *Yucca Mountain Project Stratigraphic Compendium* (CRWMS M&O 1996e, pp. 3-60 to 3-61).

4.5.4.3 Lithic Ridge Tuff

The Lithic Ridge Tuff is a thick, massive pyroclastic flow deposit (Carr, W.J. et al. 1986, p. 10-13). It ranges in thickness from 185 m (607 ft) at borehole G-2, north of the potential repository, to 304 m (997 ft) in borehole G-3/GU-3, at the south end of the repository (Figure 4.5-4). The formation is nonwelded to moderately welded and has been extensively altered to clays and zeolites. Many slight variations in the degree of welding, phenocryst ratios, and lithic-fragment content suggest that several eruptive surges are represented, which is in part supported in borehole geophysical logs. The formation is separated from the overlying dacitic lava and flow breccia (where present) by a bedded tuff unit composed mainly of fallout tephra (Table 4.5-1), and is distinguished from the Tram Tuff by a lower quartz content, the presence of sphene, and a differing content of lithic fragments (Broxton, Byers et al. 1989, Table 2).

4.5.4.4 Dacitic Lava and Flow Breccia

Dacitic lava and flow breccia overlie the Lithic Ridge Tuff in deep drill holes in the northern and western parts of Yucca Mountain, but are absent elsewhere. The thickness of the unit is 111 m (365 ft) in borehole H-1 (Rush et al. 1984, Table 1) and 249 m (817 ft) in borehole H-6 (Craig et al. 1983, Table 1). In borehole G-1, most of the unit is flow breccia made up of angular to subangular dacite fragments, commonly from 2 to 10 cm (0.8 to 4 in.) long, which are intercalated with lava blocks ranging from 1 to more than 17 m (3.3 to more than 56 ft) thick (Spengler, Byers et al. 1981, p. 36). The breccia is autoclastic, suggesting that its formation is largely due to fragmentation of semisolid and solid lava during relatively slow flow. About 8 m (26 ft) of reworked pyroclastic fallout and bedded tuff deposits underlie the flow breccia in borehole G-1 (Spengler, Byers et al. 1981, p. 37). Similar mineral constituents suggest a genetic link between these tuffs and the overlying flow breccia, and most of the upper part of the bedded interval has a volcanic texture suggesting postemplacement fusion.

4.5.4.5 Crater Flat Group

The Crater Flat Group consists of three formations of moderate- to large-volume pyroclastic flow deposits and interstratified bedded tuffs that are distinguished by their stratigraphic relations and petrologic and geochemical characteristics (Figure 4.5-1). In ascending order, these formations are the Tram, Bullfrog, and Prow Pass tuffs (Sawyer, D.A., Fleck et al. 1994, Table 1). The Bullfrog Tuff is associated with the Silent Canyon caldera complex, but sources of the Tram and Prow Pass tuffs are less certain (Sawyer, D.A., Fleck et al. 1994, p. 1,307). The tuffs of the Crater Flat Group exhibit a compositional range that falls between the high-silica rhyolites of the majority of the Paintbrush Group and the distinctive lower silica rhyolites of the Pah Canyon Tuff (Figure 4.5-12). Despite this spread of compositions, the Crater Flat tuffs may be related by a progressive deepening of the negative Eu anomaly and a decrease in La/Sm from oldest (Tram Tuff) to youngest (Prow Pass Tuff), although this observation is based on limited analyses (Broxton, Warren et al. 1989, pp. 5,978 to 5,981). The apparent trend in lanthanide-element composition could indicate progressive feldspar removal from the magma source over time (Figure 4.5-13).

The Crater Flat Group is distinguished from other pyroclastic units in the vicinity of Yucca Mountain by the relative abundance of quartz and biotite phenocrysts. In addition, the Prow Pass Tuff and, to a lesser degree, some parts of the Bullfrog Tuff contain distinctive lithic clasts of reddish-brown mudstone. At Yucca Mountain, the Crater Flat Group overlies dacitic lavas and flow breccias in the northern part of Yucca Mountain, and the Lithic Ridge Tuff in the southern part (Broxton, Byers et al. 1989, p. 38) (Figures 4.5-4 and 4.5-5). Generalized descriptions of the Tram and Bullfrog tuffs are given in Table 4.5-1, and detailed descriptions of subunits within the Prow Pass Tuff are included in Table 4.5-2.

4.5.4.5.1 Tram Tuff

There has not been a recent systematic lithostratigraphic study of the Tram Tuff that includes all boreholes at Yucca Mountain. However, numerous depositional units have been distinguished by observed changes in the abundance and types of pumice and lithic clasts in pyroclastic flow deposits and rare bedded tuff interbeds. The most easily recognized stratigraphic divisions are the lower lithic-rich unit, which in itself can be locally divided into a lower lithic-poor and an upper lithic-rich set of subunits, and an upper lithic-poor unit (Table 4.5-1). Both lithic-rich and lithic-poor units have been identified and described in several boreholes, including p#1, G-1, b#1, G-3, and H-1 (Spengler, Byers et al. 1981, pp. 17 to 18; Maldonado and Koether 1983, p. 29; Scott, R.B. and Castellanos 1984, p. 36). In borehole G-2, the upper lithic-poor unit is absent and the lithic-rich unit is well developed (Maldonado and Koether 1983, p. 29). Welding is variable throughout the Tram Tuff (Scott, R.B. and Castellanos 1984, pp. 36 to 37) and locally the large concentration of lithic clasts (such as in borehole G-2) apparently reduced the degree of welding. In general, the lithic-poor unit is more densely welded than the underlying lithic-rich unit. This can be inferred from the correlated change in geophysical logs (gamma, density, porosity) above and below the 980-m (3,215-ft) depth in borehole G-3/GU-3 (Figure 4.5-27). However, the stratigraphic position of the zone of maximum welding within the upper unit is not the same everywhere.

The Tram Tuff has the greatest light-La enrichment of the Crater Flat Group and has essentially no Eu anomaly, indicating little or no feldspar fractionation from the parent magma (Figure 4.5-13). Argillic and zeolitic alteration occurs in both units of the Tram Tuff. In the lithic-poor unit, the alteration appears to occur in two zones separated by the zone of maximum welding. Both the upper and lower parts of the formation are altered to clinoptilolite ± mordenite. In the vicinity of borehole G-1, however, analcime appears in the lower part, and in borehole USW G-2, analcime is the dominant zeolite in both the upper and lower parts.

Tram Tuff thicknesses across Yucca Mountain range from about 60 m to as much as 396 m (200 to 1,300 ft) (Figure 4.8-20). A regional isopach map by W.J. Carr et al. (1986, Figure 11) shows the thickness of the formation to be in excess of 400 m (1,310 ft) in the northern part of Crater Flat to the west.

The lithic-rich unit overlies a complex sequence of altered and weathered pyroclastic fallout deposits and minor pyroclastic flow deposits (e.g., see Diehl, S.F. and Chornack 1990, pp. 141 to 152). These pre-Tram Tuff bedded tuffs range in thickness from 50 m (164 ft) in borehole G-2 to only about 8 m (26 ft) in borehole G-3 (Figure 4.5-4) (Maldonado and Koether 1983, Table 3; Scott, R.B. and Castellanos 1984, p. 37).

4.5.4.5.2 Bullfrog Tuff

The Bullfrog Tuff, which is partially exposed only in limited outcrops near Prow Pass in the northwest corner of the Yucca Mountain site area, was penetrated wholly or partially by approximately 20 boreholes. In general, the tuff consists of welded to partially welded zeolitic upper and lower parts separated by a central zone of moderately to densely welded tuff (Carr, W.J. et al. 1986, p. 18). The Bullfrog Tuff includes a unit of reworked and weathered tuffaceous deposits (termed pre-Bullfrog Tuff bedded tuffs) (Table 4.5-1) at the base. Thicknesses are from 76 to 275 m (250 to 900 ft) (Figure 4.8-19). Regionally, W.J. Carr et al. (1986, Figure 14) show the Bullfrog Tuff to be as much as 400 m thick (1,310 ft) in a region of maximum deposition in the southern part of Crater Flat.

The pre-Bullfrog Tuff bedded tuffs consist largely of weathered pyroclastic flow deposits interbedded with thin zones of fallout tephra. S.F. Diehl and Chornack (1990, Figure 35, pp. 141 to 152) correlated five marker horizons through the sequence between boreholes G-1, G-2, G-3/GU-3, and b#1, and reported thicknesses ranging from 8 to 23 m (26 to 75 ft). The pre-Bullfrog Tuff unit in borehole SD-7 consists of medium-grained sandstone containing 10 to 15 percent small pumice grains (average size 5 mm), 15 to 20 percent quartz and feldspar grains, and 3 to 5 percent small devitrified volcanic and red siltstone lithic fragments in a fine-grained matrix (Rautman and Engstrom 1996a, p. 63).

Lithologic descriptions of the Bullfrog Tuff (Table 4.5-1) are based primarily on studies of core from boreholes G-1 and G-4 (Spengler, Byers et al. 1981, pp. 16 to 17; Spengler and Chornack 1984, pp. 73 to 76). The formation is composed of two pyroclastic flow deposits separated by an interval of pumiceous fallout. Both upper and lower deposits are simple cooling units that are moderately welded in their central portions. The middle pumiceous fallout deposit, partly to moderately welded, varies in thickness from about 20 cm to 1.5 m (8 in. to 5 ft). Rautman and Engstrom (1996a, pp. 62 to 63) recognized four pyroclastic flow units within the

Bullfrog Tuff in a study of cores from borehole SD-7. The basal part of each flow deposit includes some reworked tuffaceous materials. Except for a partially to moderately welded unit next to the top of the formation, the pyroclastic flow deposits are generally nonwelded and zeolitically altered. Pumice clasts vary from 5 to 15 percent in most units, but increase to as much as 35 to 60 percent in some zones. The phenocryst assemblage generally includes 20 to 25 percent quartz and feldspar and 5 to 10 percent biotite, hornblende, and pyroxene. The Bullfrog Tuff lacks the orthopyroxene of the overlying Prow Pass Tuff, but contains trace amounts of clinopyroxene. The unit exhibits a modest negative Eu anomaly and intermediate light-lanthanide enrichment (Figure 4.5-13). Lithic-clast content ranges from 1 to 5 percent.

Development of the devitrification zones within the Bullfrog Tuff resulted in a devitrified, vapor-phase, mineralized interior bounded by upper and lower zones that were initially vitric, but have undergone zeolitic/argillic alteration with clinoptilolite ± mordenite. The upper zeolitic zone varies in thickness from 4 m (13 ft) (borehole G-4) to as much as 45 m (148 ft) (borehole G-1), and the zeolitic alteration continues into the overlying bedded tuffs at the base of the Prow Pass Tuff. To the north, in the area of borehole G-2, the Bullfrog Tuff is entirely within the analcime zone, and the zeolitized base of the formation differs from sections to the south by the absence of clinoptilolite, containing mordenite+analcime instead. Vapor-phase crystallization is generally well developed in the middle and upper portions of the central devitrified zone. Pumice clasts are typically replaced by vapor-phase crystals, although some clasts have spherulitic and axiolitic texture. Biotite crystals are partially oxidized in vapor-phase altered zones, and siltstone lithic clasts are locally enclosed in light gray margins. Near the base of the formation, the devitrified zone overlies a thin interval of argillic alteration, which, in turn, overlies a zone dominated by zeolite mineralization that continues into the underlying pre-Bullfrog Tuff bedded tuffs.

In addition to an intervening bedded tuff unit (Tcpbt, Table 4.5-2), the Bullfrog Tuff can be differentiated from the overlying Prow Pass Tuff on the basis of phenocryst assemblage and bulk chemistry (Moyer and Geslin 1995, p. 40). Units of the Prow Pass Tuff contain altered orthopyroxene and generally nearly equal amounts of biotite. In contrast, the Bullfrog Tuff lacks pyroxene and contains abundant biotite.

4.5.4.5.3 Prow Pass Tuff

The Prow Pass Tuff is a sequence of variably welded pyroclastic deposits formed by eruptions from an unidentified source between 13.0 and 13.25 Ma (Sawyer, D.A., Fleck et al. 1994, Table 1, p. 1,307). Descriptions given below are summarized from Moyer and Geslin (1995), based primarily on studies of core samples from boreholes G-1, G-2, GU-3, G-4, UZ-14, a#1, c#1 (and nearby c#2 and c#3), and UZ#16, and from observations of exposures at Prow Pass, Busted Butte, and Raven Canyon (Figure 4.5-2).

Four pyroclastic units and an underlying interval of bedded tuff, the combined thicknesses of which range from 60 to 228 m (200 to 750 ft), compose the Prow Pass Tuff in the Yucca Mountain area (Table 4.5-2; Figure 4.8-18). The basal bedded tuffs, less than 1 m (3.3 ft) to as much as 11 m (36 ft) thick, consist of welded and zeolitically altered tuffaceous deposits that include a laminated ash deposit overlying a highly variable sequence of pumiceous fallout and pyroclastic flow deposits. A thin (approximately 0.5 m [1.6 ft]) basal breccia, containing angular

clasts of the underlying Bullfrog Tuff and, locally, other volcanic lithologies, occurs in several places.

The lowermost pyroclastic flow deposit of the Prow Pass Tuff (unit Tcp1) (Table 4.5-2), with an aggregate thickness of 25 to 70 m (82 to 230 ft), consists of three subunits separated on the basis of their lithic clast content. The subunits are generally similar, with zeolitically altered matrices; the upper and lower subunits cannot be differentiated where the middle subunit is absent. The next overlying unit (Tcp2) is a sequence of pyroclastic flow deposits that have not been subdivided because they lack distinguishing characteristics. Locally preserved ash horizons and abrupt changes in the amounts and sizes of pumice and lithic clasts, however, indicate at least three flow deposits in most boreholes studied. The aggregate thickness ranges from about 3 to 34 m (10 to 112 ft). Unit Tcp3 consists of six subunits defined by changes in the degree of welding or the intensity of vapor-phase alteration. Locally preserved, interbedded ash-fall horizons and abrupt variations in the amounts and sizes of pumice and lithic clasts mark flow boundaries. The thickness of unit Tcp3 ranges from 40 m (131 ft) to nearly 80 m (262 ft). The top unit of the Prow Pass Tuff (Tcp4), which ranges from 4 m (13 ft) to as much as 20.5 m (67 ft) thick in cored boreholes, can be divided into three irregularly distributed subunits differentiated by changes in the average diameter and percentage of pumice clasts that decrease stratigraphically upward. The contact between crystallized (including vapor-phase corroded and mineralized) and vitric (or subsequently zeolitized) rocks is typically marked by a thin horizon of argillically altered pumice clasts and the largest matrix grain. This mineralogic contact occurs at the contact of units 3 and 4 and near the contact of units 2 and 3, although the mineralogic change is locally at the contact of the moderately welded and partially welded rocks in unit 3 or in the upper part of unit 2. Rocks in units 1, 2, and 4 are typically altered to zeolite (clinoptilolite and/or mordenite near the water table) and lesser amounts of clay throughout most of Yucca Mountain. Analcime occurs in the lower part of the Prow Pass Tuff to the north (in borehole G-2), but is not found in any part of the formation to the south. Units 2 and 4 are vitric in the southwestern part of the central block, with vitric rocks in unit 4 occurring as far north as borehole H-5.

Among the various criteria used to distinguish the lithostratigraphic units of the Prow Pass Tuff from those of the next younger Calico Hills Formation, the most prominent are the ubiquitous siltstone clasts and altered orthopyroxene of the Prow Pass Tuff (Moyer and Geslin 1995, p. 40). The two formations also have different amounts of phenocrysts, proportions of quartz in the phenocryst assemblage, and chemical compositions. The Prow Pass Tuff exhibits the deepest negative Eu anomaly and least light-La enrichment of the Crater Flat Group (Figure 4.5-13), and it is distinguished by the presence of more (altered) orthopyroxene than biotite as phenocrysts and by characteristic fine-grained, oxidized lithic inclusions of red mudstone. Both the orthopyroxene and the mudstone inclusions need to be considered in evaluating interactions of the Prow Pass Tuff with radionuclides. The basal bedded tuff and sandstone units of the Calico Hills Formation serve as consistent stratigraphic marker beds in several boreholes studied (Diehl, S.F. and Chornack 1990, p. 49, Figure 32).

4.5.4.6 Calico Hills Formation

The Calico Hills Formation and the underlying bedded tuffs potentially comprise one of the most significant barriers to waste migration at Yucca Mountain. Despite its great heterogeneity, the

Calico Hills Formation has a consistently high matrix porosity (average 28 to 35 percent) and poor fracture development, which suggests an important role for matrix flow and interaction. Other properties, particularly permeability, are extremely variable and strongly dependent on mineralogy; permeability drops by about two orders of magnitude, and sorption by cation exchange rises by up to five orders of magnitude, in the transition from vitric to zeolitic character within the formation. Fine-scale variations in matrix properties occur within centimeters, and lateral continuity in properties is poor (Broxton, Chipera et al. 1993, Figures 4, 14).

The Calico Hills Formation is a complex series of rhyolite tuffs and lavas that resulted from an episode of volcanism approximately 12.9 Ma (Sawyer, D.A., Fleck et al. 1994, Tables 1, 3). Five pyroclastic units, overlying a bedded tuff unit and a locally occurring basal sandstone unit, were distinguished in the Yucca Mountain area by Moyer and Geslin (1995, pp. 5 to 8). The formation thins southward across the potential repository site area, from composite thicknesses of as much as 460 m (1,500 ft) to only about 15 m (50 ft) (Figure 4.8-17). The following descriptions are summarized from Moyer and Geslin (1995, pp. 5 to 8), whose studies are based on examinations of cores and observations of outcrops in the same boreholes and surface localities as those listed above for the Prow Pass Tuff.

The basal volcaniclastic sandstone unit of the Calico Hills Formation (unit Tacbs) (Table 4.5-2) is interbedded with rare reworked pyroclastic flow deposits; thicknesses of the unit range from 0 to 5.5 m (0 to 18 ft). The overlying bedded tuff (unit Tacbt), 9 to 39 m (30 to 128 ft) thick, is composed primarily of pyroclastic fall deposits with subordinate, primary, and reworked pyroclastic-flow deposits. Each of the five pyroclastic units forming the bulk of the Calico Hills Formation (units Tac1 to Tac5) consists of one or more pyroclastic flow deposits with similar macroscopic characteristics. The flow deposits are separated by locally preserved fall horizons; these pumice- and lithic-fall deposits are grouped arbitrarily with the superjacent pyroclastic unit. Ash-fall and ash-flow deposits beneath the potential repository block give way to lava flows to the north and east.

X-ray diffraction of drill core samples by Caporuscio et al. (1982, p. 32), Bish and Vaniman (1985, Appendix A), and Bish and Chipera (1986, Appendix A) and of outcrop samples by Broxton, Chipera et al. (1993, pp. 18 to 35) show an abundance of authigenic zeolites in all Calico Hills Formation units. Exceptions occur in the southwest part of the Central Block of Yucca Mountain (boreholes H-3 and GU-3), where the entire formation is vitric, and in borehole H-5, where the bedded tuff at the base is zeolitized but the remainder is not. The complex series of composite primary and reworked units grades laterally from completely zeolitized to unaltered vitric rock from east to west across the potential repository area. Available lanthanide data follow the generally rhyolitic pattern of little light-lanthanide enrichment and a prominent negative Eu anomaly (Figure 4.5-14). Phenocrysts predominantly are quartz, feldspar, and biotite, with trace magnetite and accessory clinopyroxene, ilmenite, allanite, and zircon.

The Calico Hills Formation is overlain by a bedded tuff unit (Tpbt1) (Table 4.5-2) that marks the base of the Topopah Spring Tuff. The formation can also be distinguished from the Topopah Spring Tuff by differences in mineralogy and chemical composition. Lithostratigraphic units of the former have phenocryst assemblages with a higher proportion of quartz and higher Ca and Ba contents than units of the latter.

4.5.4.7 Paintbrush Group

The Paintbrush Group consists of four formations, each primarily composed of pyroclastic flow deposits interstratified with small-volume pyroclastic flow and fallout tephra deposits, and, locally, lava flows and secondary volcaniclastic deposits from eolian and fluvial processes (Buesch, Spengler et al. 1996a). In ascending order, the formations include the Topopah Spring, Pah Canyon, Yucca Mountain, and Tiva Canyon tuffs. This group is one of the most widespread and voluminous caldera-related assemblages in the southwestern Nevada volcanic field (Sawyer, D.A., Fleck et al. 1994, p. 1,307). The Topopah Spring Tuff forms the host rock for the potential repository, and therefore is one of the most intensely studied formations at Yucca Mountain. Locations of eruptive centers for the Topopah Spring and Pah Canyon tuffs are uncertain, but the Claim Canyon caldera (Figure 4.5-2) is the identified source of the Tiva Canyon Tuff and possibly the Yucca Mountain Tuff (Byers et al. 1976, pp. 21 to 38; Sawyer, D.A., Fleck et al. 1994, Table 1, p. 1,308).

The Paintbrush Group is dominated by the Topopah Spring and Tiva Canyon tuffs. The Yucca Mountain and Pah Canyon tuffs are volumetrically minor, but are of potential hydrologic importance because of their high matrix porosity compared to the Tiva Canyon and Topopah Spring tuffs, which are largely densely welded with low matrix porosity. The welded tuffs also have higher fracture abundance and connectivity, providing stratified contrasts in unsaturated hydrologic properties in the Paintbrush Group rocks above the potential repository. The Topopah Spring and Tiva Canyon tuffs are compositionally zoned from minor, crystal-rich, quartz-latitic upper parts to dominant high-silica, rhyolitic, crystal-poor lower parts (a zonation also seen in the Rainier Mesa Tuff). The Paintbrush Group high-silica rhyolites show an exceptionally small compositional range (Figure 4.5-12).

Descriptions of the formations within the Paintbrush Group are generalized from detailed studies of outcrops and borehole cores by Buesch, Spengler et al. (1996a), supplemented by core descriptions obtained from Geslin et al. (1995); Geslin and Moyer (1995a); and Moyer, Geslin, and Buesch (1995). Buesch, Spengler et al. (1996a) divided the Topopah Spring and Tiva Canyon tuffs into several zones and subzones, many of which can be correlated across Yucca Mountain (Table 4.5-2). Divisions of these formations from members to the most detailed intervals indicate that both are simple cooling units within the site area and can be used as analogs for one another. The interplay among depositional, welding, crystallization, and fracturing processes produces unit contacts that range from sharp to gradational (Buesch, Spengler et al. 1996a, p. 16). Depositional contacts, such as the bases of pyroclastic flow and fallout deposits and redeposited material, are examples of sharp contacts. Tops of these deposits are typically sharp, but may be gradational where there is evidence of reworking or pedogenesis. The transition from nonwelded to densely welded tuff is typically gradational, such as near the base of the Topopah Spring Tuff in boreholes GU-3 and WT-2. Contacts of several lithostratigraphic units correspond with hydrogeologic and thermal-mechanical unit boundaries throughout Yucca Mountain and have been used in the development of three-dimensional geologic and hydrogeologic models (Table 4.5-2).

4.5.4.7.1 Topopah Spring Tuff

The Topopah Spring Tuff includes the host rock units for the potential repository and, as such, its characteristics are of direct importance to repository design, unsaturated zone hydrologic flow and radionuclide transport, and total system performance assessment. A complete description of the Topopah Spring Tuff is presented in Buesch, Spengler et al. (1996a, Appendix 2). Its thickness and distribution are discussed in Section 4.8. The features that are important to studies used in the site suitability evaluation are discussed in this section.

The Topopah Spring Tuff (Tpt) has a maximum thickness of about 380 m (1,250 ft) in the Yucca Mountain vicinity (Figure 4.8-14). The formation is divided into a lower crystal-poor member (Tptp) and an upper crystal-rich member (Tptr). Each member is divided into numerous zones, subzones, and intervals based on variations in depositional features, such as crystal content and assemblage, size and abundance of pumice and lithic clasts, distribution of welding and crystallization zones, and fracture characteristics (Buesch, Spengler et al. 1996a, pp. 19 to 21).

The Topopah Spring Tuff is compositionally zoned, with an upward chemical change from high-silica rhyolite in the crystal-poor member to quartz latite (also referred to as quartz trachyte) in the crystal-rich member (Lipman et al. 1966, p. F3; Sawyer, D.A., Fleck et al. 1994, p. 1,313). As discussed in Section 5.2.1, these two members are also clearly distinguishable on the basis of mineralogy and trace-element concentrations. Figure 4.5-15 shows the characteristic differences between quartz-latitic and rhyolitic lanthanide-element compositions that occur within the formation. The lower part of the Topopah Spring Tuff, which is the potential repository horizon, is one of the most chemically homogeneous rock types in the region (Figure 4.5-12). The homogeneity of the major-element chemistry within the high-silica rhyolite also extends to trace elements. Somewhat greater chemical variability is seen in the quartz latites. These characteristic chemical differences result in variable devitrification, vapor-phase, and low-temperature alteration minerals, which account for differences in rock texture and mineralogy between the rhyolitic and quartz-latitic rocks.

The crystal-poor member (unit Tptp, Table 4.5-2), which is characterized by less than 3 percent felsic phenocrysts, is divided into vitric rocks of the vitric zone near the base (unit Tptpv) and devitrified rocks of the upper lithophysal (unit Tptpul), middle nonlithophysal (unit Tptpmn), lower lithophysal (unit Tptpll), and lower nonlithophysal (unit Tptpln) zones; the latter four zones form the host rock for the potential repository. The vitric zone is divided primarily on the basis of degrees of welding, which range upward from a nonwelded subzone at the base, which includes partially welded rocks near the top, through a moderately welded subzone, to a densely welded subzone that caps the sequence. The vitric, densely welded subzone (unit Tptpv3), commonly referred to as the vitrophyre, is identified as an important thermal-mechanical unit (unit TSw3, Table 4.5-2).

Within the potential repository host rock (i.e., the devitrified, rhyolitic portion of the Topopah Spring Tuff) phenocrysts are minor constituents (less than 5 percent) of the rock, with the remaining more than 95 percent consisting of fine-grained devitrification minerals. These devitrification products are principally feldspars plus a variable combination of the silica polymorphs tridymite, cristobalite, and quartz. Quartz phenocryst abundance is a useful stratigraphic marker within the devitrified, rhyolitic Topopah Spring Tuff, but quartz phenocrysts

are nevertheless much less abundant (less than 0.5 percent) than groundmass quartz (approximately 20 percent) throughout this interval. The silica polymorph distributions are particularly important because of their thermal stability, dissolution properties, and their properties that create inhalation hazards.

A transitional zone, commonly referred to as the vitric-zeolitic transition, extends downward from the base of the lower nonlithophysal zone into the crystal-poor vitric zone through a stratigraphic interval ranging from about 3 to 30 m (10 to 100 ft) in thickness. This zone is composed of partly devitrified vitrophyre, in which devitrification is sporadic and localized around fractures. The most common alteration features within this zone are fractures with devitrified borders of alkali feldspar and cristobalite up to 0.3 m (1 ft.) thick. Some of the devitrified borders are downward extensions from the overlying, completely devitrified tuff. The outermost margins of devitrified fracture borders contain zeolites, smectite, and minor silica. Quartz, chalcedony, and opal are locally abundant as fracture and void fillings. There are discontinuous distributions of secondary minerals both vertically and horizontally, as well as substantial variation in abundance and proportion of the alkali feldspar, smectite, henlandite-clinoptilolite, and silica that make up the characteristic secondary-mineral assemblage.

In many parts of Yucca Mountain, the moderately welded and nonwelded subzones at the base of the crystal-poor vitric zone are overprinted by zeolite alteration zones (Buesch, Spengler et al. 1996a, p. 21). Accordingly, a "vitric-zeolitic boundary" was drawn that varies within a narrow range of stratigraphic positions, but generally coincides closely with the contact between the moderately welded subzone and the overlying densely welded subzone (Buesch and Spengler 1999a, Figures 8, 9, 10). This boundary is further defined as the contact between the Topopah Spring welded hydrogeologic unit (TSw) and the underlying Calico Hills nonwelded hydrogeologic unit (CHn, Table 4.5-2).

The vitric-zeolitic transition zone that separates vitric tuffs from underlying zeolitic tuffs is interpreted to have been an approximately planar surface, the configuration and position of which were originally related to the configuration and position of the static water table at the time of alteration (e.g., Levy 1991, p. 481). This interpretation is based largely on recognition that zeolitization requires the presence of abundant water over a long period of time (e.g., Levy 1991, p. 481), a condition that favors a laterally extensive water table rather than local perched-water tables. If valid, observations regarding the present stratigraphic and structural relations of the vitric-zeolitic transition zone within the lower Topopah Spring Tuff, as well as similar zones in other formations, have a direct bearing on interpretations regarding alteration history.

The crystal-rich member (unit Tptr, Table 4.5-2), which overlies the potential repository host horizon, is characterized by greater than 10 percent phenocrysts, with a crystal-transition subzone (Tptrnl) at the base where phenocryst abundance increases upward from 3 to 10 percent. The crystal-rich member is divided into lithophysal (unit Tptrl), nonlithophysal (unit Tptrn), and vitric (unit Tptrv) zones. Rocks in both the lithophysal and nonlithophysal zones are devitrified, so the division is based on the presence or absence of lithophysae. The vitric zone, which caps the member (unit Tptrv), is distinguished by preservation of the volcanic glass to form rocks with a vitreous luster that typically grade upward from densely welded to nonwelded. This zone is a particularly important geochemical subunit because it is relatively impermeable; impedance of

downward flow and reaction of water with quartz-latitic glass provides an important geochemical marker in unsaturated zone waters (Vaniman and Chipera 1996, p. 4,420).

Matrix materials comprise the bulk of the Topopah Spring Tuff, exclusive of open fractures, fracture fillings larger than about 0.2 mm (0.008 in.), and lithophysal cavities and xenoliths larger than about 5 mm. Texture (phenocrysts, lithic fragments, cryptocrystalline groundmass, etc.) is the most variable parameter. Microveinlets observed in thin sections are almost always filled with silica minerals and alkali feldspar, and they commonly connect with those in lithophysal cavity linings. Granophyric pumice is a significant matrix constituent because of the larger size of its crystals (up to 0.5 mm [0.02 in.]) and because the crystals commonly line cavities in pumice.

A sequence of bedded tuffaceous rocks (unit Tpbt2) occurs between the Topopah Spring Tuff and the Pah Canyon Tuff. The lower part of this unit, 5 to 15 m (16 to 50 ft) thick, consists of moderately well-sorted pumiceous tephra with a thin (2 cm [0.8 in.]) lithic-rich fallout tephra overlying a thin (2 cm [0.8 in.]) very fine-grained ash bed at the base. This thin basal bedset occurs across Yucca Mountain in core from boreholes and in surface exposures from the mountain's southwestern flank along Solitario Canyon to north of Yucca Wash near Fortymile Wash (Figure 4.5-2).

4.5.4.7.2 Pah Canyon Tuff

The Pah Canyon Tuff (Tpp, Table 4.5-2) is a simple cooling unit (Christiansen 1979, Table 1) composed of multiple flow units. The formation reaches its maximum thickness of about 70 m (225 ft) in the northern part of Yucca Mountain (Figure 4.8-12), and thins southward to zero in the vicinity of borehole UZ#16 (Moyer et al. 1996, Figures 19, 46). The Pah Canyon Tuff varies from nonwelded to moderately welded, and, throughout much of the area, vitric pumice clasts are preserved in a nondeformed matrix that was sintered or lithified by vapor-phase mineralization. Large pumice clasts contain distinctive clusters of phenocrysts. Phenocrysts in the matrix and in most pumice clasts comprise 5 to 10 percent of the rock, with a high ratio of feldspars to mafic (biotite and clinopyroxene) phenocrysts. Lithic clasts (up to 5 percent of the rock) of devitrified rhyolite are common, and clasts of porphyritic obsidian occur in some horizons. Shards occur either as poorly preserved clear glass or as devitrified material. The high saturation of porous nonwelded units, such as the Pah Canyon and Yucca Mountain units, is more effective in producing alteration where an underlying barrier to transmission becomes effective; thus, because of the relatively impermeable upper vitrophyre of the underlying Topopah Spring Tuff, the alteration of the Pah Canyon Tuff (typically to smectite) is typically more extensive than that of the overlying Yucca Mountain Tuff. Therefore, despite its minor volume, the Pah Canyon Tuff has a significant impact on reactions between unsaturated zone water and the host tuffs.

The Pah Canyon Tuff is a chemical anomaly within the Paintbrush Group. It is somewhat poorer in silica content than the high-silica rhyolites (Figure 4.5-12), and even more different from the other rhyolites in trace-element chemistry, having rare-earth-element composition more akin to quartz latites than to rhyolites (Figure 4.5-16).

A bedded tuff unit (Tpbt3, Table 4.5-2) intervenes between the Pah Canyon Tuff and the overlying Yucca Mountain Tuff where these two formations are present in the Yucca Mountain site area (Diehl, S.F. and Chornack 1990, Figure 30, Appendix 1). Several units consisting of rhyolite lava flows and fallout tephra deposits also occur in this general stratigraphic interval (e.g., the rhyolite of Black Glass Canyon, Table 4.5-2) in areas mostly northeast of Yucca Mountain, but are not present at Yucca Mountain.

4.5.4.7.3 Yucca Mountain Tuff

The Yucca Mountain Tuff (Tpy, Table 4.5-2) is a simple cooling unit that is nonwelded throughout much of the Yucca Mountain area, but is partially to densely welded where it thickens in the northern and western parts of Yucca Mountain. Although typically vitric in most locations in the central part, the tuff is increasingly devitrified where it is thick. The Yucca Mountain Tuff varies in thickness from 0 to 45 m (0 to 150 ft) (Figure 4.8-11). Locally, it includes a thin (few centimeters [1 to 2 in.]) ground layer at the base of the pyroclastic flow deposit that was originally interpreted as a pumiceous fallout tephra bed. The formation is nonlithophysal throughout Yucca Mountain, but contains lithophysae where densely welded in northern Crater Flat.

The Yucca Mountain Tuff is chemically very similar to the high-silica rhyolites of the Tiva Canyon and Topopah Spring units (Figure 4.5-12). The chondrite-normalized La patterns for this tuff are typical of high-silica rhyolites (Figure 4.5-17). Although the formation is rhyolitic, it contains both plagioclase and sanidine phenocrysts, whereas the only feldspar phenocrysts in the rhyolitic Tiva Canyon Tuff are sanidine. This two-feldspar phenocrystic assemblage is also characteristic of the rhyolitic parts of the Topopah Spring Tuff.

A bedded tuff sequence (unit Tpbt4) overlies the Yucca Mountain Tuff. In borehole GU-3, this sequence is about 15 m (50 ft) thick and is characterized by thin beds of pyroclastic fallout tephra deposits interbedded with thin, oxidized, weathered zones (Diehl, S.F. and Chornack 1990, pp. 62 to 64).

4.5.4.7.4 Tiva Canyon Tuff

The Tiva Canyon Tuff (Tpc, Table 4.5-2) is a large-volume, regionally extensive, compositionally zoned (from rhyolite to quartz latite) tuff sequence that forms most of the rocks exposed at the surface of Yucca Mountain (Day et al. 1998a, 1998b). Most vertical recharge pathways that pass through the potential repository block encounter these rocks, and the minerals therein play a large part in determining unsaturated zone groundwater composition. The thicknesses of those portions of the formation penetrated in boreholes or observed in outcrops range from less than 50 m to as much as 175 m (165 to 575 ft). Separation of the formation into a lower crystal-poor member (Tpcp) and an upper crystal-rich member (Tpcr), and into zones within each of these members, is based on criteria similar to those discussed above for the Topopah Spring Tuff.

The lowest part of the Tiva Canyon Tuff consists of densely welded to nonwelded high-silica rhyolitic glass. That interval provides another horizon of potential water accumulation in the unsaturated zone, with potential associated dissolution. Note, however, that water composition

resulting from dissolution of rhyolitic glass will be compositionally distinct from water that interacts with the upper quartz-latitic glass in the same tuff.

The rhyolitic crystal-poor member (unit Tpcp) is divided into five zones: vitric (unit Tpcpv), lower nonlithophysal (unit Tpcpln), lower lithophysal (unit Tpcpll), middle nonlithophysal (unit Tpcpmn), and upper lithophysal (unit Tpcpul). Division into subzones is based on vitric versus devitrified rocks, degree of welding, differences in pumice clasts, presence or absence of lithophysae, and fracture morphology. The crystal-poor member and overlying crystal-rich member are separated by a thin transitional subzone in which there is an upward increase in crystal content and an increase in the ratio of mafic to felsic phenocrysts.

The quartz-latitic crystal-rich member (unit Tpcr) consists primarily of devitrified, nonlithophysal material, which locally contains lithophysae near the base, and is capped by a thin (less than 1 m) vitric zone that is only locally preserved and typically has been eroded from most of Yucca Mountain. The crystal-rich nonlithophysal zone (unit Tpcrn) is divided into four subzones based upon such depositional features as abundance of phenocrysts and pumice. Much of this zone has undergone corrosion and alteration, which has significantly increased its porosity compared to the overlying and underlying rocks. The chondrite-normalized lanthanide pattern of the quartz latite (Figure 4.5-18) is similar to that of the quartz latite subunit of the Rainier Mesa Tuff (Figure 4.5-19). As discussed in Section 4.5.3.2, detailed variations of trace element concentrations within the crystal-rich member provide rather precise indications of the stratigraphic positions of various units.

4.5.4.8 Post-Tiva Canyon/Pre-Rainier Mesa Tuffs

A sequence of pyroclastic flow and fallout tephra deposits occurs between the top of the Tiva Canyon Tuff and the base of the Rainier Mesa Tuff of the Timber Mountain Group in the vicinity of Yucca Mountain (unit Tpbt5). Rocks in this stratigraphic position occur in the subsurface beneath alluvial deposits in Midway Valley on the east flank of Yucca Mountain (Figure 4.5-2) (Carr, W.J. 1992, pp. A-10 to A-14, A-19 to A-20, A-23 to A-24; Geslin and Moyer 1995a, Table 3, p. 10-12; Geslin et al. 1995, pp. 36 to 37). The sequence ranges in thickness from 0 to 61 m (0 to 200 ft) and is intermediate in composition between the Tiva Canyon and Rainier Mesa tuffs. Some units have been placed in the Timber Mountain Group (Sawyer, D.A., Fleck et al. 1994, Table 1) and others in the Paintbrush Group (Buesch, Spengler et al. 1996a, p. 5). They are described by Buesch, Spengler et al. (1996a, p. 5) as consisting of tuffaceous rocks correlated with known eruptive units based on detailed tephrostratigraphic studies, as well as other tuffaceous deposits that have not been correlated with known eruptive units. Included are units in the Timber Mountain Group referred to as rhyolite of the Loop (Sawyer, D.A., Fleck et al. 1994, Table 1) and Windy Wash lavas and tuffs (Fridrich 1999, Table 1), and units in the Paintbrush Group, such as the rhyolites of Comb Peak (Tpk) and Vent Pass (Tpv) (Buesch, Spengler et al. 1996a, p. 5). A lithic-rich unit (Tpki), informally referred to as tuff unit "x" by W.J. Carr (1992, pp. A-12 to A-23), occurs in these bedded tuffs and has been correlated with the rhyolite of Comb Peak (Buesch, Spengler et al. 1996a, p. 5).

4.5.4.9 Timber Mountain Group

The Timber Mountain Group includes all quartz-bearing pyroclastic flow and fallout tephra deposits erupted from the Timber Mountain caldera complex (Figure 4.5-2) about 11.5 Ma (Byers et al. 1976, pp. 38 to 47; Sawyer, D.A., Fleck et al. 1994, p. 1,308). The complex consists of two overlapping, resurgent calderas: an older caldera formed by the eruption of the Rainier Mesa Tuff, and a younger, nested caldera formed by the eruption of the Ammonia Tanks Tuff (Minor, Sawyer et al. 1993, p. 14; Sawyer, D.A., Fleck et al. 1994, p. 1,308).

4.5.4.9.1 Rainier Mesa Tuff

The Rainier Mesa Tuff (Tmr) is a compositionally zoned compound cooling unit consisting of high-silica rhyolite tuff overlain with a partial cooling break by a considerably thinner quartz latite tuff that is restricted to the vicinity of the Timber Mountain caldera (Byers et al. 1976, p. 39) (Figure 4.5-2). The formation does not occur across much of Yucca Mountain, but is locally exposed on the downthrown blocks of large faults in valleys on either side of the mountain (Scott, R.B. and Bonk 1984; Gibson et al. 1992, p. E-3) (Figure 4.5-2). It has also been penetrated in a few boreholes on the east side. Based on examination of cores from boreholes NRG#2, #2B, #2C, and #2D (not shown, but located between boreholes NRG#1 and NRG#3 in Figure 4.5-5), the Rainier Mesa Tuff consists of a nonlithified to lithified and partially welded pyroclastic flow deposit (Geslin and Moyer 1995a, p. 11-12; Geslin et al. 1995, pp. 27, 29). Near Yucca Mountain, a maximum thickness of 240 m (787 ft) (Fridrich 1999, Figure 10) for the Rainier Mesa Tuff was observed in the southwestern part of Crater Flat. Thicknesses reported from studies of boreholes on the east side of Yucca Mountain are generally less than 30 m (98 ft) (Geslin and Moyer 1995a, p. 11-12).

The Rainier Mesa Tuff occurrences are significant for their vitric character and are likely sources for silica and trace minerals released by chemical weathering. The formation includes both high-silica rhyolite and quartz latite subunits (Figure 4.5-12), with the quartz-latitic subunit overlying and grading into the rhyolite (Broxton, Warren, Byers et al. 1989, pp. 5,976 to 5,977). Chondrite-normalized La patterns for the subunits show light-La enrichment and no (or a minimal) Eu anomaly in the quartz latite, typical of quartz-latitic compositions at Yucca Mountain. That pattern contrasts with those of the rhyolites, which have much less light-lanthanide enrichment and a variable, but generally strong, negative Eu anomaly (Figure 4.5-19).

A nonlithified fallout-tephra deposit initially interpreted to form the basal part of the Rainier Mesa Tuff (Geslin and Moyer 1995a, p. 11-12; Geslin et al. 1995, pp. 27 to 29) is now considered to be part of an older bedded tuff sequence that also contains nonlithified pyroclastic flow deposits. This sequence, referred to as the pre-Rainier Mesa Tuff bedded tuff (Tmbt1), occupies intervals of about 17 m in boreholes NRG#2C and NRG#2D and is characterized by moderately well-sorted white pumice lapilli and volcanic lithic clasts.

4.5.4.9.2 Ammonia Tanks Tuff

The Ammonia Tanks Tuff (Tma) is not present across Yucca Mountain, but is exposed in the southern part of Crater Flat and was penetrated by one borehole in the Crater Flat area

(Fridrich 1999, Figure 10). The formation consists of welded to nonwelded rhyolite tuff, with highly variable thicknesses ranging up to about 215 m (705 ft).

4.5.4.10 Younger Basalt

The youngest volcanic rocks at and near Yucca Mountain are the basalts in Crater Flat basin and the basalt dikes on the west side of Yucca Mountain along the Solitario Canyon fault near the head of Solitario Canyon (Figure 4.5-2), just south of Drill Hole Wash, and along minor faults to the west (Day et al. 1998b; Crowe, Perry et al. 1995, pp. 2-11 to 2-12, 2-19 to 2-24). The basalts in Crater Flat basin, in the form of scoria cones, thin lava flows, and flow breccias, were erupted during four major episodes dated as 11 Ma, 3.7 Ma, 1 Ma, and approximately 0.08 Ma, respectively (Crowe, Perry et al. 1995, pp. 2-12, 2-20 to 2-25; Heizler et al. 1999, pp. 800 to 801). The thin dikes that were intruded along the Solitario Canyon fault consist of fine-grained, olivine-bearing basalt, locally with scoria and altered volcanic glass; they are dated as 10 Ma (Crowe, Perry et al. 1995, p. 2-11). Basaltic volcanism in the Yucca Mountain area is discussed in Section 12.2.

4.5.4.11 Surficial Deposits

Surficial deposits of late Tertiary and Quaternary ages are widespread in the Yucca Mountain area (Figure 4.5-2). Included is a large variety of alluvial deposits and soils that blanket the floors of all major washes and colluvial deposits that mantle many hillslopes. Detailed mapping and the stratigraphic and geochronological studies of these materials that were conducted as part of the site characterization program are discussed in Section 4.4.

4.5.5 Correlation of Lithostratigraphic, Hydrogeologic, and Thermal-Mechanical Units

Three primary stratigraphic systems were developed to investigate the distribution of lithostratigraphic, hydrogeologic, and thermal-mechanical units at Yucca Mountain. Common to all these systems are the properties of bulk rock density, grain density, and porosity. Where there are changes in these rock properties, it is reasonably expected that there are commensurate changes in many of the associated hydrogeologic and thermal-mechanical properties. Thus, it was suggested that lithostratigraphic, hydrogeologic, and thermal-mechanical units share some common boundaries (Buesch, Spengler et al. 1996a, pp. 21 to 26; Moyer et al. 1996, p. 7). Although it is acknowledged that there are differences in many of the boundaries, these differences result in large part from how individual boundaries (time-stratigraphic, hydrogeologic, or thermal-mechanical) are defined. Most of the material presented below focuses on the properties common to the three types of units; more detailed discussions of the hydrogeologic properties in the unsaturated zone and thermal-mechanical properties are presented elsewhere (Sections 8.3 and 4.7, respectively).

Lithostratigraphic units are grouped into five major hydrogeologic units in the Yucca Mountain area, based principally on major variations in the degree of welding (Montazer and Wilson 1984, pp. 14 to 19). These include the undifferentiated overburden unit (UO, surficial deposits down through the upper part of the crystal-rich member of the Tiva Canyon Tuff), Tiva Canyon welded unit (TCw), Paintbrush nonwelded unit (PTn), Topopah Spring welded unit (TSw), and Calico Hills nonwelded unit (CHn) (Table 4.5-2). The distribution and characteristics of these units are

discussed by Buesch and Spengler (1999a, pp. 24 to 33). Lithology and properties of the hydrogeologic units are discussed in Section 8.3. Correlation of lithostratigraphic features and contacts to the detailed hydrogeologic units are outlined in Buesch and Spengler (1999a, pp. 24 to 26).

Stratigraphic units with distinct thermal and mechanical properties within the volcanic rock sequence at Yucca Mountain were identified by Ortiz et al. (1985, Table 1). As with the hydrogeologic units, correlations of the boundaries of thermal-mechanical units with lithostratigraphic zones and subzones (Tables 4.5-1 and 4.5-2) are based on changes in macroscopic features that define lithostratigraphic units and the preliminary correlation of lithostratigraphic units with preliminary laboratory measurements (Buesch, Spengler et al. 1996a, Table 4). Most thermal-mechanical unit boundaries roughly correspond to lithostratigraphic contacts that mark the transition from vitric, moderately welded rocks to densely welded subzones or to the contact between the vitric, moderately welded rocks and high-temperature, devitrified rocks; additional criteria are based on the percentage of lithophysae (Table 4.5-2; Figure 4.5-33). Figure 4.5-33 illustrates the variations in porosity, density, p- and s-wave velocity, Young's modulus, and ultimate strength plotted versus depth and lithostratigraphic zone (labeled) and subzone (not labeled). Several lithostratigraphic zones have distinctive values and ranges; some minor variations within these properties are correlated to some of the subzones. Figure 4.5-33 shows a fairly typical distribution of thermal-mechanical property data, which points out the fact that, compared to the closely spaced hydrogeologic data (Flint, L.E. 1998), the thermal-mechanical data can be used to determine general properties of the units, but it is typically difficult to identify a unique contact between the units. Detailed discussions of the thermal and mechanical properties of the various thermal-mechanical units are given in Section 4.7.

4.6 SITE STRUCTURAL GEOLOGY

4.6.1 Introduction

The purpose of this section is to describe the structural geologic framework of Yucca Mountain. Geologic mapping and geophysical investigations provide the data to understand the spatial and temporal patterns of faulting and fracturing of the Miocene age volcanic bedrock at the Yucca Mountain potential repository site. An understanding of these characteristics is needed to design a potential repository for high-level radioactive wastes at Yucca Mountain and to assess its performance. Structural geologic results contribute to evaluation of the volume and quality of rock available for underground construction of a potential repository, the delineation of hydrologic flow paths, and the assessment of seismic and fault displacement hazards.

The structure of the site area is discussed first with an overview of the basic structural framework and timing of deformation (Sections 4.6.2 and 4.6.3). A more detailed discussion of the structure of the central part of the site area closest to the potential repository is then presented (Section 4.6.4), followed by summaries of structures interpreted from geophysical investigations (Section 4.6.5) and of fracture studies (Section 4.6.6). The final discussion presents a descriptive structural geologic model for Yucca Mountain (Section 4.6.7).

Definitions–To facilitate the discussion, several key structural terms are defined with meanings specific to the Yucca Mountain site area:

- **Block-Bounding Faults**–A series of north-striking predominantly normal faults that are spaced 1 to 4 km (0.6 to 2.5 mi.) apart. South of the site area, they are northeast-striking. The faults commonly have experienced hundreds of meters (thousands of feet) of Tertiary displacement of Miocene Paintbrush Group tuffs, with subordinate amounts of strike-slip motion. In some places, Quaternary displacement has been documented on these faults (Section 12.3).

- **Central Block**–An informal designation for the Yucca Crest subblock of the central Yucca Mountain structural domain. In current design concepts, the emplacement area for radioactive waste at a potential geologic repository constructed at Yucca Mountain would lie within the Central Block.

- **Cooling Joints**–Smooth, gently curved to planar discontinuities that are inferred to have formed early in the history of the volcanic rock mass, in response to contraction during cooling. Cooling joints are most easily identified where tubular structures are present on the joint surface (Barton, C.C., Howard et al. 1984). A combination of other criteria may be used to recognize cooling joints where tubular structures are absent (Throckmorton and Verbeek 1995, p. 12). These criteria include low surface roughness; smooth, continuous traces; great length relative to other fractures; parallelism with proven cooling joints nearby; presence of demonstrated early age as shown through abutting relations with fractures of other sets; and the presence of bleached margins composed of minerals that formed at high temperatures (Levy 1993, p. 544).

- **Faults**–Planar or curviplanar discontinuities along which displacement of bedrock has occurred. Because this section addresses bedrock structural geology, use of the term

"fault" is confined to structures that produced displacements of units within the bedrock. In some cases, these structures are also associated with displacements of Quaternary units. Because the numerous geologic mapping and fractured rock mass studies were subject to widely varying observation scales, bedrock exposure percentage, and stratigraphic control precision, the lower limit on fault displacement magnitudes portrayed in each study also varies widely.

- **Fault System**–A complex, commonly anastomosing array of faults that are geometrically and kinematically linked. At Yucca Mountain, the term "fault system" is generally reserved for fault arrays that have trace lengths of several kilometers (such as "block-bounding fault systems") although it has also been applied to smaller fault zones.

- **Fracture Intensity**–A general term used to describe spatial changes in the spacing or density of fractures. Intensity may be computed based on the distance between neighboring fractures and thus reported as either spacing (the distance between fractures) or frequency (number of fractures per linear distance). Areal fracture intensity may be computed in terms of fracture density (e.g., the number of fractures per unit area), or fracture trace length per unit area.

- **Intrablock Faults**–Relatively minor faults that lie entirely within the structural blocks defined by the block-bounding faults. In the Central Block, intrablock faults have 1 to 30 m (3.3 to 100 ft) of displacement, typical mapped lengths of less than 1 km (0.6 mi.), and up to a maximum mapped length of 7 km (4.3 mi.) (this maximum length represents the combined length of the Ghost Dance and Abandoned Wash faults).

- **Joint Set**–A population of joints in a defined area that are subparallel.

- **Relay Faults**–Faults that kinematically link block-bounding faults. Relay faults range in size from large zones with total displacement and rock-mass damage approaching that of block-bounding faults to small faults with characteristics similar to intrablock faults. Through most of the site, relay faults strike to the northwest; south of the site area, they strike to the north.

- **Structural Domains**–Discrete portions of the site area that are characterized by a particular structural style distinct from that of adjacent areas. The concept of structural domains can be applied at any scale. For present purposes, they are defined on the 1:24,000-scale geologic map by Day et al. (1998b). These domains are separate from the more regional tectonic domains discussed in Section 4.2 (Walker Lane, Basin and Range, Inyo-Mono) and Section 4.3 (Crater Flat).

- **Tectonic Fractures**–Discontinuities across which simple opening (face separation) or less than 10 cm (4 in.) of displacement has occurred in response to regional tectonic stresses or local stresses. In some cases, these structures have reactivated preexisting cooling joints.

4.6.2 Structural Geologic Data

Regional structural studies of Yucca Mountain began with 1:24,000-scale geologic mapping of 7.5-minute topographic quadrangles, in and near the Nevada Test Site, by the U.S. Geological Survey in the 1950s and 1960s. In the immediate vicinity of Yucca Mountain, the relevant maps from these studies are Christiansen and Lipman (1965) and Lipman and McKay (1965). These maps, although primarily reconnaissance in nature, portrayed the block-bounding faults and some intrablock faults that affected the principal Miocene ash-flow tuffs and the underlying Paleozoic rocks.

Anticipating the need for larger scale geologic mapping in the early stages of site suitability studies, renewed field investigations in the central and northern portions of Yucca Mountain resulted in the publication of a 1:12,000-scale map by R.B. Scott and Bonk (1984). The area of mapping is shown on Figure 4.6-1. Their mapping shows geologic structure in considerably greater detail than the earlier quadrangle maps. R.B. Scott and Bonk's (1984) defined numerous map units (zones) within each of the Tiva Canyon and Topopah Spring tuffs (the principal bedrock formations at Yucca Mountain [Section 4.5]), which led to the delineation of numerous minor faults not previously recognized. Although also considered to be the result of reconnaissance mapping, R.B. Scott and Bonk's (1984) map served as the primary source of bedrock geologic data at Yucca Mountain for nearly a decade. It provided a guide to help define the most favorable areas in which to concentrate further site studies. A preliminary 1:12,000-scale geologic map of the southern part of Yucca Mountain (Scott, R.B. 1992) was also completed.

Simonds et al. (1995) compiled a 1:24,000-scale fault map for Yucca Mountain, integrating new data on Quaternary to recent fault activity (e.g., neotectonic studies of fault scarps). The compilation was based in part on bedrock faults mapped by R.B. Scott and Bonk (1984) and R.B. Scott (1992). Regional compilations at smaller scales (Frizzell and Shulters 1990; Maldonado 1985) summarize the results of the quadrangle mapping and place Yucca Mountain geology in a regional context.

Two additional bedrock geologic maps are the primary products of the most recent geologic mapping activities at Yucca Mountain. A 1:24,000-scale map by Day et al. (1998b) covers an area approximately 11 by 15 km (7.0 by 9.3 miles) centered on the north-central part of the mountain (Figure 4.6-1). This area is informally referred to as the "site area." A 1:6,000-scale map of the Central Block area by Day et al. (1998a) includes a 5.25-by-7.75-km (3.26-by-4.81-mi.) area centered more directly on the potential repository area within the mountain (Figure 4.6-1).

Bedrock geologic map units correspond largely to boundaries of formations and members of formations for the 1:24,000-scale mapping (Day et al. 1998b), and to zonal contacts within these units for the 1:6,000-scale mapping (Day et al. 1998a). Tables 4.5-1 and 4.5-2 provide detailed descriptions of lithostratigraphic units and subunits that have been differentiated within the thick mid-Tertiary volcanic rock sequence at Yucca Mountain. A summary of site stratigraphy is provided in Section 4.5.

Faults with 5 m (16 ft) (or more) of displacement were recorded at 1:24,000-scale, whereas faults with as little displacement as 1 m (3 ft) were mapped in the more detailed studies. Mapping at scales larger than 1:6,000 was conducted in selected areas to show essential fault relationships not portrayed well at the smaller scales. For example, the Ghost Dance and Sundance fault zones (Figure 4.6-2), which displace bedrock units near the potential repository block, were mapped at scales ranging from 1:240 to 1:2,400. Geologic mapping of the Exploratory Studies Facility (ESF) (Figure 4.6-2) was done at a scale of 1:125.

The distribution and characteristics of fractures in volcanic bedrock units were studied in natural and cleared surface exposures, boreholes, and underground excavations. Mapping was conducted at scales of 1:240 or larger (typically 1:120 and 1:125). The largest volume of fractured rock mass data was provided by the full-periphery geologic mapping in the 8-km-long (5-mi.-long), 7.6-m-diameter (25-ft-diameter) ESF tunnel.

4.6.3 Structural Framework of Site Area

This section describes the structural framework of the site area. First the hierarchy of faulting observed at the site is discussed. Next, the application of the concept of structural domains is presented for Yucca Mountain. Finally, the section concludes with a discussion of the timing of faulting. Figure 4.6-3 provides an index map showing geographic features referred to in the text.

4.6.3.1 Hierarchy of Faulting

The structural framework of the site area consists of block-bounding faults, relay faults, and intrablock faults (see definitions in Section 4.6.1). Block-bounding faults are spaced 1 to 4 km (0.6 to 2.5 mi.) apart. In the site area (Figure 4.6-2), these faults include (from west to east) the Northern Windy Wash, Fatigue Wash, Solitario Canyon, Dune Wash, Bow Ridge, Midway Valley, Paintbrush Canyon, Busted Butte, and several unnamed faults in the southernmost part of the site area. Fault scarps commonly dip 50° to 80° to the west, with scattered dips of 40° to 50° and 80° to 90°. A subordinate component of left-lateral displacement is commonly associated with these faults as determined from slickenside orientations (Scott, R.B. and Bonk 1984; Simonds et al. 1995; Day et al. 1998a). The orientation, amount of displacement, and nature of the associated deformation varies slightly from north to south and from west to east within the site area (Figure 4.6-2). The nature of these variations is discussed in this section.

Displacement is transferred between block-bounding faults along relay faults. The Drill Hole Wash and Pagany Wash faults are examples of relay faults (Figure 4.6-2). Relay faults intersect block-bounding faults at oblique angles and provide an intrablock kinematic link between the bounding structures. As such, the relay faults (and related structures that comprise relay fault zones) are significant components of the block-bounding fault systems, particularly in the southern half of Yucca Mountain. Most relay faults are complex faulting zones. Through most of the site area (Figure 4.6-2), block-bounding faults strike to the north and relay faults strike to the northwest. South of the site area, block-bounding faults strike to the northeast and relay faults strike to the north.

Within structural blocks, small strains are accommodated along intrablock faults. Intrablock faults may represent local structural adjustments in response to displacements along the

block-bounding faults. In some cases, intrablock faults are expressions of hanging-wall or footwall deformation within a few hundred meters (about 1,000 ft) of block-bounding faults. Other intrablock faults, such as northwest-trending, narrow grabens in the southeast part of the Central Block (Day et al. 1998a), accommodate strains in narrow zones between overlapping tips of block-bounding faults. Such intrablock faults may have evolved into relay faults as a result of increased horizontal extension in the southern part of Yucca Mountain.

4.6.3.2 Structural Domains

To facilitate discussion of the structural framework of Yucca Mountain, the site area is divided into structural domains (Section 4.6.1). The concept of domains is a useful descriptive tool because it synthesizes a large area and many features into a smaller number of groups with similar characteristics. Ten structural domains within the site area are defined here and are shown on Figure 4.6-4. One other domain in the northwest corner of the site area extends farther west and is not discussed further. More detailed discussions are provided in Day et al. (1998b, pp. 12 to 17).

Each structural domain is characterized by a distinctive structural style. The distinctive structural patterns that characterize individual domains may include the nature and intensity of faulting, as well as magnitude and direction of stratal dips. The domains reflect an integrated structural response through time, and are not defined on the basis of timing of deformation or response to a particular tectonic episode. The site area structural domains are briefly described below.

4.6.3.2.1 Central Yucca Mountain Domain

The largest and structurally simplest domain is the Central Yucca Mountain domain. It comprises three east-tilted blocks bounded by west-dipping block-bounding faults, as shown on Figure 4.6-4. From west to east, these blocks are: (1) the West Ridge block, bounded on the west by the Northern Windy Wash fault and on the east by the Fatigue Wash fault; (2) the Jet Ridge block, bounded on the west by the Fatigue Wash fault and on the east by the Solitario Canyon fault; and (3) the Central Block, bounded on the west by the Solitario Canyon fault and on the east by the Bow Ridge fault.

The potential repository is located within the Central Block of the Central Yucca Mountain domain. This domain includes a narrow portion that continues to the south, where it is bounded by the Iron Ridge fault on the west and the East Ridge fault and an unnamed normal fault on the east. At the latitude of the potential repository, the West Ridge block is about 1 km (0.6 mi.) wide, the Jet Ridge block is about 2 km (1.2 mi.) wide, and the Central Block is about 3.5 to 4.0 km (2.2 to 2.5 mi.) wide. In each block, stratal dips in the Paintbrush Group ash-flow tuffs are typically 5° to 10°. Along the eastern edges of the blocks in the hanging walls of block-bounding faults, dips are locally as high as 15° to 20° (Scott, R.B. and Bonk 1984; Day et al. 1998a). The Central Yucca Mountain domain has undergone about 10 percent of post-12.7-Ma east-west extension.

The fault systems that bound the three blocks of the Central Yucca Mountain domain are internally complex, in contrast to the geologically simple east-tilted blocks. Within the Central

Yucca Mountain domain, the transfer of displacements between block-bounding faults was observed only on West Ridge. At that location, a complex northwest-trending relay fault zone crosses the ridge and links the Northern Windy Wash fault to the Fatigue Wash fault (Scott, R.B. and Bonk 1984; Day et al. 1998b). In areas south of the Central Yucca Mountain domain (discussed in Section 4.6.3.2.7), relay faults commonly transfer displacements between block-bounding faults.

Intrablock faults, such as the north-striking Ghost Dance and Abandoned Wash faults in the Central Block and the Boomerang Point fault in the Jet Ridge block, are locally prominent. These prominent intrablock faults have locally undergone tens of meters of west-side-down displacement and, individually, tend to be associated with a simple, narrow deformation zone, in contrast to the hundreds of meters (about 1,000 ft) of displacement and broad complex deformation zones commonly associated with block-bounding faults. The Central Block and, to a much lesser extent, the Jet Ridge block, contain complex intrablock faulting zones along their eastern edges (Scott, R.B. and Bonk 1984; Day et al. 1998a). This block-margin faulting, accompanied by steepening of stratal dips, reflects the internal deformation produced in the hanging wall of a complex block-bounding fault zone (Scott, R.B. 1990, p. 259; Day et al. 1998a). R.B. Scott (1990, p. 259) used the term imbricate zone to describe this intense block-margin faulting and proposed that it records deformation above a listric block-bounding fault above a shallow detachment. Details of block-margin faulting in the Central Block are discussed later.

The northern parts of the West Ridge and Jet Ridge blocks are more highly deformed than to the south. This is particularly obvious near The Prow (Figures 4.6-3, 4.6-4), where the frequency and intensity of intrablock faulting increases. Along the northwest-trending edge of Yucca Mountain, between The Prow and Castellated Ridge (Figure 4.6-3), northeast-facing, southeast-dipping strata of the Paintbrush Group are cut by a series of north-striking to north-northwest-striking normal faults that range in displacement from 2 to 70 m (6.5 to 230 ft). Eastside-down and west-side-down displacements are about equally divided (Day et al. 1998b, p. 14; Scott, R.B and Bonk 1984; Christiansen and Lipman 1965). Through the northwestern corner of the site area and to the north of the site area, the Windy Wash fault is a complex, westside-down block-bounding fault. The Fatigue Wash fault continues through The Prow area as a westside-down block-bounding fault.

4.6.3.2.2 Azreal Ridge Domain

The Azreal Ridge domain (Figure 4.6-4) is characterized by decreased east-west extension relative to the Central Yucca Mountain domain. Westside-down displacements along the Solitario Canyon fault and the Bow Ridge fault decrease to zero at hinge points within this domain. North of the hinge points, eastside-down displacements are mapped or inferred from borehole and map data. For the Solitario Canyon fault, the hinge point is in Teacup Wash (Day et al. 1998a, p. 6), and for the Bow Ridge fault, the hinge point lies beneath Quaternary alluvium east of Isolation Ridge (Dickerson and Drake 1998a, p. 255). The Azreal Ridge domain occupies the little-extended area bounded by the segments of these two faults with minimal displacement near the hinge points.

The magnitude of post-12.7-Ma extension in the Azreal Ridge domain was about 0 to 7 percent. The maximum value of 7 percent was calculated by C.J. Fridrich et al. (1999, Figure 5). In addition to the decreased extension compared to that of the Central Yucca Mountain domain, southeast stratal dips in the Paintbrush Group and a change in intrablock faulting style characterize the Azreal Ridge domain. The main ridges and washes at Yucca Mountain are generally parallel to the dip of the Paintbrush Group welded tuffs. This southeast dip is geomorphically expressed as a strong northwest-trending topographic grain. The southeasterly dipping strata in the Azreal Ridge domain comprise one limb of a broad southeast-plunging syncline. The east-dipping strata of the Central Block define the other limb. The axis of this syncline lies beneath Drill Hole Wash (Figure 4.6-3).

The long northwest-trending washes bordering the northern part of the potential repository are underlain by faults that elsewhere show evidence for dextral strike-slip and southwestside-down dip-slip motion (Scott, R.B., Bath et al. 1984, p. 18). Evidence includes subhorizontal slickensides and mullion structures on the nearly vertical Sever Wash fault and Reidel shears along the Pagany Wash fault (Day et al. 1998b, pp. 10 to 11). R.B. Scott and Bonk (1984) mapped the Drill Hole Wash fault as a dextral strike-slip fault. Evidence for this included the dextral offset of a north-striking fault by the (presumably younger) northwest-trending Drill Hole Wash fault near the southeast end of Tonsil Ridge. Day et al. (1998a) found that the intersecting fault pattern mapped by R.B. Scott and Bonk (1984) is not present. According to Day et al. (1998a, p. 8) the Drill Hole Wash fault, along which the Tiva Canyon Tuff is displaced 15 m (49 ft) down to the southwest on Tonsil Ridge, is discontinuous. The amount of stratigraphic throw decreases abruptly in both directions from where the fault crosses Tonsil Ridge. Where the Drill Hole Wash fault zone crosses the ESF 400 m (1,312 ft) to the southeast, the stratigraphic throw may be as little as 1.2 m (4 ft). Subhorizontal slickensides, indicating dextral slip, are documented along one strand of the Drill Hole Wash fault in the ESF (Day et al. 1998a, p. 8). In southern Drill Hole Wash, southeast of the ESF alignment, Spengler and Rosenbaum (1980, p. 31, Figure 2) used oriented drill core logs to infer the presence of two faults beneath surficial deposits along the northwest and southeast margins of Drill Hole Wash. The drill core showed evidence of shearing and rotation of foliation and remanent magnetization vectors. Spengler and Rosenbaum (1980, p. 31) interpreted the buried faults as sinistral strike-slip, or oblique-slip faults.

4.6.3.2.3 Yucca Wash Domain

The Yucca Wash domain is north of the Azreal Ridge domain (Figure 4.6-4). It records a northward increase in the magnitude of east-west extension, accommodated along north- to northwest-striking intrablock faults. These include several splays of the Sever Wash fault, which demonstrate increased displacement to the north, just south of Yucca Wash. This structural style is similar to that of the adjacent part of the Central Yucca Mountain domain near The Prow.

Geologic and geophysical evidence in the Yucca Wash domain argues against the existence of the Yucca Wash fault, which was proposed by R.B. Scott and Bonk (1984) as a significant strike-slip fault located beneath Yucca Wash. The base of the Pah Canyon Tuff projects across Yucca Wash with no apparent displacement, whereas the presence of a significant strike-slip fault, oriented approximately parallel to the dip of the strata, would produce significant stratigraphic throw (Dickerson 1996). Langenheim, Ponce et al. (1993) acquired ground-based

gravity and magnetic data from four traverses across Yucca Wash and three parallel traverses along the length of Yucca Wash. These data reveal a distinct high magnetic anomaly trending across Yucca Wash near borehole UE-25 WT#6. The anomaly is not offset along any northwest-striking structure, nor is a distinct magnetic plateau southeast of this anomaly offset to the northwest or southeast. These geophysical data define several north-striking anomalies, interpreted as normal faults, that can be traced beneath the wash to bedrock exposures of normal faults on both sides of Yucca Wash. Aeromagnetic data (McCafferty and Grauch 1997) show northwest-trending gradients between magnetic highs and lows that parallel the northwest-striking faults in Drill Hole, Pagany, and Sever washes. Conversely, the aeromagnetic anomalies and gradients between them are oriented along north-south trends in the Yucca Wash area, as are a number of mapped normal faults. These data suggest that the structural grain beneath Yucca Wash is dominated by north-striking normal faults that are not disrupted by a significant northwest-trending structure. The Yucca Wash fault was not recognized by either Christiansen and Lipman (1965) or Day et al. (1998a, p. 8; 1998b, p. 11).

4.6.3.2.4 Paintbrush Canyon Domain

The Paintbrush Canyon domain is located to the east of the Yucca Wash, Azreal Ridge, and Central Yucca Mountain domains (Figure 4.6-4). It is characterized by closely spaced faults that separate a series of long, narrow, north-trending and east-dipping blocks ranging in width from 0.6 to 1 km (0.4 to 0.6 mi.). The domain is bounded on its east and west sides by the Paintbrush Canyon and Bow Ridge faults, respectively. It includes prominent north-striking faults, such as the Black Glass Canyon fault, the Midway Valley fault, and the Exile Hill fault. In the northern part of the domain, fault blocks are juxtaposed along down-to-the-west normal faults that have extensive hanging-wall deformation (Dickerson and Drake 1998b, p. 12, Plate 1). This hanging-wall deformation includes graben development, numerous splays, pull-apart structures, and wide, internally sheared, massively brecciated, multi-plane main fault zones. Geophysical interpretations suggest that fault-bounded blocks buried by surficial deposits in Midway Valley define a horst-and-graben pattern (Ponce and Oliver 1996, Figure 5). Exile Hill, for example, represents a horst; another buried horst occurs to the east beneath the center of Midway Valley. These horsts are 0.3 to 0.7 km (0.2 to 0.4 mi.) wide (Ponce 1996, Plate 4; Dickerson and Drake 1998a, p. 255).

The continuity of north-trending faults from north of Yucca Wash southward through Midway Valley is a characteristic of the Paintbrush Canyon domain. Geophysical and geologic data indicate that the main faults exposed north of Yucca Wash continue southward beneath Quaternary deposits to the southern part of Midway Valley (Dickerson 1996; Dickerson and Drake 1998a, p. 254). This observation argues against the presence of the Yucca Wash fault as a major structure.

Along the eastern edge of the Paintbrush Canyon domain, the magnitude of deformation and complexity of the Paintbrush Canyon fault increase southward. There is more than 200 m (656 ft) of displacement along this fault in upper Paintbrush Canyon (Dickerson and Drake 1998b, p. 12) and more than 300 m (984 ft) of displacement near Fran Ridge (Figure 4.6-3). Beneath the southeastern part of Midway Valley, buried northeast-striking faults are inferred to have propagated from the main trace of the Paintbrush Canyon fault (Dickerson and Drake 1998a, p. 255). The horst-and-graben pattern characteristic of most of Midway Valley is either

truncated or merges with these splays (Dickerson and Drake 1998a, p. 255). At the southern end of the Paintbrush Canyon domain, the Paintbrush Canyon fault becomes a major fault system as it merges with the Dune Wash and Bow Ridge faults (Figure 4.6-4). The Paintbrush Canyon fault system collects the aggregate displacement of all of these faults. Unfortunately, the area in which these faults intersect, surely one of the most deformed and structurally complex areas of Yucca Mountain, is concealed beneath surficial deposits northwest of Busted Butte. Considered in the context of relay faults, the northwest-striking segments of the Dune Wash and Bow Ridge faults transfer displacement between their north-striking segments (to the north) and the north-striking Paintbrush fault system (to the south).

4.6.3.2.5 Fran Ridge Domain

The Fran Ridge domain is a north-south trending, largely intact block, between the Paintbrush Canyon fault and Fortymile Wash (Figures 4.6-3, 4.6-4). It includes (from north to south) Comb Peak and the bedrock tract to its south, Alice Ridge, Fran Ridge, and Busted Butte (Figure 4.6-3). The domain is characterized by less internal deformation than that found in the Paintbrush Canyon domain. Smaller faults splay eastward off the Paintbrush Canyon fault at Joey Ridge, Alice Ridge, and Fran Ridge, and indicate a greater amount of footwall deformation along the Paintbrush Canyon fault than is documented for faults in the Paintbrush Canyon domain. Although the internal deformation in most of the Fran Ridge domain is minor, there are a few intrablock faults with significant amounts of offset, such as the Busted Butte fault (75 m [246 ft]) and the fault south of Comb Peak (130 m [427 ft]). Additionally, the Fran Ridge domain is both stratigraphically and structurally higher than the adjacent Paintbrush Canyon and Fortymile Wash domains. Gaps between the topographic highs within the Fran Ridge domain are occupied by buried down-to-the-north faults that lie between Busted Butte and Fran Ridge, and between Fran Ridge and Alice Ridge. These buried faults, probably northwest-striking splays within the footwall of the Paintbrush Canyon fault, are identified by stratigraphic mismatches between outcrops on the topographic highs.

4.6.3.2.6 Fortymile Wash Domain

The Fortymile Wash domain lies east of the Fran Ridge domain (Figure 4.6-4). Geologic relationships within the Fortymile Wash domain are poorly understood because bedrock is largely concealed by Quaternary (and possibly older) surficial deposits of Jackass Flats. Data from borehole UE-25 J#13 (Figure 4.5-5) indicate that this area is down-faulted along a fault east of Fran Ridge. Also, the prevailing east dip of the Paintbrush Group strata suggests that a westside-down normal fault lies beneath the western part of Jackass Flats (east of the down-to-the-east Busted Butte fault shown east of Fran Ridge) (Figures 4.6-3, 4.6-4). This fault is possibly the Gravity fault shown on Figure 4.3-1. The northern part of the Fortymile Wash domain contains the extensively faulted rocks east of Fortymile Wash. There is no preferred orientation for faults in this area. It is not known to what extent this fault pattern characterizes other parts of the Fortymile Wash domain where bedrock is not exposed.

4.6.3.2.7 Dune Wash, East Ridge, Southwest, and Plug Hill Domains

The Dune Wash, East Ridge, Southwest, and Plug Hill domains cover the area south of the Central Yucca Mountain domain (Figure 4.6-4). These domains are associated with a significant

increase in the magnitude of extension accompanied by different structural styles (Scott, R.B. and Bonk 1984; Day et al. 1998b). The transition from the less-extended northern part of Yucca Mountain to the more-extended southern part is generally expressed on geologic maps by numerous splay faults that fan southward from block-bounding faults from the north. For example, increased east-west extension is accompanied by the southward splaying of the Solitario Canyon fault, the development of a broad, complexly faulted graben between Dune Wash and the unnamed ridge between Dune Wash and Abandoned Wash, and the convergence of several block-bounding faults along the west side of Busted Butte. In intrablock areas, the transition is expressed by the appearance of numerous closely spaced minor faults that coalesce and gain displacement to the south. These patterns are apparent in the northern part of Dune Wash and particularly near the mouth of Abandoned Wash (Scott, R.B. and Bonk 1984; Day et al. 1998b, p. 17).

In the southern part of the site area, the amount of extension, intensity of deformation, and the amount of vertical-axis rotation all increase (Scott, R.B. 1990, pp. 259, 265; Scott, R.B. 1992; Day et al. 1998b, p 17; Rosenbaum et al. 1991, pp. 1971 to 1972, Figure 10). R.B. Scott (1990, p. 259) interpreted the southward increase in deformation to reflect an increase in the area underlain by "imbricate fault zones." These zones were interpreted to be characterized by steeper eastward dips of strata and "an imbricate pattern of closely spaced, steep, west-dipping faults with minor, down-to-the-west offsets of a few meters or less" (Scott, R.B. 1990, p. 259). Clockwise vertical-axis rotations of Paintbrush Group strata increase from north to south, from 5° to 10° in the Central Block of the Central Yucca Mountain domain, to 30° at the extreme south end of Yucca Mountain, south of the site area (Rosenbaum et al. 1991, Figure 10). Northwest- to north-northwest-striking splays are common components of the north-striking block-bounding fault systems. In some places, these northwest-striking splays have developed into relay faults that transfer displacement between block-bounding faults. In the extreme southern part of Yucca Mountain (south of the site area), the strike of the Southern Windy Wash and Stagecoach Road block-bounding faults are rotated to northeasterly orientations, and the subsidiary splays are north-striking (Simonds et al. 1995).

The Dune Wash domain (Figure 4.6-4) is defined by a northwest-trending complex graben, bounded on the east side by the down-to-the-west block-bounding Dune Wash fault. Its western margin is bounded by a down-to-the-east block-bounding East Ridge fault zone with at least 120 m (394 ft) of down-to-the-east displacement, which is equal to or greater than that of the more widely known Dune Wash fault. This fault zone is approximately 100 m (328 ft) wide, contains tectonically brecciated and juxtaposed units of the Topopah Spring Tuff and, in places, exhibits higher degrees of oxidation, silicification, and alteration relative to other block-bounding faults. The East Ridge fault zone splays to the south into several faults with down-to-the-east displacement southwest of borehole UE-25 WT#17 (Figure 4.5-5) (Day et al. 1998b). The splays each have over 30 m (100 ft) of displacement. Within the interior of the graben are numerous smaller horst-and-graben structural blocks whose strata dip dominantly to the east. The structure of the graben interior is complex, with numerous, discontinuous, steeply dipping faults. The Dune Wash domain is an area depicted by R.B. Scott (1990, Figure 3) as a broad imbricate fault zone. Although intensely faulted, it is not characterized by consistent westside-down offsets, as R.B. Scott (1990, p. 259) implies by his definition and use of the term "imbricate fault zone."

In the northern end of the Dune Wash graben (southwest of borehole USW WT-1) (Figure 4.5-5), the East Ridge fault steps about 200 m (656 ft) to the west and displacement decreases. This fault places the crystal-rich member of the Tiva Canyon Tuff down against the pre-Tiva Canyon, post-Topopah Spring nonwelded tuffs (Table 4.5-2). The displacement on individual faults within the graben decreases to the north, but the overall horst-and-graben pattern is maintained. At the northern end of the graben, just south of the mouth of Abandoned Wash, the faulting resembles the closely spaced faulting that characterizes block-margin deformation in the Central Block to the north. The southern end of the Dune Wash domain, which is buried beneath Quaternary deposits southwest of Busted Butte, seems to terminate against the down-to-the-west Paintbrush Canyon fault.

The East Ridge domain lies to the west of the Dune Wash domain (Figure 4.6-4). It is bounded on the west by an unnamed block-bounding fault west of borehole WT-12, and on the east by the East Ridge fault. This domain differs from the adjacent Central Yucca Mountain domain in that the amount of intrablock faulting records a greater amount of extensional deformation. The strata strike north-northeast and dip generally 15° to 20° to the east, which is steeper than is observed in the Central Yucca Mountain domain. This domain also has numerous eastside-down faults, which splay off the western margin of the Dune Wash graben.

In the Southwest domain (Figure 4.6-4), which lies between the Iron Ridge fault and Crater Flat, north-trending, block-bounding faults are linked kinematically by northwest-trending relay faults and associated structures. These act to disperse the regional tectonic strain across several faults. An example is the complex northwest-striking relay zone between the Solitario Canyon and Iron Ridge faults, near the north end of the Southwest domain (Scott, R.B. and Bonk 1984; Day et al. 1998b, p. 10) (Figure 4.6-4). Here and elsewhere in the southern part of Yucca Mountain, northwest-striking narrow grabens commonly are associated with relay faults. The fault systems in this domain are west-dipping, upward widening arrays, with west dips ranging from relatively shallow (45° to 50°) to steep (75° to 85°). As the upward widening fault zones attain shallower dips, the amount of secondary faulting preserved in the footwall of the block-bounding fault system noticeably increases. In addition, fracturing of the footwall increases near the major relay faults.

The Plug Hill domain (Figures 4.6-4) includes low-lying hills of Tiva Canyon Tuff at the western edge of the map area as well as the Rainier Mesa Tuff exposed on Plug Hill itself (Figure 4.6-3). The northern margin of the domain is delineated by the relay structures on the southern tip of Jet Ridge. The eastern and southern margins are formed by the Solitario Canyon fault, which curves from a north strike to a more northeasterly strike. The bedrock is poorly exposed, but where present, it is composed of faulted, eastward-dipping blocks of Paintbrush Group units downdropped along the normal faults that rim the domain. Plug Hill is made up of Tiva Canyon Tuff overlain by nonwelded and welded units of the Rainier Mesa Tuff. The amount of faulting within the Rainier Mesa Tuff is difficult to detect because of poor exposures. Day et al. (1998a) mapped faults in the underlying Paintbrush Group rocks as being overlain by unfaulted Rainier Mesa Tuff, suggesting that deposition of the Rainier Mesa Tuff postdated some of the post-Paintbrush Group movement on the hanging wall of the Solitario Canyon fault. Here, as elsewhere, the Rainier Mesa Tuff is preserved only on the hanging wall of the block-bounding faults.

4.6.3.3 Timing of Deformation

In addition to the structural elements characterizing Yucca Mountain, the timing of faulting and fracturing forms an additional component of the structural geologic framework for the site. This information can be used to understand the nature and interrelationship of faults and fractures in the subsurface. Five investigations were conducted to evaluate the timing of Neogene deformation in the Yucca Mountain site area:

1. Evaluation of stratigraphic relations across faults using geologic map patterns and lithologic logs of boreholes in the vicinity of faults to discern evidence for growth or episodic fault motion

2. Evaluation of discordance in stratal dips across unconformities

3. Estimation of vertical axis rotation using spatial and temporal variations in paleomagnetic data

4. Estimation of fault slip directions derived from field measurements of fault plane orientations and slickensides, temporally constrained by stratigraphic control where available

5. Evaluation of Quaternary to recent faulting in surficial materials (neotectonic studies).

The first four investigations are summarized below; the fifth is summarized in Section 12.3.

4.6.3.3.1 Stratigraphic Relations across Faults

Among the block-bounding faults, geologic map patterns provide evidence for episodic Miocene movement along the Solitario Canyon and Fatigue Wash faults during deposition of the Paintbrush Group volcanic tuffs. For example, on the east side of Solitario Canyon, across a prominent footwall splay of the Solitario Canyon fault, the pre-Pah Canyon bedded tuffs (Tpbt2, which directly overlies the Topopah Spring Tuff) (Table 4.5-2) and the overlying Pah Canyon Tuff show evidence for stratigraphic thinning from the hanging wall to the footwall of 7 m (23 ft) and 2 m (6.5 ft), respectively (Day et al. 1998b, p. 17). The top of the Topopah Spring Tuff is offset by 13 m (43 ft), whereas the bases of the Yucca Mountain Tuff and Tiva Canyon Tuff are offset by about 3 m (10 ft). These relationships indicate that this splay of the Solitario Canyon fault was active during deposition of map unit Tpbt2 and the Pah Canyon Tuff (12.8 to 12.7 Ma), and underwent lesser movement after deposition of the Tiva Canyon Tuff (12.7 Ma).

Further evidence for episodic fault displacement is present along an east-dipping segment of the Solitario Canyon fault on the north side of Teacup Wash. The lower nonlithophysal zone of the Tiva Canyon Tuff thickens about 10 m (33 ft) from the footwall across the fault to the hanging wall (Day et al. 1998a, p. 7). Thickening in the lower part of the Tiva Canyon Tuff suggests that fault-controlled relief of about 10 m (33 ft) occurred across the fault immediately before deposition of the Tiva Canyon Tuff. Thus, up to 10 m (33 ft) of pre-Tiva Canyon Tuff displacement occurred. In addition, displacement of stratigraphic markers near the top of the Tiva Canyon Tuff may represent about 12 m (40 ft) of post-Tiva Canyon Tuff displacement.

Southeast of The Prow (Figure 4.6-3), along the steep northeast-facing slope of Yucca Wash, the pre-Yucca Mountain Tuff bedded tuffs (Tpbt3) abruptly thicken across the Fatigue Wash fault. This suggests that the fault was active during or just prior to deposition of this unit at about 12.8 to 12.7 Ma. An additional 50 m (164 ft) of post-Tiva Canyon Tuff (post-12.7 Ma) displacement also occurred. About 150 m (492 ft) to the west, a parallel fault exhibits, in its hanging wall, a 45-m-thick (148-ft-thick) rhyolite flow (map unit Tpz) (Table 4.5-2) located stratigraphically between the Pah Canyon Tuff and the pre-Yucca Mountain Tuff bedded tuffs (Tpbt3). This flow is absent in the footwall, implying that at least 45 m (148 ft) of displacement occurred after deposition of the Pah Canyon Tuff. A 16-m (52-ft) increase in Yucca Mountain Tuff thickness occurs across this fault. Also, the base of the Tiva Canyon Tuff (younger than 12.7 Ma) is displaced about 20 m (66 ft).

Some intrablock faults also may have moved episodically. In the Central Block, borehole USW UZ-7a penetrates the Ghost Dance fault; lithologic logs indicate a 30-m (98-ft) decrease in thickness of the upper lithophysal zone of the Topopah Spring Tuff (Tptpul). At the surface, geologic mapping accounts for only about 15 m (49 ft) of displacement within the Tiva Canyon Tuff. This suggests that about 15 m (49 ft) of post-Topopah Spring, pre-Tiva Canyon Tuff (12.8 to 12.7 Ma) displacement, plus about 15 m (49 ft) of post-Tiva Canyon Tuff fault displacement, occurred at this locality. Day et al. (1998a) accounts for this difference in displacement by assuming that growth faulting (represented by stratigraphic thinning across the fault) occurred during deposition of the crystal-rich member of the Topopah Spring Tuff and overlying bedded tuffs at the base of the Tiva Canyon Tuff (Table 4.5-2). This interpretation assumes that a small amount of fault-related topography existed prior to deposition of the Tiva Canyon Tuff.

Numerous minor faults on the west side of Fran Ridge and the north end of Busted Butte (splays of the Busted Butte fault) displace the top of the Topopah Spring Tuff and the superjacent pre-Pah Canyon Tuff bedded tuffs (Tpbt2) by 1 to 10 m (3.3 to 33 ft). The younger pre-Tiva Canyon Tuff bedded tuffs (Tpbt4) and the base of the Tiva Canyon Tuff are not displaced. Thus, these faults were active only during the 100-k.y. interval between the eruption of the 12.8-Ma Topopah Spring Tuff and the deposition of the 12.7-Ma Tiva Canyon Tuff.

In upper Paintbrush Canyon in the northern part of the site area, several minor faults show evidence for activity throughout deposition of the Paintbrush Group (Dickerson and Drake 1998b, pp. 14 to 15). There is decreasing offset of successively younger units along several of the faults throughout the Paintbrush Group.

In summary, stratigraphic relationships across both block-bounding and intrablock faults in the site area show evidence for activity throughout the Paintbrush Group deposition. Evidence includes apparent growth relations (stratigraphic thickening across faults) within various post-Topopah Spring, pre-Tiva Canyon units, and fault-related paleotopography at the base of the Tiva Canyon Tuff. Post-Topopah Spring, pre-Tiva Canyon displacement does not produce discernible angular discordances between successive units. This may indicate that faults of this age produced vertical displacement but not extension, or only minor displacement of the volcanic units. Characteristics of the pre-Tiva Canyon faulting phase are difficult to define because the post-Tiva Canyon Tuff deformation greatly exceeds and masks the pre-Tiva Canyon Tuff displacement. Scattered, limited exposures of the Rainier Mesa Tuff impede evaluation of

post-Rainier Mesa deformation. As summarized below, evidence in the site area suggests that the Rainier Mesa Tuff was displaced and tilted nearly the same amount as the Tiva Canyon Tuff.

4.6.3.3.2 Angular Discordance across Unconformities

Contrasts in stratal dips across unconformities offer another method of examining the timing of deformation in the Yucca Mountain area. Fridrich (1999) and C.J. Fridrich et al. (1999) systematically evaluated the progressive Miocene deformation of Yucca Mountain and Crater Flat using this method. Specifically, C.J. Fridrich et al. (1999) compiled maps that portray the amount of angular discordance between the Paintbrush Group (12.8 to 12.7 Ma) and the Timber Mountain Group (11.7 to 11.45 Ma), and between the Timber Mountain Group and 10.5-Ma basalts and sedimentary breccia sheets. Because stratified 10.5-Ma units are not exposed in the site area, and because the majority of post-11.6-Ma deformation is confined to the part of Crater Flat west of the site area, only the Paintbrush-Timber Mountain unconformity is significant with respect to the timing and magnitude of extensional deformation at Yucca Mountain.

C.J. Fridrich et al. (1999, Figure 2A) indicate that in the Yucca Mountain site area the Tiva Canyon Tuff (12.7 Ma) was tilted by 10° to 20° to the east and southeast prior to deposition of the Rainier Mesa Tuff (Tmr, 11.6 Ma). Their summary maps (C.J. Fridrich et al. 1999, Figures 3A, 4A) indicate that less than 5° of eastward tilting occurred in the site area between 11.6 and 10.5 Ma, and that less than 5° of eastward tilting occurred after 10.5 Ma. These angular relationships are not well constrained in most of the site area because units younger than the Tiva Canyon Tuff are sparsely exposed. C.J. Fridrich et al. (1999, p. 203) relied on extrapolation from northern Crater Flat, as well as a few scattered exposures in the site area (southern Boundary Ridge, Plug Hill) to establish the reported contrasts in dip between the Tiva Canyon and Rainier Mesa tuffs. R.B. Scott (1990, p. 268), using compaction foliations, suggested that there is more than 10° of discordance between the Rainier Mesa Tuff and the Tiva Canyon Tuff west and northwest of Busted Butte (including the southern Boundary Ridge area). Because no 10.5-Ma stratified rocks are present in the site area, angular relationships involving this unit, reported by C.J. Fridrich et al. (1999, p. 204), are extrapolated from the western part of Crater Flat.

In contrast to the angular relations reported by C.J. Fridrich et al. (1999) and by R.B. Scott (1990, p. 268) in outlying parts of the site area, mapping by Day et al. (1998b, p. 18) indicates minimal angular discordance between the Paintbrush and Timber Mountain groups over most of the site area. For example, the basal bedded layers in the Rainier Mesa Tuff west of Busted Butte parallel both underlying post-Tiva Canyon Tuff bedded tuff (Tpbt5) and flattened pumice in the Tiva Canyon Tuff. Thus the Tiva Canyon, post-Tiva Canyon, and Rainier Mesa tuffs are separated by disconformities, not by angular unconformities, west of Busted Butte. Day et al. (1998b, p. 18) also report little or no (5° or less) angular discordance between the Tiva Canyon Tuff and the Rainier Mesa Tuff at southern Boundary Ridge (east of Dune Wash) and Plug Hill.

Within the North Ramp of the ESF, immediately west of the Bow Ridge fault (Beason et al. 1996), additional constraints on the amount of post-Paintbrush Group, pre-Timber Mountain Group tilting are available. Depositional contacts in the uppermost part of the Tiva Canyon Tuff dip 15° to 19°E, and depositional contacts in the lowermost tuffs of the Rainier Mesa Tuff dip 10° to 18°E. However, there is significant overlap in the values for these two units; the 10° dip

appears to be measured in an anomalous segment. The steep dips on these strata relative to the strata to the west in the Central Yucca Mountain and Azreal Ridge domains are typical of block-margin deformation in the immediate hanging wall of the Bow Ridge fault. C.J. Fridrich et al. (1999, Figures 2, 3) suggest that, in the northwestern part of the site area, tilting that occurs after deposition of the Paintbrush Group, but before the Timber Mountain Group, increases to the west. They calculate maximum cumulative horizontal extension values of 15 to 30 percent and minimum values of 7 to 15 percent across the site area. Most of the extension occurred from 12.7 to 11.6 Ma.

Day et al. (1998b) mapped shallower dips and correspondingly lower extension magnitudes than those reported by C.J. Fridrich et al. (1999). In the Azreal Ridge and Yucca Wash domains, and near The Prow in the Central Yucca Mountain domain, dips of the Tiva Canyon Tuff away from block-bounding faults range from 1° to 8°SE, and are typically about 5°SE (Day et al. 1998a). Day et al. (1998a) determined these values using three-point calculations on depositional contacts in the crystal-rich member of the unit. Similar values are obtained to the south in the Central and Jet Ridge blocks of the Central Yucca Mountain domain where Day et al. (1998a) determined contact dips of 5° to 11°E, with typical values of about 7°E. In contrast, C.J. Fridrich et al. (1999, Figure 2) report, for the same area, that the Tiva Canyon Tuff was tilted 10° to 15°E prior to deposition of the Rainier Mesa Tuff, and after 11.6 Ma was tilted by several more degrees. Dip amounts similar to those reported by C.J. Fridrich et al. (1999) occur only locally in the hanging walls of block-bounding faults. The difference in reported dips may be due to a reliance by Fridrich et al. (1999) on foliation attitudes in tuffs, defined by flattened pumice and lithophysae, rather than true stratal dips. Flattening foliations in crystal-rich zones of the Tiva Canyon Tuff are 5° to 14° in the Azreal Ridge domain and 8° to 20° in the Central and Jet Ridge blocks of the central Yucca Mountain domain (Scott, R.B. and Bonk 1984; Day et al. 1998a). Day et al. (1998a) demonstrated that the dips of flattening foliations commonly exceed true stratal dips by 5° (as determined by three-point calculations on depositional contacts). Representative stratal dip values, used in the tilting-domino-extension calculation of Nur et al. (1989), yield cumulative (post-12.7-Ma) extension values that are similar to the minimum extension values of 7° to 15° reported by C.J. Fridrich et al. (1999, Figure 5B).

4.6.3.3.3 Vertical-Axis Rotations

Vertical axis rotations determined from paleomagnetic data also provide information on deformation timing at Yucca Mountain. Rosenbaum et al. (1991) summarize paleomagnetic data for the Tiva Canyon Tuff. They demonstrate a progressive north-to-south increase in post-12.7-Ma vertical-axis rotations from 0° (no rotation) at The Prow to about 30° at the south end of Yucca Mountain (10 km south of the south edge of Figure 4.6-3). Within the site map area, vertical-axis rotation varies from 0° at The Prow to about 5° at the latitude of Busted Butte (south edge of the map). The apparent north-to-south increase in vertical-axis rotations at Yucca Mountain is part of a subregional trend of northeast-to-southwest-increasing vertical-axis rotations of Miocene volcanic units (Hudson, M.R., Sawyer et al. 1994, Figure 6; Hudson, M.R., Minor et al. 1996, p. A-451; Fridrich, C.J., 1999, Figure 8). Vertical-axis rotation occurred primarily from 11.6 to 11.45 Ma. This is based on statistically identical amounts of rotation for the Bullfrog Tuff (Tcb, 13.25 Ma) and the Tiva Canyon Tuff (12.7 Ma), a slight decrease in rotation of the Rainier Mesa Tuff (11.6 Ma), and a significant decrease in rotation of the

Ammonia Tanks Tuff (Tma, 11.45 Ma). The main period of vertical-axis rotation postdates the period of maximum extension by about 1 m.y., based on the interpretation that most of the extension predated the Rainier Mesa Tuff (Hudson, M.R., Minor et al. 1996, p. A-451; Fridrich, C.J. et al. 1999, p. 210). However, the majority of tilting and extension in the site area may postdate the Rainier Mesa Tuff. Thus, extension and vertical-axis rotation in the site area may have been synchronous and accompanied oblique displacement along block-bounding faults. The curved map patterns of faults in the more highly extended and rotated area south of the site area suggest that clockwise vertical axis rotation may have continued after major east-west extension (Fridrich, C.J. et al. 1999, p. 210).

4.6.3.3.4 Fault Slip Analysis

Fault slip analysis can be used to demonstrate variations in faulting style as a function of time. In the Yucca Mountain site area for the period after 12.7 Ma, a sinistral component of displacement is consistently observed on north-striking block-bounding faults (Dickerson and Spengler 1994, p. 2371; Day et al. 1998b, p. 8). Also, a dextral component is observed on some northwest-striking faults, particularly those in the Azreal Ridge domain. R.B. Scott (1990, pp. 261 to 265) reported that striations on northwest-striking fault planes are consistent with dextral components of motion, that striations on northeast-striking faults are consistent with sinistral components, and that faults with northerly strikes show a mix of dextral and sinistral motion. However, major north-striking block-bounding faults in the site area, such as the Solitario Canyon and Paintbrush Canyon faults, have indicators of a sinistral component of slip (Dickerson and Spengler 1994, p. 2371; Day et al. 1998b, p. 8).

Fault slip data on normal and strike-slip faults preserved in bedrock at Yucca Mountain suggest that the minimum horizontal stress direction was nearly east-west at the time that bedrock fault scarps and striae were formed (R.B. Scott 1990, p. 266). This direction is consistent with the range of Middle Miocene minimum stress directions determined for this part of the Basin and Range province (Zoback et al. 1981, p. 204, Figure 9), and differs from present day west-northwesterly minimum stress directions (Stock et al. 1985). These data indicate that fault striae preserved in bedrock at Yucca Mountain record dominantly Miocene fault displacements.

Fault slip analyses that use of the excellent stratigraphic control in northern Crater Flat suggest a 12.7- to 11.6-Ma period of normal fault slip and an 11.6-Ma and younger period of oblique slip (Minor, Hudson et al. 1996). The oblique slip in northern Crater Flat was characterized by sinistral slip components on northeast-striking faults and dextral slip components on north-striking faults (Minor, Hudson et al. 1996). The fault slip directions in northern Crater Flat are compatible with a shortening direction oriented north-northeast. In the Yucca Mountain site area, post-12.7-Ma fault motions correspond to a north-northwest shortening direction. Both shortening directions are radial to the center of the Timber Mountain caldera complex to the north (Figure 4.5-2), implying that eruptive processes in the caldera influenced the subregional stress field and strain patterns throughout Crater Flat and Yucca Mountain. East of the caldera complex, the maximum horizontal extension direction is radial to the caldera margin (Minor 1995, pp. 10,525 to 10,527) and extensional faults strike northerly. Thus, regional strain effects related to the caldera complex are probably second-order effects, superimposed on north-striking faulting patterns.

4.6.3.3.5 Sequential Joint Formation and Relation to Site-Scale Structural Evolution

Patterns and relations of extensional joints (joints that originate as tensional openings, with no shear displacement) yield information on the relative age of strains with diverse orientations. Systematic sets of tectonic extension joints reflect components of the stress field in which they formed. Each tectonic joint set is interpreted to represent a distinct episode of jointing and an associated stress field. The observable sequential development of joint sets is thus interpreted to relate to systematic changes in the local or regional stress field. For each joint set, two components of the stress field at the time of fracture can be defined: the minimum compressive stress (σ_3) oriented perpendicular to the median fracture plane, and the maximum horizontal compressive stress (σ_{hmax}) oriented parallel to fracture strike. Maximum compression in the horizontal plane (σ_{hmax}) is not necessarily equivalent to either of the principal compressive stresses (σ_1 or σ_2). Thus, vertical to subvertical joints may have been generated in a normal stress field (σ_1 nearly vertical) or in a strike-slip stress field (σ_1 nearly horizontal). Fractured rock mass studies are described in more detail in Section 4.6.6; here the emphasis is on the timing of joint set formation.

Patterns and timing of tectonic joint formation at Yucca Mountain are summarized in Throckmorton and Verbeek (1995). They identify four joint sets of tectonic origin, labeled T1, T2, T3, and T4, which have median orientations (strike/dip) of N01°W/86°SW, N31°W/86°SW, N38°E/88°NW, and N82°W/88°SW, respectively (Throckmorton and Verbeek 1995, pp. 25 to 37, Table 2). Throckmorton and Verbeek (1995, p. 42) interpreted the subvertical north-striking, northwest-striking, and northeast-striking joint sets at Yucca Mountain to have developed sequentially as products of noncoaxial regional extension during Basin-and-Range faulting. In their model, each fracture set represents a distinct phase of regional extension. This requires the regional direction of maximum horizontal compressive stress to have initially rotated counterclockwise, from a north-trending σ_{hmax} to about N30°W, during the time interval between the formation of the north-striking and northwest-striking joints. During the time interval between the formation of the northwest-striking and northeast-striking joints, the model requires clockwise rotation from about N30°W to about N40°E. Subsequent analyses by other investigators (see below) question aspects of their model.

Throckmorton and Verbeek (1995, p. 27) interpreted the north-striking joints to be the oldest tectonic fracture set because they are the longest tectonic fractures, have the largest percentage of fracture ends that terminate in unfractured rock, and are only truncated by preexisting cooling joints. In certain places, the northwest-striking fracture set appears to postdate the north-striking set, but at other localities the northwest-striking fracture set terminates against the north-striking set (Sweetkind, Verbeek et al. 1995b, Plate 1). There are few examples of north-south striking fractures that appear to have renewed growth at their tips in the northwest-striking direction, resulting in a curved or even sigmoidal overall fracture shape.

In many of the locations studied by Throckmorton and Verbeek (1995), and at more recently mapped exposures, age relationships between the north-striking and northwest-striking sets are not clearly defined. The two sets commonly have ambiguous or contradictory termination relationships and, in some cases, the northwest-striking set appears to be the older. In contrast to the fracturing sequence reported by Throckmorton and Verbeek (1995, p. 44), there is no clear

evidence that the northwest-striking set is consistently younger than the north-striking set. In general, the two fracture sets appear to be coeval. Northeast-striking tectonic joints consistently terminate against cooling joints and the two sets of tectonic fractures described above (Throckmorton and Verbeek 1995, p. 33; Sweetkind, Verbeek et al. 1995a, p. 62). Thus, the northeast-striking tectonic joints formed relatively late in the sequence of fracture development.

Geologic evidence throughout the Yucca Mountain region indicates dominantly east-west extension during the deposition of the Paintbrush Group, with little evidence for a separate phase of northeast-southwest extension. Motion along north-striking, block-bounding faults, with extension directions compatible with the opening of north-striking fractures, began prior to eruption of the Paintbrush Group, and continued during and after its deposition (Scott, R.B. 1990, p. 268). Fault-slip analyses in nearby areas to the north record continuous east-west directed extension until around 8.5 Ma (Minor 1995, p. 10,524). Because joints form at very low resolved stress, north-striking fractures probably formed throughout and after the time represented by Paintbrush Group deposition, in response to east-west directed extension.

Evidence for continuous east-west directed extension and lack of consistent evidence of the relative age of the north-striking and northwest-striking tectonic fracture sets suggest that the regional direction of maximum horizontal compressive stress probably did not rotate counterclockwise, from a north-trending σ_{hmax} to about N30°W, between the formation of the two fracture sets, as suggested by Throckmorton and Verbeek (1995, p. 42). More likely, the northwest-striking fractures formed during the same time period as the north-striking fractures. Formation of northwest-striking fractures could be the result of locally rotated σ_3 directions within a regime of regional east-west directed extension. For example, initiation of sinistral slip on block-bounding faults (Simonds et al. 1995) could favor the formation of northwest-striking extension fractures within the fault-bounded blocks (Dyer 1988, p. 689).

Geometric and timing relationships observed between north- and northwest-striking joints are mirrored by similar fault relationships at Yucca Mountain, where the north- and northwest-striking faults appear to have formed coevally and were kinematically related. Studies of concurrently active normal and strike-slip faults in the southern Great Basin indicate that adjacent faults with disparate slip vectors do not require temporal changes in the stress field (e.g., Wesnousky and Jones 1994, pp. 1032 to 1033). Given the relative magnitudes of the principal stresses, where $\sigma_1 = \sigma_2 >> \sigma_3$, a complex relationship of joints and faults might arise from a relatively simple stress history. Alternatively, concurrent motion along normal and strike-slip faults could result from the interplay between active Basin and Range extension and initiation of strike-slip motion along the Walker Lane zone (Bellier and Zoback 1995, p. 588). Interaction of these two stress regimes might explain the perplexing and often ambiguous relative temporal relationships between the north-striking and northwest-striking fractures.

Northeast-striking tectonic joints are a relatively younger joint set, based on termination relationships with all other cooling joints and tectonic joints at Yucca Mountain (Throckmorton and Verbeek 1995, p. 33; Sweetkind, Verbeek, et al. 1995b, p. 45; Sweetkind, Verbeek, et al. 1995a, p. 62). Northeast-striking extension joints are consistent with the present-day direction of σ_{hmin} (equivalent to σ_3 for subvertical fractures), as determined from hydrofracture tests and orientations of borehole breakouts (Haimson et al. 1974, p. 558; Stock, J.M., Healy et al. 1985,

pp. 8693 to 8701; Stock, J.M. and Healy 1988, p. 91) and from earthquake fault plane solutions and inversion of slip vectors on active faults in the region (Rogers, A.M., Harmsen, Carr et al. 1983; Bellier and Zoback 1995, pp. 566 to 568). Fault-slip analysis in nearby areas to the north record dominantly east-west directed extension until 8.5 to 9 Ma (Minor 1995, p. 10,524), after which time the extension direction shifted toward the present-day orientation. Fault-slip analyses in nearby areas to the north (Minor 1995, p. 10,524) confirm a regional shift from dominantly east-west directed extension prior to 8.5 to 9 Ma, to northwest-oriented extension after that time.

4.6.3.3.6 Summary of Timing of Deformation

Stratigraphic relations across faults and angular relations across unconformities demonstrate that block-bounding faults were active at Yucca Mountain during eruption of the Paintbrush Group (12.8 to 12.7 Ma), and significant motion on these faults continued until after the Rainier Mesa (11.6 Ma) Tuff was deposited. Most stratal tilting in the site area occurred after 11.6 Ma and was probably synchronous with the main pulse of vertical-axis rotation, which occurred between 11.6 and 11.45 Ma. Fault slip analyses support a mid-Miocene age as the main period of motion of Yucca Mountain faults and suggest that the fault patterns at Yucca Mountain, dominated by north-striking faults, are consistent with regional strain patterns, with an overprint of caldera-related deformation in northernmost Yucca Mountain. Studies of sequential formation of tectonic extension joints, in the context of regional paleostress studies, indicate that north- and northwest-striking joint sets formed during a regional east-west extension in Paintbrush Group time, and that a prominent northeast-striking joint set formed later, probably after 9 Ma.

4.6.3.3.7 Tectonism and Alteration History

A widespread vitric-zeolitic transition zone (Section 4.5.4.7.1) is generally assumed (e.g., Levy 1991, p. 481) to have formed as an approximately planar horizontal surface. This assumption is based on the interpretation that the zone's configuration and position were originally related to the configuration and position of the static water table. The vitric-zeolitic transition zone is generally inclined in the same direction as the host rocks of the Topopah Spring Tuff, but, in places, at a lesser angle (e.g., Buesch and Spengler 1999a, Figures 8, 9, 10). The relations imply that zeolitization occurred either before or during the tilting of normal fault blocks, which formed from 12.7 to 11.45 Ma.

The timing of alteration relative to faulting and tilting was determined by examining microscopic textural evidence preserved within the zeolitized rocks in geopetal fillings. A geopetal filling is any rock feature whose form is influenced by gravity and which indicates the relation of top to bottom at the time of formation of the rock. Geopetal structures in tuffs at Yucca Mountain are pores less than 2 mm (0.08 in.) across, such as bubbles in glass shards and cavities left by dissolved shards, that have been partly to completely filled with opal, zeolite, clay, or fine-grained detritus. Of most interest are those in which the filling material was extremely fine grained and likely to have been deposited by settling from aqueous suspension. Because the upper surfaces of these fillings are planar and horizontal at the time of deposition, they serve as indicators of post-depositional tilting.

Textural relationships indicate that many geopetal fillings postdate zeolitization in the rocks in which they were deposited. Most cavities with geopetal fillings are secondary pores created by the dissolution of glass shards. Petrographic and scanning-electron-microscopic studies of partially and completely zeolitized tuffs (e.g., Levy 1984a; Vaniman, Bish, Broxton et al. 1984) indicate that large glass shards are the last primary material to be affected by alteration. The shard cavities are commonly lined with zeolite crystals, which are in turn covered by geopetal fillings, if present. Thus, geopetal filling orientations provide information on deformation that occurred subsequent to zeolitization.

Microscopic examination of thin sections provides a means for studying the orientations of the flat surfaces of the geopetal pore fillings. Measurements made in drillhole core sections commonly show two or more sets of average orientations, providing evidence that tectonic tilting was active at the time the fillings were deposited (Levy 1984a, p. 39). Textural relations within a sample from the vitric-zeolitic transition zone of the Topopah Spring Tuff indicate that the tuff was about 90 to 98 percent zeolitized by the time the last geopetal filling was deposited (Levy 1984a, p. 40). This brackets the age of alteration between the age of the Topopah Spring Tuff (12.8 Ma) and the cessation of major tectonism (11.45 Ma).

4.6.4 Central Block Geologic Structure

The emplacement area for a potential geologic repository at Yucca Mountain lies in the Central Block (Figure 4.6-4). Faulting and fracturing in this area is important to hydrologic flow and transport modeling, potential repository design, and performance assessment. The Central Block is bounded on the west by the Solitario Canyon fault, on the east by the Bow Ridge fault, and on the north by the northwest-striking Drill Hole Wash fault (Figure 4.6-5). A simplified cross section across the Central Block is shown on Figure 4.6-6. The block's southern boundary is marked by a transition to structural styles that accompany greater magnitudes of extension (Figure 4.6-4). Surface geologic mapping (Scott, R.B. and Bonk 1984; Day et al. 1998a), underground mapping of the ESF, geophysical surveys, and borehole studies show that this part of Yucca Mountain is mildly deformed. It contains widely spaced intrablock faults (Figure 4.6-7) that commonly have 1 to 10 m (3.3 to 33 ft) of displacement but rarely more than 10 m (33 ft). The Central Block's eastern and southern edges, however, are formed by numerous block-margin faults.

The cross section on Figure 4.6-6 illustrates some fundamental differences among different faults types within the Central Block. The faults include the two block-bounding fault zones (Solitario Canyon and Bow Ridge), discontinuous minor faults, the intrablock Ghost Dance fault in the Yucca Crest subblock, and faults in the more intensely faulted Boundary Ridge subblock. An obvious fundamental contrast in dip exists between the block-bounding fault zones, which dip 60° to 70° to the west, and the intrablock faults, which are nearly vertical based on mapped traces (Figure 4.6-6). The contrast in dips is probably related to the fact that major extensional faults, such as the block-bounding Bow Ridge and Solitario Canyon fault zones, root at mid-crustal levels, whereas the intrablock faults accommodate small strains and commonly exploit preexisting steep cooling joints. A fundamental contrast also exists between the discontinuous intrablock faults in the Yucca Crest subblock and the more continuous block-margin faults in the Boundary Ridge subblock. The block margin faults are inferred to be an integral part of the

Bow Ridge fault zone hanging-wall deformation and are projected to intersect with the Bow Ridge fault zone at depth.

Various Central Block cross sections (Scott, R.B. and Bonk 1984; Day et al. 1998a) (e.g., Figure 4.6-6) imply that intrablock faulting postdates most of the stratal tilting. This inference is based on structural reconstructions. If the easterly dip of the Central Block is removed, and the steep intrablock faults in both the Yucca Crest and Boundary Ridge subblocks are assumed to predate tilting, most of the faults would originally have had reverse displacement. In light of the transtensional tectonic regime that characterized this area, this is unlikely. The easterly dips were more likely established early in response to initial movement on the block-bounding faults. During initial tilting, cooling joints were rotated from subvertical dips to steeply west-dipping orientations. Growth of the intrablock faults then accompanied the continued movement on the block-bounding faults as cooling joints were linked and activated.

4.6.4.1 Prominent Intrablock Faults

Characteristics of faults in close proximity to the potential repository are of direct importance to repository design, modeling of hydrologic flow and transport, and assessment of long-term performance. Because of their proximity to the emplacement area of the potential repository, the relevant characteristics of the Ghost Dance, Sundance, and Diabolus Ridge faults are discussed in the following sections.

4.6.4.1.1 Ghost Dance Fault

The Ghost Dance fault (Figures 4.6-2, 4.6-5, 4.6-6) is the principal throughgoing structure within the central part of the Central Yucca Mountain domain (see Day et al. 1998a). It has a surface length of 3.7 km (2.3 mi.) between Abandoned Wash to the south (Figure 4.6-4) and Wren Wash to the north (Figure 4.6-8). In general, the Ghost Dance fault is a north-striking normal fault zone, steeply west-dipping (75° to 85°) with down-to-the-west displacement. Displacement, amount of brecciation, and number of associated splays vary considerably along its trace.

The Ghost Dance fault zone can be divided into three segments based on the amount of displacement (Figure 4.6-8) and brecciation. North of Split Wash, the fault is relatively narrow (2 to 4 m [6.6 to 13 ft] wide) with as much as 6 m (20 ft) of down-to-the-west displacement. The central segment of the Ghost Dance fault zone has greater westside-down displacement than the northern segment, and extends from Split Wash to Broken Limb Ridge. On Antler Ridge, cumulative displacement is 13 to 20 m (43 to 66 ft) across several splays of the Ghost Dance fault that are distributed over a map width of approximately 100 to 150 m (328 to 492 ft) (Day et al. 1998a, p. 9). Individual splays are characterized by a 1-to-2-m-wide (3.3-to-6.6-ft-wide) breccia zone. To the south on Whale Back Ridge, the fault zone is about 55 m (180 ft) wide and has about 30 m down-to-the-west displacement. There, the zone is bounded by two north-striking faults, and the eastern fault is the main splay. Locally, the immediate hanging wall of the main splay of the Ghost Dance fault is highly fractured.

On the north-facing slope of Antler Ridge, the main trace of the Ghost Dance fault forms two slightly overlapping strands in map view, which define a right-stepping pattern (Figure 4.6-9). Spengler, Braun, Martin et al. (1994, p. 11) suggested that the two strands were offset along a

younger northwest-striking fault. However, subsequent mapping by Potter, Dickerson et al. (1999, p. 7) does not support the existence of a younger strike-slip fault. They suggest that the two Ghost Dance strands, separated by about 50 m (164 ft) at the surface, merge into a single fault at depth. Abundant breccia between the two fault tips may indicate a local accommodation zone between the two faults. Alternatively, the Ghost Dance fault may have "stepped over" along a preexisting discontinuity such as a set of closely spaced, northwest-striking cooling joints (Potter, Dickerson et al. 1999, p. 7). A similar example of overlapping faults occurs on Live Yucca Ridge in the northern segment of the Ghost Dance fault (Potter, Dickerson et al. 1999, p. 8; Day et al. 1998a).

The southern segment of the Ghost Dance fault extends from Broken Limb Ridge to Abandoned Wash. At Broken Limb Ridge the fault bifurcates. One strand strikes southwest and may connect to the Abandoned Wash fault. The other strikes southeast toward, but does not connect with, the Dune Wash fault (Day et al. 1998a). Although two principal fault splays are present here, in detail the fault zone is made up of numerous fault splays. The splays both parallel the main north-striking fault trace and branch laterally and vertically from the main fault. This vertical horse-tailing is present both on the south side of Whale Back Ridge and on the north-facing slope of Broken Limb Ridge.

Amounts of displacement and brecciation along the southwestern projection of the Ghost Dance fault across Highway Ridge are considerably less than those along the central segment. Along the south-facing slope of Broken Limb Ridge, displacement is less than 6 m (20 ft) and intense fracturing in the hanging wall (in map unit Tpcpmn) (Table 4.5-2) extends about 15 m (49 ft) to the west. In the Ghost Dance Wash area (near the southern end of the ESF main drift), displacement is less than 3 m (10 ft) both on the surface and in the ESF. Deformation is also confined to a relatively narrow zone (2 m [6.6 ft]) of intense fracturing and brecciation. Displacement increases southwestward to about 17 m (56 ft) in Ghost Dance Wash, along the eastern splay of the Abandoned Wash fault (Day et al. 1998a, p. 10). The combined trace length of the Ghost Dance and Abandoned Wash faults is at least 7.4 km (4.6 mi.) (Day et al. 1998b). Mapping in the ESF has shown that both the low-displacement and high-displacement parts of the Ghost Dance fault dip 80° to 90° (depending on the position along strike) from the surface to the depth of the potential repository (Albin et al. 1997, Figure 24).

4.6.4.1.2 Sundance Fault

The structure and extent of the Sundance fault (Figure 4.6-8) is equivocal (Spengler, Braun, Martin et al. 1994, pp. 9 to 11, Figure 5; Potter, Dickerson et al. 1999). It was originally mapped as a 1.5-km-long (0.9-mi.-long) zone of nearly vertical, N30° to 40°, west-striking faults extending from Antler Ridge northwest across Split Wash to Live Yucca Ridge. Many faults, considered by Spengler, Braun, Martin et al. (1994, p. 9) to occupy a zone at least 274 m (900 ft) wide, were shown to have minor amounts of down-to-the-northeast displacements and possible components of dextral strike-slip movement. Spengler, Braun, Martin et al. (1994, p. 11) also suggested that the fault may continue both to the southeast and to the northwest for a total distance of at least 3 km (1.9 mi.). This interpretation was based on observations of structural lineaments, concentrations of brecciated rock, other northwest-trending faults, and offset of the Ghost Dance fault by about 50 m (164 ft) in a dextral sense along the Sundance fault system. R.B. Scott and Bonk (1984) did not map the Sundance fault, but, based on aerial photograph

interpretations, they inferred that several northwest-trending fractures define a 750-m-long (2,460-ft-long) zone across Live Yucca and Dead Yucca ridges, immediately west of the Ghost Dance fault.

A detailed investigation of the Sundance fault mapped a 460-m-wide (1,509-ft-wide) northwest-trending "strip" from Antler Ridge to Ammo Ridge at 1:2,400 scale (Potter, Dickerson et al. 1999). This study traced the northwest-striking Sundance fault zone for about 750 m (2,460 ft) in the northern part of the Yucca Crest subblock, from Dead Yucca Ridge to Live Yucca Ridge (Figures 4.6-3 and 4.6-8). It concluded that the Sundance fault zone is shorter than suggested by previous investigators (Potter, Dickerson et al. 1999, p. 9). At its northwest end, the Sundance fault zone was mapped to terminate abruptly north of Dead Yucca Ridge. Faults in this zone are almost exclusively characterized by northeast-side-down displacement. The maximum width of the Sundance fault zone is about 75 m (246 ft), and the cumulative northeast-side-down vertical displacement across the fault zone does not exceed 11 m (36 ft) (Potter, Dickerson et al. 1999, pp. 5 to 6). Even though some horizontal slickensides are documented, no measurable strike-slip displacement is evident along the Sundance fault.

Southeast of the mapped extent of the Sundance fault zone, the Ghost Dance fault can be projected along an essentially straight trend beneath the Quaternary deposits in Split Wash with no apparent displacement along the Sundance trend (Potter, Dickerson et al. 1999, p. 8; Day et al. 1998a). On the south slope of Antler Ridge near the projected trend of the Sundance fault zone, several northwest-striking faults occur over a 170-m-wide (558-ft-wide) area, but they can be mapped only locally in the crystal-poor member of the Tiva Canyon Tuff and do not appear to be throughgoing structures (Potter, Dickerson et al. 1999, p. 8).

Individual faults in the Sundance fault zone and elsewhere at Yucca Mountain are vertically and laterally discontinuous; one or more mechanisms of strain accommodation must operate in the Tiva Canyon Tuff to accommodate displacements in the rock volume between the discontinuous discrete fault segments. Two such mechanisms are distributed brittle deformation associated with diffuse breccia bodies and minor offsets along numerous preexisting cooling joints (Potter, Dickerson et al. 1999, pp. 13 to 14).

The ESF passes beneath the southeastern end of the Sundance fault zone as mapped by Potter, Dickerson et al. (1999), where displacement is minimal on the south flank of Live Yucca Ridge. Within the ESF, the fault is mapped within a broad zone of discontinuous, minor, northwest-striking faults and joints in the middle nonlithophysal zone of the Topopah Spring Tuff (map unit Tptpmn) (Table 4.5-2). It is similar in character to the fault zone mapped at the surface (Potter, Dickerson et al. 1999, p. 8; Day et al. 1998a). The feature identified as the Sundance fault in the ESF trends N25°W and dips 84° to the west; the amount and sense of offset is unknown, and there are subhorizontal mullion structures and slickensides developed on the polished fault surface (Albin et al. 1997, p. 44, Figure 24). It is unclear whether this fault is directly correlative with the principal strand of the Sundance fault as mapped at the surface. The fault observed in the ESF is located approximately 50 m (164 ft) north of the subsurface projection of the main trace of the Sundance fault toward the ESF, and its west dip is opposite to that observed at the surface.

4.6.4.1.3 Diabolus Ridge Fault

The Diabolus Ridge fault (Figure 4.6-8), a locally prominent intrablock fault, is unusual because it is a low-angle reverse fault (Day et al. 1998a). Maps by Lipman and McKay (1965), R.B. Scott and Bonk (1984), and Day et al. (1998a) portray the fault differently. The 1:6,000-scale map of Day et al. (1998a) depicts it as a north-northwest-striking reverse fault. This interpretation, based on the largest scale mapping, incorporates the greatest degree of stratigraphic detail.

The Diabolus Ridge fault is located about 450 m (1,476 ft) west of the northern termination of the Ghost Dance fault. At the crest of Diabolus Ridge it has about 7 m (23 ft) of west-side-down displacement of the base of the crystal-rich member of the Tiva Canyon Tuff (Figure 4.6-8). Its southern termination occurs in the Wren Wash drainage, 150 m (492 ft) south of Diabolus Ridge (Day et al. 1998a). On the northeast side of Diabolus Ridge, R.B. Scott and Bonk (1984) extended the Diabolus Ridge fault to the base of the slope and projected it beneath surficial deposits in Drill Hole Wash and onto the southwest-facing slope of Tonsil Ridge. Day et al. (1998a) demonstrated that the fault does not continue far down the northeast-facing slope of Diabolus Ridge, based on the lack of displacement of the top of map unit cpll (Table 4.5-2). The trace of the fault trends to the east just beyond the ridge crest, where it is defined by displacement of a zonal contact in the crystal-rich member of the Tiva Canyon Tuff (base of map unit Tpcr2) (Table 4.5-2). The fault dips 25° to 32°E (Day et al. 1998a), based on three-point calculations along the fault trace, the geometry of associated breccia zones, and the intersection of the fault by borehole USW SD-9 (Engstrom and Rautman 1996, p. 12). The dip may be shallower where the trace of the fault bends to the east-southeast along the crest of Diabolus Ridge.

4.6.4.2 Structural Geology of the Yucca Crest and Boundary Ridge Subblocks

The emplacement area for a potential repository at Yucca Mountain lies beneath Yucca Crest in the Yucca Crest subblock of the Central Yucca Mountain structural domain (Figure 4.6-6). The area to the east is the Boundary Ridge subblock (Figure 4.6-6). Tunnels providing access to the waste emplacement area of a potential repository would pass through the Boundary Ridge subblock into the Yucca Crest subblock. Because of the importance of these subblocks in designing and assessing the performance of a potential repository, this section provides a detailed discussion of their structural geology.

The Yucca Crest subblock comprises a relatively undeformed east-dipping block crossed by relatively sparse minor faults. Tiva Canyon Tuff units, exposed at the surface over most of this block, typically dip 4° to 8°E. The three faults described in the previous section (Ghost Dance, Sundance, and Diabolus Ridge faults) are the most prominent faults in the subblock (Figure 4.6-5). These faults have trace lengths of 0.5 to 7.5 km (0.3 to 4.7 mi.). Other faults in the subblock have maximum trace lengths of less than about 200 m (656 ft). These minor intrablock faults are marked by breccia zones that are commonly 0.1 to 1.0 m (0.3 to 3.3 ft) in width, and are both laterally and vertically discontinuous (Day et al. 1998a, 1998b). Many of the faults are parallel to the dominant orientations of cooling joints in the Tiva Canyon Tuff. The two most prominent sets of joints have orthogonal northeasterly and northwesterly strikes. These faults likely reactivated preexisting cooling joints, a conclusion supported by the presence of thin

(1 cm [0.4 in.] thick), tabular, tectonic breccia bodies along cooling joints. Such breccia-lined cooling joints are probably faults with small displacements.

Figure 4.6-7 is a representative part of the Yucca Crest subblock, reproduced from the Central Block geologic map of Day et al. (1998a). The north-striking Ghost Dance fault extends along the east edge of the map (Figure 4.6-7); and the Sundance fault crosses Purgatory Ridge near the northeast corner. The mapped faults between the Ghost Dance fault and the west-facing slope of Solitario Canyon (along the west edge of Figure 4.6-7) are short and discontinuous.

The greatest concentration of minor intrablock faults that has been mapped occurs on the south slope of Antler Ridge (Figure 4.6-10). These faults are useful examples of the relationships between minor faults that might be found in the subsurface at similar stratigraphic levels. At this location, numerous northwest-striking faults and several north- and northeast-striking faults displace contacts within the crystal-poor member of the Tiva Canyon Tuff, but most do not continue up into the crystal-rich member (Potter, Dickerson et al. 1999, p. 8). While breccia occurs along many of the faults, pods of breccia are also distributed across the slope with no apparent relation to faults. Mapping along this slope shows only one small fault, in addition to the Ghost Dance fault, that displaces the base of the crystal-rich member. However, the base of this unit is poorly exposed along most of this slope, so additional minor faults are possible. Displacement across the mapped minor faults ranges from 0.3 to 6 m (1 to 20 ft), with most between 1 and 3 m (3.3 and 10 ft). Almost all minor faults have a mapped length of less than 50 m (164 ft), and none is mapped in excess of 100 m (328 ft) long. In nearly every case, fault lengths are constrained by unfaulted contacts that cross the projected location of known faults mapped either upslope or downslope (Potter, Dickerson et al. 1999, p. 8).

The discontinuous faulting shown on Figure 4.6-10 requires that displacements are balanced by distributed deformation within the rock mass between the mapped faults. Much of the breccia colluvium on the slope may represent distributed brittle deformation in addition to discrete faulting that accommodated strain (Potter, Dickerson et al. 1999, p. 9). This deformational style is depicted on Figure 4.6-10 by a small graben bounded by northeast-striking and northwest-striking faults. The faults displace the base of map unit Tpcpmn3 by 5 and 7 m (16 and 23 ft), respectively. Downslope (to the south), the northwest-trending breccia zone appears to truncate the northeast-trending breccia zone (or the northeast-trending zone merges into the northwest-trending zone). Neither zone can be traced an appreciable distance upslope. The breccia zone that marks the northeast-trending fault cannot be traced above the base of Tpcpmn3 (in the footwall), and the top of Tpcpmn3 is not displaced along the projected trace of this fault. Instead, a northeast-trending fault located 20 m to the west displaces this contact by 5 m (16 ft). Pods of breccia occupy unit Tpcpmn3 between the two discontinuous northeast-striking faults, and appear to be a zone of distributed brittle deformation accommodating the displacement on the two northeast-trending faults. The northwest-trending fault that bounds the west side of the small graben cannot be traced upslope as a single discrete fault, but appears to branch into several smaller northwest-trending splays that displace the top of unit Tpcpmn3. Thus, one of the faults bounding this small graben steps to the northwest as it moves upsection via an accommodation zone that exhibits distributed brittle deformation and the other branches into at least three splays upsection. The result (on Figure 4.6-10) is a complex zone of deformation that is representative of a common style of deformation in the Tiva Canyon Tuff at Yucca Mountain.

Discontinuous faulting in the Yucca Crest also occurs within the Sundance fault zone. Several strands of the Sundance fault comprise a 25- to 70-m-wide (82- to 230-ft-wide) zone within the top of the middle nonlithophysal zone of the Tiva Canyon Tuff (Tpcpmn), along the lower south-facing slopes of Purgatory Ridge and Dead Yucca Ridge (Figures 4.6-3, 4.6-7) (Potter, Dickerson et al. 1999, p. 6). A single fault continues up into the crystal-rich member at the top of each ridge. Displacement of this strand (13 m [43 ft]) is less than the cumulative displacement across the broader fault zone that cuts the top of the middle nonlithophysal zone.

Map patterns of the Sundance fault zone (Figure 4.6-7) exemplify stratigraphically controlled faulting. The fault zone is broader in the crystal-poor member (Tpcp) than in the overlying crystal-rich member (Tpcr) of the Tiva Canyon Tuff, reflecting a contrast in material properties. Available experimental data suggest that the zones of the crystal-poor member (Tpcpll, Tpcpmn, Tpcpul) and the crystal-transition subzone (Tpcrl) at the base of the crystal-rich member (Table 4.5-2) have significantly greater tensile and ultimate strengths than the overlying crystal-rich subzones (Tpcr2, Tpcr3) (Boyd, Price et al. 1996a; Sections 4.7.4 and 4.7.5). The middle nonlithophysal zone (Tpcpmn) also has a greater abundance of cooling joints than either the upper lithophysal zone (Tpcpul) or the overlying crystal-rich member (Sweetkind, Barr et al. 1997, pp. 23 to 25). Thus, the broad distributed deformation in the Tpcpmn, and the upward narrowing of the fault zone through the Tpcpul and into the crystal-rich member, may be attributed to either the more brittle character of the Tpcpmn or the availability of preexisting cooling joints in the Tpcpmn for exploitation by the Sundance fault zone. Conversely, the narrower, more restricted deformation in the crystal-rich member of the Tiva Canyon Tuff may be attributed to the less brittle nature of the unit or to the lower frequency of cooling joints there. The contrast in the frequency of cooling joints between the units may therefore also reflect their differing material properties.

Lack of vertical continuity of individual fault strands through different stratigraphic levels requires a mechanism for lateral accommodation of strain within the Tiva Canyon Tuff. Strain likely occurred as distributed deformation within the breccia zones and through incremental small displacements along the numerous cooling joints. In this scenario, the faulted crystal-poor member contains numerous irregular, small blocks that have slipped or rotated along preexisting joints and synkinematic breccia zones. In contrast, the lack of cooling joints in the crystal-rich member confined the displacement to fewer discrete faults bounding larger, undeformed blocks.

The Boundary Ridge subblock, comprising the eastern and southern margins of the Central Block, is characterized by an increased density of intrablock faulting (Figure 4.6-11). Block-margin deformation along the eastern margin of the Central Block records complex deformation in the hanging wall of the Bow Ridge fault. Block-margin deformation along the southern edge indicates an along-strike transition to greater extension to the south. Along the eastern edge of the Central Block, the block-margin deformation zone is about 650 to 900 m (2,133 to 2,953 ft) wide and is characterized by steep north- and northwest-striking faults with both down-to-the-west and down-to-the-east normal displacement (Day et al. 1998a, p. 6). As much as 70 to 80 m (230 to 262 ft) of cumulative down-to-the-west displacement occurs at the north end of Boundary Ridge. Stratal dips of the Tiva Canyon Tuff steepen to 10° to 20° in the Boundary Ridge subblock, compared with the 4°– to 8°–dips within the Yucca Crest subblock.

Faults within the Boundary Ridge subblock are generally longer than faults within the Yucca Crest subblock. The largest faults in the block-margin deformation zones, particularly in the hanging wall of the Bow Ridge fault, are several kilometers long (a couple of miles) (Figure 4.6-11). These faults are inferred to intersect the Bow Ridge fault at depth. The term "imbricate fault zone" has been used to describe this series of closely spaced, steeply dipping faults associated with hanging-wall deformation along the Bow Ridge fault (Figure 4.6-5) and similar zones in the southern part of Yucca Mountain (Scott, R.B. 1990, p. 259). The term was defined as an imbricate pattern of closely spaced, steep, west-dipping faults with minor down-to-the-west offsets of a few meters or less. The term was abandoned because it is vague (Spengler and Fox 1989, p. 29) and because the block-margin deformation does not correspond to a conventional definition of the term imbricate fault zone, which is usually associated with reverse faults along the toe of large thrust faults (Day et al. 1998a).

The easternmost faults exposed in the Boundary Ridge subblock are east-dipping normal faults that crop out on Bleach Bone, Azreal, Live Yucca, Antler, and Boundary ridges (Day et al. 1998b, cross section B-B'). These faults comprise the western boundary of a hanging-wall graben (or series of grabens) bounded on the east by the Bow Ridge fault. Most of the graben (or series of grabens) is buried beneath alluvium.

Locally, compressional faulting is present in the hanging wall of the Bow Ridge fault. Near the south portal of the ESF, on the eastern flank of Boundary Ridge, an east-dipping reverse fault is exposed at the surface and dips toward the Bow Ridge fault (Figure 4.6-11). It indicates local shortening in the Bow Ridge hanging wall (Day et al. 1998b). A few meters (about 10 ft) below the surface, where intersected by the South Ramp of the ESF, this fault steepens to a near-vertical dip. Reverse faulting in the hanging wall of the Bow Ridge fault, and similar faulting within the footwall on Bow Ridge, are likely related to oblique-slip movement on the Bow Ridge fault.

There are several intrablock, northwest-striking, en echelon grabens in the southeastern part of the Central Block near Boundary Ridge (Day et al. 1998a; Scott, R.B. and Bonk 1984). These narrow (100 m [328 ft] wide), long (as much as 750 m [2,460 ft] long), steep-walled, canoe-shaped grabens, termed "synthetic grabens" by R.B. Scott (1990, p. 261), have significant internal displacement. Their bounding faults locally exceed 30 m (98 ft) of displacement, although there is minimal relative displacement between the strata on either side of each graben. On Boundary Ridge, the en echelon grabens occur between the Bow Ridge fault and the northern termination of the Dune Wash fault, and merge with the north-trending zone of block-margin hanging-wall deformation. The grabens appear to be analogous to tension gashes in shear zones and are kinematically compatible with a sinistral component of displacement on the Dune Wash and Bow Ridge block-bounding faults. Comparison between surface mapping (Day et al. 1998a) and geologic mapping in the ESF shows that these grabens are bounded by faults that dip toward the graben center. Relationships indicate that the formation of the grabens largely followed, rather than preceded, eastward tilting of the Tiva Canyon Tuff, as suggested by R.B. Scott (1990, p. 261).

Mutually crosscutting relations between north-striking and northwest-striking faults in the Boundary Ridge subblock support the interpretation that their development was apparently coeval and kinematically linked.

4.6.4.3 Deformation within the Solitario Canyon Fault System

Because faults represent potential hydrologic pathways and zones of poor rock quality, deformation along the faults bordering the potential repository area have been extensively studied. Map patterns demonstrate that tectonic mixing of various Paintbrush Group lithologies has occurred within the most intensely deformed parts of block-bounding fault systems. This is most apparent in the Solitario Canyon fault system (Scott, R.B. and Bonk 1984; Day et al. 1998a). In this up-to-400-m (1,312-ft)-wide system, lenses from stratigraphically diverse parts of the Tiva Canyon Tuff are juxtaposed. Slices of Topopah Spring Tuff are also mixed, and in some areas lenses from more than one Paintbrush Group formation are tectonically juxtaposed (Day et al. 1998a). Tectonic mixing is also apparent along the Northern Windy Wash fault system west of Prow Pass, along the Bow Ridge fault system in the saddle between Bow Ridge and Boundary Ridge, and in the Paintbrush Canyon fault system, along the west flank of Fran Ridge (Scott, R.B. and Bonk 1984; Day et al. 1998b). Individual fault strands within these tectonically mixed zones are brecciated; in some cases the fault-bounded lenses are internally brecciated.

In addition to tectonic mixing, there are areas where coherent blocks of Tiva Canyon Tuff, up to 250 m wide, dip to the west, opposite to the prevailing easterly dips of the major structural blocks (Day et al. 1998a). Locally, anticlines with axes subparallel to the fault zone are present within individual fault slices and in the immediate footwall of the Solitario Canyon fault (Day et al. 1998a). These folds are likely produced by contractional faults that have rotated volcanic strata. Mapped fold hinges may actually be small-displacement, brittle fault zones occurring at shallow structural levels. Thrust faults are mapped within the Solitario Canyon fault system and in the hanging wall of the Bow Ridge fault near the south portal of the ESF (Day et al. 1998a). The anastomosing pattern of faults that characterizes these fault systems also produced individual fault splays that cut into both the hanging wall and footwall (e.g., splays mapped on the west-facing slope of Solitario Canyon in the footwall of the Solitario Canyon fault) (Day et al. 1998a).

The Solitario Canyon fault was encountered in the western end of the Enhanced Characterization of the Repository Block Cross Drift. The drift was excavated across the eastern splay of the fault (considered to be the main splay), but stopped short of the western splay to allow for testing of that zone prior to penetrating it with a tunnel. The eastern splay has about 260 m (853 ft) of normal (down to the west) displacement where it was crossed by the drift. The lower nonlithophysal zone of the Topopah Spring Tuff (Tptpln) in the footwall is juxtaposed against the upper lithophysal zone of the Topopah Spring Tuff (Tptpul) across the fault. However, the tectonic mixing described above is also seen within the fault zone, where there is a breccia composed of clasts of the overlying lower nonlithophysal zone of the Tiva Canyon Tuff (Tpcpln). Footwall deformation (mostly brecciation) is fairly extensive in the area of the drift, extending approximately 50 m (164 ft) east of the main fault. This deformation may be associated with additional intersecting fault splays in this area (Mongano et al. 1999, pp. 59 to 65).

4.6.5 Site Scale Geophysical Investigations

Several geophysical methods, including seismic reflection, gravity, and magnetic surveys, were used to characterize the subsurface geologic structure within the potential repository site area (Majer et al. 1996; Brocher et al. 1998). A single magnetotelluric line (along YMP-3) and several vertical seismic profiles provide supplementary information (Figure 4.6-12).

4.6.5.1 Seismic Reflection Surveys

Imaging the subsurface geology at Yucca Mountain by seismic surveys is difficult for a variety of reasons. Fracturing, lithologic heterogeneities in volcanic rocks (e.g., lithophysal zones, varying degrees of welding), velocity inversions, and unsaturated rock all decrease the efficiency of seismic energy propagation. Because of the various scales of heterogeneity in the stratigraphy at Yucca Mountain, scattered waves also play a prominent role in the interpretation process (Majer et al. 1996, pp. 7 to 8).

A generally east-trending, 32-km-long (20-mi.-long) seismic reflection survey was conducted across Bare Mountain, Crater Flat, Yucca Mountain, Midway Valley, and Fortymile Wash (shown partially on Figure 4.6-12, REG-2 and REG-3) (Brocher et al. 1998, Figure 1). Where this regional profile crosses the potential repository site, the reflection data are interpreted to show a series of west-dipping normal faults that displace volcanic rocks and the Tertiary/pre-Tertiary contact at depth (Brocher et al. 1998, Figures 6, 13, 14). A prominent 1,000-m (3,280-ft) displacement of this contact occurs in the vicinity of the Ghost Dance fault. Although it projects upward toward the surface expression of the Ghost Dance fault, this subsurface fault is thought to be an unrelated older structure. The gravity gradient associated with the large displacement of the Tertiary/pre-Tertiary contact trends more easterly than the mapped trace of the Ghost Dance fault (Brocher et al. 1998, p. 965). The regional seismic reflection data also provide evidence against proposed active detachment faults at shallow depths along the Tertiary/pre-Tertiary contact beneath the potential repository (e.g., Scott, R.B. 1990, pp. 269 to 270; Hamilton 1988, p. 62). Active detachment faulting is inconsistent with the observed normal fault displacements of the Tertiary/pre-Tertiary contact (Brocher et al. 1998, Figures 6, 13, 14).

An alternative interpretation of the regional seismic work (Majer et al. 1996, Figure 47a), based on gravity data, describes the Tertiary/pre-Tertiary contact as largely unfaulted. The gravity data, however, do not have the resolution to distinguish between a faulted or unfaulted pre-Tertiary boundary beneath Yucca Mountain (Majer et al. 1997, p. 12). Likewise, the magnetic data do not constrain the nature of this contact because no magnetic contrast is assumed between the Tertiary and Paleozoic rocks (Brocher et al. 1998, p. 955).

Other, local seismic reflection lines (Figure 4.6-12) were designed to obtain lithologic and structural data in the immediate vicinity of the potential repository (Majer et al. 1996). These lines also provide data to investigate geologic relations that could provide insight into the large hydraulic gradient (Robison 1984, Figure 2) at the north end of Yucca Mountain (see Section 9.2.8). The target depth for the majority of the high-resolution seismic reflection lines in the Central Block was from 100 m (328 ft) down to repository depth (300 m [984 ft]) or greater. Gravity data were collected along all geophysical survey lines. They were initially designed to constrain interpretations of the seismic reflection data. However, as a result of difficulties

encountered in obtaining high-quality seismic reflection data, greater dependence was placed on gravity data in interpreting subsurface structure in the Yucca Mountain vicinity. Accordingly, gravity observations were used to interpret general regional structure, and to aid in interpreting shallow structure at Yucca Mountain, such as fault location and displacement.

4.6.5.2 Magnetic and Magnetotelluric Surveys

Ground magnetic surveys are used to infer fault locations and displacements at Yucca Mountain. The Topopah Spring Tuff is the most strongly magnetic Tertiary volcanic formation. Contrasts in magnetic anomalies across faults are typically interpreted to result from displacement of this formation (Bath and Jahren 1984, p. 28). Simple models can be used to interpret magnetic survey results and can be constrained by other geophysical and geologic evidence. Because aeromagnetic data respond to deeper and stronger magnetic sources than ground-based magnetic data, interpretations of aeromagnetic data address regional to subregional geologic structure, rather than site-scale geology.

Because buried faults and geological heterogeneities at Yucca Mountain are of concern for the long-term performance of the potential repository, magnetotelluric methods were used to detect and characterize these features. Magnetotelluric results can be greatly enhanced if the method is coupled with other geophysical techniques, such as gravity and magnetic surveys, and the seismic method for structural constraints.

4.6.5.3 Geophysical Investigations of Faults

A primary issue to be addressed by geophysical methods is the amount, style, depth, and continuity of faulting within the potential repository block. To illustrate how geophysical data have been used at Yucca Mountain, the geophysical signatures of two characteristic faults, the block-bounding Bow Ridge fault and the intrablock Ghost Dance fault, are summarized below. Ground-based gravity and magnetic surveys (Ponce, Langenheim et al. 1993; Ponce and Langenheim 1995), high-resolution seismic reflection surveys (Majer et al. 1996), and an aeromagnetic survey (McCafferty and Grauch 1997) were examined. In addition to the systematic characterization of these two faults, possible faults, inferred from the high-resolution seismic reflection surveys and from ground-based gravity and magnetic profiles, in the Central Block were compared to faults mapped by Day et al. (1998a).

Geophysical studies focused on the vicinity of the Ghost Dance fault because of its proximity to the potential repository. The studies incorporated surface seismic reflection at four scales (REG 2, HR-2, YMP 3 and 4, and Line 1/YMP-3), vertical seismic profiling, gravity, ground magnetic, and magnetotelluric methods (Figure 4.6-12) (Majer et al. 1996, pp. 1 to 2). Figure 4.6-13 summarizes the geophysical and geologic data along profile YMP-3. The results are consistent with a deformation zone at the mapped location of the Ghost Dance fault; however, none of the methods clearly identified the location and orientation of the Ghost Dance fault at depth (Majer et al. 1996, pp. 53 to 54). Results of the ground-based gravity surveys show small gravity lows within the mapped hanging wall of the fault on the Antler Ridge and Live Yucca Ridge traverses, but no similar anomaly exists on the WT-2 Wash traverse. Four profiles of ground-based magnetic data indicate a magnetic low about 100 m (328 ft) wide within the footwall. The magnitude of this magnetic low decreases northward, coinciding with a decrease in vertical

displacement along the fault. The Ghost Dance fault is not apparent from aeromagnetic surveys. Aeromagnetic anomalies and gradients (not shown in Figure 4.6-13) are oriented at high angles to the strike of the fault and may reflect a regional trend. The magnetotelluric data show a strong change in resistivity associated with the fault.

The Ghost Dance fault is not easily detected on standard, high-resolution seismic reflection lines (6- to 12-m [20- to 40-ft] station spacing) because individual reflections lack continuity (Majer et al. 1996, p. 8). Attenuation of individual reflectors in the upper 0.1 to 0.2 s (65 to 130 m [213 to 426 ft]) of both the stacked and migrated seismic reflection profiles occurs across the mapped projection of the Ghost Dance fault. Very-high-resolution seismic reflection lines, using station spacing of 1 to 2 m (3.3 to 6.6 ft), detected the Ghost Dance as a reflection anomaly. Individual splays of the Ghost Dance fault can be mapped on the basis of these data in WT-2 Wash, but cannot be correlated to other profiles. While it is difficult to map the Ghost Dance fault at depth based on geophysical results, there is abundant geophysical evidence for multiple subparallel fracture zones or faults associated with mapped faults, and particularly for the Ghost Dance fault (Majer et al. 1996, p. 57). There is also evidence for the presence of shallow, low-velocity material in the fault zones, presumably owing to intense fracturing and rubble zones, as indicated by seismic refraction studies (Majer et al. 1996, p. 58).

The Bow Ridge fault can only be reliably detected from ground-based gravity and aeromagnetic data. The ground-based gravity data show a distinct gravity low in the hanging wall of the fault, which occurs both south and north of Exile Hill, but dissipates farther north toward Isolation Ridge (Majer et al. 1996, Figures 92, 94, 97). A noticeable aeromagnetic high in the mapped footwall and aeromagnetic low in the mapped hanging wall characterize the Bow Ridge fault. These anomalies extend from east of Isolation Ridge southward to southern Dune Wash. The contrast across the Bow Ridge fault is greater for the area east of Pagany Wash and Sever Wash than it is for the Exile Hill area. The anomalies reverse from an apparent down-to-the-west signature southward from Exile Hill to a down-to-the-east signature from Yucca Wash northward, in agreement with the geologic understanding of displacement on the Bow Ridge fault (Day et al. 1998b; Dickerson and Drake 1998a, p. 255). Ground-based magnetic data show a distinct magnetic high from Exile Hill southward. North of Exile Hill, the magnetic signature of the fault becomes indistinct. East of Isolation Ridge, the Bow Ridge fault is again a zone of anomalously high magnetization; however, geologic verification of the fault is prohibited because of alluvial burial.

Seismic reflection data provide mixed results in locating the Bow Ridge fault. Seismic reflection profiles YMP-4 (which had poor resolution due to low stacking fold where it crossed the Bow Ridge fault) and YMP-7 show attenuation of certain reflections on either side of the approximate location of the fault on stacked profiles (Figure 4.6-12). Profile YMP-12 did not acquire usable data. Regional seismic reflection line REG-3 also crossed the surface projection of the Bow Ridge fault, but had poor resolution at shallow depth (Brocher, Hart et al. 1996, p. 34; Brocher et al. 1998, Figure 14).

The observations discussed above provide some insight into the ability of geophysical techniques to identify faults at Yucca Mountain. In general, there are fairly consistent geophysical signatures associated with the block-bounding Bow Ridge fault. Thus, it can be consistently mapped beneath Quaternary deposits with a variety of geophysical techniques (seismic reflection

is the notable exception), particularly when they are used in combination. The intrablock Ghost Dance fault, on the other hand, lacks a consistent geophysical expression. High resolution seismic reflection methods do not, in general, image the fault. Very high-resolution seismic reflection methods (station spacing of 1 to 2 m [3.3 to 6.6 ft]), image some details of the fault.

Based on the gravity and magnetic signature of the Bow Ridge fault, it is likely that any concealed faults of similar magnitude would be identified with the standard geophysical techniques used in Yucca Mountain site investigations. For example, Ponce (1996, pp. 5 to 7) used potential field data to infer the presence of several smaller, intermediate offset faults beneath surficial deposits in Midway Valley, including the Midway Valley fault. The Midway Valley fault correlates to a fault mapped on southern Bow Ridge by R.B. Scott and Bonk (1984) and by Day et al. (1998b). This interpretation was incorporated into the geologic map of Day et al. (1998b).

In conclusion, the standard geophysical techniques employed at Yucca Mountain are best suited for detection of faults with at least tens of meters (about 100 ft) of offset.

4.6.6 Fractured Rock Mass Studies

Fracture information at Yucca Mountain is used to characterize the fracture network for hydrologic flow. Fracture study data provide support for surface infiltration model development (Flint, A.L. and Flint 1994), numerical simulations of discrete fracture networks (Anna and Wallman 1997), and calculations of bulk-rock permeability for use in equivalent continuum models of the unsaturated zone (Schenker et al. 1995; Arnold et al. 1995). The data are also used to characterize the fracture network for mechanical stability of the potential repository and to better understand the paleostress history of Yucca Mountain. Results of fracture studies are summarized largely from two key documents, Sweetkind and Williams-Stroud (1996) and Sweetkind, Barr et al. (1997). Use of lithostratigraphic unit names and symbols in the following discussions is based on descriptions given in Tables 4.5-1 and 4.5-2.

4.6.6.1 Types of Fracture Studies

Fractures in the Miocene volcanic rocks at Yucca Mountain developed as cooling joints or as tectonic joints. Fracture data were obtained from: (1) mapping and observation of natural and cleared surface exposures; (2) examination of borehole cores and video logs and interpretation of borehole geophysical logs; and (3) full periphery geologic mapping and scanline surveys within the ESF (Figure 4.6-14). This section summarizes results of these studies.

4.6.6.1.1 Fracture Data from Surface Exposures

Surface fracture studies at Yucca Mountain are of two types:

1. Studies in which all fractures above a certain length within a prescribed area or along a prescribed scanline are measured. These are termed a "global inventory" by Throckmorton and Verbeek (1995, p. 5).

2. Studies in which fracture attributes are collected from members of particular fracture sets. These are termed a "selective inventory" by Throckmorton and Verbeek (1995, p. 5).

Surface fracture studies that employed the global inventory approach include mapping, detailed line survey, and photogrammetry studies (Sweetkind and Williams-Stroud 1996, pp. 18 to 21). The selective inventory approach employed observations of natural outcrops (Figure 4.6-14). Fracture data have been collected from the Tiva Canyon Tuff, the rock units included in the Paintbrush nonwelded hydrogeologic unit, the Topopah Spring Tuff, the Calico Hills Formation, and the Bullfrog Tuff (Crater Flat Group). Sweetkind and Williams-Stroud (1996) summarize much of these data.

Fracture network maps have been produced for 13 surface sites at Yucca Mountain. Nine sites are cleared exposures called pavements, which have been physically cleared by excavation or hydraulic methods (Figure 4.6-14). Mapped pavements at Yucca Mountain range in area from 300 to 1,200 m^2 (3,229 to 12,917 ft^2). Fractures were mapped from aerial photographs or manual surveys. The number of fractures measured at each pavement ranges from 100 to 1,200 (Sweetkind, Anna et al. 1997, p. 188). C.C. Barton et al. (1993, pp. 7, 25, 30, 32) summarized the methods used during the mid-1980s for mapping fracture-trace networks at cleared pavements and for measuring or describing fracture parameters, including trace length, orientation, connectivity, aperture, roughness, shear offset, trace-length density, and mineralization. At each pavement, all fractures that exceed a specific length, typically from 0.3 to 1.5 m (1 to 5 ft), were mapped. Pavement maps can provide critical information regarding termination (relative age) relations and connectivity of fracture sets.

Fracture data from pavements at Yucca Mountain are dominantly from the uppermost portions of the Paintbrush Group. Eight of 13 mapped exposures are in the Tiva Canyon Tuff, including six from the crystal-poor upper lithophysal zone (Tpcpul). Three large natural exposures of the rock units included in the Paintbrush nonwelded hydrogeologic unit (PTn) were mapped as pavements (Sweetkind, Verbeek et al. 1995a, pp. 13 to 14, Figure 1). Two pavements were cleared in the middle nonlithophysal zone of the Topopah Spring Tuff (Tptpmn) (Sweetkind, Verbeek et al. 1995b, pp. 13 to 14).

Data collected at natural outcrops using the selective inventory approach provide a descriptive inventory of the fracture network in the area being studied (Throckmorton and Verbeek 1995, pp. 6 to 7), but individual fractures were not mapped. Fracture sets were identified by inspection, primarily by subdividing fractures on the basis of orientation and relative age, and average attributes for each fracture set were measured (Throckmorton and Verbeek 1995, p. 7). Information obtained includes number of fracture sets and their relative visual prominence at the outcrop, termination (age) relationships, average orientation of each set (a representative number of fractures of each set are measured), ranges of trace length and trace height, and mineral filling.

Fifty-four outcrop stations are located on various units of the Paintbrush Group in the general vicinity of the potential repository (Figure 4.6-14). Additional outcrop data were collected from the crystal-poor basal vitrophyre of the Topopah Spring Tuff (unit Tptpv) at Busted Butte, from zeolitized pyroclastic flow units of the Calico Hills Formation at Prow Pass, and from moderately welded Bullfrog Tuff (Crater Flat Group) at Raven Canyon and Little Skull

Mountain. Fracture data were also collected during large-scale geologic mapping of an area straddling the Ghost Dance fault (Spengler, Braun et al. 1993, pp. 655 to 656). Within the area mapped near the Ghost Dance fault, all observed fractures greater than 2 m (6.6 ft) in length were mapped, and a limited suite of fracture attributes was collected.

4.6.6.1.2 Fracture Data from Subsurface Exposures in the Exploratory Studies Facility

The detailed line survey was the primary method used to collect fracture data in the ESF (Figure 4.6-15). This method provides a statistical sampling of the fracture network and is relatively rapid for obtaining directional fracture data along a traverse (La Pointe, P.R. and Hudson 1985, p. 28). In the ESF, the location of a discontinuity was measured along a horizontal datum line, and fracture attributes, including orientation, infillings, terminations, fracture length, roughness, and aperture, were recorded. (See Barr et al. [1996, pp. 16 to 18] for a complete discussion of detailed line survey methodology.) The detailed line survey method was also used to obtain fracture data at a number of surface exposures, including the ARP-1 pavement, the USW NRG-1 drill pad (McKeown 1992), various cleared areas around the North Portal of the ESF, in the vicinity of Prow Pass, and at Busted Butte.

Full-periphery maps (scale 1:125) of the tunnel walls provide the geologic context for interpreting the fracture data collected in the ESF. Lithologic contacts, fault orientations and characteristics, shear zones, and fractures greater than 1 m (3.3 ft) in length were mapped across the full periphery of the exposure. Rock mass quality ratings were routinely reported during tunnel excavation; these data generally correlate with fracture intensity. Geologic data from full-periphery geologic mapping and detailed line surveys were incorporated in this section. Fracture data are tied to lithology and location. The nature of the exposure allows detailed identification of fault and shear offsets. Although the detailed line survey method is a one-dimensional sample of fracture attributes, it provides two-dimensional data because trace lengths and termination relationships are recorded. Fracture data collected using the detailed line survey method are biased against recording fractures that are subparallel to the trace line. The North Ramp of the ESF has an orientation of N61°W, thus resulting in a bias against recording steeply dipping, northwest-striking fractures. The Main Drift of the ESF has an orientation of N3°E, resulting in a bias against recording steeply dipping, north-striking fractures. The South Ramp has an orientation of N91°E resulting in a bias against recording steeply dipping, east-striking fractures. In all portions of the tunnel, the use of a subhorizontal trace line results in a bias against recording gently dipping fractures.

A map of the fracture network was produced using close-range photogrammetric techniques along a 65-m-long (213-ft-long) exposure (Stations 3+60 to 4+25) of the Tiva Canyon Tuff in the North Ramp of the ESF (Coe 1997). Fracture attributes similar to those measured on surface pavements were obtained for each of the 1,171 fractures mapped at this locality, except that aperture, roughness, and mineral fillings were not recorded.

Fracture mapping was also conducted in the Enhanced Characterization of the Repository Block Cross Drift using the same techniques (detailed line surveys and full periphery mapping) that were used in the main ESF. The distribution of fractures, faults, and shears is similar in the Cross Drift and the ESF in terms of frequency, character, and orientation, with one exception (Mongano et al. 1999, pp. 65 to 76), the intensely fractured zone that is prominent in the Main

Drift of the ESF (Stations 42+00 to 51+50, Figure 4.6-15b) does not occur in the Cross Drift. The fracture frequency in the Cross Drift shows an increase from 2.2 to 2.9 fractures per meter between Stations 13+20 and 14+20, in the middle nonlithophysal zone, as compared to the 4.2 fractures per meter in the intensely fractured zone in the Main Drift, in the same lithostratigraphic zone. This might be due to the small amount of offset on the Ghost Dance fault in the vicinity of the Cross Drift.

The occurrence of mineral coatings along fractures is similar in both the Cross Drift and the ESF. Vapor-phase mineral coatings are nearly ubiquitous in both excavations. Calcite and opal infillings in fractures and on the lower surfaces of lithophysal cavities are common within a number of intervals in the Cross Drift and the ESF (Mongano et al. 1999, p. 79, Figure 23).

4.6.6.1.3 Fracture Data from Boreholes

Fracture data from subvertical boreholes drilled at Yucca Mountain (Figure 4.5-5) were collected, interpreted, and documented in a number of reports (e.g., Spengler, Byers et al. 1981; Scott, R.B. and Castellanos 1984; Spengler and Chornack 1984; Engstrom and Rautman 1996, pp. 19 to 23; Rautman and Engstrom 1996a, pp. 24 to 26; 1996b, pp. 22 to 26). For each borehole, coring-induced fractures were eliminated, and the total number of natural fractures (and fractures of indeterminate origin) were tabulated from core logs with 10-ft (3-m) depth intervals. Core recovery was tabulated for each 10-ft interval. Methods to account for unrecovered core and rubble zones are discussed in several reports describing stratigraphic sequences penetrated in drill holes (e.g., Rautman and Engstrom 1996a, pp. 19 to 24). The number of observed fractures was adjusted for unrecovered core by assuming that fracture density in the unrecovered core and rubble zones was the same as in the recovered core. The total number of fractures adjusted for core recovery was thus calculated by dividing the sum of the natural and indeterminate fractures by the percentage of core recovered for each 10-ft (3-m) interval (length of core run minus length of unrecovered core plus rubble zones).

Fracture frequency (number of fractures per unit length) was obtained from unoriented core, downhole video logs, or geophysical techniques, such as sonic logs. Boreholes also provide important information about variations in fracture intensity with depth and lithology. A number of difficulties were encountered when borehole fracture data were compared to data collected at the surface and in the ESF:

- Much of the borehole fracture data are based on unoriented core, and thus cannot statistically be compared to true fracture orientations measured in outcrops or in the ESF.
- Borehole data do not directly provide information on fracture lengths or termination relationships.
- Assessing in situ fracture characteristics from boreholes requires the understanding and correction of orientation and length bias inherent in borehole sampling of a fracture network.
- The air or air and foam mixture used to minimize hydrologic perturbations during drilling adversely affect core recovery and diminish the quality of downhole video logs.

4.6.6.1.4 Comparison of Data Collection Methods

The various fracture studies at Yucca Mountain result in diverse and not entirely compatible data sets. Even where the same fracture attribute was measured (e.g., trace length), different collection methods may have used different measurement criteria (e.g., different lower-limit trace-length cutoffs). A further difficulty in integrating the data sets results from comparing one-dimensional (detailed line survey) and two-dimensional (pavement maps, outcrop observations, and full-periphery maps in the ESF) data and integrating them into an accurate representation of the fracture network.

Sweetkind and Williams-Stroud (1996, p. 29); Sweetkind, Anna et al. (1997, pp. 188 to 192); and Sweetkind, Barr et al. (1997, pp. 15 to 22) have discussed various approaches and strategies for comparing and integrating diverse fracture data. Fracture studies at the surface and in the ESF yield generally consistent orientation distributions, trace-length distributions, and fracture spacing (both true spacing of individual fracture sets and average apparent spacing) (Sweetkind, Barr, et al. 1997, pp. 19 to 20). Borehole fracture data, however, have severe length and orientation bias. The orientation bias is the result of sampling subvertical fractures with a subvertical borehole. The length bias results from the general inability to evaluate the fracture trace-length distribution of the fracture population being sampled. Sweetkind, Barr et al. (1997, pp. 21 to 22) concluded that the amount of information needed to completely integrate borehole data with two-dimensional data from outcrops and the ESF is generally not available. Consequently, no attempt was made to explicitly correct borehole fracture data for possible severe length and orientation bias.

4.6.6.2 Fracture Attributes of Lithostratigraphic Units

Fracture attributes at Yucca Mountain are dependent on stratigraphic position. Therefore, characterization of fracture attributes with respect to stratigraphy is important for hydrologic flow and transport modeling, potential repository design, and performance assessment.

Fracture characteristics in pyroclastic flow units are primarily controlled by variations in degree of welding. Secondary controls that occur in specific lithostratigraphic intervals are lithophysal development, alteration, and pumice content. These factors control fracture spacing, fracture type, number of sets (orientations), continuity, and connectivity (Sweetkind and Williams-Stroud 1996, pp. 60 to 66; Sweetkind, Barr et al. 1997, pp. 62 to 67).

4.6.6.2.1 Tiva Canyon Tuff (Tpc)

The fracture network in many lithostratigraphic units within the welded, devitrified portion of the Tiva Canyon Tuff is dominated by steeply dipping fractures with northwest, north, or northeast strikes (Tables 4.6-1, 4.6-2). Fractures within the crystal-rich member are dominantly cooling joints with lengths of at least 2.5 m (8.2 ft) and spacing of 1 to 2 m (3.3 to 6.6 ft).

The upper lithophysal zone of the crystal-poor member of the Tiva Canyon Tuff (Tpcpul) is characterized by well-developed cooling joints. They generally occur as two sets of steeply dipping fractures forming a prominent rectangular pattern observable at most of the cleared pavements in this unit (Barton, C.C., Larsen et al. 1993) and at nine outcrop localities studied by Throckmorton and Verbeek (1995, p. 38). These joints range in length from 2 to 10 m (6.6 to

33 ft). Spacing ranges from 0.5 to 3 m (1.6 to 10 ft), but is variable, with local zones of closely spaced (0.5 to 1 m [1.6 to 33 ft]) joints separated by areas of more widely spaced joints (2 to 3 m). Tectonic joint sets, often 1 to 2 m (3.3 to 6.6 ft) in length, are common in this unit as well (Throckmorton and Verbeek 1995, Figure 17). The tectonic joints commonly abut the older cooling joints. Cooling joints dominate over tectonic joints in the upper lithophysal zone of the Tiva Canyon Tuff crystal-poor member (Tpcpul) (Barton, C.C., Page et al. 1989).

The middle nonlithophysal zone of the Tiva Canyon Tuff crystal-poor member (Tpcpmn) is characterized by abundant, short (1 to 2 m [3.3 to 6.6 ft] or less), curving fractures of diverse orientation (Table 4.6-1). This zone commonly exhibits closely spaced, incipient cooling joints, which are parallel to foliation and informally called "vapor-phase partings" in the ESF (Barr et al. 1996, p. 25). These partings impart a stair-step appearance to exposures at the surface where the unit corresponds to the rounded step map unit of older geologic maps (Scott, R.B. and Bonk 1984). The vapor-phase partings decrease significantly in abundance in the underlying lower lithophysal zone of the Tiva Canyon Tuff crystal-poor member (Tpcpll).

Northwest-striking cooling joint sets are more prominent and easy to identify in the lower lithophysal zone of the Tiva Canyon Tuff crystal-poor member (Tpcpll). Cooling joints range in length from 1 to 4 m (3.3 to 13 ft) and have a spacing of 0.1 to 3 m (0.3 to 10 ft). Tectonic joints in this unit are shorter (0.5 to 1 m [1.6 to 3.3 ft]) and exhibit variable spacing. Throughout most of the underlying lower nonlithophysal zone (Tpcpln), cooling joints are difficult to identify because tubular structures are rare, and roughness is not definitive. A network of short, curved, anastomosing fractures that break the rock mass into 2- to 4-cm (0.8- to 1.6-in.) fragments is locally developed in the hackly subzone (Tpcplnh) and in the lower part of the lower lithophysal zone. The base of the lower nonlithophysal zone (Tpcplnc) is characterized by a hexagonal network of cooling joints that divide the rock into abundant crude vertical columns 2 to 5 m (6.6 to 16 ft) high (the columnar zone of Scott, R.B. and Bonk 1984; Throckmorton and Verbeek 1995, p. 20). Column diameters of 0.2 to 1 m (0.6 to 3.3 ft) are common. Cooling joints that bound the columns extend upward short distances into the lower nonlithophysal zone and downward into the underlying crystal-poor vitric zone (Tpcpv) (Sweetkind, Verbeek et al. 1995a, p. 73).

4.6.6.2.2 Paintbrush Nonwelded (PTn) Hydrogeologic Unit

The stratigraphic interval that extends from the base of the densely welded and devitrified portion of the Tiva Canyon Tuff (base of Tpcpv3) downward to the top of the densely welded portion of the Topopah Spring Tuff (Tptrvl) is referred to as the Paintbrush nonwelded (PTn) hydrogeologic unit (Table 4.5-2). This interval includes the basal part of the Tiva Canyon Tuff, the Yucca Mountain Tuff, the Pah Canyon Tuff, the uppermost part of the Topopah Spring Tuff, and three informally designated intervening bedded tuff units (Moyer et al. 1996, p. 7) (Table 4.5-2). Fracture characteristics in the PTn unit are important to hydrologic modeling because of their potential role in water percolation from the surface to the potential repository host horizon.

Fracture characteristics of the pyroclastic flows within this stratigraphic interval (Table 4.6-2) are closely tied to degree of welding (Sweetkind, Verbeek et al. 1995a, p. 88); fracture intensity increases with the degree of welding. Even partly to moderately welded tuffs have higher

fracture intensity and network connectivity than interstratified nonwelded and bedded units (Sweetkind, Verbeek et al. 1995a, pp. 99 to 106; Sweetkind and Williams-Stroud 1996, p. 41). Throughout most of the central portion of Yucca Mountain, the Yucca Mountain and Pah Canyon tuffs are nonwelded (Buesch, Spengler et al. 1996a, pp. 18 to 19) and fracture intensity is low (Sweetkind, Verbeek et al. 1995a, p. 100, Table 6). North of Drill Hole Wash, the Yucca Mountain and Pah Canyon tuffs are welded and devitrified (Moyer et al. 1996, Figures 14, 19). Cooling joints are present in both units, and fracture intensity is greater than in areas to the south (Sweetkind, Verbeek et al. 1995a, pp. 82 to 83).

The crystal-poor vitric zone at the base of the Tiva Canyon Tuff (Tpcpv) has transitional fracture characteristics and physical properties related to the rapid vertical variation in degree of welding (Table 4.6-2) (Moyer et al. 1996, p. 17; Sweetkind, Verbeek et al. 1995a, p. 23). Cooling joints of the columnar subzone of the lower nonlithophysal zone (Tpclnc) are observed in surface exposures to terminate downward into a network of small, irregular cooling joints in the densely welded upper part of the crystal-poor vitric zone of the Tiva Canyon Tuff (Tpcpv3) (Sweetkind, Verbeek et al. 1995a, p. 38). Cooling joints are abundant and commonly outnumber tectonic joints in the moderately welded tuff part of the zone (Tpcpv2). Both types of joints have a limited vertical extent and terminate downward into poorly welded tuff (Tpcpv1) that has significantly greater matrix porosity and permeability (Moyer et al. 1996, Figure 24; Sweetkind, Verbeek et al. 1995a, p. 75).

The fracture characteristics of nonwelded pyroclastic flows and interstratified pyroclastic fall deposits within the Paintbrush Group are controlled primarily by variations in lithology across depositional boundaries (Sweetkind, Verbeek et al. 1995a, pp. 88 to 92). Higher pumice content and clast size are correlated to lower fracture density. Among the nonwelded units, recognizable sets of fractures are most common in the basal, nonwelded portion of the crystal-poor vitric zone of the Tiva Canyon Tuff (Tpcpv1) and in nonwelded units of the Yucca Mountain Tuff. Both generally contain 15 percent or less of pumice clasts (Moyer et al. 1996, pp. 17, 25). Nonwelded units with 30 to 70 percent pumice clasts, which include most of the bedded tuffs and nonwelded flows between the base of the Yucca Mountain Tuff and the top of the Topopah Spring Tuff, are much less intensely fractured. Definable joint sets are sparse at many localities and joint spacing is irregular (Table 4.6-2) (Sweetkind, Verbeek et al. 1995a, p. 90). Many of the fractures terminate at compositional boundaries, such as the contacts with pumice-rich fall deposits. Pumiceous tephra deposits, containing 80 percent or more of pumice clasts, generally are not fractured except for sparse weathering joints (Sweetkind, Verbeek et al. 1995a, p. 90).

The effect of clast size is difficult to separate from other important controls on fracture network development. Nevertheless, increasing clast size appears to inhibit the development of fractures (Sweetkind, Verbeek et al. 1995a, p. 91). Comparison of the three pumiceous fallout tephras within the Paintbrush Group (informal subunits Tpbt3a, Tpbt3d, and Tpbt4 of Moyer et al. [1996, Figure 3, Table 3]) reveals that the finest grained of the three (unit Tpbt4) consistently contains the most fractures. Similar relationships between joint development and grain size are known in sedimentary rocks, particularly sandstone and conglomerates (Price, N.J. 1966, pp. 142 to 144).

4.6.6.2.3 Topopah Spring Tuff (Tpt)

Fractures in the Topopah Spring Tuff are important to hydrologic modeling because of their role in hydrologic flow in and around the potential repository host horizon. The population of fractures within the crystal-rich member of the Topopah Spring Tuff (Tptr) is dominated by steeply dipping cooling joints of various orientations (Table 4.6-3) (Sweetkind, Barr et al. 1997, pp. 38 to 42). Exposed lengths of cooling joints in surface exposures range from 1 to 4 m (3.3 to 13 ft). Tectonic joints are mostly less than 1 m (3.3 ft), although some are as long as 5 m (16 ft) (Throckmorton and Verbeek 1995, pp. A-11 to A-21). Many fractures within the densely welded, crystal-rich vitrophyre of the Topopah Spring Tuff (Tptrv1) terminate upward within the overlying moderately welded pumiceous material (Tptrv2) (Barr et al. 1996, Drawing OA-46-283). The crystal-rich vitrophyre of the Topopah Spring Tuff (Tptr) is underlain by a thin (2- to 3-m [6.6- to 10-ft]) interval of devitrified tuff that contains argillically altered pumice clasts (Tptrn3). Below this zone, pumice clasts are replaced with coarsely crystalline vapor-phase minerals (Tptrn2) (Buesch, Spengler et al. 1996a, pp. 7, 19). Within the ESF, vapor-phase crystallization is intense in the upper portions of the Topopah Spring Tuff crystal-rich member (Tptrn2) between ESF Stations 12+75 to 13+36, where pumice fragments are corroded and the rock matrix contains pockets of vapor-phase minerals. The fracture intensity in this vapor-phase-altered interval is high. Below this interval (at ESF Station 13+37 and beyond), fracture frequency decreases and interfracture distance increases. This change corresponds to a vapor-phase alteration boundary within the Topopah Spring Tuff crystal-rich member and most likely indicates a change in the "brittleness" of the units (Barr et al. 1996, pp. 78 to 79).

In the ESF, fracture density in the Topopah Spring Tuff crystal-rich member decreases at the contact with the upper lithophysal zone of the crystal-poor member (Tptpul), where fracturing is infrequent and discontinuous (Barr et al. 1996, Drawing OA-46-283). In contrast to the crystal-rich member, steeply dipping cooling joints are rare in the upper lithophysal zone (Tptpul). The predominant fractures are north- and northwest-striking tectonic joints that have spacings that typically range from 0.5 to 3 m (1.6 to 10 ft) (Table 4.6-3). Tectonic fractures in the highly lithophysal rock are short, and most cannot be followed continuously for more than 3 m (10 ft). Joint surfaces are rough and pockmarked by abundant lithophysal cavities, and their traces are irregular. In many cases, the fractures appear to link lithophysae. All of these properties reflect the difficulty of propagating a smoothly continuous fracture through a rock containing numerous large voids, resulting in a network of relatively short, widely spaced, discontinuous tectonic fractures with a high proportion of blind fracture terminations (Sweetkind, Verbeek et al. 1995b, p. 42).

A network of long, relatively closely spaced joints generally characterizes the middle nonlithophysal zone of the crystal-poor member of the Topopah Spring Tuff (unit Tptpmn). At least four joint sets are interpreted to be present in this unit in the ESF, including two subvertical sets that strike northwest and northeast, a northwest-striking set with moderate dips (50°), and a northwest-striking set with about 20° dips (Albin et al. 1997, pp. 26 to 28, Table 1; Sweetkind, Barr et al. 1997, pp. 45 to 48). Northwest-striking joints are the most prevalent set throughout the unit, followed in abundance by northeast-striking joints (Albin et al. 1997, p. 26, Table 1). An intensely fractured zone is present from Stations 42+00 to 51+50, in which the overall fracture frequency is more than twice the frequency observed in other areas. Within the intensely fractured zone, a northwest-striking set, oriented N80°W to N35°W, dominates all

other joint sets. These joints are smooth, with manganese-oxide coatings and some vapor-phase mineralization (Albin et al. 1997, p. 60). The origin of the intensely fractured zone is currently unresolved.

The northwest-striking joint set with moderate dips occurs only at the north end of the ESF Main Drift; joints with intermediate dips are uncommon south of about Station 37+00. The fracture set with 20° dips is observed throughout the middle nonlithophysal zone; however, within the intensely fractured zone the set is nearly absent, comprising only 1 percent of the fractures (Albin et al. 1997, p. 26, Table 1). Within the ESF, fracture intensity in the middle nonlithophysal zone is high, with an average apparent fracture spacing of 0.36 m (1.18 ft) for fractures 1 m and longer. This value includes the effect of the intensely fractured zone between ESF Stations 42+00 to 51+50. Average apparent spacing in this unit north of the intensely fractured zone is 0.52 m (1.70 ft), and to the south, the average is 0.40 m (1.31 ft). Average apparent fracture spacing within the intensely fractured zone itself is 0.2 m (0.68 ft) (Figure 4.6-16).

The fracture network within the middle nonlithophysal zone of the crystal-poor member of the Topopah Spring Tuff (Tptpmn) has been mapped at pavements P1000 and P2001, both located on the east flank of Fran Ridge, 3 km (1.9 mi.) east of the crest of Yucca Mountain (Figure 4.6-3) (Sweetkind and Williams-Stroud 1996). Pavement P2001 exposes three mutually orthogonal cooling joint sets: two subvertical sets, striking northwest and northeast, and one subhorizontal set (Sweetkind, Verbeek et al. 1995b). Four subsequent sets of tectonic fractures are all steeply dipping; the earliest tectonic fractures are oriented north-south, followed by northwest-striking, northeast-striking, and east-west sets. The orientations of northwest- and northeast-striking joints at P2001 are similar to those observed in the ESF (Albin et al. 1997, p. 26; Sweetkind, Barr et al. 1997, p. 47). However, north-striking joints observed at P2001 and prominent at P1000 (Sweetkind and Williams-Stroud 1996, p. 40) are not well expressed in the ESF (Table 4.6-2). Detailed line survey scanlines in the ESF Main Drift have orientations of N3°E, resulting in a bias against the recording of steeply dipping, north-striking fractures. North-striking joints are locally observed within the turn from the North Ramp to the ESF Main Drift and in the east-trending alcoves (Sweetkind, Barr et al. 1997, pp. 48, 121). Orientation bias alone may not account for the small number of north-striking joints in the ESF. The presence of north-striking joints at Fran Ridge may represent real spatial variability in joint orientations in this lithostratigraphic unit (Tptpmn). North-striking joints may also be related to their proximity to the Paintbrush Canyon fault (Sweetkind, Verbeek et al. 1995b, p. 74).

Fracture intensity drops sharply and fracture character changes markedly at the contact between the middle nonlithophysal and lower lithophysal zones of the Topopah Spring Tuff (Tptpmn and Tptpll, respectively). Fractures within the middle nonlithophysal zone tend to be planar or arcuate, with low surface roughness; fractures within the lower lithophysal zone are subplanar and extremely rough. On average, fractures in the middle nonlithophysal zone are significantly longer than fractures in the lower lithophysal zone. The numerous large fractures that characterize the middle nonlithophysal zone typically terminate abruptly at the contact with the lower lithophysal zone of the Topopah Spring Tuff crystal-poor member (Tptpll). Below this contact, fractures are infrequent, with an average apparent spacing of 3.3 m (10.8 ft).

No fracture data from the surface or the ESF are available for the lower nonlithophysal zone of the Topopah Spring Tuff crystal-poor member (Tptpln). Fracture frequency from borehole core measurements for this unit typically ranges from 19.4 to 23.7 fractures per 10-ft interval (Sweetkind, Barr et al. 1997, p. 49). These fracture frequencies are high relative to the lithophysal-bearing units in the crystal-poor member of the Topopah Spring Tuff, but are similar to fracture frequencies obtained from the middle nonlithophysal zone (Figure 4.6-16).

Three sets of steeply dipping cooling joints form an incipient columnar network of joints within the crystal-poor vitrophyre of the Topopah Spring Tuff (Tptpv) (Sweetkind, Barr et al. 1997, pp. 49, 53). Also present are distinct, subhorizontal discontinuities that separate column intervals. Mean fracture spacing is 0.5 m (1.6 ft), which is smaller than that observed in most of the ESF welded, devitrified units.

4.6.6.2.4 Calico Hills Formation (Tac)

Fracture data were collected from surface exposures of zeolitically altered Calico Hills Formation in the vicinity of Prow Pass (Figure 4.6-4). In general, two steeply dipping fracture sets are present within the pyroclastic flow units, a prominent northwest-striking set and a slightly less well-developed northeast-striking set (Sweetkind, Barr et al. 1997, p. 53). The orientations of the two principal sets differ slightly between individual pyroclastic flow units, but average fracture spacing and trace length are similar, regardless of orientation. The spacing interval between discontinuities of an individual set ranges from 0.3 to 4 m (1 to 13 ft); average apparent spacing for the unit as a whole is 1 to 2 m (3.3 to 6.6 ft) (Table 4.6-4). At Prow Pass, northwest-striking joints tend to occur as a series of widely spaced northwest-trending zones. Each zone consists of a number of northwest-striking joints that are typically long (5 to 10 m [16 to 33 ft]) and closely spaced (0.5 to 1 m [1.6 to 3.3 ft]). These northwest-trending zones are spaced 50 to more than 100 m (164 to more than 328 ft) apart. Between the zones, the spacing of the northwest-striking joints is 2 to 4 m (6.6 to 13 ft) or more (Sweetkind, Barr et al. 1997, p. 55).

4.6.6.2.5 Bullfrog Tuff (Tcb)

Fracture data from the welded, devitrified middle portion of the Bullfrog Tuff were collected from surface exposures at Raven Canyon and Little Skull Mountain, at distances of 15 and 20 km (9.3 and 12.4 mi.), respectively, from central Yucca Mountain (Sweetkind, Barr et al. 1997, p. 58). The majority of fractures measured at both localities are steeply dipping. At Raven Canyon (Figure 4.5-2), cooling joints form two sets: northeast-striking with high dispersion of orientation, and north- to northwest-striking. Tectonic fractures strike dominantly northwest with a smaller number striking northeast. Average apparent spacing is 0.3 m (1 ft) at Raven Canyon and 0.4 m (1.3 ft) at Little Skull Mountain (Table 4.6-4). Fractures from Little Skull Mountain may be subdivided into seven sets of steeply dipping cooling and tectonic joints (Sweetkind, Barr et al. 1997, p. 58). Sets of cooling joints have median strike directions of N52°E, N4°E, and N60°W, respectively. The predominant tectonic joint set has a median strike direction of N34°E, with less well-expressed tectonic sets oriented at N17°E and N14°W.

4.6.6.3 Fracture Intensity and Connectivity

Fracture data from boreholes at Yucca Mountain indicate that welded flow units in the Tiva Canyon and Topopah Spring tuffs have consistently higher fracture frequencies than the surrounding nonwelded units of the PTn unit and the Calico Hills Formation (Spengler and Chornack 1984, p. 35; Scott, R.B. and Castellanos 1984, Figure 25; Engstrom and Rautman 1996; Rautman and Engstrom 1996b). Surface mapping also shows that the fracture density within nonwelded and poorly welded units is much lower than in the surrounding welded units (Table 4.6-5). The intensity of fracturing increases with degree of welding within the welded pyroclastic flows because of the presence of cooling joints, and because increasing brittleness of the rock favors an increase in the number of tectonic joints.

Fracture intensity for the various lithostratigraphic units described above is summarized by Sweetkind, Barr et al. (1997, pp. 22 to 58) and shown on Figure 4.6-16. Surface and ESF fracture data are reported in terms of spacing—the distance in meters between fractures (upper axis of Figure 4.6-16). Apparent fracture spacing from surface data is shown as bars that represent the range of values from surface studies (Figure 4.6-16). The apparent fracture spacing from ESF data is shown as a single dot. Average apparent fracture spacing in the ESF is calculated as the number of fractures observed in a particular lithostratigraphic unit divided by the distance in the tunnel in which the rocks of that unit are exposed (Sweetkind, Barr et al. 1997, pp. 19 to 20). Borehole fracture density for lithostratigraphic units is reported as the number of fractures per 10-ft (3-m) interval, adjusted for unrecovered core (Figure 4.6-16; Sweetkind, Barr et al. 1997, Tables 2-5, 8-14). Borehole data are not corrected for either orientation or trace-length bias. Although direct comparisons cannot be made, the borehole data mirror the trends in fracture intensity seen in the surface and ESF data (Sweetkind, Barr et al. 1997, pp. 58 to 62). Values for borehole fracture frequency appear along the bottom axis of Figure 4.6-16, and the scale has been reversed so that fracture intensity increases to the left and decreases to the right in both the upper and lower axes.

Different lower-limit trace-length cutoffs make it difficult to statistically compare fracture data collected by different methods. The shapes of fracture trace-length distributions at Yucca Mountain are generally consistent with a power-law or exponential model. Therefore, use of a smaller lower-limit trace-length cutoff results in the measurement of increasing numbers of fractures in a given area. Borehole fracture lengths have no lower truncation, so bias in favor of measuring short fractures is extreme. One benefit of reporting borehole fracture frequency separately from the surface and ESF data (Figure 4.6-16) is that a measure of fracture density is available from two general size classes of fractures. The surface and ESF data yield apparent fracture spacing (reported as distance between fractures) for fractures 1 m (3.3 ft) and greater. In contrast, borehole data yield fracture density (reported as number of fractures per unit distance, equivalent to 1/spacing) for all fractures larger than the diameter of the core.

Fluid flow through a fracture network depends, in part, on the degree to which the fractures are interconnected. Fracture connectivity, in turn, is dependent upon fracture size and orientation distributions, fracture density, and the fracture-system geometry, particularly the distribution of intersection types, which can be measured or described through field observations and geometric analysis of the resulting pavement maps.

One method of estimating fracture connectivity is through a graphical comparison of fracture termination relations (Barton, C.C., Larsen et al. 1993, pp. 32 to 33). Fractures may terminate in the rock matrix as a blind or dead end, may cross each other as an intersection or X termination, or may abut each other at a T or Y termination. The relative proportions of these termination types in an exposure may be expressed as ratios, using the terms of termination probability and termination percentage. Termination probability (the likelihood that a fracture will abut an earlier formed fracture) is calculated as the number of abutting intersections divided by the total number of fracture intersections (abutting and crossing). Termination percentage (the likelihood that a fracture will intersect another fracture rather than end blindly) is calculated as the number of abutting and crossing terminations divided by the total number of fracture endpoints (Table 4.6-5; Figure 4.6-17).

Fracture connectivity must be integrated with fracture intensity in an evaluation of the potential flow properties of a fracture network. Well-connected fractures may still yield very few continuous pathways, given low fracture densities. One such combination of connectivity and intensity is intersection intensity, which is calculated as the number of fracture intersections per area (number divided by square meters) for pavement map data. For scanline data from the detailed line survey, intersection intensity is reported in terms of number of fracture intersections per unit fracture trace length (Table 4.6-5; Figure 4.6-17). The calculation of intersection intensity is dependent on both fracture intensity and on network geometry. For example, a network consisting of many subparallel fractures would yield a low intensity by this measure. In general, however, this method of measuring intensity yields values that are quite consistent for both one- and two-dimensional fracture measures (Table 4.6-5; Figure 4.6-17).

Fracture termination percentage and intersection density are highest in the densely welded interiors of pyroclastic flows and lowest in the surrounding nonwelded rock (Table 4.6-5; Figure 4.6-17). The complex fracture networks in the densely welded interiors of pyroclastic flows are well connected because the development through time of multiple fracture sets promotes fracture interaction. Abundant cooling joints and early tectonic joints limited the amount of available area for subsequent fractures to propagate. Thus, many late fractures simply connect preexisting fractures. Poorly welded pyroclastic flows and nonwelded bedded units are characterized by poorly connected networks and an abundance of blind fracture terminations in rock (Table 4.6-5; Figure 4.6-17).

Fracture connectivity within the welded portions of the pyroclastic flows of the Paintbrush Group is dependent on the degree of communication between fracture networks within individual zones. High effective permeabilities, resulting from overall high fracture connectivity within the welded units at Yucca Mountain, may be inferred from air flow in wells as a result of barometric and topographic effects (Weeks, E.P. 1987, pp. 166 to 169), transient pneumatic pressure disturbances caused by the excavation of the ESF (Rousseau et al. 1999, pp. 110 to 111), and pathways analysis of a simulated fracture network in the Tiva Canyon Tuff (Anna and Wallman 1997, pp. 206 to 207). (See also Sections 8.3 and 8.4).

4.6.6.4 Structural Controls on Fracture Network Properties

4.6.6.4.1 Fracture Intensity near Fault Zones

Hydrologic models require that the width and hydraulic properties of fault zones be defined to evaluate the influence of faults on flow pathways (Wittwer et al. 1993, pp. 667, 673). The total width of the fault zone may include an area around the fault plane, here called a zone of influence, in which fracture intensity is higher, or in which some other parameter, such as orientation, changes in response to the presence of the fault.

In the ESF, overall variability in the frequency of fractures 1 m long (3.3 ft) or longer is primarily a function of lithology, not proximity to faults (Figures 4.6-15a, 4.6-15b) (Sweetkind, Barr et al. 1997, p. 68). At the large scale used for detailed mapping in the ESF, there are no sharp increases in the number of fractures longer than 1 m (3.3 ft) in close proximity to faults (Figures 4.6-15a, 4.6-15b). The relationship of fractures shorter than 1 m (3.3 ft) to faults was evaluated by visual examination of every fault in the ESF (Sweetkind, Barr et al. 1997, p. 68) that could be correlated with a fault mapped at the surface (Day et al. 1998a) (Table 4.6-6). Four principal conclusions were reached (Sweetkind, Barr et al. 1997, pp. 68, 71):

1. The width of the zone of influence on fracture frequency in the immediate vicinity of a fault is, in general, quite narrow, ranging from less than 1 m (3.3 ft) up to 10 m (33 ft) from the fault (Table 4.6-6).

2. The width of the zone of influence in the immediate vicinity of a fault generally correlates with the amount of fault offset. Intrablock faults with very small amounts of offset (1 to 5 m [3.3 to 16 ft]) have zones of influence that are 1 to 2 m (3.3 to 6.6 ft) wide. Block-margin faults with tens of meters (up to 100 ft) of offset (faults at ESF Stations 11+20 and 70+58) (Table 4.6-6) have zones of influence that range up to 6 to 10 m (20 to 33 ft) wide. The limited available data from block-bounding faults are not definitive regarding the nature of attendant fracturing. The Dune Wash fault is exposed in the ESF near Station 67+88, where the offset is 65 m (213 ft) (Sweetkind, Barr et al. 1997, Table 21), and the zone of increased fracture frequency in the vicinity of the fault is 6 to 7 m (20 to 23 ft) wide. The Bow Ridge fault has very little attendant fracturing despite the 100-m (328-ft) offset and exposure near the surface (approximately 35 m (115 ft) of overburden). Lack of deformation around the fault zone probably results from the presence of nonwelded pre-Rainier Mesa Tuff in the hanging wall of the fault.

3. The width of the zone of influence around a fault does not appear to be related to depth, at least within the ESF. The width of the zones of influence for small faults observed along the North Ramp where overburden is 50 to 60 m (164 to 197 ft) thick is similar to those of small faults observed elsewhere in the ESF where overburden thickness is two to three times greater. However, upward-splaying faults can result in apparent broad zones of influence at the surface because of the overlap of fractured zones surrounding individual fault splays.

4. The amount of deformation associated with faults may be dependent, in part, upon which lithologic unit is involved in the faulting. Faults within nonwelded to partly welded portions of the crystal-poor vitric zone of the Tiva Canyon Tuff (Tpcpv) are generally sharp, discrete breaks with minimal fault gouge or secondary shear surfaces (Table 4.6-6, faults at ESF Stations 8+45 and 10+44). Individual pumice clasts along some faults can be traced to the fault surface without visible sign of breakage, and wall rocks show little evidence of deformation. In comparison to brittle, welded rocks, nonwelded units apparently can accommodate a greater amount of extensional strain before failing by fracture.

Broad, fault-related zones of influence on the fracture network are evident at two cleared surface exposures that cross the Ghost Dance fault. One locality is the vertical cut at the USW UZ-7a drill pad; the other is the ARP-1 pavement on the south-facing slope of Antler Ridge (Figure 4.6-14). Both cleared exposures intersect a section of the Ghost Dance fault with the greatest displacement (13 to 30 m [43 to 98 ft]) and greatest number of associated fault splays.

The vertical cut at the USW UZ-7A drill pad exposes the middle nonlithophysal zone of the Tiva Canyon Tuff (Tpcpmn) in the hanging wall of the Ghost Dance fault. At the surface, the Ghost Dance fault dips steeply (75° to 87°) to the west and has variable down-to-the-west displacement (Day et al. 1998a, p. 9). A secondary, east-dipping fault with 3 to 4 m (10- to 13-ft) of offset occurs 42 m (138 ft) west of the Ghost Dance fault trace. The intervening rock is intensely broken and consists of a complex network of short fractures that bound blocks as small as 10 cm (4 in.). True fracture intensity (measured with no trace-length cutoff) is high—nearly 12 m (39 ft) of fracture trace-length per square meter of exposure (12 m/m^2 [37 ft/yd^2]); fracture connectivity is also high (Sweetkind and Williams-Stroud 1996, p. 74). Rocks of the lowermost part of the lower lithophysal zone of the Tiva Canyon Tuff (Tpcpll) are exposed in the footwall of the Ghost Dance fault at the UZ-7A exposure, but these footwall rocks do not display the intense fracturing that is exhibited in the hanging wall.

The ARP-1 pavement is located on the south flank of Antler Ridge and exposes the upper lithophysal, middle nonlithophysal, and lower lithophysal zones (Tpcpul, Tpcpmn, Tpcpll) of the Tiva Canyon Tuff. On Antler Ridge, there are 13 to 20 m (43 to 66 ft) of cumulative westside-down displacement across several splays of the Ghost Dance that are distributed over a map width of approximately 100 to 150 m (328 to 492 ft) (Day et al. 1998a, p. 9). Individual splays are characterized by 1- to 2-m-wide (6.6-ft-wide) breccia zones. The 100-m-wide (6.6-ft-wide) pavement straddles the main trace of the Ghost Dance fault and two small associated faults. The fracture network at ARP-1 is dominated by closely spaced, steeply dipping fractures striking N5°W to N25°W. There is abundant tectonic breccia present at ARP-1, and many fractures show minor amounts of offset. The closely spaced fractures and abundant brecciation at ARP-1 may be interpreted to be the result of their proximity to the Ghost Dance fault. However, it may be equally likely that the pavement exposes distributed faulting that is unrelated to the Ghost Dance fault, similar to structures mapped by Potter, Dickerson et al. (1999, pp. 8 to 9) to the east of ARP-1 on the south slope of Antler Ridge (Figure 4.6-10).

4.6.6.4.2 Links between Discontinuous Faults and the Fracture Network

Because the potential repository area contains small, discontinuous faults, the role of these faults in interacting with fracture networks is important for modeling hydrologic flow and predicting rock quality for repository design and tunneling operations. The fracture network acts as a preexisting weakness in the rock mass that can distribute strain in the form of small amounts of shear along many fractures. Evidence for distributed shear along fractures includes thin selvages of tectonic breccia along cooling joints and slip lineations along joint surfaces (Sweetkind, Potter, and Verbeek 1996, p. 5266).

Lithology plays a role in the interaction between discontinuous faults and the fracture network. Because each lithostratigraphic zone at Yucca Mountain has characteristic fracture attributes, including preferred orientations, spacing, trace length, and joint type (Sweetkind, Barr et al. 1997, p. 76), each unit is unique in its ability to deform by distributed slip along fractures. The result is stratigraphic control of structural geometry; thus, what may be a discrete break in one lithostratigraphic unit may be a broad zone of distributed deformation in another.

As an example, the discontinuous Sundance fault was studied in the potential repository area. The northwest-striking Sundance fault has as much as 12 m (39 ft) of dip-slip separation where it displaces the crystal-rich member of the Tiva Canyon Tuff (Tpcr) (Potter, Dickerson et al. 1999, pp. 5 to 6). Within the crystal-poor member (Tpcp), however, displacement is distributed across numerous discontinuous fault segments over a maximum width of about 70 m (230 ft) (Potter, Dickerson et al. 1999, p. 6). The trend of each fault segment corresponds to one of the dominant orientations of cooling joints exposed on this portion of the mountain (Barton, C.C., Larsen et al. 1993, p. 7; Barton, C.C., Page et al. 1989, p. 12). This implies that the discontinuous faults are likely to be reactivated cooling joints (Potter, Day et al. 1996; Sweetkind, Potter, and Verbeek 1996).

Similar evidence for distributed displacement is found elsewhere at Yucca Mountain. Mapped displacements of lithostratigraphic contacts are accompanied by the presence of numerous, irregular, small blocks showing evidence for minor slip or rotation and by pervasive brecciation along fracture sets and as isolated breccia bodies (Potter, Dickerson et al. 1999, pp. 8 to 9; Potter, Day et al. 1996). Stratigraphic offset in these areas is accomplished through distributed slip over a broad zone, rather than by movement along a single plane.

4.6.6.4.3 Spatial Variability of Fracture Properties

Fracture orientations are generally consistent across the central and northern part of the site area (Throckmorton and Verbeek 1995) (Figure 4.6-18). Strike directions for cooling joints identified at 15 outcrop locations and four pavements form a rectilinear network of two sets with median strike directions of N45°W and N50°E. Within the Tiva Canyon and Topopah Spring tuffs, a third cooling joint set is developed, at least locally. This set is subparallel to the flattening foliation and roughly orthogonal to the other two cooling joint sets (Throckmorton and Verbeek 1995, p. 43).

Over the same broad area, Throckmorton and Verbeek (1995, Table 2) also identified four subsequently formed joint sets of tectonic origin (Section 4.6.3.3.5). In addition, there is a set of

subhorizontal tectonic joints that have variable strikes and dips less than 10° (Throckmorton and Verbeek 1995, pp. 36 to 37). These joint sets are observable in various combinations in all of the surface outcrop data.

Sweetkind and Williams-Stroud (1996, pp. 66 to 70) also evaluated the spatial variability of fracture orientation. They combined the above data from Throckmorton and Verbeek (1995) with pavement and outcrop fracture data from the PTn hydrogeologic unit (Sweetkind, Verbeek et al. 1995a) and a limited amount of ESF data (Coe 1997). Rose diagrams depict strike distributions subdivided into lithostratigraphic categories. The results of the evaluation suggested that much of the variability seen in joint orientations across Yucca Mountain might be attributed to the variable expression of cooling joints (Sweetkind and Williams-Stroud 1996, p. 69). Cooling joints appear as a system of joint sets in all the welded units, with considerable variability of orientation. The tectonic joints described by Throckmorton and Verbeek (1995, pp. 25 to 36) were evident across the entire central portion of Yucca Mountain, especially where cooling joints were not present, such as lithostratigraphic units that are equivalent to the PTn hydrologic unit.

While there is general consistency of fracture orientations across the central and northern portions of Yucca Mountain (Throckmorton and Verbeek 1995; Sweetkind and Williams-Stroud 1996, pp. 46 to 47), there is also local variability in fracture character within individual lithostratigraphic units. An example is the intensely fractured zone exposed within the middle nonlithophysal zone of the Topopah Spring Tuff (Tptpmn) in the ESF between Stations 42+00 and 51+50, in which fracture intensity is much higher than in any other observed part of unit (Figure 4.6-15). The strike of the predominant joint set within this zone rotates clockwise approximately 20° (Albin et al. 1997, p. 60). Another example is the distribution of gently dipping cooling joints. Such joints are an important component of the fracture network in the middle portion of the Tiva Canyon Tuff in northern Yucca Mountain (the rounded step unit of Scott, R.B. and Bonk [1984]), but become much less pronounced in the central portion of Yucca Mountain. Spatial variability in fracture characteristics is also linked to welding variations in the pyroclastic flows. North of Drill Hole Wash, the Yucca Mountain and Pah Canyon tuffs become welded and devitrified (Moyer et al. 1996, Figures 14, 19). Here fracture characteristics differ distinctly from those for the distal, nonwelded portions of these pyroclastic flows exposed in the vicinity of the potential repository (Sweetkind, Verbeek et al. 1995a, pp. 82 to 83).

4.6.6.5 Correlation of Small-Scale Structures from the Surface to the Subsurface

Geologic mapping in the Central Block at the surface and within the ESF demonstrates a good correlation of structural features between the surface and subsurface. Correlation is best for faults with more than a meter of apparent vertical separation, particularly within the Tiva Canyon Tuff, where uncertainties in surface-to-ESF projections are minimal (Sweetkind, Beason et al. 1996). Along the north ramp of the ESF, the numerous faults mapped at the surface on Azreal Ridge have nearly identical expression in the surface and subsurface—the same number of faults are observed and amounts of displacement are similar (Barr et al. 1996, pp. 70 to 73). Near the southern end of the ESF Main Drift, the southern extension of the Ghost Dance fault is observed to be a single, simple fault plane that dips steeply to the west with minor displacement (1 to 2 m [3.3 to 6.6 ft]) (Albin et al. 1997, Figure 24), the same as it is mapped at the surface (Day et al. 1998a).

In some cases, the correlation of structural features between the surface and subsurface is problematic. For example, the southern splay of the Drill Hole Wash fault has a different strike, dip, and apparent vertical separation in the ESF than at the surface. At the surface, the fault strikes N30°W, dips 80° to 85°SW, and has a vertical separation of approximately 15 m (49 ft) (Day et al. 1998a, p. 8). In the ESF, the average fault strike is N10°W, the average dip is 80°SW, and apparent displacement is estimated at 1.2 m (4 ft) (Day et al. 1998a, p. 9). This variability is typical for intrablock faults observed in the subsurface in the potential repository area.

In some cases, structural features observed in the subsurface have no surface expression. The most prominent example is the zone in the southern portion of the ESF Main Drift where the Topopah Spring Tuff middle nonlithophysal zone (Tptpmn) is intensely fractured. No correlative feature is observed at the surface. Joints within this zone have some attributes typical of cooling joints, including great length, smooth, curving traces, low surface roughness, and local evidence of vapor-phase mineralization. Cooling joints are localized to individual pyroclastic flows. Thus, a cooling joint origin for the joints in the intensely fractured zone would explain their absence in surrounding units (Albin et al. 1997, p. 63).

Correlation of structures between surface and subsurface must take into account possible changes in fault geometry at depth and along strike. Structures may be correlative even though the amounts of displacement, number of splays, and width of breccia zones differ. Controls on the variability of fault geometry between surface and subsurface include free-surface and block-margin effects, preexisting weaknesses, and fault history:

- Upward splaying of faults in response to the free surface is a common, but not universal, geometry at Yucca Mountain that results in differing surface and subsurface fault expressions (Day et al. 1998a). Minor faults often increase in displacement at the block margins where major block-bounding faults influence them.

- Preexisting weaknesses can localize or distribute fault displacement. In the potential repository area, cooling joints are common lines of preexisting weakness. Since their existence and properties are dependent on lithostratigraphic units, different fault geometries can develop in different parts of the stratigraphic section, mirroring the availability of cooling joints over which to distribute displacement. What may be a discrete break in one part of the section may be a broad zone of distributed deformation in another.

- Deformation in the southwestern Nevada volcanic field is spatially and temporally associated with major pyroclastic eruptions. In some cases, the timing of fault movement is such that faults penetrate one stratigraphic unit, but not overlying units. For example, faults that predate the deposition of the Tiva Canyon Tuff would have no correlative surface structures. Similarly, cooling-related features in a particular flow, even if reactivated later, may not have a correlative surface expression.

4.6.6.6 Structural Evidence for Fast Hydrologic Pathways from Studies of Chlorine-36

The radioactive isotope ^{36}Cl is present in anomalous concentrations (relative to natural background values) in young, infiltrating waters. Elevated levels of ^{36}Cl, referred to as bomb-pulse ^{36}Cl, are the result of global fallout from more than 70 atmospheric nuclear tests conducted in the South Pacific between 1952 and 1958 (Glasstone 1962, pp. 481 to 488). These anomalous concentrations occur in chloride leached from bulk-rock samples from the ESF at Yucca Mountain (Fabryka-Martin et al. 1998, p. 93).

The occurrence of bomb-pulse ^{36}Cl in the ESF indicates the presence of flow paths capable of transmitting infiltration from the surface to depths as much as 300 m (984 ft) in less than 50 years (Fabryka-Martin et al. 1998, p. 94). Detailed characterization of the structural settings of the sample locations and their relations to infiltration rates have resulted in a conceptual model for fast pathways at Yucca Mountain (Levy, Sweetkind et al. 1997, p. 11). The model requires two conditions to transmit bomb-pulse ^{36}Cl to the sampled depth within 50 years: (1) a continuous structural path must extend from the surface to the sampled depth, and (2) the magnitude of surface infiltration must be sufficiently high to initiate and sustain at least a small component of fracture flow along the connected fracture path.

Sample localities in the ESF where multiple samples indicate bomb-pulse ^{36}Cl are generally associated with faults correlative to faults mapped at the surface (Barr et al. 1996, pp. 70 to 73; Day et al. 1998a). Hydrologic modeling results highlight the importance of geologic structures as primary controls of fast hydrologic pathways through the lithostratigraphic units equivalent to the PTn hydrogeologic unit (Fabryka-Martin et al. 1998, p. 94). Model simulations require structural disruption of PTn-equivalent units to allow a small amount of water with the bomb-pulse signature to reach the middle nonlithophysal zone of the Topopah Spring Tuff (ESF Main Drift) in 50 yr. or less (Fabryka-Martin et al. 1998, p. 94). Bomb-pulse levels of ^{36}Cl are associated with several fault types, including a block-bounding fault (Bow Ridge fault), a probable strike-slip fault (Drill Hole Wash fault), and smaller, intrablock faults (Sundance fault) (Levy, Sweetkind et al. 1997, p. 11). In the vicinity of Diabolus Ridge, an elevated $^{36}Cl/Cl$ value at the ESF sampling location does not correspond to any fault mapped in the ESF. However, geologic evidence indicates the Diabolus Ridge fault (Day et al. 1998b) might project to the subsurface at a dip of about 30° E. This conclusion is based on three-point calculations from the mapped trace of the fault where it crosses Wren Wash, the attitude of breccia zones observed along the surface trace of the fault, and intersection of a gently dipping fault by borehole USW SD-9 within poorly welded Yucca Mountain Tuff (Engstrom and Rautman 1996, p. 12). The projected subsurface location of this fault where it transects the PTn hydrogeologic unit lies almost directly above the ESF. This corresponds with bomb-pulse ^{36}Cl in samples from Stations 26+79 and 27+18. Structural features sampled in the ESF that do not have elevated $^{36}Cl/Cl$ values either do not have a connected pathway to the surface (e.g., much of the intensely fractured zone) or are faults with surface traces that coincide with areas of low infiltration rates (e.g., the southern part of the Ghost Dance fault as exposed in the ESF Main Drift) (Levy, Sweetkind et al. 1997, p. 11). Additional discussion of results of ^{36}Cl studies can be found in Section 5.3.7.3.

4.6.7 Structural Model for Yucca Mountain

To provide a comprehensive summary of the structural geology of Yucca Mountain, the structural descriptions and interpretations presented in the preceding sections are used to construct a structural model that describes the kinematic and geometric interactions among various structural elements at a variety of scales. Elements of the model then form the basis for a discussion of the genesis of structures, including the relative influences of local stratigraphy and regional tectonics.

A descriptive structural model is illustrated in a series of block diagrams (Figures 4.6-19 to 4.6-23) that portray a hierarchy of observational scales that span four orders of magnitude and the fundamental structural elements operative at each scale. Note that these diagrams are generalized and, in part, schematic and are not intended to represent all faults and fault relations shown on previous figures. The observation scales include:

- A subregional scale (Figure 4.6-20), portraying the overall structural framework of all of Yucca Mountain (approximates a map scale of 1:24,000)
- Intermediate scales (Figures 4.6-21 and 4.6-22), portraying intrablock faulting within the potential repository block from the surface to the repository level and below, and the relationships between the intrablock and the structure of the block-bounding fault zones (approximates a map scale of 1:12,000 to 1:6,000)
- Small-scale maps with relatively small (1,000 m^3 [1,308 yd^3]) volumes of rock, mainly within the Yucca Crest subblock (approximates a map scale of less than 1:6,000).

4.6.7.1 Subregional-Scale Model

Figure 4.6-20 is a block diagram of the subregional scale illustrating structural elements that shape the general aspects of Yucca Mountain. The front of the diagram is a cross section through Yucca Mountain at a northing of N749,000 (Nevada State coordinate system, in feet). Surface fault traces are generalized from the site area geologic map of Day et al. (1998b), and subsurface geology is adapted (with some modification, such as addition of second order faults and a more detailed interpretation of the top of the Paleozoic basement) from the Yucca Mountain Site Characterization Project three-dimensional geologic framework model (CRWMS M&O 2000a) (see Section 4.8). The front face of the block diagram illustrates geology in the moderately extended, south-central part of the mountain, and the top (map view) illustrates structural transitions to the less-extended northern part of the mountain. The principal structural issues at this scale are: (1) systems of block-bounding faults that are kinematically and geometrically linked, (2) hanging-wall and footwall deformation related to the large fault systems, and (3) displacement transfer between individual block-bounding faults along relay faults.

Important features shown at the subregional scale on Figure 4.6-20 are:

- The Solitario Canyon fault system, which contains complexly intersecting faults.
- Strata that steepen in the hanging wall of the Solitario Canyon and Bow Ridge faults.

- Relay faults transfer displacement between the Solitario Canyon and Iron Ridge faults.
- Intrablock faults that have steep dips.
- Dune Wash represents complex hanging-wall deformation above a system of merging block-bounding faults, dominated by the Paintbrush Canyon fault.
- Structural complexity is greatest in the southern part of Yucca Mountain.

The western part of the front face of the block (Figure 4.6-20) shows the geology of the Plug Hill domain (Figure 4.6-4), in which several strands of the Solitario Canyon fault and the southern continuation of the Boomerang Point fault are buried beneath the surficial deposits of southeastern Crater Flat. Key structural relations include the complex geometry of intersecting fault strands in the Solitario Canyon fault system, the "rollover" style of steepening of stratal dips into the Solitario Canyon fault system, and the steeper dips of intrablock fault planes relative to the block-bounding fault plane.

East of the Plug Hill domain, the front face of the block (Figure 4.6-20) crosses the northern tip of the Southwest domain (Figure 4.6-4) east of the Solitario Canyon fault system. This domain is characterized by relay faults and substantial footwall deformation. The Iron Ridge fault splays southeast from the Solitario Canyon fault system and is an example of a relay fault zone distributing displacement between two block-bounding faults.

In the vicinity of Abandoned Wash, the front face of the block (Figure 4.6-20) crosses the structurally simple central Yucca Mountain domain (Figure 4.6-4). The Abandoned Wash fault, which is interpreted to be the southern extension of the Ghost Dance fault (Day et al. 1998a, 1998b), has a steep dip that is characteristic of intrablock faults. The fault merges with a narrow northwest-trending graben that accommodates extension between the Abandoned Wash fault and the Iron Ridge relay fault zone.

The complex Dune Wash domain (Figure 4.6-4) occupies the center of the southern part of the block (Figure 4.6-20) and is clearly more deformed than the blocks that flank it. It comprises a horst-and-graben complex within a large graben and is bounded on the east by the Dune Wash fault. To the east, the diagram illustrates the merging at depth of three block-bounding faults: the Dune Wash, Bow Ridge, and Paintbrush Canyon faults. The Paintbrush Canyon fault is the "master fault" into which the extensional faults of eastern Yucca Mountain merge, and the Dune Wash domain represents the intense hanging-wall deformation above this system.

The eastern part of the block (Figure 4.6-20) shows that the Paintbrush Canyon domain (Figure 4.6-4) is a horst at this latitude, bounded on the west by the Paintbrush Canyon fault and on the east by a buried, unnamed, down-to-the-east fault exposed to the south, on the east flank of Busted Butte (Scott, R.B. 1992; Day et al. 1998b).

At the latitude of Figure 4.6-20, the Solitario Canyon-Iron Ridge and Paintbrush Canyon-Bow Ridge-Dune Wash fault systems appear to have encroached on the Central Block, which is reduced from a width of 4 km (2.5 mi.) farther north to 1.5 km (0.9 mi.) at the front face of the block diagram. This tectonic encroachment on the Central Block was accomplished by hanging-wall deformation from the east and footwall deformation from the west. Farther north, as

illustrated on the map view on the top face of the block (Figure 4.6-20), the structure becomes much simpler, and the amount of extension and fault offset decreases. For example, the myriad faults in the Dune Wash graben have less displacement northward. The Dune Wash fault dies out in the southeastern part of the Central Block, where it transfers its displacement into the block-margin deformation in the Bow Ridge fault hanging wall.

The two large fault systems (Iron Ridge-Solitario Canyon fault system and Paintbrush Canyon-Bow Ridge-Dune Wash fault system) converge toward the south end of the block (Figure 4.6-20). South of the site area, the Iron Ridge fault becomes a major relay fault that transfers displacement between the Solitario Canyon and the Stagecoach Road faults (Scott, R.B. 1992; Simonds et al. 1995).

4.6.7.2 Intermediate-Scale Model

Figures 4.6-21a and 4.6-21b illustrate structural styles at Yucca Mountain corresponding to a map scale of 1:6,000 to 1:12,000, about twice the detail of Figure 4.6-20. Comparison of the two figures shows that Yucca Mountain is structurally simpler toward the north, especially in the potential repository area. The front face of Figure 4.6-21a is located at a northing of N765,000 (Nevada State coordinate system, in feet), near the center of the potential repository area. The front face of Figure 4.6-21b is located at a northing of N740,000 (Nevada State coordinate system, in feet), which is south of the potential repository area. Additional important relations shown in Figures 4.6-21a and 4.6-21b are as follows:

- The 50° dip shown on the Paintbrush Canyon fault in Figure 4.6-21b is typical for block-bounding faults at this latitude.
- The complex faults in Dune Wash merge with the Paintbrush Canyon fault.
- Numerous splays have propagated into the footwalls of the Solitario Canyon and Iron Ridge faults.

In Figure 4.6-21a, the front face of the block passes directly through the Central Block, crossing the Bow Ridge and Solitario Canyon faults. Hanging-wall deformation is shown on the eastern edge of the Central Block, and the steeper stratal dips and more intense faulting contrast with the gentler dips and lack of significant faulting throughout most of the Central Block. At this latitude, the Ghost Dance and Sundance faults each have minor displacements (less than 5 m [16 ft] in both cases), and a footwall splay of the Solitario Canyon fault abruptly loses displacement near Yucca Crest. The complex juxtaposition of stratigraphic units in the Solitario Canyon fault system is confined to a narrow zone, west of which is a west-dipping, fault-bounded block characteristic of this part of the Solitario Canyon fault zone (and of other block-bounding faults, such as the Iron Ridge fault).

In Figure 4.6-21b, the front face of the block is situated west of Busted Butte, and crosses the Paintbrush Canyon fault and the Iron Ridge fault, as well as the intervening deformed area. At this latitude, the Paintbrush Canyon fault acquires displacement from the Bow Ridge and Dune Wash faults, which have merged with the Paintbrush Canyon fault to the north, as seen on the top face of the block. The 50° dip shown for the Paintbrush Canyon fault is characteristic of

large-displacement faults in the southern part of Yucca Mountain. In the footwalls of both the Paintbrush Canyon and Iron Ridge faults, footwall deformation includes numerous closely spaced splays that have propagated into the footwalls from the principal block-bounding faults. In the case of the Iron Ridge fault, the hanging-wall splays bound the 0.6-km-wide (0.4-mi.-wide) Central Block. At the ground surface along the southern edge of the block diagram (Figure 4.6-21b), much of the bedrock is buried beneath surficial cover that blankets low-lying topography. Highly faulted tracts beneath the extensive Quaternary cover are inferred by geologic mapping in the southern part of Yucca Mountain (Scott, R.B. 1990, Figure 3). This is illustrated to a limited degree in Figure 4.6-21b, particularly west of the Paintbrush Canyon fault where a buried complex of faults forms hanging-wall deformation beneath Dune Wash.

4.6.7.3 Small-Scale Model

Figures 4.6-22a and 4.6-23 show small-scale structures in the potential repository area, and Figure 4.6-22b shows small-scale structures immediately to the east of the potential repository area in the Boundary Ridge subblock. The figures represent about an order of magnitude larger scale than in Figure 4.6-21.

Figure 4.6-22a illustrates the following important relations and features in the potential repository area:

- Intrablock faults in the potential repository area are discontinuous and are influenced by stratigraphic variations in fracture properties.
- Cooling joints influence fault geometries.
- The Ghost Dance fault is continuous laterally. This probably reflects its origin in response to intrablock stresses rather than simply as a reactivation of cooling joints.

Figure 4.6-22b illustrates the following important relations and features immediately east of the potential repository area:

- Faulting in the hanging wall of the Bow Ridge fault is more intense than faulting in the potential repository area.
- Cooling joints influence the orientations of northwest-trending faults even in an area of intense faulting.

Figure 4.6-23 illustrates the following important relations and features in the potential repository area:

- Fracture characteristics vary by lithostratigraphic unit.
- Cooling joints are the principal control on structural style at this scale, including control on the expression of intrablock faults.
- Fractures within the lithostratigraphic units comprising the PTn hydrogeologic unit are much less pervasive than in the surrounding welded units.

- Lithophysal (Tptpll) and nonlithophysal (Tptpmn) zones in the Topopah Spring Tuff have distinctly different fracture intensities.

Figure 4.6-22a portrays an area that includes the Ghost Dance and Sundance faults within the Yucca Crest subblock of the Central Block. It illustrates the discontinuous nature of intrablock faults that pass through units of the Paintbrush Group in the Yucca Crest subblock, influenced by the specific preexisting fracture and faulting patterns that are inherent at each stratigraphic level. The network of northeast- and northwest-striking cooling joints that are well developed in this part of the Central Block, and the partial activation of these joints by minor intrablock faults, are shown here. Because the joints, which are the preexisting planes of weakness available for use by faults, are of limited individual extent, the faults that make use of them are discontinuous as well. Irregular, distributed brecciation is required to accommodate strain transfer between discontinuous, fault-activated joint surfaces. In addition, because these small, intrablock faults make use of cooling joints, they inherit steep dips. In this part of Yucca Mountain, the presence of preexisting cooling joints is a powerful influence on both the attitude and the continuity (or lack thereof) of intrablock faults.

The Ghost Dance fault is continuous as opposed to the majority of the faults in the Central Block. This is despite the strong influence exerted by preexisting joints as evidenced by splays and nearby distributed deformation. The fault is probably controlled to a greater degree by intrablock stresses than by older jointing. The Ghost Dance fault appears to pass through several formations in the Paintbrush Group, whereas smaller faults are confined to specific stratigraphic units. The apparent discontinuity in the trace of the Ghost Dance fault on the surface of the block (Figure 4.6-22a) is due to a stepover; the two strands are inferred to connect at depth. The local strain accommodation within this stepover probably occurs through slip on preexisting joints.

Figure 4.6-22b shows the nature of block-margin faulting in the hanging wall of the Bow Ridge fault system (Boundary Ridge subblock of the Central Block) (Figure 4.6-6). Block-margin deformation (Figure 4.6-22b) contains closely spaced north-trending faults that define horst-and-graben patterns and northwest-trending miniature relay structures. These structures qualitatively resemble those in the extended southern part of Yucca Mountain, such as the Dune Wash graben, though at a different scale. This faulting is more pervasive than that in the potential repository area, but the influence of preexisting cooling joints may still be present. Narrow northwest-trending grabens that are an important element of the block-margin deformation have an orientation parallel to that of a prominent cooling joint set documented in relatively undeformed parts of the Tiva Canyon Tuff elsewhere. Small discontinuous faults common to the Yucca Crest subblock are not observed in the Boundary Ridge subblock.

At the scale of 10 to 50 m (33 to 164 ft) (Figure 4.6-23), the fracture network and faults with small displacements are the principal observed structural elements. Representative elements of the fracture network within the Yucca Crest subblock of the Central Block are shown at three different stratigraphic levels: the middle portion of Tiva Canyon Tuff (Tpc), the lithostratigraphic units equivalent to the PTn hydrogeologic unit, and the middle portion of the Topopah Spring Tuff (Tpt) (Figures 4.6-23a, b, and c, respectively). The fracture network subdivides the mountain into numerous fracture-bounded blocks and forms a pervasive mesoscopic fabric element. Cooling joints act as significant preexisting weaknesses in the rock

mass and are the principal control on the style of deformation at this scale. Each lithostratigraphic zone has its own characteristic suite of cooling joint attributes (including joint orientation, spacing, and trace length) so that each zone has a different fabric of preexisting weaknesses. These differences indicate that lithostratigraphic zones respond to extensional stresses differently, resulting in a stratigraphic control of structural geometry.

A pervasive network of cooling and tectonic joints characterize the Tiva Canyon Tuff (Figure 4.6-23a). Cooling joints in the crystal-poor upper lithophysal zone (Tpcpul) and the crystal-rich member (not shown) are large, steeply dipping, and often form two orthogonal sets. Joints in the underlying middle nonlithophysal zone (Tpcpmn) are more numerous, but are shorter, forming an anastomosing network of curved joints. Evidence for tectonic activation of joints as small faults within the Tiva Canyon Tuff includes: (1) the presence of thin breccia zones along cooling joints, (2) slip lineations along fracture surfaces, and (3) common small offsets of lithologic contacts. Intrablock faults may exploit the fracture network, and certain intrablock faults may be nothing more than reactivated cooling joints. However, the differences in the nature of the joint network within each lithostratigraphic unit may govern the expression of the intrablock fault. Within the crystal-poor upper lithophysal zone (Tpcpul), extension may be accommodated by slip along a single, long cooling joint, whereas in the underlying middle nonlithophysal zone (Tpcpmn), extension may be accommodated as a broad zone of distributed deformation on several short joints. Faults, regardless of the amount of offset, commonly occur as zones of brecciation and attendant fracturing many meters wide.

Joints within the lithostratigraphic units that comprise the PTn hydrogeologic unit are much less pervasive than in the surrounding welded units (Figure 4.6-23b). There are no cooling joints in the nonwelded units and few throughgoing joints. Most joints are strata bound and terminate at lithologic contacts. Joints are widely and irregularly spaced, except within welding transitions, such as at the base of the Tiva Canyon Tuff (Figure 4.6-23b). Numerous small faults are observed in this interval, both at the surface and in the ESF. Most faults are narrow, sharp breaks, with no attendant brecciation or fracturing.

Similar to the Tiva Canyon Tuff, the Topopah Spring Tuff has a well-developed network of cooling and tectonic joints. Especially in the middle nonlithophysal zone (Tptpmn), long cooling joints of various orientations are common (Figure 4.6-23c). There is a distinct difference in fracture intensity between lithophysal (Tptpll) and nonlithophysal rock in the Topopah Spring Tuff. Most of the long cooling joints in the middle nonlithophysal zone terminate abruptly at the contact with the underlying lower lithophysal zone (Figure 4.6-23c). In the ESF, the intensely fractured zone dominates the middle nonlithophysal stratigraphic unit. Joint density more than doubles within this zone of closely spaced northwest-striking joints. Similar to the Tiva Canyon Tuff, numerous faulted joints with small displacements occur in the Topopah Spring Tuff. However, little brecciation along joint surfaces or distributed brecciation is observed within the Topopah Spring Tuff. Fault zones at the level of the Topopah Spring Tuff are narrow, and the zones of fault-related fracturing and brecciation are typically only a few meters wide.

4.6.7.4 Genetic Controls on Structural Geometry

The genesis and geometry of the various structural elements may be understood in terms of the relative influence of local stratigraphic control and regional tectonic control (Figure 4.6-24).

Local stratigraphic control may be more significant to local structures, whereas regional tectonic stresses affect structures on a subregional to regional scale. However, almost all of the structures considered in the descriptive structural models are influenced by both stratigraphic and tectonic factors.

At the mesoscopic scale, stratigraphic controls dominate the structure. For example, cooling joints are strongly influenced by stratigraphic position within the Paintbrush Group. Preferential development of cooling joints within specific zones of the Tiva Canyon and Topopah Spring tuffs provides an important primary fabric that later may be exploited by faults. The faults are formed in response to regional and local stresses.

Local stratigraphic control and regional tectonic control equally influence intrablock faults. Closely spaced discontinuous faults located along the south slope of Antler Ridge likely are localized along preexisting cooling joints in the middle nonlithophysal (Tpcpmn) and upper lithophysal (Tpcpul) zones of the Tiva Canyon Tuff (Potter, Dickerson et al. 1999, Figure 2). As discussed earlier, the Sundance fault is a larger example of this superposition. Where cooling joints are poorly developed in the crystal-rich member of the Tiva Canyon Tuff this fault occupies a well-defined single strand. Where there is a greater abundance of cooling joints, such as near the Tpcpul-Tpcpmn contact, displacement is distributed across a broader zone (Potter, Dickerson et al. 1999, pp. 13 to 14).

Local stratigraphic controls influence the largest intrablock faults in minor ways. For example, the Ghost Dance fault is relatively continuous compared to other intrablock faults in the Central Block (Day et al. 1998b). The orientation and continuity of the fault are largely due to its role as a strain accommodation zone within a major tilt block. Minor fault strands that parallel the Ghost Dance fault appear to be purely tectonic features and not activated cooling joints. Stratigraphy appears to influence the hanging-wall deformation and may also be responsible for the way cooling joints are activated to accommodate strain at stepovers. Similarly, much of the block-margin deformation produced by intrablock faulting and block-bounding fault processes is largely controlled by tectonic forces. However, ancillary structures, such as northwest-trending narrow grabens, may also be strongly influenced by stratigraphically controlled cooling joints.

Regional tectonic forces control block-bounding faults with little influence from local stratigraphy. The northern strikes of block-bounding faults in the north are due to east-west extensional stresses that were greatest from 13 to 11 Ma (Minor 1995, pp. 10, 524; Minor, Hudson et al. 1996; Fridrich, C.J. et al. 1999, pp. 202 to 203). The northeast strikes of block-bounding faults in the south reflect the southward-increasing clockwise rotation that affected Yucca Mountain between 13 and 11.45 Ma, with greatest intensity between 11.6 and 11.45 Ma (Rosenbaum et al. 1991, pp. 1971 to 1977; Hudson, M.R. et al. 1996). The latter stresses are attributed to Walker Lane-related right-lateral deformation (Fridrich, C.J. 1999, pp. 177, 193). In addition, stresses imposed by caldera-scale volcanism imposed a second-order influence that affected the kinematics of large faults (Minor 1995, pp. 10,525 to 10,527; Minor, Hudson et al. 1996). Local stratigraphic effects on block-bounding fault systems include relay fault zones that activated cooling joints in the footwalls of block-bounding faults.

In summary, the interplay between local stratigraphic and regional tectonic effects is integral to analyses of the genesis and geometry of structural elements at Yucca Mountain, particularly in the intrablock areas (Figure 4.6-24).

INTENTIONALLY LEFT BLANK

4.7 SITE GEOENGINEERING PROPERTIES

4.7.1 Introduction

This section describes the geoengineering properties of the site, with focus on the potential repository block (Figure 4.7-1). Geoengineering properties include the physical, mechanical, thermal, thermal-mechanical, and other relevant special properties of the various units of geologic material constituting the site.

This section emphasizes the description of the geoengineering properties in the repository block. Investigatory efforts were focused on the lithostratigraphic units proposed as the repository host horizon. However, the planned location of the repository host horizon was adjusted during the design and investigation. Geoengineering properties of near-surface geologic materials were investigated outside the repository block for the design of surface facilities (Figure 4.7-1). This information is included in this section.

The stratigraphic framework in which the potential repository may be constructed is described in Section 4.5. Surficial Quaternary sedimentary deposits are described in Section 4.4. The stratigraphic sequence at the site is generally a series of pyroclastic flow and fallout tephra deposits, as described in Section 4.5. Section 4.5 also includes criteria for differentiating stratigraphic units, detailed descriptions of all the volcanic units that are exposed or encountered in the subsurface within the study area, an index map showing the distribution of stratigraphic units (Figure 4.5-2), and stratigraphic tables (Tables 4.5-1 and 4.5-2).

4.7.1.1 Stratigraphic Framework for Testing

The general stratigraphy of the area is illustrated in Table 4.7-1, which has been abstracted from the more extensive stratigraphy shown in Tables 4.5-1 and 4.5-2. Figures 4.7-2, 4.7-3, 4.7-4, and 4.7-5 show a series of geologic cross sections through the site; a simplified geologic map of the Central Block area is presented in Figure 4.6-4. Rocks important to repository design are mainly within the Miocene age Paintbrush Group, which consists of welded and nonwelded ash-flow deposits. The formations within the Paintbrush Group, as shown in Table 4.7-1 and described in greater detail in Section 4.5, include, in ascending order, the Topopah Spring Tuff, the Pah Canyon Tuff, the Yucca Mountain Tuff, and the Tiva Canyon Tuff. Bedded tuffs are found separating all ash-flow units of the Paintbrush Group. These tuffs are typically nonwelded and are nonlithified to moderately lithified. They range from 0 to 10 m (0 to 33 ft) thick and contain a variety of ash-flow and ash-fall deposits, with minor reworked tuffaceous sandstones. Five of these bedded tuffs are recognized within the Paintbrush Group (Brechtel et al. 1995, p. 4-12).

Below the rocks of the Paintbrush Group is the Calico Hills Formation. Overlying the Paintbrush Group in local areas near Exile Hill are younger, nonwelded ash-flow and air-fall tuffs, including tuff unit X and the Rainier Mesa and Ammonia Tanks tuffs of the Timber Mountain Group.

The late Tertiary and Quaternary surficial sedimentary deposits of the Yucca Mountain area consist of colluvium; alluvium; eolian sand sheets, ramps, and dunes; and spring deposits (see Section 4.4). These range in age from late Pliocene to Holocene. Engineering properties of surficial deposits are described in greater detail in Section 4.7.8.

The Yucca Mountain Site Characterization Project (YMP) developed a thermal-mechanical stratigraphy to provide a systematic basis for characterizing the rock mass in the site area, based on geoengineering properties of the rock units, to facilitate analysis of the response of the rock to the repository construction, operation, and long-term performance. This stratigraphic system, based on thermal and mechanical rock characteristics that are important to repository design, was developed by designating lithologic units, in whole or in part, or a group of contiguous units, or parts, as thermal-mechanical units. Ortiz et al. (1985, p. 3) proposed this nomenclature to group rocks with similar thermal-mechanical properties. The stratigraphy originated from the observation (Lappin et al. 1982, pp. 20 to 24) that thermal properties can be correlated directly to grain density and porosity. The stratigraphy of Ortiz et al. (1985, p. 10, Table 1) includes 16 thermal-mechanical units, seven of which are shown in Table 4.7-1. The thermal-mechanical units were originally identified megascopically in terms of their welding and lithophysal cavity content.

The definition of thermal-mechanical units reflects the general degree of welding. The thermal-mechanical units correlate generally with groups of lithostratigraphic units or, in the case of the Topopah Spring Tuff, parts of a lithostratigraphic unit (Tables 4.5-2 and 4.7-1). The upper two Topopah Spring Tuff units, TSw1 and TSw2, are within the densely welded, devitrified Topopah Spring Tuff. Originally, Ortiz et al. (1985, p. 11) defined the TSw1 as containing more than 10 percent void space from lithophysal cavities and TSw2 as containing less than 10 percent void space from lithophysal cavities. However, the change in percentage of lithophysae does not occur at a consistent stratigraphic position in the crystal-poor upper lithophysal zone, and it can be difficult to identify. For this reason, the Tptpul (upper lithophysal zone)-Tptpmn (middle nonlithophysal zone) lithostratigraphic contact is now used to define the TSw1-TSw2 thermal-mechanical contact, and the top of the potential repository host horizon is now aligned with the horizon below which lithophysae content is less than 10 percent, as inferred from borehole geophysical data (CRWMS M&O 1997c, Section 7.3, pp. 36 to 38). On this basis, the top of the repository host horizon may be up to 30 m (98 ft) above the Tptpul-Tptpmn lithostratigraphic contact (Spengler and Fox 1989, pp. 26 to 27). Recently, CRWMS M&O (1997c, p. 45) indicated that the top of the repository host horizon is as high as 45 m (148 ft) above the contact north of the potential emplacement area. It appears to be 30 to 35 m (98 to 115 ft) above the contact within the potential emplacement area.

Two thermal-mechanical units, the Tiva Canyon welded unit (TCw) and the TSw1, were further subdivided into the high lithophysal and nonlithophysal zones for Exploratory Studies Facility (ESF) geotechnical studies to investigate differences in rock structure and rock mass quality within these zones (Brechtel et al. 1995, p. 4-24). The zones represent summations of the individual lithophysal and nonlithophysal lithostratigraphic zones for those units.

The uppermost identified thermal-mechanical unit is the undifferentiated overburden unit. This collection of various rock and soil types overlies the welded, devitrified Tiva Canyon Tuff. The overburden unit includes alluvium, colluvium, nonwelded, and vitric portions of the Tiva Canyon Tuff and other tuff units, such as the Rainier Mesa Tuff of the Timber Mountain Group, tuff unit X, and their associated bedded tuff units (Tables 4.5-2 and 4.7-1) (Ortiz et al. 1985, Table 1).

Most of the Tiva Canyon Tuff is contained in the TCw thermal-mechanical unit. This unit includes rock between (and including) the densely welded subzone of the vitric zone of the crystal-rich member and, where it is present, the densely welded subzone of the vitric zone of the crystal-poor member. Where the crystal-poor vitric densely welded subzone of the Tiva Canyon Tuff does not occur, the contact of the devitrified rocks in the columnar subzone and the vitric rocks in the moderately welded subzone corresponds to the base of the TCw (Buesch, et al. 1996a, p. 23). The unit is exposed on top of Yucca Crest and the ridges on the eastern flank of Yucca Mountain.

Below the TCw is the Paintbrush nonwelded thermal-mechanical unit (PTn). This unit consists of partially welded to nonwelded, vitric, and, in places, devitrified tuffs. Included in this unit are the nonwelded tuffs at the base of the Tiva Canyon Tuff, the Yucca Mountain Tuff, the Pah Canyon Tuff, the nonwelded and moderately welded tuffs at the top of the Topopah Spring Tuff, and the associated bedded tuffs.

The Topopah Spring welded thermal-mechanical unit (TSw) underlies the PTn. This unit is divided into three subunits based on volume of lithophysal cavities and the identification of the crystal-rich vitrophyre. The top subunit, TSw1, is lithophysae-rich. This subunit includes several parts of the Topopah Spring crystal-rich member (Tptr) plus the upper lithophysal part of the Topopah Spring crystal-poor member, as shown in Table 4.7-1. This upper subunit ranges from about 49 to 113 m (161 to 371 ft) thick (CRWMS M&O 1997d, p. 3-19). The middle subunit, TSw2, is lithophysae-poor and consists of the middle nonlithophysal, lower lithophysal, and lower nonlithophysal zones. The TSw2 subunit ranges in thickness from 175 to 229 m (574 to 751 ft). The vitrophyre subunit (TSw3) at the base of the TSw is about 7 to 25 m (23 to 82 ft) thick (CRWMS M&O 1997d, p. 3-19).

The Calico Hills nonwelded unit underlies the TSw unit. This unit consists of the lower, nonwelded to partially welded portion of the Topopah Spring Tuff, the Calico Hills Formation, the underlying pre-Calico Hills bedded tuff, and the upper, nonwelded portions of the underlying Prow Pass Tuff of the Crater Flat Group.

As shown in Table 4.7-1, the TSw2 thermal-mechanical unit and the lower portion of the TSw1 thermal-mechanical unit have been identified as the potential repository host horizon (CRWMS M&O 1997c, p. 37; 1997d, p. 3-5). This includes the lower portion of the Tptpul (upper lithophysal zone) lithostratigraphic unit, and the whole of the Tptpmn (middle nonlithophysal zone), Tptpll (lower lithophysal zone), and Tptpln (lower nonlithophysal zone) lithostratigraphic units.

4.7.1.2 Geographic Distribution of Data

Most of the data presented in this section was collected to support the design and construction of the ESF and the potential repository. Figure 4.7-1 shows the location of boreholes and test alcoves that were data sources used to develop the characterization data. Additional data are presented from ongoing thermal testing in the ESF. Figure 4.7-1 also shows a subsurface plan view, showing ESF stations, existing boreholes, the repository area, site locations, alcoves, topographic contours, and the coordinates of the North and South Portals. The primary focus of the data collection program was the lithostratigraphic units constituting the potential repository

horizon: the lower portion of the Tptpul (upper lithophysal zone), the Tptpmn (middle nonlithophysal zone), the Tptpll (lower lithophysal zone), and the Tptpln (lower nonlithophysal zone) (CRWMS M&O 1997d, p. 1-1). CRWMS M&O (1997f, Attachment I) presents data submittals from geologic mapping of the ESF. Additional geologic data are included from the Enhanced Characterization of the Repository Block Cross Drift (Mongano et al. 1999)

4.7.1.3 Use of Data for Three-Dimensional Rock Properties Modeling

The three-dimensional integrated site model of Yucca Mountain, consists of a geometric representation of selected rock units and structures, a geologic framework model, and a set of rock properties and mineralogy models and data sets (CRWMS M&O 2000g, p. 1-1) (Section 4.8). The framework model encompasses a 166-km^2 (64-$mi.^2$) rectangle around Yucca Mountain, and includes 50 rock units selected to meet the requirements of hydrologic and transport models and to represent the geology of Yucca Mountain. Modeled rock properties included matrix porosity, bulk lithophysal porosity, saturated hydraulic conductivity, density, and thermal conductivity. A three-dimensional model of mineral distributions was also integrated into the model. Use of data for three-dimensional rock-properties modeling is discussed in greater detail in CRWMS M&O (2000b).

Rautman (1995) and Rautman and McKenna (1997) implemented a two-dimensional geostatistical model of porosity at Yucca Mountain and developed a correlation between that porosity model and thermal conductivity. The relationship of thermal conductivity to porosity, saturation, and temperature is discussed in Section 4.7.4.2. It was assumed for modeling purposes that the spatial continuity of thermal conductivity is identical to those patterns exhibited by lithophysal porosity. This assumption was necessary because there are not enough actual measurements of thermal conductivity from which to develop a spatial continuity model of its own (Rautman and McKenna 1997, p. 13). The result is a suite of thermal conductivity models that exhibit approximately the same cross-variable correlation with porosity as do the few measured data (Rautman and McKenna 1997, p. 113). It is anticipated that such a geostatistical modeling of thermal conductivity, based on laboratory data from intact rock, may be used in numerical programs to effectively simulate the rock mass thermal conductivity behavior. There may be some uncertainties in scaling thermal conductivity data from small, intact, rock sample testing to the repository or rock mass level.

Results of geostatistical modeling of thermal conductivity and a more complete discussion of the correlation of porosity and thermal conductivity are presented in Section 4.8, in Rautman (1995), and in Rautman and McKenna (1997). Section 4.8 further discusses the control of rock material properties by large-scale geologic processes, the use of porosity as a surrogate for other material properties, the use of empirically observed correlations between selected material properties measured on the same physical specimen, principal sources of rock-properties data used for modeling, and the methodological approach and results of rock properties modeling.

4.7.2 Data

Data from laboratory testing of borehole samples and in situ testing at larger scales were analyzed to determine the geoengineering properties of the site. Testing and analyses were conducted in the context of other site properties. Experimental measurements are thus the

primary source of the geoengineering-properties database. The material presented in this section is a compilation and synthesis of data and information that have been collected under other activities and reported elsewhere. Figure 4.7-1 shows the location of boreholes, the ESF, test alcoves, and the Enhanced Characterization of the Repository Block Cross Drift that were data sources.

4.7.3 Rock Structure

4.7.3.1 Rock Structural Data from Surface Mapping, Underground Mapping, and Geophysical Studies

A description and analysis of rock structural geological data from surface mapping of fractures, detailed line surveys, and underground scanline mapping in the ESF and the Enhanced Characterization of the Repository Block Cross Drift are presented in Section 4.6. Results of pavement studies conducted at surface exposures, outcrop studies, geologic mapping, and fracture data from the ESF, as well as fracture data from boreholes, are included in that section. The data synthesis includes fracture orientation distributions, trace length distributions, fracture intensity for various stratigraphic units, fracture connectivity, and fracture aperture and mineralization. A brief summary is presented here.

The nature of jointed rock masses requires that frequency and characteristics of jointing be assessed, along with in situ stress and intact rock strength. Jointing in the rock mass is often the primary factor controlling excavation stability. Joint and fracture data are incorporated into rock mass classifications systems (discussed in Section 4.7.5.1) to estimate tunnel support requirements. Jointing can also significantly influence penetration rates of mechanical rock excavation equipment. Frequency and orientation of prominent joint sets are considered when estimating tunnel boring machine penetration rates.

Rock mass discontinuities are subdivided into groups according to their origin because the origin of jointing in the project area influences the joint characteristics, such as roughness and planarity.

As discussed in greater detail in Section 4.6.3.3, joints within the Paintbrush Group have been subdivided into early cooling joints, later tectonic joints, and joints due to erosional unloading. Each type of joint exhibits different characteristics that may affect trace length, connectivity, and orientation. Cooling joints and tectonic joints are similar in orientation but differ in surface roughness. Joints due to erosional unloading have a different orientation and tend to be cross joints terminating at preexisting joints (Sweetkind and Williams-Stroud 1996, p. 71).

Cooling joints are identified in every unit that is at least moderately welded (Sweetkind and Williams-Stroud 1996, p. 60). They occur as two nearly orthogonal sets of steeply dipping joints, with a third, subhorizontal joint set that occurs irregularly. Cooling joints are characterized as having low surface roughness, with a Joint Roughness Coefficient less than 5 (Sweetkind and Williams-Stroud 1996, p. 320). Tectonic joints have rougher surfaces (Joint Roughness Coefficient greater than 5) and occur throughout all units of the Paintbrush Group. The predominant strike is also north-south, with less frequent strike trends of northwest and northeast (Sweetkind and Williams-Stroud 1996, p. 52).

Genetic controls on joint set geometry are discussed in detail in Section 4.6.4.2. Joints due to erosional unloading were variably oriented but trended predominantly east-west (Sweetkind and Williams-Stroud 1996, p. 71). Joint orientations appear to be related primarily to lithology, with a lesser association with major structures (Sweetkind and Williams-Stroud 1996, p. 79). The dominant dip of fractures in all lithostratigraphic units was near vertical. This trend was moderated in the undifferentiated overburden (Tmr, Tpki) and the crystal-rich members of the Tiva Canyon Tuff and Topopah Spring Tuff, where fractures with moderate dips were observed (CRWMS M&O 1997d, p. 2-7).

Multiple joint sets are well developed in the Tiva Canyon Tuff (CRWMS M&O 1997d, p. 2-7). All lithostratigraphic units in the Tiva Canyon Tuff exhibit the subhorizontal joint set to some degree, as well as two sets of near-vertical joints. Nonwelded tuff rocks of the undifferentiated overburden and PTn thermal-mechanical units had fewer joints and, generally, only a single north-south trending set (CRWMS M&O 1997d, p. 2-8). Fracture attributes, including orientation, are summarized in Tables 4.6-1 to 4.6-4.

The subhorizontal joint set occurs in the crystal-rich member of the Topopah Spring Tuff, which corresponds with the upper portion of the TSw1 thermal-mechanical unit. However, it was not observed in the upper lithophysal zone (Tptpul) of the TSw1 (Tables 4.5-2 and 4.7-1). Estimated rock quality in Tptpul was distinctly better than the equivalent unit of the Tiva Canyon Tuff (Tpcpul) due to much less frequently recorded joints, as well as fewer joint sets (CRWMS M&O 1997d, p. 2-29; Sweetkind and Williams-Stroud 1996, p. 54, Figure 25).

Multiple joint sets occurred in the TSw2 thermal-mechanical unit, with dominant, near-vertical joints striking north-south and northwest. The subhorizontal joint set also occurs (CRWMS M&O 1997d, p. 2-8).

Analysis of data from the Enhanced Characterization of the Repository Block Cross Drift showed a strong correlation between fracture sets exhibited in the Cross Drift and those exhibited in the ESF (Mongano et al. 1999, p. 110).

General information on fracture intensity and apparent connectivity indicates that the highest joint frequencies and connectivities occur in the nonlithophysal units of the Tiva Canyon and Topopah Spring tuffs (Sweetkind and Williams-Stroud 1996, p. 59) (see also Table 4.6-5 and Section 4.6.6). Nonwelded tuffs of the PTn had the lowest joint frequencies and lowest observed connectivities.

Geophysical studies augmented bedrock geology structural studies and contributed to the understanding of the spatial distribution of the geoengineering properties of the rocks at Yucca Mountain. Surface and borehole geophysical studies conducted from 1979 to 1996 at Yucca Mountain are synthesized and summarized in the report *Synthesis of Borehole and Surface Geophysical Studies at Yucca Mountain, Nevada and Vicinity*. The synthesis report consists of two volumes: *Volume I: Surface Geophysics* (Majer et al. 1996), and *Volume II: Borehole Geophysics* (CRWMS M&O 1996d). The interpretations of geophysical data in the above reports are generally consistent with drilling data and have been incorporated in the latest version of the integrated site model, ISM3.1 (CRWMS M&O 2000g).

In general, the geophysical results indicate that the potential repository at Yucca Mountain is in tuffs that vary in physical properties (Majer et al. 1996). In addressing the spatial distribution of porosity (fracture porosity and matrix porosity) over the potential repository volume, the geophysical model indicates that welding, lithophysal character and content, porosity, and mineralogy vary over scales of tens of meters. The geophysical model is not able to discriminate variation in porosity caused by fracturing from large scale changes in matrix properties. However, in cases where there is good surface evidence for faulting, it appears that faulting and fracturing are the main causes for the variability in the geophysical data. The general results imply that the subsurface rock is heterogeneous and complex at a rather small scale (Majer et al. 1996).

The geophysical synthesis reports also address the amount, type, depth, and continuity of faulting in the potential repository volume. Vertical seismic profile, surface seismic surveys at four different scales, gravity and magnetic surveys, and magnetotelluric methods were all applied in the Yucca Mountain region. It was concluded that the faulting is a classic example of steeply dipping Basin and Range extensional faulting, with cross faults intersecting the normal faulting. There is abundant evidence of multiple, subparallel fracture zones or faults associated with better developed mapped faults. Surface and borehole velocity studies across Yucca Mountain indicated that, in addition to local heterogeneity, there is a general trend of increasing seismic velocity to the south, implying increasing porosity to the north (Majer et al. 1996).

4.7.3.2 Rock Structural Data from Boreholes

Rock structure data presented here were developed primarily from boreholes UE-25 NRG-1, NRG-2, NRG-2A, NRG-3, NRG-4, NRG-5, USW NRG-6, and NRG-7/7A. The Tptpmn was also described by boreholes USW SD-7, SD-9, SD-12, and UZ-14. Borehole locations are shown on Figure 4.7-1. A detailed description of the structural core logging process is presented in Brechtel et al. (1995, pp. 3-6 to 3-11).

Structural data developed from the core included core recovery, locations of fractures and vugs, fracture characteristics, hardness, weathering, rock quality designation (RQD), and lithophysal and other voids. Lithologic and structural data were presented, together with lithologic and stratigraphic units, in geology and rock structure logs. Rock structural data for each hole were also summarized in the rock structural data summary log. In this log, data concerning rock weathering, rock hardness, and fracture characteristics were summarized in 3-m (10-ft) intervals and correlated with both lithostratigraphic units and thermal-mechanical units. Variations in RQD were also graphically displayed (Brechtel et al. 1995, Appendices A to J; Kicker et al. 1997, Appendix C).

4.7.3.2.1 Core Recovery

Core recovery can be used as a general indicator of relative rock quality. Data from borehole studies indicate that rock quality calculated from core data was relatively low for all stratigraphic units. Substantial amounts of core in all lithostratigraphic units were either lost or recovered as rubble. Combining data from each of the boreholes, the amount of lost core for the Tptpmn lithostratigraphic unit was 15 percent of the total core length, as summarized in the recovery data presented in Table 4.7-2. Rubble zones accounted for 20 percent of the total length.

Figure 4.7-6 presents a series of pie charts showing core recovery, lost core, and rubble zones as a percentage of total drilling in the various thermal-mechanical units. Total lost core and rubble ranged from 28.4 percent in the TCw to 49.2 percent in the TSw2 (Brechtel et al. 1995, Table 5-1). In the lithophysae-rich portions of TCw and TSw1, the proportion of lost core and rubble zones was 32.6 percent and 51.2 percent, respectively.

The amount of lost core and rubble can also be a general indicator of the quality of the drilling technique. To limit the introduction of water and chemical additives that are typically used in core drilling, a modified method with dry, compressed air as the circulating medium was used. The effect of this dry drilling technique on the proportion of lost core and rubble was assessed by Brechtel et al. (1995, p. 5-3), who concluded that the amount of lost core and rubble was due to the fractured nature of the welded tuffs and the presence of lithophysal voids, and not due to the drilling technique.

The high proportion of lost core and rubble is attributed to the degree of small-scale fracturing of the welded rocks and the presence of other inhomogeneities, such as lithophysae and vapor-phase alteration. Fracturing also may have been induced along a subhorizontal fabric or foliation by drilling. These inhomogeneities had a large influence on core recovery and core quality, but have much less significance at the tunnel scale. Lost core and rubble zones did, however, limit core description in places where individual features could not be reconstructed.

4.7.3.2.2 Rock Quality Designation

While core recovery is related to the quality of rock encountered in a boring, it also is influenced to some degree by the drilling technique and type and size of core barrel used. The rock quality designation (RQD) (Deere 1968, p. 15) is a recovery ratio that provides an alternative estimate of in situ rock quality. This ratio is determined by considering only pieces of core that are at least 100 mm (4 in.) long. The ratio between the total length of such core recovered and the length of core drilled on a given run, expressed as a percentage, is the RQD, as follows (Deere 1968, p.15):

$$\mathrm{RQD}(\%) = \frac{\sum \text{Piece lengths} \geq 100\ \text{mm}\ (4\ \text{in.})}{\text{Interval length}} \times 100 \qquad \text{(Eq. 4.7-1)}$$

This index has been widely used as a general indicator of rock mass quality and is an input for rock mass classification systems, such as rock mass rating (RMR), and rock mass quality (Q), discussed below. Rock mass rating (RMR) and rock mass quality (Q) are indices that consider characteristics of the rock mass, such as the degree of jointing, strength, and groundwater condition, to classify the rock mass according to rock quality.

The RQD used for geotechnical design considered all breaks in the core, including those identified by geological and geotechnical staff as drilling-induced and those indeterminate as to their natural or drilling-induced origin. Differentiation among types of breaks was difficult because of the general absence of mineralization along fractures and the existence of a subhorizontal fabric similar to foliation in some of the tuff rocks. The resulting RQD, used for subsequent estimations of rock mass quality, is thus considered conservative because it indicates lower rock quality than if only natural fractures had been considered. Attempts were made to

filter the effects of drilling-induced fracturing. A parameter called enhanced RQD was calculated (Brechtel et al. 1995, pp. 5-5 to 5-9; Kicker et al. 1997, pp. 4-3 to 4-5), in which the fractures judged to be drilling-induced were disregarded, resulting in greater piece lengths. Enhanced RQD values were 1.5 to 2.2 times higher than RQD designations, which considered all fractures. However, because of the uncertainty in fracture classification and because of the large proportion of lost core and rubble, the more conservative RQD was used for rock mass quality estimations.

RQD data are presented graphically on Figure 4.7-7. RQD is generally not high in any unit because of the relatively low recovery of intact core, the high frequency of core fractures, and the inclusion of drilling-induced mechanical breaks as fractures. Using the relative rock quality descriptions based on RQD developed by Deere (1968, pp. 15 to 16), rock quality of core in the Tptpmn stratigraphic zone of the TSw2 thermal-mechanical unit ranges from poor to very poor among the boreholes evaluated. Within the Tptpmn are two intervals of generally higher RQD bounding a lower RQD interval defined by the lithophysal subzone of the Tptpmn lithostratigraphic unit. The portion of the TSw2 unit cut by the Main Drift is characterized by very low RQDs, and these low values are consistent from hole to hole. Based on RQD values, core from the TCw and PTn thermal-mechanical units are classified as poor quality rock, and core from the TSw1 is classified as very poor quality rock (Brechtel et al. 1995, p. 5-6). Locally, however, the nonlithophysal portion of the TSw1 was of higher quality and is classified as poor, instead of very poor rock.

Based on the minimal tunnel support that was required in the ESF, rock quality is much higher from an engineering standpoint than indicated by the low, borehole-data-based RQD. This is because of the inclusion of mechanical- and drilling-induced fractures, along with natural fractures, for RQD calculation, the apparent natural tendency of the lithophysal zones to produce rubble zones at the core scale that do not significantly affect stability at the tunnel scale, and the use of dry drilling in fairly brittle rocks, which may have produced more fracturing than would have been the case with mud drilling. Because the recovered core was highly fractured, it was difficult to separate features that represented continuous joints from smaller-scale incipient cracks and inhomogeneities in the rock (CRWMS M&O 1997d, p. 4-25).

Rock-mass properties are discussed in Section 4.7.5. Enhanced RQD, as assessed at the tunnel scale, was much higher than borehole enhanced RQD (discussed in greater detail in Section 4.7.5). This is, in part, because the borehole enhanced RQD values were artificially low for the reasons listed above, and also because the core data included smaller scale fractures that were not counted at the tunnel scale. Tunnel scanline enhanced RQD assessments were made by considering only joints and fractures longer than approximately 30 cm (1 ft), unless their apertures were over 3 mm (0.1 in.) (TP-234 Rev 02, *Conducting Rock Mass Quality Assessment*). Borehole-data-based RQD assessments included all fractures longer than the core diameter.

4.7.3.2.3 Rock Weathering

Qualitative rock weathering descriptors were applied to describe the average condition of the core in each core-run interval. These standard descriptors, based on recommendations of the ISRM (1981, pp. 85 to 110), are listed in Table 4.7-3. The data are presented graphically, by thermal-mechanical unit, on Figure 4.7-8.

All rock from the Tptpmn in the TSw2 unit was either fresh or slightly weathered, constituting 51 and 49 percent, respectively, of the total recovered core (Kicker et al. 1997, p. 4-5). A fairly high percentage of the core recovered from other welded tuff units, TCw and TSw1, was also fresh or slightly weathered, constituting approximately 60 to 70 percent. About 20 percent of the core length in the PTn unit was moderately weathered (Brechtel et al. 1995, p. 5-10).

4.7.3.2.4 Rock Hardness

Rock hardness is a general descriptor of the strength of the rock material. Estimated rock hardness for recovered core was determined following the procedures in Sandia National Laboratories Technical Procedure TP-233, *Geotechnical Logging of Core by Examination of Core and Video Records.* The estimated hardness classification ratings used are listed in Table 4.7-4. Hardness data are presented graphically for each thermal-mechanical unit on Figure 4.7-9. Quantitative hardness measurements on selected samples using Schmidt hammer tests are described in Section 4.7.4.3.8.

Rock in the Tptpmn of the TSw2 was generally classified from core logging as almost entirely hard (79 percent) to very hard (16 percent) (Kicker et al. 1997, Figure 4-6). Most of the rock in the other welded tuff units was estimated to be classified as very hard, hard, or moderately hard, with the highest percentage in the hard category (Brechtel et al. 1995, p. 5-12). The nonwelded rock of the PTn unit was much softer than the welded tuffs, and approximately half of the core in this unit was estimated to be in the soft or very soft category (Brechtel et al. 1995, p. 5-12).

4.7.3.2.5 Fracture Data

A detailed description of the procedure for logging fracture characteristics in core is presented in Brechtel et al. (1995, pp. 5-15 to 5-27). Complete data are presented in CRWMS M&O (1997d), Brechtel et al. (1995), and Kicker et al. (1997). Fractures judged to have been induced by drilling generally were oriented normal to the core axis and are believed to have probably formed along subhorizontal planes of incipient weakness (Brechtel et al. 1995, p. 2-10). These fractures accounted for 40 to 70 percent of the total fractures, depending on the thermal-mechanical unit (Brechtel et al. 1995, p. 2-10; Kicker et al. 1997, p. 4-10). Only natural fractures and those indeterminate as to natural or drilling-induced origin were included in evaluations of fracture inclination, frequency, infillings, and roughness. Fractures judged to be drilling-induced were excluded (Brechtel et al. 1995, p. 5-16).

Because of testing requirements that the borehole walls be kept dry and clear (i.e., protected from water and mudcake contamination), high-velocity, dry, compressed air was used as the drilling fluid (instead of mud) for core drilling. The effect of this drilling technique on fracturing in the core was difficult to establish because of limited data available for comparison (Brechtel et al. 1995, p. 5-2). As discussed in Section 4.7.3.2.1, Brechtel et al. (1995, p. 5-3) concluded that the amount of lost core and rubble was not because of the dry-drilling technique, but because of the fractured nature of the welded units and the presence of lithophysal voids. It is possible, however, that because of the brittle nature of these volcanic rocks, dry drilling may have caused more fracturing than mud drilling may have caused.

When fracture frequencies were corrected for sampling bias because of the relative orientation of the borehole with respect to the fractures, the near-vertical fractures were most numerous. This agreed well with surface mapping observations (Brechtel et al. 1995, p. 5-21).

Most fractures were clean, and fracture infillings, when observed, were rated as either thin or just surface sheen. Most frequent infilling materials were identified as white crystalline, white noncrystalline, or black dendritic minerals. Thick infillings have been observed in the ESF excavation but were not sampled effectively by drilling, possibly because of the high-velocity compressed air used as the circulation medium (Kicker et al. 1997, p. 4-12).

Additional information on fracture mineralization and aperture is presented in Section 4.6.3 and in CRWMS M&O (1997d, pp. 4-37 to 4-40).

Fracture surfaces in core samples were classified predominantly as having an irregular shape. The second most frequent fracture surface characteristic was planar. Most fracture surfaces were rated as moderately rough.

4.7.3.3 Potential Key Blocks in Underground Excavations

Key blocks are rock wedges, formed by the intersection of geologic discontinuities and an excavation surface, that are kinematically able to move into the excavation. Key-block analyses were performed to verify that ground support being installed in the ESF was adequate (Kicker et al. 1997, pp. 5-11 to 5-14, Appendix D). Analyses were done before excavation of the ESF Main Drift to compare the size of potential key blocks that might occur in the North Ramp to the size of blocks projected for the Main Drift alignment, assuming that the joint sets encountered in the North Ramp also would be encountered in the Main Drift. In addition, analyses of a 100-m (328-ft) section of the North Ramp were performed to assess the importance of the subhorizontal vapor-phase parting structure that occurs periodically in the welded units.

A key-block stability analysis software program was used to rapidly estimate maximum key-block sizes. The maximum potential key-block size is the volume of the largest key block that could potentially form, given an existing excavation configuration and a particular combination of joint-set orientations. Software used to carry out the analysis is discussed in Kicker et al. (1997, Appendix D). Specific individual joints cannot be positioned in specific locations. The analysis is nonprobabilistic, but determines the maximum potential block types and volumes based on the provided joint-set data. The software analyzes no more than three joint sets at a time. Input parameters include joint-set orientation, joint spacing, cohesion and friction angle of each joint set, and rock unit weight.

The comparative analysis of the potential key blocks in the North Ramp and the Main Drift suggested that, given similar rock mass conditions, the Main Drift would have a higher frequency of key blocks because of the orientation of joints relative to the tunnel alignment.

A second analysis was performed to predict the maximum potential size key block that could form, based on joint sets observed between Stations 12+00 and 13+00 in the ESF. Although the subhorizontal joints in this interval could have had a negative impact on tunnel stability, most key blocks that were analytically predicted could be supported by the rockbolt support system being installed. Two potential key blocks were large enough to exceed the capacity of the

rockbolt support system. However, no key blocks of this size were observed in the interval. The key-block analysis must be considered conservative because of its inherent assumptions. Observations in the constructed ESF indicate that the installed supports are adequate, and no failures of significant rock wedges have been reported.

Additional key-block analyses were performed as part of a study to analyze the deterioration of the rock mass surrounding the potential repository emplacement drifts (CRWMS M&O 2000e). A statistical description of the probable block sizes formed by fractures around the emplacement drifts was developed for each of the lithologic units of the repository host horizon. The change in drift profile resulting from progressive deterioration of the emplacement drifts was assessed both with and without backfill. Drift profiles were determined for four different time increments and three seismic levels (CRWMS M&O 2000e, p. 63).

This drift degradation analysis indicated that the seismic effect on rock fall size distribution for 1,000-, 2,000- and 5,000-yr. events is relatively minor (CRWMS M&O 2000e, p. 63). The analysis also indicated that thermal and time-dependent effects causing a reduction of joint cohesion have a minor impact on rock fall. This is based on joint cohesion being conservatively reduced from a laboratory value of 0.86 MPa to a value of 0.01 MPa after 10,000 yr. (CRWMS M&O 2000e, p. 63). Based on analysis of worst-case degradation profiles, most emplacement drift openings would not be affected by rock fall. The highest percentage of drift affected by rock fall was 16 percent in the Tptpmn unit. The Tptpmn unit also produced the largest volume of key blocks per kilometer (CRWMS M&O 2000e, p. 63). A realignment of emplacement drifts to an azimuth of approximately 75° could potentially reduce the maximum possible rock block (CRWMS M&O 2000e, p. 63).

4.7.4 Laboratory Properties of Intact Rock

4.7.4.1 Physical Properties

Bulk and physical property measurements were performed on specimens of tuff prepared from cores recovered from NRG and SD boreholes. Additional measurements were performed on samples from the Single Heater Test block and the Drift Scale Test block of the Thermal Test Facility of the ESF. The data collected include density, porosity, and mineralogy.

4.7.4.1.1 Density and Porosity

Density, a physical property defined as mass per unit volume at a specific temperature, can vary substantially within a rock mass because of variations in mineralogy, porosity, and welding. Average grain density is controlled by the rock composition, and variations in average grain density are attributable to variations in mineralogy and petrography. Porosity is a measure of the volume of voids in a solid material such as rock. It can be calculated from the relationship of average grain density and dry bulk density and also from the relationship of saturated bulk density and dry bulk density. Effective elastic constants, rock fracture, and rock rheological behavior are controlled, in large part, by the size, shape, and distribution of pores throughout the rock.

Measurements of dry bulk density, saturated bulk density, and average grain density were performed on laboratory test specimens of tuff prepared from cores recovered from NRG boreholes. Dry bulk density represents the mass measured in a dry condition, divided by the volumetric measurement of the external dimensions of a test specimen. The Sandia National Laboratories procedure TP-229, *Bulk Properties Determinations of Tuffaceous Rocks: Dry Bulk Density, Saturated Bulk Density, Average Grain Density and Porosity,* adhered to the American Society for Testing and Materials standards ASTM D 854-92, *Standard Test Method for Specific Gravity of Soils,* and ASTM C 135-86, *Standard Test Method for True Specific Gravity of Refractory Materials by Water Immersion,* with one exception. Test specimens recovered from the NRG boreholes were dried before testing to a constant weight at 110°C (230°F) and the dry bulk density was determined. The 110°C (230°F) heating temperature is slightly higher than the American Society for Testing and Materials recommended temperature. The Sandia procedure was developed to consider duration of drying cycle and maximum acceptable change in sample mass for successive cycles (Boyd et al. 1994, p. 2). The 110°C (230°F) temperature was found to satisfy the need to dry the samples to a consistent level without removing substantial amounts of water associated with the zeolite mineral structures and to evaluate grain density results on a common basis. Because excessive temperatures may damage the specimen because of differential thermal expansion along grain boundaries, a series of thermal diagnostic tests was conducted as part of this study. The tests showed that drying welded tuff specimens at 110°C (230°F) produced no noticeable damage. This was demonstrated by measuring the compressional and shear-wave velocities before and after heating welded tuff specimens. If microcracks had developed, the velocity would have decreased. The thermal cycling produced no reduction in velocity, indicating that no thermally induced microcracking had occurred.

Once the dry bulk density was measured, each specimen was saturated with distilled water. A two-stage process was used for the saturation. The specimen was first pressure-saturated at 10 MPa (1,450.4 psi) for a minimum of 1 hr., followed by a minimum of two vacuum-saturation cycles. Once the mass change for successive cycles had stabilized to within ± 0.05 percent, the saturated bulk density was computed (Boyd et al. 1994, p. 31; CRWMS M&O 1997d, p. 5-3).

The average grain density was measured using the pycnometry method. This technique consists of a two-stage measurement. First, the mass of a dry, powdered specimen was measured. Next, the powder volume was determined. These two measurements were combined to compute the average grain density. Detailed procedures for the measurement are presented in Boyd et al. (1994). Total porosity, ϕ_T, was computed from the grain density, ρ_g, and the dry-bulk density, ρ_{db}, using the expression (Boyd et al. 1996b, pp. 10, 12):

$$\phi_T = \frac{\rho_g - \rho_{db}}{\rho_g} \qquad \text{(Eq. 4.7-2)}$$

Dry bulk and saturated bulk densities, average grain density, and calculated porosity for specimens from the NRG boreholes are presented in CRWMS M&O (1997d, Section 5.1.1), Martin et al. (1994), Boyd et al. (1996a, 1996b), and Martin et al. (1995, Tables 1 to 4, pp. 28 to 39). The data are summarized by thermal-mechanical unit in Tables 4.7-5 to 4.7-8. As shown, nonwelded rocks of the undifferentiated overburden and PTn units have significantly lower bulk density and higher porosity than rocks of welded units TCw, TSw1, and TSw2. Because of the

relatively uniform composition of the tuffs, average grain density shows only small variability among different rock units. Mean dry bulk density was 1.28 g/cm^3 (79.9 lb./ft^3) in both the nonwelded units undifferentiated overburden and PTn. Mean dry bulk density in the other welded units was substantially higher and ranged from 2.12 to 2.35 g/cm^3 (132.35 to 146.71 lb./ft^3).

As part of the preheating ambient characterization of hydrologic properties, density and porosity measurements were also performed on cores from wet-drilled and dry-drilled underground boreholes in the Single Heater Test block and the Drift Scale Test block of the ESF. Grab samples from the Observation Drift of the Drift Scale Test were also tested. All tested samples were from the TSw2 thermal-mechanical unit. Complete results and procedures are discussed in CRWMS M&O (1996b, pp. 5-1 to 5-2; 1997g, pp. 5-1 to 5-11). Results are summarized in Table 4.7-9 and are generally consistent with TSw2 results from surface-based boreholes. As shown, mean bulk density ranged from 2.20 to 2.26 g/cm^3 (137.34 to 141.09 lb./ft^3), mean particle density (or grain density) ranged from 2.49 to 2.51 g/cm^3 (155.45 to 156.69 lb./ft^3), and mean porosity ranged from 9.3 to 12.5 percent.

Porosity, bulk density, and particle density were measured in additional core samples from drill holes SD-7, SD-9, and SD-12 in support of hydrologic measurements. Samples were collected at a nominal 3-ft (0.9-m), regularly spaced sampling interval on core from these boreholes. Results from SD-7, SD-9, and SD-12 are presented in Rautman and Engstrom (1996a, pp. 41 to 159), Engstrom and Rautman (1996, pp. 108 to 126), and Rautman and Engstrom (1996b, pp. 118 to 130), respectively.

L. Flint (1998, Table 1, pp. 3 to 4) used measurements of physical and hydrologic properties of the rock matrix, including porosity, bulk density, particle density, volumetric water content, saturated hydraulic conductivity, and moisture retention characteristics to divide the unsaturated zone at the site into 30 hydrogeologic subunits. The study analyzed 4,892 core samples obtained from 23 shallow and 8 deep boreholes. Procedures and results are discussed in Section 8.3 and L. Flint (1998).

4.7.4.1.2 Mineralogy

The mineralogy and petrography of the volcanic rocks at Yucca Mountain have been described extensively in studies of both drill core and outcrop samples (see Sections 5.2 and 4.5 for a summary). Mineralogy and petrography affect thermal and mechanical geoengineering properties and thus help characterize the rock mass at the site and predict performance. These properties have been modeled as discussed in Section 4.8.3 (Rock Properties Model). Because heat will be generated by the waste packages, heat transfer properties (e.g., thermal conductivity and thermal heat capacity) need to be understood so that repository performance can be assessed. Because thermal properties are largely a function of mineralogy, an understanding of these properties requires that mineralogy be determined. A three-dimensional mineralogic model for the site is discussed in Section 4.8.4.

The minerals that could affect the rock's thermal-mechanical behavior at elevated temperatures are of particular interest. These minerals include cristobalite, which undergoes a phase transition and volume change at elevated temperatures, and smectite and zeolites, which dehydrate at

elevated temperatures, with accompanying volume reduction. Other mineralogical effects associated with temperature changes include the dissolution and precipitation of silica and the dehydration of volcanic glass. All these effects, in turn, affect the thermal-mechanical properties of the rock mass. The purpose of mineralogical and petrographic analyses was to evaluate correlations between the thermal-mechanical behavior of rock samples and their mineralogical components and texture. Correlations are discussed in Section 4.7.4.2. Mineralogy and petrography are also used as input for modeling heat-induced changes during in situ thermal testing in the ESF.

In brief, both the Tiva Canyon Tuff and the Topopah Spring Tuff are zoned, ash-flow tuffs, with crystal-poor rhyolitic units at the base and crystal-rich quartz latite units at the top. Both units have devitrification, welding zones, and secondary crystallization imposed on their primary features (Section 4.5).

A suite of 97 samples from borehole NRG-6 was studied to understand the mineralogy and petrography of samples tested for thermal expansion, thermal conductivity, and mechanical properties (CRWMS M&O 1997d, p. 5-39). Borehole NRG-6 provides a relatively complete stratigraphic section from the lower part of the Tiva Canyon Tuff through most of the lower lithophysal zone of the Topopah Spring Tuff of the Paintbrush Group (Tables 4.5-2 and 4.7-1). Depths ranged from 6.77 to 330.7 m (22.2 to 1,085.0 ft). The data and procedures are summarized below.

Laboratory testing of mineralogy also was performed for the Single Heater Test and the Drift Scale Test of the Thermal Test Facility of the ESF to relate mineralogy to coupled thermal, mechanical, chemical, and hydrological processes. Analyses were performed for 10 samples from the Single Heater Test region of the Thermal Test Facility. The analyses used the matrix flushing method of Chung (1974, pp. 519 to 525) and an internal intensity standard (corundum) to quantify the phases present.

Mineral abundances were also determined for 17 samples from the Drift Scale Test block of the Thermal Test Facility of the ESF using the Rietveld method of whole X-ray pattern fitting (Snyder and Bish 1989, pp. 129 to 138; Young 1993, pp. 1 to 38). Complete procedures and results are described in Roberts and Viani (1997a, pp. 1 to 6) and CRWMS M&O (1997g, pp. 6-1 to 6-4). The method appears to yield better precision than the matrix flushing method of Chung (1974, pp. 519 to 525) used for Single Heater Test samples.

Petrographic and mineralogical data from borehole NRG-6 were obtained by an examination of all 97 core samples. Table 4.7-10 shows the summary petrographic characterization of NRG-6 specimens. More detailed mineralogical and chemical analyses were performed for selected samples using different laboratory analytical methods, including optical microscopy of thin sections with modal-point counts of identified constituents to determine composition, X-ray diffraction analysis of prepared powders to identify and estimate proportions of finely crystalline minerals, and whole-rock chemical analysis to determine the chemical composition and water content of samples (CRWMS M&O 1997d, p. 5-39).

The most obvious physical divisions are between welded and nonwelded tuff. These divisions are reflected in the variation in thermal properties discussed in Section 4.7.4.2. Invariably, in the

samples from NRG-6, the welded intervals show significant compaction, resulting in the destruction of primary porosity. With few exceptions and above the water table, the nonwelded intervals retain their primary glassy or vitric character and retain significant porosity. These intervals rarely correspond to stratigraphic rock unit boundaries because the upper and lower layers of eruptive units (on which the stratigraphic units are defined) are typically nonwelded, while the interiors of the units are welded (CRWMS M&O 1997d, p. 5-44).

Minerals identified from X-ray powder diffraction on 23 devitrified samples from NRG-6 included the silica phases (cristobalite, quartz, tridymite), feldspar (plagioclase and Na- and K-rich alkali feldspar), and a clay mineral (primarily illite). Other minerals were noted in thin sections but were not identifiable by X-ray diffraction because of their scarcity. These include small amounts of quartz present as phenocrysts, biotite, amphibole, and iron-titanium oxides (CRWMS M&O 1997d, p. 5-44).

As shown in Table 4.7-10, cristobalite is present in virtually all devitrified samples and is the dominant silica phase in most samples. Quartz is absent in all samples shallower than 139.8 m (458.7 ft) and appears abundantly only below 197.7 m (648.6 ft). Tridymite is intermittently present in samples at 129.6 m (425.3 ft) or less (in depth), and was not identified in any quartz-bearing samples. Clay (illite) is identified in many, but not all, samples in the same interval from which tridymite was identified. It also was noted that silica phase variations tend to cross the lithostratigraphic boundaries defined by Geslin et al. (1995, pp. 33 to 35) in their lithostratigraphic classification of rocks from borehole NRG-6. However, in general, the lithostratigraphic classifications (Geslin et al. 1995, pp. 33 to 35) are consistent with the mineralogical data presented in Table 4.7-10.

Results of laboratory testing (CRWMS M&O 1996b, pp. 6-1 to 6-5) of mineral abundances for samples from the Single Heater Test region of the Thermal Test Facility are presented in Table 4.7-11. Quartz and cristobalite average about 8 and 19 percent of the samples, respectively. Smectite was found in all the samples, but was generally present at less than 3 percent. The greatest variability was shown in the abundances of albite and sanidine. Clinoptilolite was present in small amounts in three of the samples. Because the method used to estimate mineral abundances is not normalized to 100 percent, the total mineral abundances do not sum to 100 percent. The average of the total is 96 ± 4 percent. This low value suggests that an unidentified phase may be present. The observed mineralogy is consistent with previous measurements of mineral abundances in core samples of Topopah Spring devitrified tuff (CRWMS M&O 1996b, p. 6-4).

Results of laboratory testing (CRWMS M&O 1997g, pp. 6-1 to 6-4) of mineral abundances for samples from the Drift Scale Test block are summarized in Table 4.7-12. All samples were from the TSw2 thermal-mechanical unit. The total abundance of the silica polymorphs is fairly uniform, although the cristobalite component varies from 4 to 31 percent, suggesting potential variability in thermal-mechanical properties at the temperatures at which cristobalite undergoes a phase change. In most samples, albite, sanidine, and cristobalite are the dominant phases, with lesser amounts of quartz. Tridymite is significant in three samples, with cristobalite being less abundant in these samples. Zeolite phases were observed in three samples, clinoptilolite in two samples, and stilbite in one sample. Compared to the analyses of samples from the Single Heater Test block (Roberts and Viani 1997b; Viani and Roberts 1996), the Drift Scale Test samples

show similar total silica polymorph content (between 33 and 41 percent). The quartz and cristobalite contents appear to be inversely related. No samples contained detectable mica phases.

Mineral hardness or abrasivity is commonly used to predict rates of tunnel boring machine cutter wear (CRWMS M&O 1997d, p. 5-45). Measurements of rock abrasivity, such as the Cerchar Abrasivity Test, have not been performed on YMP rock samples, but abrasivity can be inferred from mineral composition (CRWMS M&O 1997d, p. 5-45). The tunnel boring machine disc-cutter steel has a hardness of approximately 6.5 on the Mohs scale of hardness. Rock with a large percentage of minerals of hardness equal to or exceeding 6.5 would produce faster cutter wear than rock with a smaller percentage of hard minerals. The percentage of quartz, with a Mohs hardness of 7, is typically used for cutter wear prediction. Generally, a quartz content less than 20 percent would indicate low cutter wear, between 20 and 50 percent would indicate significant cutter wear, and greater than 50 percent would indicate high cutter wear. As shown in Tables 4.7-10, 4.7-11, and 4.7.12, the estimated combined percentage of quartz, cristobalite, and tridymite (which also have a hardness of 7) was typically between about 15 and 30 percent for borehole NRG-6 and the Single Heater Test samples and between 33 and 40 percent for the Drift Scale Test samples. Tables 4.7-10, 4.7-11, and 4.7-12 also include percentages of other hard minerals that could affect cutter wear: the feldspars, which have a Mohs hardness of 6, and the mafic minerals, which may not be encountered in significant quantities, but can have Mohs hardness near 6.5.

4.7.4.2 Thermal Properties

Data on the thermal properties of rock consist of thermal conductivity, thermal expansion, and heat capacity.

4.7.4.2.1 Thermal Conductivity

Thermal conductivity is a measure of a material's ability to transmit heat, and so relates to the ability of the host rock to conduct heat away from waste containers. Thus, thermal conductivity is an important parameter for numerically simulating the transient temperature field from heat generated by emplaced radioactive waste.

Characterization of the thermal conductivities of Yucca Mountain tuffs has been ongoing since 1980 (Lappin 1980). Data published through 1988 were reviewed by Nimick (1989), who summarized only data for which supporting documentation was available. These data were from boreholes G-1, G-2, GU-3, and G-4. The reports summarized in Nimick (1989) include Lappin et al. (1982, pp. 3 to 46), Lappin and Nimick (1985, pp. 1 to 55), Nimick and Lappin (1985, pp. 1 to 46), and Nimick et al. (1988). Nimick (1990b) presented analyses of data for the welded, devitrified portion of the Topopah Spring Tuff (units TSw1 and TSw2); experimental results for the units overlying and including CHn2 are also analyzed in Nimick (1990b). Additional measurements of thermal conductivity were performed on core specimens from Yucca Mountain by Sass et al. (1988, pp. 25 to 30, Appendix 3) using a needle probe technique. However, the uncertainty in moisture contents for these specimens is discussed in Nimick (1990a).

Data presented in this report were for 95 specimens from NRG-4, NRG-5, NRG-6, and NRG-7/7A (Brodsky et al. 1997; CRWMS M&O 1997d). The test method and test results are described and analyzed in detail in Brodsky et al. (1997, pp. 11 to 16, 27 to 35). In addition, as part of the geological and geotechnical characterization of the Single Heater Test region of the ESF Thermal Test Facility, four specimens were tested for thermal conductivity tests in 1996 (CRWMS M&O 1996b, pp. 3-1 to 3-11). Specimens for these tests were from boreholes drilled into the Single Heater Test region to accommodate placement of the heater and additional instrumentation. All specimens from the Single Heater Test region were from the TSw2 thermal-mechanical unit and the Tptpmn lithostratigraphic unit.

Twenty specimens from the Drift Scale Test block, all from the TSw2 thermal-mechanical unit, were also measured for thermal conductivity. Specimens for these tests were from boreholes drilled into the Observation Drift to accommodate instrumentation placement. Results and procedures are described in detail in CRWMS M&O (1997g, pp. 3-1 to 3-9, 3-12).

Test specimens were right-circular cylinders, approximately 12.7 mm (0.5 in.) in length and 50.8 mm (2 in.) in diameter. Moisture contents were either air dried (as received), oven dried, vacuum saturated, or partially saturated (intermediate between air dried and vacuum saturated). Tests were conducted using the guarded heat-flow meter over the temperature range of 30° to 300°C (86° to 572°F). The test specimen was placed between two heater plates controlled at different temperatures, and the heat flow was measured. Radial heat-flow losses were minimized using a cylindrical guard heater. The test procedure is given in TP-202, *Measurement of Thermal Conductivity of Geologic Samples by the Guarded-Heat-Flow-Meter Method.* The applicable American Society for Testing and Materials standard, one which relies on the same type of measurement equipment, is ASTM F 433-77, *Standard Practice for Evaluating Thermal Conductivity of Gasket Materials.* There are no significant differences between the Sandia National Laboratories procedures and the American Society for Testing and Materials procedures.

Variation of thermal conductivity with saturation for the NRG boreholes is illustrated for thermal-mechanical units for low temperatures (less than 100°C [212°F]) in Table 4.7-13. Variations for high temperatures (greater than 100°C [212°F]) are shown in Table 4.7-14. The data were compiled in this manner rather than for each 25°C (77°F) interval because thermal conductivity is not strongly temperature dependent. No data were available for tuff rocks in the undifferentiated overburden unit or for an upper portion of the TCw unit (Tpcrv, Tpcrn, Tpcpul, and Tpcmn). Additional thermal conductivity data from the TSw2 unit (Tptpmn) from the Single Heater Test block is shown in Table 4.7-15. These specimens were tested in the air-dried state (i.e., in the as-received condition). Results are consistent with results from the specimens from NRG boreholes. Thermal conductivity data from the TSw2 unit in the Drift Scale Test block are presented in Table 4.7-16. The specimens were tested in the saturated state, and results are also consistent with specimens from NRG boreholes.

Thermal conductivities are lower for dried specimens and highest for saturated specimens. Thermal conductivities, averaged over all boreholes, ranged, depending on temperature and saturation state, from 1.2 to 1.9 W/(mK) for TCw, from 0.4 to 0.9 W/(mK) for PTn, from 1.0 to 1.7 W/(mK) for TSw1, and from 1.5 to 2.3 W/(mK) for TSw2. The data show distinct differences between the nonwelded tuffs of the PTn and the welded tuffs of the TCw, TSw1, and

TSw2. PTn consistently shows the lowest conductivities, while the TCw and TSw2 units have the highest values. The thermal conductivities of TSw1 specimens are intermediate in value and are distributed over a larger range.

Evaluation of the mean values in Tables 4.7-13, 4.7-14, 4.7-15, and 4.7-16 indicates that thermal conductivity increases with saturation. Temperature, however, does not appear to have a pronounced affect on thermal conductivity. Thermal conductivity generally increased with increasing saturation and temperature. Sharp increases in thermal conductivity are observed near 100°C (212°F) for several oven-dried specimens. These increases are as yet unexplained, but they may be associated with a change in instrumentation at 100°C (212°F) or with the vaporization of remaining water. For ESF Single Heater Test block specimens, thermal conductivity appeared to increase sharply at 70°C (158°F). This response is probably associated with the change in instrumentation at that temperature (CRWMS M&O 1996b, p. 3-10). At temperatures above 100°C (212°F), thermal conductivity shows little temperature dependence. Decreases in conductivity with increasing temperature, observed in saturated specimens, are attributed to dehydration (Brodsky et al. 1997, p. 27).

Comparison of data from NRG-4, NRG-5, NRG-6, and NRG-7, and previous data from USW G-1, USW G-2, USW G-3, and USW G-4 (Nimick 1989) reported by Brodsky et al. (1997, p. 34), indicates that the two sets of data compare very well for TSw1 and TSw2. For PTn data, the values reported by Nimick (1989) are higher, by approximately a factor of two, than those reported in Brodsky et al. (1997, p. 34) and CRWMS M&O (1997d, p. 5-48). However, Nimick's database for PTn consisted of only two tests from hole USW G-2, which is almost 3 km (1.9 mi.) from the nearest NRG borehole.

The effective thermal diffusivity, or thermal conductivity divided by the product of density and specific heat of crushed tuff, was measured in two bench-scale tests (Ryder et al. 1996). The first test ran approximately 502 hours and the second 237 hours. In each test, a cylindrical volume (1.58 m^3 [55.8 ft^3]) was filled with crushed tuff particles, ranging in size from 12.5 to 37.5 mm (0.5 to 1.5 in.), to form an effective porosity of 0.48. Heat was generated by an axial heater. Temperatures near the heater reached 700°C (1,292°F), with a significant volume of material exceeding 100°C (212°F). Thermal diffusivity was estimated post-test, using three different analysis methods. Estimates of thermal diffusivity were 5.0×10^{-7} m^2/s to 6.6×10^{-7} m^2/s, of the same order of magnitude as the thermal diffusivity used for crushed backfill in the total system performance assessment for 1993 (CRWMS M&O 1997d, p. 5-52).

Attempts have been made to correlate thermal conductivity with an easily measured physical property, such as porosity, as discussed in Rautman and McKenna (1997, p. 113). The relationship between thermal conductivity and porosity, saturation, and temperature is discussed in several references. Lappin et al. (1982) documents thermal conductivities of the major silicate phases in tuff and discusses calculation of matrix conductivities from conductivities of components and measured values of porosity and saturation using the Woodside and Messmer (1961, pp. 1688 to 1699) geometric mean approach. A data compilation is presented in Nimick (1989). Nimick (1990a) introduces use of the Brailsford and Major (1964, p. 315) equation for calculating matrix thermal conductivity to replace the geometric mean equation used previously by Lappin et al. (1982), and uses the Brailsford and Major (1964, p. 315) equation for calculation

of matrix porosity. Nimick (1990b) summarizes data for 15 samples of Topopah Spring Tuff and estimates matrix conductivities and in situ thermal conductivities for the TSw1 and TSw2 thermal-mechanical units.

The porosities of samples adjacent to many of the NRG borehole thermal conductivity test specimens (from the same original piece of core) were determined. Both the geometric mean equation and the Brailsford and Major (1964, p. 315) equations were investigated and, based on the measured saturation and porosity of each specimen, the matrix conductivity for each specimen was calculated using each model. These matrix conductivities were then averaged for each model to obtain conductivity at zero porosity. The predicted change in conductivity with increasing porosity was then calculated and plotted for each model, with thermal conductivity approaching that of air as porosity reaches 1.0 (CRWMS M&O 1997d, p. 5-69). The TSw2 data appeared to cluster into three groups: high, low, and intermediate thermal conductivity. Unfortunately, lithologies also change with increasing porosity, so it is difficult to isolate the effects of changing one variable.

Modeling of thermal conductivity for the Topopah Spring welded (TSw) unit is discussed in Section 4.8.3.3.2.

4.7.4.2.2 Thermal Expansion

Thermal expansion is the tendency of a material to undergo a change in volume as a result of a change in temperature. The coefficient of linear thermal expansion is defined as the change in length per degree Celsius, expressed as a fraction of the length at 0°C (32°F). The relationship as presented by Weast (1974, p. F-112) is:

$$l_t = l_0(1 + \alpha T) \qquad \text{(Eq. 4.7-3)}$$

in which

l_0 = length at 0°C (32°F)
l_1 = length at T°C
α = coefficient of linear thermal expansion

Thermal expansion measurements on tuffs are reported in Lappin (1980) for samples from UE-25 a#1, Well J13, and G-tunnel, and in Schwartz and Chocas (1992) for 109 specimens from UE-25 a#1, USW G-1, USW G-2, USW G-4, and USW GU-3. The results of these measurements generally compare well with those of the measurements discussed below. Seventy-eight of the 109 specimens reported by Schwartz and Chocas (1992) were tested unconfined, and 31 were tested at nominally 10 MPa (1,450.4 psi) confining pressure.

Thermal expansion tests were also performed on 120 specimens from NRG-4, NRG-5, NRG-7/7A, and SD-12. The unconfined tests (from NRG boreholes) are reported in Brodsky et al. (1997). Five SD-12 specimens were tested under confined conditions and are reported in Martin et al. (1997). In addition, nine thermal expansion tests were performed in August 1996 as part of the geological and geotechnical characterization of the Single Heater Test part of the ESF

Thermal Test Facility (CRWMS M&O 1996b). Specimens for these tests were from boreholes drilled to accommodate placement of the heater and additional instrumentation. All specimens from the Single Heater Test region were from the TSw2 thermal-mechanical unit and the Tptpmn lithostratigraphic unit. Seventeen TSw2 specimens from the Drift Scale Test block were also tested for thermal expansion as part of the ambient, preheating characterization program (CRWMS M&O 1997g). Because previous work had shown that, for welded tuff, moisture content has no appreciable effect on thermal expansion (Brodsky et al. 1997, p. 36), all specimens were tested in the air-dried state. Measurements were made through two cycles of heating and cooling. Results of in situ determinations of thermal expansion for the Drift Scale Test are discussed in Section 4.7.5.2.

Thermal expansion measurements were made using a push-rod dilatometer. Test specimens were right-circular cylinders, approximately 50.8 mm (2 in.) in length and 25.4 mm (1 in.) in diameter. Moisture contents were either air dried (as received), oven dried, or vacuum saturated. Tests were conducted at ambient pressure over the temperature range of 30°C (86°F) to more than 300°C (572°F). Temperature was ramped at 1°C (33.8°F) per minute. Specimens under saturated conditions were tested up to 100°C (212°F). The test procedure is given in TP-203, *Measurement of Thermal Expansion of Geologic Supplies Using a Push Rod Dilatometer.* The closest applicable American Society for Testing and Materials standard is ASTM E 228-85 (reapproved 1989), *Standard Test Method for Linear Thermal Expansion of Solid Materials with a Vitreous Silica Dilatometer.* This standard describes equipment similar to that used in TP-203. An additional applicable American Society for Testing and Materials standard is ASTM D 4535-85, *Standard Test Methods for Measurement of Thermal Expansion of Rock Using a Dilatometer.* The procedures given in ASTM E 228-85 and TP-203 do not differ significantly.

Temperature and displacement data were obtained throughout a heating and cooling cycle to determine the coefficient of thermal expansion. Coefficients of thermal expansion change with temperature, so calculations were performed over specified temperature intervals. Mean thermal expansion coefficients were calculated over 25°C (77°F) intervals from data obtained at the endpoints of the interval. Instantaneous coefficients of thermal expansion were calculated from linear least-square fits to data contained within 5°C (41°F) windows spaced 25°C (77°F) apart. The instantaneous coefficient of thermal expansion data are given in Brodsky et al. (1997, pp. 39 to 40, B-23 to B-42, Appendix E).

Mean coefficients of thermal expansion from surface-based borehole specimens are presented by thermal-mechanical unit and saturation in Table 4.7-17 for heating phases and in Table 4.7-18 for cooling phases. Thermal expansion data exist for the TCw, PTn, TSw1, and TSw2 thermal-mechanical units. The mean thermal expansion coefficient does show some borehole-to-borehole variation, which is obscured by the data averaging in these tables. Complete data are presented in Brodsky et al. (1997, Appendices B, E). The mean thermal expansion coefficient was highly temperature dependent and ranged, depending on temperature and saturation state, from 6.6×10^{-6}/°C to 50×10^{-6}/°C for TCw; from negative values to 16×10^{-6}/°C for PTn; from 6.3×10^{-6}/°C to 44×10^{-6}/°C for TSw1; and from 6.7×10^{-6}/°C to 37×10^{-6}/°C for TSw2. Data also are summarized by thermal-mechanical unit and are plotted as a dimensionless ratio versus temperature in CRWMS M&O (1997d, p. 5-61) and in Brodsky et al. (1997, p. 35-46, Appendix E).

Additional data for TSw2 thermal-mechanical unit (Tptpmn) samples from the Single Heater Test region of the ESF Thermal Test Facility are presented in Table 4.7-19. The mean thermal expansion coefficients for these samples ranged from 7.5×10^{-6} to 52×10^{-6}/°C and, as shown, were temperature dependent during the heating cycle. Complete data and analysis are presented in CRWMS M&O (1996b, pp. 3-10 to 3-17, Appendix A).

Statistical summaries for mean coefficients of thermal expansion for specimens from the Drift Scale Test block are given in Table 4.7-20 for two cycles of heating and cooling. Complete data and analysis are presented in CRWMS M&O (1997g, pp. 3-12 to 3-27, Appendices A, B). Single Heater Test and Drift Scale Test values are generally consistent. There is more variability in the Drift Scale Test data, but that study included a much larger sampling volume. Drift Scale Test mean values are consistently higher than those for the Single Heater Test and are generally higher during cooling. However, the mean Single Heater Test values are typically within one standard deviation of the mean Drift Scale Test values.

The data presented in Tables 4.7-17 to 4.7-20 indicate that at a transition temperature of 150° to 200°C (302° to 392°F) the mean thermal expansion coefficient increases more steeply for the welded tuff (TCw, TSw1, TSw2) but decreases for the nonwelded tuff (PTn). A transition is expected in the welded devitrified specimens because of phase changes in tridymite and cristobalite. These minerals occur, with or without quartz, as primary devitrification products in many samples of Yucca Mountain welded tuffs. Phase transitions in synthetic tridymite occur at approximately 117° and 163°C (242.6° to 325.4°F), and in synthetic cristobalite at approximately 272°C (521.6°F) (Papike and Cameron 1976, p. 64 to 65) and involve notable changes in volume. Phase transition temperatures have been shown to vary significantly due to lattice variations found in natural occurrences of these minerals, which are usually mixed phase material (Thompson and Wennemer 1979). Previous and current work on the mineralogy of welded tuff from TCw, TSw1, TSw2, and TSw3 suggests that these mixed phase assemblages are dominant. Hysteresis is associated with the phase changes because the phases invert at higher temperature during heating than during cooling (Brodsky et al. 1997, p. 41).

Some specimens that displayed sensitivity to transition temperature were analyzed to assess the role of the maximum test temperature. Specimens from approximately the same depth and same borehole were tested to different temperatures. The results showed that as long as the maximum test temperature remained below the transition temperature, the specimens did not permanently change dimension (Brodsky et al. 1997, p. 44).

The sharp increase in mean coefficients of thermal expansion, beginning at approximately 200°C (392°F) in welded tuffs, is not attributed to thermally induced fracturing or differential expansion, because these behaviors would not be significant during the second heating phase, and the Drift Scale Test data indicate sharp increases for both cycles (CRWMS M&O 1997g, pp. 3-12 to 3-14). Three specimens from the Drift Scale Test suite of tests did not show the increase in mean coefficients of thermal expansion at elevated temperature. Two of these specimens appeared to initiate phase changes below 200°C (392°F), and one specimen appeared to undergo essentially no phase change. This difference in behavior is attributed to different concentrations of cristobalite and tridymite. Details are presented in CRWMS M&O (1997g, pp. 3-12 to 3-14).

Thermal expansion was independent of saturation state for welded specimens but did depend on saturation state for the nonwelded specimens (Brodsky et al. 1997, p. 36). Nonwelded specimens with high moisture contents contracted during testing near 100°C (212°F), causing a temporary sharp decrease in the mean thermal expansion coefficient at approximately 100°C (212°F). This is presumed to be because of reduction of pore water and dehydration of hydrated glass. However, there is insufficient information to determine a mechanism for the shrinkage. The expansion characteristics of the welded specimens, on the other hand, seemed to be independent of saturation state, and the curves for different saturation states are similar (Brodsky et al. 1997, p. 36).

A suite of confined thermal expansion tests was conducted to determine if strain hysteresis and transition temperature effects would be suppressed by elevated confining pressures. These test results are discussed in detail in Martin et al. (1997). Because confining pressure effects for specimens tested between 1 and 30 MPa (145.0 to 4,351.2 psi) were very small (Martin et al. 1997, p. 24), data from these pressures were averaged together and compared with data from unconfined tests. At temperatures below approximately 150°C (302°F), the coefficient of thermal expansion is slightly lower for unconfined tests than for confined tests. However, at higher temperatures (150° to 250°C [302° to 482°F]), the mean values approach one another, and the scatter among the unconfined tests encompasses the results for the confined tests. Over the higher temperature range, coefficients of thermal expansion, therefore, appear to be independent of confining pressure (CRWMS M&O 1997d, p. 5-64).

The effect of specimen size was investigated using samples from Busted Butte and from boreholes USW G-1, USW G-2, USW GU-3, and USW G-4 (CRWMS M&O 1997d, p. 5-63). The original test data included five sets of tests that illustrate size effects. For all depths except the Calico Hills (Tac) unit sampled in USW G-2, mean thermal expansion coefficients are higher for small specimens than for large specimens. However, the difference in mean values is always within the error in the measurement or within one standard deviation of the mean, and data were insufficient to formulate conclusions about size effect (CRWMS M&O 1997d, p. 5-63).

The correlation between thermal properties and mineralogy was very poor but may be explained in several ways. First, the data set is very limited. Second, the mineralogical analyses were not performed on the test specimens themselves but on pieces of rock taken from near the test specimens. Third, hysteresis in the thermal expansion data may be influenced by other rock properties besides mineralogy, such as lithophysae content, and a larger database and further analyses would be required to separate the influences of each of these variables (Brodsky et al. 1997, p. 68).

4.7.4.2.3 Heat Capacity

Heat capacity is the amount of heat required to change the temperature of a substance by a given amount. It is defined (Halliday and Resnick 1974, p. 359) as:

$$H = \frac{\Delta J}{\Delta T} \qquad \text{(Eq. 4.7-4)}$$

in which

ΔJ = quantity of heat in joules (J)
ΔT = change in temperature in degrees Kelvin (K).

The database for heat capacity measurements consists of theoretical values calculated by Nimick and Connolly (1991) from chemical and mineralogical data, and from experimental values reported in Brodsky et al. (1997, pp. 48, 51 to 54, Appendix F).

Bulk chemical analyses of 20 tuff samples from Yucca Mountain were used to calculate heat capacities of the solid components of the tuffs as a function of temperature. The data were combined with grain density, matrix porosity, lithophysal cavity abundance, mineral abundance, in situ saturation, and the properties of water to estimate rock mass thermal capacitances. Calculations were completed for nine thermal-mechanical units (TCw, PTn, TSw1, TSw2, TSw3, CHn2v, CHn1z, and CHn2z) over the temperature range of 25° to 275°C (77° to 527°F) (CRWMS M&O 1997d, p. 5-66). Summary mineralogic and chemical data are reported in Connolly and Nimick (1990) and thermal capacitance calculations and results are given in Nimick and Connolly (1991). Data for TSw1 and TSw2 are presented later in this section in comparison with experimentally determined values.

Heat capacity was measured for 10 air-dried specimens from UE-25 NRG-4 and UE-25 NRG-5. The test method and test results are described and analyzed in detail in Brodsky et al. (1997, pp. 20 to 23, 47 to 49).

Test specimens were air-dried, right-circular cylinders approximately 57.0 mm (2.24 in.) in length and 50.8 mm (2 in.) in diameter. Tests were conducted over the temperature range of 30° to 300°C (86° to 572°F) using an adiabatic pulse calorimeter. This instrument applies a known quantity of electrical energy to a specimen and measures the resulting rise in specimen temperature. The test procedure is presented in TP-204, *Measurement of Specific Heat of Geologic Samples by Adiabatic Pulse Calorimetry.* The closest applicable American Society for Testing and Materials procedure is ASTM D 4611-86, *Standard Practice for Specific Heat of Rock and Soil.* This standard is based on the drop calorimeter method and provides less accurate results than the adiabatic calorimeter method given in TP-204 (CRWMS M&O 1997d, p. 5-56).

Thermal capacitance, which is heat capacity multiplied by specimen density, is summarized for TSw1 and TSw2 in Table 4.7-21 and plotted on Figure 4.7-10, along with data from Nimick and Connolly (1991). A complete data presentation is included in Brodsky et al. (1997, pp. 47 to 49) and CRWMS M&O (1997d, pp. 5-66 to 5-68). Thermal capacitance is higher for TSw2 than for TSw1. Mean thermal capacitance ranges from 1.6 J/cm^3/K to 2.1 J/cm^3 /K for TSw1 and from 1.8 J/cm^3/K to 2.5 J/cm^3/K for TSw2 (Table 4.7-21).

Experimentally determined values of heat capacity increased with temperature, reaching a localized peak of 2.4 and 2.1 J/cm^3/K at approximately 150° to 170°C (302° to 338°F) for the TSw1 and TSw2 units, respectively. This peak may be related to a phase change. However, the data presented here were insufficient to correlate peaks more specifically. The peaks in specific heat at these temperatures do occur at a temperature range associated with the phase change in

tridymite (163°C [325.4°F]). It is also evident that there were no significant changes in measured specific heat for these air-dried specimens at 100°C (212°F), indicating that dehydration effects were minor (Brodsky et al. 1997, p. 49).

Values of thermal capacitance calculated by Nimick and Connolly (1991) from chemical and mineralogical data are given in Figure 4.7-10, along with the experimental data. For both the theoretical and experimental data, values for TSw2 are higher than for TSw1. The theoretical data show a decrease at 100°C (212°F) due to the heat of vaporization of water. The test specimens were air dried and showed no comparable decrease. The two sets of data roughly coincide. However, it should be noted that without the decrease at 100°C (212°F) in the calculated data, the discrepancy between measured and calculated values for TSw1 would be maintained (CRWMS M&O 1997d, p. 5-67).

4.7.4.3 Mechanical Properties

A comprehensive series of mechanical property measurements was conducted on specimens prepared from cores recovered from NRG and SD boreholes. The measurements included elastic constants, strength, and deformation moduli for specimens from the thermal-mechanical units. One objective of the measurements was to establish a baseline set of properties to study the vertical and lateral variability of bulk and mechanical properties at Yucca Mountain. Boyd et al. (1995) noted there was little lateral variability in properties among the NRG boreholes along the axis of the North Ramp, as determined by results of tests on core samples from the NRG borehole series. However, there is significant vertical variability due to large differences in lithology, and smaller differences in smaller scale fabric and pore-structure characteristics.

Tests were performed on specimens of tuff prepared from cores recovered from NRG and SD boreholes. The size of the specimen required for each type of measurement was important in the selection of appropriate samples for testing. The other key factor in sample selection was the absence of fractures and large lithophysae, greater than about 1 cm (0.4 in.), which could affect test results.

Additional laboratory testing of mechanical properties was performed on 22 samples from the Single Heater Test block of the ESF Thermal Test Facility to characterize the area's intact rock properties. Testing and results are described in detail in CRWMS M&O (1996b, pp. 4-1 to 4-12). Unconfined compression tests were also performed on 16 specimens from the TSw2 thermal-mechanical unit from boreholes in the Drift Scale Test block. Details are presented in CRWMS M&O (1997g, pp. 4-1 to 4-13).

4.7.4.3.1 Static and Dynamic Elastic Constants

Young's modulus and Poisson's ratio, the primary mechanical deformation indices of rock, are indicators of the elastic response of the rock to stress. Static Young's moduli and Poisson's ratios were computed from the stress-strain data obtained for the specimens tested in confined and unconfined compression. In addition, dynamic elastic moduli were computed from compressional and shear-wave velocities measured under ambient laboratory conditions.

Test procedures for confined and unconfined compression are discussed in the following sections. The test procedure for compressional and shear-wave velocity measurements involved measurement of ultrasonic compressional and shear-wave velocities, both parallel and normal to the axis of the test specimen (CRWMS M&O 1997d, p. 5-77). One compressional and two orthogonally polarized shear waves were measured parallel to the axis. One compressional and one polarized shear wave, with a vibration direction parallel to the core axis, were measured in the radial direction. These data were used to compute the elastic anisotropy of the specimen. In addition, the compressional and shear-wave velocity, combined with specimen density, were used to compute the dynamic Young's modulus and Poisson's ratio. Details of the test procedure used for the ultrasonic compressional and shear-wave velocity measurements are given in Martin et al. (1997, pp. 6 to 7).

Detailed results of experiments conducted on specimens from cores recovered from boreholes UE-25 NRG-2, UE-25 NRG-3, UE-25 NRG-4, UE-25 NRG-5, USW NRG-6, and USW NRG-7/7A are presented in Martin et al. (1994, Tables 1 to 4, pp. 25 to 35; 1995, Tables 1 to 4, pp. 26 to 38) and Boyd et al. (1996a, Tables 1 to 4, pp. 29 to 44; 1996b, Tables 1 to 4, pp. 26 to 36). Tables 4.7-22 and 4.7-23 list the mean and standard deviation of static Young's moduli (elastic moduli) and Poisson's ratios for thermal-mechanical units and for individual lithostratigraphic units. In general, the Young's modulus of the tuff depends on welding. Nonwelded tuffs are weak and exhibit low Young's moduli. In contrast, the welded tuffs are stronger and exhibit significantly greater Young's moduli. In borehole NRG-6, for example, the moduli range from less than 1 GPa (1.45×10^5 psi) for the nonwelded units to near 40 GPa (5.8×10^6 psi) for the welded units. The greatest moduli are observed for specimens recovered from units TCw and TSw2. The Young's moduli observed on specimens from TSw1 are somewhat lower than those for the other welded units. The standard deviation in the Young's moduli for each thermal-mechanical unit is large. Specimens separated by very small vertical distances, having nominally the same texture and composition, exhibited large changes in moduli (CRWMS M&O 1997d, p. 5-97).

For specimens from the TSw2 thermal-mechanical unit in the Single Heater Test block of the ESF Thermal Test Facility, elastic constants calculated from unconfined compression tests were fairly consistent, with a mean Young's modulus of 32.4 GPa (4.7×10^6 psi) and a mean Poisson's ratio of 0.17. Complete test results and analysis are presented in CRWMS M&O (1996b, pp. 4-3 to 4-6, 4-9 to 4-12).

Elastic constants calculated from unconfined compression tests on specimens from the TSw2 thermal-mechanical unit (Tptpmn lithostratigraphic unit) in the Drift Scale Test block were slightly higher than values from the Single Heater Test block (CRWMS M&O 1997g, p. 4-13), but were generally consistent with values from NRG borehole samples. The mean Young's modulus was 36.8 GPa (5.3×10^6 psi) and the mean Poisson's ratio was 0.201. Standard deviations for both constants were slightly smaller than either of the other two test suites. Complete results and analysis are presented in CRWMS M&O (1997g, pp. 4-6 to 4-13).

Dynamic Young's moduli were computed from the velocity and density data. Dynamic moduli exceed static moduli. In general, the ratio of dynamic to static moduli is less than two. The difference is greatest at lower moduli and decreases as the moduli increase (CRWMS M&O 1997d, p. 5-97).

Compressional and shear-wave velocities were measured in the dry and in the saturated condition on each specimen tested in unconfined and confined compression. Table 4.7-24 presents a summary of the velocities measured for wave propagation parallel to the axis of the dry specimens. The compressional and shear-wave velocities are greatest in the TCw and TSw2 welded units and lowest in the nonwelded PTn units (CRWMS M&O 1997d, p. 5-80). The compressional wave velocity increases with saturation, and the shear-wave velocity decreases. These effects are consistent with theoretical models of seismic waves in porous media.

The anisotropies of specimens tested in unconfined and confined compression were calculated from the ultrasonic velocity data. The anisotropy ranges from less than 5 to 15 percent. Of the densely welded units, the TSw1 unit exhibited the largest anisotropy, probably due to the presence of oriented lithophysae and vapor-phase altered zones (CRWMS M&O 1997d, p. 5-80).

4.7.4.3.2 Compressive Strength

Compressive strength of a rock is its ability to withstand compressive stress without failure. Compressive strength of intact rock is measured in the laboratory by subjecting a cylindrical test piece to a compressive load parallel to its axis until it fails. Compressive strength is the maximum stress at failure and is computed from the maximum load and the cross-sectional area of the test piece. Confined (or triaxial) compressive strength is determined by subjecting the cylindrical test specimen to a uniform lateral confining pressure, in addition to the axial load.

4.7.4.3.3 Unconfined Compressive Strength

Unconfined compressive strengths of a wide range of tuff samples from the Yucca Mountain area have been measured and reported by a number of workers (Olsson and Jones 1980; Olsson 1982; Price and Jones 1982, pp. 12, 16, Table 3; Price and Nimick 1982; Price, Jones et al. 1982; Price, Nimick et al. 1982; Price 1983; Price et al. 1984; Nimick et al. 1985). Compressive strengths of the various units of the Paintbrush Group from the USW G-1 to G-4 borehole series are given in Price et al. (1985).

For unconfined compression tests described in Brechtel et al. (1995, pp. 6-1 to 6-5) and CRWMS M&O (1997d, p. 5-77), ground, right-circular cylindrical specimens of tuff were tested to failure at a constant strain rate of 10^{-5}/s under ambient temperature and pressure conditions. Nominal specimen size was 101.6 mm (4 in.) in length and 50.8 mm (2 in.) in diameter. The specimens were saturated with distilled water. Testing was performed following the procedures in ASTM D 3148-96, *Standard Test Method for Elastic Moduli of Intact Rock Core Specimens in Uniaxial Compression,* and International Society of Rock Mechanics procedure "Suggested Methods for Determining Uniaxial Compressive Strength and Deformability of Rock Materials" (Bieniawski et al. 1981, pp. 111 to 116). Static Young's modulus and Poisson's ratio were computed by performing linear least-squares fits to the stress-and-strain data collected between 10 and 50 percent of the fracture strength. The reported fracture strength was the maximum stress exerted on the specimen.

Results of unconfined compression tests on specimens from NRG and SD boreholes indicate that the unconfined compressive strengths vary, depending on the rock's welding, porosity, and fabric (CRWMS M&O 1997d, p. 5-102). Welded tuffs exhibited higher strengths than

nonwelded tuffs. Within the welded units, the variations in strengths are related to the presence and size of lithophysae and vapor-phase altered zones. Table 4.7-25 compares the mean and standard deviation of uniaxial compressive strength for thermal-mechanical units and individual lithostratigraphic units. The data are described in greater detail in CRWMS M&O (1997d, pp. 5-102 to 5-113).

The modes of fracture in most of the unconfined compression tests were very similar. In most cases, the fractures terminated in the endcaps of the specimens. There often was no evidence of shear cone development in the specimens.

Specimens from TCw typically exhibit the greatest strengths—strengths in excess of 300 MPa (43,512 psi) were observed for this unit. In contrast, the weakest specimens are from the PTn unit, with strengths generally less than 10 MPa (1,450.4 psi). Large variability is observed for TSw1 and TSw2. The strengths for these units vary from 25 to 250 MPa (3,626 to 36,260 psi) and show no consistent trend between strength and depth (CRWMS M&O 1997d, p. 5-102).

In most cases, very little inelastic volumetric strain (dilatancy) is observed in tests on the welded TCw, TSw1, and TSw2 tuffs (CRWMS M&O 1997d, p. 5-139). Many crystalline rocks begin to dilate at stresses as low as 50 percent of the fracture strength. However, in the welded tuffs, little nonlinearity in the volumetric strain is observed until the specimens are very near failure. The manner in which cracks grow and interact in tuff appears different from that observed in other crystalline rocks in which microcrack porosity is dominant. The data suggest that axial cracks extend without interacting with other cracks until failure is imminent. Similar effects also have been reported by Brace et al. (1966, pp. 3950 to 3951) and Scholz (1968, p. 1428).

Results of unconfined compression tests on TSw2 samples from the Single Heater Test block of the ESF Thermal Test Facility (CRWMS M&O 1996b, pp. 4-9, 4-12) showed a large scatter in strengths similar to that observed in other testing of Yucca Mountain tuffs (Brechtel et al. 1995, pp. 6-2 to 6-5; CRWMS M&O 1997d, p. 5-102). Unconfined compressive strengths ranged from 75.1 to 243.8 MPa (10,892 to 35,360 psi), with a mean of 143.2 MPa (20,770 psi) and a standard deviation of ± 50.3 MPa (7,295.4 psi) (CRWMS M&O 1996b, p. 4-9). Moisture contents for these specimens were not controlled, and differences in moisture contents may have contributed to the scatter in strengths. The mode of failure for all specimens was dominated by brittle axial cracking. There was no correlation between strength and mode of failure, and all of the specimens failed violently (CRWMS M&O 1996b, p. 4-9).

Results of unconfined compression tests on 16 samples from the TSw2 thermal-mechanical unit (Tptpmn lithostratigraphic unit) from the Drift Scale Test block of the ESF also showed a large scatter in strengths. Complete data and analysis are presented in CRWMS M&O (1997g, pp. 4-6 to 4-13). Strengths ranged from 71.3 to 324.1 MPa (10,341 to 47,007 psi), with a mean value of 176.4 MPa (25,585 psi) and a standard deviation of ± 66 MPa (9,572.5 psi). The highest and lowest strengths were obtained on specimens that were in relatively close proximity (only 4 m [13 ft] apart). Neither of these two specimens had notable surface features that might predict anomalous behavior. The mean, unconfined compressive strength value from the Drift Scale Test block, like the mean values of Young's modulus and Poisson's ratio, is higher than the mean values obtained for samples from the Single Heater Test block. This difference is believed to be at least partly attributable to minor differences in the testing program, although it

may indicate spatial variability within the Thermal Testing Facility of the ESF (CRWMS M&O 1997g, p. 4-13).

4.7.4.3.4 Confined Compressive Strength

Confined compression experiments were carried out on cores with a length-to-diameter ratio of two and nominal diameters of 25.4 or 50.8 mm (1 or 2 in.) (Brechtel et al. 1995, p. 6-14; CRWMS M&O 1997d, p. 5-78). All specimens were tested saturated, in a drained condition. The general procedure for testing the specimens was the same as for the unconfined compression tests, except that the specimens were jacketed in Cu and deformed in a pressure vessel at a fixed confining pressure. The procedure used for the measurements generally conformed to International Society of Rock Mechanics "Suggested Methods for Determining the Strength of Rock Materials in Triaxial Compression" (Vogler and Kovari 1981, pp. 123 to 127), and ASTM D 2664-86, *Standard Test Method for Triaxial Compressive Strength of Undrained Rock Core Specimens Without Pore Pressure Measurements.* Deviations from these procedures are discussed in CRWMS M&O (1997d, p. 5-78). Measurements were performed at confining pressures of 5 and 10 MPa (725.2 and 1,450.4 psi), and pressure was held constant to ± 0.1 MPa (14.5 psi). The instrumented specimens were monotonically loaded to failure at a nominal strain rate of 10^{-5}/s. Young's modulus and Poisson's ratio were computed between 10 and 50 percent of the stress difference at failure.

Results of confined compression tests indicate that the axial stress difference at failure increases with increasing confining pressure (CRWMS M&O 1997d, p. 2-22). Strength parameters calculated from confined compression test results are listed in Table 4.7-26. The specimens tested in confined compression failed in shear (i.e., the fractures formed on shear planes with little evidence of axial splitting). In most cases, a visibly evident shear plane developed. However, there was no evidence of conjugate fracture sets forming in any of the specimens (CRWMS M&O 1997d, p. 5-114).

To examine effects of temperature, 17 confined compression experiments were also performed at a nominal temperature of 150°C (302°F) on specimens recovered from borehole USW SD-9 (CRWMS M&O 1997d, p. 5-78). All of the measurements were conducted on specimens from thermal-mechanical unit TSw2. Measurements were conducted at effective confining pressures of 1, 5, and 10 MPa (145,725.2, and 1,450.4 psi), with a pore pressure of 5 MPa (725.2 psi). The experiments were performed at a nominal strain rate of 10^{-6}/s. The confining pressure was held constant to ± 0.25 MPa (36.3 psi), and the pore pressure was maintained constant at 5.00 ± 0.25 MPa (725.2 ± 36.3 psi). The elevated temperature was generated by means of band heaters positioned on the outside of the pressure vessel. The temperature was monitored inside the pressure vessel with a thermocouple positioned at the midpoint of the specimen.

The high-temperature confined compression test data indicated a clear increase in strength between 1 and 5 MPa (145 and 725.2 psi) (CRWMS M&O 1997d, p. 5-116). However, there was no apparent increase in the mean strength of the tuff between 5 and 10 MPa (725.2 and 1,450.4 psi) confining pressure. Comparison of room and elevated temperature (150°C [302°F]) tests suggested that the effect of temperature on the strength of welded tuff from thermal-mechanical unit TSw2 was small. Similarly, Young's moduli and Poisson's ratios, measured at

elevated temperatures (150°C [302°F]), were not significantly different from those measured at room temperature (CRWMS M&O 1997d, p. 5-116).

The heterogeneity in the tuff poses a problem in analyzing the effect of pressure on strength in terms of Mohr-Coulomb criteria. As seen with the unconfined compression test data, strengths may vary by as much as a factor of two, even over a limited depth interval. Without a suite of nominally identical specimens, a Mohr-Coulomb failure envelope is difficult to establish. Data are judged to be incomplete for the PTn and CHn1 units (CRWMS M&O 1997d, p. 5-140).

4.7.4.3.5 Tensile Strength

Indirect tensile strength tests, commonly referred to as Brazilian tests, were carried out using a procedure adhering to ASTM D 3967-95, *Standard Test Method for Splitting Tensile Strength of Intact Rock Core Specimens.* The test is simple in principle. A load is applied to a cylindrical specimen with its axis normal to the loading direction. Tensile stress develops in the center of the cylinder. The force is increased until the specimen fails by an extension fracture along the diametral loading plane. The tensile strength is computed from the force at failure.

Indirect tensile strength tests were performed on specimens from boreholes NRG-2, UE-25 NRG-3, UE-25 NRG-4, USW NRG-6, and USW NRG-7/7A (Brechtel et al. 1995, p. 6-14; CRWMS M&O 1997d, p. 5-119). Nominal specimen size was 38.1 mm (1.5 in.) in length and 50.8 mm (2 in.) in diameter. Results are summarized in Table 4.7-27 and presented in greater detail in CRWMS M&O (1997d, pp. 5-119, 5-123 to 5-131).

Tensile strengths generally range from 0.2 to 16 MPa (29 to 2,320.6 psi). The weakest specimens are from the nonwelded PTn thermal-mechanical unit. The greatest strengths are observed in the TCw welded tuff. In general, TSw1 is weaker than TSw2. However, there is significant scatter in TSw2 data.

4.7.4.3.6 Shear Strength

Mathematical simulation of rock response to mining and drilling requires the use of failure criteria for the rock. One commonly used criterion is Mohr-Coulomb, which defines the limiting state of stress for static equilibrium with the material at which inelastic deformation begins (Jaeger and Cook 1979). The criterion itself is expressed as follows:

$$\tau = C_0 + \sigma \tan\phi \qquad \text{(Eq. 4.7-5)}$$

in which

- τ = shear stress on the failure plane at the onset of failure
- C_0 = cohesion
- σ = normal stress on the failure plane at the onset of failure
- ϕ = angle of internal friction

The shear stress at the onset of failure is also the shear strength of rock, which is defined by its two components: cohesion (C_0) and the angle of internal friction (ϕ). Results of unconfined

compressive tests and triaxial (confined) compression tests can be used to determine τ and ϕ. As noted in the discussion of compression test results (Sections 4.7.4.3.3 and 4.7.4.3.4), because of the heterogeneity in the tuff, it is difficult to establish a Mohr-Coulomb failure envelope without a suite of nominally identical specimens. Section 4.7.5.3 discusses the use of rock mass indices to estimate in situ strength parameters.

4.7.4.3.7 Time-Dependent (Creep) Behavior

If a solid is subjected to a load (stress) within its elastic limit, it instantaneously experiences an amount of deformation (strain), which disappears on removal of the load. If the load is maintained at the same level, the solid will continue to deform beyond the instantaneous deformation at a slow rate, depending on the level of the applied stress. This continuing deformation with time, in spite of no increase in stress, is referred to as time-dependent deformation or "creep deformation."

Seven creep experiments were performed on right-circular cylinders of TSw2 tuff recovered from borehole NRG-7/7A (CRWMS M&O 1997d, p. 5-79). The specimens had a length-to-diameter ratio of 2:1 and a specimen diameter of 50.8 mm (2 in.). The experiments were performed at a constant confining pressure of 10 MPa (1,450.4 psi) and a temperature of 225°C (437°F). The procedure used for these measurements was based on ASTM D 4406-93, *Standard Test Method for Creep of Cylindrical Rock Core Specimens in Triaxial Compression.* Measurements were carried out in a compact creep apparatus, described by Martin et al. (1995, pp. 11 to 13). The key features of the system included independent controls for the confining pressure, pore pressure, temperature, and axial force producing the differential stress on the sample. Loading continued under constant temperature, differential stress, and confining pressure until the sample failed or the experiment was terminated. The procedure is described in detail in CRWMS M&O (1997d, p. 5-79).

Results of creep measurements on specimens from the TSw2 thermal-mechanical unit (Tptpmn lithostratigraphic unit) are presented in Table 4.7-28. The experiments were conducted at nominal differential stresses of 40, 70, 100, and 130 MPa (5,801.5, 10,152, 14,504, and 18,855 psi), at a fixed confining pressure of 10 MPa (1,450.4 psi), and at a temperature of 225°C (437°F). The duration of the experiments ranged from 2.55×10^6 s to 5.90×10^6 s (30 to 68 days). At higher stress differences, the data show very small increases in the axial strain. The experiments conducted at stress differences between 40 and 100 MPa (5,801.5 and 14,504 psi) show smaller strain accumulations, and for the test conducted at a differential stress of 40 MPa (5,801.5 psi), no strain accumulation was observed (CRWMS M&O 1997d, p. 5-140). Each test was terminated before the specimen failed.

4.7.4.3.8 Hardness

Schmidt hammer rebound hardness measurements were conducted on samples from the NRG holes to produce early strength estimates and to supplement the rock mechanics test data. The measurements were performed following International Society of Rock Mechanics suggested methods (Bamford et al. 1981, pp. 101 to 102), and the analysis of the results incorporates suggested improvements to the International Society of Rock Mechanics methods by Goktan and Ayday (1993). Pieces of core were selected on nominal 3-m (10-ft) intervals downhole and

clamped in a testing anvil weighing a minimum of 20 kg (44.1 lb). A group of 20 rebound hardness measurements were then conducted. The data are presented in detail in Brechtel et al. (1995, pp. 6-21 to 6-23).

Results of Schmidt hammer measurements are summarized in Table 4.7-29. Estimates of uniaxial compressive strength based upon a correlation with Schmidt hammer data gave reasonable predictions for the TCw and TSw2 thermal-mechanical units but overestimated strength in the PTn and TSw1 units (Brechtel et al. 1995, p. 2-12).

4.7.4.3.9 Correlations and Parametric Effects for Mechanical Properties

Anisotropy–In general, rock properties often depend on the direction of measurement relative to such characteristics as bedding, schistosity, and dominant orientation of layered silicate minerals. Anisotropy of specimens tested in confined and unconfined compression was calculated from ultrasonic velocity data. The anisotropy ranges from -5 to 15 percent (CRWMS M&O 1997d, p. 5-139). The TSw1 thermal-mechanical unit exhibited the largest anisotropy, probably because of the presence of oriented lithophysae and vapor-phase altered zones. Price et al. (1984) found that dynamic elastic moduli for samples of the densely welded Topopah Spring member from borehole USW GU-3 showed that anisotropy of elastic properties for orientations parallel and perpendicular to the rock fabric is insignificant.

Lithophysae–The units of the Topopah Spring Tuff contain varying amounts of lithophysae. Lithophysae are described in greater detail in Section 4.5. They are generally spherical to sometimes slightly flattened cavities of up to several tens of centimeters (91 ft or more) in diameter. The lithophysal cavities often have on their inner wall a thin layer of feldspars, silica minerals, and other vapor-phase mineral deposits (Figure 4.5-8). The functional porosity, which is the total of lithophysal pore volume, nonlithophysal pore volume, and volume of clay minerals, has been related by Price and Bauer (1985) to Young's modulus and unconfined compressive strength.

Porosity–The vertical variability in the elastic and strength properties of the tuffs at Yucca Mountain is large. Even considering the data within thermal-mechanical units, the scatter for each property is large. Variations of a factor of two or more are common. Price and Bauer (1985) sorted the elastic and fracture properties of tuff according to porosity in an attempt to compare specimens with similar properties. They observed a good correlation between modulus and porosity. However, there is still significant scatter in the moduli, even for similar samples with nearly identical porosities. In spite of the apparent correlation of modulus with porosity for porosities between 8 and 60 percent, it is still difficult to predict modulus based on porosity data (CRWMS M&O 1997d, p. 5-133).

A similar correlation exists between ultrasonic wave velocities and porosity. Based on data collected on NRG and SD specimens, compressional and shear-wave velocities decrease with increasing porosity (CRWMS M&O 1997d, p. 5-133). However, as with Young's modulus, at each porosity there is large scatter in the measured velocities.

The distribution of strengths observed in unconfined compression tests similarly correlates with porosity (CRWMS M&O 1997d, p. 5-133). As with the elastic properties, the strength decreases

with increasing porosity and there is substantial scatter at each porosity. Even within a very narrow range of porosities, and presumably similar composition and distribution of lithophysae and vapor-phase altered zones, the variability in strength is large. Most of this scatter has been attributed to differences in pore distribution (Price et al. 1993).

Temperature Effects–The effect of temperature on the TSw2 welded tuff produced somewhat conflicting results (CRWMS M&O 1997d, p. 5-133). The application of moderate confining pressure (5 or 10 MPa [725.2 or 1,450.4 psi]) resulted in a significant increase in the stress difference at failure. However, comparing data collected at ambient temperature with those at elevated temperature at low confining pressures indicates that the effect of temperature on strength is small. More data are needed to assess the influence of temperature on strength.

Effect of Sampling on Parametric Studies–The current data set does not adequately isolate parametric effects, such as temperature, pressure, and saturation, because of the large variability in properties between lithologic units and within lithologic units (CRWMS M&O 1997d, p. 5-137). Samples were selected to characterize vertical variability within the thermal-mechanical units. Comparisons were made with samples from different depths in the boreholes, and attempts were made to group properties to define how temperature and confining pressure influence behavior in a specific rock unit. However, variability between samples may be greater than the parametric effect being investigated.

The data have not been evaluated against the requirements for design and performance assessment, and there may be some omissions in the current data set. For example, no confined strength measurements are available for nonwelded tuff units. However, in general, the parametric effects have been investigated in both welded tuffs and nonwelded tuffs.

Scaling Intact Properties–Scaling of baseline data on intact rock properties for site and time may be important for modeling approaches that do not assume an equivalent continuum. In this case, the intact properties of rock blocks between fractures represent an intermediate size between the rock mass and the lab sample.

Two important parameters for scaling intact properties are the volume of the rock and the duration of the applied stress at elevated temperature. Price (1986) studied the effect of sample size on the unconfined compressive strength and elastic moduli of welded tuff using TSw2 welded specimens recovered from Busted Butte, adjacent to Yucca Mountain. The data show a decrease of more than a factor of two in compressive strength as the specimen diameter increases from 25.4 to 228.6 mm (1 to 9 in.).

The data pertaining to time dependence reveal an inconsistency. The study of strain rate dependence for Busted Butte specimens shows that subcritical crack propagation substantially affects failure strengths (CRWMS M&O 1997d, 5-141). However, failure strengths for SD-12 specimens at room temperature were not different from those of SD-9 at 150°C (302°F). Because subcritical crack propagation is a thermally activated process, if strain-rate dependence is observed, it is expected that some temperature dependence also would be observed (CRWMS M&O 1997d, p. 5-141).

4.7.4.3.10 Mechanical Properties of Fractures

Discontinuities such as joints, bedding planes, faults, and fractures cause the properties of a rock mass in situ to be different from those of intact rock tested in the laboratory. In general, strength and deformational properties of the rock mass will be lower than those measured in the laboratory. An understanding of the mechanical properties of discontinuities is necessary to evaluate their effect on rock mass properties.

Most rock masses contain natural fractures that are called joints if they show little or no visible offset. The presence of these features in the rock mass has important effects on the overall thermal-mechanical response of the rock mass. They can increase the compliance, reduce the strength, alter the thermal conductivity, and act as pathways for fluid movement. Because of their potential importance in design and performance assessment, fracture properties, such as normal stiffness, shear stiffness, cohesion, and coefficient of friction, are important.

Natural fractures from boreholes UE-25 NRG-4, USW NRG-6, USW NRG-7, USW SD-9, and USW SD-12 were tested for stiffness and strength. Tests are reported in Olsson and Brown (1994, 1997). These studies used the rotary shear technique for measuring fracture stiffness and shear strength. This technique has been used for at least 20 years and has certain advantages over other configurations for shear testing. Details on implementation of this test technique are given in Olsson and Brown (1997).

In the rotary shear tests, the specimens were composed of two short, hollow tubes of rock that were divided at mid-height by the fracture to be tested. Specimens were prepared from the as-received core by subcoring perpendicular to the fracture. Outer specimen diameters ranged from 44.3 to 82.0 mm (1.74 to 3.22 in.). Test specimens were potted into metal specimen holders with gypsum cement. The metal specimen holders were then bolted into the load frame. Stress was applied normal to the fracture while the change in fracture aperture was measured with linear variable differential transformers. Torque was then applied to cause sliding on the interface, and shear displacements were measured. All samples were sheared at constant normal stress at room temperature and in the air-dried condition. Further details are given in Olsson and Brown (1997, pp. 9 to 13).

For each test, Olsson and Brown (1994, 1997) reported the normal stress, shear and normal stiffness functions, shear strength, residual shear strength, and dilation angle at peak shear stress. Also, the friction angle, ϕ, and cohesion, C, were reported for each of four thermal-mechanical units. Data are summarized in Tables 4.7-30, 4.7-31, and 4.7-32 and in CRWMS M&O (1997d, pp. 5-142 to 5-149).

The normal stiffness for Yucca Mountain fractures increases with increasing normal stress, as is typical for interfaces of any type (Olsson and Brown 1994, 1997). However, there is wide variability from fracture to fracture, which is indicated by the large standard deviations in Table 4.7-32. The coefficient of friction seems to be slightly greater for TSw2 than for TSw1, but the one standard deviation band includes essentially all the other values. The small number of tests conducted on TCw and CHn1 do not provide assurance that the data are representative (CRWMS M&O 1997d, p. 5-146).

There are too few data to draw quantitative conclusions about fracture strengths for TCw and CHn1. For TSw1 and TSw2, where there are more data, the friction angle, expressed as tan ϕ, seems to be slightly greater for TSw2 than for TSw1, 0.87 (ϕ = 41°) ± 0.09 versus 0.77 (ϕ = 38°C) ± 0.08, respectively (CRWMS M&O 1997d, p. 5-146). The roughness characteristics of the fracture surfaces agree qualitatively with the simple mathematical model of Brown (1995), derived from fracture data in many other rock types.

4.7.5 Rock-Mass Properties

Analyses to support the design of the repository are required to address the potential impacts of seismic, thermal, and mechanical loading. These analyses require knowledge of rock properties at the rock-mass scale as inputs. Mechanical properties are known to be very different for strong, jointed, in situ rock masses than for small, intact samples tested in the laboratory. These differences, termed "scale effects," are attributed to the influence of the size of the rock-mass-affected inhomogeneities, such as jointing.

In situ thermal testing is being conducted at the Thermal Test Facility of the ESF to better understand rock-mass behavior and the coupled thermal, mechanical, hydrological, and chemical processes that may occur from radioactive waste emplacement in the rock mass of the potential repository. The ESF Thermal Test comprises a Single Heater Test and a long-term Drift Scale Test. Preheating characterization studies (CRWMS M&O 1996b, 1997g) and early data and analysis from the Single Heater Test (CRWMS M&O 1997h) and the Drift Scale Test (CRWMS M&O 1998a) have contributed significantly to the understanding of rock-mass behavior. The Single Heater Test was initiated in August 1996. The heater was deactivated in May 1997, and monitoring continued for an additional 9 months during the cool-down period. The Drift Scale Test, initiated in December 1997, is ongoing. Planned durations for the heating and cooling phases of the Drift Scale Test are 4 years each (CRWMS M&O 1997g, p. 2-1).

For the Single Heater Test, instrumentation was installed within (and on) the rock mass encompassed by the test block to record measurements during both the heating and cool-down periods. Thermomechanical measurements included temperature measurements using thermocouples, resistance temperature devices, and thermistors. Mechanical instrumentation included multiple-point borehole extensometers, tape extensometers, surface-mounted wire extensometers, load cells on rockbolts, and an NX borehole jack. Additional instrumentation was installed to measure hydrological and chemical properties (CRWMS M&O 1999c, pp. 3-7 to 3-8).

The Drift Scale Test consists of a nearly 50-m-long (164-ft-long), 5-m-diameter (16.4-ft-diameter) heated drift, a connecting drift, an observation drift, a plate-loading niche, and a data-collection system niche. Thermal, mechanical, hydrologic, and chemical responses are measured with about 3,700 sensors in boreholes or on the drift surface. Now in the heating phase, temperatures of the more than 10,000 m^3 (353,145 ft^3) of rock will be elevated above 100°C (212°F), while the temperature along the drift wall will reach 200°C (392°F) (CRWMS M&O 1997g, p. 2-1). Rock mass deformation modulus has been determined in the Drift Scale Test block by means of plate-loading tests near the entrance to the heated drift (CRWMS M&O 1998a, pp. 6-14 to 6-16). See Section 11 for additional information on thermal testing.

4.7.5.1 Rock-Mass Classification

Rock mass quality (Q) data were collected in preconstruction exploration boreholes, in the ESF and in the Enhanced Characterization of the Repository Block Cross Drift. The rock mass quality (Q) system (Barton et al. 1974, pp. 192 to 198) and the rock mass rating (RMR) system (Bieniawski 1989, pp. 51 to 72) were employed in ESF construction activities as the basis of empirical design of excavation ground support and empirical correlation with rock mass properties. These two indices are rock classification methods that consider characteristics of the rock mass, such as the degree of jointing, the interaction of joints to form blocks, joint surface frictional characteristics, rock strength, rock stress, and hydrologic conditions. Rock mass quality indices and the parameters used to determine the indices, are derived from direct observations of rock mass characteristics.

The calculation of rock mass rating (RMR) requires six parameters that consider the strength of the rock, the RQD, the joint spacing, the condition of joint surfaces, the groundwater environment, and a factor for the adjustment of joint orientation toward the excavation, as shown in the following equation:

$$RMR = C + I_{RQD} + JS + JC + JW + AJO \qquad \text{(Eq. 4.7-6)}$$

in which

RMR = a dimensionless number from 0 to 100
C = the strength parameter
I_{RQD} = the RQD parameter
JS = the joint spacing parameter
JC = the joint surface condition parameter
JW = the groundwater parameter
AJO = the adjustment for joint orientation

Table 4.7-33 correlates ranges of rock mass rating (RMR) with relative descriptions of rock quality. Parameter values are assigned based on classification guidelines presented by Bieniawski (1989, Table 4-4, p.62). Adjustments for joint orientation can be made to the rock mass rating (RMR) to account for the effects of the direction-of-mining approach. When application of the rock mass rating (RMR) index is limited to estimation of rock-mass mechanical properties in drift-design methodology, adjustment for joint orientation is not applied. Borehole estimates of rock mass rating (RMR) do not include adjustment for joint orientation, because joint orientations cannot be determined from core. The scanline data does include the adjustment for joint orientation factor, because joint orientations can, in fact, be evaluated with respect to the tunnel axis. Borehole RQD was calculated as described in Section 4.7.3, while rock mass RQD was calculated from tunnel scanline data using two methods described in CRWMS M&O (1997d, pp. 6-7, 6-29). Rock mass rating (RMR) values for boreholes and for ESF scanlines are presented in Brechtel et al. (1995), Kicker et al. (1997), SNL (1995), and CRWMS M&O (1997d, 1997g). RMR values for the Enhanced Characterization of the Repository Block Cross Drift are given in Mongano et al. (1999).

Rock mass quality (Q), as defined by Barton et al. (1974, p. 193), is calculated from six parameters:

$$Q = \left(\frac{RQD}{Jn}\right) * \left(\frac{Jr}{Ja}\right) * \left(\frac{Jw}{SRF}\right) \qquad \text{(Eq. 4.7-7)}$$

in which

RQD = rock quality designation
Jn = joint set number
Jr = joint roughness number
Ja = joint alteration number
Jw = joint water reduction number
SRF = stress reduction number

The first term (RQD/Jn) describes the block size, the second term (Jr/Ja) describes interblock shear strength, and the third term (Jw/SRF) describes the effect of the active stress. Relative classes of rock quality based on the overall value of rock mass quality (Q) have been assigned by Barton et al. (1974, pp. 208, 210, and 212, Figures 4, 5, and 6) and are presented in Table 4.7-34.

Data and methodology used to estimate rock mass quality (Q) and rock mass rating (RMR) from the core data are described in Brechtel et al. (1995), Kicker et al. (1997), and CRWMS M&O (1997d). In the methodology, Q was estimated for every 3-m (10-ft) interval of the core log. Some parameters used to calculate the Q or RMR index could not be determined from core, and values for each interval were, therefore, estimated by Monte Carlo simulations from distributions of the parameter, which were based on surface mapping and mapping of the North Ramp Starter Tunnel. The approach assumed that the value of each parameter was independent of the other parameters in each interval.

Rock mass quality data were also generated for 5-m (16.4-ft) intervals of the ESF and the Enhanced Characterization of the Repository Block Cross Drift, based on scanline observations made on the excavation surface. Scanline refers to the determination of parameters along linear traces within the interval, as opposed to a detailed mapping of the features in the interval. The methodology used for the scanline rock mass quality determinations is described in CRWMS M&O (1997d). In addition, Q data were also determined from full-peripheral field mapping of the ESF, following the procedure *Underground Geologic Mapping*, NWM-USGS-GP-32, Rev. 0. Complete data and detailed analyses are presented in CRWMS M&O (1997d, pp. 6-1 to 6-65, Appendices B, C; 1997g, pp. 8-1 to 8-13). Cross Drift data and analyses are presented in Mongano et al. (1999, pp. 92 to 103).

Both the Q and the RMR empirical rock classification systems were applied in the ESF. These classification systems were determined in the ESF based on two separate sets of mapping data, including scanline field mapping data and full-peripheral field mapping data. Rock mass quality (Q) and rock mass rating (RMR) data were collected for each 5-m (16.4-ft) interval of tunnel. To smooth the spatial variability along adjacent 5-m (16.4-ft) intervals of the ESF, a nine-term moving average rock-mass property value was determined for each interval, such that the value

of a particular interval was averaged together with the values of the four preceding intervals and the four succeeding intervals (CRWMS M&O 1997f, p. 54).

Rock mass quality assessments from the two data sets from the ESF are shown on Figures 4.7-11 and 4.7-12. Rock mass rating (RMR) data (Figure 4.7-11) typically show higher rock mass quality compared to rock mass quality (Q) data (Figure 4.7-12). Scanline and full-peripheral data are in very good agreement throughout the ESF, with the exception of the TSw1 thermal-mechanical unit in the North Ramp. A comparison of rock mass quality (Q) values in the TSw1 shows that the greatest difference between the two data sources occurs over the interval from approximately Station 19+00 to Station 28+00, corresponding primarily to the Topopah Spring crystal-poor upper lithophysal zone (Tptpul) (CRWMS M&O 1997f, p. 54). There is an observable structural difference along the tunnel alignment within the Tptpul in the North Ramp, such that the rock exposure is significantly smoother and less fractured above the springline compared to below the springline (CRWMS M&O 1997f, p. 54). The scanline Q assessment was conducted above the springline and therefore does not reflect the lower quality rock below the springline.

An empirical method for assessing the Q system parameter, called the stress-reduction factor (Kirsten 1988), was applied to both scanline and full-peripheral data sets in the ESF, resulting in the determination of a modified Q value. The method and analysis are described in detail in CRWMS M&O (1997f, pp. 57, 60 to 69). The Q values calculated by the Kirsten approach, defined as $Q_{modified}$, are typically higher for both data sets and are generally in closer agreement to the RMR values.

Table 4.7-35 presents a concise statistical description of rock mass quality in the ESF. Cumulative frequency of occurrence for each thermal-mechanical unit, from both scanline and full-peripheral data, is shown on Figure 4.7-13 for RMR data, on Figure 4.7-14 for Q data, and on Figure 4.7-15 for $Q_{modified}$ data. This cumulative frequency of occurrence of rock mass quality data is summarized in Table 4.7-35, with frequencies of occurrence of 5, 20, 40, 70, and 90 percent. These frequencies correspond to the five rock mass quality categories as defined by Hardy and Bauer (1991) and serve as the basis for evaluating the potential range of rock-mass conditions. Table 4.7-35 also includes the original borehole values used in the ESF ground support design analysis. As shown, these values resulted in conservative estimates of rock mass quality and a conservative ground support system.

Comparison of data obtained from exploratory drilling with early scanline data obtained from the ESF allowed the identification of potential biases in the data sets (CRWMS M&O 1997d, p. 6-48). The most significant potential sources of bias are directional bias, bias because of the effect of scale (the smaller amount of structural data available from a borehole), and bias because of sample disturbance during borehole drilling. Comparison of rock mass quality projected from boreholes to the scanline assessment data from the ESF excavations shows that the borehole data generally produced conservative estimates. The TCw was the only exception, where the impacts of normal faults on the rock were not well represented in the core data, as the predominantly vertical boreholes did not provide a good sampling of fault impact on the brittle tuff rocks.

Borehole core-based RQD, a parameter influencing rock mass quality indices, was much lower than the RQD as assessed at the tunnel scale. This is because of the character of the core

recovered from drilling. The tuff rocks are extensively fractured, which causes a large amount of rubble, lost core, and high fracture frequency. Attempts to filter drilling-induced fractures from the RQD calculations (enhanced RQD) increase the values by factors of 1.5 to 2.2 for different thermal-mechanical units. However, RQD values from the tunnel scale were still greater by a factor of 1.5 to 3.1. The RQD in the tunnel assessments is based on the frequency of fractures that are observed at the tunnel scale, which excludes many fractures that affect the core. In addition, although the extent of rubble or highly fractured intervals was included in the tunnel assessment of RQD, those types of features were less common than observed in the core. Joint frequencies were higher in core data, because core data included smaller scale fractures that were not counted at the tunnel scale. This resulted in small values of the joint spacing parameter in the core-based RMR. Joint set numbers in the core were based on fractures observed in the TCw, which had both more joint sets and higher frequencies of jointing than other units. Jn values used for the PTn and TSw1 were higher than revealed by the excavation.

As shown in Table 4.7-35, lowest rock mass quality was observed in the TCw thermal-mechanical unit. The TCw also had the greatest variability. Rock mass quality was lowest in the most densely welded lithostratigraphic units, Tpcpul and Tpcpmn, in the Tiva Canyon Tuff (CRWMS M&O 1996d, p. 2-29). It was higher in the less densely welded upper and lower portions. This correlates with analysis of the fracture mapping for TCw, which consistently indicates more joint sets and higher joint frequency. In addition, the North Ramp penetrates the TCw in a zone of normal faulting, which contributed to the broken character of the TCw rocks (CRWMS M&O 1997d, p. 2-29).

Table 4.7-35 also indicates that the PTn unit showed consistently high rock mass quality. Typically, only one set of joints was evident in the PTn, which had limited impact on the excavation. Rock strength was low in this unit, with some intervals being nonlithified. Shear failures were observed on the sides of the tunnels in some of the weaker PTn materials. However, they were localized and have not affected the long-term stability of the excavation.

Rock mass quality was higher in the TSw1 unit than in the corresponding portions of the TCw (CRWMS M&O 1997d, p. 2-29). Jointing was less well developed. Poor rock mass quality, anticipated in the upper lithophysal zone (Tptpul), was not observed. Jointing was not well developed and was generally limited to one set. The inhomogeneities in the Tptpul, caused by large lithophysae and relatively small cracking of the rock, had little negative effect on the rock mass at the excavation scale. Where the middle nonlithophysal zone (Tptpmn) in the TSw2 was exposed in excavations of the Main Drift, rock mass quality was relatively high.

The ESF ground support guidelines (CRWMS M&O 1996c) specify ranges of rock mass quality for associated ground support (Classes I through V). Based on these guidelines and rock mass quality indices from early ESF scanline data, ground support requirements were projected for each thermal-mechanical unit. Table 4.7-36 presents the recommended ground support with respect to the specified range of rock mass-quality (Q) values. Classes I and II specify welded-wire fabric and rockbolts, with tighter rockbolt spacing for Class II. Class III uses the Class II arrangement of rockbolts and welded-wire fabric, but with the addition of shotcrete. However, although called for by design, shotcrete was never used, except in the starter tunnel, because of the actual conditions observed during excavation. Classes IV and V use W8 circular steel sets and lagging, with tighter set spacing and full lagging for Class V.

Table 4.7-37 lists the projected proportion of the tunnel within each thermal-mechanical unit that would require the support suggested by the guidelines. The scanline rock mass quality data suggested that the majority of tunnel excavation could be supported with rockbolts and welded-wire fabric in the undifferentiated overburden, PTn, TSw1, and TSw2 units (CRWMS M&O 1997d, p. 6-59). The rock mass quality distribution in the TCw unit, however, projected heavier ground supports than required for the other units. Comparisons of projected and installed ground support (Section 4.7.7.3.4) are integral to the construction monitoring activities (CRWMS M&O 1997a).

Rock mass quality data were determined in the Enhanced Characterization of the Repository Block Cross Drift from detailed line surveys following the same procedures used in the ESF. Rock mass rating (RMR) values were determined both including and excluding lithophysae. Lithophysae were found to have only a minimal effect on the determination of rock mass rating (RMR) (Mongano et al. 1999, pp. 94 to 95). Generally, there was good correlation with results for the same rock units in the ESF. A summary of rock mass rating (RMR) values in the Cross Drift is presented in Mongano et al. (1999, Table 12, p. 95). Rock mass quality (Q) values were determined for the Cross Drift both with and without the Kirsten approach, but the $Q_{modified}$ value, determined using Kirsten's approach, was used as the actual reported Q value. Rock mass quality (Q) ratings matched very closely with the predicted Q ratings based on values obtained in the ESF, but were higher than anticipated (Mongano et al. 1999, p. 101). A summary of rock mass quality (Q) ratings in the Cross Drift is presented in Mongano et al. (1999, Table 14.2, pp. 100 to 101).

Two ground support classes were considered for the Cross Drift: systematic bolting and steel sets (Mongano et al. 1999, p. 103). The high rock mass quality (Q) values that were determined indicated, however, that very little support was required in the stratigraphic units exposed in the Cross Drift, other than occasional spot bolting.

4.7.5.2 Rock-Mass Thermal Properties

Correlations have been developed or proposed for thermal-mechanical properties at the rock-mass scale (Nimick and Connolly 1991). Thermal conductivity at the intact scale has been shown to be a function of porosity, saturation, and temperature. Differences at the rock-mass scale are projected to be related to the additional fracture porosity, which should be a small effect. Similarly, the heat capacity of intact rock is expected to be an adequate predictor of heat capacity at the rock mass scale.

Preliminary thermal-mechanical analyses for design have been performed in an attempt to project laboratory thermal expansion data to the rock-mass scale, as described in Jung et al. (1993). The preliminary thermal-mechanical analyses indicated a maximum upward displacement of almost 30 cm (11.8 in.) at the surface, 300 years after waste emplacement. Most of this displacement would originate in the TSw2 unit (CRWMS M&O 1997d, p. 7-16). The rock in the immediate vicinity of the repository was predicted to be in compression, but the tensile stress nearer the surface (TCw thermal-mechanical unit) was predicted to be relatively high (approximately 5 MPa [725.2 psi]). This behavior could potentially result in the opening of preferential pathways for water infiltration or gas migration. However, thermal expansion data for the analyses in Jung et al. (1993, p. 4-10) came primarily from borehole laboratory thermal

expansion testing results. Data from the in situ thermal tests being conducted in the ESF are expected to be more representative of rock-mass behavior than the laboratory test results and are used for updating and expanding the three-dimensional thermal-mechanical analysis for the repository. The resulting, more realistic material models are expected to predict lower stresses (Jung et al. 1993; CRWMS M&O 1997d, p. 7-16).

Before the onset of heating in both the Single Heater Test block and the Drift Scale Test block of the ESF Thermal Test Area, baseline laboratory and in situ testing were performed to characterize thermal, mechanical, hydrological, and chemical properties, local geology, in situ hydrology, and local rock mass quality of the area to be tested (CRWMS M&O 1996b, 1997g). Results of the baseline characterization are generally consistent with results of previous studies in the same thermal-mechanical unit and lithostratigraphic unit.

Data collected from the Single Heater Test through May 1997 (CRWMS M&O 1997h) indicate that the temperature distribution around the heater was radially symmetric and that conduction thus appears to be the primary mode of heat transfer through the rock mass (CRWMS M&O 1997h, p. 6-2). However, some anomalous temperature gauge readings may indicate convective heat transport in fractures. The available thermal data also indicate the formation of a dry-out zone extending radially outward roughly 1 m (3.3 ft) from the heater to approximately the 100°C (212°F) isotherm (CRWMS M&O 1997h, p. 6-4). Although there is generally good overall agreement between calculated and measured temperatures, numerical simulations of thermal behavior did not accurately predict the observed thermal data. This is likely due to limitations imposed by the equivalent continuum model, which is the conceptual model on which the numerical simulations are based. A complete data presentation and analysis is given in CRWMS M&O (1997h).

The thermal expansion coefficient of the rock mass was determined from selected multipurpose borehole extensometer displacements and temperatures. The calculated rock-mass thermal expansion coefficient ranged from between about 4×10^{-6}/°C and 6×10^{-6}/°C. Rock-mass thermal expansion was calculated from the in situ data, including temperature change for a given axial length from ambient gauge length and measured thermal displacement over the gauge length. Only the data from multipurpose borehole extensometers with relatively uniform temperature were used (MPBX-1 and MPBX-3). Because of displacement direction reversals after day 90 of the test, the calculated rock-mass thermal expansion coefficients presented in Table 4.7-38 are only for data through day 90. Analytical calculation of the thermal expansion coefficients for the longest gauge lengths available near the end of the heating cycle produced the results presented in Table 4.7-39. A more complete discussion, along with complete data, is given in SNL (1997b), CRWMS M&O (1997h, pp. 5-27 to 5-28), and CRWMS M&O (1999c, Section 9.1).

Rock-mass thermal expansion coefficients calculated from the Single Heater Test are generally lower than laboratory determined values for the same TSw2 unit.

Rautman (1995) developed a correlation between thermal conductivity and a two-dimensional geostatistical model of porosity at Yucca Mountain. The relationship of laboratory measurements of thermal conductivity to porosity, saturation, and temperature is summarized in Section 4.7.4.2, and the use of these data for three-dimensional rock properties modeling is

discussed in Section 4.7.1.3. Results of geostatistical modeling of thermal conductivity, and a more complete discussion of the correlation of porosity and thermal conductivity, are presented in Section 4.8 and in Rautman (1995). See Section 11 for more information on thermal loading.

4.7.5.3 Rock-Mass Mechanical Properties

4.7.5.3.1 Rock-Mass Strength

Rock-mass mechanical properties have been estimated using the approach proposed by Hardy and Bauer (1991). This approach uses laboratory test data and rock mass rating (RMR) to estimate mechanical properties at the rock mass scale for use in equivalent continuum analyses. The estimated properties are listed in Table 4.7-40 for each thermal-mechanical unit and rock mass rating (RMR) values at 40 percent cumulative frequency of occurrence. Ranges of the rock mass properties are estimated, based on rock mass rating (RMR) from scanline data and the average of the appropriate intact rock property. Complete analysis is presented in CRWMS M&O (1997d, pp. 7-2 to 7-12, Appendix B). Two sets of empirical rock-mass-strength criteria, Yudhbir et al. (1983, pp. B-1 to B-8) and Hoek and Brown (1988, pp. 31 and 34), were adopted for the Drift Design Methodology, and an average of the two predicted strengths was used to develop a power law relationship of rock-mass strength versus confining pressure. Design parameters for rock-mass elastic modulus (Serafim and Pereira 1983), Poisson's ratio, and Mohr-Coulomb strength were developed for each thermal-mechanical unit.

Rock-mass strengths, based on the empirical strength criteria of Yudhbir et al. (1983, pp. B-1 to B-8) and Hoek and Brown (1988, pp. 31, 34), have been developed for the thermal-mechanical units (CRWMS M&O 1997d, p. 7-6, Table 7-3). Information required for obtaining rock-mass strength includes rock mass quality indices, intact rock uniaxial compressive strengths, and the triaxial compressive strength data. The rock-mass-strength criteria were generated for the five categories of rock mass quality, based on frequency of occurrence of 5, 20, 40, 70, and 90 percent, (presented in Section 4.7.5.1).

The equation proposed by Yudhbir et al. (1983, p. B-4) for calculation of rock mass strength is:

$$\sigma_1 = A\sigma_c + B\sigma_c \left(\frac{\sigma_3}{\sigma_c}\right)^{\alpha} \qquad \text{(Eq. 4.7-8)}$$

in which

- σ_1 = strength of the rock mass
- A = a dimensionless parameter, dependent on the rock mass rating (RMR)
- σ_c = intact rock uniaxial compressive strength
- α, B = rock material constants, dependent on rock type
- σ_3 = confining stress

The value of A for the rock mass is obtained from the design rock mass rating (RMR_D) by the following equation from Yudhbir et al. (1983, p. B-6):

$$A = e^{0.0765(RMR_D)-7.65} \quad \text{(Eq. 4.7-9)}$$

The material constants B and α are related to the rock type and are determined by a curve fitting of the confined, compressive-strength test results.

Table 4.7-41 lists the values of B and α, as well as σ_c, for each unit. For the TCw thermal-mechanical unit, NRG core triaxial test data were used to determine B and α, using the method outlined in Hardy and Bauer (1991) and Lin et al. (1993). These data were originally published in Brechtel et al. (1995, pp. 8-5 to 8-6). For the undifferentiated overburden and PTn thermal-mechanical units, NRG uniaxial compression and Brazilian tensile-strength tests were used to determine B and α, with modifications of the method suggested by Hardy and Bauer (1991) and Lin et al. (1993). These data were originally published in Brechtel et al. (1995, pp. 8-5 to 8-6). For the TSw1 and TSw2 thermal-mechanical units, triaxial test data from samples from SD-9 and SD-12 were used to determine B and α, using the method outlined in Hardy and Bauer (1991) and Lin et al. (1993). Only five data points for each unit were available to evaluate these constants.

The Hoek and Brown (1988, pp. 31, 34) rock-mass-strength criterion is shown in Equation 4.7-10:

$$\sigma_1 = \sigma_3 + \sqrt{m\sigma_c\sigma_3 + s\sigma_c^2} \quad \text{(Eq. 4.7-10)}$$

in which

σ_1 = strength of the rock mass
σ_3 = confining stress
m = a constant that depends on the properties of the rock = $m_i e^{(RMR-100)/28}$
σ_c = intact rock uniaxial compressive strength
s = a constant that depends on the extent to which the rock is fractured = $e^{(RMR-100)/9}$

The parameter m_i is the constant for intact rock and is determined by curve fitting of the confined compressive-strength test data. Values for m_i are listed in Table 4.7-41. Data sources and derivations are given in CRWMS M&O (1997d, pp. 7-4 to 7-5).

The design rock-mass strengths for each rock mass quality category were calculated by averaging the strengths determined from both Yudhbir et al. (1983, pp. B-3 to B-6) and Hoek and Brown (1988, pp. 31, 34) criteria, following the procedure of Hardy and Bauer (1991).

A power law relationship of the form:

$$\sigma_1 = A + B\sigma_3^C \quad \text{(Eq. 4.7-11)}$$

was employed to describe the nonlinear design rock mass strength. The parameters A, B, and C were determined by curve fitting the strength envelopes using a least-square method and are included in Table 4.7-40 for 40 percent cumulative frequency for each thermal-mechanical unit.

The design rock-mass-strength envelopes for the TSw2 unit, based on ESF scanline data, are presented on Figure 4.7-16. Complete design rock-mass strength envelopes for other thermal-mechanical units and resulting power law constants are given for all rock-mass classes in each thermal-mechanical unit in CRWMS M&O (1997d, pp. 7-6 to 7-12).

The Mohr-Coulomb strength parameters, including cohesion and angle of internal friction, and the dilation angle are commonly used to describe rock-mass strength in numerical analysis. The strength parameters were developed from the least-square curve fits of strength data pairs (σ_1, σ_3) produced using the power law criterion described above and summarized for 40 percent frequency in Table 4.7-40. The linear relation for strength (σ_1) and confining pressure (σ_3) is defined in the form of the following equation:

$$\sigma_1 = \sigma_c + N\sigma_3 \qquad \text{(Eq. 4.7-12)}$$

in which

σ_c = uniaxial compressive strength
N = confinement factor

The parameters σ_c and N were then used to create a Mohr-Coulomb failure criterion relating the shear and normal stress on the plane of failure to cohesion and angle of internal friction by the following equation:

$$\tau = C_0 + \sigma_n \tan\phi \qquad \text{(Eq. 4.7-13)}$$

in which

C_0 = cohesion $= \sigma_c/\sqrt{N}$
ϕ = angle of internal friction $= 2(\tan^{-1}\sqrt{N} - 45^\circ)$

The least-square best fit was performed over the range of confining pressures, from 0 to 3 MPa (0 to 435.1 psi), which is representative of the projected range in minimum principal stresses near the boundary of the excavations. Table 4.7-40 includes the resulting Mohr-Coulomb strength parameters for 40 percent cumulative frequency of occurrence. Complete results are presented in CRWMS M&O (1997d, p. 2-31).

The nonassociated flow rule, suggested by Michelis and Brown (1986), which uses a dilation angle equal to half the internal friction angle, was considered suitable for the tuff (Hardy and Bauer 1991), and the resulting values for dilation angles are also listed in Table 4.7-40, with complete results presented in CRWMS M&O (1997d, p. 7-12).

Two additional empirical methods were used for assessing rock-mass-strength properties: the Geological Strength Index (Hoek and Brown 1988) and the Rock Mass Index (Palmstrom 1996a, 1996b). Properties estimated included rock mass elastic modulus; cohesion; friction angle; unconfined compressive strength; and tensile strength, joint cohesion, and friction angle.

Complete analyses and results are presented in CRWMS M&O (1997f, pp. 69, 74). Results indicated that the original rock-mass property assessment methodologies were conservative.

4.7.5.3.2 Rock-Mass Elastic Moduli

Serafim and Pereira (1983) developed a correlation between the RMR and the rock-mass elastic modulus (E) that was recommended for use by Hardy and Bauer (1991). The correlation is shown in the following equation:

$$E = 10^{(RMR-10)/40} \qquad \text{(Eq. 4.7-14)}$$

in which

E is measured in GPa

Because the equation does not incorporate the intact rock elastic modulus, the predicted rock-mass elastic modulus can exceed the intact rock elastic modulus at high RMR values. An upper-bound limit of the rock-mass modulus was, therefore, set equal to the intact rock modulus (Table 4.7-41). Calculated rock-mass moduli based on design RMR values are shown for 40 percent cumulative frequency of occurrence in Table 4.7-40. Complete results are presented in CRWMS M&O (1997d, p. 7-13).

Rock-mass moduli determined by using the Geological Strength Index and Rock Mass Index described in Section 4.7.5.3.1 resulted in modulus values that significantly exceeded the mean intact value for the undifferentiated overburden, PTn, and TSw1 thermal-mechanical units, based on field mapping data (CRWMS M&O 1997f, p. 48). The Rock Mass Index empirical methodology applied in this analysis resulted in a significantly smaller range of E values that is more consistent with the intact value for these units. The Rock Mass Index method may be a more appropriate empirical methodology for assessing rock-mass modulus for the range of rock mass quality values in the ESF (CRWMS M&O 1997f, p. 74).

Empirical relationships to estimate Poisson's ratio from RQD are not available. The mean values for intact rock Poisson's ratios from the laboratory tests for each thermal-mechanical unit are adopted as the rock-mass Poisson's ratios. Table 4.7-40 includes the results. No adjustments for rock-mass category are recommended.

Rock-mass elastic moduli were also determined in situ as part of the Single Heater Test, using the NX borehole jack (Goodman jack). Results, procedures, and analysis are described in SNL (1997b) and in CRWMS M&O (1997h, pp. 5-24, 5-29). This borehole instrument was periodically inserted into a single borehole drilled roughly horizontal and perpendicular to the Single Heater Test heater and pressurized at various locations along the borehole. Jack pressure and loading platen displacements were monitored, and rock-mass modulus was determined from the pressure and displacement curve.

Borehole jack tests were run before heater startup in August 1996 and again in October 1996, November 1996, and March 1997. Temperatures were measured in the borehole for each set of tests before insertion of the jack using a portable thermocouple probe at various points, and by manually taking temperature readings using a handheld thermocouple reader. Jacking tests were

run along the borehole at various depths. All borehole jack testing followed ASTM D 4971-89 (1989, reapproved 1994) with minor exceptions.

The NX borehole jack consisted of two hydraulically activated steel loading platens approximately 20.3 cm (8 in.) long, which applied a unidirectional load to a nominal 7.62-cm-diameter (3-in.-diameter) borehole wall. The maximum jack pressure was 69 MPa (10,008 psi), and the maximum platen displacement was 0.63 cm (0.25 in.). Jack pressure was applied using an Enerpak hand pump. The jack was inserted into the borehole, and platens were slowly expanded until the pressure just began to rise. The resulting linear variable-displacement transducer readings represent initial borehole diameter and were used for calculations of borehole wall displacement under pressure. The jack pressure was increased in increments to the desired maximum pressure and then decreased in similar increments. Typically, the jack was pressurized in 3.44 MPa (500 psi) increments to 55.2 MPa (8,000 psi), and then back to zero, with linear variable-displacement transducer readings recorded during both loading and unloading.

Field rock-mass moduli from borehole jack testing in the Single Heater Test block are given in Table 4.7-42, along with the rock temperature at the time of the test. Rock modulus values ranged from about 3 to 23 GPa (4.35×10^5 to 3.34×10^6 psi) (CRWMS M&O 1997h, p. 5-29). The data show thermally induced stiffening of the rock mass in the region near the heater, with rock-mass moduli in this region increasing from 8 GPa (1.16×10^6 psi) in November 1996 to 23 GPa (3.34×10^6 psi) in March 1997. This modulus increase is likely because of the closing of fractures by rock matrix thermal expansion.

Ambient in situ rock-mass moduli calculated from Single Heater Test borehole jacking are lower than laboratory values determined for intact specimens, which are in turn lower than values determined from Q/RMR rock mass quality estimates. This is consistent with previous in situ experiments conducted in welded tuff in G-tunnel, which indicated that the modulus values for in situ tests were about half the intact laboratory-determined value of about 23 to 35 GPa (3.34×10^6 to 5.08×10^6 psi) (CRWMS M&O 1997h, p. 5-29).

Two plate-loading tests were conducted as part of the Drift Scale Test, in May and June 1998, to measure the rock-mass modulus for ambient and thermally perturbed rock. They were performed in a plate-loading niche at the southeastern corner of the Drift Scale Test block (CRWMS M&O 1998a, pp. 6-14 to 6-15). The test was designed to mechanically load the rock in a horizontal orientation using large, square-shaped flatjacks that press against both ribs of the plate-loading test niche. A steel frame was constructed between the ribs of the plate-loading test niche to provide a reaction force for the flatjacks. The plate-loading test data suggest, using simplified analytical techniques, a rock mass modulus ranging from 11.5 to 29.7 GPa (1.67×10^6 to 4.31×10^6 psi) at the plate-loading niche. These data show that the higher values for modulus were obtained on the hot side of the plate-loading niche, that is, the side closer to the heated drift (CRWMS M&O 1998a, pp. 6-25 to 6-27). See Section 11 for more information on thermal loading.

4.7.6 In Situ Stress Conditions

Design of the potential repository requires knowledge of the magnitude, direction, and variability of the preconstruction in situ state of stress for the analysis and design of stable underground openings, as well as for the prediction of short-term and long-term rock mass deformation. Detailed results of in situ stress measurements in tuffs at Yucca Mountain or at Rainier Mesa are contained in several references (Hooker et al. 1971, Table 2; Haimson et al. 1974, Table 1, p. 560; Tyler and Vollendorf 1975, Table 1; Ellis and Ege 1976; Ellis and Magner 1980, Table 10, p. 26; Warpinski et al. 1981, pp. 58 to 70; Zimmerman and Vollendorf 1982, pp. 11 to 17; Stock et al. 1984, p. 9, 1985). These references also discuss details of testing techniques and potential limitations and errors.

Table 4.7-43 presents a summary of the estimated in situ stress at the repository horizon. The direction of the maximum principal stress is vertical, due to lithostatic load. At the repository level, the vertical stress, on the average, has been assumed to be 7.0 MPa (1,015.3 psi) (Stock et al. 1984; CRWMS M&O 1995a, p. 6-163, Assumption TDSS 001). Horizontal stresses are expected to be lower and to range from 3.5 to 4.2 MPa (507.6 to 609.2 psi), although the range may be as wide as 2.1 to 7.0 MPa (304.6 to 1,015.3 psi). These in situ stress values were generally confirmed by a stress profile calculated for the ESF test area (Stock and Healy 1988, pp. 87 to 93), which showed a vertical stress of 6.0 MPa (870.2 psi) at a depth of 300 m (984 ft). Horizontal stress for the same depth ranged from 2.1 to 4.2 MPa (304.6 to 609.2 psi).

Horizontal in situ stresses at the potential repository site are expected, generally, to be low. Consequently, failure modes around underground openings during construction are expected to be primarily controlled by geologic structures. Horizontal to vertical stress ratios for the minimum and maximum horizontal stresses are close, indicating a weak horizontal stress anisotropy. Lateral stresses and their effects would thus be expected to be similar for all drift orientations (CRWMS M&O 1997d, p. 3-23).

Hydraulic fracturing tests performed for ambient characterization of the Drift Scale Test block measured in situ stresses in the TSw2 unit (SNL 1997a, p. 2; CRWMS M&O 1997g, pp. 10-9, 10-13 to 10-15). Results were generally consistent but revealed somewhat lower in situ stresses than previously estimated. Tests were conducted in borehole ESF-AOD-HDFR#1, drilled from the Thermal Test Facility alcove in the ESF, at depths approximately 240 to 249 m (787 to 817 ft) below ground surface. The downhole testing equipment consisted of a hydraulic fracturing, straddle-packer system, which was lowered to predetermined hydraulic fracturing test intervals. An impression-packer orienting tool was used to obtain an oriented trace of the induced hydraulic fracture on the borehole wall, and test interval pressure and flow rate were digitally monitored.

A series of five successful hydraulic fracturing tests were conducted in the Drift Scale Test block, but only one test yielded what were considered reliable results. Based on these test results, the principal horizontal stresses around this borehole are estimated to be (SNL 1997a, p. 20):

$$\sigma_h = 1.7\ (\pm\ 0.1)\ \text{MPa}\ (246.6 \pm 14.5\ \text{psi})\ \text{acting in the N75°W}\ (\pm\ 14°)\ \text{direction}$$

in which

σ_h = least horizontal principal stress

$\sigma_H = 2.9 (\pm 0.4)$ MPa (420.6 ± 58.0 psi) acting in the N15°E ($\pm$ 14°) direction

in which

σ_H = largest horizontal principal stress

Because vertical stress was not measured in these tests, it was approximated as the weight of the overburden at the depth of the tests from the surface, as follows (SNL 1997a, p.15):

$$\sigma_v = 4.7 \text{ MPa } (681.7 \text{ psi})$$

in which

σ_v = vertical stress

Although the measured horizontal stresses are only moderately differential, both are smaller than the vertical stress. This measured stress regime, one of low horizontal magnitudes, is in accord with the dominant local normal faults. The north-northeastern maximum horizontal stress direction is subparallel to the average strike of these faults and is supported by previous measurements in the Yucca Mountain area (Zoback and Healy 1984, pp. 691 to 692). Additional details of procedures, results, and interpretations are presented in SNL (1997a) and CRWMS M&O (1997g, pp. 10-9, 10-13 to 10-15).

4.7.7 Excavation Characteristics of the Rock Mass

Geotechnical monitoring data were developed during excavation of the North Ramp Starter Tunnel and Upper Tiva Canyon Alcove to provide the basis for design verification (SNL 1995, abstract). The North Ramp Starter Tunnel was constructed to launch the 7.6-m-diameter (25-ft-diameter) tunnel boring machine to construct the ESF North Ramp, Main Drift, and South Ramp. The Upper Tiva Canyon Alcove was excavated off the North Ramp Starter Tunnel to provide access for site characterization testing. Design verification studies are being performed to monitor and observe the long-term behavior of openings in the range of rock conditions to be encountered in the potential repository host rock, to observe and evaluate the construction of the ESF (with respect to implications for potential repository construction and performance), and to collect information for design of the ventilation systems in the potential repository (DOE 1988, Section 8.3.1.15.1.8).

4.7.7.1 Excavation Methods

Both SNL (1995) and CRWMS M&O (1997a) address evaluations of mining methods and monitoring of ground support systems and drift stability. Rock mass quality evaluations, an evaluation of as-built mapping data, and blast vibration monitoring were performed as part of the mining methods evaluation. An evaluation of rock structure data from surface and underground mapping is presented in Section 4.7.3; an evaluation of rock mass quality data is presented in

Section 4.7.5; and blast monitoring is discussed in this section and in CRWMS M&O (1997d, pp. 7-18 to 7-20). The Enhanced Characterization of the Repository Block Cross Drift was excavated by a conventional tunnel boring machine, with a starter tunnel excavated by drill and blast methods. Rock mass quality data from the Enhanced Characterization of the Repository Block Cross Drift are presented in Section 4.7.5.1 and in Mongano et al. (1999, pp. 88 to 108).

The North Ramp Starter Tunnel, Upper Tiva Canyon Alcove, Alcove 2, and sections of the Thermal Test Facility (Thermal Testing Facility Alcove) were excavated by drilling and blasting. Controlled blasting procedures were implemented to minimize blast-induced damage to the excavation perimeter. Blast damage can result in loosening of the surrounding rock mass, which increases ground support requirements and long-term maintenance. The ESF design requirements (YMP 1997, p. 3-67) estimated that the rock mass altered by the excavation process will be within 1.5 m (5 ft) of the excavated surface.

Additional criteria for blast vibration limits, based on measurements of peak particle velocity, were developed for the excavation perimeter and nearby structural elements. They are listed in Table 4.7-44. These vibration criteria are specified without reference to the dominant frequency. Application of peak particle velocity to distance relationships is required to obtain estimated peak particle velocity to within 1 m (3.3 ft) of the blast. Far-field monitoring used seismic equipment with peak frequency ranges of 250 Hz.

Excavation of the North Ramp Starter Tunnel and Upper Tiva Canyon Alcove produced substantial overbreak on existing structural features, even with the use of perimeter blasting procedures. Monitoring of the blasts indicated that reduced quantities of explosives detonated per delay (and long-period delays) were successful in controlling peak particle velocities. Observations suggested that measurable blast damage was limited to within 1 m (3.3 ft) of the excavation perimeter.

During construction of Bow Ridge Fault Alcove and a portion of the Thermal Test Facility (Thermal Testing Facility Alcove), construction monitoring consisted of monitoring ground motion (peak particle velocity), observing damage in the rock surrounding the excavation, and visually observing the number of borehole half-casts remaining on the excavation perimeter. Half-casts of perimeter trim holes were mapped on the east and west walls of Upper Tiva Canyon Alcove. Half-casts were rare on the east wall. They occurred more frequently on the west wall, but occurred irregularly. The half-cast distribution may be attributed to drilling and blasting practices or to structural geologic controls, such as joint spacing and orientation (CRWMS M&O 1997a).

Geophones were attached to steel set 90, adjacent to the entrance of Upper Tiva Canyon Alcove, and recorded a peak particle velocity of 330 mm/s (13 in./s) in the direction of the North Ramp axis during blasts 5 and 6. These geophones measured blast vibrations with frequencies below 250 Hz and peak particle velocities well below the 1,250 mm/s (49 in./s) criterion in Table 4.7-44.

Visual observations of blasting damage at Upper Tiva Canyon Alcove were made by video borescope records of inspection boreholes at distances of 0.9, 1.5, and 2.5 m (3, 5, and 8 ft) from the excavation perimeter. On the basis of observed debris in the holes, rock damage in the holes,

and overbreak of the excavation, the blasting effects extended up to 1 m (3.3 ft) from the excavation perimeter. No damage was evident at 1.5 m (5 ft) from the perimeter.

Comparison of Upper Tiva Canyon Alcove far-field blasting results to results obtained during construction of the North Ramp Starter Tunnel Top Heading (SNL 1995, pp. 4-1 to 4-14) indicates similar trends.

A similar monitoring program, performed during construction of part of the Thermal Test Facility (Alcove 5), successfully produced both near-field and far-field blast vibration data. An attenuation relationship was developed by combining the two data groups and was used to project the peak particle velocity at a distance of 1 m (3.3 ft) from the excavation perimeter for comparison to the criteria in Table 4.7-44. The calculation indicated that rock 1 m (3.3. ft) from the excavation perimeter would be most strongly impacted by detonation of the trim holes, because they are closest and contain the highest quantity of explosive because of the number of holes. Application of the attenuation relationship predicted peak particle velocities between 703 and 720 mm/s (27.7 and 28.3 in./s), which would exceed the criterion of 700 mm/s (27.5 in./s) at 1 m (3.3 ft) by a maximum of 3 percent. Data scatter in the peak particle velocities used to develop the attenuation relationship is very large; it is therefore highly likely that the criteria were not exceeded. Furthermore, most of the data are developed from blast holes where the explosive was tamped and fully coupled to the hole perimeter. Trim holes were loaded with decoupled charges (smaller diameter than the hole) and were not tamped. Peak particle velocities predicted for all other holes were well below the 700 mm/s (27.5 in./s) criterion.

Blast monitoring results at the Thermal Test Facility suggest that damage to the rock was limited to within 1.5 m (5 ft) of the excavation boundary. Peak particle velocities at 1 m (3.3 ft) from the excavation boundary appeared to satisfy the blast-vibration limits. Other observations on drilling and blasting results for the Thermal Test Facility are summarized in CRWMS M&O (1997a).

4.7.7.2 Potential Health Hazards during Excavation

Potential health hazards during excavation include the effects of minerals that become airborne during tunneling operations, which can produce respiratory ailments. Specific safety and health concerns related to rock mass mineralogies at Yucca Mountain include respiratory effects of the zeolite erionite and the silica minerals, including quartz and cristobalite, encountered during daily underground activities. These minerals occur in varying proportions in the different lithologies and geochemical environments at Yucca Mountain, as reported in Vaniman et al. (1996, Section 6).

Health-related mineral issues associated with airborne particles released by excavation operations at Yucca Mountain were evaluated by combining quantitative X-ray diffraction analyses of mineral distributions with published information on mineral toxicity and carcinogenicity. There are several minerals that may be of potential concern as airborne particles during construction or operation, but the risk posed by most of these can be minimized by safe, modern mining practices (e.g., by maintaining low dust levels and adequate ventilation). The crystalline silica minerals (quartz, tridymite, cristobalite, and opal-CT) fall into this category. These minerals are classed by the International Agency for Research on Cancer as probable

human carcinogens, and they are ubiquitous at Yucca Mountain. The risk posed by these minerals can probably be mitigated by proper dust control.

Apart from vitric and vitrophyre zones at Yucca Mountain, amounts of the crystalline silica minerals are typically 3 to 40 percent by weight. All of the excavations in vitric tuff (e.g., the nonwelded tuff occurring at the base of the Topopah Spring Tuff and the lower Topopah Spring vitrophyre) will involve rocks with inherently low abundances of crystalline silica. Of the three crystalline silica phases (quartz, cristobalite, and tridymite), only small amounts of quartz (less than 1 to 7 percent by weight) and cristobalite (0 to 4 percent by weight), with no occurrences of tridymite in such vitric tuffs, have been found. Total crystalline silica abundances in these vitric tuffs are all 7 percent or less; typical abundances are about 4 percent by weight. These low abundances of crystalline silica contrast with abundances in devitrified rhyolitic Topopah Spring Tuff (in which the ESF and the potential repository horizon are located). In these devitrified rocks, the total crystalline silica abundances are typically about 30 to 40 percent by weight. The silica minerals in these devitrified rocks are generally quartz and cristobalite, with more variable and generally lesser occurrences of tridymite.

Some potentially hazardous minerals, such as palygorskite and sepiolite, have occurrences limited to fractures, so exposures to these minerals will likely be very small, particularly if low dust levels are maintained. Consequently, these minerals probably do not pose a risk at Yucca Mountain. In addition, palygorskite, in particular, is usually at depths shallower than the potential repository horizon.

Mordenite occurs in fractures in the Topopah Spring Tuff and in the zeolitized units below the potential repository horizon. Although published data suggest that mordenite is not carcinogenic, a prudent approach will be to minimize exposures to airborne mordenite, using methods appropriate for crystalline silica.

Erionite, because of its apparently extremely high carcinogenic potential, may pose a risk if encountered in sufficient quantity, even when standard, modern mining practices are followed. Erionite, a natural fibrous zeolite that occurs in the rocks at Yucca Mountain, is listed as a known human carcinogen by recognized international agencies (e.g., the International Agency for Research on Cancer). No safe exposure levels have been established for erionite, and no federal health and safety standards are in place that specifically regulate exposure to erionite, aside from 29 CFR 1910, Labor: Occupational Safety and Health Standards. Although the U.S. regulatory agencies do not specifically address erionite, its morphology and the International Agency for Research on Cancer classification strongly suggest that it be treated at least as carefully as asbestos.

Erionite occurrence at Yucca Mountain appears to be restricted to zones immediately below the potential repository horizon and just below the Tpcplnc/Tpcpv2 boundary in the lower Tiva Canyon Tuff. Thus, it may only be a concern wherever underground workings penetrate into the basal vitrophyre of the Topopah Spring member or when tunneling from the surface penetrates the Tpcplnc/Tpcpv2 boundary.

Knowledge of mineral abundances and variability in the Topopah Spring Tuff can be used to predict the hazardous mineral abundances in given dust loads produced by mining (Harrington

1998). In addition to the implications for understanding and predicting hazardous mineral exposures during potential repository excavation, the data in the study are pertinent to predictions of silica dissolution and transport under a repository-induced thermal load.

Dust and wall-rock samples were analyzed from tunnel boring machine water-use and surfactant-use test intervals, as well as from routine tunnel boring machine operations in the east-west Cross Drift at Yucca Mountain. Variation in tunnel boring machine mining method, from water application to water plus surfactant to dry, produced significant variations in dust quantity, but no measurable variations in dust mineralogy. Dust production was diminished by about half with water application at the cutter head, but adding surfactant to the applied water caused increased dust production that was comparable to the dust produced during dry excavation (Harrington 1998, p. 35).

Constituent minerals of the unexcavated bulk rock are fractionated by tunnel boring machine fragmentation. Silica mineral abundances in the respirable size materials in the Tptpul horizon vary individually, but are cumulatively only 60 to 75 percent of their abundance in the unexcavated rock (Harrington 1998, p. 36).

The crystalline silica minerals (quartz, cristobalite, and tridymite) were the only hazardous minerals of significance in the east-west Cross Drift; zeolites were detected in small amounts, but did not include the hazardous zeolite erionite. Among the silica minerals, the fractionation systematics of cristobalite, which diminishes in abundance with decreasing particle size, differed from those of tridymite and quartz, which reach a maximum abundance in the 1,000 to 10 μm size range (Harrington 1998, p. 36).

A three-dimensional mineralogic model was developed for Yucca Mountain to support the analyses of hydrologic properties, radionuclide transport, repository performance, and repository design, as well as mineral health hazards. Mineralogic model Version 3.0 includes quartz, tridymite, and cristobalite + opal-CT, so that all of the silica polymorphs are considered (CRWMS M&O 2000c, p. 18). The three-dimensional mineralogic model allows prediction of possible locations of the carcinogenic zeolite erionite. Such predictions can be used as a basis for planning work in suspect zones.

Safety and health concerns for the YMP are addressed by the *Safety and Health Plan* (YMP 1998), which includes respiratory protection. Control measures regarding mineralogic respiratory hazards are performed according to Harris (1995) for erionite and McManus (1996) for silica. These measures include monitoring, engineering control, and proper personal protective equipment when tunneling activities are occurring in areas where these minerals are of concern. These measures should also be considered during repository design.

4.7.7.3 Excavation Characteristics

Ground support in the ESF include rockbolts, lattice girders, steel-fiber reinforced shotcrete, and steel sets (CRWMS M&O 1997d, p. 7-20). Wire mesh and channel straps are used to control loose materials between rockbolts. Rockbolt monitoring was accomplished using rockbolt load cells and instrumented rockbolts. Convergence pins were attached to the lattice girders in the first 10 m (33 ft) of the ESF to monitor the displacement of these components of the ground

support system. Vibrating wire strain gauges and convergence pins were attached to steel sets throughout the ESF to monitor the changes in rock loading. Convergence pin arrays and borehole extensometers were installed in rock supported by Swellex bolts (CRWMS M&O 1997d, p. 7-20).

4.7.7.3.1 Rockbolt Load

Rockbolt load cells were installed along the North Ramp Starter Tunnel and on the highwall at the North Portal. Installation procedures are detailed in SNL (1995, pp. 4-6 to 4-8). All bolts had some load bleed-off and have settled into generally stable trends in which bolt loads are relatively constant. No load increases that would indicate rock loosening were observed from the time of installation to June 1996. Current bolt loads range from 0.1 to 16.0 percent of the bolt yield strength (CRWMS M&O 1997d, p. 7-21).

Instrumented rockbolts were installed in Upper Tiva Canyon Alcove, as described in SNL (1995, p. 4-6). Stable bolt loads were similar to those observed in rockbolt load cells. Bolt loads appeared to remain well below the bolt yield strength (SNL 1995, p. 4-6).

Eight rockbolt load cells were also installed as part of the Single Heater Test to evaluate the effects of elevated temperature on bolt performance. Complete data and analysis are presented in SNL (1997b) and CRWMS M&O (1997h, pp. 5-26 to 5-27). Four rockbolts were installed on the heated side of the thermomechanical alcove below the level of the heater, and four additional bolts were installed on the opposite, cool side of the alcove. Each load cell contained three strain gauges, and the total load acting on the cell was calculated by averaging the measurements from all three.

In Table 4.7-45 (CRWMS M&O 1997h, p. 5-27), the Single Heater Test rockbolt load cell data are presented as load and time from the start of heating, or day zero. As shown, there is a general decrease in load measured in all the load cells, although the decreases are all less than 7 percent of the initial load (CRWMS M&O 1997h, p. 5-27). The average decrease is 1.37 percent for rockbolts on the ambient (cool) side and 3.45 percent for rockbolts on the heated side. The two largest decreases were measured in the rockbolt load cells that were nearest the heater, RB-1 and RB-2 (CRWMS M&O 1997h, p. 5-27).

4.7.7.3.2 Portal Lattice Girder Deformation

Deformation of the portal lattice girders embedded in shotcrete was tracked using convergence data collected by a tape extensometer. The deformations have remained fairly constant after the initial settling (SNL 1995, p. 4-8), and the monitoring data from June 1995 to June 1996 showed a continuing trend of no closure (CRWMS M&O 1997a).

4.7.7.3.3 Steel Set Deformation

Vibrating wire strain gauges were installed on 33 steel sets from January 1995 through June 1996. The strain gauges were attached to the steel sets, both before and after installation in the tunnel. When the gauges were attached before installation, stress changes in the web of the steel sets because of jacking loads were monitored during the steel set installation process.

Strain changes that occurred during jacking installation indicated a generally similar pattern of tensile and compressive stress change in the steel. Changes in the crown of the steel set were the most uniform. The measured strain changes during jacking indicated stress changes between 10 and 180 MPa (1,450.4 and 26,107 psi) (CRWMS M&O 1997a, p. 6-3).

Strain magnitudes remained generally constant after installation was complete, suggesting that rock loading around the steel sets monitored was not occurring. Most of the steel sets were installed in the TCw and in the undifferentiated overburden units. Similar long-term trends indicating no increase of steel set load were observed for steel sets in the PTn, TSw1, and TSw2 units (CRWMS M&O 1997d, p. 7-21).

4.7.7.3.4 Installed Ground Support versus Rock-Mass Quality Projections

Installed (as-built) ground support has been compared to ground support as projected based on the rock mass quality determined for 5-m (16.4-ft) intervals for the ESF (CRWMS M&O 1997d, p. 7-22; 1997f, pp. 69, 73). Projected ground support classes were defined as a function of the rock mass quality (Q) value to provide the recommended ground support to cover the expected range of ground conditions. The as-built, installed ground support classes are shown in Figure 4.7-17, together with the spatial distribution of $Q_{modified}$ values. The installed ground support class was generally in agreement with, or more conservative than, the scanline-based $Q_{modified}$ value (CRWMS M&O 1997f, p. 69).

4.7.8 Engineering Properties of Surficial Material

4.7.8.1 Surficial Sedimentary Deposits

The late Tertiary and Quaternary surficial sedimentary deposits of the Yucca Mountain area consist of colluvium, fan alluvium, eolian sand sheets, ramps and dunes, and spring discharge or marsh deposits (see Section 4.4). These range in age from late Pliocene to Holocene. The deposits are grouped into eight major units, plus locally important eolian and marsh deposits. Quaternary stratigraphy and deposit distribution are described in detail in Section 4.4.3. Distribution of alluvium and colluvium is included in the Central Block geologic map (Figure 4.6-5).

Late Pliocene and early Pleistocene deposits consist predominantly of debris flows with sparse, bedded fluvial sediments. They occur as dissected fans and fan remnants that are adjacent to bedrock ranges and, less commonly, as isolated outcrops several kilometers (a couple of miles) from the ranges. These deposits are moderately indurated, coarse, angular, unsorted gravel, with minor amounts of sand-sized to clay-sized material (Wesling et al. 1992, p. 23-32; Lundstrom et al. 1995).

Middle to late Pleistocene deposits consist of fan alluvium, fluvial and eolian sands, and local lenses of volcanic ash. These deposits generally overlie older alluvial deposits on middle to upper pediment slopes, and they occur in larger stream valleys.

Eolian deposits occur as dunes and sand sheets in and adjacent to the Amargosa Valley. Ramps of fine, well-sorted sand, as much as 50 m (164 ft) thick, flank many of the hills bordering the

Amargosa Valley and near Yucca Mountain at Busted Butte. Fluvial sand sheets occur along major streams and along drainages downstream from dunes.

Holocene deposits in the Yucca Mountain area consist of fluvial sand and gravel and eolian sand. Holocene deposits occur mainly as thin, broad fans downstream from incised stream channels on pediment slopes. Eolian sand deposits consist of well-sorted fine sand that occurs as small dunes and irregularly shaped sheets in the Amargosa Valley.

Man-made fill overlies colluvial and alluvial material at the North Portal Pad, an area approximately 800 to 1,200 ft (244 to 366 m) by 600 to 700 ft (183 to 213 m) where the ESF tunnel portal was constructed. Muck piles along the eastern side of the North Portal Pad rise to about 17 to 30 ft (5.2 to 9.1 m) above the pad surface (CRWMS M&O 1999a, p. 1-2). They are believed to consist almost entirely of rock excavated from the ESF tunnel (CRWMS M&O 1999a, p. 6-1).

4.7.8.2 Surface Soil Investigations

A preliminary geotechnical investigation was conducted between October 1998 and March 1999 for the design of the potential Waste Handling Building at the North Portal Pad. The investigation included:

- Review of existing information
- Drilling, logging, and sampling one new borehole (UE-25 RF#13)
- In situ penetration tests
- Laboratory gradation and water content tests on soil samples from borehole UE-25 RF#13
- Downhole seismic logging in borehole UE-25 RF#13
- Seismic refraction surveys
- Laboratory dynamic response tests
- Laboratory testing for shear modulus and damping on soil and rock samples from UE-25 RF#13.

Results are presented in CRWMS M&O (1999a), and those results relevant to soils geoengineering properties are summarized here.

Based on available information, including construction records, the North Portal Pad fill material consists of coarse granular alluvium and colluvium, and tuffaceous rocks excavated from various sources. The materials were placed in a manner that was not well documented (CRWMS M&O 1999a, p. 6-1), and so is not considered an engineered fill (CRWMS M&O 1999a, p. 3-12). At borehole UE-25 RF#13, a thickness of 12.5 ft (3.8 m) of pad fill was encountered (CRWMS M&O 1999a, p. 6-1).

Beneath the fill, boring information indicates 12.5 to 87 ft (3.8 to 26.5 m) of alluvium and colluvium. The fines content was generally low. Modified California drive samples taken in borehole UE-25 RF#13 indicate a predominance of sand-size material, generally with gravels. Some layers of mostly gravel were encountered. Near the base of the alluvium and colluvium unit, fine-grained sands and silty sands, having only scattered gravels, were encountered (CRWMS M&O 1999a, p. 6-1).

Based on boring data and exposures in Fortymile Wash, it appears that the alluvium and colluvium in this area are highly variable. Several layers of calcite-cemented material (caliche) are present in the soil column. Uncemented layers are also common, which would cause rapid changes in soil strength with depth (CRWMS M&O 1999a, p. 6-2).

High blow counts, generally greater than 50, were recorded for most of the alluvial and colluvial material encountered in borehole UE-25 RF#13, based on an equivalent SPT N_1 value (standard penetration test result corrected to overburden pressure of 1 ton/ft^2 (0.09 MPa). However, the alluvial and colluvial material from about 35 to 42 ft (10.7 to 12.8 m) below ground surface appeared to be significantly less dense than the overlying and underlying alluvial and colluvial material. The one modified California sample driven in this interval yielded an equivalent SPT N_1 value of 12 (CRWMS M&O 1999a, p. 6-2). The dense nature of the alluvial and colluvial material was also indicated by the relatively high values of shear-wave velocity measured in the downhole survey of borehole UE-25 RF#13. Because of the dense, granular nature of the materials, it is appropriate to use the drained shear strength for general characterization and analyses, and cohesion is assumed to be zero (CRWMS M&O 1999a, p. 6-2).

There have been numerous other investigations to determine the physical properties of native soils in the site vicinity, primarily the North Portal and the Midway Valley areas. Investigations to assess the surface soils in the vicinity of the ESF were conducted primarily between the mid-1980s to the early 1990s. Between 1984 and 1985, three studies (Neal 1985, 1986; Ho et al. 1986) addressed surface facilities and soils. Neal (1985) presents the general boring logs for eight exploratory borings (UE-25, RF#1 through #8) in the vicinity of Exile Hill. Neal (1986) incorporates three additional holes (UE-25, RF#9, #10, and #11) and extends the depth of one of the original holes (UE-25, RF#3). The total depth of penetration ranges from 60 to 301 ft (18.3 to 91.7 m), and detailed logs are presented. In addition, the study contains some of the basic physical properties of the alluvium and cored rock. A study in 1986 (Ho et al. 1986, pp. 6 to 29) involved four test trenches in the western portion of Midway Valley and south of Exile Hill. The test pits, in general, corresponded to exploratory boring locations UE-25, RF#1, #2, #3, and #5. The study presents detailed information on shallow (11 to 13 ft [3.4 to 3.9 m]) alluvium stratigraphy, physical properties, and engineering characteristics of the native soils.

YMP scientists investigated surficial materials for the North Ramp Surface Facility of the ESF (McKeown 1992). The report is based on data from geologic mapping, pavement mapping, 73 test pits, laboratory test data on samples from seven test pits, and four drill holes: RF-1, RF-10, and RF-11, located in Midway Valley, and UE-25-NRG-1 located at the North Portal start station (McKeown 1992, p. 6).

The study found (McKeown 1992, p. 13) that topsoil typically ranges from 0 to 3 ft (0 to 0.9 m) of silty sand (SM), silty sand with gravel (SM), poorly graded gravel with sand (GP-GM), and

silty gravel with sand (GM). The topsoil is relatively loose and contains roots. The soil at the site is primarily colluvium and alluvium, generally composed of silty sand (SM) and silty gravels (GM, GP-GM), with fines ranging from 4 to 30 percent. Some clayey sand (SC) and clayey gravel (SC, GC), with fines ranging from 29 to 40 percent, are present but in very small amounts. Physical property data and test pit logs for seven portal-pad test pits and 39 road alignment test pits are reported (McKeown 1992, Appendix 1). These seven portal-pad test pits are representative of materials and foundation conditions for the ESF North Ramp Surface Facility. The soil is caliche-cemented from just below the surface to several feet deep adjacent to the hill and decreasing away from the hill.

All the soil in the North Ramp Surface Facility pad area is carbonate-cemented to some degree. The carbonate-cemented soil may be ripped to facilitate excavation. The prevalence of secondary carbonate-cementation throughout the pad area indicates that foundation-bearing capacities determined by disturbed sampling methods or physical properties will be conservative. Practical methods to sample and test the gravelly materials at the site do not exist. Soil material had to be jack-hammered for removal for ring-density tests because of the soil cementation. However, in-place and relative densities were determined and can be used to assess the bearing capacity of the material. The material appears to be adequate for founding the relatively temporary, low-load structures contemplated. A suggested design value for bearing capacity is 1.1 ton/ft^2 (0.10 MPa) per foot of footing width, plus 1.9 ton/ft^2 (0.18 MPa) per foot of depth (McKeown 1992, p. 18). Calculations, estimated settlement, and references were also reported (McKeown 1992).

Test pits along the road alignments indicate that soils generally consist of poorly graded silty gravel, with varying amounts of sand, cobbles, and boulders. Slope recommendations based on natural slopes are that the colluvium and alluvium will stand at 1:1 for temporary slopes and 1.5:1 for permanent slopes (McKeown 1992, p. 18). Occupational Safety and Health Administration requirements may dictate actual slopes used.

Because the material commonly has from 5 to 15 percent fines, initial fill placement tests should be performed using both laboratory compaction and relative density tests to establish the appropriate method of construction control. Both testing methods may be needed unless blending of materials is planned, because soils are present with less than 5 to 15 percent fines as well as more than 5 to 15 percent fines.

Calcium carbonate cementation is present on the slopes along the base of Exile Hill, but was found to have not developed significantly in the area of the proposed leach field (McKeown 1992, pp. 17 to 18). Material excavated from one test pit, MWV-P-32, consisted mostly of gravel with silt and sand, and silty sand with gravel.

Between 1988 and 1989, Holmes & Narver conducted two studies of three potential borrow-pit areas for the ESF (Holmes & Narver 1989; Daffern and Thummala 1988). These reports present estimated quantities of Type I and II aggregate and fill material. A gravel pit exists near the northeast side of Fran Ridge in Nevada Test Site Area 25 (McKeown 1992). The pit supplies select fill, road gravel, and backfill.

4.7.9 Summary

Geoengineering properties data were developed from both laboratory and field testing. These properties have been described in the context of their relevance for design and construction of the potential repository and include rock structure, potential key blocks, rock physical properties (porosity, density, and mineralogy), rock thermal properties (thermal conductivity, thermal expansion, and heat capacity), rock mechanical properties (elastic constants, compressive strength, shear strength, creep behavior, hardness, and fracture properties), rock mass properties, in situ stress, excavation characteristics, and engineering properties of surficial material. These data are used in designing the potential repository, evaluating the behavior of the natural system under thermal loading (Section 11), and assessing long-term performance.